



# THÈSE DE DOCTORAT DE L'UNIVERSITÉ PSL

Préparée à l'École Normale Supérieure

# Vagues océaniques déferlantes : Modélisation mathématique, résolution numérique et limite de viscosité évanescente

Soutenue par

Alan RIQUIER

Le 9 septembre 2025

École doctorale nº386

Sciences Mathématiques de Paris Centre

Spécialité

**Mathématiques** 

Préparée au

Département de Mathématiques et Applications

Composition du jury :

Christophe BESSE

Directeur de Recherche Institut de Mathématiques de Toulouse

Didier BRESCH

Directeur de Recherche Université Savoie Mont-Blanc

Anne-Laure DALIBARD

Professeure des universités

Sorbonne Université

Emmanuel DORMY

Directeur de Recherche École Normale Supérieure

Christophe LACAVE

Chaire Professeur Junior

Université Savoie Mont-Blanc

David LANNES

Directeur de Recherche Université de Bordeaux

Catherine SULEM

Professor

University of Toronto

Président

Rapporteur

Examinatrice

Directeur de thèse

Invité

Rapporteur

Examinatrice



 $\grave{A}$  mes parents

 $\grave{A}\ mes\ ami\cdot e\cdot s$ 

## **Abstract**

The work presented here is concerned with *breaking water waves*, a well-known phenomenon arising as an oceanic wave approaches the shore: its crest starts to move faster than the trough up front, which ultimately leads to the appearance of an overhanging region that quickly curls over while falling down until it collides with the water lying below. An important contemporary issue concerns the incorporation of the viscous dissipation associated with the breaking into the many models that have been introduced to describe the ocean. This is mostly done empirically.

In the present work, we follow a different path: we aim at modelling wave breaking up to the free surface self-intersection (the "splash" singularity), relying thus on a more geometrical approach to the subject.

The first part of this thesis will be devoted to the motivation of a set of equations that describes overhanging waves in the inviscid irrotational regime, with either a one-dimensional or a two-dimensional free surface. This is done by setting aside the commonly used Eulerian framework and working in (pseudo)Lagrangian coordinates instead. This should be seen as an extension of the Zakharov–Craig–Sulem formulation of the Water Waves problem. The non-canonical Hamiltonian structure of these partial differential equations is investigated and it is shown that in the absence of breaking, they can be reduced to the usual set of equations. Emphasis is put on the various physical assumptions that are made along the way.

In a second moment, we come back to these very hypotheses and put them to the test. This is done numerically using a Navier-Stokes based computational framework based on the Finite-Element Method (FEM). The major novelty compared to other studies lies in the use of the Arbitrary Lagrangian-Eulerian method (ALE), which diminishes the interpolation error greatly. The viscosity can therefore be decreased to values that allow the comparison with the inviscid solution (computed using another wode, based on potential theory in the complex plane) to be carried out.

Over a flat topography, it is found that both the free-surface and bed boundary layers are sufficiently well-behaved as to not perturb the bulk irrotational flow. Water being characterised by a relatively small viscosity, the consequence is that, in this regime the inviscid models accurately describe the oceanic flow. We do not prove this assertion rigorously, however.

Difficulties seem to arise, however, when a non-flat topography is considered. Indeed, the typical velocities associated with the wave are high enough to eventually trigger boundary layer separation near curved-enough portions of the bed, resulting in vorticity being shed in the initially irrotational flow, far from the topography. The convergence to the inviscid solution is therefore compromised.

On AI-generated content. The author swears on his honour that the content of the present document is entirely human-generated and that no AI-based algorithm has been used during the conception of this work, aside from the following logo which was generated using midjourney.com.



**Declaration of interests.** The author reports no conflict of interest.

Cover picture taken by Josh Sorenson (shared under the pexels.com license, an irrevocable, worldwide, perpetual, non-exclusive and royalty-free right to use, copy, modify or adapt the image for non-commercial purposes).

Supplementary materials. Video animations are attached to the figures labelled using the camera symbol They can be found on the author's personal website, following this link: https://ariquier.gitlab.io/thesis/thesis.html or scanning the following QR code.



## Résumé

Cette thèse porte sur le déferlement des vagues océaniques, un phénomène physique que l'on observe principalement sur les littoraux mais que l'on trouve aussi dans l'océan lointain. Explicitons la définition adoptée ici : lorsque les non-linéarités (comprendre l'amplitude) deviennent importantes, la crête d'une vague peut se mettre à se propager à une vitesse supérieure à celle du creux qui la précède, résultant éventuellement en un enfourchement de ce dernier. Lorsque cela se produit, nous parlons de déferlement. Le rouleau ainsi créé tombe immanquablement sur la surface d'eau plus avenante. À partir de là, une quantité importante de structures de petite échelle apparaissent (gouttes, écume, turbulence, etc.), conduisant à l'augmentation du tourbillon (de la vorticité) et, de ce fait, de la dissipation énergétique. Un enjeu scientifique contemporain consiste en la caractérisation précise de cette dissipation et sa prise en compte dans les modèles océaniques.

Cependant, le travail présenté dans les pages qui suivent n'abordera pas cette facette du problème. À la place, nous allons nous intéresser à la dynamique présente avant le recoupement de l'interface par elle-même (une singularité que la communauté anglo-saxonne a astucieusement nommé le *splash*).

Dans un premier temps, nous allons introduire un ensemble d'équations à dérivées partielles qui décrivent l'évolution de la surface libre de l'océan, l'eau étant considérée comme non-visqueuse, le tourbillon étant supposé évanescent et l'air étant complètement négligé. Ces équations, que nous nous proposons d'appeler équations des vagues déferlantes, sont obtenues formellement à partir de principes physiques généraux (description continue de la matière, densité homogène et uniforme de l'eau, etc.). La structure hamiltonienne non-canonique de ce système sera par la suite explicitée. Nous montrerons aussi que, en l'absence de déferlement, elles se réduisent à une formulation bien-connue du problème, dite de Zakharov, Craig et Sulem.

Pour arriver à ce système d'équations, deux hypothèses importantes doivent être réalisées : négliger la viscosité et supposer un tourbillon nul. La seconde partie de ce travail consistera en une discussion de ces dernières. Pour cela, nous adopterons une approche numérique permettant d'approximer la solution des équations de Navier–Stokes à surface libre. Le schéma mis au point diffère de ceux qu'il est coutume d'utiliser pour ce problème. En effet il met en œuvre la méthode Lagrangien–Eulerien Arbitraire (ALE) pour l'advection et la discrétisation est réalisée par la Méthode des Éléments Finis (FEM).

Ce schéma numérique sera d'abord utilisé pour étudier la couche limite apparaissant sous l'interface eau—vide, lorsque le fond de l'eau est plat. Il nous sera alors possible de conclure que le tourbillon ainsi généré n'empêche nullement la solution de faible viscosité de converger vers la solution irrotationnelle de l'équation d'Euler, étant donné que son support devient arbitrairement petit.

Par contre, l'étude de topographies non-plate mettra en lumière un phénomène physique absent du système limite : le décollement de la couche limite présente au fond de l'eau. En effet, il peut arriver que l'écoulement irrotationnel associé au passage d'un train d'onde d'amplitude finie ait une vélocité suffisamment importante pour venir arracher des tourbillons des régions de forte courbure et les transporter jusqu'à proximité immédiate de la surface. Ce phénomène ne semble pas disparaître dans la limite de viscosité évanescente et contrecarre, de ce fait, la convergence vers la solution irrotationnelle.

# Acknowledgements - Remerciements

During the last three years, I had the chance to carry out research on a topic I chose and I even got paid for that. I am deeply grateful to the taxpayers in France for this opportunity. The results obtained during my Ph.D. belong to them.

This work consists in a contribution of size  $\varepsilon \ll 1$  to the total scientific knowledge deciphered by the human kind. It is based in its entirety on the results obtained by my predecessors and colleagues. My warmest thanks go to the scientific community, and in particular to the people whose work constitutes the foundations of my infinitesimal contribution. I could have said that I lack the space to provide a complete list of these persons, but this manuscript actually ends with such a list: its bibliography.

Je remercie grandement le Département de Physique de l'Université de Genève, celui de l'ENS et le département de Mathématiques de l'Université Dauphine-PSL qui ont transformé le tourbillon chaotique que j'étais en tourbillon chaotique instruit.

Je remercie énormément toutes les personnes étant passées par le Département de Mathématiques et Applications de l'ENS au cours de ces trois dernières années pour leur chaleureux accueil et leur bienveillance. En particulier je remercie Fabienne pour sa patience infinie face à mon incapacité flagrante à préparer une mission correctement.

Je souhaite remercier chaleureusement Alexandre M. pour m'avoir ouvert les yeux concernant la beauté de la Science, et en particulier celle de la Physique et des Mathématiques. Je ne serais pas là où je suis aujourd'hui sans lui.

I would like to thank the wonderful people I met during the conferences I attended during my doctorate. In particular those I met at the second and third Advanced Summer Schools on Mathematical Fluid Dynamics, held in 2023 and 2025 in Corsica. I surely wish to acknowledge the participants and the organisers of the Conférence Jeunes Chercheur euse s du GdR Géophys 2023, of the CANUM 2024, the EFDC1, the Journées de l'Hydrodynamique 2024, the FreeFEM days 2024 and the CIMAV 2025 too. Finally, I sincerely thank the persons that invited me to present my work a few times: M. Benoit, V. Duchêne, A. Duran, B. Fabrèges, F. Hecht, M. Kazakova, C. Lacave, F. Marche, G. Richard, G. Sadaka and P. Vigneaux.

I would like to thank D. Bresch, C. Lacave, K. Moffatt, J. Neufeld, C. Sulem and S. Tobias who kindly provided support to my numerous applications to post-docs and fellowships. It eventually worked out pretty well!

Je remercie assertivement la fine équipe de maths du Palais de la Découverte : Robin J., Noëlle K., Marjolaine L. et Guillaume R. pour leur accueil, leur confiance et leur bienveillance.

Je remercie sincèrement mes deux rapporteurs, D. Bresch et D. Lannes, d'avoir pris le temps de se frayer un chemin à travers les broussailleuses pages qui composent ce tapuscrit, non sans difficulté j'en suis sûr.

Je remercie résolument les membres de mon jury : C. Besse, D. Bresch, A.-L. Dalibard, E. Dormy, C. Lacave, D. Lannes et C. Sulem pour la patience dont ils et elles vont devoir se munir afin de me lire et de m'écouter parler (certain·e·s pour la n<sup>ème</sup> fois qui plus est).

Je remercie félinement la défunte petite Lulu pour ses câlins, ronronnements et sa gloutonnerie sans limite.

Je remercie éminemment T. Alazard, D. Bresch, G. Beck, T. Fradin, C. Lacave, O. Hénot, L. Oruba, E. Rebouillat, P. Saulgeot, M. Wallon, et P. Wang pour les joyeux moments passés ensemble, aussi bien en conférence qu'au laboratoire, mais aussi pour les discussions enrichissantes que nous avons pu avoir en de nombreuses occasions.

Je remercie affectionnément ma famille proche pour les efforts qu'ils et elles ont fournis dans le but de

comprendre ce que je faisais ces dernières années et pour avoir su cacher leurs nombreuses désapprobations vis-à-vis de mes choix de carrière. De plus, je remercie conjonctionnellement mes parents pour leur soutien infaillible et inconditionnel.

Je remercie similairement et affectueusement Jeanne B., Louis C., Mohammed C., Abel C., Alejandro E., Fred F., Loïc F., Coline F., Clem L., Sophie L., Johanne P., Alexandre P., Annabel S., Léo T., Louis T., Milla V., et Maxime Z. pour la patience infinie qu'ils et elles ont fournie afin de me supporter aussi bien lors de mon ascension du Mont-Thèse que d'une manière générale (cette liste a été classée alphabétiquement, n'y voyez pas une quelconque façon de vous départager non plus).

Je ne remercie absolument pas la vaisselle, qui n'a toujours pas trouvé le bon goût de se faire toute seule. Je remercie énormément mon directeur de thèse Emmanuel Dormy pour sa patience, son originalité, sa camaraderie, sa bienveillance et son infaillible enthousiasme. Il a cru en moi à un moment où j'en avais grandement besoin, sans quoi le travail présenté ici n'aurait jamais abouti.

Je remercie amoureusement Johanne P. qui a dû me supporter dans des moments assez difficiles ces dernières années. Je n'y serais clairement pas arrivé sans elle.

...et je remercie comiquement le site lalanguefrancaise.com pour son dictionnaire d'adverbes sans lequel j'aurais probablement eu grand mal à arriver harmonieusement au bout de ces remerciements...

# Contents

English	ab	stract	vii
Résumé	er	n français	ix
Acknow	led	gements	хi
Introdu	cti	on et résumé plus substantiel en français	1
	Ι	La description eulérienne des vagues océaniques	2
		I.1 Le système de Navier-Stokes à surface libre	3
		I.2 Le système d'Euler à surface libre	4
		${\it I.3} \qquad {\it Les \'equations des vagues oc\'eaniques, dites de Zakharov-Craig-Sulem} \ . \ . \ . \ . \ . \ .$	5
		I.4 Adimensionnement	5
		La description lagrangienne et les équations des vagues déferlantes	6
		Un schéma numérique pour les équations de Navier-Stokes à surface libre	8
		Limite de viscosité évanescente et déferlement	10
	V	1 0 1	11
		9	12
		V.2 Cas d'une marche de courbure finie	13
Chapter	0.	Introduction	<b>15</b>
	Ι	Mathematical results on the Water Waves problem	16
		I.1 The free-surface Navier-Stokes equations	16
		I.2 The free-surface Euler equations	17
		I.3 The Water Waves equations	18
	II	Boundary layers and the vanishing viscosity limit	20
	III	Wave Breaking	22
		III.1 Instabilities triggering wave breaking	23
		III.2 Numerical simulations of breaking waves	23
		III.3 The shape of water waves	24
	IV	Scope of the present work	25
		ŭ ŭ	25
		IV.2 On the limit of vanishing viscosity in (Breaking) Water Waves	25
Mathe	ma	atical Modelling of Breaking Water Waves	27
Chapter	1.	The Eulerian description of Water Waves	29
		I.1 Derivative of volume integrals	29
		v 1	31
			32
	II	Boundary conditions	34
		II.1 The inviscid boundary conditions	35
		II.2 The viscous boundary conditions	36
		II.3 Neglecting the air	36

		II.4	The kinematic condition, Eulerian advection
	<b>TTT</b>	II.5	Surface tension
	111		imensionalisation
		III.1	The linear wave solution
		III.2	The non-dimensional Euler problem
		III.3	The non-dimensional Navier-Stokes problem
		III.4	Surface tension
	IV		tionality
		IV.1	The vorticity
		IV.2	Non-dimensionalisation
	V		Vater Waves equations
		V.1	Motivating the equations
		V.2	On the Dirichlet–to–Neumann operator
		V.3	Hamiltonian structure
		V.4	Water Waves on a manifold
Chapter	<b>2</b> .		Lagrangian framework and the Breaking Waves equations 61
	Ι		ngian Fluid Mechanics
		I.1	The label space
		I.2	Conservation of mass
		I.3	Conservation of momentum
		I.4	Boundary conditions
		I.5	Irrotationality and Bernoulli's equation
		I.6	Water Waves solutions in the lagrangian frame
	II	The B	reaking Waves equations
		II.1	The geometric approach
		II.2	A less geometric derivation
		II.3	Hamiltonian structure
		II.4	Non-dimensionalisation
	III	What	is a breaking wave?
		III.1	Definition
		III.2	Reduction to the Water Waves equations
On the	. T	/anisk	ning Viscosity Limit in Water Waves 87
			•
			erical methods for the free-surface Navier-Stokes system
	Ι		inite Element Method
		I.1	The weak formulation of $(1.54)$
		I.2	Time discretisation
		I.3	Matrix creation
	II		ary Lagrangian-Eulerian advection
		II.1	General velocities on the continuous level
		II.2	Numerical analysis of the ALE scheme and implementation
		II.3	Two special choices of mesh velocities
	III	Imple	mentation
		III.1	Recomputing the mesh
		III.2	Parallelisation
	IV	Code	validation
		IV.1	Comparison to analytical solutions
		IV.2	Numerical convergence
		IV.3	Cross-validation
		IV.4	Validating the 3d code
Chapter	4	Visco	sity and the shape of breaking Water Waves
			conditions for breaking waves

		I.1 Constructing the initial conditions		
	тт	I.2 Comparison between different initial conditions		
		The Re $\rightarrow +\infty$ limit		
	111	I Viscous dissipation near the free surface		
		III.1 Vorticity generation at fluid interfaces		
		III.2 The free–surface boundary layer		
		III.3 What about no-slip/Dirichlet conditions?		
	IV	Regularisation of free surfaces due to viscosity		
		IV.1 Time evolution of the curvature		
		IV.2 Asymptotic expansion and scaling	•	. 137
Chapter	<b>5</b> .	Irrotationality of Water Waves and topography		
	Ι	Motivation: why should water waves be irrotational?		
	II	Non-convergence to the irrotational solution		
		II.1 Stability of the boundary layer laying over a flat topography: the non-breaking		
		case		. 142
		II.2 Adding a rectangular step on the bed		. 142
		I Boundary layer separation		
	IV	Separation from a smooth step		. 148
		IV.1 Constructing the topography		. 148
		IV.2 Does separation persist around smooth obstacles?		. 148
	V	A plea for a theory of boundary layers on curved concave walls		. 152
		V.1 The Navier-Stokes equations in the Frénet frame		. 152
		V.2 Formal asymptotic regimes		. 154
	VI	I Concluding remarks		. 156
Chapter	-1.	. Conclusions and perspectives		. 157
Chapter	Α.	. Mathematical tools and notations		. 159
Chapter	I.	Functional setting		
	_	I.1 Function spaces		
		I.2 Pseudo-Differential operators		
		I.3 Miscellaneous		
	П	Differential Geometry 101		
	11	II.1 Smooth manifolds		
		II.2 Differential operations on manifold		
Chapter	B	A plenty of calculus identities		162
Спарил	J.	Notations and disambiguations		
		A plenty of identities		
	11	II.1 First order identities		
		II.2 Chain rule		
	TTT			
	111	I Common differential operators in arbitrary orthogonal coordinates systems		
		III.1 The Christoffel symbols		
		III.2 Differential operators		. 165

## Introduction et résumé substantiel en français

"La mer Qu'on voit danser le long des golfes clairs A des reflets d'argent La mer Des reflets changeants Sous la pluie"

> "La mer Au ciel d'été confond Ses blancs moutons Avec les anges si purs La mer bergère d'azur Infinie"

Charles Trenet, La Mer (1946)

La modélisation mathématique des vagues (océaniques ou capillaires) et des phénomènes naturels qui leur sont associés constitue un travail scientifique de longue haleine, dont il convient de placer l'origine à l'étude des forces de flottaison par Archimède au IIIème siècle avant notre aire, et qui se poursuit encore aujourd'hui. En effet l'océan est un système physique d'une grande complexité dont la description par l'approche de la mécanique des fluides ne peut se faire que par le prisme de modèles réduits obtenus par approximations successives, échouant de ce fait à capturer la dynamique océanique globale. Pourtant, au regard des enjeux climatiques contemporains, l'étude de cette dernière se doit d'obtenir une grande attention de la part du monde académique (IPCC 2019, 2023). Il a été établi de longue date que l'océan joue un rôle prépondérant dans grand nombre de phénomènes de transport et de régulation climatique.

Une difficulté inhérente à ce problème est le couplage entre différentes échelles qu'il est difficile de modéliser conjointement. Par exemple, la dissipation énergétique associée au déferlement (petite échelle) a un impact non-négligeable sur la dynamique côtière (échelle moyenne). La mise en place d'un dialogue entre les différentes dimensions, du point de vue de la modélisation mathématique, est un enjeu contemporain fascinant (voir par exemple la recension récente de Seenath 2025).

Dans ce travail, nous allons nous intéresser à une facette bien particulière de la description de la surface de l'océan, de petite échelle puisqu'il sera rarement question de plus d'une crête de vague à la fois, à savoir le déferlement des vagues océaniques. L'accent sera mis sur le régime côtier, où le fond de l'eau joue un rôle important sur la dynamique surfacique, mais certaines conclusions (notamment celles du chapitre 2) trouveront sans souci une généralisation à des profondeurs plus importantes (par rapport à la longueur d'onde d'une vague).

La majorité des modèles océaniques de petite échelle ne parviennent pas à décrire le déferlement. Pour cause, il est souvent supposé que l'interface peut être vue comme le graphe d'une fonction. Adopter un point de vue lagrangien, c'est-à-dire suivre la trajectoire de chaque élément infinitésimal du fluide plutôt que de

s'intéresser à la vitesse de ce dernier en un point donné, permet de s'affranchir de cette hypothèse. Cette observation a été mis en œuvre par Longuet-Higgins and Cokelet (1976, 1978) pour l'élaboration du premier schéma numérique permettant de simuler des vagues océaniques déferlantes, en supposant la viscosité et le tourbillon évanescents. Des suites de ce travail important, d'autres auteurs-rices ont mis en place des schémas numériques avec la même finalité (citons par exemple Vinje and Brevig (1981), Baker, Meiron, et al. (1982), Dold et al. (1986) ou encore Grilli et al. (1989)).

Il fallut attendre la fin des années quatre-vingt-dix pour lever l'hypothèse d'irrotationnalité dans les méthodes numériques et s'intéresser aux effets de la viscosité. En effet supposer un tourbillon évanescent permet d'utiliser le potentiel de vitesse et ainsi reformuler le problème avec des variables résidant sur l'interface (et éventuellement sur le fond) uniquement. Cette réduction de la dimension ne peut plus être réalisée avec un fluide visqueux pour lequel le tourbillon ne reste pas nécessairement nul (Longuet-Higgins 1992; Lundgren and Koumoutsakos 1999). De ce fait, il fallut attendre la puissance informatique nécessaire à la réalisation de simulations non-linéaires en deux et trois dimensions d'espace pour approximer numériquement la solution des équations de Navier-Stokes à surface libre. Surprenamment, le schéma d'advection de l'interface communément adopté est eulerien, mais il n'est jamais supposé que l'interface est le graphe d'une fonction, bien entendu. Des exemples de schémas numérique de la sorte sont décris dans les publications de Chen et al. (1999), Iafrati (2009), Deike, Popinet, et al. (2015), Lubin and Glockner (2015), Deike, Melville, et al. (2016), Di Giorgio et al. (2022) ou encore Mostert et al. (2022), pour ne citer qu'eux.

L'emploi de ces méthodes numériques ne fut en aucun cas uniquement cosmétique. En effet, Longuet-Higgins (1978) a par exemple utilisé sa méthode pour mettre en évidence le mécanisme à l'origine du déferlement: l'instabilité super-harmonique. Cette dernière correspond à un développement exponentiel de l'amplitude des modes de longueur d'onde plus courte que celle de la vague, ayant pour effet de ralentir le creux en amont d'une crête, tout en accélérant cette dernière. Le développement de cette instabilité a par la suite été étudié plus précisément par Tanaka (1983, 1985). Bien que ces études aient été menées en eaux profondes, Tanaka et al. (1987) ont montré qu'il s'agit aussi d'un mécanisme présent lorsque le fond joue un rôle dans la dynamique.

Le travail que nous présentons ici est scindé en deux parties. Premièrement, nous allons présenter une reformulation des équations d'Euler irrotationnelles à surface libres, adoptant la même philosophie que celle de Zakharov (1968), Craig and Sulem (1993), avec une description lagrangienne de l'interface, permettant ainsi de décrire des vagues déferlantes jusqu'au recoupement de l'interface, en deux et trois dimensions d'espace. Le cas d'une interface de dimension un ayant déjà été traité par Craig (2017), nous n'apportons qu'une extension de son travail aux surfaces paramétrisées. Dans un second temps, nous allons mettre au point un schéma numérique pour l'équation de Navier-Stokes à surface libre. À la différence des études déjà citées, l'advection de l'interface passera par l'advection de tout le maillage selon la méthode lagrangien-eulerien arbitraire (Hirt et al. 1974). Cela permettra de réduire grandement l'erreur d'interpolation et ainsi diminuer la viscosité jusqu'à des valeurs permettant la comparaison avec la solution des équations d'Euler à surface libre, approximée selon la méthode du dipole décrite, justifiée, implémentée et testée en détails par Dormy and Lacave (2024). Cette comparaison entre solutions visqueuses et non-visqueuse sera réalisée avec des conditions de type Navier ou Dirichlet imposées au niveau du fond de l'eau. Nous essaierons de dégager une loi générale concernant la validité de l'approximation d'irrotationnalité du flot et du bon emploi des modèles sans viscosité.

Dans une optique d'accessibilité internationale, cette thèse a été rédigée en anglais. Nous fournissons tout de même, dans les quelques pages qui suivent, un résumé détaillé du contenu de chaque chapitre en français. Pour assurer la continuité de la lecture, certaines figures seront reproduites à l'identique (avec toutefois leur légende traduite).

#### La description eulérienne des vagues océaniques

Commençons simplement par un tour d'horizon des différentes façons de décrire les écoulements océanique non-loin des côtes. Cela permettra d'expliciter les approximations généralement faites et de voir apparaître les difficultés auxquelles il faudra se confronter afin d'obtenir un ensemble d'équations décrivant les lames déferlantes.

Hypothèse	Interprétation physique	Traduction mathématique
H1	La matière est un continuum	Modélisation via des EDPs
H2	Les fluides possèdent des densités homogènes	Incompressibilité (1.2)
H3	L'eau et l'air sont immiscibles	$\Gamma_i(t)$ est une surface de dimension $d$
H4	L'eau et l'air sont newtoniens avec des viscosités	(1.7), (1.8)
	homogènes	
H5	Pas de partie émergée, c'est-à-dire qu'il existe tou-	( <b>H5</b> ) ou ( <b>H5</b> , bis)
	jours une couche d'eau entre le sol et l'air	
H6	L'eau n'a pas de viscosité ( $\nu_{\rm w}=0$ )	Le système d'Euler (1.53)
H7	L'air a une densité nulle	$\rho_{\rm a}=0$
H8	La vague ne déferle pas	$\Gamma_i(t)$ est le graphe de $h(t, \vec{x})$
H9	Absence de tension de surface	$\gamma_{\rm w} = 0$
H10	Le fond de l'eau est représentable par le graphe	$\Gamma_b$ peut être vu comme $b(\vec{x})$
	d'une fonction constante dans le temps	
H11	L'écoulement possède un tourbillon évanescent	$\omega = 0$

**Tableau** – Les hypothèses généralement réalisées pour décrire la surface de l'océan. Elles sont toutes discutées en détails dans la première partie de ce travail.

#### I.1. Le système de Navier-Stokes à surface libre

Considérons un fluide newtonien de viscosité  $\nu$  et densité  $\rho$  homogènes (**H2** et **H4**; les hypothèses qui serons faites étant résumées dans le tableau ci-dessus), modélisé comme un continuum (**H1**). L'évolution conjointe de sa vitesse  $\boldsymbol{u}$  et de sa pression p en tout point contenu dans une portion  $\Omega(t)$  de l'espace  $\mathbb{R}^{d+1}$  (avec d=1 ou 2 la dimension de l'interface entre l'eau et l'air) est décrite par les équations de Navier et Stokes, dont la formulation eulérienne est

$$\partial_t \boldsymbol{u} + \boldsymbol{u} \cdot \nabla \boldsymbol{u} + \frac{1}{\rho} \nabla p = \nu \Delta \boldsymbol{u} + \boldsymbol{g}$$

$$\nabla \cdot \boldsymbol{u} = 0,$$

avec g l'accélération de la pesanteur.

Pour utiliser ces équations dans le cadre d'une description de l'océan dans un régime littoral, un certain nombre d'hypothèses supplémentaires doivent être faites. Déjà, nous supposons que le domaine  $\Omega(t)$  s'étend à l'infini dans les directions spatiales horizontales et qu'il est compris entre le fond de l'océan  $\Gamma_b$ , supposé fixe, et l'interface entre l'eau et l'air  $\Gamma_i(t)$  (H3, H5). Des représentations schématiques de cette configuration géométrique sont disponibles en figures 1.6 et 1.7. Les composantes horizontales sont dénotées  $\vec{x}$ , à l'aide d'une flèche afin de souligner qu'elles sont de dimension d, tandis que la composante verticale est appelée z.

Dans le cadre eulérien théorique, l'évolution de l'interface entre l'eau et l'air est décrite en supposant que cette dernière peut être représentée comme le graphe d'une fonction  $h(t, \vec{x})$  (**H8**). L'équation de transport conduit alors à

$$\partial_t h = oldsymbol{u} \cdot oldsymbol{n} \qquad ext{où} \qquad oldsymbol{n} = egin{bmatrix} - ec{
abla} h \\ 1 \end{bmatrix},$$

où il est implicitement entendu que la valeur de u est prise au niveau de l'interface  $z = h(t, \vec{x})$ . Nous dénotons par  $\vec{\nabla}$  la partie horizontale du gradient et n correspond alors à un vecteur perpendiculaire à la surface non-normalisé. Un grand nombre d'auteur-rices appellent cette équation la condition cinématique. Il paraît un peu trop réducteur d'utiliser le terme condition étant donné qu'il ne s'agit nullement d'une contrainte de bords mais d'une EDP d'évolution se suffisant à elle-même.

Dans l'intégralité de ce travail, l'air est considéré comme ayant une densité nulle (**H7**). Cette hypothèse peut sembler quelque peu drastique étant donné que le vent est responsable de l'essentiel de la génération des vagues en haute mer (Janssen 2004). Sur des intervals de temps courts (de l'order de quelques périodes), cela peut toutefois se justifier. Il conviendra aussi de négliger les effets dûs à la tension superficielle (**H9**), principalement car il ne s'agit pas du sujet de la présente étude. Dans ce cas particulier, nous ajoutons une contrainte vectorielle dynamique au niveau de l'interface, à savoir que les contraintes normales s'annulent

au niveau de l'interface,

$$p\hat{\boldsymbol{n}} - \nu\rho \Big[\boldsymbol{\nabla}\boldsymbol{u} + (\boldsymbol{\nabla}\boldsymbol{u})^{\top}\Big] \cdot \hat{\boldsymbol{n}} = 0 \qquad \text{sur } \Gamma_{i}(t),$$

avec  $\hat{n}$  le vecteur unitaire normal à l'interface pointant en dehors de l'eau. Notons que cette condition comporte une partie normale et une partie tangentielle.

Enfin, il reste à prescrire des conditions sur le fond  $\Gamma_b$  afin de clore le système. Deux possibilités se présentent à nous pour ce faire. Il est par exemple commun de supposer que les molécules composant le fluide sont libres de glisser sur le fond sans contrainte, la condition de glissement ou de Navier. À l'inverse, on suppose parfois que les molécules adhèrent aux parois du fait de la viscosité, ce qui les empêche de se mouvoir, la condition de non-glissement ou de Dirichlet. Elles se matérialisent par

$$\left\{ oldsymbol{u} \cdot \hat{oldsymbol{n}} &= 0 \\ \hat{oldsymbol{n}} imes \left[ oldsymbol{\nabla} oldsymbol{u} + (oldsymbol{\nabla} oldsymbol{u})^{ op} 
ight] \cdot \hat{oldsymbol{n}} &= 0 \end{array} 
ight\} \quad ext{(Navier)}$$

Comme nous le verrons aux chapitres 4 et 5, la première engendre bien moins de difficultés que la seconde. En particulier il existe une vaste littérature mathématique concernant la limite de faible viscosité avec condition de Navier (sans surface libre), comme par exemple les études de Iftimie and Planas (2006), Iftimie and Sueur (2011), Masmoudi and Rousset (2012) ou encore Gérard-Varet and Lacave (2013). Cependant, la condition de Dirichlet semble mieux représenter la réalité, bien qu'elle soit dotée de la fâcheuse tendance à générer des couches limites, que l'on peut interpréter, quitte à trop simplifier pour l'instant, comme des zones de tourbillon intense à proximité des bords. Des couches limites peuvent aussi apparaître dans le cas de conditions de Navier, mais elles sont un ordre plus faible en intensité. Remarquons qu'avec ces deux conditions, le fluide n'a pas la possibilité de pénétrer le fond de l'océan.

Les équations présentées succinctement ci-dessus constituent le système de Navier-Stokes à surface libre. Ce dernier a été étudié mathématiquement par quelques courageux-ses auteurs-rices. Dans le cas de conditions de Dirichlet au fond, nous pouvons ainsi mentionner les travaux de Beale (1981), Allain (1987) ou encore Guo and Tice (2013c) concernant le caractère localement bien-posé de ces équations. En prenant de petites conditions initiales, il est même possible de dégager des résultats de caractère bien-posé globaux en temps (Beale 1984, Nishida and Teramoto 2004, Guo and Tice 2013a,b). Si la condition de Dirichlet se voit remplacée par la condition de Navier, l'auteur ne connaît que le résultat local en temps de Bresch and Noble (2011). Enfin, le cas d'un fond infiniment profond a été traité par Masmoudi and Rousset (2017), où la limite de viscosité évanescente a, de surcroît, été établie. Le système limite est l'objet de ce qui suit.

#### I.2. Le système d'Euler à surface libre

L'essentiel du travail que nous présentons ici concerne les effets de la viscosité de l'eau sur l'écoulement océanique côtier (avec la prudence qu'il est nécessaire de prendre, nos résultats étant pour l'essentiel bidimensionnels). Effectivement, la viscosité de l'eau étant relativement faible (ou, plus précisément, les nombres de Reynolds océaniques étant habituellement grands), une hypothèse naturelle consiste à la négliger totalement (**H6**). Si l'on pose formellement  $\nu = 0$  dans les équations de Navier-Stokes incompressibles, nous obtenons les équations d'Euler (tout aussi incompressibles),

$$\partial_t u + u \cdot \nabla u + \frac{1}{\rho} \nabla p = g$$

$$\nabla \cdot u = 0.$$

Pour autant, il est loin d'être acté que dans la limite  $\nu \to 0$ , la solution du système visqueux présenté en section I.1 finisse par devenir une solution du système ci-dessus, et ce du fait de l'influence des bords. En effet, en posant  $\nu=0$  dans les équations de Navier-Stokes, nous perdons la plus forte dérivée (le laplacien vectoriel). De ce fait, il n'est pas possible de conserver la même quantité de conditions de bords et il ne reste qu'à espérer que les contraintes excédentaires ne poserons pas de problèmes (le chapitre 5 nous montrera que parfois elles le font). Pour fermer le système d'Euler, il y a besoin d'une condition spatiale en moins. Cela est fait sans ambiguïté dans la littérature scientifique en imposant

$$p=0$$
 à l'interface  $\Gamma_i(t)$ 

$$\boldsymbol{u} \cdot \hat{\boldsymbol{n}}_b = 0$$
 au fond  $\Gamma_b$ ,

avec  $\hat{n}_b$  le vecteur unitaire perpendiculaire à la surface  $\Gamma_b$ . En l'absence de fond, le résultat remarquable de Masmoudi and Rousset (2017) assure la convergence de petites solutions de viscosité  $\nu > 0$  vers de petites solutions du système d'Euler. Ce dernier ayant aussi été étudié mathématiquement par Lindblad (2005), Coutand and Shkoller (2007) ou encore Zhang and Zhang (2008).

#### I.3. Les équations des vagues océaniques, dites de Zakharov-Craig-Sulem

Comme il est coutume en dynamique des fluides, le tourbillon  $\boldsymbol{\omega} = \boldsymbol{\nabla} \times \boldsymbol{u}$  est une quantité que l'on espère garder petite. En effet l'étude du système présenté en sec. I.2 est grandement simplifiée si l'on suppose  $\boldsymbol{\omega} = 0$ , c'est-à-dire l'*irrotationnalité* de l'écoulement (**H11**). Cette hypothèse ne se fait que rarement sans intérêt personnel. Elle conduit en effet à l'expression de la vitesse  $\boldsymbol{u}$  comme le gradient d'un potentiel  $\boldsymbol{\nabla} \phi$ , astucieuse substitution. Cependant, bien que la validité de cette réécriture ne ferait nullement débat si la dynamique de l'océan pouvait être correctement modélisée par le système d'Euler (du fait de la loi de conservation de la circulation de Kelvin : théorème 1.6 ci-après), il peut arriver que les effets visqueux, petits mais présents, conduisent à quelques complications (prenant souvent la forme d'un décrochement de couche limite).

Nous reléguons à plus tard la périlleuse question de la stabilité des couches limites. Pour l'instant, nous préférons discuter des conséquences de l'hypothèse d'irrotationnalité du point de vue de la modélisation. Dans son article fondateur, Zakharov (1968) a remarqué qu'en introduisant la variable  $\psi(t,\vec{x}) = \phi(t,\vec{x},z=h(t,\vec{x}))$ , la valeur du potentiel calculée au niveau de la surface libre  $\Gamma_i(t)$ , alors les équations des vagues prennent une forme hamiltonienne en tous points ressemblante à celle des équations de la mécanique (mais en dimension infinie). Avec les notations modernes introduites par Craig and Sulem (1993), cela s'écrit

$$\left\{ \begin{array}{lcl} \partial_t h & = & \delta_\psi \mathbf{H} \\ \partial_t \psi & = & -\delta_h \mathbf{H}. \end{array} \right. \quad \text{avec} \quad \mathbf{H}[h,\psi] = \frac{1}{2} \int_{\mathbb{R}} \psi \operatorname{DtN}[h] \psi + \frac{1}{2} \int_{\mathbb{R}} g h^2,$$

où DtN[h] $\psi$  est l'opérateur de Dirichlet-vers-Neumann, associant à  $\psi$  la dérivée normale  $\partial_n \phi$  du potentiel évaluée au niveau de l'interface ; la dérivée variationnelle de H selon  $\psi$  étant dénotée  $\delta_{\psi}$ H. L'utilisation de cet opérateur permet de réécrire le système d'Euler à surface libre à l'aide de quantités définies sur l'interface uniquement, selon

$$\begin{cases} \partial_t h = \mathrm{DtN}[h]\psi \\ \\ \partial_t \psi = -gh - \frac{1}{2} \big| \vec{\nabla} \psi \big|^2 + \frac{1}{2} \frac{ \big[ \mathrm{DtN}[h]\psi + \vec{\nabla} \psi \cdot \vec{\nabla} h \big]^2}{1 + |\vec{\nabla} h|^2}. \end{cases}$$

De cette manière, la dimension du problème a été réduite d'une unité. Bien que fortement non-linéaire, les Équations aux Dérivées Partielles ci-dessus ont été grandement étudiées (parmi ces travaux, nous mentionnons ceux de Lannes (2005, 2013b), Ambrose and Masmoudi (2009a,b), Alazard, Burq, et al. (2014a,b), Alazard and Delort (2015a,b) ou encore les travaux à faible régularité récents de Ai et al. (2022, 2024)).

#### I.4. Adimensionnement

L'analyse mathématique comme l'approximation numérique des solutions des trois systèmes fondamentaux discutés ci-dessus est une tâche bien souvent fastidieuse. Dans certains cas, il est possible d'utiliser des modèles plus simples (comme, par exemple, ceux de Barré de Saint-Venant, Serre, Green and Naghdi ou encore Korteweg and de Vries). Pour comprendre les régimes de validités de ces modèles comme pour les justifier rigoureusement, la stratégie habituellement employée consiste à adimensionner les équations, c'est-à-dire à redéfinir les diverses variables et quantités dans le but de laisser apparaître des paramètres que l'on pourrait faire tendre vers zéro ou vers l'infini. Dans notre cas, nous faisons apparaître trois grandeurs sans dimension physique,

$$\varepsilon = \frac{\text{amplitude}}{\text{hauteur d'eau}} \qquad \mu = \frac{\text{hauteur d'eau}}{\text{longueur d'onde}} \qquad \text{Re} = \frac{\text{hauteur d'eau} \cdot \text{vitesse de groupe}}{\nu}$$

En suivant la procédure décrite au chapitre 1 (sec. III, notamment le tableau 1.2), le système de Navier-Stokes à surface libre devient le suivant,

$$\begin{split} \mu \partial_t \boldsymbol{u}_\mu + \varepsilon \boldsymbol{u}_\mu \cdot \boldsymbol{\nabla}_\mu \boldsymbol{u}_\mu &= -\frac{1}{\varepsilon} \vec{\nabla} p - \frac{\hat{\boldsymbol{z}}}{\varepsilon} + \frac{1}{\mathrm{Re}} \Delta_\mu \boldsymbol{u}_\mu \\ \partial_t h + \varepsilon \vec{\boldsymbol{u}} \cdot \vec{\nabla} h &= \boldsymbol{u}_z \\ p \hat{\boldsymbol{n}} &= \frac{\varepsilon}{\mathrm{Re}} \Big[ \boldsymbol{\nabla}_\mu \boldsymbol{u}_\mu + (\boldsymbol{\nabla}_\mu \boldsymbol{u}_\mu)^\top \Big] \cdot \hat{\boldsymbol{n}}, \end{split}$$

avec la vitesse  $\boldsymbol{u}_{\mu}$  et les opérateurs  $\boldsymbol{\nabla}_{\mu}$  et  $\boldsymbol{\Delta}_{\mu}$  redimensionnés (donc avec l'indice  $\mu$ ) définis en section III.3 du chapitre 1. Les autres équations constituantes se transforment de façon relativement inintéressantes. À partir là, la version adimensionnée du système d'Euler s'obtient formellement en prenant  $\mathrm{Re} = +\infty$ . Un grand nombre de régimes asymptotiques correspondant à des faibles profondeurs peuvent être obtenus dans le cas  $\mu \ll 1$  (cf. Lannes (2013b, 2020) ou bien Duchêne (2021)). Cependant, la limite que nous allons discuter tout du long de la seconde partie de ce travail sera celle de viscosité évanescente,  $\mathrm{Re} \to +\infty$ .

#### II. La description lagrangienne et les équations des vagues déferlantes

Discutons maintenant d'une généralisation des équations des vagues océaniques de Zakharov, Craig et Sulem au cas des courbes et surfaces paramétrisées évoluant selon un schéma lagrangien, complétant ainsi le travail de Craig (2017). Cela permet de lever l'hypothèse de non-déferlement (**H8**).

Nous présentons ici une motivation des équations dans le cas d'une espace physique bi-dimensionnel (d=1) afin d'alléger les notations. Le cas général est traité en détails dans le chapitre 2 (mais nous rappellerons les résultats en fin de section). Représentons donc l'interface entre l'eau et l'air par une courbe paramétrisées  $\gamma(t,\cdot):\mathbb{R}\to\mathbb{R}^2$ , supposée continue et infiniment différentiable pour le moment, et dont la paramétrisation dépend du temps. Cela suppose déjà que le volume de fluide  $\Omega(t)$  est d'un seul tenant (et donc qu'il n'y a ni goutte, ni bulle, ni écume) et simplement connexe (donc que l'interface ne s'est pas recoupée elle-même). Une représentation schématique de cette configuration est proposée en figure 2.6. L'évolution de la paramétrisation se fait de façon lagrangienne, selon

$$\partial_t \gamma(t,s) = u(t,\gamma(t,s)),$$

c'est-à-dire : chaque point de l'interface se meut à la vitesse du fluide ;  $\gamma(t,s)$  représente donc l'élément de fluide initialement à la position  $\gamma(0,s)$ .

Comme dans le cas eulérien, l'hypothèse d'irrotationnalité est absolument essentielle pour cette approche. En effet, dans un domaine simplement connexe (ce qui est souvent le cas avant le recoupement de l'interface), elle permet l'introduction du potentiel de vitesse  $\phi$  (une extension à des domaines multiplement connexes a été discutée par Ambrose, Camassa, et al. 2022). Comme pour des vagues non-déferlantes, définissons aussi  $\psi(t,s) = \phi(t,\gamma(t,s))$  la valeur du potentiel au niveau de la surface libre. En substituant  $u = \nabla \phi$  dans l'équation d'advection lagrangienne présentée ci-dessus, nous obtenons alors

$$\begin{split} \partial_t \pmb{\gamma}(t,s) &= \pmb{\nabla} \phi \Big(t, \pmb{\gamma}(t,s) \Big) = \Big[ \hat{\pmb{n}}(t,s) \cdot \pmb{\nabla} \phi \Big(t, \pmb{\gamma}(t,s) \Big) \Big] \hat{\pmb{n}}(t,s) + \Big[ \hat{\pmb{\tau}}(t,s) \cdot \pmb{\nabla} \phi \Big(t, \pmb{\gamma}(t,s) \Big) \Big] \hat{\pmb{\tau}}(t,s) \\ &= \frac{\text{DtN}[\pmb{\gamma}] \psi}{\left| \partial_s \pmb{\gamma} \right|} (t,s) \hat{\pmb{n}}(t,s) + \frac{\partial_s \psi}{\left| \partial_s \pmb{\gamma} \right|} (t,s) \hat{\pmb{\tau}}(t,s) \\ &= \frac{\text{DtN}[\pmb{\gamma}] \psi(t,s)}{\left| \partial_s \pmb{\gamma}(t,s) \right|^2} \Big( \partial_s \pmb{\gamma} \Big)^\perp + \frac{\partial_s \psi(t,s)}{\left| \partial_s \pmb{\gamma}(t,s) \right|^2} \Big( \partial_s \pmb{\gamma} \Big), \end{split}$$

les vecteurs unitaires  $\hat{\boldsymbol{\tau}}(t,s)$  et  $\hat{\boldsymbol{n}}(t,s)$  étant, par définition, une base orthonormée de  $\mathbb{R}^2$  pour chaque temps  $t \geqslant 0$  et chaque abscisse curviligne  $s \in \mathbb{R}$ . L'opérateur  $\mathrm{DtN}[\boldsymbol{\gamma}]\psi$  est défini d'une façon similaire à sa version eulérienne.

L'obtention d'une équation d'évolution pour  $\psi$  se fait rapidement en appliquant à de multiples reprises la règle de la chaîne et en utilisant l'équation de Bernoulli. Il est aussi possible de ne travailler qu'avec

des quantités lagrangiennes, c'est-à-dire repérées par une système de coordonnées dépendant du temps et évoluant à la vitesse du fluide. Ce point-de-vue alternatif est discuté au chapitre 2. Au final nous obtenons

$$\begin{split} \partial_t \psi(t,s) &= \partial_t \Big( \phi \Big(t, \pmb{\gamma}(t,s) \Big) \Big) = \Big( \partial_t \phi \Big) \Big(t, \pmb{\gamma}(t,s) \Big) + \partial_t \pmb{\gamma}(t,s) \cdot \pmb{\nabla} \phi \Big(t, \pmb{\gamma}(t,s) \Big) \\ &= -g \gamma_z(t,s) + \frac{1}{2} \Big| \pmb{\nabla} \phi \Big(t, \pmb{\gamma}(t,s) \Big) \Big|^2 \\ &= -g \gamma_z(t,s) + \frac{1}{2} \left( \frac{\text{DtN}[\pmb{\gamma}] \psi}{|\partial_s \pmb{\gamma}|} \right)^2 (t,s) + \frac{1}{2} \left( \frac{\partial_s \psi}{|\partial_s \pmb{\gamma}|} \right)^2 (t,s), \end{split}$$

avec  $\gamma_z$  la composante verticale de  $\gamma$ . Une fois encore, il a été possible de réécrire le système d'Euler irrotationnel à surface libre à l'aide de quantités définies sur l'interface uniquement.

Il est aussi possible d'obtenir ce système dans l'espace physique tri-dimensionnel, lorsque la surface libre est vue comme une surface paramétrisée  $\gamma(t, \cdot): \mathbb{R}^2 \to \mathbb{R}^3$ . Pour ce faire, introduisons quelques notations au préalable. La paramétrisation étant bi-dimensionnel, nous abusons des notations de la section I et dénotons par  $\vec{s} = [s^1, s^2]$  la paramétrisation de l'interface. Il s'agit d'une paramétrisation régulière si  $\partial_{s^1} \gamma \times \partial_{s^2} \gamma \neq 0$ , ce qui permet de définir un vecteur normal unitaire  $\hat{n}$  par la même occasion. Les vecteurs tangents  $\tau_1 = \partial_{s^1} \gamma$  et  $\tau_2 = \partial_{s^2} \gamma$  ne peuvent en aucun cas être supposés perpendiculaire étant donné que, même s'ils sont choisis initialement ainsi, il n'y a aucune raison qu'ils le restent par la suite. De ce fait, à t et  $\vec{s}$  fixés, les trois vecteurs  $\hat{n}$ ,  $\tau_1$  et  $\tau_2$  ne forment pas une base orthonormal de  $\mathbb{R}^3$  et il n'est plus possible de décomposer  $\nabla \phi$  aussi simplement qu'en deux dimensions d'espace. Cette difficulté est résolu par l'utilisation de la métrique  $\mathbf{g}$ , définie comme

$$\mathbf{g} = \begin{bmatrix} \partial_{s^1} \boldsymbol{\gamma} \cdot \partial_{s^1} \boldsymbol{\gamma} & \partial_{s^1} \boldsymbol{\gamma} \cdot \partial_{s^2} \boldsymbol{\gamma} \\ \partial_{s^2} \boldsymbol{\gamma} \cdot \partial_{s^1} \boldsymbol{\gamma} & \partial_{s^2} \boldsymbol{\gamma} \cdot \partial_{s^2} \boldsymbol{\gamma} \end{bmatrix}.$$

Pour une paramétrisation régulière  $\gamma(t, \vec{s})$  de  $\Gamma_i(t)$ ,  $\mathbf{g}(t, \vec{s})$  est définie positive et fournie donc un produit scalaire sur l'espace tangent  $\mathbf{T}_{\vec{s}}\Gamma_i(t)$ . Cette propriété essentielle nous permet de décomposer  $\nabla \phi$  et nous obtenons le système lagrangien suivant,

$$\begin{cases} \partial_t \boldsymbol{\gamma} = \frac{\mathrm{DtN}[\boldsymbol{\gamma}] \psi}{\sqrt{\det(\mathbf{g})}} \hat{\boldsymbol{n}} + \begin{bmatrix} \partial_{s^1} \psi & \partial_{s^2} \psi \end{bmatrix} \mathbf{g}^{-1} \begin{bmatrix} \partial_{s^1} \boldsymbol{\gamma} \\ \partial_{s^2} \boldsymbol{\gamma} \end{bmatrix} \\ \partial_t \psi = -g \gamma_z + \frac{1}{2} \left( \frac{\mathrm{DtN}[\boldsymbol{\gamma}] \psi}{\left| \partial_s \boldsymbol{\gamma} \right|} \right)^2 + \frac{1}{2} \begin{bmatrix} \partial_{s^1} \psi & \partial_{s^2} \psi \end{bmatrix} \mathbf{g}^{-1} \begin{bmatrix} \partial_{s^1} \psi \\ \partial_{s^2} \psi \end{bmatrix}. \end{cases}$$

En fait, cette forme fonctionne aussi pour une interface de dimension un, avec  $\mathbf{g} = |\partial_s \gamma|$ , et se généraliser aux dimensions supérieures. Ces équations sont aussi établies par une approche géométrique au chapitre 2, ayant l'avantage de laisser apercevoir plus de structure sous-jacente, au prix d'une grande quantités de notations superfétatoires.

Une question naturelle concerne la structure hamiltonienne de ce système : la dynamique découle-t-elle encore d'une hamiltonien, comme dans la formulation eulérienne, ou non ? La réponse est en demieteinte : une structure hamiltonienne existe mais elle n'est nullement canonique. En effet, si l'on définit la fonctionnelle suivante,

$$H[\boldsymbol{\gamma}, \boldsymbol{\psi}] = \frac{1}{2} \int_{\mathbb{R}^d} \boldsymbol{\psi} \operatorname{DtN}[\boldsymbol{\gamma}] \boldsymbol{\psi} + \frac{g}{2} \int_{\mathbb{R}^d} (\gamma_z^2) \, \hat{\boldsymbol{z}} \cdot \hat{\boldsymbol{n}} \, \sqrt{\det(\mathbf{g})},$$

alors nous parvenons à dégager la structure suivante,

$$\left\{ \begin{array}{ll} \partial_t \boldsymbol{\gamma} & = & \displaystyle \frac{\boldsymbol{n}}{\det \mathbf{g}} & \displaystyle \frac{\delta \mathbf{H}}{\delta \psi} & + \text{ partie tangentielle} \\ \partial_t \psi & = & \displaystyle -\frac{\boldsymbol{n}}{\det \mathbf{g}} & \displaystyle \frac{\delta \mathbf{H}}{\delta \boldsymbol{\gamma}} & + \text{ partie tangentielle}. \end{array} \right.$$

Bien que quelque peu décevante, l'absence de canonicité n'est guère surprenante : la partie tangentielle des équations ne contribue pas à la forme de l'interface, elle n'encode que le glissement des éléments de fluide sur cette dernière. Notons toutefois que la forme symplectique qui apparaît dans les équations génère

effectivement une structure hamiltonienne, au sens élargi de Olver (1980) ou Kuksin (2000). Remarquons tout de même une certaine forme de normalisation du fait de  $|\mathbf{n}|^2 = \det \mathbf{g}$ .

À l'aide de toutes ces considérations sur la paramétrisation de la surface libre, il nous est possible de formuler une définition mathématique du déferlement de la solution de ce système.

**Définition 2.22.** Au temps  $t \ge 0$ , la vague représentée par l'interface  $\Gamma_i(t)$  a déferlé si la différentielle de l'application  $\vec{s} \mapsto \vec{s} + \vec{\gamma}(t, \vec{s})$ , vue comme une fonction de  $\mathbb{R}^d \to \mathbb{R}^d$ , n'est pas inversible en un certain  $\vec{s}$ .

En comparant cette définition avec celles données dans la littérature expérimentale (Galvin 1968; Wiegel 1964), nous voyons qu'il s'agit en réalité de la définition d'une déferlante plongeante (plunging breaker). Les autres types de houle s'étant brisée étant caractérisés par des gouttes ou de l'écume, nous ne pouvons les modéliser de la façon présentée ici. Remarquons que par le théorème de la fonction inverse, cette définition nous fournit une autre caractérisation (non-équivalente) du déferlement :  $\vec{s} \mapsto \vec{s} + \vec{\gamma}(t, \vec{s})$  est injective si la vague (la solution) n'a pas déferlé. Le lien avec la vision usuelle de la brisure d'une vague comme un choc hyperbolique se comprend aussi au travers de cette définition.

L'injectivité de  $\vec{s} \mapsto \vec{X}_t(\vec{s}) = \vec{s} + \vec{\gamma}(t, \vec{s})$  en l'absence de déferlante nous permet de définir son inverse  $\vec{X}_t^{-1}(\vec{x})$  sans ambiguïté. Cela permet d'expliciter un lien entre variables lagrangienne  $\vec{s}$  et eulérienne  $\vec{x}$  horizontale. Dans le cas d'un espace ambient bi-dimensionnel (d=1), nous parvenons à montrer que les quantités

$$\varphi(t,x) = \psi \Big(t, X_t^{-1}(s)\Big) \qquad \text{et} \qquad h(t,x) = \gamma_z \Big(t, X_t^{-1}(s)\Big)$$

sont des solutions du système de Zakharov-Craig-Sulem. De ce fait, les équations des vagues déferlantes peuvent effectivement être vues comme une extension des équations des vagues océaniques, avec équivalence en l'absence de déferlement.

#### III. Un schéma numérique pour les équations de Navier-Stokes à surface libre

L'utilité de l'hypothèse d'irrotationnalité (H11) a été mise en lumière dans les deux sections précédentes. Il convient toutefois de motiver son emploi. C'est le sujet de la seconde partie de ce travail, débutant ici. Nous nous proposons d'approximer numériquement la solution des équations de Navier-Stokes à surface libre (le système le plus fondamental, résultant du plus faible nombre d'hypothèses physiques) afin de comprendre les effets de la viscosité sur les écoulements océaniques de petite échelle (de l'ordre d'une longueur d'onde en faible profondeur).

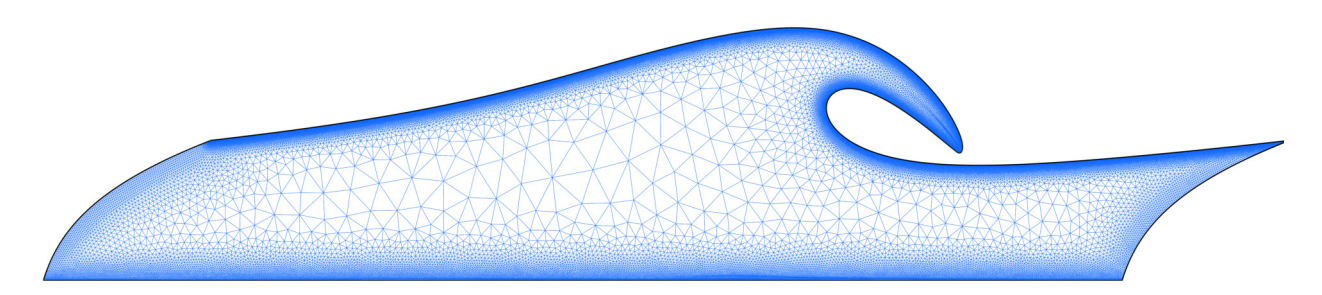


Figure 3.14 (reproduction) – Exemple de maillage obtenu dans le cadre d'une simulation de vague déferlante à un nombre de Reynolds Re =  $10^5$ . Celui-ci contient  $N_v = 59\,532$  sommets,  $N_t = 117\,729$  triangles et  $N_e = 174\,258$  arrêtes.

Commençons donc par décrire la méthode numérique employée. Contrairement à grand nombre d'études déjà mentionnées, nous allons adopter un schéma d'advection lagrangien pour l'interface et employé la méthode des éléments finis, implémentée via l'interface c++ FreeFEM (Hecht 2012).

Lorsque l'évanescence du tourbillon n'est pas supposée (et cela ne peux être fait dans le cas des équations de Navier-Stokes à surface libre, comme nous allons le voir), il devient nécessaire de mailler l'intégralité du domaine fluide. Cela est fait à l'aide de triangles (cf. fig 3.14, reproduite ci-dessous). Ce faisant, transporter

l'interface de façon lagrangienne ne peut être réalisé sans transporter le reste du maillage. Pour cela, nous employons la méthode lagrangien-eulérien arbitraire (ALE, Hirt et al. 1974) qui consiste à choisir une vitesse  $\boldsymbol{v}$  propre au maillage.

Avec un schéma temporel de type Euler implicite, en dénotant par  $(\boldsymbol{u}^n, p^n)$  l'état du système après n pas de temps, chacun de taille  $\delta t^n$  calculée selon la condition CFL, et  $\boldsymbol{v}^n$  la vitesse du maillage à ce même pas de temps, il est possible d'obtenir la formulation variationnelle du problème, nécessaire pour implémenter la méthode des éléments finis (FEM). Soit donc l'espace fonctionnel suivant,

$$\boldsymbol{H}^1_{\Gamma_b}(\Omega) = \Big\{\boldsymbol{u} \in \left(H^1(\Omega)\right)^{d+1} \text{ t.q. } \boldsymbol{u} \cdot \hat{\boldsymbol{n}}_b = 0 \text{ sur } \Gamma_b\Big\},$$

correspondant à la condition de Navier (avec une adaptation rapide pour ce qui est des conditions de Dirichlet sur  $\Gamma_b$ ). Nous avons alors le problème suivant : trouver deux fonctions  $\boldsymbol{u}^{n+1} \in \boldsymbol{H}^1_{\Gamma_b}(\Omega^n)$  et  $p^{n+1} \in L^2(\Omega^n)$  telles que

$$\int_{\Omega^n} \left[ \boldsymbol{w} \cdot \frac{\boldsymbol{u}^{n+1} - \boldsymbol{u}^n}{\delta t^n} + \boldsymbol{w} \cdot \left( \boldsymbol{u}^n - \boldsymbol{v}^n \right) \cdot \nabla \boldsymbol{u}^{n+1} + \frac{2}{\text{Re}} \, \mathbf{S}(\boldsymbol{w}) : \mathbf{S}(\boldsymbol{u}^{n+1}) \right.$$
$$\left. - p^{n+1} \nabla \cdot \boldsymbol{w} - q \nabla \cdot \boldsymbol{u}^{n+1} - \boldsymbol{w} \cdot \boldsymbol{g} \right] \, \mathrm{d}\boldsymbol{x} = 0,$$

pour tout  $\boldsymbol{w} \in \boldsymbol{H}^1_{\Gamma_b}(\Omega^n)$  et  $q \in L^2(\Omega^n)$ . Le domaine  $\Omega^n$  étant le domaine de fluide au pas de temps n.  $\mathbf{S}(\boldsymbol{u})$  correspond à la partie symétrique du tenseur gradient de  $\boldsymbol{u}$ . Il suffit ensuite de transporter chaque point de  $\Omega^n$  à la vitesse  $\boldsymbol{v}^n$  pour obtenir  $\Omega^{n+1}$ . Noter la présence du terme  $\boldsymbol{v}^n \cdot \nabla \boldsymbol{u}^{n+1}$ , assurant que le mouvement du domaine  $\Omega^n$  soit bien compensée. La justification de ce terme sera effectuée en section II du chapitre 3. La formulation faible présentée ci-dessus fonctionne aussi bien au niveau continu qu'une fois une triangulation du domaine  $\Omega^n$  réalisée. À la connaissance de l'auteur, aucune justification rigoureuse de la méthode ALE n'a été proposée. Il est formellement établi que l'ordre de la méthode correspond à l'ordre du schéma d'advection de  $\Omega^n$  au chapitre 3.

Deux choix de vitesse du maillage  $\boldsymbol{v}^n$  sont discutés. Déjà, remarquons que si l'on prend un schéma purement lagrangien, pour lequel  $\boldsymbol{v}^n = \boldsymbol{u}^n$ , alors la non-linéarité disparaît complètement du système de Navier-Stokes. Par contre, dans le cas d'une condition de Navier imposée sur  $\Gamma_b$ , il n'est pas totalement assuré que la géométrie du fond sera conservée (bien que ce soit le cas au niveau continu). Pour palier à ce problème, une autre possibilité est de calculer  $\boldsymbol{v}^n$  en résolvant numériquement le problème elliptique suivant,

$$\begin{cases}
\Delta \mathbf{v}^n = 0 & \operatorname{dans} \Omega^n \\
\mathbf{v}^n = \mathbf{u}^n & \operatorname{sur} \Gamma_i^n \\
\mathbf{v}^n = 0 & \operatorname{sur} \Gamma_b,
\end{cases}$$

à chaque pas de temps. De cette façon le schéma est purement eulérien sur le fond  $\Gamma_b$ , et purement lagrangien au niveau de l'interface  $\Gamma_i(t)$ . Les deux méthodes seront utilisées dans les pages qui suivent.

L'implémentation de ce schéma numérique est fait via FreeFEM. En particulier, la génération et le transport du maillage lui sont délégués, de même que la génération des matrices. Dans l'objectif de satisfaire la condition LBB, des éléments de Taylor–Hood  $\mathbb{P}^2 \times \mathbb{P}^1$  sont utilisés. La méthode s'avère relativement lente, en particulier du fait de la nécessité de recalculer les matrices à chaque pas de temps. De ce fait, l'interface pré-existante entre FreeFEM et PETSc est utilisée afin de paralléliser le code via une décomposition du domaine (Dolean et al. 2015) et la méthode des multi-grilles géométriques.

La validation du code est réalisée de différentes manières. Premièrement, avec une faible viscosité (Re =  $10^5$ ), la solution numérique est comparée à une solution analytique de faible amplitude : l'onde de Stokes de première ordre en la non-linéarité  $\varepsilon$ . La différence entre les deux reste de l'ordre de  $\varepsilon^2$ , de sorte qu'il n'est pas possible d'attribuer cette erreur à la solution analytique ou au schéma numérique.

Les solutions analytique tenant compte de la viscosité sont rares. Un second test est réalisé en comparant le temps d'amortissement  $\tau$  d'une onde de Stokes de faible amplitude, obtenu numériquement, au cas théorique calculé par Lamb (1932). Comme  $\tau = O(\text{Re})$ , une viscosité assez forte est utilisée (Re =  $10^2$ ). Une fois encore, la différence reste de l'ordre de  $\varepsilon^2$ . On remarque toutefois via ce cas-test que, sans donner de meilleurs résultats, la méthode de Crank-Nicolson se montre bien plus instable que le schéma Euler implicite en temps.

Enfin, un dernier contrôle est réalisé en comparant la solution à faible viscosité (Re = 10<sup>6</sup>) à la solution du système d'Euler à surface libre dans le cas d'une vague déferlante, selon une condition initiale irrotationnelle construite selon le modèle de Baker, Meiron, et al. (1982), calculée à l'aide de la méthode des dipoles décrite par Dormy and Lacave (2024). La faible différence entre les deux approximations numériques permet à la fois de conclure de la robustesse des deux méthodes, mais aussi de la convergence de la solution visqueuse vers la solution irrotationnelle dans ce cas précis.

#### IV. Limite de viscosité évanescente et déferlement

Cette partie se base sur notre étude (Riquier and Dormy 2024b). Il y est question de la limite de faible viscosité ( $\text{Re} \to +\infty$ ) avec un fond plat sur lequel nous venons imposer la condition de Navier, et une condition initiale conduisant au déferlement de la vague. Dans la direction horizontale, l'écoulement est supposé périodique.

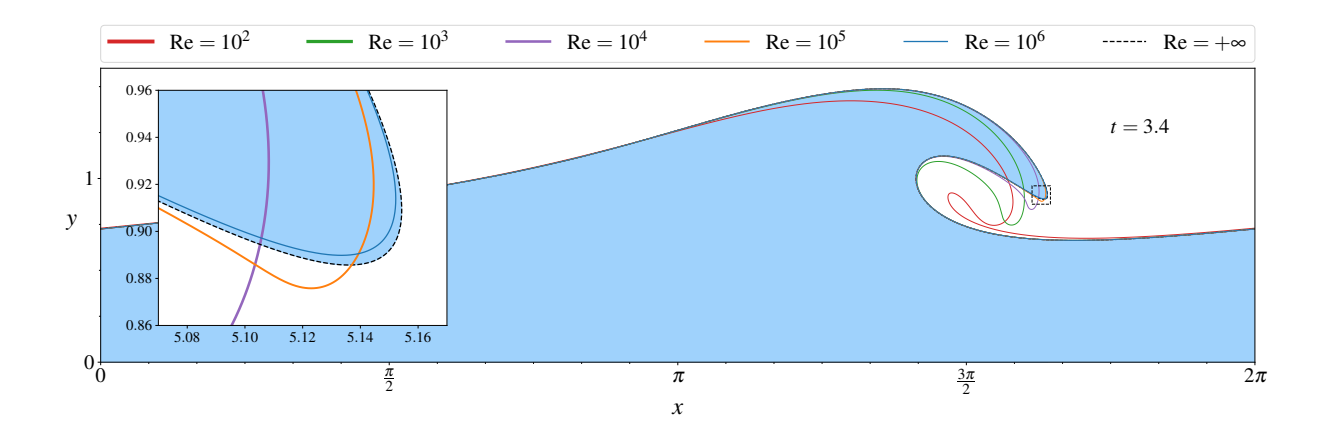


Figure 4.6 (reproduction) – Comparaison des surfaces libres obtenues par approximation de la solution visqueuse ( $\text{Re} = 10^2 \rightarrow 10^6$ ) et de la solution non-visqueuse irrotationnelle ( $\text{Re} = +\infty$ ), cette dernière étant calculée à l'aide de la méthode du dipole de Dormy and Lacave (2024).

La condition initiale est construite de sorte à être irrotationnelle. Pour ce faire, nous prenons une interface initiale  $h(0,x) = h_0 + a\cos(kx)$  (avec  $h_0 = k = 1$ , et donc une longueur d'onde  $\lambda = 2\pi$ ) correspondant à une onde linéaire d'amplitude a = 0.5, puis nous calculons la vitesse initiale en résolvant numériquement le problème elliptique suivant,

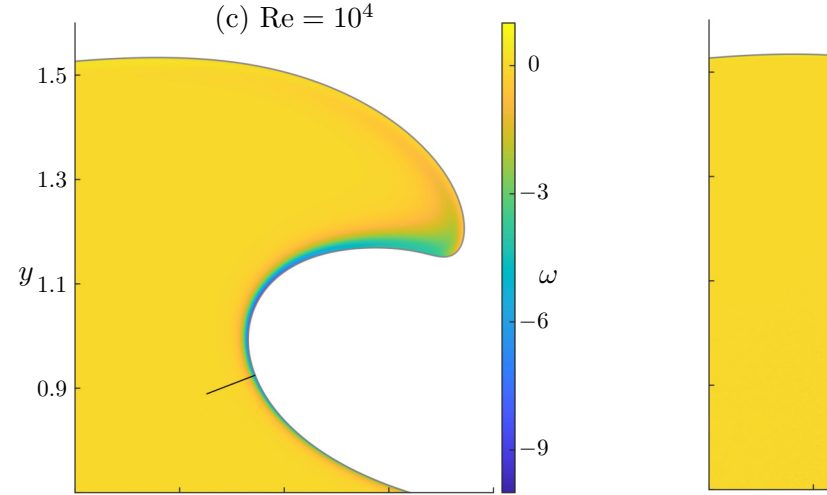
$$\left\{ \begin{array}{lcl} \Delta\phi_0 &=& 0 & \mathrm{dans}\; \Omega(0) \\ \partial_n\phi_0 &=& \boldsymbol{u}_{\mathrm{in}}\cdot\hat{\boldsymbol{n}} & \mathrm{sur}\; \Gamma_i(0) = \{z=h_0+a\cos(kx)\} \\ \partial_n\phi_0 &=& 0 & \mathrm{sur}\; \Gamma_b = \{z=0\}, \end{array} \right.$$

avec la vitesse initiale  $u_{in}$  correspondant à une extension d'amplitude finie d'une onde de Stokes d'ordre 1, c'est-à-dire

$$\label{eq:u_in_loss} \boldsymbol{u}_{\rm in} \cdot \hat{\boldsymbol{n}} = a \sqrt{gk \, \tanh(kh_0)} \cdot \frac{\sin(kx)}{\sqrt{1 + k^2 a^2 \sin^2(kx)}} \left(1 - \frac{ka}{\tanh(kh_0)} \cdot \cos(kx)\right).$$

La vitesse initiale est alors  $\boldsymbol{u}(t=0) = \boldsymbol{\nabla}\phi_0$ , assurant ainsi un tourbillon initialement nul.

Des simulations utilisant la condition initiale que nous venons de décrire ont été réalisées avec des valeurs du nombre de Reynolds variant de  $Re = 10^2$  à  $Re = 10^6$ . Dans la figure 4.6 (reproduite ci-dessus dans une version tronquée), ces solutions numériques sont comparées avec celle du système d'Euler à surface libre (irrotationnelle, calculée à l'aide du code de Dormy and Lacave (2024)). La convergence est alors observée.



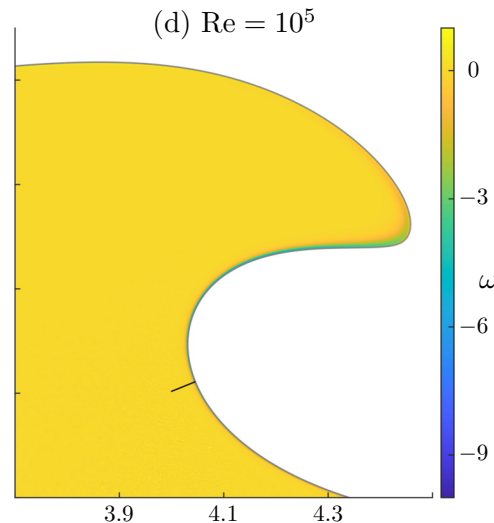


Figure 4.13 (reproduction) – Le tourbillon  $\omega = \partial_x u_z - \partial_z u_x$  au temps t = 2.9 pour Re =  $10^4$  et  $10^5$ . Les lignes noires seront utilisées au chapitre 4 dans l'objectif d'étudier la taille et le profil de la couche limite.

Afin de comprendre la convergence constatée plus finement, il semble utile de s'intéresser à la dissipation énergétique. En effet, de rapides manipulations du système de Navier-Stokes nous permettent d'obtenir le bilan d'énergie globale suivant,

$$\frac{1}{2}\frac{\mathrm{d}}{\mathrm{d}t}\left(\int_{\Omega(t)}\boldsymbol{u}^2\right) + \frac{1}{2}\frac{\mathrm{d}}{\mathrm{d}t}\left(\int_{\mathbb{T}}(\gamma_z)^2\hat{n}_z\Big|\partial_s\gamma\Big|\right) + \frac{2}{\mathrm{Re}}\int_{\Omega(t)}\mathbf{S}(\boldsymbol{u}):\mathbf{S}(\boldsymbol{u}) = 0.$$

Le dernier terme est responsable de la dissipation visqueuse. D'un point de vue local, nous avons l'équation dévolution de l'énergie cinétique,

$$\left[\partial_t + \boldsymbol{u} \cdot \boldsymbol{\nabla}\right] \left(\frac{\boldsymbol{u}^2}{2}\right) - \boldsymbol{u} \cdot \boldsymbol{g} + \boldsymbol{u} \cdot \boldsymbol{\nabla} p = \frac{1}{\mathrm{Re}} \cdot \boldsymbol{u} \cdot \Delta \boldsymbol{u} = -\frac{1}{\mathrm{Re}} \, \left[\boldsymbol{\nabla} \cdot \left(\omega \boldsymbol{u}^\perp\right) + \omega^2\right].$$

Il est intéressant de remarquer que la dissipation énergétique a lieue dans le support du tourbillon. Pour cette raison, cette dernière quantité est affichée en figure 4.13 (reproduite ci-dessus dans une version abrégée). Une nappe de tourbillon apparaît à proximité immédiate de l'interface. Il s'agit en réalité d'une couche limite de Navier (tourbillon uniformément borné en Re et contenu dans une mince région de taille  $\mathrm{Re}^{-\frac{1}{2}}$ ). Dans la limite  $\mathrm{Re} \to +\infty$ , cette couche limite disparaît donc, expliquant ainsi la convergence constatée vers la solution irrotationnelle.

Bien entendu, cette conclusion ne tient qu'avant le recoupement de l'interface par elle-même. Les phénomènes physiques en jeu lorsque cela se produit ne semble pas encore bien compris mais il est établi que cela conduit à la génération de structures turbulentes, et donc à une plus importante quantité de dissipation énergétique.

La réalisation des mêmes simulations avec une condition de Dirichlet imposée au niveau de  $\Gamma_b$  conduit à des conclusions identiques pour les valeurs de Re considérées. En effet la couche limite de Dirichlet (tourbillon d'intensité Re $^{\frac{1}{2}}$  localisée à une distance Re $^{-\frac{1}{2}}$  du bords) semble stable pour ces valeurs de viscosité.

#### V. L'hypothèse d'irrotationnalité et l'influence de la topographie

Intéressons-nous maintenant à l'épineuse question de la préservation de l'irrotationnalité. En effet, il a déjà été acté que ses implications sont d'une grande importance du point de vue de la modélisation mathématique des vagues océaniques : lorsque la vitesse découle d'un potentiel, le système d'Euler à surface libre se réduit en un système d'équations de dimension moindre à partir desquelles il est possible de justifier nombre de modèles réduits correspondant à des régimes asymptotiques.

Intuitivement, une perte d'irrotationnalité, c'est-à-dire une génération de tourbillon, ne peut être le fait que de deux phénomènes physiques : la turbulence due au recoupement de l'interface, et un décrochement de couche limite au niveau des obstacles sous-marins. Il a déjà été établi que nous ne parvenons pas à modéliser le comportement d'une vague dans le premier cas. Nous allons donc traiter du second en essayant de déstabiliser la couche limite gisant au fond de l'eau lorsque la condition de Dirichlet (physiquement plus motivée) est prescrite.

#### V.1. Cas d'une marche rectangulaire

Le premier cas que nous traitons est celui représenté schématiquement en figure 5.3: un obstacle rectangulaire, donc avec deux coins, placés au fond de l'eau. La condition initiale est construite de la même façon qu'à la section IV, avec une amplitude a=0.1 cette fois-ci, de sorte à ne pas voir de déferlement. L'évolution du tourbillon est visible en figure 5.6 (reproduite ci-dessous, quoique tronquée).

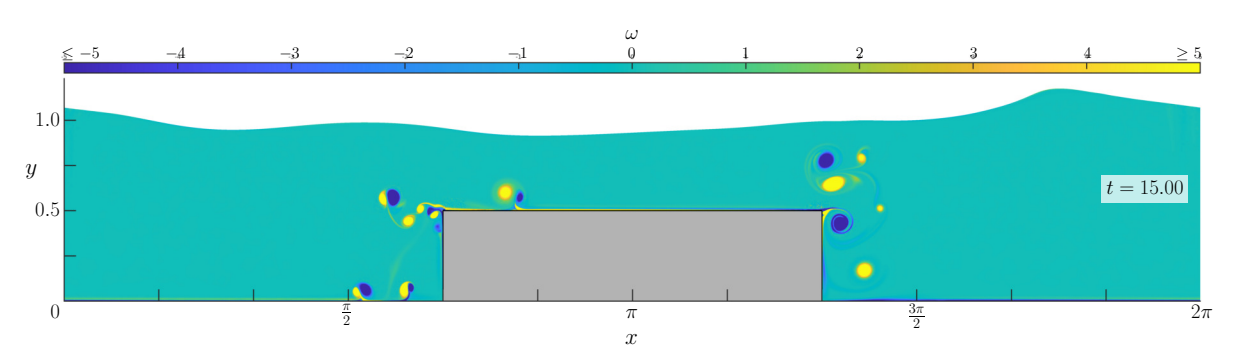


Figure 5.6 (reproduction) – Évolution du tourbillon dans une simulation de vague d'amplitude initiale a = 0.1 au-dessus d'une marche rectangulaire avec un nombre de Reynolds  $Re = 10^5$ .

On remarque un détachement de la couche limite au niveau des coins du rectangle. De part la nature oscillante de l'écoulement, ce détachement prend la forme d'une succession de filaments positifs et négatifs, qui s'enroulent sur eux-mêmes sous l'effet de l'instabilité de Kelvin-Helmholtz. Au final, après le passage d'une crête et d'un creux, la résultante peut être vue comme une paire de tourbillons contra-rotatifs, évoluant sous l'influence des autres tourbillons déjà présent et de l'écoulement potential d'arrière-plan. Lorsque la viscosité diminue, chaque vortex semble devenir de plus en plus singulier : ce phénomène ne devrait pas disparaître à partir d'une certaine valeur de Re.

Une question naturelle est alors : est-ce que la présence de ces tourbillons peut venir perturber la surface libre ? Pour répondre à cette question, nous avons réalisé la même simulation que celle présentée dans la figure 5.6 pour d'autres valeurs (plus petites) du nombre de Reynolds. Ces résultats sont comparés, encore une fois, avec la solution non-visqueuse irrotationnelle approximée à l'aide de la méthode des dipoles (Dormy and Lacave 2024). Le résultat est visible en figure 5.4 (reproduite ci-dessous).

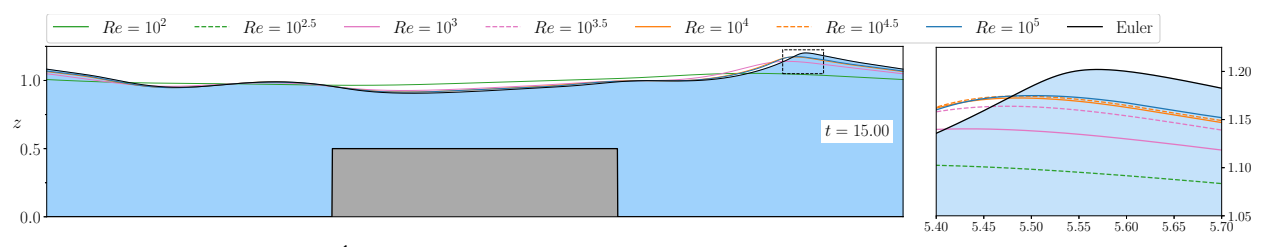


Figure 5.4 (reproduction) – Évolution des interfaces correspondant à diverses simulations de vagues d'amplitude initiale a=0.1 au-dessus d'une marche rectangulaire avec un nombre de Reynolds compris entre  $Re=10^2$  et  $Re=10^5$ . La solution du système d'Euler à surface libre, calculée à l'aide du code de Dormy and Lacave (2024) et la même condition initiale irrotationnelle est aussi présentée.

Contrairement aux résultats présentés dans la section IV, la convergence de la solution visqueuse vers la solution irrotationnelle lorsque  $Re \to +\infty$  est cette fois-ci remise en question. En effet, on remarque que la solution des équations de Navier-Stokes à surface libre semble converger vers une limite qui ne correspond pas à la solution non-visqueuse et irrotationnelle. Bien que l'effet soit faible, la différence constatée semble augmenter dans le temps, au fur et à mesure que des tourbillons son émis et que l'écoulement ressemble de plus en plus à un gaz de tourbillons.

#### V.2. Cas d'une marche de courbure finie

La présence d'un détachement de la couche limite dans le cas de coins anguleux n'est nullement surprenant. En effet, pour un nombre de Reynolds donné, il existe un angle à partir duquel ce décrochement aura lieu (Sychev et al. 1998). Mais est-ce toujours le cas pour une marche lissée de sorte à ce que la courbure de cette dernière soit finie? Pour étudier cette question, nous utilisons la méthode dites de mollification afin de construire une topographie prenant toujours la forme d'une marche mais avec un rayon de courbure r minimal. Un exemple d'une telle simulation est présenté dans la figure 5.13 (reproduite ci-dessous).

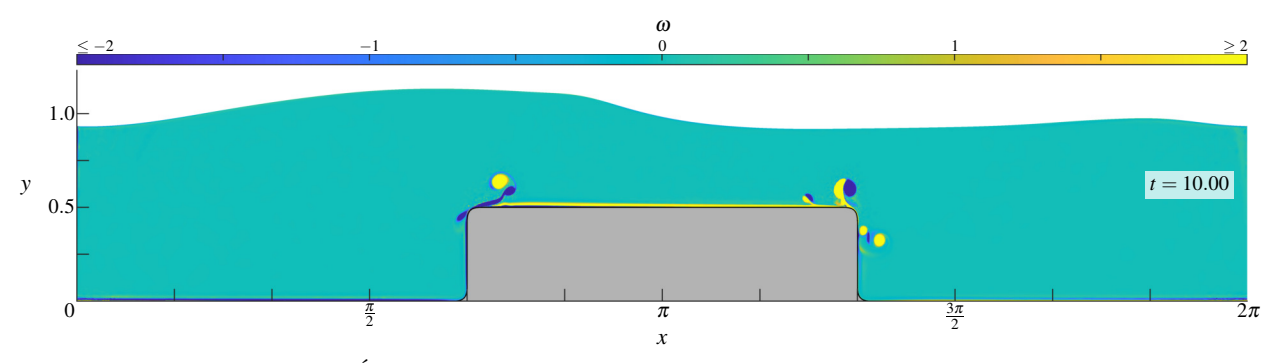


Figure 5.13 (reproduction) – Évolution du tourbillon lors d'une simulation de vague d'amplitude initiale a = 0.1 au-dessus d'une marche rectangulaire lisse (rayon de courbure r = 0.1) avec un nombre de Reynolds de Re =  $10^5$ .

Bien que le tourbillon émis soit plus faible, le décollement de la couche limite reste néanmoins présent malgré une topographie lisse. En fait cette dernière apparaît une fois un seuil de courbure franchi. Ce seuil semble dépendre du nombre de Reynolds.

Les implications de cette observation sont multiples. Déjà, elle contrevient à l'usage de modèles irrotationnels dans le cas d'un fond non-plat avec une topographie de trop forte courbure. Par la suite, elle empêche de la même façon la solution visqueuse de converger vers la solution irrotationnelle lorsque  $\text{Re} \to +\infty$ , le système limite est tout autre. Enfin, il n'est pas possible de conclure de l'absence de turbulence pour des valeurs encore plus élevée de Re. Des conclusions plus complètes seront présentées à la fin du chapitre 5.

Voilà qui conclut notre résumé en français du travail qui va suivre. Le caractère trop succin de ces dernières pages doit probablement laisser au lecteur un goût d'incomplétude ainsi qu'un grand nombre de questions. Nous espérons qu'il n'en sera pas de même des suites de la lecture des pages qui suivent.

# Chapter

# Introduction

"[T]he next waves of interest, that are easily seen by everyone and which are usually used as an example of waves in elementary courses, are water waves. As we shall soon see, they are the worst possible example, because they are in no respects like sound and light; they have all the complications that waves can have."

"[S]ince the wave is not so simple, the shocks are much more contorted, and the wave over-curves itself [...]. This is what happens when waves come into the shore, and the real complexities in nature are well revealed in such a circumstance. No one has yet been able to figure out what shape the wave should take as it breaks. It is easy enough when the waves are small, but when one gets large and breaks, then it is much more complicated."

Richard P. Feynman, The Feynman Lectures on Physics (1965)

Water Waves might be one of the easiest scientific subject to describe to a non-scientist: everybody has seen them (not only at the surface of the ocean but also in a glass of water for instance), everybody has the chance of observing their oscillatory nature. Their physical and mathematical description, a process that can arguably be traced back to the discovery of Archimedes' principle, remains however, even to this very day, a challenging scientific problem. Indeed, they exhibit complex behaviours whose understanding is far from complete.

Among the many difficulties that may arise, the breaking phenomenon plays an important role. Intuitively, it corresponds to the moment the surface of the water rolls up onto itself, due to the crest of the wave travelling faster than the trough up front, before collapsing due to its own mass, creating a formidable amount of small-scale secondary structures (droplets, bubbles, turbulence, vortex filaments and foam). Unfortunately, it cannot be overlooked easily as it is mainly responsible for the viscous dissipation arising on small time scales, through the generation of vorticity happening after the *splash* singularity has occurred, *i.e.* after the free surface self-intersected.

As difficult as it might be, studying water waves is of fundamental importance in the modern era. Generally speaking, the ocean plays an important role in the global Earth system and its impact on climate change has been widely and thoroughly studied (IPCC 2019, 2023). From the viewpoint of Fluid Mechanics, the ocean might be one of the most difficult configuration possible: it is a large-scale stratified fluid with

a free surface whose temperature, salt density and viscosity are not homogeneous, evolving in a rotating spherical-like frame with irregular boundaries and which lies below either a lighter fluid or large portions of its buoyant solid phase. A total account of all physical processes happening in the ocean is not conceivable at the present stage of scientific knowledge. Therefore many hypotheses must be made in order to carry out any theoretical study, preventing a complete global description. Water waves, in particular, are associated with some important climate-related natural disasters, like e.g. tsunamis or coastlines wearing away. Their generation, evolution and associated strength must hence be evaluated thoroughly in order to increase the accuracy of forecasting methods and eventually come up with adaptive solutions.

It seems unlikely that independent scientific communities could provide meaningful answers to these important issues (and their possible future consequences) without interacting with each other openly. Indeed, such a complex problem should be tackled in every possible ways and the theoretical, computational, experimental and observational works should be considered as a whole. With that in mind, the work presented here aims at using methods from both the theoretical and the computational world extensively. The text is therefore written in a way primarily accessible to people originating from either of these communities.

In the pages that constitute this introductory chapter, we will try our best to provide a survey of important mathematical and physical results regarding water waves and related physical processes, without making the distinction between the different possible approaches to the same problem. Of course, the present considerations are subject to the author's personal affinity with theoretical and computational studies and, therefore, not all experimental work may be referred to. After this, certainly incomplete, *state of the art* discussion, we shall motivate the work done in the present doctoral thesis to understand why it has been carried out and where its conclusions lie.

#### Mathematical results on the Water Waves problem

In the vast majority of the theoretical result the author is aware of, the Water Waves problem relates to the mathematical description of a homogeneous incompressible, possibly viscous, fluid subject to a constant gravitational force. It is usually encompassed between a possibly unfathomable solid boundary: the bed and a time-varying interface between the fluid and the void (or a lighter secondary fluid which is commonly disregarded): the free surface. In the present work, the former will also be referred to as the bottom, the topography, the bathymetry or, simply, the ground. In light of the physical properties of the ocean, we understand that this already corresponds to a greatly simplified framework. In chapter 1, we shall give a thorough motivation of the Partial Differential Equations (PDEs, or models) emerging once a few hypotheses have been made.

#### I.1. The free-surface Navier-Stokes equations

Describing viscous fluids, the Navier-Stokes equations are widely considered as the most fundamental laws of fluid mechanics. They were obtained independently by Navier (1821) and by Stokes (1845). Using modern notations, they read

$$\partial_t \boldsymbol{u} + \boldsymbol{u} \cdot \nabla \boldsymbol{u} + \frac{1}{\rho} \nabla p = \nu \Delta \boldsymbol{u} + \boldsymbol{g}$$

$$\nabla \cdot \boldsymbol{u} = 0,$$

where u is the fluid's velocity, p its pressure,  $\rho > 0$  its density and  $\nu > 0$  its kinematic viscosity (both being supposed homogeneous). These equations will be discussed thoroughly in chapter 1. For the moment, we will only mention some of their general properties.

In the whole space  $\mathbb{R}^d$  ( $d \leq 4$ ), the existence of global (in time) weak (turbulente) solutions has been established in the pioneering article of Leray (1934b). In two space dimensions (d=2), the uniqueness of these weak solutions has been established by Lions and Prodi (1959) (it is also a byproduct of Leray 1934a). Solutions that are even weaker are known to exist in any dimension (Hopf 1950). The global existence of unique stronger smooth solutions has been shown by Ladyženskaya (1958) in 2d for arbitrary initial data, and in 3d for small initial data by Fujita and Kato (1964). An extension of this last case to arbitrarily large initial data does not seem to raise any interest.

The case of a solid boundary will not be treated thereafter as it would be too long, but we must mention the book of Temam (1984). In order to describe viscous free-surface water waves, the Navier-Stokes equations should be supplemented with boundary conditions. Neglecting the air lying above the water and the effects of surface tension, it is natural to assume that the complete stress tensor vanishes on the time-dependent free surface  $\Gamma_i(t)$  (i standing for interface, see figures 1.6, 1.7, 2.6, 2.3 for the notations),

$$p\hat{\boldsymbol{n}} - \nu\rho \Big[\boldsymbol{\nabla}\boldsymbol{u} + (\boldsymbol{\nabla}\boldsymbol{u})^{\intercal}\Big] \cdot \hat{\boldsymbol{n}} = -\gamma\kappa\hat{\boldsymbol{n}} \qquad \text{on } \Gamma_i(t),$$

with  $\hat{n}$  the normal vector pointing in the air/void domain,  $\kappa$  the surface curvature (or the sum of the principal curvatures in space dimension  $d \geqslant 3$ ) and  $\gamma$  the surface tension coefficient. Should a bottom topography  $\Gamma_b$  exist, the associated boundary conditions can be of free-slip/Navier type of no-slip/Dirichlet type,

$$\left\{ oldsymbol{u} \cdot \hat{oldsymbol{n}} = 0 \\ \hat{oldsymbol{n}} \times \left[ oldsymbol{\nabla} oldsymbol{u} + (oldsymbol{\nabla} oldsymbol{u})^{ op} \right] \cdot \hat{oldsymbol{n}} = 0 \end{array} \right\} \quad ext{(free-slip/Navier)} \qquad \qquad oldsymbol{u} = 0 \quad ext{(no-slip/Dirichlet)}.$$

An early mathematical result regarding this system is the one of Solonnikov (1977), in which is considered a bounded domain whose boundary is entirely free (like e.g. a droplet). The more physically motivated case of a periodic or infinite horizontal fluid encompassed between a topography  $\Gamma_b$  and a free surface  $\Gamma_i(t)$  was first mathematically studied by Beale (1981), in which a local existence result is proved when surface tension is present and the no-slip/Dirichlet boundary condition is assumed. This result has later been extended to the case of vanishing surface tension by Allain (1987) or Guo and Tice (2013c). Assuming small initial conditions also yields global existence results, with surface tension (Beale 1984; Nishida and Teramoto 2004) or without it (Guo and Tice 2013a,b). Many of these studies use the lagrangian formulation of fluid mechanics (which will be introduced in chapter 2, the underlying idea being to use the fluid itself as a time-dependent coordinate system) and therefore, as a byproduct, apply to breaking water waves too. The case of an infinitely deep ocean has been treated in Masmoudi and Rousset (2017). To the author's knowledge, the case of slip/Navier boundary conditions imposed on  $\Gamma_b$  has only been treated by Bresch and Noble (2011).

As already mentioned, most results regarding the free-surface Navier-Stokes system are proved using the Lagrangian formulation of the equations. This somewhat eludes the difficult question of the interface advection scheme. Studies based on the Eulerian formulation (i.e. the one that has been introduced above) cannot do so: in order to close the set of equations, another one must be added to the formulation in order to describe the free surface at all times. This is usually achieved assuming that the fluid's interface corresponds to the graph of some function  $h: \mathbb{R}^{d-1} \to \mathbb{R}$ , depending only on the horizontal variable(s). When d=2 (i.e. when the free surface  $\Gamma_i(t)$  is a one-dimensional curve), h evolves through

$$\partial_t h = oldsymbol{u} \cdot oldsymbol{n} \qquad \text{with} \qquad oldsymbol{n} = egin{bmatrix} -\partial_x h \\ 1 \end{bmatrix}.$$

The vector  $\mathbf{n}$  is the non-normalised vector normal to  $\Gamma_i(t)$  associated with h. Adaptations to a higher dimension is straightforward. It is implicitly understood that the value of  $\mathbf{u}$  is taken on the free surface. Unfortunately, assuming that the free surface is represented by the graph of a function prevents any result to hold for breaking waves. To overcome this limitation, we shall work, as of chapter 2, with parametrised curves (when d=2) and surfaces (when  $d \geq 3$ ). We would like to remind the reader that the various equations appearing in this introduction will be motivated thoroughly in chapter 1.

#### I.2. The free-surface Euler equations

Both water and air are viscous fluids, but their viscosity being relatively small it may seem like a good idea to neglect the viscous term appearing in the Navier-Stokes equations in this particular case, yielding Euler's incompressible equations,

$$egin{aligned} \partial_t oldsymbol{u} + oldsymbol{u} \cdot oldsymbol{
abla} oldsymbol{u} + oldsymbol{1} \cdot oldsymbol{
abla} oldsymbol{p} &= oldsymbol{g} \ oldsymbol{
abla} \cdot oldsymbol{u} &= oldsymbol{0}. \end{aligned}$$

If the reader is not convinced by the above thorough and rigorous explanation of why we are allowed to use the inviscid equations, they would be completely right. We shall discuss the relevance of the viscosity in water waves in the second part of this work.

In the absence of boundary, the existence of global smooth solutions was established by Hölder (1933) and Wolibner (1933). Weaker solutions with bounded vorticity are also known to exist since the work Yudovich (1963). Later, Delort (1991) obtained an existence result for any initial vorticity in  $H^{-1}(\mathbb{R}^2)$  only (the notations for function spaces are defined in appendix A), as is the case of vortex sheets. A wider panorama of the results regarding Euler's equations is available in the classical books of Chemin (1995) or Majda and Bertozzi (2002). In all these mentioned results, the vorticity, defined as

$$\boldsymbol{\omega} = \boldsymbol{\nabla} \times \boldsymbol{u},$$

plays an important role. As we will see, it is directly linked with the viscous dissipation (should it be considered) and assuming its evanescence allows to introduce the velocity potential  $\phi$ , such that  $\boldsymbol{u} = \boldsymbol{\nabla} \phi$ , once some geometrical assumptions have been made on the fluid-containing domain.

Euler's equations being a first-order (in space and time) set of PDEs, closing the system once a wall has been added is done with less boundary conditions than for the Navier-Stokes equations (second order in space). In the case of a free surface, it is assumed that the pressure difference across the interface is exactly given by the surface tension. When there is no upper fluid, this yields

$$p = \gamma \kappa$$
 on  $\Gamma_i(t)$ .

Similarly, should a bottom topography exist, we can simply close the system by assuming that the fluid does not penetrate it. This is formalised as

$$\boldsymbol{u} \cdot \hat{\boldsymbol{n}}_b = 0$$
 on  $\Gamma_b$ ,

with  $\hat{n}_b$  the unit vector normal to the topography. Even though this natural condition seems to hold only for regular walls, it actually does not prevent to perform non-linear analysis on rather irregular domains too (Gérard-Varet and Lacave 2013).

Mathematical results regarding the inviscid water waves problem including a non-vanishing vorticity are scarce. This is mainly due to impossibility to rewrite the problem in d-1 space dimension(s) (whereas such simplification can be carried out when  $\omega=0$ ). Nevertheless this did not prevent (Lindblad 2005) to obtain a first local well-posedness result in 2d for a vanishing surface tension coefficient in infinite depth. Coutand and Shkoller (2007) then obtained a similar result with possibly non-vanishing  $\gamma$ . Finally, the three-dimensional case was treated in Zhang and Zhang (2008). When a bottom topography is not neglected, Castro and Lannes (2014, 2015) have been able to rewrite the problem with two (d-1)-dimensional quantities together with the d-dimensional vorticity  $\omega$  in order to obtain a well-posedness result and a rigorously defined shallow water asymptotic regime.

Some recent theoretical studies (Desjardins et al. 2020; Fradin 2025) have been interested in modelling the large-scale ocean instead. To this end, a flat one-dimensional free surface is imposed and a non-constant stratified density is studied.

#### I.3. The Water Waves equations

Assuming that the vorticity vanishes identically in the fluid domain, i.e. that  $\omega=0$ , it is allowed to work with the velocity potential  $\phi$  (as long as the water domain remains simply connected). Then, a surprising result due to Zakharov (1968) states that the irrotational water waves problem can be entirely and unambiguously rephrased using two (d-1)-dimensional quantities: the free-surface elevation  $\eta$  and the value  $\psi$  of the potential  $\phi$  on the interface  $\Gamma_i(t)$ . Furthermore, he showed that the resulting set of equations is in fact Hamiltonian with a canonical symplectic structure. Introductions to Hamiltonian PDEs and their associated structures can be found in the books of Kuksin (2000) or Craig (2000). The set of equations originally obtained by Zakharov has later been rewritten by Craig and Sulem (1993) using the Dirichlet-to-Neumann operator  $\text{DtN}[\eta]\psi$ , associating to  $\psi$  the value of  $\partial_n \phi$  on the free surface, thus removing every occurring to  $\phi$  in the equations. Should we follow their method, we obtain the most studied Water Waves

equations, also called the Zakharov-Craig-Sulem formulation of the problem,

$$\begin{cases} \partial_t \eta = \mathrm{DtN}[\eta] \psi \\ \\ \partial_t \psi = -g \eta - \frac{1}{2} \big| \vec{\nabla} \psi \big|^2 + \frac{1}{2} \frac{ \big[ \mathrm{DtN}[\eta] \psi + \vec{\nabla} \psi \cdot \vec{\nabla} \eta \big]^2}{1 + |\vec{\nabla} \eta|^2}, \end{cases}$$

with  $\vec{\nabla}$  denoting the gradient in the horizontal direction(s) only (see chapter 1) and g is the gravitational acceleration of the earth. The associated Hamiltonian is

$$\mathbf{H}[\eta,\psi] = \frac{1}{2} \int_{\mathbb{R}} \psi \, \mathrm{DtN}[\eta] \psi + \frac{1}{2} \int_{\mathbb{R}} g \eta^2 \qquad \text{such that} \qquad \left\{ \begin{array}{rcl} \partial_t \eta & = & \delta_\psi \mathbf{H} \\ \partial_t \psi & = & -\delta_\eta \mathbf{H}. \end{array} \right.$$

A minor modification should be made in order to take the surface tension into account. The major advantage of this formulation is that it somewhat reduces the study of non-breaking irrotational water waves to the study of the Dirichlet-to-Neumann operator  $DtN[\eta]\psi$  (e.g. Craig, Schanz, et al. 1997). However, its discovery tragically eluded the use of the lagrangian frame (as in the pre-DtN study of Craig, Sulem, and Sulem 1992). All's well that ends well: Craig (2017) was able to obtain a lagrangian formulation of the Water Waves equations in 2d (1d interface), thus describing overturning waves. In the present work, we will extend his new formulation to two-dimensional free surfaces, *i.e.* to the three-dimensional physical world (which happens to be the one the author lives in).

The mathematical analysis of the irrotational Water Waves problem did not wait for the Zakharov-Craig-Sulem formulation to appear. Indeed, the first local existence results are those of Nalimov (1974, infinite depth, without surface tension), Yosihara (1982, with a bottom, without surface tension) and Craig (1985, with a bottom, without surface tension). These pioneering results all assumed small initial data. The first local well-posedness results that lifted this assumption were those of Beyer and Günther (1998, capillary waves on the unit sphere) and Wu (1997, infinite depth, without surface tension). This last result was then extended to the three-dimensional case in Wu (1999). Lannes (2005) then obtained a well-posedness result in 2d and 3d with a topography. The case of non-vanishing surface tension coefficient was treated by Ambrose and Masmoudi (2009a,b, infinite depth) and by Ming and Zhang (2009, with a finite depth), in which the vanishing surface tension limit was also investigated. Better estimates of the time of existence have been obtained in Wu (2009, 2d, infinite depth, without surface tension) or Lannes (2013b, 2d or 3d, with a bottom). The previously mentioned results are not sharp, however. Indeed, employing results from paradifferential calculus (Bony 1981, Alinhac 1986), Alazard and Métivier (2009) obtained a paradifferential representation of the Dirichlet-to-Neumann operator whose utilisation allowed to obtained less regular solutions of the Water Waves equations without any assumption on the bottom topography. This was done in Alazard, Burq, et al. (2014a,b, with and without surface tension), making good use of results from Alazard, Burq, et al. (2011b) too. More recent results following this path are those of Wu (2019) and Ai et al. (2024).

A key assumption made by the previously mentioned results is the criterion formulated originally by Taylor (1950), stating that on the interface, the normal acceleration of the fluid should not get any higher than the normal component of the gravitational acceleration. Using Euler's momentum equation, this amounts to assume that

$$-\hat{\boldsymbol{n}}\cdot\boldsymbol{\nabla}p\Big|_{\Gamma_{i}(t)}\geqslant \mathrm{constant}>0,$$

with  $\hat{n}$  pointing outside of the fluid domain. In fact, Ebin (1987) showed that if the above condition does not hold initially, then the Water Waves problem is ill-posed.

For small regular initial data, the three-dimensional problem (two-dimensional free surface) enjoys better decay rates (due to dispersive effects) thant its 2d counterpart. Therefore, the first global existence results have been obtained in 3d by Wu (2010) and Germain et al. (2012), in deep water without surface tension and by Deng et al. (2017) with  $\gamma > 0$ . The more difficult two-dimensional case has been treated by Alazard and Delort (2015a,b), Ionescu and Pusateri (2015) and more recently by Ai et al. (2022) (all of these results without any topography and with vanishing capillary effects).

The case of two fluids with an interface, more physically relevant, is somewhat more involved due to the possible appearance of the Kelvin–Helmholtz instability (a modern treatment of which can be found in Benjamin and Bridges 1997a,b), or the Rayleigh-Taylor one in the breaking case. These issues have been

recently addressed from the mathematical point of view by Lannes (2013a) or Lannes and Ming (2015). In these studies, it is proved that both the gravity and the surface tension have a regularising effect on small length scales. The viscosity may have one too. In the author's opinion, it corresponds to the underlying mechanisms that prevents the splash (and splat) singularity to happen (Fefferman et al. 2016, Coutand and Shkoller 2014, 2016), while it can happen in the single-fluid formulation (Castro, Córdoba, et al. 2013, see also Castro, Córdoba, et al. 2019 or Coutand and Shkoller 2019 for the case of a viscous single fluid). Indeed, in 2d, as a wave breaks, it ultimately encloses an incompressible air pocket which has no other possibility but to flee the entrapment region with a high velocity below the plunging crest (this interpretation should be easier to understand by taking a look at one of the numerous schematic pictures appearing in this work, like e.g. figs. 1.14 or 2.6). In 3d, the air can leave from the sides and so such difficulty should not always happen.

A major difficulty inherent to free-surface inviscid flows is the appearance of small divisors in many estimates at the linear level. An introduction to these kinds of problem can be found in the book of Craig (2000). Most of the time, this issue is solved using a Nash (1956)–Moser (1966) iteration scheme (which is to be seen as a regularised Newton method). Such method was e.g. used to study standing waves by Iooss, Plotnikov, and Toland (2005), i.e. surface waves that are periodic in time and space and enjoy some symmetric properties. A similar method was later used by Iooss and Plotnikov (2009) to study the so-called diamond waves, which can be seen as a two-dimensional equivalent of Stokes' waves, as well as non-symmetric periodic wave trains (Iooss and Plotnikov 2011). We mention the recent work of Alazard and Shao (2025) who came up with a way to bypass the small divisors-related issues without relying on a Nash–Moser iterative method using tools from paradifferential calculus.

Incorporating emerging boundaries to the study remains a challenging topic. Indeed, the results mentioned in the previous paragraphs all set aside this possibility. However, the interaction of waves and structures is an important contemporary subject: it allows to model ice shelves, floating bodies or beaches for instance. Alazard, Burq, et al. (2011a) treated vertical walls using a periodic reflection method. The study of de Poyferré (2019) and that of Ming and Wang (2021) observed that the problem could be treated for small values of the contact angle. More recently, Lannes and Ming (2024) were able to treat more general cases at the linear level. The inherent difficulties associated with the boundary conditions do not seem to be easier to handle with reduced models, unfortunately (Beck and Lannes 2022).

Finally, we would like to mention two interesting applications of the well-posedness theory. For instance, Alazard, Baldi, et al. (2018) studied the controllability of the water waves equations from an arbitrary small region of the domain. Then, Alazard and Zuily (2024) proved a conservation result for water waves that is similar to the Virial theorem of classical mechanics.

There exists a vast and plenteous literature interested in asymptotic regimes of the Water Waves equations. We do not treat it thoroughly as it remains somewhat distant to the work presented here. We refer the reader to the book of Lannes (2013b) or the *mémoire d'habilitation* of Duchêne (2021) for comprehensible introductions to these topics. A few of these irrotational regimes will be discussed at the beginning of chapter 5.

#### II. Boundary layers and the vanishing viscosity limit

An important part of our work will be concerned with the appearance of boundary layers in the flow associated with viscous water waves. A possible interpretation of the results of Swann (1971) and Chemin (1996) is that, when considering flows with very small viscosities (more rigorously speaking, flows with high values of the Reynolds number), the only things that eventually prevent the use of Euler's equations instead of the Navier-Stokes system are boundaries. Indeed, the former are first-order in space while the latter are second-order. Therefore, closing the two systems when boundaries are present is done using different numbers of boundary conditions. As the viscosity decreases, the difficult question is what happens to the excess condition? This is an important example of a singular limit.

To the author's knowledge, the only available mathematical result regarding this limit in the case of Water Waves is the one of Masmoudi and Rousset (2017), in infinite depth and without surface tension. The second part of the present work will be devoted to investigating numerically the case of finite depth

with either the free-slip/Navier boundary conditions or the no-slip/Dirichlet ones. Indeed, experimental evidences of Grue and Kolaas (2017) shows that boundary layers appear below the free surface as well as the water bed.

Why should we study the vanishing viscosity limit in the first place? As mentioned in the previous section, both water and air are nearly inviscid fluids on large scales (high Reynolds number). Therefore, should the limit hold, the difference between the solutions of Euler's equations and of the Navier-Stokes system should be small, thus motivating the use of inviscid models like the Water Waves equations, or any of their asymptotic regimes.

Any good book on Fluid Dynamics contains an introduction to boundary layer theory from the viewpoint of Physics (Batchelor (1967), Landau and Lifshitz (1987) or Guyon et al. (2012) being common examples). More recent references include the *grimoires* of Sychev et al. (1998), Schlichting and Gersten (2017) and Ruban (2018). Shorter introductory reviews can also be found in the introductions of the articles of Widmann and Tropea (2015) and Nguyen van yen, Waidmann, et al. (2018).

Let us first discuss the free-slip/Navier conditions in the absence of free surfaces. On non-flat topographies, they give rise to a vorticity sheet of size  $\nu^{\frac{1}{2}}$  (with  $\nu$  the viscosity) in which the vorticity is uniformly bounded in  $\nu$  (Iftimie and Planas 2006; Iftimie and Sueur 2011). The limit  $\nu \to 0$  has been shown to hold by e.g. Masmoudi and Rousset (2012). More recently, Gérard-Varet, Lacave, et al. (2018) obtained a similar result on rough domains: the Navier-type condition seems rather well-behaved. Numerical evidences by Nguyen van yen, Farge, et al. (2011) and Nguyen van yen, Waidmann, et al. (2018) show that this might not remain true for a viscosity-dependent slip length (which does not seem relevant for water waves).

Unfortunately, the most physically motivated boundary conditions are of no-slip/Dirichlet type. Indeed, fluids lying on walls tend to stick to them due to viscous interactions, thus creating some drag which is absent from the limit Euler system. Such vorticity sheet are characterised, in contrast with the Navier boundary layers, by a vorticity which scales as  $\nu^{-\frac{1}{2}}$ . When this vorticity remains confined in the vicinity of the wall, the size of the Dirichlet-type boundary layer is still  $\nu^{\frac{1}{2}}$  so that, formally, we can expect convergence to a vortex sheet. Whether this assertion actually holds remains an open question. Indeed, since the pioneering experimental work of von Kármán (1911), we know that there exists cases where the vorticity generated near the wall is shed in the bulk flow. It may even happen that a turbulent behaviour arises, for which the viscous dissipation does not disappear as  $\nu \to 0$ , thus preventing Euler's equation to be the correct asymptotic system.

In his well-known 1904 article, Prandtl proposed a reduced set of equations to study the behaviour of Dirichlet-type vortical layers, through a formal rescaling of the Navier-Stokes equations. Later, Goldstein (1948) explicited instabilities arising in Prandtl's equations, characterised by an adverse pressure gradient, that is, a pressure gradient working in the a direction opposite to the flow's direction outside the vorticity sheet. These computations were extended to higher order by Stewartson (1958), without disproving the conclusions of Goldstein (1948) however. The influence of this adverse pressure gradient have been studied mathematically by Dalibard and Masmoudi (2019). In fact, the analytical literature regarding Prandtl's system is extensive. To name but a few, Gérard-Varet and Dormy (2010) actually proved that Prandtl's equations are in fact linearly ill-posed in Sobolev spaces, while it has been shown many times that the analytical framework was better behaved (see Oleinik (1966) for a global well-posedness result with a somewhat non-physical assumption of monitonicity of the background flow, or Sammartino and Caflisch (1998a) for a local well-posedness result). Indeed, in this latter regime, Sammartino and Caflisch (1998b) have been able to construct solutions of the Navier-Stokes system in the half-space by gluing solutions of the inviscid Euler system and of Prandtl's system. The threshold between the analytical framework and the Sobolev regularity has been found by Gérard-Varet and Masmoudi (2015) to correspond to some Gevrey space.

In light of the shortcomings of Prandtl's equation to provide an accurate and precise explanation for the separation mechanism, a finer model has been conjectured: the triple deck theory (Stewartson 1974) in which the boundary layer is split into three small portions (the decks). However, this system does not seem to behave any better in Sobolev spaces (Dietert and Gérard-Varet 2022; Gérard-Varet, Iyer, et al. 2023). A similar conclusion holds for the Interactive Boundary Layer model, in light of the result of Dalibard, Dietert, et al. (2017).

Whether, generally speaking, the presence of a boundary layer actually prevents the vanishing viscosity limit to hold or not remains a complex topic. In light of Kato (1984)'s result, the convergence to Euler's inviscid solution is only a matter of boundary layers. More precisely, Kato proved that this result holds on

a time interval [0,T] if and only if the following criterion,

$$\nu \int_0^T \mathcal{E}(\boldsymbol{u}(t)) dt \longrightarrow 0$$
 as  $\nu \to 0$ ,

is verified, with  $\mathcal{E}(\boldsymbol{u})$  the enstrophy defined on the fluid domain  $\Omega$  as

$$\mathcal{E}(\boldsymbol{u}) = \int_{\Omega} \left| \boldsymbol{\nabla} \boldsymbol{u} \right|^2.$$

This is the exact term arising in the energy equation for the Navier-Stokes equation with Dirichlet boundary conditions. A most striking second part of Kato's theorem asserts that we can replace  $\omega$  with a neighbourhood of size  $O(\nu)$  and still have equivalence with the vanishing viscosity limit. The information on the convergence Navier-Stokes  $\to$  Euler is thus entirely contained in a boundary layer whose size is even smaller than the standard boundary layer thickness  $O(\nu^{\frac{1}{2}})$  (for a bounded domain  $\Omega$  with Dirichlet boundary conditions only). Later, Kelliher (2007) showed, among other equivalent formulations of Kato's criterion, that the term  $|\nabla u|^2$  could in fact be replaced with the squared vorticity  $\omega^2$ . Mathematical results that effectively obtained a convergence result with Dirichlet boundary layers are scarce. We mention the work of Sammartino and Caflisch (1998b) for the case of a flat plate and the more recent work of Drivas et al. (2024) regarding the Prandtl–Batchelor theorem. An interpretation of this last result, also motivated by the pioneering work of Stokes (1847) on oscillating boundary layers, is that an oscillating or periodic flow might stabilise the vorticity lying in the vicinity of the wall and thus prevent separation and turbulence to happen. We shall come back to this observation in the second part of this work in the particular case of water waves.

Before moving on, we wish to make a short  $d\acute{e}tour$  through the theory of vortices and oceanic flows. Indeed, singular limits associated with viscous flows are also present in other fields and it can be enlightening to discuss them. For instance, Gallagher, Gallay, and Lions (2005) considered the two-dimensional Navier-Stokes equations on the whole space  $\mathbb{R}^2$  whose initial vorticity is a Dirac mass, yielding an Oseen vortex. The vanishing viscosity limit is not so straightforward in such case as the 2d Euler equation with an initial Dirac mass vorticity is not defined (indeed, the previously mentioned result of Delort (1991) provides solutions for initial vorticities in  $H^{-1}$  only, and  $\delta_x \in H^{-1-\varepsilon}$  for every  $\varepsilon > 0$ ). This result was later extended by Gallagher and Gallay (2005) to consider solutions of the Navier-Stokes equations whose initial vorticity is a (Radon) measure. Another example of singular limit is found in the oceanographical work of Dalibard and Saint-Raymond (2018), concerned with the Munk equation. They show that separation does occur on certain parts of the boundary and, using geometrical considerations, construct a solution converging to a non-trivial limit system.

# III. Wave Breaking

When arriving to the shore, water waves (or, more precisely, waves crests) ultimately break. Such well-known phenomenon happens in the open ocean too. Surprisingly, this is quite a long standing scientific subject with very recent developments (McAllister et al. 2024). Wiegel (1964) and Galvin (1968) proposed an experimental classification of breaking waves into four subcategories: spilling, surging, collapsing and plunging breakers. Only the last one can be effectively modelled mathematically. Indeed, plunging breakers are characterised by an overhanging region while the others all possess small-scales attributes (droplets, bubbles, foam or white water), making the water-air interface description rather unpleasant (to say the least). In chapter 2, we shall propose a definition of (plunging) wave breaking, a stronger two-dimensional version being

**Definition** (Wave breaking). At time  $t \ge 0$ , let  $\gamma(t, \cdot) : \mathbb{R} \to \mathbb{R}^2$  a parametrisation of the free surface of the wave. We say that  $\gamma(t, \cdot)$  has broken if its horizontal component, denoted  $\gamma_x(t, \cdot)$  fails to be injective.

Such mathematical definition will be made clearer soon enough. We clearly see why it fails to describe other types of breaking: in such cases, the interface cannot be represented by a parametrised curve  $\gamma(t, \bullet)$  (or a parametrised surface in 3d) because of non-connected components.

Working with a parametrised interface has many advantages: it allows wave breaking (in the sense of the above definition) but it also enables the use of lagrangian coordinates, following the fluid elements. This shall

be put to the test in the first part of this work. Beforehand, we would like to review the physical literature on the subject (the mathematical one has already been exposed in sec. I) for the sake of completeness.

#### III.1. Instabilities triggering wave breaking

As observed in the review articles of Peregrine (1983) and Banner and Peregrine (1993), the instabilities arising for finite amplitudes waves, leading to the breaking phenomenon, have been identified principally in the deep water regime. Benjamin and Feir (1967) showed that deep water periodic waves of frequency  $\omega$  could transfer energy at an exponentially increasing rate to neighbouring modes of frequency  $\omega \pm \delta$ , with  $\delta$  depending on the wave's steepness. The resulting wavetrain is modulated (see the experimental results shown in fig. 2 of Benjamin 1967), meaning that an amplitude-increasing envelope appears, eventually reaching the breaking threshold.

The Benjamin-Feir instability explains an increase of amplitude happening in periodic wavetrains but fails at explaining the breaking phenomenon itself. The *superharmonics* instability, originally found by Longuet-Higgins (1978) and later confirmed by Tanaka (1983, 1985), does it. More detailed and comprehensible accounts can be found in the works of Tanaka et al. (1987) or Jillians (1989). The underlying idea is simple: considering a periodic wave train with wave number  $k_0$  and steepness  $k_0a$ , once a certain steepness threshold  $k_0a_c$  has been reached, the modes associated to wavenumbers  $k > k_0$  (i.e. superharmonic modes) will become unstable. The resulting effect will be a substantial decrease of the front-facing part of the wave, coupled with an increase of the backward-facing part, resulting in a steepening which ultimately leads to breaking. It is interested to note that his instability occurs before the thresholding 120° limitting corner wave has been reached.

In three space dimensions, there exists another amplitude-related instability discovered by McLean et al. (1981) (discussed in greater details in McLean 1982), called the type-II instability, resulting in a span-wise modulation of the amplitude (as in the Benjamin-Feir two-dimensional instability).

On shallow waters, Banner and Peregrine (1993) argue that the modulational instabilities become less important and that the steepening of the wavetrain is due to the slowly varying topography. On the other hand, in the near-shore analysis the superharmonics instability remains important to understand the breaking mechanism, as shown by Tanaka et al. (1987).

#### III.2. Numerical simulations of breaking waves

Analytical solutions of the Water Waves problem in the presence of an overhanging region are, unfortunately, currently not available. Therefore, since the original work of Longuet-Higgins and Cokelet (1976, 1978), most non-experimental results regarding wave breaking have been of computational nature. They can essentially be split up into two categories: irrotational inviscid simulations based on potential theory using the Lagrangian framework, and two-fluids simulations of the Navier-Stokes system using an Eulerian advection scheme.

The fact that the two-dimensional inviscid Water Waves problem can be recast, when the vorticity is identically zero, as a one-dimension problem on the interface, has motivated authors to study irrotational breaking water waves as early as the seventies. Longuet-Higgins and Cokelet (1976) mapped the deep-water problem to the unit disk embedded in the complex plane and used tools from potential theory to compute the normal velocity numerically at each time iteration. This method was later extended by New et al. (1985) to take in account the effects of a non-flat water bed (mapping the physical domain to an annulus instead of a disk). Vinje and Brevig (1981) carried out a similar study on a flat topography by dropping out the map from the physical space to the disk. Soon after, Baker, Meiron, et al. (1982) introduced well-studied reformulations of the inviscid problem, cast in the complex plane: the *vortex* and *dipole* methods (recently justified rigorously in Dormy and Lacave (2024), using methods of Arsénio et al. (2020)). The numerical method of Dold et al. (1986), described more thoroughly in Dold (1992), was the first to completely set aside the complex plane and use the Boundary Integral Method instead. This method was improved by Grilli et al. (1989) so that, as soon as the needed computational power became available, three-dimensional simulations were carried out (Guyenne and Grilli 2006; Pomeau, Le Berre, et al. 2008).

Since recasting the equations on the free surface cannot be accomplished in the viscous case, the Navier-Stokes simulations only became possible at the very end of the nineties (setting aside the work of Monaghan

(1994), based on the Smoothed-Particles Hydrodynamics method). The pioneering work of Chen et al. (1999) successfully set what would become the standard way to simulate viscous breaking waves, that is a two-fluids formulation with an Eulerian interface tracking scheme (like the Volume of Fluid method (Nichols and Hirt 1975) or the level-set method of Osher and Sethian (1988)). The book of Sethian (1999) contains an enjoyable introduction to these implicit interface representation procedures. An interesting aspect of these methods is that they provide a description of the post-splash dynamics, even though there does not seem to exist any theoretical justification of the accuracy of the data generated in this manner to the author's knowledge. For instance, Iafrati (2009) was able to study the vorticity generation (and hence, the energy dissipation) happening right after the free surface self-intersection in 2d. The three-dimensional case was later studied by Di Giorgio et al. (2022). Following a similar method, Lubin and Glockner (2015) observed numerically the appearance of air filaments wraping around the cylindrical air pocket obtained when the overhanging region of a plunging breaker falls down on itself. The capillary effects on breaking waves have been studied thoroughly in Deike, Popinet, et al. (2015) and Deike, Melville, et al. (2016), making use of the Gerris library (Popinet 2003, 2009), in order to tune-up a turbulence model. This last project was later extended in Mostert et al. (2022). Hydrodynamical instabilities arising after the breaking has been triggered were the subject of the work of Lubin, Kimmoun, et al. (2019).

Surprisingly, even though they describe the same physical phenomenon, the inviscid studies are rarely compared with viscous ones, and *vice-versa*. Moreover, the scientific questions addressed using Euler's equations seem to be completely disjoint from the ones for which the Navier-Stokes system is used. The numerical method described in chapter 3 aims at taking the best of both worlds.

#### III.3. The shape of water waves

The numerical methods mentionned in the previous section were not (all) developed for the sole satisfaction of reproducing highly nonlinear physics. They have also been used extensively to motivate more general physical laws. For instance, there exists a long-standing debate concerned with the shape of the air pocket lying below the overhanging region. Longuet-Higgins (1982) overlayed a *cubic upwelling* curve which matches conspicuously well its envelope. However, the fluid dynamics community seems to prefer the  $\sqrt{3}$ -ellipse of New (1983), even though the resulting comparison is far less convincing to the author's opinion.

A somewhat more concerned long-standing question is could a finite-time cusp-like singularity appear? Put differently, in the inviscid and irrotational regime, starting from an initially smooth datum, could the free-surface fail to remain  $C^1$  and see an triangular crest appear before the splash singularity occurs? Numerical evidences of a curvature blow-up are rare, mainly because most numerical methods tend to be regularised (using Fourier truncation or any other technique). Fontelos and De La Hoz (2010) claim to have proved that, should such singularity appear, then it should take the form of a logarithmic spiral. However, taking a closer look at their proof, they actually showed that self-similar solutions could lead to such solution, but it is nowhere argued that this is the only possibility. However, starting from an initial condition with non-vanishing circulation, they provide an interesting numerical simulation with a plausible logarithmic singularity. Another type of curvature blow-up was conjectured in the work of Baker and Xie (2011), starting from a second-order Lagrangian Stokes wave in deep water. The author did not manage to reproduce their difficult simulation to put it to the test, however.

Regarding the theoretical approach of this issue, Longuet-Higgins (1980a,b) proposed analytical solutions of the potential problem in the complex planes whose free surface (that is, the p=0 implicitly defined curve in his framework) approaches a cusp-like singularity (in infinite time unfortunately). An interpretation of his work is as follows: carrying out an extension of the pressure outside the fluid domain, the cusp would correspond to a saddle-point lying on the p=0 line. Later, Pomeau and Le Berre (2012) studied self-similar cone-like solutions of the free-surface Euler equation in order to obtain scaling laws followed by the solution as the singularity appears. Whether their work applies to initially smooth ocean-like free surfaces remains an open question.

# IV. Scope of the present work

In the following pages, we will propose a mathematical basis for a theory of wave breaking up to the splash singularity. We will motivate a set of equations that describe this phenomenon, in the spirit of the Water Waves equations, starting from the most basic physical laws and hypotheses. Emphasis shall be put upon the well-foundedness of two major assumptions: neglecting viscosity and the vorticity. To be more precise, let us describe in depth our programme.

#### IV.1. Mathematical modelling of Breaking Water Waves

In the first part of this work, we discuss the straight path starting from the most basic physical assumptions (matter is continuous, water is homogeneous, etc.) and leading to the most general models of fluid mechanics (Euler's, the Navier-Stokes and the Water Waves equations). This will be done in chapter 1. Most of the subsequent chapters will correspond to short or long detours, in which these assumptions will be motivated, disproved or bypassed, eventually leading to a different destination. In the remaining of chapter 1, the structure of the Zakharov-Craig-Sulem shall be discussed and water waves on any curved surface will be carried out using tools from differential geometry.

The second chapter aims at extending Craig (2017)'s work on overhanging waves to parametrised free surfaces. Indeed, in his original article, a generalisation of the Water Waves equations for parametrised one-dimensional free surfaces is carried out, thus describing the breaking phenomenon. Loosely speaking, they can be seen as a Lagrangian version of the Water Waves equations introduced as follows: let  $\gamma(t, \cdot) : \mathbb{R} \to \mathbb{R}^2$  a (smooth for the moment) parametrisation of the water-void interface in two dimension. Let  $\psi$  the value of the velocity potential on this very interface. Then both these quantities evolve through the Breaking Waves equations (a name proposed by the author)

$$\begin{cases} \partial_t \gamma = \frac{\mathrm{DtN}[\gamma]\psi}{|\partial_s \gamma|} \hat{\boldsymbol{n}} + \frac{\partial_s \psi}{|\partial_s \gamma|} \hat{\boldsymbol{\tau}} \\ \partial_t \psi = -g \gamma_z + \frac{1}{2} \left( \frac{\partial_s \psi}{|\partial_s \gamma|} \right)^2 + \frac{1}{2} \left( \frac{\mathrm{DtN}[\gamma]\psi}{|\partial_s \gamma|} \right)^2, \end{cases}$$

with s the arbitrarily-chosen curvilinear coordinate,  $\hat{\tau}$  the unit tangent vector to the interface,  $\hat{n} = \hat{\tau}^{\perp}$  the unit normal vector to the free surface and  $\mathrm{DtN}[\gamma]\psi$  the curvilinear Dirichlet-to-Neumann operator. Their generalisation to two-dimensional free surfaces will be introduced in chapter 2 (eqs. 2.16). This set of equations enjoys a non-canonical Hamiltonian structure (2.17) through the following Hamiltonian functional,

$$\mathrm{H}[\pmb{\gamma}, \psi] = \frac{1}{2} \int_{\mathbb{R}^d} \psi \, \mathrm{DtN}[\pmb{\gamma}] \psi + \frac{g}{2} \int_{\mathbb{R}^d} (\gamma_z^2) \, \hat{\pmb{z}} \cdot \hat{\pmb{n}} \, |\partial_s \pmb{\gamma}|.$$

We will also prove that as long as no breaking happens, they can be reduced to the usual Water Waves equations.

#### IV.2. On the limit of vanishing viscosity in (Breaking) Water Waves

Having motivated a set of equations for breaking waves in the inviscid irrotational regime, a natural question is: are the effects of viscosity really negligible? The second part of this work will try to provide an answer to this question, even though it actually raises even more questions by trying to do so.

Comparisons between the viscous and invicid irrotational solutions of the Water Waves problem will be handled numerically. To this end, we will introduce a computational scheme to approximate the solution of the Navier–Stokes system in chapter 3, which differs significantly from the other numerical methods the author is aware of. Indeed, the advection is made explicit through the use of the Arbitrary Lagrangian–Eulerian method (Helluy et al. 2005), allowing to decrease the interpolation error as to decrease the viscous dissipation to values that were never achieved with the purely Eulerian methods mentioned in sec. III.2. However, in contrast with these previous studies, the simulation must stop as soon as the interface intersects itself. The implementation using FreeFEM (Hecht 2012), parallelisation and validation of this framework will also be discussed thoroughly.

Chapter 4 will make use of this code to investigate the viscosity effects on a one-dimensional interface, over a flat topography. This is done comparing the viscous solution to the inviscid irrotational one, computed through the robust method of Dormy and Lacave (2024). A sample result is shown in figure 4.6, allowing to conjecture the convergence with the slip/Navier set of boundary conditions.

In chapter 5, no-slip/Dirichlet conditions will be imposed on a non-flat topography in order to investigate the stability of the resulting boundary layer. This is first done for a sharp rectangular step lying at the bottom, for which vorticity separation can be seen (fig. 5.6) but also with a smooth mollified step, for which the separation happens as soon as a curvature threshold has been reached. The most striking aspect of the detached vorticity is that is does not seem to disappear in the limit of vanishing viscosity limit, therefore preventing the limitting system (should it exist) to be the (irrotational) Water Waves equations.

I

# Mathematical Modelling of Breaking Water Waves

This first part is devoted to the introduction of a unified framework for the study of Breaking Waves.

We first introduce the physical laws of fluid dynamics before discussing the usual Eulerian description of Water Waves.

This description fails at describing the breaking phenomenon. Hence, in a second time, we introduce the lagrangian description of the water-air interface and derive a new mathematical model that describes overhanging waves up to the "splash" singularity.

# The Eulerian description of Water Waves

"I don't like sand. It's coarse and rough and irritating... and it gets everywhere"

Anakin Skywalker, In: Star Wars: Episode II – Attack of the Clones (2002, dir. G. Lucas)

The mathematical description of the ocean has always been a most studied, yet challenging question in Fluid Mechanics. Indeed the variety of physical, chemical and sometimes even biological phenomena at stake, coupled with a delicate mixing of scales, obliges us to make strong assumptions (simplifications) about the flow in order to ease the computations.

This chapter is devoted to the physical derivation of the mathematical laws that describe the ocean in the near-shore regime (soon to be defined). We will emphasize and discuss the physical relevance of each assumption we make along the way. We will also discuss asymptotic regimes of the obtained equations in a rigorous manner.

The description of the water-air interface will be made in an Eulerian way, hence assuming that a wave cannot overturn. A way to overcome this limitation will be introduced in the next chapter.

# I. The Navier-Stokes equations

Let us start with a physical motivation of the Navier–Stokes equations<sup>1</sup>. We are interested in a macroscopic description of matter and therefore suppose that it can be described as a continuum **(H1)**. We consider a fluid of density  $\rho(t, \boldsymbol{x})$  and dynamic viscosity  $\mu(t, \boldsymbol{x})^2$ , occupying a time-varying region  $\Omega(t)$  of the space  $\mathbb{R}^{d+1}$  (with dimension d=1 or 2; see figure 1.1). For now, both  $\rho$  and  $\mu$  are not assumed constant. Typical values of  $\rho$  and  $\mu$  in the fluids at stake are given in table 1.1.

The state of the physical system is represented by the instantaneous and localised velocity  $\boldsymbol{u}(t,\boldsymbol{x})$  and pressure  $p(t,\boldsymbol{x})$ . In order to derive a system of partial differential equations for  $\boldsymbol{u}$ , p,  $\rho$  and  $\mu$ , we follow classical fluid dynamics books<sup>3</sup>. A more rigorous derivation of the Navier-Stokes equations (or Euler's equations) is related to Hilbert's sixth problem which remains open to this day.

#### I.1. Derivative of volume integrals

The formal (physical) motivation of the Navier-Stokes equations we shall present here relies on vector calculus identities and manipulations

<sup>&</sup>lt;sup>2</sup>As we shall assume the incompressibility of the flow later on (hypothesis **H2**), we won't talk about the second viscosity here.

Fluid	$\rho[\rm kgm^{-3}]$	$\mu  [\mathrm{Pa} \mathrm{s}]$
Water Seawater Air	$1.00 \cdot 10^3 \\ 1.02 \cdot 10^3 \\ 1.29$	$1.01 \cdot 10^{-3}  1.09 \cdot 10^{-3}  1.81 \cdot 10^{-5}$

**Table 1.1** – Typical values of  $\rho$  and  $\mu$  at a temperature of 20 [°C]. The values for the seawater are taken at with a salinity of 35%.

<sup>&</sup>lt;sup>1</sup>Historical note: these equations were first obtained in Navier (1821), with a small oversight that was corrected in his following publications. They were later (re)obtained in Stokes (1845).

<sup>3</sup>See e.g., the classical books of Batchelor (1967), Granger (1995), Johnson (1997), Lamb (1932) or Landau and Lifshitz (1987) in english; Guyon et al. (2012) or Huerre (2012) in french.

 $^{1}i.e.$  at time t, the map  $\Sigma_{t}: \mathring{\mathcal{V}} \to \mathcal{V}(t) \subset \mathbb{R}^{d+1}$  is  $C^{1}$ , bijective with  $C^{1}$  inverse.

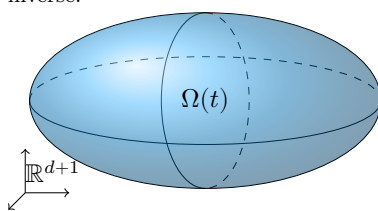


**Figure 1.1** – A general domain  $\Omega(t)$  containing the fluid.

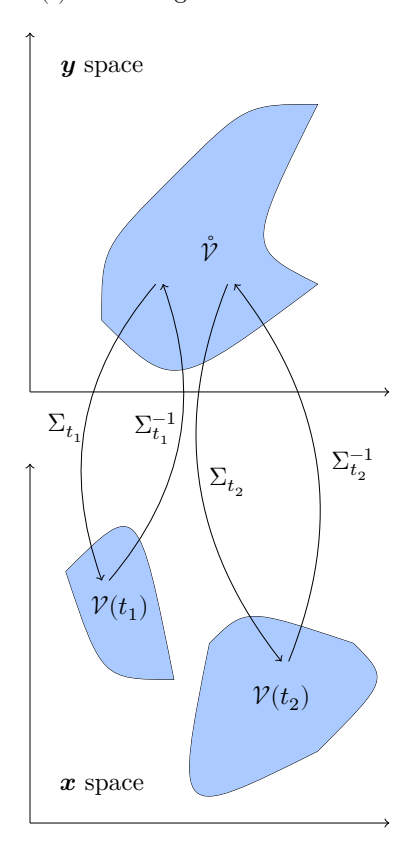


**Figure 1.2** – The configuration of lemma 1.1.

of volume integrals. Before we begin this process, let us prove an extremely usefull identity. Let  $\mathring{\mathcal{V}}$  a bounded subset of  $\mathbb{R}^{d+1}$ . Let  $\Sigma_t$  a  $C^1$ -diffeomorphism from the fixed volume  $\mathring{\mathcal{V}}$  to a bounded subset  $\mathcal{V}(t) \subset \mathbb{R}^{d+1}$  with  $C^1$  time dependency (see figure 1.2)<sup>1</sup>. Let us define the velocity of the points  $\boldsymbol{x}$  in the domain  $\mathring{\mathcal{V}}$ ,

$$\boldsymbol{v}(t,\boldsymbol{x}) = \left\lceil \frac{\partial \Sigma_t}{\partial t} \circ \Sigma_t^{-1} \right\rceil (\boldsymbol{x})$$

We are then able to prove the following result, sometimes called Reynolds' transport theorem,

**Lemma 1.1** (Reynolds 1903).

$$\frac{\mathrm{d}}{\mathrm{d}t} \left( \int_{\mathcal{V}(t)} f(t, \boldsymbol{x}) \, d\boldsymbol{x} \right) = \int_{\mathcal{V}(t)} \partial_t f(t, \boldsymbol{x}) + \boldsymbol{\nabla} \cdot \left( f(t, \boldsymbol{x}) \boldsymbol{v}(t, \boldsymbol{x}) \right) \mathrm{d}\boldsymbol{x}$$

*Proof.* From the definition of  $\Sigma_t$ , we have

$$\int_{\mathcal{V}(t)} f(t, \boldsymbol{x}) \, \mathrm{d}\boldsymbol{x} = \int_{\mathring{\mathcal{V}}} f\Big(t, \Sigma_t(\boldsymbol{y})\Big) \det\Big(\mathbf{J}_{\boldsymbol{y}} \Sigma_t\Big) \, \mathrm{d}\boldsymbol{y},$$

where  $\mathbf{J}_{\boldsymbol{y}}\Sigma_t = \left(\boldsymbol{\nabla}_{\boldsymbol{y}}\Sigma_t\right)^{\top}$  is the Jacobian<sup>2</sup> of the transformation  $\Sigma_t$ . The second integral having a domain independent of t, we can intervert the derivative and integral sign,

$$\frac{\mathrm{d}}{\mathrm{d}t} \left( \int_{\mathcal{V}(t)} f(t, \boldsymbol{x}) \, \mathrm{d}\boldsymbol{x} \right) = \int_{\mathring{\mathcal{V}}} \partial_t f\left(t, \Sigma_t(\boldsymbol{y})\right) \det\left(\mathbf{J}_{\boldsymbol{y}} \Sigma_t\right) \mathrm{d}\boldsymbol{y} 
+ \int_{\mathring{\mathcal{V}}} \left[ \boldsymbol{\nabla} f\left(t, \Sigma_t(\boldsymbol{y})\right) \cdot \partial_t \Sigma_t(\boldsymbol{y}) \right] \det\left(\mathbf{J}_{\boldsymbol{y}} \Sigma_t\right) \mathrm{d}\boldsymbol{y} 
+ \int_{\mathring{\mathcal{V}}} f\left(t, \Sigma_t(\boldsymbol{y})\right) \, \partial_t \det\left(\mathbf{J}_{\boldsymbol{y}} \Sigma_t\right) \mathrm{d}\boldsymbol{y}.$$

The third integral can be related to v through the use of Jacobi's identity for differentiating a determinant,

$$\begin{split} \partial_t \Big( \det \big( \mathbf{J}_{\boldsymbol{y}} \boldsymbol{\Sigma}_t \big) \Big) &= \det \big( \mathbf{J}_{\boldsymbol{y}} \boldsymbol{\Sigma}_t \big) \ \operatorname{tr} \Big[ \big( \mathbf{J}_{\boldsymbol{y}} \boldsymbol{\Sigma}_t \big)^{-1} \cdot \partial_t \big( \mathbf{J}_{\boldsymbol{y}} \boldsymbol{\Sigma}_t \big) \Big] \\ &= \det \big( \mathbf{J}_{\boldsymbol{y}} \boldsymbol{\Sigma}_t \big) \ \operatorname{tr} \Big[ \big( \mathbf{J}_{\boldsymbol{x}} \boldsymbol{\Sigma}_t^{-1} \circ \boldsymbol{\Sigma}_t(\boldsymbol{y}) \big) \cdot \mathbf{J}_{\boldsymbol{y}} \Big( \partial_t \boldsymbol{\Sigma}_t(\boldsymbol{y}) \Big) \Big] \\ &= \det \big( \mathbf{J}_{\boldsymbol{y}} \boldsymbol{\Sigma}_t \big) \ \operatorname{tr} \Big[ \mathbf{J}_{\boldsymbol{x}} \Big( (\partial_t \boldsymbol{\Sigma}_t) \circ \boldsymbol{\Sigma}_t^{-1}(\boldsymbol{x}) \Big) \circ \boldsymbol{\Sigma}_t(\boldsymbol{y}) \Big] \\ &= \det \big( \mathbf{J}_{\boldsymbol{y}} \boldsymbol{\Sigma}_t \big) \ \operatorname{tr} \Big[ \mathbf{J}_{\boldsymbol{x}} \boldsymbol{v} \Big( t, \boldsymbol{\Sigma}_t(\boldsymbol{y}) \Big) \Big] \\ &= \det \Big( \mathbf{J}_{\boldsymbol{y}} \boldsymbol{\Sigma}_t \big) \ \operatorname{tr} \Big[ \boldsymbol{\nabla}_{\boldsymbol{x}} \boldsymbol{v} \Big( t, \boldsymbol{\Sigma}_t(\boldsymbol{y}) \Big) \Big] \\ &= \det \Big( \mathbf{J}_{\boldsymbol{y}} \boldsymbol{\Sigma}_t \big) \ \boldsymbol{\nabla}_{\boldsymbol{x}} \cdot \boldsymbol{v} \Big( t, \boldsymbol{\Sigma}_t(\boldsymbol{y}) \Big), \end{split}$$

where  $\operatorname{tr}(A)$  denotes the trace of the matrix A. We have use the fact that  $\nabla_{\boldsymbol{y}} \Sigma_t$  is invertible at all times, the fact that  $\operatorname{tr}(A) = \operatorname{tr}(A^\top)$  and the properties of the inverse of a Jacobian matrix. Doing the reverse transformation we find that

$$\frac{\mathrm{d}}{\mathrm{d}t} \left( \int_{\mathcal{V}(t)} f(t, \boldsymbol{x}) \, \mathrm{d}\boldsymbol{x} \right) = \int_{\mathcal{V}(t)} \partial_t f + \boldsymbol{v} \cdot \boldsymbol{\nabla} f + f \, \boldsymbol{\nabla} \cdot \boldsymbol{v}$$

<sup>&</sup>lt;sup>2</sup>The chosen notations about vector calculus are described in appendix B, in which are also listed some usefull identities.

$$= \int_{\mathcal{V}(t)} \partial_t f + \boldsymbol{\nabla} \cdot \Big( f \boldsymbol{v} \Big),$$

as desired.  $\Box$ 

The lemma 1.1 will be used extensively in the present work. Observe that for a solenoidal vector field v, i.e. a field such that

$$\nabla \cdot \boldsymbol{v} = 0$$
,

we have another relation

$$\nabla \cdot (fv) = v \cdot \nabla f.$$

**Remark 1.2.** The regularity of the boundary  $\partial \mathcal{V}(t)$  doesn't change the result. By extending the diffeomorphism to a small neighborhood outside the boundary, we can bypass this issue.

When  $\mathbf{v} = \mathbf{u}$  the velocity of the fluid, then  $\mathcal{V}(t)$  is seen as moving with the flow from the fixed reference frame of the observer. This is called the *Eulerian* point of vue, which shall be investigated in the present chapter. On the other hand, when  $\mathbf{v} = 0$ , the reference frame is that of the fluid elements<sup>1</sup>. This is the  $Lagrangian^2$  point of vue, more suited to the study of breaking waves, as we shall see. When  $\mathbf{v}$  is neither  $\mathbf{u}$  nor 0, we shall speak of the  $Arbitrary\ Lagrangian-Eulerian\ (ALE)^3$  point of vue, as will be used in the numerical method described in chapter 3.

#### I.2. The continuity equation and incompressibility

Historically, the first mathematical law of fluid dynamics stems from the conservation of mass. It can arguably be traced back to da Vinci's pioneering analogy between sections of trees and rivers' flow rates<sup>4</sup>. Until the end of this chapter, we use the Eulerian  $(\boldsymbol{v}=\boldsymbol{u})$  point of vue. Let  $\mathcal{V}(t) \subset \Omega(t)$  a bounded volume with closed boundary  $\partial \mathcal{V}(t)$  which moves with the fluid. The massive elements originally in  $\mathcal{V}(0)$  will be in  $\mathcal{V}(t)$  by definition. Hence the total mass in  $\mathcal{V}(t)$ , defined by

$$M\big[\mathcal{V}(t)\big] = \int_{\mathcal{V}(t)} \rho(t, \boldsymbol{x}) \,\mathrm{d}\boldsymbol{x},$$

is conserved. The physical interpretation is that each fluid element keeps the same mass throughout the experiment. Owing to lemma 1.1 with v = u, this means that

$$\frac{\mathrm{d}}{\mathrm{d}t} M \left[ \mathcal{V}(t) \right] = \frac{\mathrm{d}}{\mathrm{d}t} \left( \int_{\mathcal{V}(t)} \rho(t, \boldsymbol{x}) \, \mathrm{d}\boldsymbol{x} \right)$$

$$= \int_{\mathcal{V}(t)} \partial_t \rho + \boldsymbol{\nabla} \cdot \left( \rho \boldsymbol{u} \right) \qquad \text{by lemma 1.1}$$

$$= 0 \qquad \text{by hypothesis}$$

As this must be true within each material volume<sup>5</sup>, we have the *continuity equation* in the fluid,

$$\partial_t \rho + \boldsymbol{\nabla} \cdot (\rho \boldsymbol{u}) = 0. \tag{1.1}$$

Let us now assume that the density of the fluid in consideration is homogeneous (H2),

$$\rho(t, \boldsymbol{x}) = \rho_{\mathrm{flu.}} > 0 \qquad \text{in } \mathcal{V}(t),$$

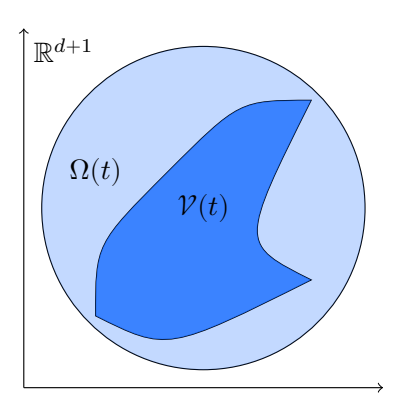


Figure 1.3 – The arbitrary material domain  $\mathcal{V}(t) \subset \Omega(t)$ .

<sup>1</sup>Note that since we have made the continuum hypothesis (H1), we cannot speak of fluid particle. Instead we use the term fluid element, which can be thought of as an infinitesimal volume of fluid.

<sup>2</sup>Lagrange (1781)

<sup>3</sup>Hirt et al. (1974)

<sup>4</sup> "All the branches of trees, each degree of their height, combined, are equal to the size of their trunk.

All the branches of waters, in each degree of their length being of equal movement, are equal to the size of their origin"

- Leonardo da Vinci (1500)

Translated and cited in the review article of Marusic and Broomhall (2021).

<sup>&</sup>lt;sup>5</sup>*i.e.* each volume  $\mathcal{V}(t)$  moving with velocity  $\boldsymbol{u}$ .

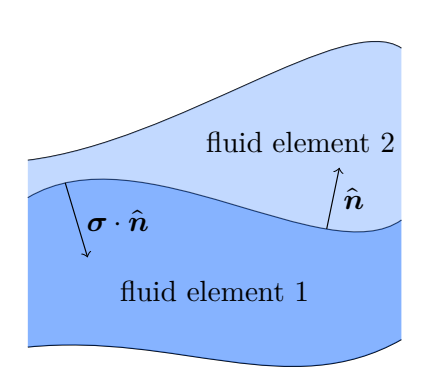


**Figure 1.4** – The superficial force applied by the fluid element 2 on the fluid element 1 in the inviscid case.

<sup>2</sup>Indeed.

$$\begin{split} \int_{\partial \mathcal{V}(t)} &- p(t, \boldsymbol{y}) \hat{\boldsymbol{n}} \, \mathrm{dS}(\boldsymbol{y}) = \\ &= \int_{\partial \mathcal{V}(t)} - p(t, \boldsymbol{y}) \mathbb{1} \cdot \hat{\boldsymbol{n}}(t, \boldsymbol{y}) \, \mathrm{dS}(\boldsymbol{y}) \\ &= \int_{\partial \mathcal{V}(t)} \boldsymbol{\sigma}(t, \boldsymbol{y}) \cdot \hat{\boldsymbol{n}}(t, \boldsymbol{y}) \, \mathrm{dS}(\boldsymbol{y}) \end{split}$$

at all time  $t \ge 0$ . In the large-scale analysis of the ocean and of the atmosphere, this is unambiguously false. The density of water and air are stratified in such regimes. However, as we are interested only in the near-shore oceanic scale, the density fluctuations of both these fluids can be neglected on short time scales. This important hypothesis quickly leads to the *incompressibility condition*,

$$\nabla \cdot \boldsymbol{u} = 0. \tag{1.2}$$

Should we consider a two-fluids interface (e.g. water and air), each fluid will be incompressible in its domain. No mixing could happen without transgressing the homogeneity assumption. Hence we must also suppose that, in the presence of an interface, the two fluids under consideration are immiscible (H3).

#### I.3. The momentum equation

A second law of fluid mechanics can be obtained from Newton's fundamental law of dynamics applied to a fluid element. Let us once again consider a material volume  $\mathcal{V}(t)$ . The fluid's momentum lying within  $\mathcal{V}(t)$  is defined as

$$P[V(t)] = \int_{V(t)} \rho(t, \boldsymbol{x}) \boldsymbol{u}(t, \boldsymbol{x}) d\boldsymbol{x}.$$

Its rate of change is related to the force which is exerted on each fluid element inside V(t),

$$\frac{\mathrm{d}}{\mathrm{d}t} \mathbf{P} \big[ \mathcal{V}(t) \big] = \int_{\mathcal{V}(t)} \mathbf{F}(t, \boldsymbol{x}) \, \mathrm{d}\boldsymbol{x}. \tag{1.3}$$

Typically, the total force can be split into an exterior part  $\rho g$  (gravity in our case), only depending on the fluid's nature and state via the  $\rho$  prefactor, and an intrinsic contribution from the neighboring fluid elements  $\nabla \cdot \sigma$ , with the tensor  $\sigma$  called the *stress tensor*.

Why the divergence? Since the intrinsic contribution stems from the other fluid elements (fig. 1.4), it corresponds to a force applied on the boundary of the element<sup>1</sup> under consideration. The stress tensor  $\sigma$  represents this very boundary force and Gauß's theorem gives us the corresponding volume force through

$$\int_{\mathcal{V}(t)} \boldsymbol{F}_{\text{boundary}} = \int_{\partial \mathcal{V}(t)} \boldsymbol{\sigma}(t, \boldsymbol{y}) \cdot \hat{\boldsymbol{n}}(t, \boldsymbol{y}) \, \mathrm{dS}(\boldsymbol{y}) = \int_{\mathcal{V}(t)} \boldsymbol{\nabla} \cdot \boldsymbol{\sigma}(t, \boldsymbol{x}) \, \mathrm{d}\boldsymbol{x}.$$

Intuitively, the stress  $\sigma$  depends on the fluid's local state and is thus a (possibly non-linear) function of its properties p,  $\rho$ ,  $\mu$  and u. Let us investigate the easiest shapes of  $\sigma$  commonly used.

I.3.1. Stress tensor for inviscid fluids. The simplest element-wise boundary force we can think of is the *pressure* p. It is applied in the direction perpendicular to the interface in the direction pointing inside the fluid element (fig. 1.4), resulting in<sup>2</sup>

$$\label{eq:sigma} {\pmb\sigma}(t,{\pmb x}) = -p(t,{\pmb x}) \cdot \mathbbm{1}_{d\times d},$$

where  $\mathbb{1}_{d\times d}$  is the identity matrix in dimension d=2 or 3. This leads to the following volume force

$$\int_{\mathcal{V}(t)} \mathbf{F}_{\text{boundary}} = \int_{\mathcal{V}(t)} -\mathbf{\nabla} p(t, \mathbf{x}) \, d\mathbf{x}. \tag{1.4}$$

<sup>&</sup>lt;sup>1</sup>Recall that a fluid element is in fact an infinitesimal volume.

Putting (1.3) and (1.4) together and applying lemma 1.1, we obtain the following integral equation,

$$\int_{\mathcal{V}(t)} \partial_t \left( \rho_{\text{flu.}} \boldsymbol{u} \right) + \boldsymbol{\nabla} \cdot \left( \rho_{\text{flu.}} \boldsymbol{u} \otimes \boldsymbol{u} \right) = \int_{\mathcal{V}(t)} - \boldsymbol{\nabla} p + \rho_{\text{flu.}} \boldsymbol{g}$$
(1.5)

As in section I.2, the control volume V(t) being arbitrary, the integrands on each side of (1.5) must be equal everywhere in the domain  $\Omega(t)$ ,

$$\partial_t (\rho_{\mathrm{flu.}} \boldsymbol{u}) + \boldsymbol{\nabla} \cdot (\rho_{\mathrm{flu.}} \boldsymbol{u} \otimes \boldsymbol{u}) = -\boldsymbol{\nabla} p + \rho_{\mathrm{flu.}} \boldsymbol{g}.$$

Making use the incompressibility of the flow (1.2), due to the homogeneity hypothesis  $\mathbf{H2}^1$ , this can also read

$$\partial_t \boldsymbol{u} + \left(\boldsymbol{u} \cdot \boldsymbol{\nabla}\right) \boldsymbol{u} = -\frac{1}{\rho_{\text{flu.}}} \boldsymbol{\nabla} p + \boldsymbol{g}. \tag{1.6}$$

The couple (1.2)–(1.6) are Euler's equations<sup>2</sup>. They describe the motion of inviscid fluids. Both water and air have small viscosities (table 1.1) so it would seem like a good idea to neglect it. In forthcoming chapters, we shall discuss the well-foundedness of this assumption in details. To put it in a concise manner, things are not that easy...

I.3.2. Stress tensor for Newtonian fluids. A major drawback of Euler's equations (1.2)–(1.6) is that a fluid element traveling parallel to another does not drag it along. This is at the heart of d'Alembert's paradox<sup>3</sup>.

To introduce this physical phenomenon, one must take into account the effects of viscosity into the stress tensor. The simplest possibility is to assume that the viscosity is homogeneous,

$$\mu(t, \mathbf{x}) = \mu_{\text{flu}}$$
 everywhere in  $\Omega(t)$ , (1.7)

(typical values of  $\mu_{\text{flu.}}$  for water, seawater and air are given in table 1.1) and proportional to the symmetric part of the gradient tensor (H4), so that<sup>4</sup> (see fig. 1.5 for a schematic representation)

$$\boldsymbol{\sigma}(t, \boldsymbol{x}) = -p \mathbb{1}_{d \times d} + 2\mu_{\text{flu}} \mathbf{S}(\boldsymbol{u}), \tag{1.8}$$

where

$$\mathbf{S}(\boldsymbol{u}) = \frac{1}{2} \Big[ \boldsymbol{\nabla} \boldsymbol{u} + \Big( \boldsymbol{\nabla} \boldsymbol{u} \Big)^t \Big].$$

A fluid for which this holds is said to be *newtonian*. Its kinematics is given by the following equation in the material volume  $\mathcal{V}(t)^5$ ,

$$\begin{split} \int_{\mathcal{V}(t)} \partial_t \Big( \rho_{\text{flu.}} \boldsymbol{u} \Big) + \boldsymbol{\nabla} \cdot \Big( \rho_{\text{flu.}} \boldsymbol{u} \otimes \boldsymbol{u} \Big) = \\ &= \int_{\mathcal{V}(t)} - \boldsymbol{\nabla} p + \mu_{\text{flu.}} \Delta \boldsymbol{u} + \rho_{\text{flu.}} \boldsymbol{g}. \end{split}$$

As it should hold for all material volumes  $\mathcal{V}(t)$ , we actually have

$$\partial_t \boldsymbol{u} + \left(\boldsymbol{u} \cdot \boldsymbol{\nabla}\right) \boldsymbol{u} = -\frac{1}{\rho_{\text{flu}}} \boldsymbol{\nabla} p + \nu_{\text{flu}} \Delta \boldsymbol{u} + \boldsymbol{g}. \tag{1.9}$$

The couple (1.2)–(1.9) are called the incompressible Navier–Stokes equations, which describe newtonian fluids. The quantity

$$u_{\rm flu.} = \frac{\mu_{\rm flu.}}{\rho_{\rm flu.}}$$

<sup>1</sup>The continuity equation (1.1) can also be used and yields the same result, with a non-constant positive  $\rho$ .

<sup>2</sup>Originally obtained in Euler (1757)

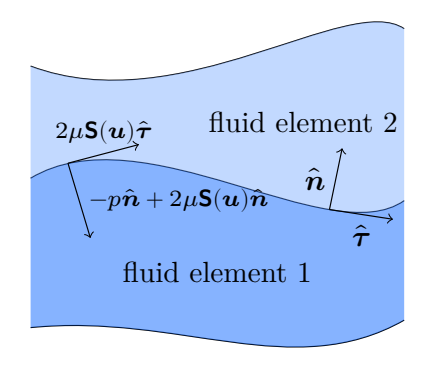


**Figure 1.5** – The superficial force applied by the fluid element 2 on the fluid element 1 in the viscous case.

<sup>3</sup>d'Alembert (1752) showed that an incompressible inviscid fluid cannot apply a drag onto a solid body.

<sup>4</sup>For a compressible fluid, the stress tensor has more terms and another parameter called the second viscosity. This is of no use here.

<sup>5</sup>Indeed,

$$\boldsymbol{\nabla}\cdot\boldsymbol{\mathbf{S}}(\boldsymbol{u}) = \frac{1}{2}\Delta\boldsymbol{u}$$

since the incompressibility condition (1.2) quickly yields that

$$\nabla \cdot \left( \nabla u \right)^t = 0.$$

is the kinematic viscosity of the fluid.

Remark 1.3. In both Euler's equations (1.2)–(1.6) and the Navier-Stokes equations (1.2)–(1.9), the time evolution of the pressure is not explicitly given, *i.e.* there is no equation for  $\partial_t p$ . In fact the pressure evolves in order to ensure the incompressibility of the flow; it can be seen as a Lagrange multiplier enforcing the incompressibility constraint. This statement can be made rigorous (Evans 2010, sec. 8.4.4, thm. 6).

# II. Boundary conditions

We now discuss the various boundary conditions that are typically used in the study of Water Waves in an Eulerian framework. To this end, let us introduce the two space domains  $\Omega_{\rm w}(t)$  and  $\Omega_{\rm a}(t)$  containing, respectively, the water and the air, see figs. 1.6 and 1.7 below. Note that these domains are time-varying. They are open in  $\mathbb{R}^{d+1}$ .

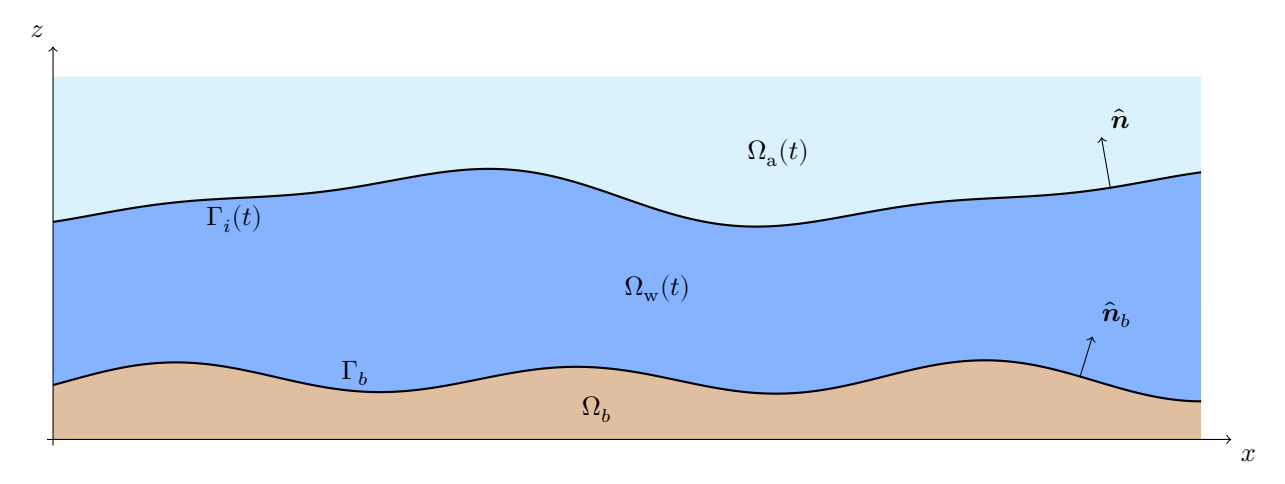


Figure 1.6 – 2d schematic representation of the water domain  $\Omega_{\rm w}(t)$ , the air domain  $\Omega_{\rm a}(t)$  and the soil domain  $\Omega_b$ . Their interfaces are  $\Gamma_i(t)$  and  $\Gamma_b$ .

 $^1{
m Mathematically},$  this amounts to

$$\Gamma_i(t) = \overline{\Omega_{\rm w}(t)} \cap \overline{\Omega_{\rm a}(t)},$$

and

$$\Gamma_b = \overline{\Omega_{\rm w}(t)} \cap \overline{\Omega_b}.$$

The latter does not depend on time even though  $\Omega_{\rm w}(t)$  does. This is because we assume that no contact between the air  $\Omega_{\rm a}(t)$  and the topography  $\Omega_b$  happens.

We denote by  $\Gamma_i(t)$  the water-air interface and by  $\Gamma_b$  the bottom boundary of the domain<sup>1</sup>, *i.e.* the contact surface between the water and the soil  $\Omega_b$ . We suppose that there is no interface between the air  $\Omega_a(t)$  and the bottom  $\Omega_b$ , *i.e.* 

$$\overline{\Omega_{\rm a}(t)}\cap\overline{\Omega_b}=\emptyset. \tag{H5}$$

The Euler equations (1.2)–(1.6) or the Navier-Stokes equations (1.2)–(1.9) describe the water in the domain  $\Omega_{\rm w}(t)$  and the air in  $\Omega_{\rm a}(t)$ . Whether the former equations are preferred to the latter is one of the fundamental question that will be discussed in the present work.

Remark 1.4. We assume the existence of a bottom boundary  $\Gamma_b$  and a soil domain  $\Omega_b$ , see fig. 1.6. We could also have supposed that the water column extends to infinity in the z negative direction. This is called the *deep-water* regime. As we will be interested in the wave breaking phenomenon, which happens mostly near the shore, we shall not discuss the deep-water regime, only motivated for the study of the

the open ocean.

Since Euler's equations are first-order in space while the Navier-Stokes equations are second-order, different boundary conditions must be used in both cases. We shall discuss both separately.

#### II.1. The inviscid boundary conditions

Should we assume that both water and air are inviscid **(H6)**, Euler's equations must be used in both  $\Omega_{\rm a}(t)$  and  $\Omega_{\rm w}(t)$ . On the bottom boundary  $\Gamma_b$ , we suppose that water does not penetrate the solid bottom.

$$\boldsymbol{u} \cdot \hat{\boldsymbol{n}}_b = 0 \quad \text{on } \Gamma_b,$$
 (1.10)

with  $\hat{\boldsymbol{n}}_b$  the unit vector perpendicular to the topography  $\Gamma_b$ , pointing into  $\Omega_{\rm w}(t)$ , see fig. 1.6. This will be referred to as the *impenetrability* condition later on.

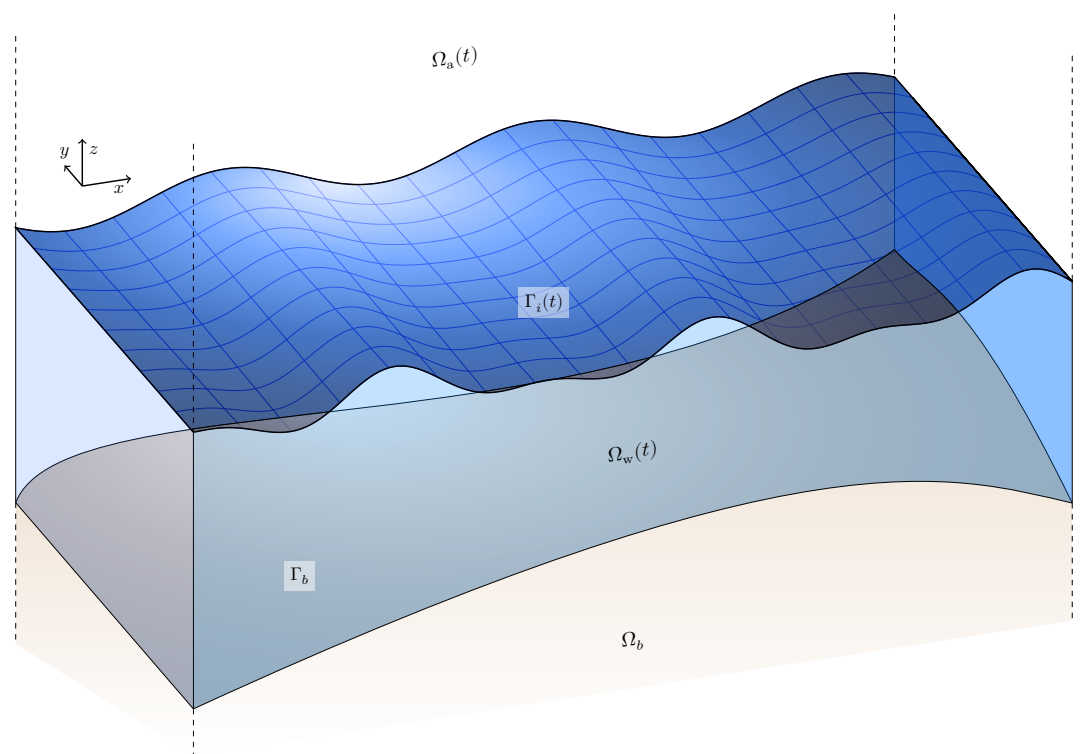


Figure 1.7 – 3d schematic representation of the water domain  $\Omega_{\rm w}(t)$ , the air domain  $\Omega_{\rm a}(t)$  and the soil domain  $\Omega_b$ . Their interfaces are  $\Gamma_i(t)$  and  $\Gamma_b$ .

On the top interface, we assume that the pressure is continuous during the change of phase, as well as the normal component of the velocity<sup>1</sup>,

$$p_{\rm a} = p_{\rm w}$$
 and  $\boldsymbol{u}_{\rm a} \cdot \hat{\boldsymbol{n}} = \boldsymbol{u}_{\rm w} \cdot \hat{\boldsymbol{n}}$  on  $\Gamma_i(t)$ , (1.11)

with  $\hat{\boldsymbol{n}}$  the unit vector perpendicular to  $\Gamma_i(t)$ , pointing into the water domain  $\Omega_{\rm w}(t)^2$ . This will be called the *dynamic* boundary condition afterward.

Finally, we need a boundary condition for the air. To this end, we suppose that this fluid is at rest far from the free surface,

$$\mathbf{u}_a = 0 \quad \text{at } z \to +\infty.$$
 (1.12)

<sup>&</sup>lt;sup>1</sup>We cannot enforce the continuity of the tangential component of the velocity through the interface without getting an ill-posed problem (i.e. absence of solution). Indeed the jump of tangential velocity is fundamental. It corresponds to a vorticity sheet localised on  $\gamma_i(t)$ , which will be studied afterward.

 $<sup>^2 \</sup>text{We}$  use  $\boldsymbol{u}_{\rm w}$  and  $p_{\rm w}$  (respectively  $\boldsymbol{u}_{\rm a}$  and  $p_{\rm a})$  to denote the solution of Euler's equations in the water domain  $\Omega_{\rm b}(t)$  (resp.  $\Omega_{\rm a}(t)).$ 

#### II.2. The viscous boundary conditions

Should we use the Navier-Stokes equations instead, the boundary conditions (1.10) and (1.12) remain valid while (1.11) must be slightly modified and some new conditions must be added.

On the free surface  $\Gamma_i(t)$ , we now assume that both component of the velocity are continuous,

$$\boldsymbol{u}_{\mathrm{w}} = \boldsymbol{u}_{\mathrm{a}} \qquad \text{on } \boldsymbol{\Gamma}_{i}(t), \tag{1.13a} \label{eq:local_state}$$

and the normal stress is also continuous through the interface,

$$-p_{\mathbf{w}}\hat{\boldsymbol{n}} + 2\mu_{\mathbf{w}}\mathbf{S}(\boldsymbol{u}_{\mathbf{w}})\hat{\boldsymbol{n}} = -p_{\mathbf{a}}\hat{\boldsymbol{n}} + 2\mu_{\mathbf{a}}\mathbf{S}(\boldsymbol{u}_{\mathbf{a}})\hat{\boldsymbol{n}} \quad \text{on } \Gamma_{i}(t). \quad (1.13b)$$

On the bottom, two viscous conditions can be added. First the *Navier conditions*, where the impenetrability (1.10) is supplemented with the contraint that the tangential stress vanishes,

These conditions are known to prevent the appearance of a boundary layer in most cases<sup>1</sup>. However they are difficult to motivate from a physical perspective. Instead we could use the *no-slip*, or *Dirichlet* boundary conditions, saying that the velocity vanishes identically on the bottom,

$$\boldsymbol{u}_{\mathrm{w}} = 0 \quad \text{on } \Gamma_b.$$
 (1.15)

This condition, more physically relevant, shall create a boundary layer localised in the vicinity of the bottom  $\Gamma_b$ . We will discuss in chapter 5 its stability in order to conclude about the use of the irrotationality assumption (**H11**, yet to be discussed).

#### II.3. Neglecting the air

The boundary conditions (BCs) discussed in secs. II.1 and II.2 can be greatly simplified should we neglect the effects of air. Before discussing this assumption (H7), let us state the resulting BCs. Formally, this corresponds to letting  $\rho_{\rm a} \to 0$  and  $\mu_{\rm a} \to 0$ .

II.3.1. Inviscid BCs without air. The impenetrability (1.10) condition is not affected. Moreover, the far-field condition (1.12) makes no sense anymore. In the end, there the dynamic condition remains, taking the easier form

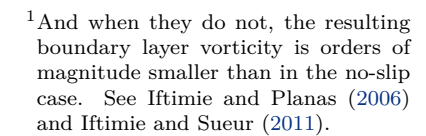
$$p_{\mathbf{w}} = 0 \qquad \text{on } \Gamma_i(t). \tag{1.16}$$

The vacuum above the water exerts no pressure over the interface. Another approach to this BC is to assume that air only applies a constant pressure  $p_a$ , the atmospheric pressure, on water. Since pressure only appears in Euler equations (1.2)–(1.6) through a gradient, it is possible to redefine the pressure up to the constant  $p_a$  without any impact on the velocity. This also yields (1.16).

II.3.2. Viscous BCs without air. Redefining  $p_{\rm w}$  up to the atmospheric pressure  $p_a$ , as was done above, and formally letting  $\mu_{\rm a}$  vanish, we get the so-called *stress-free* boundary conditions

$$p_{\mathbf{w}}\hat{\boldsymbol{n}} - 2\mu_{\mathbf{w}}\mathbf{S}(\boldsymbol{u}_{\mathbf{w}}) \cdot \hat{\boldsymbol{n}} = 0$$
 on  $\Gamma_{i}(t)$ . (1.17)

The water stress-tensor  $\boldsymbol{\sigma}_{\rm w}$  vanishes identically on the water-void interface.



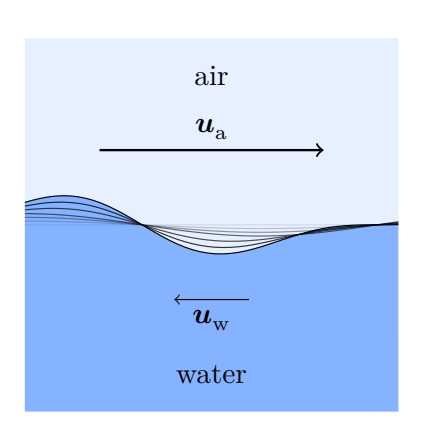


Figure 1.8 – Schematic representation of the development of the Kelvin-Helmholtz instability at the interface between water and air.

To what extent is **H7** well-motivated in the theoretical study of water waves? The answer is rather simple: it is rarely the case. Indeed waves are mainly generated by wind during a process that starts far from the shore<sup>1</sup>. The idea is simple: looking at (1.13), we can see that variations in the air pressure on the free surface generates perturbations in the water. This phenomenon coupled with the Kelvin-Helmholtz instability (fig. 1.8) arising at the interface between to fluids in the presence of a jump of tangential velocity, explain the appearance of waves at the surface of the ocean.

Hence, it seems unreasonable to neglect the effects of the air to study a phenomenon generated by these very effects. However, on short time-scales, in the near shore analysis and before the splash<sup>2</sup> has occured, we will rely on this assumption. In such conditions, air is responsible for the detachment of droplets near the crest of the wave, in the form of a spray. This hypothesis amounts to assuming that this won't have any impact on the overall shape of the wave. Furthermore, since no breaking will be permitted in this chapter (H8 below), that will not be an issue.

#### II.4. The kinematic condition, Eulerian advection

It has already been emphasised that both the water and air domains,  $\Omega_{\rm w}(t)$  and  $\Omega_{\rm a}(t)$ , are time-dependent. Indeed the interface  $\Gamma_i(t)$  moves with the fluid; it is composed of material fluid elements. Hence one must prescribe an advection scheme for this free surface. Most theoretical studies use the lagrangian framework, where the interface corresponds to the zero-value of a certain function  $F: \mathbb{R}_+ \times \mathbb{R}^d \to \mathbb{R}, ^3$ 

$$\Gamma_i(t) = \left[F(t, {\:\raisebox{3.5pt}{\text{\circle*{1.5}}}})\right]^{-1} \Bigl(\{0\}\Bigr).$$

The corresponding advection scheme is to solve the *transport equation* for F, in both fluids  $\Omega_{\rm w}(t) \cup \Gamma_i(t) \cup \Omega_{\rm a}(t)$ , with velocity  $\boldsymbol{u}_{\rm wa}$  built from  $\boldsymbol{u}_{\rm w}$ ,  $\boldsymbol{u}_{\rm a}$  and their boundary values,

$$\partial_t F + \boldsymbol{u}_{wa} \cdot \boldsymbol{\nabla}_{\boldsymbol{x}} F = 0. \tag{1.18}$$

This advection scheme is at the heart of the *eulerian* framework, subject of the present chapter. It is the basis of most numerical methods that have been used to study breaking water waves in the viscous case: the level-set method and the Volume of Fluids (VOF) method<sup>4</sup>.

However this general framework is not suited for theoretical studies as is. A more tractable form can be made assuming that no breaking occurs  $(\mathbf{H8})$ , *i.e.* supposing that F has the following shape<sup>5</sup>

$$F(t, \mathbf{x}) = F(t, \vec{x}, z) = z - h(t, \vec{x}). \tag{1.19}$$

The fact that the free surface is represented by the graph of a function h prevents the use of this framework to study breaking water waves, where h would need to be a multi-valued function. We shall see in chapter 2 that dropping out the eulerian formalism<sup>6</sup>, and replacing it with a lagrangian scheme, allows us to overcome this difficulty.

For now, let us rewrite the transport equation (1.18) using the hypothesis (1.19) above,<sup>7</sup>

$$\partial_t h + \vec{u} \cdot \vec{\nabla} h = u_z, \tag{1.20}$$

with  $\vec{\nabla} = (\partial_x, \partial_y)$  in 3d and  $\vec{\nabla} = \partial_x$  in 2d. Of course eq. (1.20) only makes sense when  $z = h(t, \vec{x})$ . It is called the *eulerian advection* 

<sup>1</sup>Janssen (2004, ch. 3), Kinsman (1965), Lamb (1932, art. 350).

<sup>2</sup>The moment the interface of the wave intersects itself after having broken, see fig. 1.14 below.

Notation. In this work, we make a distinction between vectors in  $\mathbb{R}^{d+1}$ , denoted in boldface like  $\boldsymbol{u}$ , and others lying in  $\mathbb{R}^d$ , with an overhead arrow  $\vec{u}$ . The latter will be usefull to represent quantities lying on the interface  $\Gamma_i(t)$  or on the topography  $\Gamma_b$ .

<sup>3</sup>Some hypotheses must be done on F in order to have a well-defined d-dimensional interface. Indeed F = 0 would give a space-filling free surface (whatever that means). In order to avoid such pathological cases, it is common to assume that F is (weakly) differentiable once with non-vanishing gradient.

$$|\nabla_{\boldsymbol{x}}F(t,\boldsymbol{x})|\neq 0$$

for all x, at all time  $t \ge 0$ . Such function can be constructed using e.g. the eikonal equation.

<sup>4</sup>see *e.g.* Chen et al. (1999), Deike, Melville, et al. (2016) and Deike, Popinet, et al. (2015), Di Giorgio et al. (2022), Mostert et al. (2022).

<sup>5</sup>Recall that vectors in  $\mathbb{R}^d$  (d=2 or 3) are denoted using boldface symbols (e.g. u), while vectors in  $\mathbb{R}^{d-1}$  are written with overhead arrows  $\vec{u}$ .

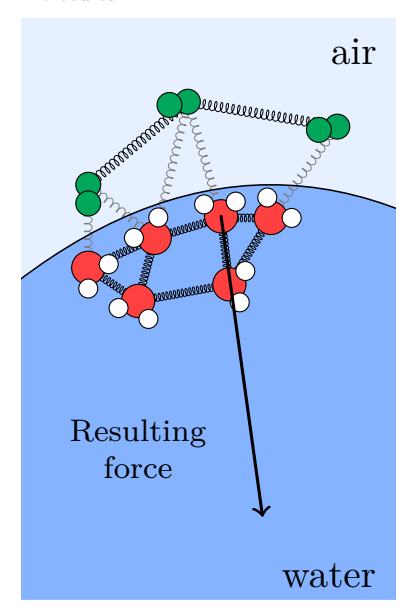
<sup>6</sup>In the following, the eulerian formalism shall referred to the advection equation after (1.19) has been assumed. The general eulerian viewpoint does not have such flaw. The issue here is (1.19)

 $^7 \vec{u}$  corresponds to the xy-projection of the velocity u,

$$ec{u} = u_x \qquad \qquad ext{for } d = 1,$$
  $= egin{bmatrix} u_x \ u_y \end{bmatrix} \qquad ext{for } d = 2.$ 

In the same manner,  $\boldsymbol{\nabla}_{\vec{x}}$  is  $\partial_x$  in 2d and  $(\partial_x,\partial_y)^T$  in 3d.

<sup>1</sup>Air is not only composed of dinitrogen molecules.



 $\odot$ : H<sub>2</sub>O molecule

 $\mathbb{C}: \mathbb{N}_2$  molecule

Figure 1.9 – Physical motivation of the surface tension: the molecular forces applied on a water molecule lying on the surface.

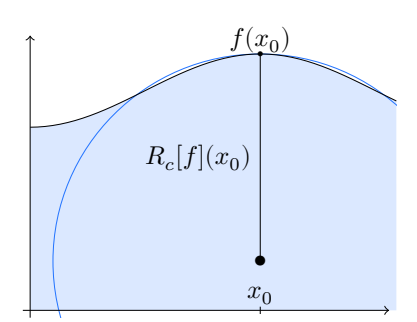


Figure 1.10 – The curvature radius  $R_c[f]$  of a function f at point  $x_0$ . The circle tangent to the graph of f at point  $x_0$  is shown in blue. Its radius is exactly  $R_c[f]$ .

equation. Most authors consider it as a boundary condition, referred to as the *kinematic condition*, even though it is an evolution equation by itself.

#### II.5. Surface tension

The capillary effects can be taken into account inside the dynamic boundary conditon directly (or neglected **(H9)**). Physically, surface tension arises from differences in intermolecular forces corresponding to water-water, dinitrogen-dinitrogen and dinitrogen-water molecular bonds<sup>1</sup>. Indeed the latter is weaker, which leads to a superficial force on the free surface which tends to decrease the curvature, *i.e.* to smooth out the boundary  $\Gamma_i(t)$  (fig. 1.9).

Let us define the signed curvature  $\kappa[f]$  of a twice-differentiable function  $f \in C^2(\mathbb{R}^{d+1})$ ,

$$\kappa[f] = \begin{cases} \frac{\partial_{xx} f}{\left(1 + (\partial_x f)^2\right)^{\frac{3}{2}}} &, \\ \frac{\left(1 + (\partial_x f)^2\right) \partial_{yy} f + \left(1 + (\partial_y f)^2\right) \partial_{xx} f - 2 \partial_x f \partial_y f \partial_{xy} f}{\left(1 + (\partial_x f)^2 + (\partial_y f)^2\right)^{\frac{3}{2}}} &, \end{cases}$$

respectively for d=1 and d=2. When d=1, the inverse of the curvature is called the *curvature radius*  $R_c[f] = \left(\kappa[f]\right)^{-1}$ . It corresponds to the radius of the circle tangent to the function f at a point x (fig. 1.10). When d=2, the curvature is the sum of the inverse curvature radius in the x direction and the inverse curvature radius in the y direction.

The effects of surface tension can be encompassed in the dynamic boundary conditions (1.16) and (1.17) directly. At the interface between two fluids, surface tension is represented by a jump in normal stress proportional to the curvature. When there is only one fluid, this leads to

$$p_{\mathbf{w}} = -\gamma_{\mathbf{w}} \kappa[\eta], \tag{1.21a}$$

$$p_{\rm w}\hat{\boldsymbol{n}} - 2\mu_{\rm w}\mathbf{S}(\boldsymbol{u}_{\rm w})\cdot\hat{\boldsymbol{n}} = -\gamma_{\rm w}\kappa[\eta]\hat{\boldsymbol{n}}, \tag{1.21b}$$

on  $\Gamma_i(t)$  for, respectively, an inviscid fluid and a viscous fluid. The factor  $\gamma_{\rm w}$  is the surface tension coefficient of the water-void interface. Its strength is of the order of  $7 \cdot 10^{-3} \, [{\rm N \cdot m^{-1}}]$ . For small values of  $\gamma_{\rm w}$  the effects of curvature tends to smooth out the interface. It will be argued in chapter 4 that this superficial force is the prevailing regularising mechanism, an order of magnitude stronger than viscosity.

#### III. Non-dimensionalisation<sup>‡</sup>

Euler's momentum equation (1.6) is invariant under the following rescaling of the variables

$$m{u}(t,m{x}) 
ightarrow \lambda^{-1} m{u} \Big( \lambda t, \lambda^2 m{x} \Big) \quad ext{and} \quad p(t,m{x}) 
ightarrow \lambda^{-2} p \Big( \lambda t, \lambda^2 m{x} \Big), \quad (1.22 ext{a})$$

for  $\lambda > 0$ . This is also trivially the case of the other constitutive equations (1.2), (1.10) and (1.16). However the Navier-Stokes momentum equation (1.9) does not follow this scaling without redefining

the viscosity. The eulerian surface advection equation (1.20) can also be rescaled in the following manner

$$h(t, \vec{x}) \to \lambda^{-2} h(\lambda t, \lambda^2 \vec{x}).$$
 (1.22b)

These scale invariance properties gives a hint at the possibility to nondimensionalise the set of equations we have obtained in the last two sections.

In order to carry out the complete non-dimensionalisation of the equations, we need to introduce a certain number of typical physical scales. We shall use most of the ones of Johnson (1997)<sup>1</sup>. Even though this choice is completely arbitrary, doing it in this manner has the advantage of letting a few dimensionless parameters appear, most of them shall be usefull to investigate the asymptotic regimes.

<sup>&</sup>lt;sup>1</sup>We could use more fiducial scales, as in Lannes (2013b), or less.

Scale	corresponding to	used to redefine
λ	Maximum distance between two crests (i.e. the maximum wavelength)	$x, y, \vec{x}$
$h_0$	Average depth of the water column	z,h,b
$\varepsilon h_0$	Typical size of a wave	$\eta$
$\varepsilon \lambda \sqrt{gh_0}$	The velocity potential's typical order of magnitude	$\phi$
$\varepsilon \sqrt{gh_0}$	Horizontal velocity of a linear shallow water wave	$u_x,u_y,\vec{u}$
$\varepsilon\mu\sqrt{gh_0}$	Vertical velocity of a linear shallow water wave	$u_z$
$ ho_{ m w} g h_0$	Mean pressure on the bottom	p
$\lambda/\sqrt{gh_0}$	Period of a linear wave in shallow water	t
$\varepsilon \sqrt{gh_0^{-1}}$	Scaling of the vorticity	$\omega$

**Table 1.2** – The chosen typical scales to non-dimensionalise the equations. The parameters  $\mu$  and  $\varepsilon$  will be defined in eq. (1.24).

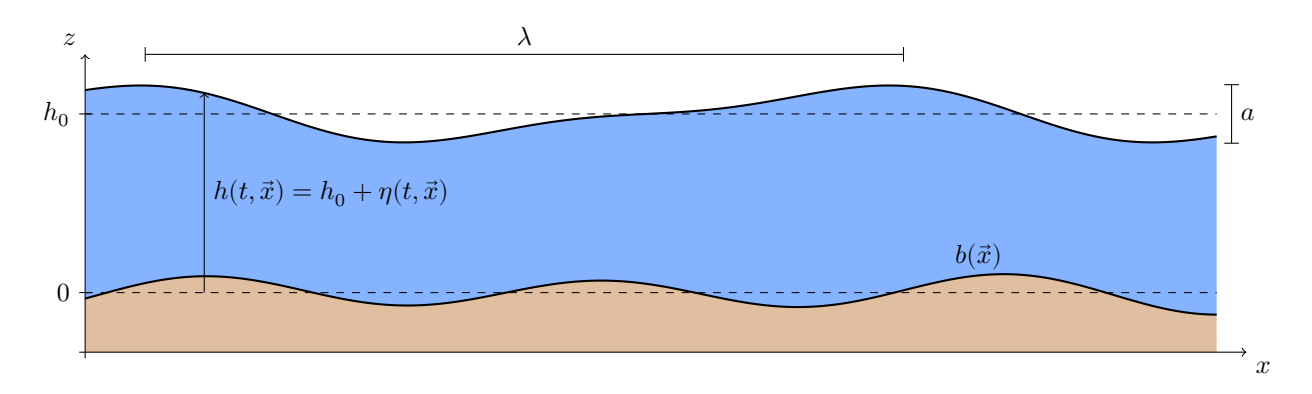


Figure 1.11 – Graphical definition of the typical scales used to non-dimensionalise the equations, in 2d (the 3d case is identical).

The various quantities we will use are defined in table 1.2 and represented graphically in fig. 1.11. For instance, we introduce the new non-dimensional space variables  $x^{\dagger}$  and  $y^{\dagger}$  as

$$x = \lambda x^{\natural}$$
 and  $y = \lambda y^{\natural}$ . (1.23)

Other non-dimensional variables  $z^{\natural}$ ,  $h^{\natural}$ ,  $b^{\natural}$ ,  $\boldsymbol{u}^{\natural}$ ,  $t^{\natural}$  and  $p^{\natural}$  are defined in a similar manner from table 1.2. We also define the wave height  $\eta$  from

$$h(t, \vec{x}) = h_0 + \eta(t, \vec{x}).$$

Notation. The superscript  $\natural$ , used to represent non-dimensional quantities, is a non-standard notation. It is pronounced "natural" so it seemed like a good idea to use it. It is difficult to find a non-overwhelming notation to carry out the non-dimensionalisation. We tried our best to keep it simple.

We can define the non-dimensional version  $\eta^{\natural}$  from table 1.2 too. The two non-dimensional parameters  $\varepsilon$  and  $\mu$  are

$$\varepsilon = \frac{a}{h_0}$$
 the non-linearity/steepness parameter, (1.24a)

$$\mu = \frac{h_0}{\lambda}$$
 the shallowness parameter. (1.24b)

#### III.1. The linear wave solution

In order to motivate the typical scales chosen in table 1.2, we will recall a well-known solution of the incompressible free-surface Euler equations (1.6, 1.2, 1.20, 1.16, 1.10). Indeed, using a parameter asymptotic expansion argument up to first order in  $\varepsilon$ , we find a space—and—time periodic solution.

We work in 2d and suppose, without proof, that  $u_x,u_z,p$  and  $\eta$  can be expressed as a power series in  $\varepsilon$ ,

$$\eta(t,x) = \sum_{j=1}^{+\infty} \varepsilon^j \eta_j(t,x),$$

and similar for  $u_x, u_z$  and p. We assume that the topography is of order 2,  $b = \mathcal{O}(\varepsilon^2)$ . Inserting this into (1.6, 1.2, 1.20, 1.16, 1.10), we get the following first-order solution<sup>1</sup>

$$\eta_1(t,x) = h_0 \cos(kx - \omega t) \tag{1.25a}$$

$$u_{x,1}(t,x,z) = \omega h_0 \frac{\cosh(kz)}{\sinh(kh_0)} \cos\Bigl(kx - \omega t\Bigr) \eqno(1.25b)$$

$$u_{z,1}(t,x,z) = \omega h_0 \frac{\sinh(kz)}{\sinh(kh_0)} \sin\Bigl(kx - \omega t\Bigr) \eqno(1.25c)$$

with  $k = 2\pi/\lambda$  the wave number and the (angular) frequency

$$\omega(k) = \sqrt{gk \cdot \tanh(kh_0)}. \tag{1.25d}$$

This solution is plotted in fig. 1.12.<sup>2</sup> Eq. (1.25d) is the linear dispersion relation. When  $z \approx h_0$  and  $\mu \ll 1$ , we have<sup>3</sup>

$$\eta_1 \sim a$$
  $u_{x,1} \sim \varepsilon \sqrt{gh_0}$   $u_{z,1} \sim \varepsilon \mu \sqrt{gh_0}$ 

in accordance with table 1.2. This also explains the scaling of the time variable t from the angular frequency  $\omega$ .

#### III.2. The non-dimensional Euler problem

Inserting the substitutions of type (1.23) into (1.6, 1.2, 1.20, 1.16, 1.10) yields the non-dimensional form of the free-surface Euler equations. We shall detail the method on the momentum equation (1.6). To do so, we will make intensive use of the following lemma.

**Lemma 1.5** (Non-dimensionalisation). Let the substitution  $x = x_0 x^{\natural}$  and  $f \in C^1$  a function. Let  $f^{\natural}(x^{\natural}) = f(x)$ , then

$$\partial_x f(x) = \frac{1}{x_0} \partial_{x^\natural} f^\natural(x^\natural).$$

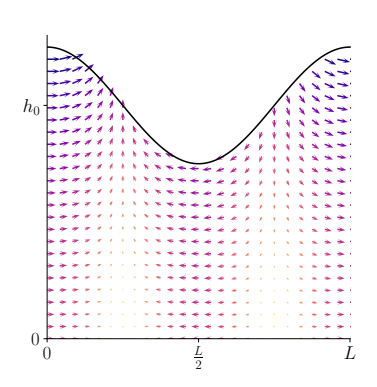


Figure 1.12 – The linear wave solution: interface  $\eta$  and velocity u.

 $^{1}$ see e.g. Johnson (1997), sec. 2.1.

<sup>2</sup>To understand the  $h_0$  prefactor in (1.25), recall that  $\varepsilon h_0 = a$ .

<sup>3</sup>Indeed in the shallow water regime  $\mu \ll 1$ ,

$$\begin{split} & \omega(k) \approx k \sqrt{g h_0} \\ & \frac{\cosh(kz)}{\sinh(kh_0)} \approx \frac{1}{\tanh(kh_0)} \approx \frac{1}{2\pi\mu} \\ & \frac{\sinh(kz)}{\sinh(kh_0)} \approx 1. \end{split}$$

40

*Proof.* This is a direct application of the chain rule.<sup>1</sup>

Using redefinitions like (1.23), defined from table 1.2 and applying lemma 1.5, we carry out the non-dimensionalisation in a straightforward manner. Indeed we have

$$\begin{split} \partial_t \vec{u} &= \varepsilon \ \mu g \ \partial_{t^\natural} \vec{u}^\natural & \partial_t u_z = \varepsilon \ \mu^2 g \ \partial_{t^\natural} u_z^\natural \\ \left( \vec{u} \cdot \vec{\nabla} \right) \vec{u} &= \varepsilon^2 \mu g \ \left( \vec{u}^\natural \cdot \vec{\nabla}^\natural \right) \vec{u}^\natural & \left( \vec{u} \cdot \vec{\nabla} \right) u_z = \varepsilon^2 \mu^2 g \ \left( \vec{u}^\natural \cdot \vec{\nabla}^\natural \right) u_z^\natural \\ u_z \partial_z \vec{u} &= \varepsilon^2 \mu g \ u_z^\natural \partial_{z^\natural} \vec{u}^\natural & u_z \partial_z u_z = \varepsilon^2 \mu^2 g \ u_z^\natural \partial_{z^\natural} u_z^\natural \\ \vec{\nabla} p &= \rho_{\mathbf{w}} \mu g \ \vec{\nabla}^\natural p^\natural & \partial_z p &= \rho_{\mathbf{w}} g \ \partial_{z^\natural} p^\natural \end{split}$$

Inserting this into (1.6), one needs to separate the (x,y)-component from the z-equation as they scale differently, yielding

$$\partial_{t^{\natural}} \vec{u}^{\natural} + \varepsilon \left( \boldsymbol{u}^{\natural} \cdot \boldsymbol{\nabla}^{\natural} \right) \vec{u}^{\natural} = -\frac{1}{\varepsilon} \quad \vec{\nabla}^{\natural} p^{\natural}, \tag{1.27a}$$

$$\partial_{t^{\natural}} u_z^{\natural} + \varepsilon \left( \boldsymbol{u}^{\natural} \cdot \boldsymbol{\nabla}^{\natural} \right) u_z^{\natural} = -\frac{1}{\varepsilon} \frac{1}{\mu^2} \partial_{z^{\natural}} p^{\natural} - \frac{1}{\varepsilon \mu^2}. \tag{1.27b}$$

The factor  $\varepsilon \mu^2$  appearing in eq. (1.27b) can be seen as a Froude number Fr<sup>2</sup>, corresponding to the ratio of horizontal velocity and group velocity in shallow water.

Applying the same procedure to (1.2, 1.20, 1.16) quickly yields the following non-dimensional equations

$$\partial_{t^{\dagger}} \eta^{\dagger} + \varepsilon \vec{u}^{\dagger} \cdot \vec{\nabla}^{\dagger} \eta^{\dagger} = u_z \quad \text{with prefactor } \varepsilon \mu \sqrt{gh_0}, \quad (1.27d)$$

$$p^{\dagger} = 0$$
 with prefactor  $\rho_{\rm w} g h_0$ . (1.27e)

Regarding the impenetrability condition (1.10), we will suppose that it can also be represented as the graph of a, at least once differentiable, function  $(H10)^3$ . This condition will be lifted in the following chapter. The vector normal to  $\Gamma_b$  is given by<sup>4</sup>

$$\hat{\boldsymbol{n}}_{b} = \frac{1}{\sqrt{1 + \left|\vec{\nabla}b\right|^{2}}} \begin{bmatrix} -\vec{\nabla}b \\ 1 \end{bmatrix} = \frac{1}{\sqrt{1 + \left|\varepsilon\vec{\nabla}^{\dagger}b^{\dagger}\right|^{2}}} \begin{bmatrix} -\varepsilon\vec{\nabla}^{\dagger}b^{\dagger} \\ 1 \end{bmatrix}. \quad (1.27f)$$

This gives the non-dimensional impenetrability condition,

$$\varepsilon \vec{u}^{\dagger} \cdot \vec{\nabla}^{\dagger} b^{\dagger} = \mu u_z^{\dagger}, \tag{1.27g}$$

with prefactor  $\varepsilon \sqrt{gh_0}$ , on  $\Gamma_b = \{z = b(\vec{x})\}.$ 

The system (1.27) shall be referred to as the non-dimensional freesurface Euler problem.

#### III.3. The non-dimensional Navier-Stokes problem

The method used to carry out a non-dimensional form of the Navier-Stokes equations (1.9, 1.2, 1.20, 1.17, 1.14) is identical to that of the previous section. However, one needs to be cautious with the viscosity term. Indeed one has

$$\Delta \vec{u} = \frac{\varepsilon \sqrt{g h_0}}{h_0^2} \Big[ \mu^2 \Big( \partial_{x^\natural x^\natural} + \partial_{y^\natural y^\natural} \Big) \vec{u}^\natural + \partial_{z^\natural z^\natural} \vec{u}^\flat \Big]$$

<sup>1</sup>Indeed, let  $y(x^{\sharp}) = x_0 x^{\sharp}$  the change of variable. We then have  $f^{\sharp} = f \circ y$  so

П

$$\begin{split} \partial_{x^\natural} f^\natural(x^\natural) &= \partial_{x^\natural} y(x^\natural) \cdot \Big(\partial_x f \circ y\Big)(x^\natural) \\ &= x_0 \Big(\partial_x f \circ y\Big)(x^\natural). \end{split}$$

Non-dimensionalisation is just a matter of pushforwards and pullbacks (appendix A).

<sup>2</sup>the cancelled prefactor of (1.27a) is

 $\varepsilon \mu g$ ,

while the prefactor of (1.27b) is  $\varepsilon \mu^2 g$ .

<sup>3</sup>That is, there exists  $b \in C^1$  such that  $\Gamma_b = \{ (\vec{x}, b(\vec{x})) \text{ for all } \vec{x} \in \mathbb{R}^d \}.$ 

<sup>4</sup>following an argument similar to that

Notation. In 2d (d=1),

$$\vec{\nabla}^{\natural} = \partial_{-1}$$
.

$$oldsymbol{
abla}^{
abla} = \left[\partial_{x^{
abla}}, \partial_{z^{
abla}}
ight]^t,$$

while in 3d (d=2),

$$\vec{\nabla}^{\natural} = \left[\partial_{- \natural}, \partial_{- \natural}\right]^t$$

$$\boldsymbol{\nabla}^{\natural} = \left[\partial_{x^{\natural}}, \partial_{y^{\natural}}, \partial_{z^{\natural}}\right]^t.$$

$$\Delta u_z = \frac{\varepsilon \mu \sqrt{gh_0}}{h_0^2} \Big[ \mu^2 \Big( \partial_{x^\natural x^\natural} + \partial_{y^\natural y^\natural} \Big) u_z^\natural + \partial_{z^\natural z^\natural} u_z^\natural \Big].$$

Inserting this into 1.9 and dividing by the same prefactors than those of (1.27a) and (1.27b), we see the following non-dimensional number appear,

$$\frac{\nu_{\rm w}}{\mu h_0 \sqrt{gh_0}} = \frac{1}{\mu} \frac{1}{\text{Re}},\tag{1.29}$$

where Re corresponds to the *Reynolds number*, quantifying whether the viscous effects are important in the flow (Re  $\approx 1$ ) or not (Re  $\gg 1$ ). This yields the following non-dimensional momentum equations

$$\partial_{t^{\natural}} \vec{u}^{\natural} + \varepsilon \left( \boldsymbol{u}^{\natural} \cdot \boldsymbol{\nabla}^{\natural} \right) \vec{u}^{\natural} = -\frac{1}{\varepsilon} \quad \vec{\nabla}^{\natural} p^{\natural} \qquad + \frac{1}{\operatorname{Re}} \frac{1}{\mu} \Delta^{\natural}_{\mu} \vec{u}^{\natural}, \qquad (1.30a)$$

$$\partial_{t^{\natural}} u_z^{\natural} + \varepsilon \left( \boldsymbol{u}^{\natural} \cdot \boldsymbol{\nabla}^{\natural} \right) u_z^{\natural} = -\frac{1}{\varepsilon} \quad \partial_{z^{\natural}} p^{\natural} - \frac{1}{\varepsilon \mu^2} + \frac{1}{\operatorname{Re}} \frac{1}{\mu} \Delta_{\mu}^{\natural} u_z^{\natural}, \quad (1.30b)$$

where the non-dimensional Laplace operator is given by

$$\Delta^{\natural}_{\mu} = \mu^2 \Big( \partial_{x^{\natural} x^{\natural}} + \partial_{y^{\natural} y^{\natural}} \Big) + \partial_{z^{\natural} z^{\natural}}.$$

The non-dimensional stress-free (1.17) and Navier (1.14) conditions<sup>1</sup> are

$$p^{\dagger} \hat{\boldsymbol{n}} - \frac{\varepsilon}{\text{Re}} \left[ \boldsymbol{\nabla}_{\mu}^{\dagger} \boldsymbol{u}_{\mu}^{\dagger} + \left( \boldsymbol{\nabla}_{\mu}^{\dagger} \boldsymbol{u}_{\mu}^{\dagger} \right)^{2} \right] \cdot \hat{\boldsymbol{n}} = 0$$
$$\hat{\boldsymbol{n}} \times \left[ \boldsymbol{\nabla}_{\mu}^{\dagger} \boldsymbol{u}_{\mu}^{\dagger} + \left( \boldsymbol{\nabla}_{\mu}^{\dagger} \boldsymbol{u}_{\mu}^{\dagger} \right)^{2} \right] \cdot \hat{\boldsymbol{n}} = 0$$

The non-dimensional gradient tensor is defined as

$$oldsymbol{
abla}_{\mu}^{
abla} oldsymbol{u}_{\mu}^{
abla} = egin{bmatrix} \mu ec{
abla}^{
abla} ec{u} & \mu^2 ec{
abla}^{
abla} u_z^{
abla} \ (\partial_{z^{
abla}} ec{u}^{
abla})^t & \mu \partial_{z^{
abla}} u_z^{
abla} \end{bmatrix}.$$

The system (1.30,1.27d) will be called the non-dimensional free-surface Navier-Stokes problem afterward. In most cases, we will set  $\mu=\varepsilon=1$  for simplicity. The resulting Euler system will be identical to the dimensional one (with the added  $\natural$  superscript) due to the scaling property (1.22). On the other hand, the Navier-Stokes one will have a prefactor Re<sup>-1</sup> in place of the viscosity  $\nu_{\rm w}$ . Formally, as Re  $\to +\infty$ , both problem become identical<sup>2</sup>. As we will see, this does not mean that Euler's solution will correspond to the Navier-Stokes solution as Re  $\to +\infty$ ...

#### III.4. Surface tension

Should we include the surface tension into our model, *i.e.* lifting hypothesis **H9**, another non-dimensional coefficient shall appear. Indeed, denoting by  $\kappa^{\natural}$  the curvature with the couple (x, y) replaced by the couple  $(x^{\natural}, y^{\natural})$ , we rapidly get that

$$\frac{\gamma_{\rm w}}{\rho_{\rm w}gh_0}\kappa[\eta] = \frac{\gamma_{\rm w}}{\rho_{\rm w}gh_0\lambda}\kappa^{\natural}[\varepsilon\mu\eta^{\natural}] = \frac{\kappa^{\natural}[\varepsilon\mu\eta^{\natural}]}{{\rm We}} = \frac{\kappa^{\natural}[\varepsilon\mu\eta^{\natural}]}{\mu{\rm Bo}},$$

with We Weber's number and Bo stands for Bond's number, related by a factor  $\mu$  in the special case of water waves with this scaling.

Notation. The  $\mu$  rescaled derivative and vector fields are defined as

$$\begin{split} \boldsymbol{\nabla}^{\natural}_{\mu} &= \left[ \mu \vec{\nabla}^{\natural}, \partial_{z^{\natural}} \right], \\ \boldsymbol{u}^{\natural}_{\mu} &= \left[ \vec{u}^{\natural}, \mu u^{\natural}_{z} \right], \end{split}$$

so that

$$\Delta^{\natural}_{\mu} = \boldsymbol{\nabla}^{\natural}_{\mu} \cdot \boldsymbol{\nabla}^{\natural}_{\mu}.$$

These rescaled quantities will sometimes appear by themselves, as in the definition of the non-dimensional velocity potential  $\phi^{\natural}$ .

**Notation.** We recall the definition of the various non-dimensional numbers defined up to here,

$$\begin{split} \mu &= \frac{h_0}{\lambda} & \text{shallowness} \\ \varepsilon &= \frac{a}{h_0} & \text{non-linearity} \\ \text{Re} &= \frac{h_0 \sqrt{g h_0}}{\nu_{\text{w}}} & \text{Reynolds} \\ \text{We} &= \frac{\rho_{\text{w}} g h_0 \lambda}{\gamma_{\text{w}}} & \text{Weber} \\ \text{Bo} &= \frac{\rho_{\text{w}} g \lambda^2}{\gamma_{\text{m}}} & \text{Bond} \end{split}$$

$$\hat{m{n}} = rac{1}{\sqrt{1+\left|arepsilon \mu ec{
abla}^{
abla} \eta^{
abla}
ight|}} egin{bmatrix} -arepsilon \mu ec{
abla}^{
abla} \eta^{
abla} \ 1 \end{bmatrix}.$$

<sup>&</sup>lt;sup>1</sup>The no-slip/Dirichlet condition remains identical. The normal vector is already non-dimensional so it does not change. However it depends on  $\varepsilon$  and  $\mu$ ,

<sup>&</sup>lt;sup>2</sup>Aside from the bottom boundary condition whose effects will be discussed in chapters 4 and 5.

# IV. Irrotationality

A major simplifying hypothesis we can make is to "assume that the flow is *irrotational*" (H11), *i.e.* assuming that the *vorticity* vanishes identically in  $\Omega_{\rm w}(t)$ , at all time  $t\geqslant 0$ . We will put this assumption to the test in chapter 5. It is commonly made in theoretical studies of water waves but rarely motivated from a physical perspective. We postpone this discussion for now while carrying out the resulting simplifications.

#### IV.1. The vorticity

Vorticity is a 2-form  $^1$  built from the fluid velocity  $\boldsymbol{u}$  using the exterior derivative d as such

$$\boldsymbol{\omega} = \mathrm{d}(\boldsymbol{u}^{\flat}). \tag{1.31}$$

This definition has the advantage of being independent from ambient space dimension d. In two-dimensional space (d = 1), this yields the well-known definition (up to an isomorphism)

$$\omega \equiv - \boldsymbol{\nabla} \cdot \boldsymbol{u}^{\perp} = \partial_x u_z - \partial_z u_x.$$

In 3d (d=2),  $\check{\omega}$  is isomorphic to the usual (pseudo)vector defined through the curl,

$$\boldsymbol{\omega} \equiv \boldsymbol{\nabla} \times \boldsymbol{u}$$
.

In general, should we work in higher dimension,  $\omega$  would be isomorphic to a vector in  $\mathbb{R}^{\binom{d+1}{2}}$ , *i.e.* an skew-symmetric matrix. We see that with the language of differential geometry we can bypass such technicalities. This also highlights the covariant nature of the vorticity.

Assuming irrotationality amounts to assume that

$$\boldsymbol{\omega} = 0. \tag{H11}$$

П

A consequence of Kelvin's circulation theorem<sup>2</sup> is that, should this be the case initially in an inviscid fluid, then it would remain so at subsequent times. To see this, let us consider a surface  $\mathcal{S} \subset \Omega_{\mathrm{w}}(t)$  and define the associated *circulation* 

$$\Gamma[S] = \oint_{\partial S} \boldsymbol{u} \cdot d\boldsymbol{s} = \int_{S} \check{\omega}.$$

Now, if  $\mathcal{S}(t)$  depends on time, has a piecewise once-differentiable boundary, and is a material surface, meaning that every constitutive point moves with the fluid at velocity  $\boldsymbol{u}$ , we are able to state the conservation of the circulation in time. This is Kelvin's circulation theorem.

**Theorem 1.6** (Kelvin 1869). Let S(t) a material surface with piecewise  $C^1$  boundary  $\partial S(t)$ , moving in an incompressible and inviscid fluid. Then  $\Gamma$  is conserved,

$$\frac{\mathrm{d}\Gamma}{\mathrm{d}t} = 0.$$

*Proof.* In order to establish Kelvin's circulation theorem, we cannot use Reynolds' transport lemma 1.1 as we are not considering volume integrals (when d=2). Instead, more work is needed to establish it.

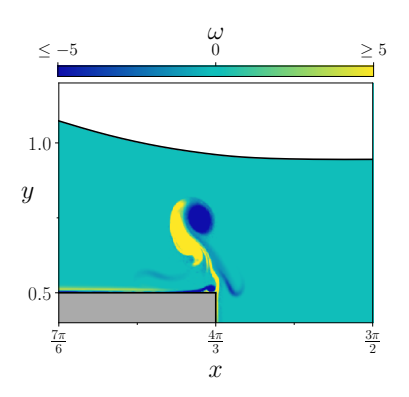


Figure 5.10 (reproduced) — The vorticity near an obstacle. Vortices are detached from the bottom boundary layer as a wave of sufficient height passes above (more details in the original caption).

<sup>1</sup>A primer in differential geometry is available in appendix A. We simply recall that 1-forms can be identified with vector field,  $\boldsymbol{u} \simeq \boldsymbol{u}^{\flat}$ , where the  $\flat$  and  $\sharp$  operators allow to move from the world of differential forms (covariant vectors) and (contravariant) vector fields.

In 2d,  $\boldsymbol{u}^{\perp}$  denotes the  $\frac{\pi}{2}$  counter-clockwise rotation

$$oldsymbol{u}^\perp = egin{bmatrix} -u_z \ u_x \end{bmatrix}.$$

<sup>2</sup>This fundamental result of fluid mechanics is a generalisation of Helmholtz (1858)'s work (later translated in english, Helmholtz 1867). He used it to justify his bold theory: "vortex atoms" (Kelvin 1867). In our case, Helmholtz would be enough to prove that the flow remains irrotational.

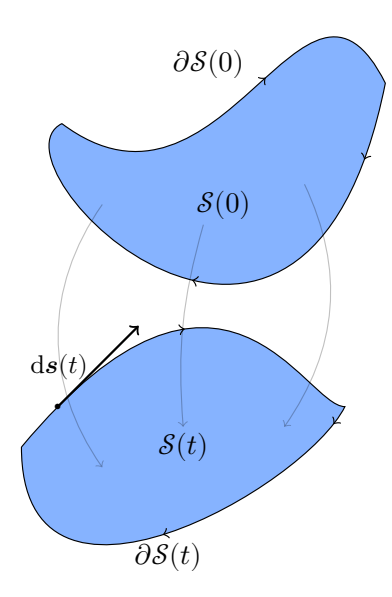


Figure 1.13 – Notations for thm. 1.6.

Let  $\alpha(t, \cdot): [0, L] \to \Omega_{\mathrm{w}}(t)$  a parametrisation of  $\partial \mathcal{S}(t)$ . By hypothesis  $\alpha$  is at least piecewise  $C^1$  in its second argument. Without loss of generality we can assume that it is  $C^1$  (by concatenation). As the points of  $\mathcal{S}(t)$  move at velocity  $\boldsymbol{u}$ , we have

$$\partial_t \boldsymbol{\alpha}(t,s) = \boldsymbol{u}\Big(t, \boldsymbol{\alpha}(t,s)\Big).$$

In these conditions, we can directly compute the time-derivative of  $\Gamma[\mathcal{S}(t)],$ 

$$\begin{split} \frac{\mathrm{d}}{\mathrm{d}t} \Gamma \Big[ \mathcal{S}(t) \Big] &= \frac{\mathrm{d}}{\mathrm{d}t} \oint_{\partial \mathcal{S}(t)} \boldsymbol{u} \cdot \mathrm{d}\boldsymbol{s}(t) \\ &= \frac{\mathrm{d}}{\mathrm{d}t} \int_0^L \boldsymbol{u} \Big( t, \boldsymbol{\alpha}(t,s) \Big) \cdot \partial_s \boldsymbol{\alpha}(t,s) \, \mathrm{d}s \\ &= \int_0^L \partial_t \boldsymbol{u} \Big( t, \boldsymbol{\alpha}(t,s) \Big) \cdot \partial_s \boldsymbol{\alpha}(t,s) \, \mathrm{d}s \\ &+ \int_0^L \Big[ \boldsymbol{\nabla}_{\boldsymbol{x}} \boldsymbol{u} \Big( t, \boldsymbol{\alpha}(t,s) \Big) \cdot \partial_t \boldsymbol{\alpha}(t,s) \Big] \cdot \partial_s \boldsymbol{\alpha}(t,s) \, \mathrm{d}s \quad (*) \\ &+ \int_0^L \boldsymbol{u} \Big( t, \boldsymbol{\alpha}(t,s) \Big) \cdot \partial_{ts} \boldsymbol{\alpha}(t,s) \, \mathrm{d}s \quad (\dagger) \end{split}$$

Concerning the term (\*), we have

$$\begin{split} (**) &= \int_0^L \left[ \boldsymbol{\nabla}_{\boldsymbol{x}} \boldsymbol{u} \Big( t, \boldsymbol{\alpha}(t,s) \Big) \cdot \boldsymbol{u} \Big( t, \boldsymbol{\alpha}(t,s) \Big) \right] \cdot \partial_s \boldsymbol{\alpha}(t,s) \, \mathrm{d}s \\ &= \int_0^L \left[ \boldsymbol{\nabla}_{\boldsymbol{x}} \left( \frac{|\boldsymbol{u}|^2}{2} \right) \Big( t, \boldsymbol{a}(t,s) \Big) \right] \cdot \partial_s \boldsymbol{\alpha}(t,s) \, \mathrm{d}s \\ &= \oint_{\partial \mathcal{S}(t)} \boldsymbol{\nabla}_{\boldsymbol{x}} \left( \frac{|\boldsymbol{u}|^2}{2} \right) \cdot \mathrm{d}\boldsymbol{s}(t) = 0. \end{split}$$

Finally, the last term (†) is

$$\begin{split} (\dagger) &= \int_0^L \boldsymbol{u} \Big( t, \boldsymbol{\alpha}(t,s) \Big) \cdot \partial_s \boldsymbol{u} \Big( t, \boldsymbol{\alpha}(t,s) \Big) \, \mathrm{d}s \\ &= \int_0^L \boldsymbol{u} \Big( t, \boldsymbol{\alpha}(t,s) \Big) \cdot \boldsymbol{\nabla} \boldsymbol{u} \Big( t, \boldsymbol{\alpha}(t,s) \Big) \cdot \partial_s \boldsymbol{\alpha}(t,s) \, \mathrm{d}s \\ &= \oint_{\partial S(t)} \boldsymbol{u} \cdot \boldsymbol{\nabla} \boldsymbol{u} \cdot \mathrm{d}\boldsymbol{s}(t). \end{split}$$

In the end, using Euler's equation (1.6), we get

$$\frac{\mathrm{d}}{\mathrm{d}t}\Gamma \Big[\mathcal{S}(t)\Big] = \oint_{\partial \mathcal{S}(t)} \! \Big( \boldsymbol{g} - \frac{1}{\rho_{\mathrm{w}}} \cdot \boldsymbol{\nabla} p \Big) \cdot \mathrm{d}\boldsymbol{s}(t) = 0.$$

**Remark 1.7.** A quick inspection of the above proof shows that Kelvin's theorem 1.6 remains true for a barotropic fluid where the density is a function of the pressure only.

**Identity.** For all practical purposes, we recall that

$$egin{aligned} oldsymbol{
abla} \left(rac{|oldsymbol{u}|^2}{2}
ight) = & oldsymbol{
abla} oldsymbol{u} \cdot oldsymbol{u} = oldsymbol{u} \cdot oldsymbol{
abla} oldsymbol{u} + oldsymbol{u} imes \left(oldsymbol{
abla} imes oldsymbol{u}
ight) \ = & oldsymbol{u} \cdot oldsymbol{
abla} oldsymbol{u} + oldsymbol{u} imes \left(oldsymbol{
abla} imes oldsymbol{u}
ight) \end{aligned}$$

44

**Remark 1.8.** In the case of a viscous fluid with viscosity  $\nu$ , we have (Batchelor 1967, eq. 5.2.7)

$$\frac{\mathrm{d}\Gamma}{\mathrm{d}t} + \nu \oint_{\partial S(t)} \mathbf{\nabla} \times \boldsymbol{\omega} = 0.$$

The term  $\nabla \times \boldsymbol{\omega}$  is sometimes called the *palinstrophy*. Adaptations in 2d is straightforward.

An important consequence of assumption **H11** is the existence of a velocity potential  $\phi$ . Indeed, the domain  $\Omega_{\rm w}(t)$  remains simply connected up to the splash (fig. 1.14), which cannot happen in the Eulerian formulation of the problem, owing to hypothesis **H8**. We can hence use Poincaré's lemma<sup>1</sup> to write

$$\boldsymbol{u} = \boldsymbol{\nabla}\phi. \tag{1.33}$$

This decomposition simplifies considerably the Euler system (1.27). Indeed, the momentum equation becomes a vanishing gradient,

$$\nabla \left( \partial_t \phi + \frac{\left| \nabla \phi \right|^2}{2} + \frac{p}{\rho_{\rm w}} + gz \right) = 0.$$

This quickly leads to

$$\partial_t \phi + \frac{\left| \nabla \phi \right|^2}{2} + \frac{p}{\rho_w} + gz = f(t), \tag{1.34}$$

for some function f depending on time only. Redefining the velocity potential as

$$\phi(t, \boldsymbol{x}) \longrightarrow \phi(t, \boldsymbol{x}) + \int_0^t f(\tau) d\tau + f(0)t,$$

we are able to omit the function f.<sup>2</sup> Should the flow be steady, we would get Daniel Bernoulli's equation<sup>3</sup>,

$$\frac{\boldsymbol{u}^2}{2} + gz + \frac{p}{\rho_{\mathbf{w}}} = 0,$$

everywhere in the fluid domain. Evaluating (1.34) on an free-surface point  $z=1+\eta(t,\vec{x})$  yields

$$\left. \partial_t \phi \right|_{z=1+\eta(t,\vec{x})} + \left. \frac{\left| \nabla \phi \right|^2}{2} \right|_{z=1+\eta(t,\vec{x})} + g\eta = 0.$$
 (1.35a)

We shall refer to this equation as Bernoulli's equation aferward. We have used the dynamic condition (1.16) to eliminate the pressure. At the same time, the incompressibility condition (1.2) trivially becomes Laplace's equation<sup>4</sup>

$$\Delta \phi = 0. \tag{1.35b}$$

Finally, the impenetrability condition (1.10) becomes a Neumann boundary condition for  $\phi$ ,

$$\partial_{n_b} \phi = \hat{\boldsymbol{n}}_b \cdot \boldsymbol{\nabla} \phi = 0, \tag{1.35c}$$

on  $\Gamma_b$ . The system (1.35,1.20) shall be recast onto a set of two equation on the interface  $\Gamma_i(t)$  only defining the Dirichlet-to-Neumann operator. This will be the subject of the next section.

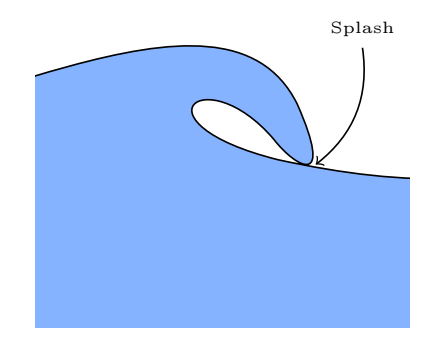


Figure 1.14 – The splash singularity corresponds to the moment the free surface intersects itself in the post-breaking phase. If hypothesis H7 is lifted, the splash cannot happen, as is shown in Fefferman et al. (2016) and Coutand and Shkoller (2019)

<sup>1</sup>stated and quickly showed in a short note (Poincaré 1886), taken up again shortly after in Poincaré (1887). It states that on a simply connected open subset of  $\mathbb{R}^n$ , every closed 1-form is exact.

<sup>2</sup>This has no effect on the physics since the relevant information is encompassed in the gradient of  $\phi$ .

<sup>3</sup>Bernoulli (1738)

<sup>4</sup>Laplace (1798 (an VII))

#### IV.2. Non-dimensionalisation<sup>†</sup>

We quickly obtain the scaling of  $\check{\omega}$  presented in table 1.2 by inserting the non-dimensional forms of both  $\nabla$  and u into the definition (1.31) of the vorticity. We quickly get<sup>1</sup>

$$\boldsymbol{\omega}^{\natural} = d \left( \begin{bmatrix} \vec{u}^{\natural} \\ \mu^2 u_z^{\natural} \end{bmatrix}^{\flat} \right). \tag{1.36}$$

This motivates the introduction of a non-dimensional velocity potential  $\phi^{\natural}$  (and **H11** allows it) such that

$$oldsymbol{
abla}^
atural^
atural} \phi^
atural} = egin{bmatrix} ec{u}^
atural} ec{u}^
atura$$

Its scaling given in table 1.2 is, once again, chosen in light of the  $\mathcal{O}(\varepsilon)$  linear wave solution,

$$\phi(t,x,z) = \frac{a\omega}{k} \frac{\cosh(kz)}{\sinh(kh_0)} \sin\Bigl(kx - \omega(k)t\Bigr) \stackrel{z \approx h_0 \ll \lambda}{\propto} \varepsilon \lambda \sqrt{gh_0}.$$

Inserting this into Bernoulli's equation (1.35), along with (1.27g) and (1.27c) yields

$$\begin{split} \partial_{t^\natural}\phi^\natural + \frac{\varepsilon}{2} \left( \left| \vec{\nabla}^\natural \phi^\natural \right|^2 + \frac{1}{\mu^2} \left( \partial_{z^\natural}\phi^\natural \right)^2 \right) + \eta^\natural &= 0 & \text{on } \Gamma_i(t), \quad (1.37\text{a}) \\ \Delta^\natural \phi^\natural &= 0 & \text{in } \Omega_\text{w}(t), \quad (1.37\text{b}) \\ \varepsilon \mu \vec{\nabla}^\natural b^\natural \cdot \vec{\nabla}^\natural \phi^\natural &= \partial_{z^\natural}\phi^\natural & \text{on } \Gamma_b. \quad (1.37\text{c}) \end{split}$$

The physical relevance of irrotationality **H11** is the subject of an entire part of this work, chapter 5. Indeed, in the viscous setting, the appearance of boundary layers near obstacles lying on the bottom can lead to vortices being shed and avected in the fluid domain. We will also discuss this hypothesis in light of the wave generation mechanism.

Remark 1.9. (Dimensional quantities or not?) For the rest of this work, we shall only work using dimensionless quantities. Hence we drop out the  $\natural$  superscript for now on. Furthermore, we will set  $\varepsilon = \mu = 1$  (recall that the choice of  $\lambda$ , a and  $h_0$  is arbitrary) except when it is relevant to assume otherwise. Sections in which the values of  $\varepsilon$  and  $\mu$  are of interest shall enjoy a highlight in their title, as the present one or sec. III.

# V. The Water Waves equations

A surprising feature of the Bernoulli system (1.35) is that it can be written in terms of quantities depending on  $\vec{x}$  only, hence diminishing the equations instrinsic dimension by one. Indeed, as originally noted by Zakharov (1968), should be define the trace of the potential on  $\Gamma_i(t)$ ,

$$\psi(t,\vec{x}) = \phi\Big(t,\vec{x},z = \eta(t,\vec{x})\Big), \tag{1.38}$$

we are able to recast (1.35) in terms of  $\eta$  and  $\psi$  only. Furthermore, the resulting system of equations enjoys a particularly interesting feature: it is Hamiltonian. Later, Craig and Sulem (1993) were able to rewrite

<sup>1</sup>We have

$$reve{\omega} = arepsilon \sqrt{rac{g}{h_0}} reve{\omega}^{
atural}.$$

Furthermore, working in the dimension-dependant curl operator yields the usual definitions of the vorticity.

this very system in terms of  $\eta$  and  $\psi$  only by means of the well-studied Dirichlet-to-Neumann operator. The resulting set of equations is called the Water Waves system, sometimes also referred to as the Zakharov-Craig and Sulem formulation.

#### V.1. Motivating the equations

Using the definition (1.38) of the free-surface potential  $\psi$ , a quick application of the chain rule yields

$$\partial_t \psi = \partial_t \phi + \partial_t \eta \cdot \partial_z \phi \tag{1.39a}$$

$$\vec{\nabla}\psi = \vec{\nabla}\phi + \vec{\nabla}\eta \cdot \partial_z\phi,\tag{1.39b}$$

with  $\phi$  evaluated on the interface  $z=\eta(t,\vec{x})$ . Intuitively, it seems difficult to express  $\partial_z \phi$  as a function of  $\psi$  and  $\eta$  only. It is however possible using the gentle properties of Laplace's equation. To this end, we introduce the Dirichlet-to-Neumann operator  $DtN[\eta, b]\psi$  as

$$\mathrm{DtN}[\eta,b]\psi = \sqrt{1 + \left|\vec{\nabla}\eta(t,\vec{x})\right|^2} \ \partial_n \phi \Big(t,\vec{x},z = \eta(t,\vec{x})\Big). \tag{1.40}$$

This operator is linear<sup>1</sup> in  $\psi$  but highly nonlinear in both  $\eta$  and b. Indeed both functions appear through the shape of the domain  $\Omega_{\rm w}(t)$  in which  $\phi$  is computed. We can also write

$$DtN[\eta, b]\psi = \partial_z \phi \Big|_{z=\eta} - \vec{\nabla} \phi \Big|_{z=\eta} \cdot \vec{\nabla} \eta = \partial_t \eta, \tag{1.41}$$

using (1.20) and the definition of the normal vector  $\hat{\boldsymbol{n}}$ ,

$$\hat{\boldsymbol{n}} = \frac{1}{\sqrt{1 + |\vec{\nabla}\eta|^2}} \begin{bmatrix} -\vec{\nabla}\eta\\1 \end{bmatrix}. \tag{1.42}$$

This quickly leads to<sup>2</sup>

$$\partial_z \phi \Big|_{z=\eta} = \frac{\mathrm{DtN}[\eta,b] \psi + \vec{\nabla} \psi \cdot \vec{\nabla} \eta}{1 + |\vec{\nabla} \eta|^2}.$$

Inserting this into (1.39a) yields the equation for the time evolution of  $\psi$ , (all appearances of  $\phi$  being implicitly expressed on  $z = \eta$ )

$$\begin{split} \partial_t \psi &= \partial_t \phi + \partial_t \eta \cdot \partial_z \phi \\ &= -g \eta - \frac{1}{2} \left[ \left| \vec{\nabla} \phi \right|^2 + \left( \partial_z \phi \right)^2 \right] + \text{DtN}[\eta, b] \psi \cdot \partial_z \phi \quad \text{by (1.35a), (1.41)} \\ &= -g \eta - \frac{1}{2} \left| \vec{\nabla} \psi \right|^2 + \frac{1}{2} \frac{\left[ \text{DtN}[\eta, b] \psi + \vec{\nabla} \psi \cdot \vec{\nabla} \eta \right]^2}{1 + |\vec{\nabla} \eta|^2}. \end{split}$$

Indeed, we have

$$\begin{split} \left|\vec{\nabla}\phi\right|^2 + \left(\partial_z\phi\right)^2 &= \left|\vec{\nabla}\psi\right|^2 - 2\vec{\nabla}\psi\cdot\vec{\nabla}\eta\partial_z\psi + \left(1 + \left|\vec{\nabla}\eta\right|^2\right)\left(\partial_z\phi\right)^2 \\ &= \left|\vec{\nabla}\psi\right|^2 - 2\vec{\nabla}\psi\cdot\vec{\nabla}\eta\frac{\text{DtN}[\eta,b]\psi + \vec{\nabla}\psi\cdot\vec{\nabla}\eta}{1 + |\vec{\nabla}\eta|^2} + \frac{\left[\text{DtN}[\eta,b]\psi + \vec{\nabla}\psi\cdot\vec{\nabla}\eta\right]^2}{1 + |\vec{\nabla}\eta|^2} \end{split}$$

 $^2 \it{i.e.}$  there exists a functional  ${\rm H}[\eta,\psi]$  such that

$$\partial_t \eta = -rac{\delta H}{\delta \psi}$$
  $\partial_t \psi = -rac{\delta H}{\delta n}$ 

with  $\frac{\delta}{\delta\eta}$  and  $\frac{\delta}{\delta\psi}$  denoting the variational derivatives. These are Hamilton's equations. We shall prove this below.

<sup>1</sup>by linearity of Laplace's equation

<sup>2</sup>Details of the computations,

$$\begin{split} \partial_z \phi \Big|_{z=\eta} = & \text{DtN}[\eta, b] \psi \\ & + \left. \vec{\nabla} \phi \right|_{z=\eta} \cdot \vec{\nabla} \eta \\ = & \text{DtN}[\eta, b] \psi + \vec{\nabla} \psi \cdot \vec{\nabla} \eta \\ & - \left| \vec{\nabla} \eta \right|^2 \cdot \partial_z \phi \Big|_{z=\eta} \end{split}$$

using (1.41) and (1.39b).

so that

$$\begin{split} -\frac{1}{2} \Big[ \Big| \vec{\nabla} \phi \Big|^2 + \Big( \partial_z \phi \Big)^2 \Big] + \mathrm{DtN}[\eta, b] \psi \cdot \partial_z \phi &= -\frac{1}{2} \Big| \vec{\nabla} \psi \Big|^2 - \frac{1}{2} \frac{\Big[ \mathrm{DtN}[\eta, b] \psi + \vec{\nabla} \psi \cdot \vec{\nabla} \eta \Big]^2}{1 + |\vec{\nabla} \eta|^2} \\ &+ \vec{\nabla} \psi \cdot \vec{\nabla} \eta \frac{\mathrm{DtN}[\eta, b] \psi + \vec{\nabla} \psi \cdot \vec{\nabla} \eta}{1 + |\vec{\nabla} \eta|^2} \\ &+ \mathrm{DtN}[\eta, b] \psi \cdot \frac{\mathrm{DtN}[\eta, b] \psi + \vec{\nabla} \psi \cdot \vec{\nabla} \eta}{1 + |\vec{\nabla} \eta|^2} \\ &= -\frac{1}{2} \Big| \vec{\nabla} \psi \Big|^2 + \frac{1}{2} \frac{\Big[ \mathrm{DtN}[\eta, b] \psi + \vec{\nabla} \psi \cdot \vec{\nabla} \eta \Big]^2}{1 + |\vec{\nabla} \eta|^2} \end{split}$$

as wanted.

The resulting system of equations is exactly the Water Waves problem,

$$\begin{cases} \partial_t \eta = \text{DtN}[\eta, b] \psi & (1.43\text{a}) \\ \partial_t \psi = -g \eta - \frac{1}{2} \left| \vec{\nabla} \psi \right|^2 + \frac{1}{2} \frac{\left[ \text{DtN}[\eta, b] \psi + \vec{\nabla} \psi \cdot \vec{\nabla} \eta \right]^2}{1 + |\vec{\nabla} \eta|^2}. & (1.43\text{b}) \end{cases}$$

As already mentionned, the unknowns  $\eta$  and  $\psi$  are functions of t and  $\vec{x}$  only, *i.e.* the use of the Dirichlet-to-Neumann operator has effectively reduced the dimension of the problem by one. These equations (1.43) have been extensively studied since their first appearance thirty-two years ago<sup>1</sup>. In particular, should their solution be regular enough, it has been rigorously established<sup>2</sup> that we can use  $(\eta, \psi)$  to define a couple (u, p) solutions of Euler's system (1.27).

#### V.2. On the Dirichlet-to-Neumann operator

We have been able to reduce the space dimension of the Euler–Bernoulli system (1.35) by introducing the operator  $\mathrm{DtN}[\eta,b]\psi$ . In this section we prove that  $\mathrm{DtN}[\eta,b]$  is a well-defined operator from  $\mathring{H}^{\frac{1}{2}}(\mathbb{R}^d)/\mathbb{R}$  to  $H^{-\frac{1}{2}}(\mathbb{R}^d)^{3,4}$ , and state some of its important properties. While we are at it, we introduce material that will be usefull in subsequent chapters. We momentarily forget about the time dependency of all quantities. This section is adapted from Alazard (2021, 2024) and Lannes (2005, 2013b).

V.2.1. **Harmonic extension.** We assume that the upper interface and the bottom topography are Lipschitz functions, *i.e.*  $\eta, b \in W^{1,\infty}(\mathbb{R}^d)$  (we could consider less regular topographies). We are interested in solving the Laplace problem with Dirichlet data  $\psi \in \mathring{H}^{\frac{1}{2}}(\mathbb{R}^d)/\mathbb{R}$ ,

$$\begin{cases}
\Delta \phi = 0 & \text{in } \Omega_{\mathbf{w}} \\
\phi = \psi & \text{on } \Gamma_{i} \\
\partial_{n} \phi = 0 & \text{on } \Gamma_{b}.
\end{cases}$$
(1.44)

A direct application of Lax and Milgram's theorem<sup>5</sup> does not yield the result as  $\psi$  is not in regular enough. However, the *almost-flat* nature of the domain allows us to still find such  $\psi$ .

Let  $\mathcal{S} = \mathbb{R}^d \times (0,1)$  the flat strip. Introduce the diffeomorphism  $\Sigma$ , allowing to go back and forth between  $\mathcal{S}$  and the fluid domain (fig.

<sup>1</sup>in Craig and Sulem (1993).

<sup>5</sup>Lax and Milgram (1955)

<sup>&</sup>lt;sup>2</sup>Alazard, Burq, et al. (2013).

<sup>&</sup>lt;sup>3</sup>The same property holds if we see  $\mathrm{DtN}[b,\eta]$  as a map between non-homogeneous Sobolev spaces  $H^{\frac{1}{2}}(\mathbb{R}^d)$  and  $H^{-\frac{1}{2}}(\mathbb{R}^d)$ . See Alazard (2024) for instance.

<sup>&</sup>lt;sup>4</sup>Definitions of the various function spaces considered in this work can be found in appendix A.

1.15),

$$\begin{array}{cccc} \Sigma: & \mathcal{S} & \longrightarrow & \Omega_{\mathrm{w}} \\ & \left(\vec{x},z\right) & \longmapsto & \left(\vec{x},b(\vec{x})+\left(1+\eta(\vec{x})-b(\vec{x})\right)z\right) = (\vec{X},Z). \end{array}$$

The fact that it is a diffeomorphism, i.e. that it has an inverse transformation, is a consequence of  $\mathbf{H5}$  which can be rephrased (and slightly made stronger) as

$$\inf_{\vec{x} \in \mathbb{R}^d} \left( 1 + \eta(t, \vec{x}) - b(t, \vec{x}) \right) \geqslant \delta > 0, \tag{H5, bis}$$

at all time t, for some constant  $\delta>0$ .  $\Sigma$  can be continuously extended (since  $\eta,b\in W^{1,\infty}(\mathbb{R}^d)$ ) to encompass the bottom  $\Gamma_b$  and the interface  $\Gamma_i$  by  $\Sigma(\cdot,0):\mathbb{R}^d\to\Gamma_b$  and  $\Sigma(\cdot,1):\mathbb{R}^d\to\Gamma_i$ .

Let  $\chi \in \mathcal{D}(\mathbb{R})$  a smooth even function such that  $\chi(x) = 1$  for  $|x| < \frac{1}{2}$  and  $\chi(x) = 0$  for |x| > 1 (fig. 1.16). Introduce the extension  $\psi_{\mathcal{S}}^{\dagger}$  of  $\psi$  in  $\mathcal{S}$  as

$$\psi_{\mathcal{S}}^{\dagger}(\vec{X},Z) = \frac{1}{\sqrt{2\pi}^d} \int_{\mathbb{R}^d} \chi\Big((1-Z) \Big|\vec{\xi}\Big| \Big) \mathcal{F}[\psi](\vec{\xi}) e^{i\vec{\xi}\cdot\vec{X}} \, \mathrm{d}\vec{\xi}.$$

We check readily that  $\psi^\dagger_{\mathcal{S}}({\:\raisebox{3.5pt}{\text{\circle*{1.5}}}},1)=\psi$  and that  ${f \nabla}\psi^\dagger_{\mathcal{S}}\in L^2(\mathcal{S})$  since

$$\left\| \boldsymbol{\nabla} \psi_{\mathcal{S}}^{\dagger} \right\|_{L^{2}(\mathcal{S})} \leqslant C \left\| \psi \right\|_{\mathring{H}^{\frac{1}{2}}(\mathbb{R}^{d})}.$$

This last regularity property is essential.<sup>1</sup> We now push  $\psi^{\dagger}_{\mathcal{S}}$  to the physical domain  $\Omega_{\rm w}$  through  $\Sigma$ , defining

$$\psi^{\dagger} = \psi_{\mathcal{S}}^{\dagger} \circ \Sigma.$$

Since  $\eta, b \in W^{1,\infty}(\mathbb{R}^d)$  we can show that  $\nabla \psi^{\dagger} \in L^2(\Omega_{\mathbf{w}})$  and  $\psi^{\dagger}|_{z=\eta} = \psi$ . Introduce the space  $H^1_{\Gamma_i}(\Omega_{\mathbf{w}})$  of functions  $f \in H^1(\Omega_{\mathbf{w}})$  vanishing on the interface but not necessarily on the bottom. More precisely,

$$\begin{split} H^1_{\Gamma_i}(\Omega_{\mathbf{w}}) & \stackrel{\text{def}}{=} \overline{\mathcal{D}\!\left(\Omega_{\mathbf{w}} \cup \Gamma_b\right)}^{H^1(\Omega)} \\ & = \overline{\mathcal{D}\!\left(\Omega_{\mathbf{w}} \cup \Gamma_b\right)}^{\mathring{H}^1(\Omega)}, \end{split}$$

where the second equality stems from prop. 2.3(iii) in Lannes (2013b). It is a Hilbert space for the scalar product of  $\mathring{H}^1(\Omega)$ ,

$$\left\langle f,g\right\rangle _{\mathring{H}^{1}\left(\Omega\right)}=\left\langle \mathbf{\nabla}f,\mathbf{\nabla}g\right\rangle _{L^{2}\left(\Omega\right)}.$$

Applying the Lax-Milgram theorem, or even Riesz' theorem<sup>2</sup> we can find a function  $u \in H^1_{\Gamma_*}(\Omega_{\mathbf{w}})$  such that

$$\int_{\Omega} \nabla u \cdot \nabla v = -\int_{\Omega} \nabla \psi^{\dagger} \cdot \nabla v,$$

for all  $v \in H^1_{\Gamma_i}(\Omega_{\mathbf{w}})$ . Then  $\phi = u + \psi^{\dagger}$  is a weak solution of (1.44) with Dirichlet data  $\psi \in \mathring{H}^{\frac{1}{2}}(\mathbb{R}^d)/\mathbb{R}$ , as wanted.

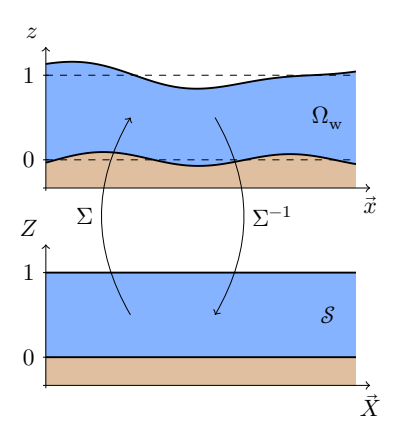


**Figure 1.15** – The diffeomorphism between  $\Omega_{\rm w}$  and  $\mathcal{S}$ .

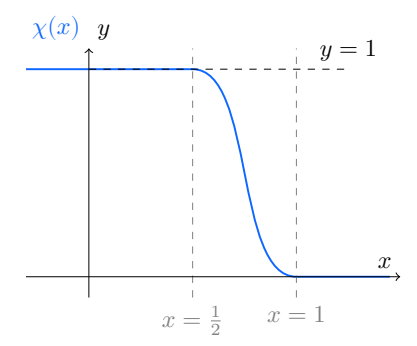


Figure 1.16 – The function  $\chi$ . Its graph for x < 0 can be imagined easily through its even nature.

<sup>1</sup>It is obtained from Plancherel's formula and lemma 2.20 of Lannes (2013b).

 $^2$ Riesz (1909)

<sup>3</sup>This function u is the weak solution of the following problem,

$$\left\{ \begin{array}{rcl} \Delta u &=& -\Delta \psi^{\dagger} & \text{ in } \Omega_{\rm w} \\ u &=& 0 & \text{ on } \Gamma_i \\ \partial_{n} u &=& -\partial_{n} \psi^{\dagger} & \text{ on } \Gamma_b. \end{array} \right.$$

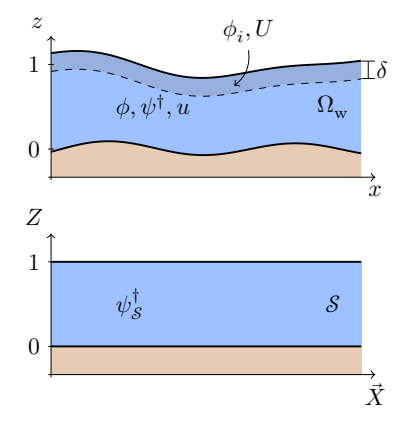


**Figure 1.17** – Where are the quantities used in secs. V.2.1 and V.2.2 defined?

<sup>1</sup>We state the result for the  $H^{\frac{1}{2}}(\mathbb{R}^d)$  to prevent a tedious discussion on the dual of the Beppo-Levi space  $\mathring{H}^{\frac{1}{2}}(\mathbb{R}^d)/\mathbb{R}$ .

 $^{2}$  *i.e.* the identity

$$\int_{\mathcal{V}} \phi \Delta \psi - \boldsymbol{\nabla} \phi \cdot \boldsymbol{\nabla} \phi = \int_{\partial \mathcal{V}} \phi \partial_n \psi,$$

obtained easily from Green (1828)'s theorem.

V.2.2. Trace. Application of the classical Sobolev trace theory in  $\Omega_{\rm w}$  to  $\nabla \phi$  would not yield an optimal result. Indeed, introducing the auxiliary function

$$\phi_i(\vec{x}, z) = \phi(\vec{x}, z + \eta(\vec{x})),$$

for values of z sufficiently close to 1 (fig. 1.17) the trace of  $\phi$  on  $\Gamma_i$  is just the value of  $\phi_i$  when z=1. As  $\eta \in W^{1,\infty}(\mathbb{R}^d)$ ,  $\phi_i$  enjoys the same regularity as  $\phi$ . The Dirichlet–to–Neumann map is then given by

$$\mathrm{DtN}[\eta,b]\psi = \left[ \left( 1 + \left| \vec{\nabla} \eta \right|^2 \right) \partial_z \phi_i - \vec{\nabla} \eta \cdot \vec{\nabla} \phi_i \right] \Big|_{z=1} = U \Big|_{z=1}.$$

Straightforward computations shows that

$$\begin{split} U \in L^2_z L^2_{\vec{x}} &= L^2 \Big( (1-\delta,1); L^2 \Big( \mathbb{R}^d \Big) \Big) \\ \partial_z U &= -\vec{\nabla} \cdot \Big( \vec{\nabla} \phi_i - \Big( \partial_z \phi_i \Big) \vec{\nabla} \eta \Big) \in L^2_z H^{-1}_{\vec{x}} = L^2 \Big( (1-\delta,1); H^{-1} \Big( \mathbb{R}^d \Big) \Big), \end{split}$$

for  $\delta$  defined in (H5, bis). We conclude using theorem 3.1 of Lions and Magenes (1968)

$$\mathrm{DtN}[\eta,b]\psi \in C\Big((1-\delta,1);H^{-\frac{1}{2}}(\mathbb{R}^d)\Big)$$

and extension by continuity quickly yields that  $\mathrm{DtN}[\eta, b]$  indeed maps  $\mathring{H}^{\frac{1}{2}}(\mathbb{R}^d)/\mathbb{R}$  to  $H^{-\frac{1}{2}}(\mathbb{R}^d)$ .

V.2.3. Standard properties. Assuming now that  $\eta$  and b are smooth for simplicity, for  $\psi_1,\psi_2\in H^{\frac{1}{2}}(\mathbb{R}^d)^1$  given, we denote by  $\phi_1$  and  $\phi_2$  their harmonic extensions constructed in sec. V.2.1 (it exists as  $H^{\frac{1}{2}}(\mathbb{R}^d)$  is continuously embedded in  $\mathring{H}^{\frac{1}{2}}(\mathbb{R}^d)/\mathbb{R}$ ). A rapid application of Green's first identity<sup>2</sup> yields

$$\int_{\mathbb{R}^d} \psi_1 \operatorname{DtN}[\eta, b] \psi_2 = \int_{\Omega_{\mathbf{w}}} \boldsymbol{\nabla} \phi_1 \cdot \boldsymbol{\nabla} \phi_2.$$

From this identity we quickly get the following lemma.

**Lemma 1.10** (Lannes 2013b, prop. 3.9). The  $DtN[\eta, b]$  operator enjoys the following properties,

1. **Symmetry.** It is symmetric with respect to the  $H^{-\frac{1}{2}} - H^{\frac{1}{2}}$  pairing,

$$\left\langle \mathrm{DtN}[\eta,b]\psi_1,\psi_2\right\rangle_{H^{-\frac{1}{2}}\times H^{\frac{1}{2}}} = \left\langle \mathrm{DtN}[\eta,b]\psi_2,\psi_1\right\rangle_{H^{-\frac{1}{2}}\times H^{\frac{1}{2}}}.$$

2. **Positivity.** It is positive for the same pairing,

$$\left\langle \operatorname{DtN}[\eta, b] \psi_1, \psi_1 \right\rangle_{H^{-\frac{1}{2}} \times H^{\frac{1}{2}}} \geqslant 0.$$

The same holds for the  $(\mathring{H}^{\frac{1}{2}}(\mathbb{R}^d)/\mathbb{R})^* - \mathring{H}^{\frac{1}{2}}(\mathbb{R}^d)/\mathbb{R}$  pairing and even for the  $L^2(\mathbb{R}^d)$  scalar product, should  $DtN[\eta, b]\psi_1$  be an element of  $L^2(\mathbb{R}^d)$ .

V.2.4. Symbolic representation. Should we choose  $b = \eta = 0$ , then we have an explicit formula for the symbol of DtN[0, 0],

$$\mathrm{DtN}[0,0] = \mathrm{Op}(a_0) \quad \text{with} \quad a_0(\vec{x},\vec{\xi}) = \left|\vec{\xi}\right| \tanh\left(\left|\vec{\xi}\right|\right)$$

This can be seen appyling the DtN[0,0] operator to the Fourier mode  $e^{i\vec{\xi}\cdot\vec{x}}$ . The symbol  $a_0$  belongs to the class  $S^1(\mathbb{R}^d)$ . Craig, Schanz, et al. (1997) proved that DtN[ $\eta$ ,0], while highly nonlinear in  $\eta$ , is analytical in this very variable<sup>1</sup>. Its first order and second order (in  $\eta$ ) symbols  $a_1$  and  $a_2$  are

<sup>1</sup>for  $\eta$  small.

$$\begin{split} &a_1({\:\raisebox{3.5pt}{\text{$\bullet$}}},\vec{\xi}) = \vec{\xi} \cdot \eta \vec{\xi} - a_0 \eta a_0, \\ &a_2({\:\raisebox{3.5pt}{\text{$\bullet$}}},\vec{\xi}) = -\frac{1}{2} \big| \vec{\xi} \big|^2 \eta^2 a_0 + a_0 \eta a_0 \eta a_0 - \frac{1}{2} a_0 \eta^2 \big| \vec{\xi} \big|^2. \end{split}$$

This decomposition has been used numerically in the pioneering work of Craig and Sulem (1993).

#### V.3. Hamiltonian structure

As already pointed out, Zakharov (1968) noticed that the Water Waves system (1.43) possesses a natural Hamiltonian structure. Indeed, should we define the following functional

$$H[\eta, \psi] = \frac{1}{2} \int_{\mathbb{R}} \psi(\vec{x}) \operatorname{DtN}[\eta] \psi(\vec{x}) \, d\vec{x} + \frac{1}{2} \int_{\mathbb{R}} g \eta^{2}(\vec{x}) \, d\vec{x}$$
$$= K[\eta, \psi] + V[\eta], \tag{1.46}$$

called the *energy* or Hamiltonian, then we will show that the system (1.43) can be put in the form

$$\partial_t \eta = \delta_\psi \mathbf{H}, \tag{1.47a}$$

$$\partial_t \psi = -\delta_n \mathbf{H}. \tag{1.47b}$$

We will now provide a proof of this important fact. The computations that will follow are purely formal (i.e. in the  $H^{\infty}(\mathbb{R}^d)$  sense). A more rigorous treatment can be found in Lannes (2013b, sec. 3.3)

V.3.1. Variation of V in  $\eta$ . The variation of the potential term in (1.46) is computed readily,

$$\begin{split} \mathbf{V}[\eta+h] &= \frac{g}{2} \int_{\mathbb{R}^d} \Bigl( \eta(\vec{x}) + h(\vec{x}) \Bigr)^2 \, \mathrm{d}\vec{x} \\ &= \frac{g}{2} \int_{\mathbb{R}^d} \Bigl( \eta(\vec{x})^2 + 2\eta(x)h(\vec{x}) + h(\vec{x})^2 \Bigr) \, \mathrm{d}\vec{x} \\ &= \mathbf{V}[\eta] + \int_{\mathbb{R}^d} g\eta(\vec{x}) \cdot h(\vec{x}) \, \mathrm{d}\vec{x} + O\Bigl( \|h\|^2 \Bigr). \end{split}$$

V.3.2. Variation of K in  $\psi$ . Using the symmetry of the DtN[ $\eta$ , b] operator (lemma 1.10(1)), we can quickly get  $\delta_{\psi}$ K,

$$\begin{split} \mathbf{K}[\eta,\psi+h] &= \frac{1}{2} \int_{\mathbb{R}^d} \Bigl( \psi(\vec{x}) + h(\vec{x}) \Bigr) \mathbf{DtN}[\eta] \Bigl( \psi(\vec{x}) + h(\vec{x}) \Bigr) \, \mathrm{d}\vec{x} \\ &= \int_{\mathbb{R}^d} \Bigl( \frac{1}{2} \psi \mathbf{DtN}[\eta] \psi + h \mathbf{DtN}[\eta] \psi \Bigr) + O\Bigl( \|h\|^2 \Bigr) \\ &= \mathbf{K}[\eta,\psi] + \int_{\mathbb{R}} h \mathbf{DtN}[\eta] \psi + O\Bigl( \|h\|^2 \Bigr). \end{split}$$

Notation.  $\delta_{\psi} H$  is the Fréchet partial derivative of H with respect to the function  $\psi$ .

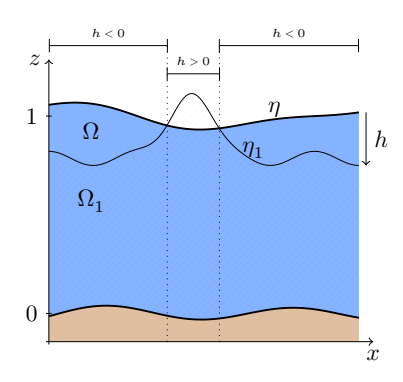


**Figure 1.18** – Variation of  $K[\eta, \psi]$  with respect to  $\eta$ . Visual definitions.

V.3.3. Variation of K in  $\eta$ . This is where things get more involved. Let  $\eta_h = \eta + h$ , where h is a small variation. Let  $\phi$  and  $\phi_h$  the corresponding solutions of the Dirichlet problems associated with the Dirichlet-Neumann operator,

$$\begin{split} \operatorname{DtN}[\eta_h] : \left\{ \begin{array}{rcl} \Delta\phi_h &=& 0 & \text{in } \Omega_h \\ \phi_h &=& \psi & \text{on } z = \eta_h(\vec{x}) \\ \partial_n\phi_h &=& 0 & \text{on } z = b(\vec{x}) \end{array} \right. \\ \operatorname{DtN}[\eta] : \left\{ \begin{array}{rcl} \Delta\phi &=& 0 & \text{in } \Omega \\ \phi &=& \psi & \text{on } z = \eta(\vec{x}) \\ \partial_n\phi &=& 0 & \text{on } z = b(\vec{x}) \end{array} \right. \end{split}$$

Of course  $\Omega$  (respectively  $\Omega_h$ ) denotes the water column encompassed between the graph of b and  $\eta$  (resp. b and  $\eta_h$ ). Green's identity quickly leads to

$$\begin{aligned} 2\mathbf{K}[\eta+h,\psi] &= \int_{\mathbb{R}^d} \psi G[\eta+h] \psi \\ &= \int_{\mathbb{R}^d} \int_b^{\eta+h} \left| \boldsymbol{\nabla} \phi_h \right|^2 \\ &= \left( \int_{\{h<0\}} + \int_{\{h>0\}} \right) \int_b^{\eta_h} \left| \boldsymbol{\nabla} \phi_h \right|^2 \\ &= I_-[\eta+h,\psi] + I_+[\eta+h,\psi] \end{aligned}$$

This decomposition of the integral is possible since both  $\eta$  and  $\eta_h$  are continuous. This is equivalent to decomposing  $h=h_++h_-$  with  $h_+=\max\{h,0\}$  and  $h_-=\min\{h,0\}$ . The derivative being a linear operator, we can compute  $K[\eta+h_+,\psi]$  and  $K[\eta+h_-,\psi]$  separately<sup>1</sup>, and we must get the same expression at the end. Let us treat each term independently.

The first term  $I_{-}$  corresponds to  $\vec{x} \in \mathbb{R}^{d}$  such that  $\eta(\vec{x}) > \eta_{h}(\vec{x})$ , i.e.  $h(\vec{x}) < 0$  (figure 1.18). In that case,  $\phi$  is defined in  $\Omega_{h}$  and we can write

$$\begin{split} \phi\Big(\vec{x},\eta_h(\vec{x})\Big) &= \phi\Big(\vec{x},\eta(\vec{x}) + h(\vec{x})\Big) \\ &= \phi\Big(\vec{x},\eta(\vec{x})\Big) + \partial_z \phi\Big(\vec{x},\eta(\vec{x})\Big) \cdot h(\vec{x}) + O\Big(h^2\Big) \\ &= \psi(\vec{x}) + \partial_z \phi\Big(\vec{x},\eta(\vec{x})\Big) \cdot h(\vec{x}) + O\Big(h^2\Big) \\ &= \phi_h\Big(\vec{x},\eta_h(\vec{x})\Big) + \partial_z \phi\Big(\vec{x},\eta(\vec{x})\Big) \cdot h(\vec{x}) + O\Big(h^2\Big) \end{split} \tag{1.49}$$

so that

$$\begin{split} I_{-}[\eta+h,\psi] &= \int_{\{h(\vec{x})<0\}} \int_{b}^{\eta_{h}} \left| \nabla \phi_{h} \right|^{2} \\ &= \int_{\{h(\vec{x})<0\}} \int_{b}^{\eta_{h}} \left| \nabla \phi_{h} \right|^{2} + \int_{\{h(\vec{x})<0\}} \int_{b}^{\eta} \left| \nabla \phi \right|^{2} - \int_{\{h(\vec{x})<0\}} \int_{b}^{\eta} \left| \nabla \phi \right|^{2} \\ &= I_{-}[\eta,\psi] + \int_{\{h(\vec{x})<0\}} \int_{b}^{\eta_{h}} \left| \nabla \phi_{h} \right|^{2} - \int_{\{h(\vec{x})<0\}} \int_{b}^{\eta+h} \left| \nabla \phi \right|^{2} + \int_{\{h(\vec{x})<0\}} \int_{\eta}^{\eta+h} \left| \nabla \phi \right|^{2} \end{split}$$

To handle the last integral, we use the fact that

$$\int_{\eta}^{\eta+h} \left|\boldsymbol{\nabla}\phi\right|^2 = \int_{\eta}^{\eta+h} \left[\left|\boldsymbol{\nabla}\phi\right|^2\!\left(\vec{x},\eta(\vec{x})\right) + \partial_z\!\left|\boldsymbol{\nabla}\phi\right|^2\!\left(\vec{x},\tilde{z}\right)h(\vec{x})\right]\,\mathrm{d}z$$

<sup>1</sup>This method shall be used to investigate the Hamiltonian structure of the Breaking Waves equations in sec. II.3 of chapter 2.

$$= \left| \boldsymbol{\nabla} \phi \right|^2 \! \left( \vec{x}, \eta(\vec{x}) \right) \cdot h(\vec{x}) + O\! \left( h^2 \right),$$

for some  $\tilde{z} \in (\eta + h, \eta)$  (this is the Taylor-Cauchy formula). Regarding the first and second integrals, we can now use

$$\begin{split} & \int_{\{h<0\}} \int_{b}^{\eta_{h}} \left| \boldsymbol{\nabla} \phi_{+} \right|^{2} - \left| \boldsymbol{\nabla} \phi \right|^{2} \\ & = \int_{\{h<0\}} \left( \phi_{h} \partial_{n} \phi_{h} \big|_{z=\eta_{h}} - \phi \partial_{n} \phi \big|_{z=\eta_{h}} \right) \\ & = \int_{\{h<0\}} \left( \phi_{h} \partial_{n} \phi_{h} \big|_{z=\eta_{h}} - \left[ \phi_{h} \big|_{\eta_{h}} + \partial_{z} \phi \big|_{\eta} \right] \partial_{n} \left[ \phi_{h} \big|_{\eta_{h}} + \partial_{z} \phi \big|_{\eta} \right] \right) \\ & = -\int_{\{h<0\}} \left( \partial_{z} \phi \big|_{\eta} \partial_{n} \phi_{h} \big|_{\eta_{h}} + \phi_{h} \big|_{\eta_{h}} \partial_{n} \partial_{z} \phi \big|_{\eta} \right) \cdot h \\ & = -2 \int_{\{h<0\}} \partial_{y} \phi \big|_{\eta} \partial_{n} \phi_{h} \big|_{\eta_{h}} \cdot h = -2 \int_{\{h<0\}} h \cdot \partial_{z} \phi \partial_{n} \phi \big|_{\eta} \\ & = -2 \int_{\{h<0\}} \mathrm{DtN}[\eta, b] \psi \cdot \partial_{z} \phi \big|_{\eta} \cdot h, \end{split}$$

where we have used multiple times the identities (1.49) and the symmetry property of the Dirichlet-to-Neumann operator. Combining everything we get

$$\begin{split} I_{-}[\eta+h,\psi] - I_{-}[\eta,\psi] &= \int_{\{h<0\}} h \cdot \left[ \left( \left( \partial_z \phi \right)^2 + \left( \vec{\nabla} \phi \right)^2 \right) \Big|_{z=\eta} - 2 \Big( \mathrm{DtN}[\eta,b] \psi \cdot \partial_z \phi \Big) \Big|_{z=\eta} \right] \\ &= \int_{\{h<0\}} h \cdot \left[ \left( 1 + \left( \vec{\nabla} \eta \right)^2 \right) \left( \partial_z \phi \right)^2 + \left| \vec{\nabla} \psi \right|^2 - 2 \Big[ \mathrm{DtN}[\eta,b] \psi + \vec{\nabla} \eta \cdot \vec{\nabla} \psi \Big] \partial_z \phi \Big] \Big|_{z=\eta} \\ &= \int_{\{h<0\}} h \cdot \left[ \left| \vec{\nabla} \psi \right|^2 - \frac{\left( \mathrm{DtN}[\eta,b] \psi + \vec{\nabla} \eta \cdot \vec{\nabla} \psi \right)^2}{1 + \left( \vec{\nabla} \eta \right)^2} \right]. \end{split}$$

We won't treat in details the case  $h(\vec{x}) > 0$  since it leads to similar computations and an identical result, namelly

$$I_+[\eta+h,\psi] - I_+[\eta,\psi] = \int_{\{h>0\}} h \cdot \left[ \left| \vec{\nabla} \psi \right|^2(x) - \frac{\left( \mathrm{DtN}[\eta,b] \psi + \vec{\nabla} \eta \cdot \vec{\nabla} \psi \right)^2}{1 + \left( \vec{\nabla} \eta \right)^2} \right].$$

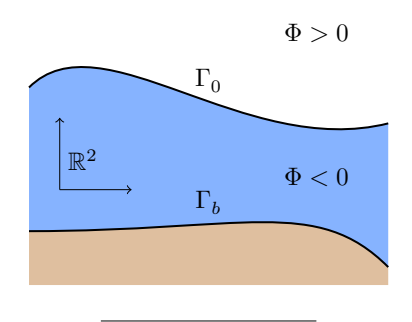
One just needs to remember that this time,  $\phi_h$  is defined in  $\Omega$  but  $\phi$  is not defined in all  $\Omega_h$  (fig. 1.18). We thus get the variationnal derivative of K with respect to  $\eta$ ,

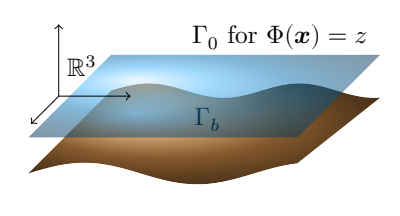
$$\delta_{\eta} \mathbf{K}(h) = \frac{1}{2} \int_{\mathbb{R}} h \cdot \left[ \left| \vec{\nabla} \psi \right|^2 (x) - \frac{\left( \mathrm{DtN}[\eta, b] \psi + \vec{\nabla} \eta \cdot \vec{\nabla} \psi \right)^2}{1 + \left( \vec{\nabla} \eta \right)^2} \right].$$

This finally establishes (1.47).

#### V.4. Water Waves on a manifold

Before moving on to a discussion on asymptotic regimes, we would like to present a reformulation of (1.43) on a d-dimensional (hyper)surface embedded in  $\mathbb{R}^{d+1}$ . In this manner, we shall express the Water Waves equations on a spherical shell (as in the earth system) or on the d-torus. In this way, we will also introduce most of the tools that shall





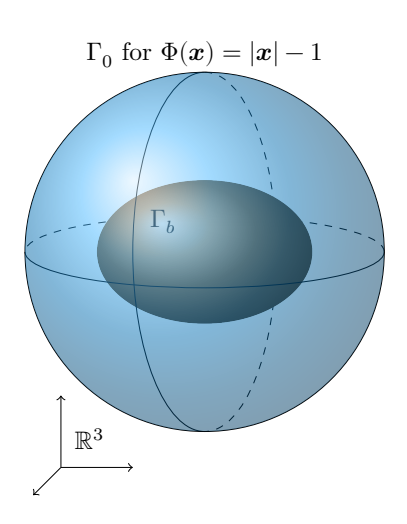


Figure 1.19 – (up) Schematic representation in 2d of the unperturbed surface  $\Gamma_0$  for a general gravitational potential  $\Phi$ . (middle) Case of the flat ocean. (down) Spherical ocean.

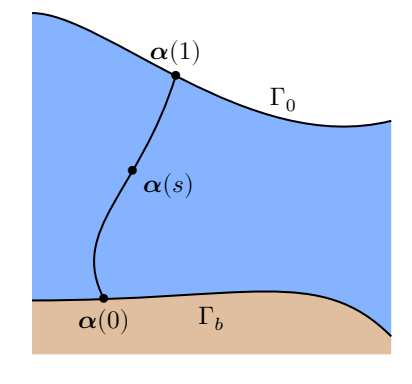


Figure 1.20 – An admissible path between  $\Gamma_b$  and  $\Gamma_0$  in 2d.

be used to motivate the Breaking Waves equations in the following chapter.

Let  $\Phi: \mathbb{R}^{d+1} \to \mathbb{R}$  a smooth function, representing a gravitational potential. We suppose that 0 is regular value of  $\Phi$  so that  $\Gamma_0 = \Phi^{-1}(\{0\})$  can be equipped with a d-dimensional oriented riemannian manifold structure (fig. 1.19). It represents the stationary (unperturbed) free surface.

If the ocean has no bottom, then the unperturbed fluid domain can be taken as

$$\Omega_0 = \big\{ \boldsymbol{x} \in \mathbb{R}^{d+1} : \Phi(\boldsymbol{x}) < 0 \big\}.$$

This is e.g. the case of an infinitely deep flat ocean. Should a topography exist, the fluid domain can be defined as follows: let  $\Gamma_b$  a surface in  $\mathbb{R}^d$  without boundary. In the absence of perturbation of  $\Gamma_0$ , hypothesis (**H5**, bis) amounts to assume that each point of  $\Gamma_b$  is a distance al least  $\delta > 0$  of  $\Gamma_0$ :

$$\inf_{\boldsymbol{x}\in\Gamma_b}\mathrm{dist}\big(\boldsymbol{x},\Gamma_0\big)=\delta>0.$$

Using the link between  $\Gamma_0$  and  $\Phi \in C^{\infty}(\mathbb{R}^{d+1})$ , this also means that

$$\sup_{\boldsymbol{x}\in\Gamma_b}\Phi(\boldsymbol{x})=-C(\delta)<0,$$

for some non-decreasing function C of  $\delta$ . To rigorously define  $\Omega$ , we shall need the following definition,

**Definition 1.11.** An admissible path connecting  $\Gamma_b$  to  $\Gamma_0$  is a parametrised continuous curve  $\boldsymbol{\alpha}:[0,1]\to\mathbb{R}^{d+1}$  whose endpoints lie on  $\Gamma_b$  and  $\Gamma_0$  respectively and whose interior points never cross either  $\Gamma_b$  or  $\Gamma_0(\text{fig. 1.20})$ . More precisely, we have  $\boldsymbol{\alpha}(0)\in\Gamma_b$ ,  $\boldsymbol{\alpha}(1)\in\Gamma_0$  and

$$\alpha(s) \notin \Gamma_b \cup \Gamma_0$$
, for all  $s \in (0,1)$ 

Then  $\Omega_0$  is the set of points lying on an admissible path connecting  $\Gamma_b$  and  $\Gamma_0$  (and which are not endpoints),

$$\Omega_0 = \Big\{ \boldsymbol{x} \in \mathbb{R}^{d+1} : \exists \boldsymbol{\alpha} \text{ admissible path s.t. } \boldsymbol{\alpha}(s) = \boldsymbol{x} \text{ for } s \in (0,1) \Big\}.$$

It is easy to see that  $\Omega_0$  defined in such manner is an open subset of  $\mathbb{R}^{d+1}$  with boundaries  $\Gamma_0$  and  $\Gamma_b$ .

Having defined  $\Gamma_0$  as the zero level-set of  $\Phi$ , it follows that a solution of the Euler–Bernoulli system (1.35) is  $\phi = 0$ . Indeed Bernoulli's equation (1.34) in  $\Omega_0$  is simply

$$\partial_t \phi + \frac{1}{2} |\nabla \phi|^2 + \Phi + p = 0.$$

Evaluated on the unperturbed free surface  $\Gamma_0,$  both  $\Phi$  and p vanish, yielding the system

$$\begin{cases} \Delta \phi &= 0 & \text{in } \Omega \\ \partial_t \phi + \frac{1}{2} |\nabla \phi|^2 &= 0 & \text{on } \Gamma_0 \\ \partial_n \phi &= 0 & \text{on } \Gamma_b \\ \phi(t=0) &= 0. \end{cases}$$

whose solution is  $\phi = 0$ , *i.e.* there is no motion due to the gravitational interaction on the interface.

V.4.1. Water Waves as a perturbation of  $\Gamma_0$ . How to introduce a surface perturbation  $\eta$  as in (1.43)? The idea is to use the unit vector  $\hat{\boldsymbol{n}}_0$ , normal to  $\Gamma_0$ . To define it in a rigorous manner, we use the  $C^{\infty}$  inclusion  $\iota:\Gamma_0\hookrightarrow\mathbb{R}^{d+1}$ . Let  $\vec{s}\in\Gamma_0^{-1}$ , the associated unit normal vector  $\hat{\boldsymbol{n}}_0(\vec{s})$  is defined by

$$\hat{\boldsymbol{n}}_0(\vec{s}) = \left[ \frac{\boldsymbol{\nabla} \boldsymbol{\Phi}}{\left| \boldsymbol{\nabla} \boldsymbol{\Phi} \right|} \circ \iota \right] (\vec{s}).$$

It is well defined since  $\Phi$  is a submersion (its gradient does not vanish in the vicinity of  $\Gamma_0$ ). Let  $\eta_t:\Gamma_0\to\mathbb{R}$  a function depending continuously on the time t. We define a new, time-dependent surface  $\Gamma_i(t)$  as the image of the following map

$$\begin{array}{cccc} \boldsymbol{f}[\eta_t] & : & \Gamma_0 & \longrightarrow & \mathbb{R}^{d+1} \\ & \vec{s} & \longmapsto & \iota(\vec{s}) + \eta_t(\vec{s}) \hat{\boldsymbol{n}}_0(\vec{s}). \end{array}$$

In the flat case, i.e. in the usual formulation of the Water Waves equations,  $\Gamma_i(t)$ , defined in this manner, is always a regular surface. Using it, we define the fluid volume  $\Omega(t)$  as long as  $\Gamma_i(t) \cap \Gamma_b = \emptyset$ . Whenever  $\Gamma_0$  is a curved surface, a curvature-based criterion on  $\eta_t$  must be specified in order to prevent self-intersections. Put differently, we must enforce a criterion to make  $\boldsymbol{f}[\eta_t]$  not only an immersion, but an embbeding.

The easiest such criterion is based on the extremas of  $\Gamma_0$ 's curvature. Indeed, for a certain  $\vec{s} \in \Gamma_0$ , let  $\kappa_1, ..., \kappa_d$  the principal curvatures of the base water surface  $\Gamma_0^2$ . Introduce  $\Gamma_h$  the parallel surface at a fixed (signed) distance h to  $\Gamma_0$  (fig. 1.22), that is, the image of  $\boldsymbol{f}[h]$ . For  $h \geq 0$ ,  $\Gamma_h$  lies in the "air" (*i.e.* where  $\Phi \geq 0$ ) while for h < 0,  $\Gamma_h$  lies in the "water" domain, where  $\Phi < 0$ .

We can relate the principal curvatures  $\kappa_{1,h},...,\kappa_{d,h}$  of  $\Gamma_h$  to  $\kappa_1,\cdots,\kappa_d$  in the following manner,

$$\kappa_{i,h} = \frac{\kappa_i}{1 + h\kappa_i} \qquad \text{for } i = 1, \cdots, d.$$

This is shown in e.g. Brechner (1992), cor. 5.4.2. The latter relation stipulates that  $\Gamma_h$  possesses a cusp in the *i*-th principal direction at  $\vec{s}$  as soon as

$$h > \pm \frac{1}{\kappa_i}$$

depending on whether  $\Gamma_0$  is locally concave  $(\kappa_i > 0)$  or convex  $(\kappa_i < 0)$  in the *i*-th direction at  $\vec{s}$  (fig. 1.23). Therefore, should we choose  $h_+, h_- \in \mathbb{R}$  such that

$$h_- > \left[\inf_{\vec{s} \in \Gamma_0} \min_{i=1,\cdots,d} \kappa_i(\vec{s})\right]^{-1} \quad \text{and} \quad h_+ < \left[\sup_{\vec{s} \in \Gamma_0} \max_{i=1,\cdots,d} \kappa_i(\vec{s})\right]^{-1},$$

with straightforward adaptations to globally convex or concave surfaces, then we can choose  $h_- < \eta_t < h_+$  and be sure that the mapping  $f[\eta_t]$  is an embedding. However, this condition is far from optimal as a small curvy region prevents large perturbations to arise in almost planar zones far away.

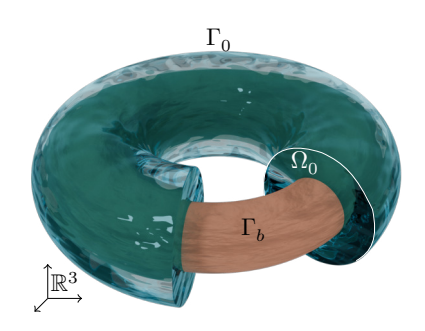


Figure 1.21 – Water Waves on the 2–torus. Parts of the interface  $\Gamma_0$  and of  $\Omega$  have been truncated in order to highlight the bottom topography  $\Gamma_b$ .

<sup>1</sup>Motivated by the work we have done so far on the flat ocean case, we denote using an overhead arrow  $\vec{\phantom{a}}$  the points of  $\Gamma_0$ . As  $\Gamma_0$  is defined as a subset of  $\mathbb{R}^{d+1}$ , we could also write  $\vec{s} \in \mathbb{R}^{d+1}$ . Hence the point of this notation is to emphasise that  $\vec{s}$  belongs to  $\Gamma_0$  as well as  $\mathbb{R}^{d+1}$ .

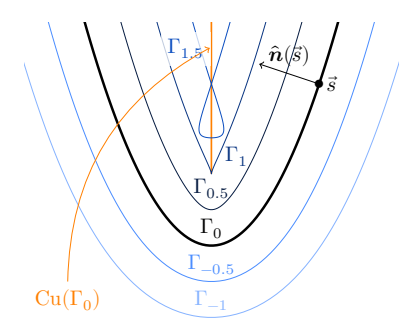


Figure 1.22 – The parallel curves to a parabola  $\Gamma_0$  of maximum curvature 1.

<sup>2</sup>Technically, the  $\kappa_1,...,\kappa_d$  are defined as eigenvalues of  $\Gamma_0$ 's second fundamental form.

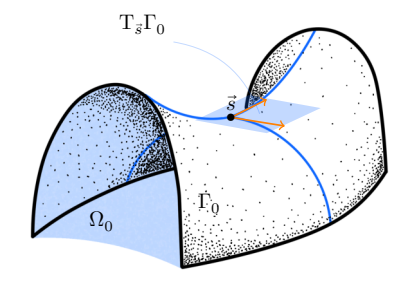


Figure 1.23 – The principal curvatures at  $\vec{s} \in \Gamma_0$ . The orange vectors are the principal directions. The blue curves are the associated geodesics, whose respective curvature at  $\vec{s}$  are exactly the principal curvatures.

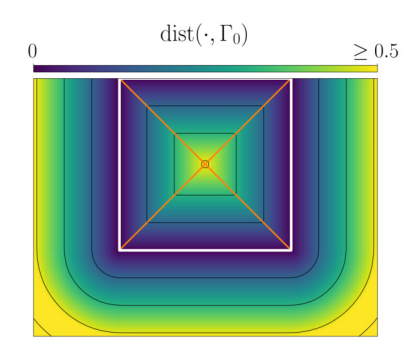
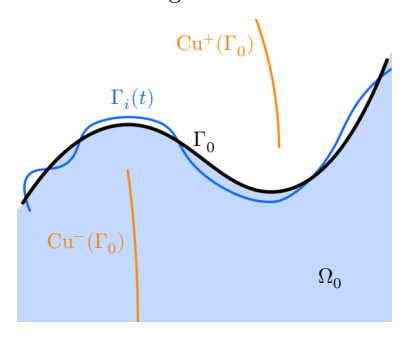


Figure 1.24 – Distance function to the unit square (in white), with isolines in black. The cut locus is shown in orange.



**Figure 1.25** – A perturbation  $\Gamma_i(t)$  of the steady surface  $\Gamma_0$ . Its outer and inner cut loci,  $\operatorname{Cu}^+(\Gamma_0)$  and  $\operatorname{Cu}^+(\Gamma_0)$ , are shown in orange.

 $^1{\rm A}$  parametrisation of  $L_{\vec s}$  is

$$\mathbf{r}_{\vec{s}}(u) = \iota(\vec{s}) + \hat{\mathbf{n}}_0(\vec{s})u,$$

for  $u \in \mathbb{R}$ .

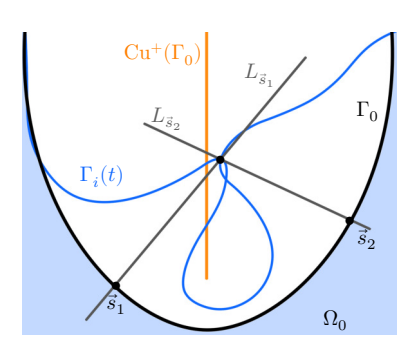


Figure 1.26 – Proof of lemma 1.12.

V.4.2. The cut locus criterion. A better geometrical argument leads to a more optimal requirement on  $\eta_t$  to yield a regular surface  $\Gamma_i(t)$ . The distance  $\mathrm{dist}(\boldsymbol{x},A)$  of a point  $\boldsymbol{x} \in \mathbb{R}^{d+1}$  to a subset  $A \in \mathbb{R}^{d+1}$  is defined as

$$\operatorname{dist}(\boldsymbol{x},A) = \inf_{\boldsymbol{y} \in A} \left| \boldsymbol{x} - \boldsymbol{y} \right|.$$

We define the  $cut\ locus\ {\rm Cu}(\Gamma_0)$  of  $\Gamma_0$  in two different ways. The first definition, analytical, relies on the singular support (defined in A.12) as

$$\mathrm{Cu}(\Gamma_0) = \left[\mathrm{sing}\,\mathrm{supp}\,\operatorname{dist}({\:\raisebox{3.5pt}{\text{\circle*{1.5}}}},\Gamma_0)\right] - \Gamma_0.$$

This definition, while practical, does not give much insight on the shape of  $\mathrm{Cu}(\Gamma_0)$ . Therefore we also provide a geometric definition. To this end, we introduce an auxiliary set, the separating set  $\mathrm{Se}(\Gamma_0)$  associated with  $\Gamma_0$ . It consists in points  $\boldsymbol{x} \in \mathbb{R}^{d+1} - \Gamma_0$  lying on at least two distance-minimising line segments from  $\boldsymbol{x}$  to  $\Gamma_0$  (fig. 1.24). Owing to thm. 3.30 of Basu and Prasad (2023), there holds that

$$Cu(\Gamma_0) = \overline{Se(\Gamma_0)}.$$

Examples of cut loci of various planar curves and surfaces are represented in figure 1.24, 1.25 or 1.27. The proof that both definitions are equivalent can be found in Basu and Prasad (2023, lemma 3.7).

From the set  $\mathrm{Cu}(\Gamma_0)$  can be extracted a geometric sufficient condition on  $\eta_t$  to yield a regular perturbation surface  $\Gamma_i(t)$ . Indeed, let

$$\operatorname{Cu}^-(\Gamma_0) = \operatorname{Cu}(\Gamma_0) \cap \Omega_0$$
 and  $\operatorname{Cu}^+(\Gamma_0) = \operatorname{Cu}(\Gamma_0) - \operatorname{Cu}^-(\Gamma_0)$ 

(see fig. 1.25). Intuitively, the idea is to choose  $\eta_t$  in order to prevent  $\Gamma_i(t)$  to cross  $\operatorname{Cu}^{\pm}(\Gamma_0)$ . This can be formalised as follows.

We denote by  $L_{\vec{s}} \subset \mathbb{R}^{d+1}$  the line that passes through  $\iota(\vec{s})$  in the normal direction  $\hat{\boldsymbol{n}}_0(\vec{s})^1$  (fig. 1.26). Introduce the functions

$$d^{\pm}(\vec{s}) = \mathrm{dist}\Big(\iota(\vec{s}), L_{\vec{s}} \cap \mathrm{Cu}^{\pm}(\Gamma_0)\Big).$$

Then we have

**Lemma 1.12.** Let  $\eta_t:\Gamma_0\to\mathbb{R}$  a  $C^\infty$  function such that

$$d^- < \eta_t < d^+$$

then the map  $\mathbf{f}[\eta_t]$  is an embedding and the associated surface  $\Gamma_i(t)$  is a regular submanifold of  $\mathbb{R}^{d+1}$ .

*Proof.* The idea is to show that if  $f[\eta_t]$  fails to be one-to-one, then  $\Gamma_i(t)$  crosses  $Cu(\Gamma_0)$  somewhere.

Thus, assume that  $\vec{s}_1, \vec{s}_2 \in \Gamma_0$  are such that

$$f[\eta_t](\vec{s}_1) = f[\eta_t](\vec{s}_2)$$
 while  $\vec{s}_1 \neq \vec{s}_2$ .

Without loss of generality, we will assume that  $f[\eta_t](\vec{s}_1)$  (see fig. 1.26) lies outside of  $\Omega_0$ , *i.e.*  $0 < \eta_t(\vec{s}_1)$  and  $0 < \eta_t(\vec{s}_2)$ . The opposite case is treated in a similar manner (with minus signs added when needed). By eventually swapping  $\vec{s}_1$  and  $\vec{s}_2$ , we can write  $\eta_t(\vec{s}_1) < d^+(\vec{s}_1)$ . Then, by definition of  $\mathrm{Cu}(\Gamma_0)$ ,

$$\operatorname{dist}\!\left(\boldsymbol{f}[\eta_t](\vec{s}_1), \Gamma_0\right) = \eta_t(\vec{s}_1).$$

Indeed, the shortest path joining  $f[\eta_t](\vec{s}_1)$  and  $\Gamma_0$  is the straight one passing through  $\iota(\vec{s}_1)$  in a perpendicular direction. Thus, the straight perpendicular path joining  $\iota(\vec{s}_2)$  and  $f[\eta_t](\vec{s}_2) = f[\eta_t](\vec{s}_1)$  is not the shortest. Therefore  $\eta_t(\vec{s}_2) > d^+(\vec{s}_2)$ .

Finally, as  $f[\eta_t]$  is a diffeomorphism between a manifold and its image, its image inherits the manifold structure of  $\Gamma_0$  and  $f[\eta_t]$  is an embedding, as wanted.

An admissible surface elevation  $\eta_t$  satisfies the hypotheses of lemma 1.12 and is such that  $\Gamma_i(t) \cap \Gamma_b = \emptyset$ .

V.4.3. The Water Waves equations in local frame. Given an admissible surface elevation  $\eta_t$ , we define the perturbed water domain  $\Omega(t)$  using the method that has been used to define  $\Omega_0$ , using admissible paths between  $\Gamma_b$  and  $\Gamma_i(t)$ .

The surface advection equation on  $\eta_t$  is now stated. Introduce the gradient of  $\eta_t$  using its differential as such,

$$\vec{\nabla}\eta_t = \left(\mathrm{d}\eta_t\right)^{\sharp} \in \mathrm{T}\Gamma_0.$$

At each  $\vec{s} \in \Gamma_0$ , it can be identified with a vector in  $T_{\iota(\vec{s})}\mathbb{R}^{d+1} \simeq \mathbb{R}^{d+1}$  using the differential of the canonical injection,  $\iota_*(\vec{\nabla}\eta_t)$ . The analogue of (1.20) on a curved surface  $\Gamma_0$  is then

$$\partial_t \eta_t = \left[ \hat{\boldsymbol{n}}_0 - \iota_*(\vec{\nabla} \eta_t) \right] \cdot \left( \boldsymbol{\nabla} \phi_t \circ \boldsymbol{f}[\eta_t] \right) = \mathrm{DtN}[\eta_t] \psi,$$

for  $\psi_t$  now defined as  $\psi_t = \phi_t \circ \boldsymbol{f}[\eta_t]$ . This is an equation on  $\Gamma_0$ . As in the flat case,  $\hat{\boldsymbol{n}}_0 - \iota_*(\vec{\nabla}\eta_t)$  is a vector field everywhere perpendicular to  $\Gamma_i(t)^1$ .

In order to derive the equation for  $\psi_t$ , we shall work in a coordinate chart. Indeed, the structure of  $\psi_t$  makes it difficult to handle globally. Let  $\vec{s} \in \Gamma_0$  and choose an open set  $U_{\vec{s}} \subset \mathbb{R}^{d+1}$  containing  $\iota(\vec{s})$  along with a diffeomorphism  $\Psi: U_{\vec{s}} \to \mathbb{R}^{d+1}$  (fig. 1.27). We denote the i-th components of  $\Psi$  as  $x^i$ . We assume that in this coordinate system  $\Gamma_0$  is represented by

$$\vec{r} \in \Gamma_0 \iff x^{d+1}(\vec{r}) = 0,$$

and that  $x^{d+1}$  corresponds to the unit normal coordinate,

$$\left.\frac{\partial}{\partial x^{d+1}}\right|_{\vec{s}} = \hat{\boldsymbol{n}}(\vec{r}), \qquad \text{for each } \vec{r} \in U_{\vec{s}} \cap \Gamma_0,$$

with extension in the normal direction. Therefore, we can also assume that  $U_{\vec{s}}$  extends up to  $\operatorname{Cu}(\Gamma_0)$  but it exhibits a coordinate singularity on any further extension. Since  $\Gamma_0$  is embedded in  $\mathbb{R}^{d+1}$ , the couple  $(V_{\vec{s}},\Xi)=(U_{\vec{s}}\cap\Gamma_0,\Psi|_{\Gamma_0})$  is a chart on  $\Gamma_0$  centered at  $\vec{s}$ . We can then write  $\iota=\Xi\circ\Psi^{-1}$ .

In the local coordinate frame  $x^j$ , the points of  $\Gamma_i(t)$  are represented in a way that does not fail to remind us something, namelly

$$(\Psi \circ \boldsymbol{f}[\eta_t])(\vec{s}) = \begin{bmatrix} x^1(\vec{s}) \\ \vdots \\ x^d(\vec{s}) \\ \eta_t(\vec{s}) \end{bmatrix}.$$
 (1.50)

The link between the potential  $\phi$  and its trace  $\psi$  is computed readily,

$$\psi_t \circ \Xi^{-1} = \phi_t \circ \boldsymbol{f}[\eta_t] \circ \Xi^{-1}$$
 by definition,

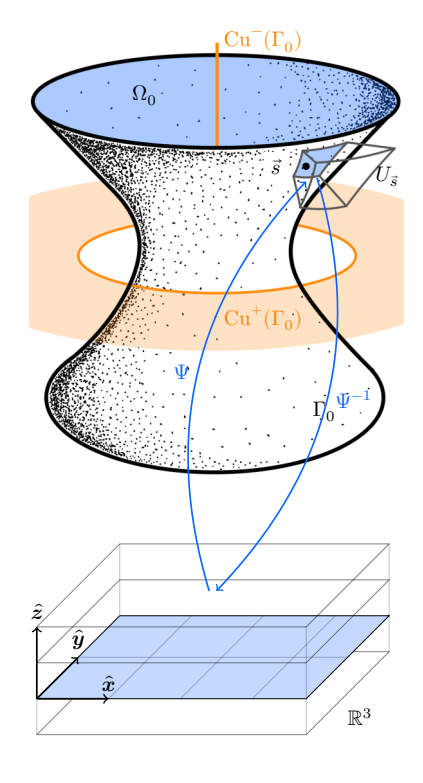


**Figure 1.27** – The cut locus of a surface. The chart  $U_{\vec{s}}$  around  $\vec{s}$  and the associated diffeomorphism.

<sup>1</sup>Indeed, through a quick computation we notice that

$$\hat{\boldsymbol{n}}_0 - \iota_*(\vec{\nabla}\eta_t) = \boldsymbol{f}[\eta_t]_* \hat{\boldsymbol{n}}_0.$$

$$\begin{split} &= \phi_t \circ \Psi^{-1} \circ \Psi \circ \boldsymbol{f}[\eta_t] \circ \Xi^{-1} & \quad \Psi \text{ being a diffeomorphism,} \\ &= \left[ \phi_t \circ \Psi^{-1} \right] \! \left( \vec{r}, \left( \eta_t \circ \Xi^{-1} \right) \! (\vec{r}) \right) & \text{using } (1.50), \end{split}$$

with  $\vec{r}$  a vector in  $\Xi(\Gamma_0) \subseteq \mathbb{R}^d$ . This shows that we can just work with the quantities  $\psi_t \circ \Xi^{-1}$ ,  $\phi_t \circ \Psi^{-1}$  and  $\eta_t \circ \Xi^{-1}$  as was done in the flat ocean case (sec. V.1). Following the same procedure<sup>1</sup>, the resulting equations (on  $\Gamma_0$ ) are exactly (1.43),

$$\begin{cases} \partial_t \eta_t = \mathrm{DtN}[\eta_t] \psi_t \\ \\ \partial_t \psi_t = \Phi \circ \boldsymbol{f}[\eta_t] - \frac{1}{2} \big| \vec{\nabla} \psi_t \big|_{\Gamma_0}^2 + \frac{1}{2} \frac{ \left[ \mathrm{DtN}[\eta] \psi_t + \mathbf{g}_{\Gamma_0} (\vec{\nabla} \psi_t, \vec{\nabla} \eta_t) \right]^2}{1 + |\vec{\nabla} \eta_t|_{\Gamma_0}^2}. \end{cases}$$

The geometrical information is implicitly encoded in the metric  $\mathbf{g}_{\Gamma_0}$ . It thus remains to elucidate its nature. If  $\langle \cdot, \cdot \rangle$  denotes the euclidean scalar product of  $\mathbb{R}^{d+1}$ , then the induced metric on  $\Gamma_0$  corresponds to its pullback by the inclusion  $\iota$ ,

$$\mathbf{g}_{\Gamma_0}(\cdot, \cdot) = \iota^* \langle \cdot, \cdot \rangle.$$

and  $\left| \vec{\nabla} \psi_t \right|_{\Gamma_0}^2$  is the associated norm.

V.4.4. Water Waves on the 2-sphere  $\mathbb{S}^2$ . A quick application of the rather abstract computations made above yields the water waves equations on the sphere. More precisely, we now write down the above system in the usual coordinate chart of the sphere given by the coordinate functions  $\theta, \varphi : \mathbb{S}^2 - \{\vec{N}, \vec{S}\} \to (0, \pi) \times (0, 2\pi)^2$ . Their action is defined through

$$(\theta, \varphi)^{-1} = \begin{bmatrix} \sin(\theta)\cos(\varphi) \\ \sin(\theta)\sin(\varphi) \\ \cos(\theta) \end{bmatrix}.$$

In this case we have  $\operatorname{Cu}(\mathbb{S}^2) = \{0\}$  so a surface perturbation  $\eta_t$  is admissible if  $\eta_t > -1$  everywhere on  $\mathbb{S}^2$ . The euclidean metric  $\mathbf{g}$ ,

$$\mathbf{g} = \mathrm{d}x^1 \otimes \mathrm{d}x^1 + \mathrm{d}x^2 \otimes \mathrm{d}x^2 + \mathrm{d}x^3 \otimes \mathrm{d}x^3,$$

gives rise to an intrinsic metric  $\mathbf{g}_{\mathbb{S}^2}$  on  $\mathbb{S}^2$  through the inclusion map  $\iota: \mathbb{S}^2 \hookrightarrow \mathbb{R}^3$ , namelly

$$\mathbf{g}_{\mathbb{S}^2} = \iota^* \mathbf{g} = \mathrm{d}\theta \otimes \mathrm{d}\theta + \sin^2(\theta) \mathrm{d}\varphi \otimes \mathrm{d}\varphi.$$

This metric contains the intrinsic geometric information of the sphere. Expressing the differential of a  $C^{\infty}$  function f using  $\theta, \varphi$  yields

$$\mathrm{d}f = \frac{\partial f}{\partial \theta} \mathrm{d}\theta + \frac{\partial f}{\partial \varphi} \mathrm{d}\varphi.$$

Its gradient  $\nabla f$  corresponds to the unique tangent vector such that<sup>3</sup>

$$\mathrm{d}f = \mathbf{g}_{\mathbb{S}^2}(\vec{\nabla}f, \bullet) \qquad \textit{i.e.} \qquad \vec{\nabla}f = \frac{\partial f}{\partial \theta}\frac{\partial}{\partial \theta} + \frac{1}{\sin^2(\theta)}\frac{\partial f}{\partial \varphi}\frac{\partial}{\partial \varphi}.$$

The coefficients appearing in the water waves equations on curved surfaces can be computed in the chart associated to  $\theta$  and  $\varphi$ ,

$$\mathbf{g}_{\mathbb{S}^2}(\vec{\nabla}\psi_t,\vec{\nabla}\eta_t) = \mathrm{d}\psi_t \Big(\vec{\nabla}\eta_t\Big) = \frac{\partial\psi_t}{\partial\theta}\frac{\partial\eta_t}{\partial\theta} + \frac{1}{\sin^2(\theta)}\frac{\partial\psi_t}{\partial\varphi}\frac{\partial\eta_t}{\partial\varphi}$$

<sup>1</sup>The computations are identical, except for the metric tensor **g** that is yet to be discussed.

 $^2\vec{N}$  and  $\vec{S}$  being respectively the north pole and the south pole of  $\mathbb{S}^2$ 

Should we use a normalised basis vector (sometimes denoted  $\hat{\varphi}$  or  $\hat{e}_{\varphi}$ ) instead, we would have the usual decomposition of the gradient vector on a unit spherical shell,

<sup>3</sup>Recall that  $\frac{\partial}{\partial \varphi}$  is not normalised.

$$ec{
abla}f = rac{\partial f}{\partial heta}\hat{oldsymbol{ heta}} + rac{1}{\sin( heta)}rac{\partial f}{\partial arphi}\hat{oldsymbol{arphi}}.$$

$$\left|\vec{\nabla}\psi_t\right|_{\mathbb{S}^2}^2 = \mathbf{g}_{\mathbb{S}^2}(\vec{\nabla}\psi_t,\vec{\nabla}\psi_t) = \left(\frac{\partial\psi_t}{\partial\theta}\right)^2 + \frac{1}{\sin^2(\theta)}\left(\frac{\partial\psi_t}{\partial\varphi}\right)^2$$

**Remark 1.13.** The Water Waves equations on  $\mathbb{S}^2$  could be usefull to describe ocean planets. However, to give an accurate description of such system, they should be rewritten in a rotating frame.

V.4.5. **Discussion.** Deriving the water waves equations on any smooth surface did not yield a surprising result: it is nothing but (1.43) with a different, non-flat, metric. Yet, it provided geometrical intuition that shall be used to describe breaking waves in the next chapter. Before doing so, we would like to make a few observations that, we believe, may be important to have in mind before moving on.

First, even though these equations describe the movement of  $\Gamma_i(t)$ , they are written on the unperturbed surface  $\Gamma_0$ . This presupposes a one-to-one correspondence between the two. While it seems unreasonable to drop out the very idea of a connection between  $\Gamma_0$  and  $\Gamma_i(t)$ , the one that has been chosen here (the normal perturbation  $\boldsymbol{f}[\eta_t]$ ) is too sharp and actually prevents this model from capturing the breaking phenomenon.

Moreover, at the very core of this method lies the implicit shape of the zero level-set of the gravitational potential,  $\Phi^{-1}(\{0\}) = \Gamma_0$ . Water waves can then be seen as time-dependant perturbations of this rest frame. In particular, if a perturbation  $\eta_t$  actually happens to yield another level-set of  $\Phi$ ,

$$\boldsymbol{f}[\eta_t](\Gamma_0) = \Phi^{-1}(\{\alpha\}),$$

for some  $\alpha \in \mathbb{R}^*$ , then the constant  $\alpha$  could be incorporated into the velocity potential  $\phi$ , yielding a steady perturbation. These kinds of  $\eta_t$  do not correspond to water waves in the physical sense since it lacks a time-dependent nature.

Finally, we observe that the geometrical analysis of admissible perturbations  $\eta_t$  eventually led us to find out about a new kind of singularity at which the present depiction of water waves fails: the *self-intersecting singularity* which, owing to lemma 1.12, only happens if  $f[\eta_t]$  crosses the cut locus. This shortcoming is intrinsic to the mathematical modelling. Indeed the universe does not break as soon as two water droplets collide.

Hypothesis	Physical description	Associated equation
H1	Matter is continuous	All of them
H2	Fluid is homogeneous	Incompressibility $(1.2)$
H3	Non-mixing of two phases	$\Gamma_i(t)$ exists and is d-dimensional
H4	Fluid is newtonian with homogeneous viscosity	(1.7), (1.8)
H5	No dry region, i.e. there is always water be-	$(\mathbf{H5}) \text{ or } (\mathbf{H5}, \text{ bis})$
	tween the air region and the bottom	
H6	Fluid is inviscid ( $\nu_{\rm w} = 0$ )	Euler's system $(1.6)$ , $(1.10)$ and $(1.16)$
H7	Neglecting the air	$\rho_{\rm a} = 0$
H8	The wave does not break	$\Gamma_i(t)$ is the graph of $h(t, \vec{x})$
H9	Neglecting surface tension	$\gamma_{\rm w} = 0$
H10	The bottom topography is single-valued	$\Gamma_b$ is the graph of $b(\vec{x})$
H11	The flow is irrotational	$\breve{\omega}=0$

**Table 1.3** – Reminder of the hypotheses that were made when deriving the equations describing eulerian water waves.

**Remark 1.14.** In this chapter, three sets of equations have been motivated from a physical perspective. For the sake of clarity and accessibility of the following chapters, we wrap up the considerations of the present one and recall these sets of equations (and the assumptions that **were not made** to motivate them).

1. The free–surface incompressible Euler system. (¬H8, ¬H10, ¬H11)

$$\begin{cases} \partial_t \boldsymbol{u} + \boldsymbol{u} \cdot \nabla \boldsymbol{u} = -\nabla p + \boldsymbol{g} & \text{in } \Omega(t) & (1.53a) \\ \nabla \cdot \boldsymbol{u} = 0 & \text{in } \Omega(t) & (1.53b) \\ p = 0 & \text{on } \Gamma_i(t) & (1.53c) \\ \boldsymbol{u} \cdot \hat{\boldsymbol{n}}_b = 0 & \text{on } \Gamma_b & (1.53d) \end{cases}$$

2. The free-surface incompressible Navier-Stokes system. (¬H6, ¬H8, ¬H10, ¬H11)

$$\begin{cases} \partial_t \boldsymbol{u} + \boldsymbol{u} \cdot \nabla \boldsymbol{u} = \frac{1}{\text{Re}} \Delta \boldsymbol{u} - \nabla p + \boldsymbol{g} & \text{in } \Omega(t) & (1.54\text{a}) \\ \nabla \cdot \boldsymbol{u} = 0 & \text{in } \Omega(t) & (1.54\text{b}) \end{cases}$$

$$p \hat{\boldsymbol{n}} - \frac{2}{\text{Re}} \mathbf{S}(\boldsymbol{u}) \cdot \hat{\boldsymbol{n}} = 0 & \text{on } \Gamma_i(t) & (1.54\text{c}) \end{cases}$$

$$\boldsymbol{u} \cdot \hat{\boldsymbol{n}}_b = 0 & \text{on } \Gamma_b & (1.54\text{d}) \end{cases}$$

$$\hat{\boldsymbol{n}}_b \times \mathbf{S}(\boldsymbol{u}) \cdot \hat{\boldsymbol{n}}_b = 0 & \text{on } \Gamma_b & (1.54\text{e}) \end{cases}$$

Should we assume, furthermore, that the interface is singe-valued  $(\mathbf{H8})$ , then both (1.53) and (1.54) are supplemented with the interface advection equation  $(\mathbf{1.20})$ .

3. The Water Waves/Zakharov-Craig and Sulem system. (¬H10)

$$\begin{cases} \partial_t \eta = \text{DtN}[\eta, b] \psi & (1.55a) \\ \partial_t \psi = -g \eta - \frac{1}{2} |\vec{\nabla} \psi|^2 + \frac{1}{2} \frac{\left[ \text{DtN}[\eta, b] \psi + \vec{\nabla} \psi \cdot \vec{\nabla} \eta \right]^2}{1 + |\vec{\nabla} \eta|^2}. & (1.55b) \end{cases}$$

### The Lagrangian framework and the Breaking Waves equations

"Happy we'll be beyond the sea And never again I'll go sailing"

Bobby Darin, Beyond the sea (1959)

The celebrated Eulerian framework for water waves that has been introduced in the previous chapter fails at describing a breaking wave (in a sense soon to be defined). This shortcoming is not due to the eulerian advection equation (1.18) itself but rather from the assumed shape of the function

$$F(\boldsymbol{x},t) = z - h(t,\vec{x}), \tag{1.19, reminder}$$

chosen to implicitly describe the interface. Indeed, numerous numerical studies (see sec. III.2 in the introduction for citations) based on the Navier-Stokes equations (1.54) with an eulerian advection scheme have been able to pass the breaking point, and even the splash singularity. The mathematical description of breaking waves, however, most often rely on a parametrisation of the interface and an explicitly lagrangian scheme to describe the motion of the fluid elements lying on the free surface.

In the present chapter, we propose a self-contained introduction to lagrangian fluid dynamics; we use it to introduce the Breaking Waves equations, a (pseudo-)Lagrangian analogue of the Water Waves equations describing overturning waves in two and three physical space dimensions, extending the unpublished work of Craig (2017); we discuss their hamiltonian structure before finally discussing equivalent mathematical definitions of wave breaking (and of the splash singularity). We hope to convince the reader that the lagrangian framework is not only a useful tool, but more generally a good mindset in our case.

### I. Lagrangian Fluid Mechanics

 $\rightarrow$  Hypotheses not made (see table 1.3): ( $\neg$ **H8**,  $\neg$ **H10**,  $\neg$ **H11**)

We begin this chapter with a thorough presentation of the laws governing fluid dynamics in the lagrangian framework, that is in a time-dependent coordinate system in which points with fixed coordinate follow the fluid elements. Most standard textbooks choose to *label* the fluid elements using the fluid domain at a time

 $t_0$ . We proceed differently to encompass changes of coordinates that shall be used later, in sec. II. The present approach is based on the book by Bennett (2006), as well as the work of Salmon (1988, 2020).

### I.1. The label space

Before writing the equations of fluid dynamics in a time-dependent coordinate system, we would like to discuss precisely how to build such frame and introduce some useful notations. As in chapter 1, we consider a fluid filling a physical time-dependent domain  $\Omega(t) \subseteq \mathbb{R}^{d+1}$  (d=1 or 2) with boundary  $\partial \Omega(t)$ . For now, we assume that this very fluid is inviscid but we shall treat the viscous case afterward.

The label space  $\mathring{\Omega}$  is a fixed subset of  $\mathbb{R}^{d+1}$  such that, at all time  $t \geqslant 0$ , there exists a  $C^1$ -diffeomorphism  $X_t \equiv X(t, \cdot) : \mathring{\Omega} \to \Omega(t)$  with inverse  $A_t \equiv A(t, \cdot) : \Omega(t) \to \mathring{\Omega}$  such that

$$oldsymbol{u}(t,oldsymbol{x}) = \left[ rac{\partial oldsymbol{X}_t}{\partial t} \circ oldsymbol{A}_t 
ight] (oldsymbol{x}),$$

i.e. the "velocity" of the diffeomorphism X corresponds to the flow's velocity u. A schematic representation is visible in figure 2.1. In the following, we shall draw the distinction between physical points  $x \in \Omega(t)$  and label points  $a \in \mathring{\Omega}$ . Consequently, the physical velocity of the point  $a \in \mathring{\Omega}$  is exactly the fluid's velocity,

$$\partial_t \mathbf{X}(t, \mathbf{a}) = \mathbf{u}(t, \mathbf{X}(t, \mathbf{a})). \tag{2.1}$$

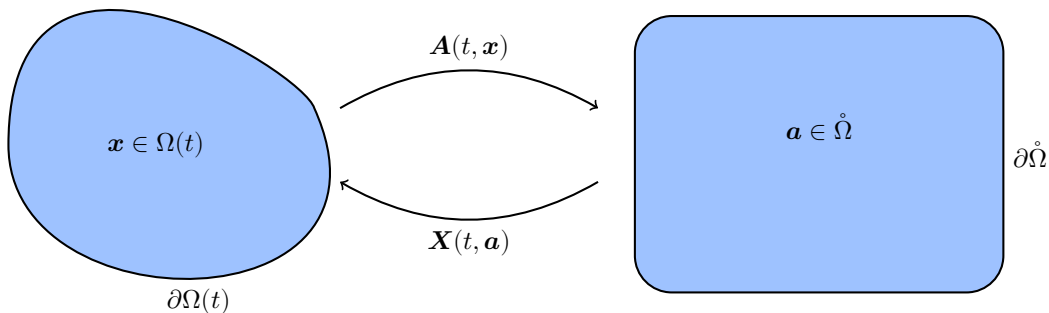


Figure 2.1 – The physical space and the label space, coupled through the time-dependent diffeomorphisms  $X_t$  with inverse  $A_t$ .

This motivates the usage of the word *label* to describe the point  $\mathbf{a} \in \mathring{\Omega}$ . Indeed,  $\mathbf{a}$  labels the fluid element initially present at  $\mathbf{X}(0, \mathbf{a})$  and whose position at time  $t \ge 0$  is  $\mathbf{X}(t, \mathbf{a})$ .

Many choices of label spaces  $\mathring{\Omega}$  can be made. Most commonly,  $\mathring{\Omega} = \Omega(t=0)$  is chosen (fig. 2.2). This amounts to freeze the elements' position in time and describe the subsequent evolution of the system in this slice of space-time. Making this choice introduces useful simplifications of the equations. In the present work, we follow a different path however.

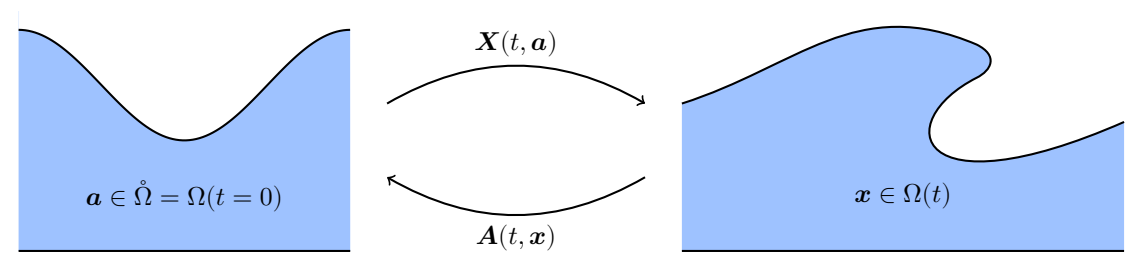


Figure 2.2 – A peculiar choice of label space: freezing the time.

Before stating the equations of fluid dynamics in the label space (the a space), we quickly turn to the

jacobian matrix associated with the transformation

$$\mathbf{J}(t,\boldsymbol{a}) = \left(\boldsymbol{\nabla}_{\boldsymbol{a}}\boldsymbol{X}\right)^{\top}(t,\boldsymbol{a}) = \left[\frac{\partial X_i}{\partial a_j}(t,\boldsymbol{a})\right]_{i,j}, \qquad \text{with inverse} \qquad \mathbf{J}^{-1}(t,\boldsymbol{x}) = \left(\boldsymbol{\nabla}_{\boldsymbol{x}}\boldsymbol{A}\right)^{\top}(t,\boldsymbol{x}) = \left[\frac{\partial A_i}{\partial x_j}(t,\boldsymbol{x})\right]_{i,j}.$$

This quantity shall be of fundamental importance in the following as it makes the link between differential operators in the  $\boldsymbol{x}$  space and the ones in the  $\boldsymbol{a}$  space. Furthermore, the conservation of mass will be rephrased as an evolution equation on this very quantity. Yakubovich and Zenkovich (2001) even proposed to write down every ideal fluid dynamics equation using  $\boldsymbol{J}$  as the sole variable.

**Remark 2.1.** In section II of chapter 3, we will rewrite the equations of fluid dynamics in any time-dependent frame in order to motivate the Arbitrary Lagrangian-Eulerian (ALE) method, thus extending the present framework.

### I.2. Conservation of mass

In sec. I.1 of chapter 1, we established Reynolds' transport lemma using exactly the lagrangian frame (without naming it). As this result leads readily to the continuity equation (1.1), it seems reasonable to state that combining elements from the proof of lemma 1.1 with the physical axiom "mass is conserved" would yield a lagrangian equation for mass conservation. Indeed, let  $\mathcal{V}(t) \subset \Omega(t)$  a material volume and denote  $\mathring{V} = A(t, \mathcal{V}(t))$ , then straightforward computations yield

$$0 = \frac{\mathrm{d}}{\mathrm{d}t} \left( \int_{\mathcal{V}(t)} \rho(t, \boldsymbol{x}) \, \mathrm{d}\boldsymbol{x} \right) = \frac{\mathrm{d}}{\mathrm{d}t} \left( \int_{\mathring{\mathcal{V}}} \mathring{\rho}(t, \boldsymbol{a}) \, \det \left( \mathbf{J}(t, \boldsymbol{a}) \right) \mathrm{d}\boldsymbol{a} \right) = \int_{\mathring{\mathcal{V}}} \partial_t \left[ \mathring{\rho}(t, \boldsymbol{a}) \, \det \left( \mathbf{J}(t, \boldsymbol{a}) \right) \right] \mathrm{d}\boldsymbol{a},$$

where for each eulerian quantity  $\theta(t, \mathbf{x})$ , we denote its value in lagrangian space as  $\mathring{\theta}(t, \mathbf{a}) = \theta(t, \mathbf{X}(t, \mathbf{a}))$ . Since the control volume  $\mathcal{V}(t)$  is arbitrary, we conclude that

$$\partial_t \Big[ \mathring{\rho}(t, \boldsymbol{a}) \, \det \Big( \mathbf{J}(t, \boldsymbol{a}) \Big) \Big] = 0 \qquad \text{for all } \boldsymbol{a} \in \mathring{\Omega} \text{ and } t \geqslant 0.$$
 (2.2)

This is the lagrangian equivalent of the continuity equation (1.1). Should the fluid be incompressible with a constant density  $\mathring{\rho} > 0$ , then we obtain the lagrangian incompressibility condition

$$\partial_t \Bigl( \det(\mathbf{J}) \Bigr) = 0. \tag{2.3}$$

This equation obviously stipulates that the volume of any material volume  $\mathcal{V}(t)$  does not change in time. Manipulations as the one made in the proof of lemma 1.1 show that it is in fact equivalent to the eulerian incompressibility condition (1.2).

**Remark 2.2.** With the label space corresponding to the initial fluid domain  $\mathring{\Omega} = \Omega(t=0)$ , as in fig. 2.2, the situation is even easier since  $X(0, \cdot)$  is the identity, so that  $\det \left( \mathbf{J}(t, \cdot) \right) = 1$  at all time  $t \ge 0$ .

### I.3. Conservation of momentum

Euler's momentum equation (1.6) was also obtained through the use of Reynolds' transport lemma 1.1. Therefore, the same type of computations as above yield

$$\frac{\mathrm{d}}{\mathrm{d}t} \left( \int_{\mathcal{V}(t)} \rho(t, \boldsymbol{x}) \boldsymbol{u}(t, \boldsymbol{x}) \, \mathrm{d}\boldsymbol{x} \right) = \frac{\mathrm{d}}{\mathrm{d}t} \left( \int_{\mathring{\mathcal{V}}} \mathring{\rho}(t, \boldsymbol{a}) \partial_t \boldsymbol{X}(t, \boldsymbol{a}) \, \det \left( \mathbf{J}(t, \boldsymbol{a}) \right) \, \mathrm{d}\boldsymbol{a} \right) \\
= \int_{\mathring{\mathcal{V}}} \frac{\partial}{\partial t} \left[ \mathring{\rho}(t, \boldsymbol{a}) \partial_t \boldsymbol{X}(t, \boldsymbol{a}) \, \det \left( \mathbf{J}(t, \boldsymbol{a}) \right) \right] \, \mathrm{d}\boldsymbol{a} \\
= \int_{\mathring{\mathcal{V}}} \mathring{\rho}(t, \boldsymbol{a}) \, \det \left( \mathbf{J}(t, \boldsymbol{a}) \right) \partial_{tt} \boldsymbol{X}(t, \boldsymbol{a}) \, \mathrm{d}\boldsymbol{a} \qquad \text{using (2.2)}$$

$$= \int_{\mathring{\mathcal{V}}} \left[ \mathring{\boldsymbol{F}} - \left( \boldsymbol{\nabla}_{\boldsymbol{x}} p \right) \left( t, \boldsymbol{X}(t, \boldsymbol{a}) \right) \right] \, \mathrm{d}\boldsymbol{a} \left( \boldsymbol{\mathsf{J}}(t, \boldsymbol{a}) \right) \mathrm{d}\boldsymbol{a},$$

with  $\mathring{F}$  the volume forces, *i.e.* gravity and eventually viscosity in our case. The pressure term can be handled using the chain rule (we recall that a summary of vector calculus identities is available in appendix B),

$$\boldsymbol{\nabla}_{\boldsymbol{x}} p = \boldsymbol{\nabla}_{\boldsymbol{x}} \boldsymbol{A} \cdot \left[ \left( \boldsymbol{\nabla}_{\boldsymbol{a}} \mathring{p} \right) \left( t, \boldsymbol{A}(t, \boldsymbol{\cdot}) \right) \right].$$

Since the material volume  $\mathring{\mathcal{V}}$  is arbitrary, setting  $\mathring{\boldsymbol{F}} = \mathring{\rho} \boldsymbol{g}$  the gravity, we obtain easily the lagrangian form of Euler's momentum equation (1.6),

$$\mathring{\rho}\partial_{tt}\boldsymbol{X} = -\Big[\boldsymbol{\nabla}_{\boldsymbol{x}}\boldsymbol{A}\Big(t,\boldsymbol{X}(t,\boldsymbol{\cdot})\Big)\Big]\cdot\boldsymbol{\nabla}_{\boldsymbol{a}}\mathring{p} + \mathring{\rho}\boldsymbol{g}.$$

Notice that, in contrast with the eulerian form, the non-linearity appears now in the pressure term. Furthermore, this relation holds for non-constant values of  $\mathring{\rho}$ . Finally, we observe that it has a form very similar to Newton's second law.

**Remark 2.3.** Recasting the above equation in the eulerian frame is done readily by noticing that the left-hand side is exactly the material derivative,

$$\partial_{tt} \boldsymbol{X}(t,\boldsymbol{a}) = \partial_t \left[ \boldsymbol{u} \big(t,\boldsymbol{X}(t,\boldsymbol{a}) \big) \right] = \left( \partial_t \boldsymbol{u} \big) \big(t,\boldsymbol{X}(t,\boldsymbol{a}) \big) + \partial_t \boldsymbol{X}(t,\boldsymbol{a}) \cdot \big( \boldsymbol{\nabla}_x \boldsymbol{u} \big) \big(t,\boldsymbol{X}(t,\boldsymbol{a}) \big).$$

**Remark 2.4.** We could also obtain the pressure term without relying on the eulerian formulation at all. This is more involved, however. A standard reference carrying out such computations is Bennett (2006, sec. 3.2)

The gravitational force usually takes the form of a potential in the eulerian frame,  $\mathbf{F} = \nabla_x \Phi$ . This allows to obtain a more tractable form of Euler's equation in the label space, namelly

$$\nabla_{a} X \cdot \partial_{tt} X = \nabla_{a} \left[ \mathring{\Phi} - \frac{\mathring{p}}{\rho} \right], \tag{2.4}$$

where we used the fact that  $A_t^{-1} = X_t$ , yielding a useful link between  $\nabla_x A$  and  $\nabla_a X$ . We stress that, for now, the computations that have been carried out do not depend on the chosen coordinate systems, either the eulerian one or the lagrangian one. We won't work out the lagrangian formulation of the Navier-Stokes momentum equation since it won't be used thereafter (see Bennett (2006, chapter 5) for the case of a rectangular coordinate system).

### I.4. Boundary conditions

Coming back to the particular case of water waves, we now assume that the physical water domain  $\Omega(t)$ , at time  $t \ge 0$ , is encompassed between two d-dimensional surfaces  $\Gamma_b$ , the water's bed, and  $\Gamma_i(t)$ , the free surface (see figure 2.3), both extending to infinity in the  $\vec{x}$  direction(s). Rigorously speaking,  $\Omega(t)$  is defined using the notion of admissible paths (definition 1.11). Extensions to infinite water depth is straightforward.

Euler's equation in the label space constitutes the basic PDE used to describe water waves. As in the eulerian frame, it should be supplemented with the correct set of boundary conditions in order to describe water waves correctly. To express them in a simple manner, we shall make some hypothesis regarding the chosen label space  $\mathring{\Omega}$ .

**Definition 2.5.** A label space  $\mathring{\Omega} \subset \mathbb{R}^{d+1}$  is said to be admissible should it enjoy the following properties:

1. Like the physical domain of a non-breaking wave, it is an "extrusion" of the d-dimensional space. That is, each point  $\mathbf{a} \in \mathring{\Omega}$  can be written as

$$\boldsymbol{a} = \left(\vec{a}, b\right)$$
 with  $\vec{a} \in \mathbb{R}^d$  and  $-\beta(\vec{a}) \leqslant b \leqslant h(\vec{a})$ .

- 2. The free surface is labeled by the set  $\mathring{\Gamma}_i = \{(\vec{a}, b) : b = h(\vec{a})\} \subset \mathring{\Omega}$ .
- 3. The lagrangian water's bed  $\mathring{\Gamma}_b$  corresponds to the condition  $b = \beta(\vec{a})$ .

The easiest way to achieve such admissible label space is to take  $\mathring{\Omega}=\Omega(0)$  for an initially non-breaking water domain with single-valued bed (i.e. **H10** should hold, as in fig. 2.2). We could be more restrictive as to assume that  $\beta=0$  and  $h=h_0$  and end up with a flat strip  $\mathring{\Omega}=\mathbb{R}^d\times[0,h_0]$ . This has the advantage of transforming the normal derivative in physical space to a simple  $\partial_b$  in the label space. Finally, notice that we cannot make the lagrangian free surface  $\mathring{\Gamma}_i$  time-dependent as it would be in contradiction with the lagrangian advection (2.1).

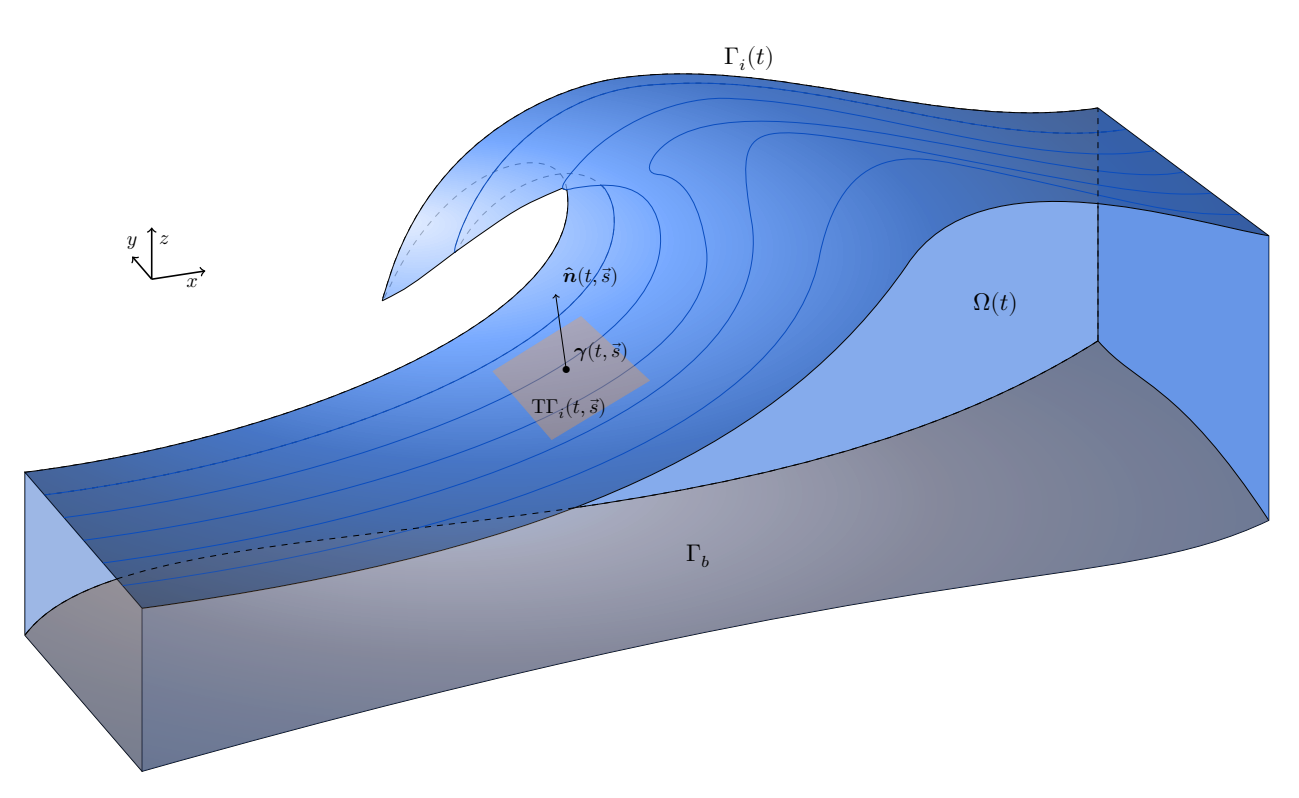


Figure 2.3 – Schematic representation of the three-dimensional water domain  $\Omega(t)$  with (possibly overturning) interface  $\Gamma_i(t)$ .

I.4.1. The kinematic condition. Physically speaking, it states that the fluid elements lying on the free surface should remain on the free surface. This is trivially satisfied by the interface elements  $a \in \mathring{\Gamma}_i$  as a consequence of (2.1).

I.4.2. **The dynamic condition.** In the absence of surface tension (**H9**), the pressure is assumed to be constant on the interface, *i.e.* 

$$\dot{p}(t, \vec{a}, b = h(\vec{a})) = 0.$$
 (2.5)

I.4.3. The non-penetration condition. The fluid elements should never cross the physical boundary  $\Gamma_b$ . Pushing (1.10) into the label space yields

$$\partial_t \boldsymbol{X} \Big( t, \vec{a}, b = \beta(\vec{a}) \Big) \cdot \hat{\boldsymbol{n}}_b \Big( t, \boldsymbol{X} \Big( t, \vec{a}, b = \beta(\vec{a}) \Big) \Big).$$

We can go deeper by implicitly describing the water's bed as the implicit equation B(x) = 0 for some differentiable function  $B: \mathbb{R}^{d+1} \to \mathbb{R}$  (whose zero-value level-set happens to be  $\beta$  pushed to the physical space). The non-normalised normal vector is merely the gradient  $n_b = \nabla B$ . This allows to rephrase the non-penetration condition in a more enlightening fashion,

$$0 = \partial_t \boldsymbol{X} \Big( t, \vec{a}, b = \beta(\vec{a}) \Big) \cdot \boldsymbol{\nabla}_{\boldsymbol{x}} B \Big( t, \boldsymbol{X} \Big( t, \vec{a}, b = \beta(\vec{a}) \Big) \Big)$$

$$= \partial_t \bigg[ B \Big( t, \boldsymbol{X} \Big( t, \vec{a}, b = \beta(\vec{a}) \Big) \Big) \bigg], \tag{2.6}$$

that is, fluid elements laying on  $\Gamma_b$  initially remain on it at all subsequent times  $t \ge 0$ .

The set of equations (2.3-2.6) is the Water Waves problem written in an admissible label space  $\mathring{\Omega}$ . This formulation encompasses overturning waves up to the moment the splash has occurred. In sec. I.3 of the introduction, we have reviewed the mathematical literature regarding this set of equations (or equivalent lagrangian formulations).

### I.5. Irrotationality and Bernoulli's equation

The vorticity can be written in the lagrangian frame but this would not be enlightening. Instead, we propose to take a completely different route by introducing the Cauchy invariant. It appears in the equation as we follow the path that usually leads to the vorticity equation in the eulerian frame, *i.e.* starting from the lagrangian form of Euler's equation (2.4), we rewrite it in a way that involves potential terms only,

$$\partial_t \left( \boldsymbol{\nabla_a} \boldsymbol{X} \cdot \partial_t \boldsymbol{X} \right) = \frac{1}{2} \boldsymbol{\nabla_a} \left( \left| \partial_t \boldsymbol{X} \right|^2 \right) + \boldsymbol{\nabla_a} \left( \mathring{\Phi} - \frac{\mathring{p}}{\rho} \right). \tag{2.7}$$

Taking the (lagrangian) curl of the above system yields a surprising relation,

$$\partial_t \left( \nabla_{\boldsymbol{a}} \times \left( \nabla_{\boldsymbol{a}} \boldsymbol{X} \cdot \partial_t \boldsymbol{X} \right) \right) = \partial_t \boldsymbol{\varpi} = 0,$$

with  $\varpi$  Cauchy's invariant, also called the lagrangian vorticity (even though it does not exactly correspond to the eulerian vorticity  $\omega$  written in the lagrangian frame). Integrating the above equation on a fixed two-dimensional surface  $\mathring{\mathcal{S}} \subseteq \mathring{\Omega}$  yields Kelvin's circulation theorem 1.6 readily. Therefore, the quantity  $\varpi$  can also be named the *circulation density*. We shall use this last nomenclature in the following. The explicit link between  $\varpi$  and  $\omega$  is

$$\boldsymbol{\omega} \circ \boldsymbol{X}_t = \frac{1}{\det(\boldsymbol{\mathsf{J}})} \, \boldsymbol{\nabla}_{\boldsymbol{a}} \boldsymbol{X} \cdot \boldsymbol{\varpi},$$

with straightforward adaptation in the two-dimensional case. The above formula is obtained easily using the index notation (Bennett 2006).

The above link between the eulerian vorticity and the circulation density shows that  $\boldsymbol{\varpi}=0$  in  $\mathring{\Omega}$  if and only if  $\boldsymbol{\omega}=0$  in  $\Omega(t)$ . This can also be seen as a consequence of Kelvin's circulation theorem. Furthermore, since  $\mathring{\Omega}$  is an admissible domain, it is simply connected. Therefore, in the irrotational case (H11) we can introduce a lagrangian velocity potential  $\varphi:\mathring{\Omega}\to\mathbb{R}$  such that

$$\nabla_{a}\varphi = \nabla_{a}X \cdot \partial_{t}X.$$

By the chain rule, we have simply  $\varphi = \mathring{\phi} = \phi \circ X_t$  the eulerian velocity potential. Inserting this definition inside (2.7), we obtain exactly Bernoulli's equation (1.35a) pushed to the label space (after a redefinition of the velocity potential  $\varphi$  to incorporate the eventual constant as in sec. IV of chapter 1),

$$\partial_t \varphi - \frac{1}{2} \left| \partial_t \mathbf{X} \right|^2 + \frac{\mathring{p}}{\rho} = \mathring{\Phi}. \tag{2.8}$$

On the free surface  $b = h(\vec{a})$ , the pressure identically vanishes. From the above set of equation, we shall motivate the Breaking Waves equations of Craig (2017) in sec. II below, thus shedding light on its purely lagrangian nature.

**Remark 2.6.** The sign in front of the  $u^2$  term in the above equation differs from the one in (1.35a). This is due to  $\partial_t \varphi$  being the material derivative of  $\varphi$ .

### I.6. Water Waves solutions in the lagrangian frame

Before discussing a new formulation of the Water Waves equation obtained from the lagrangian form of Bernoulli's equations (2.8), we would like to discuss known solutions of the Water Waves problem in the label space.

I.6.1. **Gerstner (1802)'s wave.** Historically, this was the first solution ever obtained of the free-surface lagrangian Euler system (2.3–2.6) in infinite depth. It happens to be the only finite-amplitude solution with a closed formula. Denoting the two-dimensional components of X as (X, Z), erstner's solution it is

$$\begin{split} X(t,a,b) &= a - \frac{e^{kb}}{k} \, \sin \! \left( k(a-ct) \right) \\ Z(t,a,b) &= b + \frac{e^{kb}}{k} \, \cos \! \left( k(a-ct) \right) , \end{split}$$

for  $a \in \mathbb{R}$ ,  $b \in (-\infty, 0]$ ,  $k = 2\pi/\lambda$  (with  $\lambda$  the wavelength as before) and  $c^2 = g/k$  the wave's velocity in deep water. A representation of this solution is shown in fig. 2.4.

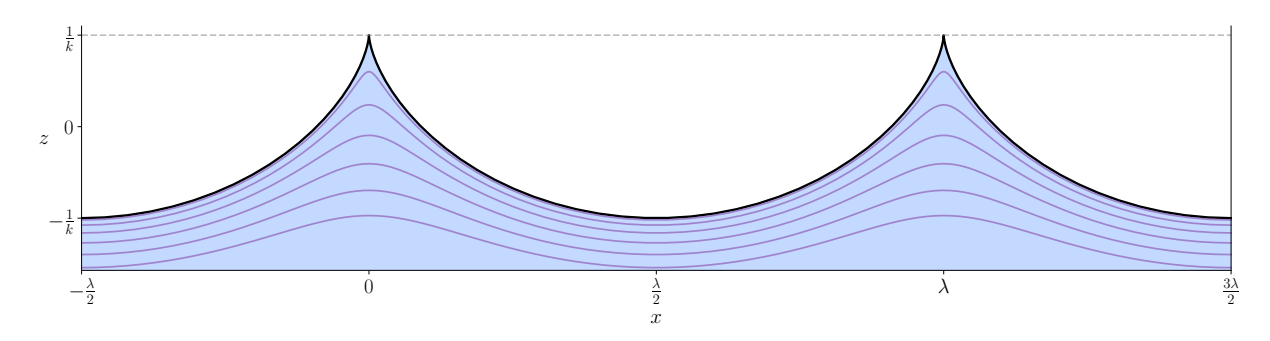


**Figure 2.4** – Visualisation of Gerstner's solution of the Water Waves problem for different values of b, i.e. for different amplitudes, up to the threshold value b = 0 for which each crest becomes a cusp.

For b=0, the free surface becomes a sharply tipped interface. Positive values of b yield non-physical self-intersecting interfaces. More work is needed to append a physical interpretation to this solution (*i.e.* translating vertically the solution so that the interface corresponds to a zero-mean perturbation of the z=0 rest state).

Surprisingly, Gerstner's solution is rotational. Indeed, its circulation density is given by

$$\varpi(t,a,b)=2\sqrt{gk}e^{2kb}\neq 0,$$

which decreases exponentially with the depth. As shown in Blaser et al. (2024), a direct consequence is that the mean drift may vanish, and in fact it does so. This solution is sometimes referred to as the trochoidal wave solution since, for fixed value of b, it corresponds to the parametric equation of an inverted trochoid. Clamond (2007) obtained higher order Gerstner-like solutions over arbitrary depths.

I.6.2. Lagrangian Stokes (1847) waves. In his original paper, Stokes obtained a second order solution of the lagrangian free-surface Euler equations in infinite depth which was later extended to seventh order by Clamond (2007). We only provide the fifth order solution to preserve our reader's mental health,

$$\begin{split} kX(t,a,b=0) &= Ka - \left(\varepsilon + \varepsilon^3 + \frac{47}{24}\,\varepsilon^5\right) \sin\!\left(K\theta\right) - \frac{1}{3}\,\varepsilon^4\,\sin\!\left(2K\theta\right) - \frac{5}{72}\,\varepsilon^5\,\sin\!\left(5K\theta\right) \\ kY(t,a,b=0) &= \frac{1}{2} \Big(\varepsilon^2 + \varepsilon^4\Big) + \Big(\varepsilon - \frac{1}{24}\,\varepsilon^5\Big) \cos\!\left(K\theta\right) + \frac{1}{6}\,\varepsilon^4\,\cos\!\left(2K\theta\right) + \frac{1}{24}\,\varepsilon^5\,\cos\!\left(3K\theta\right) \\ \text{with} \quad K &= k \Big[1 - \varepsilon^2\Big] \qquad \text{and} \qquad \theta = a - c(k)t \quad \text{with} \quad c(k) = \sqrt{\frac{g}{k}}\,\left[1 + \frac{1}{2}\,\varepsilon^2 + \frac{1}{8}\,\varepsilon^4\right], \end{split}$$

with, contrary to chapter 1,  $\varepsilon = ka$  where k is the wavenumber and a the amplitude of the first order wave. This solution is compared to the classical eulerian Stokes solution at orders 1, 3, 4 and 5 in figure 2.5, using the original computations of Stokes (1880).

The surprising aspect, shown in Clamond (2007) but also observed in figure 2.5, is that the lagrangian solution converges faster than its eulerian counterpart. To the author's knowledge, however, it has not been

established that both series converge to the same solution. The first order solution has e.g. been used as an initial condition by Baker and Xie (2011) to investigate the formation of a singularity in the deep water regime.

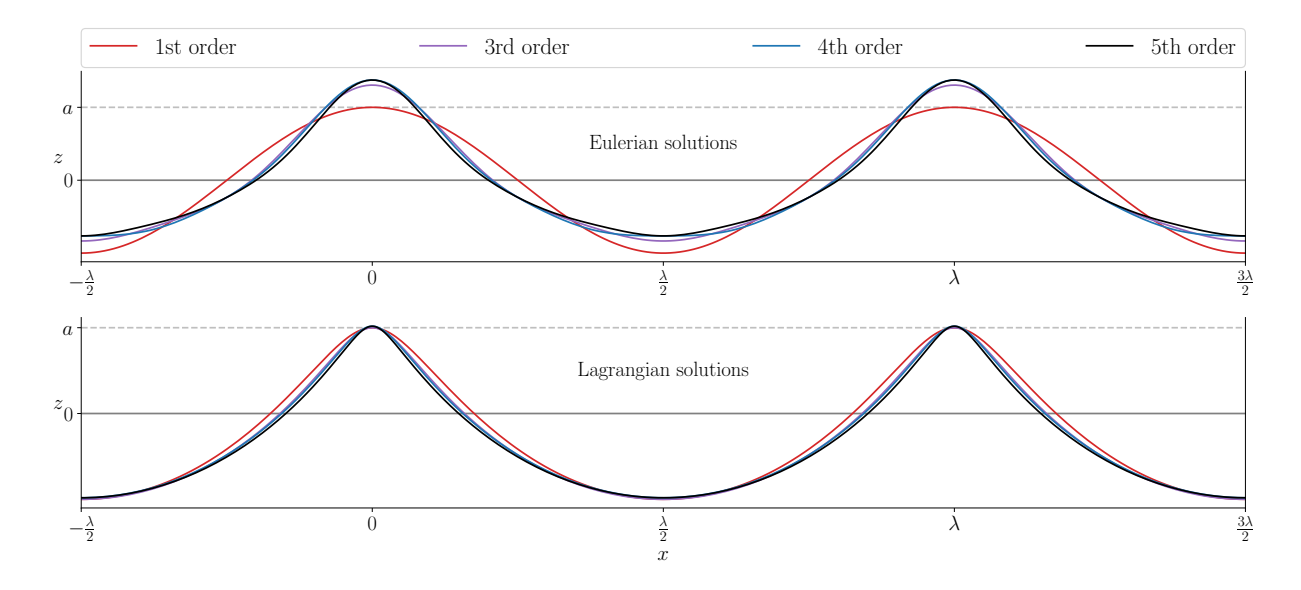


**Figure 2.5** – Eulerian and lagrangian Stokes waves at time t = 0 up to  $5^{th}$  order.

### II. The Breaking Waves equations

 $\rightarrow$  Starting from here (H11) is made (see table 1.3)

Switching from the eulerian frame to the lagrangian one permits to study overturning waves. Therefore, replacing the eulerian advection equation (1.20) by its lagrangian counterpart (2.1) and working with quantities defined on the label space should allow us to carry out a new set of equation, the lagrangian counterpart of the Water Waves equations (1.43). To do so, we follow the unpublished work of Craig (2017), finding a more general formulation that also work in three space dimensions.

At first, we shall work without specifying an intrinsic coordinate system on the interface  $\Gamma_i(t)$ , using a geometric approach. This has the advantage to yield a dimension-independent formulation. However the resulting, rather abstract, set of equation won't be very practical. Therefore we will introduce, in a second time, a set of coordinates on the interface (that is, a parametrisation of the latter). The one-dimensional resulting system (d=1) will enjoy some very nice properties while the two-dimensional one will be quite more involved. Finally, we wish to investigate the non-canonical hamiltonian structure of the resulting system, postponing a general discussion on wave breaking to the next section.

### II.1. The geometric approach

Our objective is to rewrite the Water Waves problem (in either the lagrangian or the eulerian frame) as a set of equation on the free surface  $\Gamma_i(t)$  only, as was done to obtain the Zakharov–Craig and Sulem formulation (1.43) in the non-breaking case. We hereby do it employing the language of differential geometry (see appendix A for a brief review) as it yields a set of equations that does not depend on the dimension d. For the moment, we assume that every quantity is smooth in order to correctly motivate the Breaking Waves equations.

Let d = 1 or 2 the intrinsic dimension of the interface. A schematic representation of the problem at hand in 2d (respectively in 3d) is visible in figure 2.6 (resp. fig. 2.3). The fluid domain is once again denoted

using  $\Omega(t) \subset \mathbb{R}^{d+1}$ , with bottom boundary  $\Gamma_b$  (not necessarily a graph) and free surface  $\Gamma_i(t)$ . Both  $\Gamma_b$  and  $\Gamma_i(t)$  are assumed to extend to infinity in the  $\vec{x}$  direction(s), with a finite difference separating them (H5). To this physical domain  $\Omega(t)$  corresponds, at each time  $t \geq 0$ , a label space  $\mathring{\Omega} \subset \mathbb{R}^{d+1}$  with time-dependent diffeomorphism  $X(t, \cdot) : \mathring{\Omega} \to \Omega(t)$ . We do not need to assume that  $\mathring{\Omega}$  is admissible (def. 2.5) for now.

Extending  $X(t, \cdot)$  or it inverse  $A(t, \cdot)$  by continuity, we can define the lagrangian representation  $\mathring{\Gamma}$  of the free surface  $\Gamma_i(t)$ . We suppose that  $\mathring{\Gamma}$ , as a subset of  $\mathbb{R}^{d+1}$ , does not self-intersect. It can therefore be equipped with the structure of a riemannian d-dimensional manifold, embedded in  $\mathbb{R}^{d+1}$ . We shall write down the Water Waves problem on this very manifold.

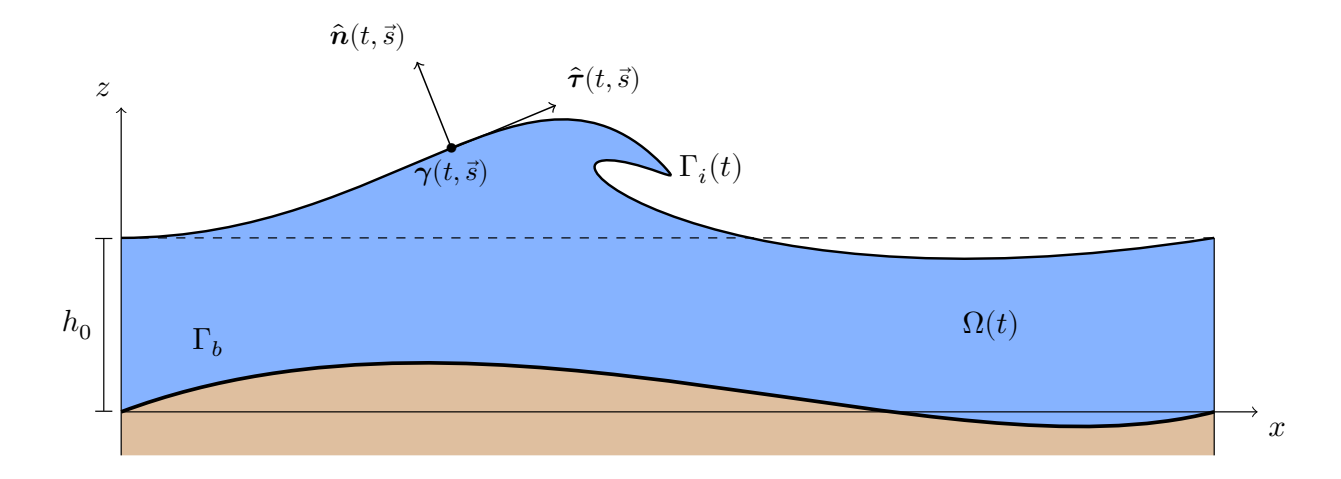


Figure 2.6 – Two-dimensional representation of the physical domain with the different quantities used in this section.

II.1.1. Notations. Reusing our notation for d-dimensional quantities, elements of  $\mathring{\Gamma}$  are written in lower-case,  $\vec{s} \in \mathring{\Gamma}$  for instance, while elements of the tangent space are denoted with upper-case letters  $\vec{V} \in \mathbf{T}_{\vec{s}}\mathring{\Gamma}$ . Correspondingly, (d+1)-dimensional element will be written as  $\boldsymbol{x} \in \mathbb{R}^{d+1}$ , without making the difference between elements of  $\mathbb{R}^{d+1}$  and those of  $\mathbf{T}_{\boldsymbol{x}}\mathbb{R}^{d+1} \simeq \mathbb{R}^{d+1}$ .

We introduce the two unknown quantities that define unambiguously the flow, namely the time-dependent surface embedding  $\gamma(t, \bullet): \mathring{\Gamma} \to \Gamma_i(t) \subset \mathbb{R}^{d+1}$  and the free-surface velocity potential  $\psi(t, \bullet): \mathring{\Gamma} \to \mathbb{R}$ . The former corresponds to the trace of  $X(t, \bullet)$  since

$$\mathring{\boldsymbol{\Gamma}} = \boldsymbol{A} \Big( t, \boldsymbol{\Gamma}_i(t) \Big) \qquad \Longrightarrow \qquad \boldsymbol{\gamma}(t, \boldsymbol{\cdot}) = \boldsymbol{X}(t, \boldsymbol{\cdot}) \Big|_{\mathring{\boldsymbol{\Gamma}}},$$

while the latter is defined as the trace of the lagrangian potential

$$\psi(t, {\boldsymbol{\cdot}}) = \varphi(t, {\boldsymbol{\cdot}}) \Big|_{\mathring{\mathbf{r}}} = \phi \Big(t, {\boldsymbol{\gamma}}(t, {\boldsymbol{\cdot}}) \Big).$$

Remark 2.7. We used the term *label space* extensively here but we did not assume that it was constructed from the lagrangian diffeomorphism introduced in section I. Indeed, X could be any time-dependent change of coordinates with fixed domain. This important degree of freedom will be used to change (or preserve) the surface parametrisation in time without changing its overall shape. Technically, the set of equations that we are trying to obtain are written in an arbitrary lagrangian-eulerian frame (as the one that will be introduced in sec. II below).

II.1.2. The advection equation. The remark made above states that using the mere lagrangian advection equation (2.1) on the interface  $\mathring{\Gamma}$  is somewhat reductive. Indeed, leaving the lagrangian interpretation aside, we could allow the element  $\vec{s}$  to slip arbitrarily on the free surface  $\Gamma_i(t)$  without effectively changing its overall shape, as long as it is done continuously in order to prevent it from "colliding" with another element. This is in fact a geometric equivalent of the relabelling symmetry. However, by doing so we would drop out the physical intuition that  $\vec{s} \in \mathring{\Gamma}$  effectively labels the exact same fluid element at all time.

Consider the following generalised advection scheme (where  $\vec{s} \in \mathring{\Gamma}$  no longer labels a physical fluid element starting from now),

$$\underbrace{\partial_t \boldsymbol{\gamma}(t, \vec{s})}_{\in \ \mathbb{R}^{d+1}} = \underbrace{\left[\boldsymbol{u}\!\left(t, \boldsymbol{\gamma}(t, \vec{s})\right) \cdot \hat{\boldsymbol{n}}(t, \vec{s})\right] \hat{\boldsymbol{n}}(t, \vec{s})}_{\in \ \mathcal{N}_{\boldsymbol{\gamma}(t, \vec{s})} \Gamma_i(t)} + \underbrace{\boldsymbol{\gamma}(t, \vec{s})_* \vec{V}(t, \vec{s})}_{\in \ \mathcal{T}_{\boldsymbol{\gamma}(t, \vec{s})} \Gamma_i(t)}, \tag{2.9}$$

where  $\vec{V}(t, \cdot): \mathring{\Gamma} \to \mathring{\Gamma}$  is a time-dependent vector field allowing the element  $\vec{s}$  to slip freely on  $\Gamma_i(t)$ ,  $\gamma(t, \cdot)_*: \mathring{\Gamma} \to \Upsilon\Gamma_i(t)$  is the derivative (or *pushforward*) of the time-dependent embedding  $\gamma$  which takes tangent vector fields on  $\mathring{\Gamma}$  to tangent vector fields on  $\Gamma_i(t)$  (we could have used the  $\nabla \gamma^{\top}$  notation instead),  $\Upsilon_{\gamma(t,\vec{s})}\Gamma_i(t)$  being the tangent space of  $\Gamma_i(t)$  at  $\gamma(t,\vec{s})$  and where  $N_{\gamma(t,\vec{s})}\Gamma_i(t)$  is the *normal space* of  $\Gamma_i(t)$  at  $\gamma(t,\vec{s})$ , such that

$$\mathbb{R}^{d+1} \simeq \mathcal{T}_{\gamma(t,\vec{s})} \mathbb{R}^{d+1} = \left( \mathcal{T}_{\gamma(t,\vec{s})} \Gamma_i(t) \right) \oplus \left( \mathcal{N}_{\gamma(t,\vec{s})} \Gamma_i(t) \right). \tag{2.10}$$

The normal space of  $\Gamma_i(t)$  at  $\gamma(t, \vec{s})$  is spanned by real multiples of  $\hat{\boldsymbol{n}}(t, \vec{s})$ , the unit normal vector at  $\gamma(t, \vec{s})$  pointing out of  $\Omega(t)$ .

Notice that changing the vector field  $\vec{V}$  does not change the geometry of the interface  $\Gamma_i(t)$ , only the normal velocity contributes to its evolution. Among the many choices of *sliding* velocity field  $\vec{V}$ , we wish to discuss three important ones,

1. The "Let's move with the flow!" choice, where

$$oldsymbol{\gamma}(t,ec{s})_*ec{V}(t,ec{s}) = oldsymbol{u}ig(t,oldsymbol{\gamma}(t,ec{s})ig) - ig[oldsymbol{u}ig(t,oldsymbol{\gamma}(t,ec{s})ig)\cdot\hat{oldsymbol{n}}(t,ec{s})ig]\hat{oldsymbol{n}}(t,ec{s}),$$

so that  $\partial_t \gamma = u \circ \gamma$  is the lagrangian advection (2.1) on the interface. This choice will be made in the numerical method presented in chapter 3 and used in chapters 4 and 5.

- 2. The "Who needs tangential velocity anyway?" choice, obtained setting  $\vec{V} = 0$ . It makes the computations easier but does not seem particularly interesting aside from that.
- 3. The "I like the arclength parametrisation" choice, preserving the arclength when d=1. It will be constructed later, in lemma 2.13.

II.1.3. The velocity potential and the Dirichlet-to-Neumann map. Since hypothesis (H11) has been made, the velocity potential  $\phi: \Omega(t) \to \mathbb{R}$  can be used. Exploiting the relation between  $\psi$  and  $\phi$ , we obtain readily that

$$\begin{split} \mathrm{d}\psi(t,\boldsymbol{\cdot}) &= \mathrm{d}\Big[\phi\Big(t,\boldsymbol{\gamma}(t,\boldsymbol{\cdot})\Big)\Big] = \mathrm{d}\big[\boldsymbol{\gamma}(t,\boldsymbol{\cdot})^*\phi(t,\boldsymbol{\cdot})\big] = \boldsymbol{\gamma}(t,\boldsymbol{\cdot})^*\big[\mathrm{d}\phi(t,\boldsymbol{\cdot})\big] \\ \text{and} \quad \psi(t,\vec{s})_* &= \phi\Big(t,\boldsymbol{\gamma}(t,\vec{s})\Big)_* \circ \boldsymbol{\gamma}(t,\vec{s})_*, \end{split}$$

with  $\gamma(t, \cdot)^*$  the *pullback* operation. The exterior derivative defines an intrinsic, coordinate-independent, notion of derivative on  $\Gamma_i(t)$  and  $\mathring{\Gamma}$ , linked through the above relation. However, making use of the riemannian structure (*i.e.* the metric) of  $\Gamma_i(t)$ , inherited from  $\mathbb{R}^{d+1}$ , we can also define the gradients  $\nabla \phi$  and  $\nabla \psi$ .

Let us be cautious here in order to define correctly the metrics. Let  $\iota:\Gamma_i(t)\hookrightarrow\mathbb{R}^{d+1}$  the inclusion map. At fixed  $\boldsymbol{x}\in\Gamma_i(t)$  and  $\vec{s}\in\mathring{\Gamma}$ , we define the two time-dependent metrics

$$\begin{split} \mathbf{h}(t, \boldsymbol{x}) : \mathrm{T}_{\boldsymbol{x}} \Gamma_i(t) \times \mathrm{T}_{\boldsymbol{x}} \Gamma_i(t) \to \mathbb{R} & \text{such that} & \mathbf{h}(t, \boldsymbol{x}) = \iota^* \mathbf{g}_{d+1} \\ \mathbf{g}(t, \vec{s}) : \mathrm{T}_{\vec{s}} \mathring{\Gamma} \times \mathrm{T}_{\vec{s}} \mathring{\Gamma} \to \mathbb{R} & \text{such that} & \mathbf{g}(t, \vec{s}) = \boldsymbol{\gamma}(t, \vec{s})^* \mathbf{h} \big(t, \boldsymbol{\gamma}(t, \vec{s})\big), \end{split}$$

with  $\mathbf{g}_{d+1}$  the Euclidean metric on  $\mathbb{R}^{d+1}$  and we recall that the pullback metric has been defined in appendix A. Using the second metric tensor (also called the first fundamental form of the surface), we define the gradient  $\nabla \psi$  using the  $\sharp$  isomorphism,

$$\vec{\nabla}\psi = d\psi^{\sharp}$$
 i.e. for all  $\vec{V} \in T_{\vec{s}}\mathring{\Gamma}$ ,  $\mathbf{g}(\vec{\nabla}\psi, \vec{V}) = d\psi(\vec{V})$ .

The gradient  $\nabla \phi$  is defined without ambiguity from the Euclidean metric. The metric  $\mathbf{h}(t)$  contains the intrinsic geometry of the surface  $\Gamma_i(t)$ . Since we are interested in recasting the fixed manifold  $\mathring{\Gamma}$ , we will instead use the time-dependent metric  $\mathbf{g}(t)$ , giving to  $\mathring{\Gamma}$  a time-varying Riemannian manifold structure.

Notice that this structure is well-defined as long as  $\gamma(t, \cdot)$  remains a diffeomorphism from  $\mathring{\Gamma}$  to  $\Gamma_i(t)$ , *i.e.* as long as no singularity has appeared (for instance a splash or a cusp).

As in the flat case, we would like to express  $\nabla \phi$  using  $\psi$  and  $\gamma$ . To this end, we introduce some useful notations. First, let  $\mathfrak{g}(t, \vec{s})$  the determinant of the surface metric  $\mathbf{g}$ , permitting to transform surface integrals on  $\Gamma_i(t)$  to integrals on  $\mathring{\Gamma}$  through

$$\int_{\Gamma_i(t)} f(\boldsymbol{y}) \, dS(\boldsymbol{y}) = \int_{\mathring{\Gamma}} f(\boldsymbol{\gamma}(t, \vec{s})) \sqrt{\mathfrak{g}(t, \vec{s})} \, d\vec{s}.$$

This allows to define the *Dirichlet-to-Neumann* map in a normalised manner.

$$DtN[\boldsymbol{\gamma}]\psi(t,\vec{s}) = \sqrt{\mathfrak{g}(t,\vec{s})} \, \mathbf{g}_{d+1} \Big( \nabla \phi \Big( t, \boldsymbol{\gamma}(t,\vec{s}) \Big), \, \hat{\boldsymbol{n}}(t,\vec{s}) \Big),$$
(2.11)

with  $\hat{\boldsymbol{n}}(t,\vec{s})$  the unit-length vector, normal to  $\Gamma_i(t)$  at  $\boldsymbol{\gamma}(t,\vec{s})$  and pointing out of  $\Omega(t)$ . Should  $\partial_n \in \mathcal{N}_{\boldsymbol{\gamma}(t,\vec{s})}\Gamma_i(t)$  be a normal vector, then

$$\hat{\boldsymbol{n}}(t,\vec{s}) = \pm \frac{1}{\sqrt{\mathbf{g}_{d+1}(\partial_n,\partial_n)}} \left. \frac{\partial}{\partial n} \right|_{\boldsymbol{\gamma}(t,\vec{s})}$$

with the plus or minus ensuring a correct orientation. The normalisation chosen to define  $\mathrm{DtN}[\gamma]\psi$  will become clear when we will investigate the Hamiltonian structure of the Breaking Waves equations. To obtain this very system of equations, we need to state and prove two technical results. The first one is concerned with the component of the metric tensor seen as a matrix in a coordinate frame.

**Lemma 2.8.** Let  $\vec{s} \in \mathring{\Gamma}$ . Let  $\left(U_{\vec{s}}, \{s^j\}\right)$  a chart about  $\vec{s}$  in  $\mathring{\Gamma}$  and  $\left(V_{\gamma(t,\vec{s})}, \{y^j\}\right)$  another one about  $\gamma(t, \vec{s})$  in  $\Gamma_i(t)$ . We write, on the tangent planes  $T_{\vec{s}}\mathring{\Gamma}$  and  $T_{\gamma(t,\vec{s})}\Gamma_i(t)$ ,

$$\begin{split} g_{ij} &= \left[\mathbf{g}(t,\vec{s})\right]_{ij} = \mathbf{g}(t,\vec{s})(\partial_{s^i},\partial_{s^j}) & and & g^{ij} &= \left[\mathbf{g}(t,\vec{s})^{-1}\right]_{ij} \\ h_{ij} &= \left[\mathbf{h}\left(t,\pmb{\gamma}(t,\vec{s})\right)\right]_{ij} = \mathbf{h}\left(t,\pmb{\gamma}(t,\vec{s})\right)(\partial_{y^i},\partial_{y^j}) & and & h^{ij} &= \left[\mathbf{h}\left(t,\pmb{\gamma}(t,\vec{s})\right)^{-1}\right]_{ij}. \end{split}$$

Then the quantities defined above are related through

$$g_{ij} = \sum_{k=1}^d \sum_{\ell=1}^d \frac{\partial (y^k \circ \gamma)}{\partial s^i} \frac{\partial (y^\ell \circ \gamma)}{\partial s^j} h_{k\ell} \qquad and \qquad h^{k\ell} = \sum_{i=1}^d \sum_{j=1}^d \frac{\partial (y^k \circ \gamma)}{\partial s^i} \frac{\partial (y^\ell \circ \gamma)}{\partial s^j} g^{ij}.$$

*Proof.* In a coordinate system, we see readily that

$$\gamma(t,\vec{s})_* \left( \left. \frac{\partial}{\partial s^j} \right|_{\vec{s}} \right) = \sum_{k=1}^d \frac{\partial (y^k \circ \gamma)}{\partial s^j} \left. \frac{\partial}{\partial y^k} \right|_{\gamma(t,\vec{s})}.$$

From the definition of the metrics  $\mathbf{h}$  and  $\mathbf{g}$ , we get

$$\begin{split} g_{ij} &= \mathbf{g}(t, \vec{s}) \left( \left. \frac{\partial}{\partial s^i} \right|_{\vec{s}}, \left. \frac{\partial}{\partial s^j} \right|_{\vec{s}} \right) = \mathbf{h} \Big( t, \gamma(t, \vec{s}) \Big) \left( \sum_{k=1}^d \frac{\partial (y^k \circ \gamma)}{\partial s^i} \left. \frac{\partial}{\partial y^k} \right|_{\gamma(t, \vec{s})}, \sum_{\ell=1}^d \frac{\partial (y^\ell \circ \gamma)}{\partial s^j} \left. \frac{\partial}{\partial y^\ell} \right|_{\gamma(t, \vec{s})} \right) \\ &= \sum_{k=1}^d \sum_{\ell=1}^d \frac{\partial (y^k \circ \gamma)}{\partial s^i} \frac{\partial (y^\ell \circ \gamma)}{\partial s^j} \mathbf{h} \Big( t, \gamma(t, \vec{s}) \Big) \left( \left. \frac{\partial}{\partial y^k} \right|_{\gamma(t, \vec{s})}, \left. \frac{\partial}{\partial y^\ell} \right|_{\gamma(t, \vec{s})} \right) = \sum_{k=1}^d \sum_{\ell=1}^d \frac{\partial (y^k \circ \gamma)}{\partial s^i} \frac{\partial (y^\ell \circ \gamma)}{\partial s^i} h_{k\ell}, \end{split}$$

which is exactly the first relation. To obtain the second, we denote by **A** the matrix with components  $A_{ij} = \partial_{s^i}(y^j \circ \gamma)$ , so that we can rephrase the above relation in matrix notation (by slightly abusing the notation for **h** and **g** to identify them with their matrices in a coordinate frame) as

$$\mathbf{g}(t,\vec{s}) = \mathbf{A}\mathbf{h} \big(t, \pmb{\gamma}(t,\vec{s})\big) \mathbf{A}^{\top}.$$

71

By definition, each matrix in the above algebraic equation is invertible. Taking the inverse yields the second relation.

The above result can ne used to obtain a link between the tangential component of  $\nabla \phi$  and  $\nabla \psi$ . This provides a useful decomposition of  $\nabla \phi$  as the sum of a tangential and a normal component as follows.

**Lemma 2.9.** As in the previous lemma, let  $\vec{s} \in \mathring{\Gamma}$  and  $\left(U_{\vec{s}}, \{s^j\}\right)$  a chart about  $\vec{s}$  in  $\mathring{\Gamma}$ . Contrary to the previous lemma, we work now in  $\mathbb{R}^{d+1}$  so let  $\left(W_{\gamma(t,\vec{s})}, n, \{y^j\}\right)$  a chart about  $\gamma(t, \vec{s})$  in  $\mathbb{R}^{d+1}$  such that n is a normal coordinate and  $\{y^j\}$  are tangential coordinates. Then we can write

$$\boldsymbol{\nabla}\phi \Big(\boldsymbol{\gamma}(t,\vec{s})\Big) = g^{nn} \Big(t,\boldsymbol{\gamma}(t,\vec{s})\Big) \frac{\partial \phi}{\partial n} \Big(t,\boldsymbol{\gamma}(t,\vec{s})\Big) \left. \frac{\partial}{\partial n} \right|_{\boldsymbol{\gamma}(t,\vec{s})} + \sum_{j=1}^d \sum_{k=1}^d g^{jk}(t,\vec{s}) \frac{\partial \psi}{\partial s^j}(t,\vec{s}) \, \boldsymbol{\gamma}(t,\vec{s})_* \left( \left. \frac{\partial}{\partial s^k} \right|_{\vec{s}} \right),$$

where  $g^{nn} = 1/\mathbf{g}_{d+1}(\partial_n, \partial_n)$  on the interface. The normal term can be related to the Dirichlet-to-Neumann operator rapidly.

*Proof.* Using the notations of lemma 2.8, we define the representation of the Euclidean metric  $\mathbf{g}_{d+1}$  in the  $(n, \{y^j\})$  coordinate system on a point  $\gamma(t, \vec{s})$  of the free surface  $\Gamma_i(t)$ ,

$$\begin{split} g_{nn}\Big(t,\pmb{\gamma}(t,\vec{s})\Big) &= \mathbf{g}_{d+1}\left(\left.\frac{\partial}{\partial n}\right|_{\pmb{\gamma}(t,\vec{s})},\left.\frac{\partial}{\partial n}\right|_{\pmb{\gamma}(t,\vec{s})}\right) \\ \text{and} \qquad h_{ij}\Big(t,\pmb{\gamma}(t,\vec{s})\Big) &= \mathbf{h}\Big(t,\pmb{\gamma}(t,\vec{s})\Big)\left(\left.\frac{\partial}{\partial y^i}\right|_{\pmb{\gamma}(t,\vec{s})},\left.\frac{\partial}{\partial y^j}\right|_{\pmb{\gamma}(t,\vec{s})}\right) = \mathbf{g}_{d+1}\left(\left.\frac{\partial}{\partial y^i}\right|_{\pmb{\gamma}(t,\vec{s})},\left.\frac{\partial}{\partial y^j}\right|_{\pmb{\gamma}(t,\vec{s})}\right). \end{split}$$

Since, by of the decomposition 2.10, we have  $\mathbf{g}_{d+1}(\partial_n, \partial_{y^j}) = 0$ , the quantities  $g_{nn}$  and  $\{h_{ij}\}$  completely describe the Euclidean metric  $\mathbf{g}_{d+1}$  on a point of the free surface  $\Gamma_i(t)$ .

We have the following decomposition of the differential  $d\phi$  at a point  $\gamma(t, \vec{s})$ ,

$$\mathrm{d}\phi\big|_{\pmb{\gamma}(t,\vec{s})} = \frac{\partial\phi}{\partial n}\,\mathrm{d}n\big|_{\pmb{\gamma}(t,\vec{s})} + \sum_{i=1}^d \frac{\partial\phi}{\partial y^j}\,\mathrm{d}y^j\big|_{\pmb{\gamma}(t,\vec{s})}.$$

Setting  $g^{nn}=g_{nn}^{-1}$ , we can use the above expansion of  $d\phi$  to obtain the following representation of the gradient vector in  $\mathbf{T}_{\gamma(t,\vec{s})}\mathbb{R}^{d+1}$ ,

$$\nabla \phi = g^{nn} \frac{\partial \phi}{\partial n} \left. \frac{\partial}{\partial n} \right|_{\gamma(t,\vec{s})} + \sum_{i=1}^{d} \sum_{j=1}^{d} h^{ij} \frac{\partial \phi}{\partial y^{j}} \left. \frac{\partial}{\partial y^{i}} \right|_{\gamma(t,\vec{s})}. \tag{\dagger}$$

We can rephrase the second term using lemma 2.8 and the chain rule in a coordinate frame, yielding

$$\begin{split} \sum_{i=1}^{d} \sum_{j=1}^{d} h^{ij} \frac{\partial \phi}{\partial y^{i}} \left. \frac{\partial}{\partial y^{i}} \right|_{\boldsymbol{\gamma}(t,\vec{s})} &= \sum_{i=1}^{d} \sum_{j=1}^{d} \sum_{k=1}^{d} \sum_{\ell=1}^{d} \frac{\partial (y^{i} \circ \boldsymbol{\gamma})}{\partial s^{k}} \frac{\partial (y^{j} \circ \boldsymbol{\gamma})}{\partial s^{\ell}} g^{k\ell} \frac{\partial \phi}{\partial y^{j}} \left. \frac{\partial}{\partial y^{i}} \right|_{\boldsymbol{\gamma}(t,\vec{s})} \\ &= \sum_{k=1}^{d} \sum_{\ell=1}^{d} g^{k\ell} \frac{\partial \psi}{\partial s^{k}} \boldsymbol{\gamma}(t,\vec{s})_{*} \left( \left. \frac{\partial}{\partial s^{k}} \right|_{\vec{s}} \right), \end{split}$$

which yields exactly lemma 2.9 once plugged into (†). (Maybe Einstein's summation convention is a clever idea after all.)

Lemma 2.9 also permits to write down the (Euclidean) norm of  $\nabla \phi$  in an interesting geometrical form. Indeed, at an interface point  $\gamma(t, \vec{s})$ , we have

$$\left|\nabla\phi\right|^2 = g^{nn} \left(\frac{\partial\phi}{\partial n}\right)^2 + \sum_{i=1}^d \sum_{j=1}^d g^{ij} \frac{\partial\psi}{\partial s^i} \frac{\partial\psi}{\partial s^j}.$$

We can rewrite this in a coordinate independent manner as

$$\boldsymbol{u}^2\big(t,\boldsymbol{\gamma}(t,\vec{s})\big) = \left|\boldsymbol{\nabla}\phi\right|^2\big(t,\boldsymbol{\gamma}(t,\vec{s})\big) = \left(\frac{\mathrm{DtN}[\boldsymbol{\gamma}]\psi(t,\vec{s})}{\sqrt{\mathfrak{g}(t,\vec{s})}}\right)^2 + \mathbf{g}(t,\vec{s})\big(\vec{\nabla}\psi(t,\vec{s}),\vec{\nabla}\psi(t,\vec{s})\big).$$

The above right-hand side contains quantities defined on  $\mathring{\Gamma}$  only, as wanted.

II.1.4. The Breaking Waves equations: geometric form. We now have all the tools required to motivate the Breaking Waves equations in their most general form, that is in a way that does not depend on the reference label space  $\mathring{\Gamma}$ . Coming back to Bernoulli's equation on the interface (1.35a) and the generalised advection scheme (2.9), using the geometric decomposition and the Dirichlet-to-Neumann operator introduced above, the latter becomes

$$\partial_t \gamma(t, \vec{s}) = \frac{\text{DtN}[\gamma]\psi(t, \vec{s})}{\sqrt{\mathfrak{g}(t, \vec{s})}} \, \hat{\boldsymbol{n}}(t, \vec{s}) + \gamma(t, \vec{s})_* \vec{V}(t, \vec{s}). \tag{2.12a}$$

To obtain an evolution equation for  $\psi$ , we combine the above advection scheme with Bernoulli's equation as such.

$$\begin{split} \partial_t \psi(t, \vec{s}) &= \partial_t \Big[ \phi \Big( t, \gamma(t, \vec{s}) \Big) \Big] = (\partial_t \phi) \Big( t, \gamma(t, \vec{s}) \Big) + \partial_t \gamma(t, \vec{s}) \cdot \nabla \phi \Big( t, \gamma(t, \vec{s}) \Big) \\ &= g \cdot \gamma(t, \vec{s}) - \frac{1}{2} \Big| \nabla \phi \Big( t, \gamma(t, \vec{s}) \Big) \Big|^2 + \left( \frac{\text{DtN}[\gamma] \psi(t, \vec{s})}{\sqrt{\mathfrak{g}(t, \vec{s})}} \right)^2 + \mathbf{g}(t, \vec{s}) \Big( \vec{\nabla} \psi(t, \vec{s}), \vec{V}(t, \vec{s}) \Big) \\ &= \underbrace{-g \Big( z \circ \gamma(t, \vec{s}) \Big)}_{\text{gravity}} + \underbrace{\frac{1}{2} \frac{\Big( \text{DtN}[\gamma] \psi(t, \vec{s}) \Big)^2}{\mathfrak{g}(t, \vec{s})} + \mathbf{g}(t, \vec{s}) \Big( \vec{\nabla} \psi(t, \vec{s}), \vec{V}(t, \vec{s}) - \frac{1}{2} \vec{\nabla} \psi(t, \vec{s}) \Big)}_{\text{inertia}}, \end{split}$$
 (2.12b)

with  $z \circ \gamma$  the z component of  $\gamma$ . The set of equations (2.12) are the Breaking Waves equations (a name proposed by the author but which remains to be accepted by the community) in their most general geometric form. As advertised, all the terms that appear only involve  $\psi$  or  $\gamma$ , i.e. the full Water Waves problem (1.53) has been written on the, possibly overturning, interface  $\Gamma_i(t)$ , pulled back to a fixed label space  $\mathring{\Gamma}$ . Notice that the quantities  $\text{DtN}[\gamma]\psi$ ,  $\hat{n}$ ,  $\mathfrak{g}$ ,  $\mathfrak{g}$  and even  $\nabla \psi$  all depend implicitly on  $\gamma$ .

**Remark 2.10.** Should we have chosen a fully lagrangian advection scheme (i.e. setting  $\vec{V} = \vec{\nabla} \psi$ ), the above system would become

$$\begin{cases} \partial_t \pmb{\gamma} = \frac{\mathrm{DtN}[\pmb{\gamma}] \psi}{\sqrt{\mathfrak{g}}} \, \hat{\pmb{n}} + \pmb{\gamma}_* \vec{\nabla} \psi \\ \\ \partial_t \psi = -g \Big(z \circ \pmb{\gamma}\Big) + \frac{1}{2} \frac{\Big(\mathrm{DtN}[\pmb{\gamma}] \psi\Big)^2}{\mathfrak{g}} + \frac{1}{2} \, \mathbf{g} \, \Big(\vec{\nabla} \psi, \vec{\nabla} \psi\Big) \,. \end{cases}$$

In this specific case, we have the link with the lagrangian potential  $\psi = \varphi|_{\mathring{\Gamma}}$  and we can use (2.8) instead of (1.35a) in order to obtain (2.12b) more easily.

**Remark 2.11.** On the other hand, setting  $\vec{V} = 0$  (*i.e.* keeping the normal velocity advection only) yields only a slightly different system,

$$\begin{cases} \partial_t \gamma = \frac{\mathrm{DtN}[\gamma]\psi}{\sqrt{\mathfrak{g}}} \, \hat{\boldsymbol{n}} + \gamma_* \vec{\nabla}\psi \\ \\ \partial_t \psi = -g \Big(z \circ \gamma\Big) + \frac{1}{2} \frac{\Big(\mathrm{DtN}[\gamma]\psi\Big)^2}{\mathfrak{g}} - \frac{1}{2} \, \mathbf{g} \, \Big(\vec{\nabla}\psi, \vec{\nabla}\psi\Big) \,. \end{cases}$$

**Remark 2.12.** Reading the motivation of (2.12) presented here once again, our concerned reader might notice that these equations actually represent "possibly overturning water waves" in  $\mathbb{R}^{d+1}$  for all  $d \ge 1$ .

### II.2. A less geometric derivation

The geometric approach presented above is rather convenient to express the equations in a concise manner. However, presented in this way, the equations may not be easy to work with. We could set  $\mathring{\Gamma} = \mathbb{R}^d$  and write these equations in a coordinate frame advected with the flow instead. It would suffice to write down each element in a coordinate system, as was done in sec. II.1.3. We propose a different way of obtaining the system (2.12) expressed in a coordinate system, which is not based on tools from differential geometry.

II.2.1. The one-dimensional case. Let  $s \in \mathbb{R}$  the curvilinear coordinate of the time-varying jordan curve (i.e. a smooth curve which does not self-intersect)  $\gamma(t, \cdot) : \mathbb{R} \to \mathbb{R}^2$  representing  $\Gamma_i(t)$ , i.e.

$$\Gamma_i(t) = \bigcup_{s \in \mathbb{R}} \pmb{\gamma}(t,s) \qquad \text{such that} \qquad \left|\partial_s \pmb{\gamma}\right| \neq 0.$$

Since  $\Gamma_i(t)$  can be seen as a perturbation of the flat oceanic surface  $\{z=h_0\}$  (fig. 2.6), we assume the decomposition

$$\label{eq:gamma_tau} \pmb{\gamma}(t,s) = \begin{bmatrix} \lambda s + \gamma_x(t,s) \\ h_0 + \gamma_z(t,s) \end{bmatrix}.$$

Note that in the above decomposition, the parameter s cannot carry an intrinsic physical dimension. Adaptations to the arclength parametrisation is made by removing the  $\lambda$  factor. We can introduce unit tangent and normal vectors  $\hat{\tau}$  and  $\hat{n}$  at  $\gamma(t,s)$  through

$$\hat{m{ au}}(t,s) = rac{\partial_s m{\gamma}(t,s)}{\left|\partial_s m{\gamma}(t,s)
ight|} \qquad ext{and} \qquad \hat{m{n}}(t,s) = \hat{m{ au}}^\perp(t,s),$$

with  $\hat{\tau}^{\perp}$  the  $\frac{\pi}{2}$  counter-clockwise rotation of  $\hat{\tau}$  (fig. 2.6). At all interface points  $\gamma(t, s)$ , the set  $(\hat{\tau}, \hat{n})$  forms an orthonormal basis of  $\mathbb{R}^{d+1}$ . In 2d (d=1), we can easily construct such orthonormal basis; this shall not remain an easy task in the 3d case. Expanding the gradient vector  $\nabla \phi$  in this coordinate system yields

$$\begin{split} \boldsymbol{\nabla}\phi \Big(t,\boldsymbol{\gamma}(t,s)\Big) &= \Big(\hat{\boldsymbol{n}}(t,s)\cdot\boldsymbol{\nabla}\phi \Big(t,\boldsymbol{\gamma}(t,s)\Big)\Big)\hat{\boldsymbol{n}}(t,s) + \Big(\hat{\boldsymbol{\tau}}(t,s)\cdot\boldsymbol{\nabla}\phi \Big(t,\boldsymbol{\gamma}(t,s)\Big)\Big)\hat{\boldsymbol{\tau}}(t,s) \\ &= \Big(\hat{\boldsymbol{n}}(t,s)\cdot\boldsymbol{\nabla}\phi \Big(t,\boldsymbol{\gamma}(t,s)\Big)\Big)\hat{\boldsymbol{n}}(t,s) + \Big(\partial_s\boldsymbol{\gamma}(t,s)\cdot\boldsymbol{\nabla}\phi \Big(t,\boldsymbol{\gamma}(t,s)\Big)\Big)\frac{\partial_s\boldsymbol{\gamma}(t,s)}{\big|\partial_s\boldsymbol{\gamma}(t,s)\big|^2} \\ &= \frac{\mathrm{DtN}[\boldsymbol{\gamma}]\psi(t,s)}{\big|\partial_s\boldsymbol{\gamma}(t,s)\big|}\hat{\boldsymbol{n}}(t,s) + \frac{\partial_s\psi(t,s)}{\big|\partial_s\boldsymbol{\gamma}(t,s)\big|}\frac{\partial_s\boldsymbol{\gamma}(t,s)}{\big|\partial_s\boldsymbol{\gamma}(t,s)\big|}, \end{split}$$

with the Dirichlet-to-Neumann operator  $DtN[\gamma]\psi$  defined by the above equation. One can check that this definition is consistent with the more geometrical one (2.11).

The generalised advection equation (2.9) is rephrased in a more tractable way as

$$\partial_{t} \boldsymbol{\gamma}(t,s) = \left(\hat{\boldsymbol{n}}(t,s) \cdot \boldsymbol{\nabla} \phi \left(t, \boldsymbol{\gamma}(t,s)\right)\right) \hat{\boldsymbol{n}}(t,s) + v(t,s) \hat{\boldsymbol{\tau}}(t,s) \\
= \frac{\text{DtN}[\boldsymbol{\gamma}] \psi(t,s)}{\left|\partial_{s} \boldsymbol{\gamma}(t,s)\right|} \hat{\boldsymbol{n}}(t,s) + v(t,s) \hat{\boldsymbol{\tau}}(t,s) \tag{2.15a}$$

where v is an arbitrary time-dependent function representing the tangential velocity. Aside from the choices v = 0 and  $v = \mathbf{u} \cdot \hat{\boldsymbol{\tau}}$ , the following lemma provides an interesting choice for v (in one space dimension d = 1 only).

**Lemma 2.13.** Suppose that  $\gamma(0,s)$  corresponds to the arclength parametrisation of  $\Gamma_i(0)$  and that v is chosen such that  $\partial_s v = \kappa u \cdot \hat{\boldsymbol{n}}$ , with  $\kappa$  the curvature. Then  $\gamma(t,s)$  corresponds to the arclength parametrisation of  $\Gamma_i(t)$  at all subsequent times  $t \geq 0$ .

*Proof.* In the arclength parametrisation, the following useful relations hold (the Frénet-Serre formulas),

$$\partial_{s}\hat{\boldsymbol{\tau}} = \kappa \hat{\boldsymbol{n}}$$
 and  $\partial_{s}\hat{\boldsymbol{n}} = -\kappa \hat{\boldsymbol{\tau}}$ .

Therefore,

$$\begin{split} \partial_t \Big( \big| \partial_s \gamma \big|^2 \Big) &= 2 \partial_{ts} \gamma \cdot \partial_s \gamma = 2 \big| \partial_s \gamma \big| \partial_s \Big( \partial_t \gamma \Big) \cdot \partial_s \gamma \\ &= 2 \big| \partial_s \gamma \big| \partial_s \Big( \Big( \boldsymbol{u} \cdot \hat{\boldsymbol{n}} \Big) \hat{\boldsymbol{n}} + v \hat{\boldsymbol{\tau}} \Big) \cdot \hat{\boldsymbol{\tau}} = 2 \big| \partial_s \gamma \big| \Big( \hat{\boldsymbol{n}} \partial_s u_n - \kappa u_n \hat{\boldsymbol{\tau}} + \hat{\boldsymbol{\tau}} \partial_s v + \kappa v \hat{\boldsymbol{n}} \Big) \cdot \hat{\boldsymbol{\tau}} \\ &= 2 \Big( \partial_s v - \kappa u_n \Big), \end{split}$$

which vanishes if and only if  $\partial_s v = \kappa u_n$ . We have used the fact that  $|\partial_s \gamma| = 1$  and we denoted  $u_n = \mathbf{u} \cdot \hat{\mathbf{n}}$ .  $\square$  **Remark 2.14.** The above lemma shall be used later, in sec. IV of chapter 4 to derive an evolution equation for the curvature  $\kappa$ .

It remains to obtain the evolution equation for  $\psi$ . This is done from the chain rule, as usual,

$$\begin{split} \partial_t \psi(t,s) &= \partial_t \Big( \phi \Big( t, \gamma(t,s) \Big) \Big) = \partial_t \phi \Big( t, \gamma(t,s) \Big) + \partial_t \gamma(t,s) \cdot \nabla \phi \Big( t, \gamma(t,s) \Big) \\ &= -g \Big( h_0 + \gamma_z(t,s) \Big) - \frac{1}{2} \Big| \nabla \phi \Big( t, \gamma(t,s) \Big) \Big|^2 + \left( \frac{\text{DtN}[\gamma] \psi(t,s)}{\left| \partial_s \gamma(t,s) \right|} \right)^2 + v(t,s) \frac{\partial_s \psi(t,s)}{\left| \partial_s \gamma(t,s) \right|} \\ &= -g \gamma_z(t,s) + \frac{1}{2} \left( \frac{\text{DtN}[\gamma] \psi(t,s)}{\left| \partial_s \gamma(t,s) \right|} \right)^2 + \frac{\partial_s \psi(t,s)}{\left| \partial_s \gamma(t,s) \right|} \left( v(t,s) - \frac{1}{2} \frac{\partial_s \psi(t,s)}{\left| \partial_s \gamma(t,s) \right|} \right), \end{split} \tag{2.15b}$$

where we have incorporated the constant  $-gh_0$  into the time derivative of  $\psi$  without changing either the physical velocity  $\nabla \phi$  or the free surface parametrisation  $\gamma$ . The two equations (2.15) are the *Breaking Waves* equations in one dimension (i.e. for a two-dimensional physical space). As in the geometric case, they take more concise forms when choosing a purely lagrangian advection scheme or setting v = 0. In the former case, these equations can be obtained more directly from the lagrangian version of Bernoulli's equation (2.8).

**Remark 2.15.** One can check that the system (2.15) is in fact exactly (2.12) written on  $\Gamma = \mathbb{R}$ . Indeed, the various quantities appearing in (2.12) can be rephrased, in this particular case, as

$$\begin{split} g_{ij} &= g_{11} = \mathbf{g}(\partial_s, \partial_s) = \left|\partial_s \boldsymbol{\gamma}\right|^2 \\ \vec{\nabla} \psi &= \frac{1}{|\partial_s \boldsymbol{\gamma}|^2} \frac{\partial \psi}{\partial s} \left. \frac{\partial}{\partial s} \right|_s \\ \mathbf{g} &= \left|\partial_s \boldsymbol{\gamma}\right|^2 \\ \mathbf{g} &\left(\vec{\nabla} \psi, \vec{\nabla} \psi\right) = \left(\frac{\partial \psi}{|\partial_s \boldsymbol{\gamma}|}\right)^2 \\ \mathbf{g} &\left(\vec{\nabla} \psi, \vec{V}\right) = \frac{v}{|\partial_s \boldsymbol{\gamma}|} \frac{\partial \psi}{\partial s}. \end{split}$$

We remark that v is the component of  $\vec{V}$  along the *normalised* basis  $\left|\partial_s \gamma\right|^{-1} \partial_s$ . Notice that the parameter space  $\mathbb{R}$  is not equipped with the standard Euclidean metric but with the one deriving from the parametrisation  $\gamma$ .

II.2.2. The two-dimensional equations. When d=1, we have been able to construct an orthonormal frame  $(\hat{s}, \hat{n})$  on which the gradient  $\nabla \phi$  was expanded readily. For a two-dimensional surface, we won't be able to use the rotation operator  $a^{\perp}$  as it is not defined for vectors  $a \in \mathbb{R}^{d+1}$ . Instead, more work shall be needed.

Let  $\gamma(t, \cdot): \mathbb{R}^d \to \mathbb{R}^{d+1}$  a global regular parametrisation of the smooth free surface  $\Gamma_i(t)$ , that is: each point  $\boldsymbol{y} \in \Gamma_i(t)$  can be written as  $\boldsymbol{y} = \gamma(t, \vec{s})$  for some unique  $\vec{s}$ , and we have

$$\partial_{s_1} \boldsymbol{\gamma} \times \partial_{s_2} \boldsymbol{\gamma} \neq 0$$
 everywhere.

This means that the tangent vectors  $\partial_{s_1} \gamma$  and  $\partial_{s_2} \gamma$  are nowhere pointing in the same direction. A new difficulty is that we cannot ensure that  $\partial_{s_1} \gamma \cdot \partial_{s_2} \gamma = 0$  at all time, even if we assume that it holds initially. In a sense, the intrinsic coordinate system of  $\Gamma_i(t)$  is advected with the flow and can thus becomes quite twisted. A unit normal vector is defined as

$$\hat{\boldsymbol{n}}(t,\vec{s}) = \frac{\partial_{s_1} \boldsymbol{\gamma} \times \partial_{s_2} \boldsymbol{\gamma}}{\left|\partial_{s_1} \boldsymbol{\gamma} \times \partial_{s_2} \boldsymbol{\gamma}\right|}.$$

Its existence everywhere is ensured by the regularity assumption. However, to ensure that  $\hat{n}$  points outside of the fluid domain  $\Omega(t)$  everywhere, we must also assume that the parametrisation  $\gamma$  possesses the correct orientation. Should it be the case initially, then it will remain so until a coordinate singularity appears.

We would like that  $\Gamma_i(t)$  corresponds to a perturbation of the flat infinite oceanic surface  $\Gamma_0 = \{z = h_0\}$ . Therefore we propose to see the parametrisation  $\gamma$  as a perturbation of the flat Euclidean space  $\mathbb{R}^d$ ,

$$\gamma(t,\vec{s}) = \begin{bmatrix} \lambda \vec{s} + \vec{\gamma}(t,\vec{s}) \\ h_0 + \gamma_z(t,\vec{s}) \end{bmatrix}.$$

Expanding the gradient  $\nabla \phi$  is rather involved. Indeed, since  $\{\partial_{s^1} \gamma, \partial_{s^2} \gamma, \hat{n}\}$  is not an orthonormal basis, we cannot expand it directly onto this basis. By construction,  $\hat{n}$  is already unitary and orthogonal to the two other vectors. We therefore only need to work on the two others. In order to build an orthonormal basis of the tangent plane from  $\partial_{s^1} \gamma$  and  $\partial_{s^2} \gamma$ , we use the Gram-Schmidt orthonormalisation process which yields, at each  $\vec{s} \in \mathbb{R}^d$  and each time  $t \geq 0$ , an orthonormal basis  $\{\hat{s}_1, \hat{s}_2\}$ 

$$\hat{\boldsymbol{s}}_1 = \hat{\boldsymbol{\tau}}_1 = \frac{\partial_{s^1} \boldsymbol{\gamma}}{\left|\partial_{s^1} \boldsymbol{\gamma}\right|} \qquad \text{and} \qquad \hat{\boldsymbol{s}}_2 = \frac{1}{\sqrt{1 - (\hat{\boldsymbol{\tau}}_1 \cdot \hat{\boldsymbol{\tau}}_2)^2}} \left[ \hat{\boldsymbol{\tau}}_2 - (\hat{\boldsymbol{\tau}}_1 \cdot \hat{\boldsymbol{\tau}}_2) \hat{\boldsymbol{\tau}}_1 \right] \qquad \text{with} \quad \hat{\boldsymbol{\tau}}_j = \frac{\partial_{s^j} \boldsymbol{\gamma}}{\left|\partial_{s^j} \boldsymbol{\gamma}\right|},$$

for j=1 or 2. The set  $\{\hat{s}_1, \hat{s}_2, \hat{n}\}$  forms an orthonormal basis of  $\mathbb{R}^{d+1}$  along which we can expand the gradient vector, yielding (all terms being evaluated at time t, physical position  $\gamma(t, \vec{s})$  or label-space position  $\vec{s}$ ),

$$\begin{split} & \boldsymbol{\nabla} \phi = (\hat{\boldsymbol{n}} \cdot \boldsymbol{\nabla} \phi) \hat{\boldsymbol{n}} + (\hat{\boldsymbol{s}}_1 \cdot \boldsymbol{\nabla} \phi) \hat{\boldsymbol{s}}_1 + (\hat{\boldsymbol{s}}_2 \cdot \boldsymbol{\nabla} \phi) \hat{\boldsymbol{s}}_2 \\ & = \frac{\operatorname{DtN}[\boldsymbol{\gamma}] \psi}{\left| \partial_{s_1} \boldsymbol{\gamma} \times \partial_{s_2} \boldsymbol{\gamma} \right|} \hat{\boldsymbol{n}} + (\hat{\boldsymbol{\tau}}_1 \cdot \boldsymbol{\nabla} \phi) \hat{\boldsymbol{\tau}}_1 + \frac{1}{1 - (\hat{\boldsymbol{\tau}}_1 \cdot \hat{\boldsymbol{\tau}}_2)^2} \bigg[ \Big( \Big( \hat{\boldsymbol{\tau}}_2 - (\hat{\boldsymbol{\tau}}_1 \cdot \hat{\boldsymbol{\tau}}_2) \hat{\boldsymbol{\tau}}_1 \Big) \cdot \boldsymbol{\nabla} \phi \Big) \Big( \hat{\boldsymbol{\tau}}_2 - (\hat{\boldsymbol{\tau}}_1 \cdot \hat{\boldsymbol{\tau}}_2) \hat{\boldsymbol{\tau}}_1 \Big) \bigg] \\ & = \frac{\operatorname{DtN}[\boldsymbol{\gamma}] \psi}{\left| \partial_{s_1} \boldsymbol{\gamma} \times \partial_{s_2} \boldsymbol{\gamma} \right|} \hat{\boldsymbol{n}} + \frac{(\hat{\boldsymbol{\tau}}_1 \cdot \boldsymbol{\nabla} \phi) \hat{\boldsymbol{\tau}}_1 + (\hat{\boldsymbol{\tau}}_2 \cdot \boldsymbol{\nabla} \phi) \hat{\boldsymbol{\tau}}_2 - (\hat{\boldsymbol{\tau}}_1 \cdot \hat{\boldsymbol{\tau}}_2) \Big[ (\hat{\boldsymbol{\tau}}_1 \cdot \boldsymbol{\nabla} \phi) \hat{\boldsymbol{\tau}}_2 + (\hat{\boldsymbol{\tau}}_2 \cdot \boldsymbol{\nabla} \phi) \hat{\boldsymbol{\tau}}_1 \Big] \\ & = \frac{\operatorname{DtN}[\boldsymbol{\gamma}] \psi}{\left| \partial_{s_1} \boldsymbol{\gamma} \times \partial_{s_2} \boldsymbol{\gamma} \right|} \hat{\boldsymbol{n}} + \frac{\left| \partial_{s^2} \boldsymbol{\gamma} \right|^2 \partial_{s^1} \psi \, \partial_{s^1} \boldsymbol{\gamma} + \left| \partial_{s^1} \boldsymbol{\gamma} \right|^2 \partial_{s^2} \psi \, \partial_{s^2} \boldsymbol{\gamma} - (\partial_{s^1} \boldsymbol{\gamma} \cdot \partial_{s^2} \boldsymbol{\gamma}) \left[ \partial_{s^1} \psi \, \partial_{s^2} \boldsymbol{\gamma} + \partial_{s^2} \psi \, \partial_{s^1} \boldsymbol{\gamma} \Big] \\ & = \frac{\operatorname{DtN}[\boldsymbol{\gamma}] \psi}{\left| \partial_{s_1} \boldsymbol{\gamma} \times \partial_{s_2} \boldsymbol{\gamma} \right|} \hat{\boldsymbol{n}} + \frac{1}{\det(\mathbf{g})} \left[ \partial_{s^1} \psi \quad \partial_{s^2} \psi \right] \begin{bmatrix} \left| \partial_{s^2} \boldsymbol{\gamma} \right|^2 & -\partial_{s^1} \boldsymbol{\gamma} \cdot \partial_{s^2} \boldsymbol{\gamma} \\ -\partial_{s^1} \boldsymbol{\gamma} \cdot \partial_{s^2} \boldsymbol{\gamma} & \left| \partial_{s^1} \boldsymbol{\gamma} \right|^2 \\ -\partial_{s^1} \boldsymbol{\gamma} \cdot \partial_{s^2} \boldsymbol{\gamma} & \left| \partial_{s^1} \boldsymbol{\gamma} \right|^2 \end{bmatrix} \begin{bmatrix} \partial_{s^1} \boldsymbol{\gamma} \\ \partial_{s^2} \boldsymbol{\gamma} \end{bmatrix} \\ & = \frac{\operatorname{DtN}[\boldsymbol{\gamma}] \psi}{\left| \partial_{s_1} \boldsymbol{\gamma} \times \partial_{s_2} \boldsymbol{\gamma} \right|} \hat{\boldsymbol{n}} + \left[ \partial_{s^1} \psi \quad \partial_{s^2} \psi \right] \mathbf{g}^{-1} \begin{bmatrix} \partial_{s^1} \boldsymbol{\gamma} \\ \partial_{s^2} \boldsymbol{\gamma} \end{bmatrix}, \end{split}$$

where  $\mathbf{g}^{-1}$  is the inverse of the intrinsic metric tensor

$$\mathbf{g} = \begin{bmatrix} |\partial_{s^1} \boldsymbol{\gamma}|^2 & \partial_{s^1} \boldsymbol{\gamma} \cdot \partial_{s^2} \boldsymbol{\gamma} \\ \partial_{s^1} \boldsymbol{\gamma} \cdot \partial_{s^2} \boldsymbol{\gamma} & |\partial_{s^2} \boldsymbol{\gamma}|^2 \end{bmatrix}.$$

We notice, furthermore, that  $|\partial_{s_1} \boldsymbol{\gamma} \times \partial_{s_2} \boldsymbol{\gamma}|^2 = \det(\mathbf{g})$  from a standard property of the cross product in  $\mathbb{R}^3$ . Using the decomposition of  $\nabla \phi$  and remembering the link between  $\mathbf{g}$  and  $\boldsymbol{\gamma}$ , we obtain that

$$\left| \nabla \phi \right|^2 = \frac{\left( \text{DtN}[\gamma] \psi \right)^2}{\det(\mathbf{g})} + \left[ \partial_{s^1} \psi \quad \partial_{s^2} \psi \right] \mathbf{g}^{-1} \begin{bmatrix} \partial_{s^1} \psi \\ \partial_{s^2} \psi \end{bmatrix}.$$

We can now state the two-dimensional Breaking Waves equations. The interface advection equations is simply

$$\begin{split} \partial_t \pmb{\gamma}(t,\vec{s}) &= \Big( \hat{\pmb{n}}(t,\vec{s}) \cdot \pmb{\nabla} \phi \Big(t,\pmb{\gamma}(t,\vec{s}) \Big) \Big) \hat{\pmb{n}}(t,\vec{s}) + v_1(t,\vec{s}) \hat{\pmb{\tau}}_1(t,\vec{s}) + v_2(t,\vec{s}) \hat{\pmb{\tau}}_2(t,\vec{s}) \\ &= \frac{\text{DtN}[\pmb{\gamma}] \psi(t,\vec{s})}{\sqrt{\det(\mathbf{g})(t,\vec{s})}} \, \hat{\pmb{n}}(t,\vec{s}) + v_1(t,\vec{s}) \hat{\pmb{\tau}}_1(t,\vec{s}) + v_2(t,\vec{s}) \hat{\pmb{\tau}}_2(t,\vec{s}), \end{split} \tag{2.16a}$$

for abirtrary tangential velocities  $v_1$  and  $v_2$ . In the meantime, the equation for the potential becomes

$$\partial_t \psi = \partial_t \phi + \partial_t \gamma \cdot \nabla \phi 
= -g \gamma_z + \frac{1}{2} \frac{\left( \text{DtN}[\gamma] \psi \right)^2}{\det(\mathbf{g})} + \begin{bmatrix} \partial_{s^1} \psi & \partial_{s^2} \psi \end{bmatrix} \mathbf{g}^{-1} \left( \begin{bmatrix} |\partial_{s^1} \gamma| v_1 \\ |\partial_{s^2} \gamma| v_2 \end{bmatrix} - \frac{1}{2} \begin{bmatrix} \partial_{s^1} \psi \\ \partial_{s^2} \psi \end{bmatrix} \right), \tag{2.16b}$$

with, once again, straightforward adaptations should the advection scheme be fully lagrangian or normal only.

**Remark 2.16.** As in the one-dimensional case, we recover the geometric form (2.12) of the Breaking Waves equations by making the following identifications,

**Remark 2.17.** (Giving to Caesar what belongs to Caesar) The one-dimensional system (2.15) was first written in Craig (2017), where different tangential velocities have been discussed. The author only extended this formulation to two-dimensional free surfaces.

**Remark 2.18.** In the above motivation of the Breaking Waves equations, we assumed that both the interface  $\gamma$  and the potential  $\psi$  are in fact smooth. At a fixed time, taking a glance back at the equations, we see that these are well-defined for interfaces in  $W^{1,\infty}(\mathbb{R}^d)$  and potentials in  $H^1(\mathbb{R}^d)$  only.

### II.3. Hamiltonian structure

Unfortunately, the canonical Hamiltonian structure (1.47) of the usual Water Waves equations (1.43) does not extend to the Breaking Waves equations. Indeed, as already noticed by Benjamin and Olver (1982) (making use of the extension of Noether's theorem to Hamiltonian systems derived in Olver 1980) or Bridges and Donaldson (2011), a Hamiltonian structure does exist but it is not canonical for the pair of variables  $(\gamma, \psi)$ . We shall work in the d-dimensional reference frame  $\mathbb{R}^d$  (with straightforward adaptations to a general reference Riemannian manifold  $\mathring{\Gamma}$ ). The energy associated with the system (2.12) is

$$\begin{split} \mathrm{H}[\boldsymbol{\gamma}, \boldsymbol{\psi}] &= \frac{1}{2} \int_{\mathbb{R}^d} \boldsymbol{\psi} \, \mathrm{DtN}[\boldsymbol{\gamma}] \boldsymbol{\psi} + \frac{g}{2} \int_{\mathbb{R}^d} (\gamma_z^2) \, \hat{\boldsymbol{z}} \cdot \hat{\boldsymbol{n}} \, \sqrt{\mathfrak{g}} \\ &= \underbrace{\frac{1}{2} \int_{\Gamma_i(t)} \boldsymbol{\phi} \, (\hat{\boldsymbol{n}} \cdot \boldsymbol{\nabla} \boldsymbol{\phi})}_{\mathrm{K}[\boldsymbol{\gamma}, \boldsymbol{\psi}]} + \underbrace{\frac{g}{2} \int_{\Gamma_i(t)} \boldsymbol{z}^2(\hat{\boldsymbol{z}} \cdot \hat{\boldsymbol{n}})}_{\mathrm{U}[\boldsymbol{\gamma}]}. \end{split}$$

K represents the kinetic energy while U corresponds to the gravitational potential energy of the interface. We now understand the choice of normalisation of the Dirichlet-to-Neumann operator: it removes the  $\sqrt{\mathfrak{g}}$  that appears when transforming an integral on  $\mathring{\Gamma}$  to an integral on  $\Gamma_i(t)$ . The fact that this Hamiltonian functional corresponds to the actual *physical* energy of the system can be see multiplying the full Euler equation (1.6) by  $u = \nabla \phi$  and making use of the various boundary conditions to carry out integrations by parts.

We now compute the variational derivatives of H with respect to  $\psi$  and  $\gamma$ . This last two quantities are no longer considered time-dependent. We should not even use the fact that they are solutions of the Breaking Waves equations (2.16). Therefore, in the following, the interface described by  $\gamma$  shall be denoted by  $\Gamma$ .

The parametric Dirichlet-to-Neumann operator possesses the same properties as the standard one, *i.e.* it is positive definite and symmetric. Hence, variation of K along  $\psi$  (for the  $L^2(\mathbb{R}^d)$  scalar product) is rather easy to obtain,

$$\mathrm{K}[\boldsymbol{\gamma}, \boldsymbol{\psi} + \boldsymbol{h}] = \int_{\mathbb{R}^d} (\boldsymbol{\psi} + \boldsymbol{h}) \, \mathrm{DtN}[\boldsymbol{\gamma}](\boldsymbol{\psi} + \boldsymbol{h})$$

$$\begin{split} &= \mathrm{K}[\boldsymbol{\gamma}, \boldsymbol{\psi}] + \int_{\mathbb{R}^d} h \, \mathrm{DtN}[\boldsymbol{\gamma}] \boldsymbol{\psi} + O\Big(h^2\Big) \\ &= \mathrm{K}[\boldsymbol{\gamma}, \boldsymbol{\psi}] + \int_{\mathbb{R}^d} h \, \frac{\delta \mathrm{K}}{\delta \boldsymbol{\psi}} + O\Big(h^2\Big). \end{split}$$

Since U does not depend on  $\psi$ , we have that  $\delta_{\psi}H = \delta_{\psi}K$ , and we see that

$$m{n}\cdot\partial_tm{\gamma}=rac{\delta H}{\delta\psi} \qquad ext{or} \qquad \partial_tm{\gamma}=rac{\delta H}{\delta\psi}rac{m{n}}{\det(m{g})},$$

with n the non-normalised normal vector. Splitting the one-dimensional and two-dimensional computations, the variation of the potential energy U with respect to  $\gamma$  is computed as

$$\begin{aligned} &(\mathrm{1d}) &(2\mathrm{d}) \\ &\mathrm{U}[\boldsymbol{\gamma}+\boldsymbol{h}] = \frac{g}{2} \int_{\mathbb{R}} (\gamma_z + h_z) \partial_s (\gamma_x + h_x) &= \frac{g}{2} \int_{\mathbb{R}^2} \left( \gamma_z + h_z \right)^2 \hat{\boldsymbol{z}} \cdot \left( \partial_1 (\boldsymbol{\gamma} + \boldsymbol{h}) \times \partial_2 (\boldsymbol{\gamma} + \boldsymbol{h}) \right) \\ &= \mathrm{U}[\boldsymbol{\gamma}] + g \int_{\mathbb{R}} \frac{\gamma_z^2}{2} \partial_s h_x + \gamma_z h_z \partial_s \gamma_x &= \mathrm{U}[\boldsymbol{\gamma}] + g \int_{\mathbb{R}^2} \gamma_z h_z \hat{\boldsymbol{z}} \cdot \boldsymbol{n} + \frac{\gamma_z^2}{2} \hat{\boldsymbol{z}} \cdot \left( \partial_1 \boldsymbol{h} \times \partial_2 \boldsymbol{\gamma} + \partial_1 \boldsymbol{\gamma} \times \partial_2 \boldsymbol{h} \right) \\ &= \mathrm{U}[\boldsymbol{\gamma}] + g \int_{\mathbb{R}} \gamma_z (h_z \partial_s \gamma_x - h_x \partial_s \gamma_z) &= \mathrm{U}[\boldsymbol{\gamma}] + g \int_{\mathbb{R}^2} \gamma_z h_z \hat{\boldsymbol{z}} \cdot \boldsymbol{n} + \gamma_z \boldsymbol{h} \cdot \left( \partial_2 \gamma_z \hat{\boldsymbol{z}} \times \partial_1 \boldsymbol{\gamma} - \partial_1 \gamma_z \hat{\boldsymbol{z}} \times \partial_2 \boldsymbol{\gamma} \right) \\ &= \mathrm{U}[\boldsymbol{\gamma}] + g \int_{\mathbb{R}} \gamma_z \boldsymbol{h} \cdot \boldsymbol{n} &= \mathrm{U}[\boldsymbol{\gamma}] + g \int_{\mathbb{R}^2} \gamma_z h_z \hat{\boldsymbol{z}} \cdot \boldsymbol{n} + \gamma_z \boldsymbol{h} \cdot \left( \boldsymbol{n} \cdot \hat{\boldsymbol{x}} + \boldsymbol{n} \cdot \hat{\boldsymbol{y}} \right) \\ &= \mathrm{U}[\boldsymbol{\gamma}] + \int_{\mathbb{R}} \boldsymbol{h} \cdot \frac{\delta \mathrm{U}}{\delta \boldsymbol{\gamma}} &= \mathrm{U}[\boldsymbol{\gamma}] + \int_{\mathbb{R}^2} \boldsymbol{h} \cdot \frac{\delta \mathrm{U}}{\delta \boldsymbol{\gamma}}. \end{aligned}$$

In both cases, we obtain that

$$g\gamma_z = \frac{\delta \mathbf{U}}{\delta \boldsymbol{\gamma}} \cdot \frac{\boldsymbol{n}}{\det(\mathbf{g})}.$$

This results extends to higher dimensions as well.

Finally, the variation of the kinetic term along  $\gamma$  is more involved. The idea is to suppose that the variation h lies along the normal  $\hat{n}$  to the free surface  $\Gamma_i(t)$  (see figure 2.7) and further decompose it as a positive part and a negative part. The tangential variation cannot contribute to the dynamic of the system as it corresponds to a mere reparametrisation. Hence, we assume

$$h(\vec{s}) = h(\vec{s})\hat{n}$$
  $h(\vec{s}) = h_{+}(\vec{s}) + h_{-}(\vec{s})$  and  $h_{+} = \max\{h, 0\}$  and  $h_{-} = \min\{h, 0\}$ 

We can carry out the computations for  $h_+$  and  $h_-$  independently without loss of generality, because of the linearity of the derivative. We shall only provide details for the  $h_+$  part.

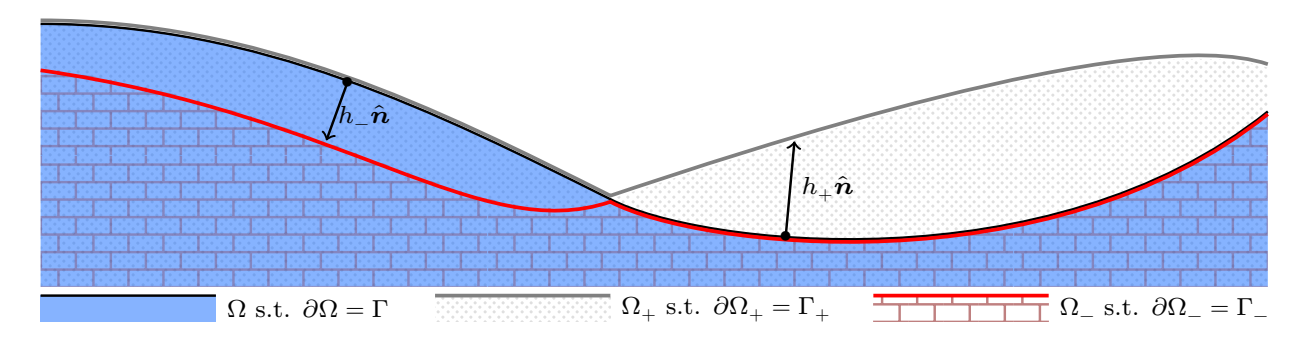


Figure 2.7 – Notations used to compute the variational derivative of the Hamiltonian  $H[\gamma, \psi]$  with respect to  $\gamma$ . The bottom boundary  $\Gamma_b$  is not shown.

Let us define  $\gamma_+ = \gamma + h_+ \hat{n}$ . Since  $h_+ \geqslant 0$ , we have  $\Omega \subseteq \Omega_+$  (figure 2.7). With these notations at hand, we define the solutions  $\phi$  and  $\phi_+$  of the following Dirichlet problems associated with the Dirichlet-to-Neumann operators

$$\mathrm{DtN}[\gamma_+] : \left\{ \begin{array}{cccc} \Delta\phi_+ &=& 0 & \mathrm{in} \ \Omega_+ \\ \phi_+ &=& \psi & \mathrm{on} \ \Gamma_+ \\ \partial_n\phi_+ &=& 0 & \mathrm{on} \ \Gamma_b \end{array} \right. \quad \text{and} \quad \mathrm{DtN}[\gamma] : \left\{ \begin{array}{cccc} \Delta\phi &=& 0 & \mathrm{in} \ \Omega \\ \phi &=& \psi & \mathrm{on} \ \Gamma \\ \partial_n\phi &=& 0 & \mathrm{on} \ \Gamma_b \end{array} \right. .$$

We have to be careful about what we actually mean by the boundary condition  $\phi = \psi$  and  $\phi_+ = \psi$  on  $\Gamma$  and  $\Gamma_+$  respectively. We actually want

$$\phi(\gamma(\vec{s})) = \psi(\vec{s})$$
 and  $\phi_+(\gamma_+(\vec{s})) = \psi(\vec{s})$ .

We are now in position to derive a useful relation on the boundary, keeping in mind that  $\phi_+$  is defined in  $\Omega$  whereas  $\phi$  is not defined in all of  $\Omega_+$  (figure 2.7).

$$\begin{split} \phi_+ \circ \gamma(s) &= \phi_+ \Big[ \gamma_+(\vec{s}) - h_+(\vec{s}) \hat{\boldsymbol{n}}(\vec{s}) \Big] \\ &= \psi(\vec{s}) - h_+(\vec{s}) \hat{\boldsymbol{n}}(\vec{s}) \cdot \Big( \boldsymbol{\nabla} \phi_+ \circ \gamma_+(\vec{s}) \Big) + O\Big(h^2\Big) \\ &= \phi \circ \gamma(\vec{s}) - h_+(\vec{s}) \hat{\boldsymbol{n}}(\vec{s}) \cdot \Big( \boldsymbol{\nabla} \phi_+ \circ \gamma_+(\vec{s}) \Big) + O\Big(h^2\Big) \\ &= \phi \circ \gamma(\vec{s}) - h_+(\vec{s}) \hat{\boldsymbol{n}}(\vec{s}) \cdot \Big( \boldsymbol{\nabla} \phi \circ \gamma(\vec{s}) \Big) + O\Big(h^2\Big). \end{split}$$

In general, we should always keep in mind that  $\phi|_{\Gamma} = \phi_{+}|_{\Gamma} + O(h)$ . We cannot postpone the computation of  $\delta_{\gamma}K$  any further; it is now time to make use of the above relation. Let us begin with

$$\begin{split} \mathrm{K}[\boldsymbol{\gamma} + h_{+} \hat{\boldsymbol{n}}, \boldsymbol{\psi}] &= \frac{1}{2} \int_{\mathbb{R}^{d}} \boldsymbol{\psi} \, \mathrm{DtN}[\boldsymbol{\gamma} + h_{+} \hat{\boldsymbol{n}}] \boldsymbol{\psi} \\ &= \frac{1}{2} \int_{\Gamma_{+}} \phi_{+} \partial_{n} \phi_{+} = \mathrm{K}[\boldsymbol{\gamma}, \boldsymbol{\psi}] + \frac{1}{2} \int_{\Gamma_{+}} \phi_{+} \partial_{n} \phi_{+} - \int_{\Gamma} \phi \partial_{n} \phi \\ &= \mathrm{K}[\boldsymbol{\gamma}, \boldsymbol{\psi}] + \frac{1}{2} \left[ \int_{\Omega} \left| \boldsymbol{\nabla} \phi_{+} \right|^{2} - \int_{\Omega} \left| \boldsymbol{\nabla} \phi \right|^{2} + \int_{\Omega_{+} - \Omega} \left| \boldsymbol{\nabla} \phi_{+} \right|^{2} \right]. \end{split}$$

We denote by  $\mathbf{g}$  the intrinsic metric of  $\Gamma$  (and we won't need the metric on  $\Gamma_+$ ). We first compute the last integral appearing in the above relation, using the Taylor-Cauchy formula,

$$\begin{split} \int_{\Omega_{+}-\Omega} \left| \boldsymbol{\nabla} \phi_{+} \right|^{2} &= \int_{\mathbb{R}^{d}} \int_{0}^{h(\vec{s})} \left[ \left| \boldsymbol{\nabla} \phi_{+} \right|^{2} \left( \boldsymbol{\gamma}(\vec{s}) + \sigma \hat{\boldsymbol{n}}(\vec{s}) \right) \right] \sqrt{\det(\mathbf{g})(\vec{s})} \, \mathrm{d}\sigma \, \mathrm{d}\vec{s} \\ &= \int_{\mathbb{R}^{d}} \int_{0}^{h(\vec{s})} \left[ \left| \boldsymbol{\nabla} \phi_{+} \right|^{2} \left( \boldsymbol{\gamma}(\vec{s}) \right) + h_{+}(\vec{s}) \partial_{n} \left( \left| \boldsymbol{\nabla} \phi_{+} \right|^{2} \left( \boldsymbol{\gamma}(\vec{s}) + \tilde{h} \hat{\boldsymbol{n}}(\vec{s}) \right) \right) + O(h^{2}) \right] \sqrt{\det(\mathbf{g})(\vec{s})} \, \mathrm{d}\sigma \, \mathrm{d}\vec{s} \\ &= \int_{\mathbb{R}^{d}} \int_{0}^{h(\vec{s})} h_{+}(\vec{s}) \left| \boldsymbol{\nabla} \phi_{+} \right|^{2} \left( \boldsymbol{\gamma}(\vec{s}) \right) \sqrt{\det(\mathbf{g})(\vec{s})} \, \mathrm{d}\vec{s} + O(h^{2}) \\ &= \int_{\mathbb{R}^{d}} \int_{0}^{h(\vec{s})} h_{+}(\vec{s}) \left| \boldsymbol{\nabla} \phi \right|^{2} \left( \boldsymbol{\gamma}(\vec{s}) \right) \sqrt{\det(\mathbf{g})(\vec{s})} \, \mathrm{d}\vec{s} + O(h^{2}). \end{split}$$

The two other integrals provide a link with the Dirichlet-to-Neumann operator,

$$\begin{split} \int_{\Omega} \left( \left| \boldsymbol{\nabla} \phi_{+} \right|^{2} - \left| \boldsymbol{\nabla} \phi \right|^{2} \right) &= \int_{\Gamma} \phi_{+} \partial_{n} \phi_{+} - \phi \partial_{n} \phi \\ &= \int_{\Gamma} \left( \phi_{+} - h_{+} \partial_{n} \phi_{+} \right) \partial_{n} \left( \phi_{+} - h_{+} \partial_{n} \phi_{+} \right) - \phi \partial_{n} \phi \\ &= \int_{\Gamma} \left[ - h_{+} (\partial_{n} \phi_{+}) (\partial_{n} \phi) - \phi \partial_{n} \left( h_{+} \partial_{n} \phi_{+} \right) \right] + O(h^{2}) \end{split}$$

$$\begin{split} &= -2 \int_{\Gamma} h_+(\partial_n \phi_+)(\partial_n \phi) + O(h^2) & \qquad \qquad \left(\text{symmetry of DtN}[\gamma]\right) \\ &= -2 \int_{\mathbb{R}^d} h_+ \frac{\left(\text{DtN}[\gamma] \psi\right)^2}{\det(\mathbf{g})} \, \sqrt{\det(\mathbf{g})} + O(h^2). \end{split}$$

The same relation is obtained for the negative perturbation  $h_{-}$ . Combining the above equations we obtain finally

$$\begin{split} \mathrm{K}[\boldsymbol{\gamma} + h_{+} \hat{\boldsymbol{n}}, \boldsymbol{\psi}] - \mathrm{K}[\boldsymbol{\gamma}, \boldsymbol{\psi}] &= \int_{\mathbb{R}^{d}} \frac{1}{2} \left[ \mathbf{g} \left( \vec{\nabla} \boldsymbol{\psi}, \vec{\nabla} \boldsymbol{\psi} \right) - \frac{\left( \mathrm{DtN}[\boldsymbol{\gamma}] \boldsymbol{\psi} \right)^{2}}{\det(\mathbf{g})} \right] \, \boldsymbol{n} \cdot \left( h \hat{\boldsymbol{n}} \right) + O(h^{2}) \\ &= \int_{\mathbb{R}^{d}} \frac{\delta \mathrm{K}}{\delta \boldsymbol{\gamma}} \cdot \hat{\boldsymbol{n}} h + O(h^{2}). \end{split}$$

Remark 2.19. We do not compute the variation of K in the tangential direction since it will not contribute to the dynamics of the system. Indeed, the symplectic form  $\mathbf{J}(\gamma)$  that will be introduce below only sees the normal component of  $\delta_{\gamma}$ H.

In the end, we can put both the one-dimensional and the two-dimensional Breaking Waves equations (2.15,2.16) in the following "Hamiltonian" form,

$$\begin{cases} \partial_t \gamma &= \frac{n}{\det \mathbf{g}} & \frac{\delta \mathbf{H}}{\delta \psi} + \text{tangential terms} \\ \partial_t \psi &= -\frac{n}{\det \mathbf{g}} & \frac{\delta \mathbf{H}}{\delta \gamma} + \text{tangential terms} \end{cases}$$
(2.17)

The tangential terms correspond to the non-physical information concerning the position of the labels  $\gamma(t, \vec{s})$  on the interface  $\Gamma_i(t)$ . They do not contain information about the shape of  $\Gamma_i(t)$  and they disappear should we set the tangential velocity  $\vec{V} = 0$ .

We now extract the symplectic structure of the system (2.17). It is, in contrast with the Water Waves system (1.47), non-canonical. That is, the operator appearing in front of the variational derivatives of the Hamiltonian H is not the symplectic matrix J. Instead, we define the following operator

$$\mathbf{J}(\boldsymbol{\gamma}) = \begin{bmatrix} 0 & -\mathbf{g}_{d+1}(\boldsymbol{n}, \boldsymbol{\cdot}) \\ \boldsymbol{n} & 0 \end{bmatrix}.$$

We see readily that  $\mathbf{J}(\boldsymbol{\gamma})^2 = -\det(\mathbf{g})\mathbb{1}_{d+1}$ . Therefore, system (2.17) can also be written as

$$\partial_t \begin{bmatrix} \pmb{\gamma} \\ \psi \end{bmatrix} = \frac{\mathbf{J}(\pmb{\gamma})}{|\mathbf{J}(\pmb{\gamma})|^2} \begin{bmatrix} \delta_{\pmb{\gamma}} \mathbf{H} \\ \delta_{\psi} \mathbf{H} \end{bmatrix} + \text{ tangential terms} \qquad \text{or} \qquad -\mathbf{J}(\pmb{\gamma}) \partial_t \begin{bmatrix} \pmb{\gamma} \\ \psi \end{bmatrix} = \begin{bmatrix} \delta_{\pmb{\gamma}} \mathbf{H} \\ \delta_{\psi} \mathbf{H} \end{bmatrix} + \text{ tangential terms}$$

In particular, working with the  $\vec{V} = 0$  equations, we obtain the conservation of the energy  $H | \gamma(t), \psi(t) |$ .

**Remark 2.20.** The one-dimensional symplectic structure was obtained by Craig (2017) following the same type of argument. However he used a functional scalar product defined on the interface  $\Gamma_i(t)$ , which depends implicitly on the parametrisation  $\gamma$ . Therefore he obtained an non-normalised symplectic structure.

**Remark 2.21.** Olver (1980) extended the definition of a symplectic structure to consider operators **J** depending gently on the unknowns. The present formulation is encompassed into this generalisation.

Of course the computations carried out in this section are purely formal. A more rigorous approach would be to follow the method introduced in Lannes (2005, 2013b): working in a fixed flat domain  $\mathcal{S}$  instead of  $\Omega$ . The author has not yet tried to implement this method. We however mention the work of Bridges and Donaldson (2011), in which the authors carried out a lagrangian formulation of the Breaking Waves problem and obtained the associated Hamiltonian structure. However, their formulation is not phrased on the interface only as both their Lagrangian and Hamiltonian functionals are integrals taken on the full two-dimensional (with a 1d interface) flat strip  $\mathcal{S}$ . Their resulting system does not follow a canonical structure either.

### II.4. Non-dimensionalisation

To obtain a non-dimensional formulation of the Breaking Waves equations, one should be careful. Indeed, all parametrisations do not carry the same intrinsic physical dimension. For instance the arclength parametrisation is a length by construction but, working in a label space looking like a flat strip  $\mathcal{S} = \mathbb{R}^d \times [0,1]$ , the corresponding vertical parameter cannot be a length as it extends from 0 to 1, no matter what the physical height of the water column is.

Having in mind that  $\vec{s}$  does not always correspond to a length, we notice that all terms appearing in (2.12, 2.15 or 2.16) do not depend on the dimension of  $\vec{s}$ . Indeed each term involving  $\vec{\nabla}$  is counter-balanced by another. Therefore, in the following we shall assume that  $\vec{s}$  has no dimension to make the computations easier, without loss of generality.

We only provide the non-dimensionalisation of the one-dimensional Breaking Waves system (2.15) for the sake of simplicity. The chosen fiducial scales are defined in table 2.1. We use the same scaling laws as for the non-breaking case (table 1.2).

Scale	corresponding to	used to redefine
λ	Maximum distance between two crests (i.e. the maximum wavelength)	$x, \gamma_x, \gamma_{b,x}$
$h_0$	Average depth of the water column	$z, \gamma_{z,x}$
$\varepsilon h_0$	Typical size of a wave	$\gamma_z$
$\varepsilon \lambda \sqrt{gh_0}$	The velocity potential's typical order of magnitude	$\phi, \psi$
$\lambda/\sqrt{gh_0}$	Period of a linear wave in shallow water	t

**Table 2.1** – The chosen typical scales to non-dimensionalise the Breaking Waves equations (2.15). The parameters  $\mu$  and  $\varepsilon$  are, respectively, the shallowness and the steepness/non-linearity parameters (defined in (1.24)).

II.4.1. The normal and tangential vectors<sup>1</sup>. Since the horizontal and vertical components are rescaled in different manners, the non-dimensionalisation process will unfortunately break the evolution equation on  $\gamma$  into two parts. The normalisation factor  $|\partial_s \gamma|$  becomes

$$\left|\partial_s \boldsymbol{\gamma}\right|^2 = \left(\partial_s \gamma_x\right)^2 + \left(\partial_s \gamma_z\right)^2 = \lambda^2 \left[\left(1 + \partial_s \gamma_x^{\natural}\right)^2 + \varepsilon^2 \mu^2 \left(\partial_s \gamma_z^{\natural}\right)^2\right] = \lambda^2 \left|\partial_s \boldsymbol{\gamma}^{\natural}\right|^2,$$

where the interface parametrisation if written as

$$oldsymbol{\gamma}^{
atural} = egin{bmatrix} s + \gamma_x^{
atural} \ 1 + arepsilon \mu \gamma_z^{
atural} \end{bmatrix} = rac{1}{\lambda} oldsymbol{\gamma}.$$

The unit tangent and normal vectors are then written as

$$\hat{m{ au}} \equiv \hat{m{ au}}(m{\gamma}) = rac{1}{|\partial_s m{\gamma}|} egin{bmatrix} \lambda + \partial_s m{\gamma}_x \ \partial_s m{\gamma}_z \end{bmatrix} = rac{1}{|\partial_s m{\gamma}^{\sharp}|} egin{bmatrix} 1 + \partial_s m{\gamma}_x^{\sharp} \ arepsilon \mu \partial_s m{\gamma}_z^{\sharp} \end{bmatrix} = \hat{m{ au}}(m{\gamma}^{\sharp}) = m{ au}$$
 and  $\hat{m{n}} = m{n}^{\sharp}$ .

The unit normal vectors  $\hat{\tau}$  and  $\hat{n}$  do not carry an intrinsic physical dimension. Therefore they do not change under the process described above. However, to emphasise that they are now written in terms of  $\gamma^{\natural}$ , we denote them as  $\hat{\tau}^{\natural}$  and  $\hat{n}^{\natural}$ .

II.4.2. The Dirichlet-to-Neumann operator<sup> $\downarrow$ </sup>. The normalisation chosen for DtN[ $\gamma$ ] $\psi$  cancels the normalisation of  $\hat{n}$ . We therefore have

$$\begin{split} \mathrm{DtN}[\boldsymbol{\gamma}]\psi &= \left(\lambda + \partial_s \gamma_x\right) \partial_z \phi - (\partial_s \gamma_z) (\partial_s \phi) \\ &= \frac{\varepsilon \lambda \sqrt{gh_0}}{\mu} \begin{bmatrix} -\varepsilon \mu \partial_s \gamma_z^{\natural} \\ 1 + \partial_s \gamma_x^{\natural} \end{bmatrix} \cdot \begin{bmatrix} \mu \partial_{x^{\natural}} \phi^{\natural} \\ \partial_{z^{\natural}} \phi^{\natural} \end{bmatrix} \\ &= \frac{\varepsilon \lambda \sqrt{gh_0}}{\mu} \left| \partial_s \gamma^{\natural} \middle| \left( \hat{\boldsymbol{n}}(\boldsymbol{\gamma}^{\natural}) \cdot \boldsymbol{\nabla}_{\mu}^{\natural} \right) \phi^{\natural} = \frac{\varepsilon \lambda \sqrt{gh_0}}{\mu} \, \mathrm{DtN}^{\natural}[\boldsymbol{\gamma}^{\natural}] \psi^{\natural}, \end{split}$$

using the notations defined in sec. III.3 of chapter 1. In the rescaled domain  $\Omega^{\natural}(t^{\natural})$ ,  $\psi^{\natural}$  and  $\phi^{\natural}$  are related through the following elliptic problem,

$$\left\{egin{array}{lll} \Delta^{
abla}_{\mu}\phi^{
abla} &=& 0 & ext{in }\Omega^{
abla}(t^{
abla}) \ \phi^{
abla} &=& \psi^{
abla} & ext{on }\Gamma^{
abla}_i(t^{
abla}) \ \widehat{m{n}}^{
abla}_b\cdotm{
abla}^{
abla}_\mu\phi^{
abla} &=& 0 & ext{on }\Gamma^{
abla}_b, \end{array}
ight.$$

with  $\hat{n}_b^{\sharp} = \hat{n}(\gamma_b^{\sharp})$  the normal vector to the non-dimensional bottom parametrisation  $\gamma_b^{\sharp}$  obtained from the dimensional one, denoted by  $\gamma_b$ , using the scaling described in table 2.1.

II.4.3. The non-dimensional equations. Carrying out the process described in sec. III of chapter 1, we obtain the following set of non-dimensional equations

$$\begin{cases}
\partial_{t^{\natural}} \boldsymbol{\gamma}^{\natural} = \frac{\varepsilon}{\mu} \frac{\text{DtN}^{\natural} [\boldsymbol{\gamma}^{\natural}] \psi^{\natural}}{\left| \partial_{s} \boldsymbol{\gamma}^{\natural} \right|} \hat{\boldsymbol{n}} (\boldsymbol{\gamma}^{\natural}) + v^{\natural} \hat{\boldsymbol{\tau}} (\boldsymbol{\gamma}^{\natural})
\end{cases}$$
(2.18a)

$$\begin{cases}
\partial_{t^{\natural}} \boldsymbol{\gamma}^{\natural} = \frac{\varepsilon}{\mu} \frac{\operatorname{DtN}^{\natural}[\boldsymbol{\gamma}^{\natural}] \psi^{\natural}}{\left| \partial_{s} \boldsymbol{\gamma}^{\natural} \right|} \hat{\boldsymbol{n}}(\boldsymbol{\gamma}^{\natural}) + v^{\natural} \hat{\boldsymbol{\tau}}(\boldsymbol{\gamma}^{\natural}) \\
\partial_{t^{\natural}} \psi^{\natural} = -\gamma_{z}^{\natural} + \frac{1}{2} \frac{\varepsilon}{\mu^{2}} \left( \frac{\operatorname{DtN}^{\natural}[\boldsymbol{\gamma}^{\natural}] \psi^{\natural}}{\left| \partial_{s} \boldsymbol{\gamma}^{\natural} \right|} \right)^{2} + \frac{\partial_{s} \psi^{\natural}}{\left| \partial_{s} \boldsymbol{\gamma}^{\natural} \right|} \left[ v^{\natural} - \frac{1}{2} \frac{\partial_{s} \psi^{\natural}}{\left| \partial_{s} \boldsymbol{\gamma}^{\natural} \right|} \right].
\end{cases} (2.18a)$$

Splitting the first two equation into vertical and horizontal parts yields a relation in which every  $\varepsilon$  and every  $\mu$  appear,

$$\partial_{t^{\natural}} \gamma_x^{\natural} = \frac{\varepsilon}{\mu} \frac{\text{DtN}^{\natural} [\gamma^{\natural}] \psi^{\natural}}{\left| \partial_s \gamma^{\natural} \right|} \hat{n}_x^{\natural} + v^{\natural} \hat{\tau}_x^{\natural} = -\varepsilon^2 \frac{\text{DtN}^{\natural} [\gamma^{\natural}] \psi^{\natural}}{\left| \partial_s \gamma^{\natural} \right|^2} \partial_s \gamma_z^{\natural} + \frac{v^{\natural} (1 + \partial_s \gamma_x^{\natural})}{\left| \partial_s \gamma^{\natural} \right|}$$
(2.19a)

$$\partial_{t^{\natural}} \gamma_z^{\natural} = \frac{1}{\mu^2} \frac{\operatorname{DtN}^{\natural} [\gamma^{\natural}] \psi^{\natural}}{\left| \partial_s \gamma^{\natural} \right|} \hat{n}_z^{\natural} + \frac{v^{\natural}}{\varepsilon \mu} \hat{\tau}_z^{\natural} = \frac{1}{\mu^2} \frac{\operatorname{DtN}^{\natural} [\gamma^{\natural}] \psi^{\natural}}{\left| \partial_s \gamma^{\natural} \right|^2} (1 + \partial_s \gamma_x^{\natural}) - \frac{v^{\natural} \partial_s \gamma_z^{\natural}}{\left| \partial_s \gamma^{\natural} \right|}. \tag{2.19b}$$

Future works on this set of equations shall decide which notation should prevail. The former is easier to write down but some dependencies on  $\varepsilon$  or  $\mu$  are hidden in the notations. This issue does not arise in the latter.

We mention that carrying out asymptotic regimes of the above set of equations is not straightforward. Indeed, one should first define an average velocity to do so. When no breaking happens, this can be done over a vertical line starting from the topography and ending on the free surface (Lannes 2013b). In the case of an overhanging wave, the questions seems far from trivial...

In the remaining section, we will work in the non-dimensional framework, but we will set  $\varepsilon = \mu = 1$  to simplify the presentation. We will also drop out the \u00e4 superscript.

### What is a breaking wave?

In this ultimate section, we would like to discuss wave breaking. Indeed, depending on the author, the words breaking waves can mean different things. We would like to propose a mathematical definition of wave breaking (somewhat in the spirit of the experimental classification of Wiegel (1964) and later extended by Galvin (1968)). With this definition, we will show (when d=1) that the Breaking Waves equations can in fact be reduced to the Water Waves equations as long as no breaking happens.

### III.1. Definition

Let us remind the reader some of the hypotheses that we make regarding the water domain  $\Omega(t)$  at time  $t \ge 0$ . We assume that the water (modelled as a continuous (H1) fluid) does not mix with the air (H3) and that no dry region exists (H5). The following discussion applies to viscous or inviscid fluids, with or without surface tension. We recall the expansion of the parametrisation  $\gamma$  of the interface as a horizontal and a vertical part as

$$\boldsymbol{\gamma}(t,\vec{s}) = \begin{bmatrix} \vec{s} + \vec{\gamma}(t,\vec{s}) \\ 1 + \gamma_z(t,\vec{s}) \end{bmatrix}$$

When d=1, we have  $\vec{\gamma}=\gamma_x$ . We then propose the following definition,

**Definition 2.22** (Breaking). At time t > 0 the wave represented by the interface  $\Gamma_i(t)$  has broken if the differential of  $\vec{s} \mapsto \vec{s} + \vec{\gamma}(t, \vec{s})$ , seen as a function  $\mathbb{R}^d \to \mathbb{R}^d$ , fails to be invertible for some  $\vec{s}$ .

For continuously differentiable surface parametrisations  $\gamma(t, \cdot)$ , by the inverse function theorem this amounts to say that  $\vec{\gamma}(t, \cdot)$  fails to be injective. Another way to see it is that there exists a point  $\vec{s}$  such that the tangent plane  $\Gamma_i(t)$  (represented as a plane in  $\mathbb{R}^{d+1}$  defined by the normal  $\hat{\boldsymbol{n}}(t, \vec{s})$ ) is vertical, *i.e.* the normal vector  $\hat{\boldsymbol{n}}(t, \vec{s})$  is horizontal.

Should we compare our definition with the classification of Wiegel (1964) (or Galvin 1968), this corresponds to a *plunging breaker*. The other types of breaking waves present in this classification (spilling, collapsing or surging breakers) are characterised by foam, bubbles, droplets or turbulence. These phenomena cannot be described by the present model. For instance, a droplet would correspond to a disconnected component of  $\Omega(t)$ ; thus yielding a non-continuous label function  $X(t, \cdot)$ .

Remark 2.23. Coming back to equation (2.18) with explicit  $\varepsilon$  and  $\mu$ , setting aside the arbitrary tangential velocity  $v^{\natural}$  for a moment, we see from (2.19a) that wave breaking is a  $O(\varepsilon^2)$  nonlinear phenomenon. Indeed, if the initial parametrisation is graph-like, i.e.  $\gamma_x^{\natural}(0,s) = 0$ , then the breaking occurs should  $\partial_s \gamma_x^{\natural}(t,s) \leqslant 1$  somewhere, which should happen for  $\varepsilon$  bigger than some threshold.

### III.2. Reduction to the Water Waves equations

With the definition 2.22 of wave breaking, we have the following result for a one-dimensional free surface,

**Proposition 2.24.** Let d=1 and  $(\gamma, \psi)$  smooth solutions of the breaking waves equations (2.18) (with  $\varepsilon = \mu = 1$ ), that do not break (in the sense of definition 2.22) on the time interval  $[0, T_b)$ . Introduce the following functions,

$$X_t(s) = s + \gamma_x(t,s) \qquad , \qquad \eta(t,x) = \gamma_z \Big(t, X_t^{-1}(x)\Big) \qquad and \qquad \varphi(t,x) = \psi\Big(t, X_t^{-1}(x)\Big).$$

They are well defined for all  $t \in [0, T_b)$  and the couple  $(\eta, \varphi)$  is a smooth solution of the Water Waves equations (1.43).

The above proposition should hold for less regular solutions of the Breaking Waves equations (2.18). However, as long as the existence of solutions of this system has not been investigated, we prefer to state the above result without discussing the regularity of, hopefully existing, solutions.

*Proof.* The idea of the following argument is to use  $\gamma_x$  as a space variables. Owing to the inverse function theorem, this can only be done if  $\partial_s \gamma_x > -1$  everywhere, *i.e.* if no breaking occurs.

At fixed time  $t < T_b$ , let  $X_t(s) = s + \gamma_x(t,s)$ . The map  $s \mapsto X_t(s)$  allows a correspondence between the parameter s and the physical variable x. The inverse function theorem states that it is invertible at fixed time  $t < T_b$ , by the definition 2.22 of wave breaking. We thus define  $X_t^{-1}$  the inverse of  $X_t$ , making the correspondence between x and s. It has the following properties (at fixed time t),

$$\left[X_t\circ X_t^{-1}\right](x)=x \qquad \qquad \left[X_t^{-1}\circ X_t\right](s)=s \qquad \qquad (2.20a)$$

$$\partial_x X_t^{-1}(x) = \left[ \left( \partial_s X_t \right) \circ X_t^{-1}(x) \right]^{-1} = \left[ 1 + \partial_s \gamma_x \left( t, X_t^{-1}(x) \right) \right]^{-1}. \tag{2.20b}$$

With this  $s \leftrightarrow x$  correspondence at hand, we can define the usual variables of the water waves system,

$$\eta(t,x) = \gamma_2\Big(t,X_t^{-1}(x)\Big) \qquad \text{and} \qquad \varphi(t,x) = \psi\Big(t,X_t^{-1}(x)\Big). \tag{2.21}$$

Finding the equations for the time evolution of  $\eta$  and  $\varphi$  now carried out.

Two useful identities. Derivatives of  $\eta$  and  $\varphi$  with respect to x can be related to  $\gamma_z$  and  $\psi$  in the following manner,

$$\begin{split} \partial_x \eta(t,x) &= \partial_x \Big( \gamma_z \Big( t, X_t^{-1} \Big) \Big) = \Big[ \partial_s \gamma_z \Big] \Big( t, X_t^{-1} \Big) \cdot \partial_x X_t^{-1} = \frac{\partial_s \gamma_z}{1 + \partial_s \gamma_x} \Big( t, X_t^{-1} \Big) \\ \partial_x \varphi(t,x) &= \partial_x \Big( \psi \Big( t, X_t^{-1} \Big) \Big) = \frac{\partial_s \psi}{1 + \partial_s \gamma_x} \Big( t, X_t^{-1} \Big) \end{split} \tag{2.22}$$

where we made use of (2.20) multiple times.

The normal and tangent vectors. It is now easy to compute the tangent and normal vectors as functions of  $\eta$  and x. By an abuse of notations, we define

$$\hat{\boldsymbol{\tau}}(t,x) = \hat{\boldsymbol{\tau}}\Big(t,X_t^{-1}(x)\Big) = \frac{\partial_s \boldsymbol{\gamma}}{\left|\partial_s \boldsymbol{\gamma}\right|}\Big(t,X_t^{-1}\Big) \qquad \text{and} \qquad \hat{\boldsymbol{n}}(t,x) = \hat{\boldsymbol{\tau}}(t,x)^{\perp}$$

so that, using the same argument as in (2.22), we see that

$$\partial_x \gamma \left(t, X_t^{-1}\right) = \frac{\partial_s \gamma}{1 + \partial_s \gamma_x} \left(t, X_t^{-1}\right) = \partial_x \begin{bmatrix} x \\ \eta(t, x) \end{bmatrix} = \begin{bmatrix} 1 \\ \partial_x \eta(t, x) \end{bmatrix},$$

so that, assuming that  $\partial_s \gamma_x > -1$  (by assumption on the non-vanishing behaviour of  $\partial_s \gamma_x$  for all  $s \in \mathbb{R}$ , if it is initially positive, it will remain so at all subsequent times until the breaking occurs),

$$\hat{\pmb{\tau}}(t,x) = \frac{1}{\sqrt{1+(\partial_x\eta)^2}} \begin{bmatrix} 1 \\ \partial_x\eta \end{bmatrix} \quad \text{ and } \quad \hat{\pmb{n}}(t,x) = \frac{1}{\sqrt{1+(\partial_x\eta)^2}} \begin{bmatrix} -\partial_x\eta \\ 1 \end{bmatrix}.$$

Adaptation of the above formula for right-to-left parametrisations of  $\Gamma_i(t)$  is straightforward.

The equation for  $\gamma_x$ . Before computing  $\partial_t \eta$  and  $\partial_t \varphi$ , it is interesting to see what the equation for  $\gamma_x$  becomes (as it should not appear in the final system). Since  $\gamma_x(t, X_t^{-1}) = x$ , we have

$$\begin{split} 0 &= \partial_t \Big( \gamma_x \Big( t, X_t^{-1} \Big) \Big) \\ &= \partial_t \gamma_x \Big( t, X_t^{-1} \Big) + \Big[ 1 + \partial_s \gamma_x \Big] \Big( t, X_t^{-1} \Big) \cdot \partial_t X_t^{-1} (x). \end{split}$$

Hence, making use of the equation for the evolution of  $\gamma_x$  (2.19a) we get

$$\partial_t X_t^{-1} = -\frac{1}{1 + \partial_s \gamma_x \left( t, X_t^{-1} \right)} \left[ \frac{\text{DtN}[\boldsymbol{\gamma}] \psi}{|\partial_s \boldsymbol{\gamma}|} \, \hat{n}_x + v \, \hat{\tau}_x \right] \left( t, X_t^{-1} \right), \tag{2.23}$$

a very useful relation for the rest of this proof.

The equation for  $\gamma_z$ . We now have all the tools to compute the time evolution of  $\eta$  and  $\varphi$  from the Breaking Waves system (2.18). We begin by transforming the equation on  $\gamma_z$  on an equation for the evolution of  $\eta$ ,

$$\begin{split} \partial_t \eta(t, \boldsymbol{\cdot}) = & \partial_t \left[ \gamma_z \Big( t, X_t^{-1} \Big) \right] \\ = & \partial_t \gamma_z \Big( t, X_t^{-1} \Big) + \partial_s \gamma_z \Big( t, X_t^{-1} \Big) \, \partial_t X_t^{-1} \\ = & \left( \frac{\operatorname{DtN}[\gamma] \psi}{|\partial_s \gamma|} \, \hat{n}_z \right) \Big( t, X_t^{-1} \Big) + \Big( v \hat{\tau}_z \Big) \Big( t, X_t^{-1} \Big) \\ & - \frac{\partial_s \gamma_z \Big( t, X_t^{-1} \Big)}{1 + \partial_s \gamma_x \Big( t, X_t^{-1} \Big)} \left[ \frac{\operatorname{DtN}[\gamma] \psi}{|\partial_s \gamma|} \, \hat{n}_x + v \, \hat{\tau}_x \right] \Big( t, X_t^{-1} \Big) \\ = & \frac{\operatorname{DtN}[\gamma] \psi}{|\partial_s \gamma|} \Big( t, X_t^{-1} \Big) \left[ \hat{n}_z - \frac{\partial_s \gamma_z \Big( t, X_t^{-1} \Big)}{1 + \partial_s \gamma_x \Big( t, X_t^{-1} \Big)} \, \hat{n}_x \right] \end{split}$$

$$\begin{split} &= \left[ \hat{\boldsymbol{n}} \cdot \boldsymbol{\nabla} \phi \Big( t, \boldsymbol{\gamma} \Big( t, \boldsymbol{X}_t^{-1} \Big) \right) \right] \frac{1 + (\partial_x \eta)^2}{\sqrt{1 + (\partial_x \eta)^2}} \\ &= & \sqrt{1 + (\partial_x \eta)^2} \, \hat{\boldsymbol{n}} \cdot \boldsymbol{\nabla} \phi \Big( t, \boldsymbol{\gamma} \Big( t, \boldsymbol{X}_t^{-1} \Big) \Big) = \mathrm{DtN}[\eta] \varphi \end{split}$$

where  $DtN[\eta]$  is the usual Dirichlet-Neumann operator, used in (1.43). We recover the advection equation on  $\eta$  that appears in (1.43). The most striking aspect of the above computation lies in the remarkable cancelling of the two terms involving the arbitrary tangential velocity v.

The equation for  $\psi$ . We now find the evolution of  $\varphi$  following the same procedure,

$$\begin{split} \partial_t \varphi(t, \boldsymbol{\cdot}) &= \partial_t \psi \Big( t, X_t^{-1} \Big) + \partial_s \psi \Big( t, X_t^{-1} \Big) \cdot \partial_t X_t^{-1} \\ &= -\eta + \frac{1}{2} \left[ \frac{\operatorname{DtN}[\gamma] \psi}{|\partial_s \gamma|} \right]^2 + \frac{\partial_s \psi}{|\partial_s \gamma|} \left[ v - \frac{\partial_s \psi}{|\partial_s \gamma|} \right] \\ &- \frac{\partial_s \psi}{1 + \partial_s \gamma_x} \Big( t, X_t^{-1} \Big) \left[ \frac{\operatorname{DtN}[\gamma] \psi}{|\partial_s \gamma|} \, \hat{n}_x + v \, \hat{\tau}_x \right] \Big( t, X_t^{-1} \Big) \\ &= -\eta + \frac{1}{2} \left[ \frac{\operatorname{DtN}[\eta] \varphi}{\sqrt{1 + (\partial_x \eta)^2}} \right]^2 + \frac{\partial_x \varphi}{\sqrt{1 + (\partial_x \eta)^2}} \left[ v - \frac{1}{2} \frac{\partial_x \varphi}{\sqrt{1 + (\partial_x \eta)^2}} \right] \\ &- \partial_x \varphi \left[ \frac{v}{\sqrt{1 + (\partial_x \eta)^2}} - \frac{\partial_x \eta \operatorname{DtN}[\eta] \varphi}{1 + (\partial_x \eta)^2} \right] \\ &= -\eta - \frac{1}{2} \Big( \partial_x \varphi \Big)^2 + \frac{1}{2} \left[ \left( \frac{\operatorname{DtN}[\eta] \varphi}{\sqrt{1 + (\partial_x \eta)^2}} \right)^2 + \left( \frac{\partial_x \varphi \, \partial_x \eta}{\sqrt{1 + (\partial_x \eta)^2}} \right)^2 + \frac{\partial_x \eta \, \partial_x \varphi \operatorname{DtN}[\eta] \varphi}{1 + (\partial_x \eta)^2} \right] \\ &= -\eta - \frac{1}{2} \Big( \partial_x \varphi \Big)^2 + \frac{1}{2} \frac{\Big( \operatorname{DtN}[\eta] \varphi + \partial_x \eta \, \partial_x \varphi \Big)^2}{1 + (\partial_x \eta)^2}, \end{split}$$

exactly the second equation in (1.43). Once again, the two terms involving v cancelled each other.

Of course, with the definition 2.22 of a breaking wave, the condition " $\partial_s \gamma_x > -1$  everywhere" may fail to hold because of a ill-chosen arbitrary velocity v. This should not happen with the three possible choices discussed in sec. II.1.2.

## $\prod$

# On the Vanishing Viscosity Limit in Water Wayes

In the previous part we have presented different models describing (possibly breaking) water waves. Most of the simplifications arise while neglecting the viscosity (H6) together with the irrotationality assumption (H11).

In the present part of our work, these two assumptions are discussed in details using numerical methods that are introduced in chapter 3. Chapter 4 is concerned with breaking waves over a flat topography. In this case both (H6) and (H11) are shown to hold. On the other hand, when considering finite-amplitude water waves over obstacles, the latter assumption does not remain true because of the former. This is the subject of chapter 5. This turns out to compromise greatly the vanishing viscosity limit.

## Chapter 3

### Numerical methods for the free-surface Navier-Stokes system

"the human requires a background grid through which to see his universe"

Frank Herbert, Dune (1965)

We are interested in investigating the effects of viscosity on water waves. This question is far from settled as, phrased like so, it is quite formidable. Therefore we need to limit the scope over which we shall provide a first answer to this problem. That is, we will only consider initially irrotational solutions to the free–surface, incompressible, Navier-Stokes system (1.54) with the Lagrangian advection scheme introduced in chapter 2.

In all cases, the set of equations (1.54) must be investigated in some way. We propose to do so numerically. The description of the computational strategy was unfortunately left out of Riquier and Dormy (2024a,b) to keep these publications short enough. This chapter is an opportunity to present our numerical methods thoroughly.

To the author's knowledge, the first Navier-Stokes simulation of breaking waves is that of Chen et al. (1999). Since that time, available computational power has greatly increased, allowing finer simulations, three-dimensional numerical domains and more accurate interface tracking procedures. However, in all the numerical studies that the author was able to find, the considered flow is two-phased, incorporates surface tension and the interface is followed through an Eulerian advection scheme. On the other hand, since the pioneering numerical work of Longuet-Higgins and Cokelet (1976, 1978) and that of Baker, Meiron, et al. (1982), the inviscid studies seem to favour the Lagrangian advection scheme and mostly overlook the air entrainment (maybe in light of the theoretical results of Fefferman et al. (2016) and Coutand and Shkoller (2019)).

Our method aims at taking the best of both worlds in order to bridge the gap between viscous and inviscid studies. Indeed we use a Lagrangian interface advection scheme and neglect the air. In the meantime the flow is not assumed irrotational and the turbulence is not encompassed through the use of a turbulent viscosity. Surface tension won't be included in the simulation so that only the consequences of hypothesis (**H6**) are investigated.

### I. The Finite Element Method

At the very heart of any numerical scheme stands the idea of casting a set of Partial Differential Equations (PDEs) into an algebraic system, solvable by a computer. Contrary to the Finite Difference Method The author acknowledges the thorough discussions with G. Sadaka on the use of FreeFEM.

 $^{1}$ Galerkin (1915)

<sup>2</sup>The FEM is e.g. described in depth in the classical books of Ern and Guermond (2021a,b,c). We also mention the fluid–oriented books of Pironneau (1989) and John (2016). Here we shall only give an introduction to FEM for the sake of completeness and to explain some important optimisations.

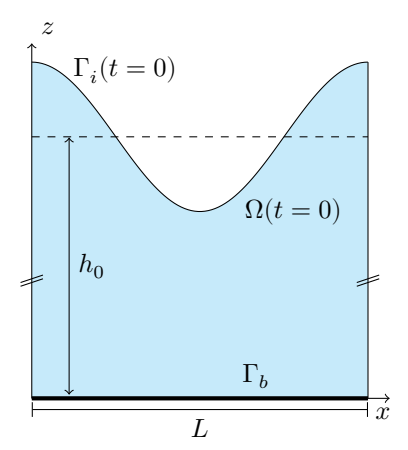


Figure 3.1 – Schematic representation of the initial domain in 2d (d=1). The initial condition will be described in sec. I.1.

<sup>3</sup>e.g. Chen et al. (1999), Deike, Popinet, et al. (2015), Di Giorgio et al. (2022), Iafrati (2009), Lubin and Glockner (2015), and Mostert et al. (2022). (FDM) and the Finite Volume Method (FVM) which use the *strong* formulation of the PDE and approximate the differential operators, the Finite Element Method (FEM) provides a procedure to discretise the weak formulation of a linear elliptic problem by approximating the functions themselves, using a well-behaved finite set of basic functions. In a way, this method falls into the more general category of Galerkin's methods.<sup>1,2</sup>

### I.1. The weak formulation of (1.54)

We briefly recall the problem at hand, motivated in chapter 1. At a time  $t\geqslant 0$ , we consider a time-varying domain  $\Omega(t)\subset \mathbb{R}^{d+1}$  encapsulated between a rigid bottom topography  $\Gamma_b$  and a moving water-void interface  $\Gamma_i(t)$  (fig. 3.1). The domain is assumed periodic in the x direction.

The corresponding non-dimensional problem is reminded for completeness and self-containdness of the present chapter,

$$\begin{cases}
\partial_{t}\boldsymbol{u} + \boldsymbol{u} \cdot \boldsymbol{\nabla} \boldsymbol{u} - \frac{1}{\operatorname{Re}} \Delta \boldsymbol{u} + \boldsymbol{\nabla} p &= -\hat{\boldsymbol{z}} & \text{in } \Omega(t) \\
\boldsymbol{\nabla} \cdot \boldsymbol{u} &= 0 & \text{in } \Omega(t) \\
p\hat{\boldsymbol{n}} - \frac{2}{\operatorname{Re}} \mathbf{S}(\boldsymbol{u}) \cdot \hat{\boldsymbol{n}} &= 0 & \text{on } \Gamma_{i}(t) \\
\boldsymbol{u} \cdot \hat{\boldsymbol{n}}_{b} &= 0 & \text{on } \Gamma_{b} \\
\hat{\boldsymbol{n}}_{b} \times \mathbf{S}(\boldsymbol{u}) \cdot \hat{\boldsymbol{n}}_{b} &= 0 & \text{on } \Gamma_{b}.
\end{cases}$$
(1.54, rem.)

**Remark 3.1.** The Reynolds number Re is defined in (1.29) using  $h_0$  as the characteristic length of the system. This is well-motivated in the shallow water regime as it appears naturally. Yet, most viscous studies<sup>3</sup> prefer the deep water scaling with characteristic length  $\lambda$ , the (longest) wave-length, and characteristic velocity  $\sqrt{g\lambda}$ . Their Reynolds number is denoted by

$$\operatorname{Re}_{\mathrm{dw}} = \frac{\sqrt{g\lambda^3}}{\nu_{\mathrm{w}}} = \frac{1}{\mu^{\frac{3}{2}}} \operatorname{Re}$$

There are several alternative choices of non-dimensionalisation. In our case, we have  $\mu^{-\frac{3}{2}}\approx 15.75$ .

Remark 3.2. We will also consider the system (1.54) with the Navier bottom condition replaced by the no-slip/Dirichlet condition. The corresponding system (1.9,1.2,1.17,1.15) will be referred to as (1.54D) in the following.

As already stated, the FEM makes use of the weak formulation of (1.54). In order to compute it, we introduce the following vector-valued functions spaces<sup>4</sup>

$$\begin{split} & \boldsymbol{H}_{\Gamma_b}^1\Big(\Omega(t)\Big) = \Big\{\boldsymbol{v} \in \Big(H^1\Big(\Omega(t)\Big)\Big)^{d+1} \text{ s.t. } \boldsymbol{v} \cdot \hat{\boldsymbol{n}}_b = 0 \text{ on } \Gamma_b\Big\} \\ & \boldsymbol{H}_{\Gamma_b,0}^1\Big(\Omega(t)\Big) = \Big\{\boldsymbol{v} \in \Big(H^1\Big(\Omega(t)\Big)\Big)^{d+1} \text{ s.t. } \boldsymbol{v} = 0 \text{ on } \Gamma_b\Big\} \end{split}$$

The former shall be used for (1.54) while the latter enforces the no-slip condition associated to (1.54D). The conditions " $\boldsymbol{v} \cdot \hat{\boldsymbol{n}}_b = 0$  on  $\Gamma_b$ " and " $\boldsymbol{v} = 0$  on  $\Gamma_b$ " must be understood in the sense of Sobolev traces.

<sup>&</sup>lt;sup>4</sup>We remind the reader that the definitions of the standard function spaces can be found in appendix B.

Let  $\mathbf{v} \in C^{\infty}(\Omega(t))^{d+1} \cap \mathbf{H}^1_{\Gamma_b}(\Omega(t))$  and  $q \in C^{\infty}(\Omega(t))$  some test functions. We take the inner product between  $\mathbf{v}$  and the first equation of (1.54) before interating on all of  $\Omega(t)$ . Then, multiple applications of Green's identity yield

$$\int_{\Omega(t)} \left[ \boldsymbol{v} \cdot \frac{\partial \boldsymbol{u}}{\partial t} + \boldsymbol{v} \cdot \left( \boldsymbol{u} \cdot \boldsymbol{\nabla} \right) \boldsymbol{u} + \frac{1}{\operatorname{Re}} \boldsymbol{\nabla} \boldsymbol{v} : \boldsymbol{\nabla} \boldsymbol{u} - p \boldsymbol{\nabla} \cdot \boldsymbol{v} - \boldsymbol{v} \cdot \boldsymbol{g} \right] \, \mathrm{d}\boldsymbol{x} = \int_{\Gamma_b \cup \Gamma_i(t)} \left[ -p \boldsymbol{v} + \frac{1}{\operatorname{Re}} \boldsymbol{v} \cdot \boldsymbol{\nabla} \boldsymbol{u} \right] \cdot \hat{\boldsymbol{n}} \, \mathrm{d}\boldsymbol{S}.$$

Most authors, like Guermond et al. (2012), start from the  $\nabla \cdot \sigma(p, \boldsymbol{u})$  ( $\sigma(p, \boldsymbol{u})$  being the stress tensor defined in (1.8)) term in (1.54) (instead of the Laplacian  $\Delta \boldsymbol{u}$ ), making the computations somewhat simpler. We choose to work out the variational form in this manner since it is quite enlightening. Thus, applying the stress-free boundary condition (1.17), the integral on  $\Gamma_i(t)$  becomes

$$\int_{\Gamma_i(t)} \left[ -p \boldsymbol{v} + \frac{1}{\mathrm{Re}} \boldsymbol{v} \cdot \boldsymbol{\nabla} \boldsymbol{u} \right] \cdot \hat{\boldsymbol{n}} \, \mathrm{d}S = -\frac{1}{\mathrm{Re}} \int_{\Gamma_{i,t}} \boldsymbol{v} \cdot \left( \boldsymbol{\nabla} \boldsymbol{u} \right)^\top \cdot \hat{\boldsymbol{n}} \, \mathrm{d}S.$$

To obtain a similar integral contribution of the bottom boundary  $\Gamma_b$ , we must expand  $\nabla u \cdot \hat{n}$  as a normal and tangential component and use the no-penetration condition  $v \cdot \hat{n} = 0$ . This is done in 2d in Riquier and Dormy (2024b) but the same procedure applies in any dimension (Guermond et al. 2012). Indeed,

$$\begin{split} \int_{\Gamma_b} \left[ -p \boldsymbol{v} + \frac{1}{\mathrm{Re}} \boldsymbol{v} \cdot \boldsymbol{\nabla} \boldsymbol{u} \right] &\cdot \hat{\boldsymbol{n}} \, \mathrm{d}S = \frac{1}{\mathrm{Re}} \int_{\Gamma_b} \hat{\boldsymbol{n}} \times \left( \hat{\boldsymbol{n}} \times \boldsymbol{v} \right) \cdot \left[ \hat{\boldsymbol{n}} \times \left( \boldsymbol{\nabla} \boldsymbol{u} \cdot \hat{\boldsymbol{n}} \right) \right] & \text{using } \boldsymbol{v} = \left( \boldsymbol{v} \cdot \hat{\boldsymbol{n}} \right) \hat{\boldsymbol{n}} - \hat{\boldsymbol{n}} \times \left( \hat{\boldsymbol{n}} \times \boldsymbol{v} \right) \\ &= -\frac{1}{\mathrm{Re}} \int_{\Gamma_b} \hat{\boldsymbol{n}} \times \left( \hat{\boldsymbol{n}} \times \boldsymbol{v} \right) \cdot \left[ \hat{\boldsymbol{n}} \times \left( (\boldsymbol{\nabla} \boldsymbol{u})^\top \cdot \hat{\boldsymbol{n}} \right) \right] \mathrm{d}S & \text{using the Navier condition } (\boldsymbol{1.14}) \\ &= -\frac{1}{\mathrm{Re}} \int_{\Gamma_b} \boldsymbol{v} \cdot \left( \boldsymbol{\nabla} \boldsymbol{u} \right)^\top \cdot \hat{\boldsymbol{n}} \, \mathrm{d}S & \text{since, once again, } \boldsymbol{v} \cdot \hat{\boldsymbol{n}} = 0. \end{split}$$

Notice that, in chapter 1, the chosen direction of the normal to the bottom  $\Gamma_b$  is  $\hat{\boldsymbol{n}}_b = -\hat{\boldsymbol{n}}$ . Hence the two boundaries contribute in the same manner. The boundary integral can then be transformed into a volume integral, using periodic boundary conditions and invoking the divergence theorem,

$$\frac{1}{\operatorname{Re}} \int_{\Gamma_0 \cup \Gamma_{i,t}} \boldsymbol{v} \cdot \left( \boldsymbol{\nabla} \boldsymbol{u} \right)^{\top} \cdot \hat{\boldsymbol{n}} \, \mathrm{d}S = \frac{1}{\operatorname{Re}} \int_{\partial \Omega(t)} \boldsymbol{v} \cdot \left( \boldsymbol{\nabla} \boldsymbol{u} \right)^{\top} \cdot \hat{\boldsymbol{n}} \, \mathrm{d}S \\
= \frac{1}{\operatorname{Re}} \int_{\Omega(t)} \left[ \boldsymbol{\nabla} \boldsymbol{v} : \left( \boldsymbol{\nabla} \boldsymbol{u} \right)^{\top} \right] \mathrm{d}\boldsymbol{x}.$$

The weak incompressibility condition is obtained readily multiplying (1.2) by q and integrating over  $\Omega(t)$ ,

$$\int_{\Omega(t)} q \, \boldsymbol{\nabla} \cdot \boldsymbol{v} \, \mathrm{d} \boldsymbol{x} = 0.$$

The weak formulation of (1.54) follows by considering  $\boldsymbol{v} \in \boldsymbol{H}_{\Gamma_b}^1 \left( \Omega(t) \right)$  and  $q \in L^2(\Omega(t))$  only and adding the integrals that have been computed above. This yields the time-dependent weak problem of finding  $\boldsymbol{u} \in C^1 \left( [0,T]; \boldsymbol{H}_{\Gamma_b}^1 \left( \Omega(t) \right) \right)$  and  $p \in L^{\infty} \left( [0,T]; L^2(\Omega(t)) \right)$  such that

$$\begin{split} \int_{\Omega(t)} \left[ \boldsymbol{v} \cdot \frac{\partial \boldsymbol{u}}{\partial t} \, + \boldsymbol{v} \cdot \left( \boldsymbol{u} \cdot \boldsymbol{\nabla} \right) \boldsymbol{u} + \frac{2}{\mathrm{Re}} \, \mathbf{S}(\boldsymbol{v}) : \mathbf{S}(\boldsymbol{u}) \\ - p \boldsymbol{\nabla} \cdot \boldsymbol{v} - q \boldsymbol{\nabla} \cdot \boldsymbol{u} - \boldsymbol{v} \cdot \boldsymbol{g} \right] \, \mathrm{d}\boldsymbol{x} &= 0, \end{split} \tag{3.1}$$

 $\label{eq:continuous} \textit{for all } \boldsymbol{v} \in \boldsymbol{H}^1_{\Gamma_b} \Big( \Omega(t) \Big) \textit{ and } q \in L^2(\Omega(t)) \textit{ and at all time } t \in [0,T].$ 

**Remark 3.3.** In most theoretical studies, the incompressibility condition (1.2) is incorporated in the definition of the velocity function

<sup>1</sup>Therefore lifting the constrain on the regularity of both functions.

<sup>2</sup>Here is used the fact that

$$egin{aligned} oldsymbol{
abla} oldsymbol{v} : \left[ oldsymbol{
abla} oldsymbol{u} + \left( oldsymbol{
abla} oldsymbol{u} 
ight)^{ op} 
ight] = \ &= 2 \, oldsymbol{
abla} oldsymbol{v} : oldsymbol{S}(oldsymbol{u}) : oldsymbol{S}(oldsymbol{u}), \end{aligned}$$

because  $\mathbf{S}(\boldsymbol{u})$  is symmetric by definition.

<sup>1</sup>It is shown in the classical book of Temam (1984) that this does not deteriorate the structure of the function space: it remains a Hilbert space for a certain associated inner product.

 $^2$ Recall that Bo stands for Bond's number, defined as

$$Bo = \frac{\rho_{wgh_0^2}}{\gamma_w},$$

in our  $\mu = 1$  case.

<sup>3</sup>That is,

$$\kappa = \kappa_1 + \kappa_2$$
.

Extension to any arbitrary space dimension is straightforward.

<sup>4</sup>numerically costly.

<sup>5</sup>A comparison between the two shall be given in sec. IV

<sup>6</sup>Euler (1768)

space  $H^1_{\Gamma_b}(\Omega(t))$ .<sup>1</sup> This has the advantage of completely eliminating the pressure from consideration. However such manipulation remains, to this day, purely theoretical as no conformal finite element space with the incompressibility constraint inherently incorporated into it was found (John 2016, sec. 3.2).

Should we consider surface tension, the same type of computations quickly leads to the modified integral formulation  $^2$ 

$$\int_{\Omega(t)} \left[ \boldsymbol{v} \cdot \frac{\partial \boldsymbol{u}}{\partial t} + \boldsymbol{v} \cdot \left( \boldsymbol{u} \cdot \boldsymbol{\nabla} \right) \boldsymbol{u} + \frac{2}{\text{Re}} \, \mathbf{S}(\boldsymbol{v}) : \mathbf{S}(\boldsymbol{u}) - p \boldsymbol{\nabla} \cdot \boldsymbol{v} \right.$$

$$- q \boldsymbol{\nabla} \cdot \boldsymbol{u} - \boldsymbol{v} \cdot \boldsymbol{g} \right] \, d\boldsymbol{x} = \int_{\Gamma_{i}(t)} \kappa \text{Bo}^{-1} \boldsymbol{v} \cdot \hat{\boldsymbol{n}} \, dS. \tag{3.2}$$

In 2d, the curvature  $\kappa$  is unambiguously defined. In 3d,  $\kappa$  corresponds to twice the mean curvature of the interface (de Gennes et al. 2002).<sup>3</sup>

In the same manner, should we be interested in the Dirichlet problem (1.54D), we would only need to replace the function space  $\boldsymbol{H}^1_{\Gamma_b}(\Omega(t))$ by  $\boldsymbol{H}^1_{\Gamma_b,0}(\Omega(t))$  in the problems (3.1) or (3.2).

### I.2. Time discretisation

Before discussing how to apply the FEM to the spatial problem (3.1), we briefly describe the time-stepping scheme that has been chosen to discretise the  $\partial_t \boldsymbol{u}$  term. It is not surprising that the major difficulty comes from the non-linear term  $\boldsymbol{u} \cdot \nabla \boldsymbol{u}$ . In order to prevent the use of a non-linear solver<sup>4</sup>, we chose to keep the first  $\boldsymbol{u}$  explicitly described using a single-step forward Euler method, at the cost of the symmetry of the associated stiffness matrix (yet to be discussed).

If  $(\boldsymbol{u}^n,p^n)$  denotes the state of the numerical system after n time steps, two different schemes have been tried, both yielding similar results<sup>5</sup>.

I.2.1. The implicit scheme. In this scheme, all remaining terms are treated using a backward Euler method<sup>6</sup>, yielding the following space-only variational formulation,

Given a  $\delta t^n > 0$  and a state  $(\boldsymbol{u}^n, p^n)$ , find  $\boldsymbol{u}^{n+1} \in \boldsymbol{H}^1_{\Gamma_b}(\Omega(t))$  and  $p^{n+1} \in L^2(\Omega(t))$  such that

$$\int_{\Omega^n} \left[ \boldsymbol{v} \cdot \frac{\boldsymbol{u}^{n+1} - \boldsymbol{u}^n}{\delta t^n} + \boldsymbol{v} \cdot \left( \boldsymbol{u}^n \cdot \boldsymbol{\nabla} \right) \boldsymbol{u}^{n+1} + \frac{2}{\mathrm{Re}} \; \mathbf{S}(\boldsymbol{v}) : \mathbf{S}(\boldsymbol{u}^{n+1}) - p^{n+1} \boldsymbol{\nabla} \cdot \boldsymbol{v} - q \boldsymbol{\nabla} \cdot \boldsymbol{u}^{n+1} - \boldsymbol{v} \cdot \boldsymbol{g} \right] \, \mathrm{d}\boldsymbol{x} = 0,$$

for all  $\mathbf{v} \in \mathbf{H}^1_{\Gamma_b}(\Omega(t))$  and  $q \in L^2(\Omega(t))$  and at all time  $t \in [0,T]$ .  $\Omega^n$  is the domain after n time iterations. The domain advection scheme will be discussed in sec. II below.

<sup>7</sup>Crank and Nicolson (1947)

I.2.2. The Crank-Nicolson scheme. Another possibility is to make use of the Crank and Nicolson scheme<sup>7</sup> to achieve second-order time-accuracy while still having a single-step method,

Given a  $\delta t^n > 0$  and a state  $(\boldsymbol{u}^n, p^n)$ , find  $\boldsymbol{u}^{n+1} \in \boldsymbol{H}^1_{\Gamma_b}(\Omega(t))$  and  $p^{n+1} \in L^2(\Omega(t))$  such that

$$\begin{split} \int_{\Omega^n} \boldsymbol{v} \cdot \frac{\boldsymbol{u}^{n+1} - \boldsymbol{u}^n}{\delta t^n} \, \mathrm{d}\boldsymbol{x} + \frac{1}{2} \int_{\Omega_t} \left[ \boldsymbol{v} \cdot \left( \boldsymbol{u}^n \cdot \boldsymbol{\nabla} \right) \boldsymbol{u}^{n+1} + \frac{2}{\mathrm{Re}} \, \mathbf{S}(\boldsymbol{v}) : \mathbf{S}(\boldsymbol{u}^{n+1}) - p^{n+1} \boldsymbol{\nabla} \cdot \boldsymbol{v} - q \boldsymbol{\nabla} \cdot \boldsymbol{u}^{n+1} - \boldsymbol{v} \cdot \boldsymbol{g} \right] \, \mathrm{d}\boldsymbol{x} \\ + \frac{1}{2} \int_{\Omega_t} \left[ \boldsymbol{v} \cdot \left( \boldsymbol{u}^n \cdot \boldsymbol{\nabla} \right) \boldsymbol{u}^n + \frac{2}{\mathrm{Re}} \, \mathbf{S}(\boldsymbol{v}) : \mathbf{S}(\boldsymbol{u}^n) - p^n \boldsymbol{\nabla} \cdot \boldsymbol{v} - q \boldsymbol{\nabla} \cdot \boldsymbol{u}^n - \boldsymbol{v} \cdot \boldsymbol{g} \right] \, \mathrm{d}\boldsymbol{x} = 0, \end{split}$$

for all  $\boldsymbol{v} \in \boldsymbol{H}^1_{\Gamma_h}(\Omega(t))$  and  $q \in L^2(\Omega(t))$  and at all time  $t \in [0,T]$ .

The time step  $\delta t^n > 0$  does not remain fixed throughout the simulation. It will be chosen using a FEM-equivalent of the CFL condition<sup>1</sup>. It will be discussed in sec. III below.

#### I.3. Matrix creation

Having chosen a time discretisation, both problems I.2.1 and I.2.2 can be viewed as elliptic, in the sense that "the information at one point  $\boldsymbol{x} \in \Omega(t)$  depends on the information at all other points". The FEM was developed to handle such situation on non-rectangular geometries and exploiting the stabler nature of the weak formulation. Its objective is to transform I.2.1 or I.2.2 into (possibly very huge but finite) algebraic systems that can be handled numerically. The resulting equation must hence take the form

$$\mathbf{A}u = \mathbf{b}.\tag{3.3}$$

We call  $\mathbf{A} \in \mathbb{R}^{N \times N}$  the *stiffness* matrix,  $\mathbf{u} \in \mathbb{R}^{N}$  is the *discrete solution* and  $\mathbf{b} \in \mathbb{R}^{N}$  is the *right-hand side*, with N the *number of degrees of freedom*.

I.3.1. **Meshing.** The first step that must be followed in order to obtain a finite system like (3.3) from a given elliptic problem is to triangulate the domain at hand. We rapidly describe the method in two space dimensions and provide clues as to how to extend this method in 3d.

Let  $\Omega$  a bounded, connected open subset of  $\mathbb{R}^2$  with Lipschitz boundary  $\partial\Omega$  (fig. 3.2, up). For some chosen precision h>0, its corresponding Delaunay triangulation<sup>3</sup>  $\mathcal{T}^h(\Omega)$  can be constructed following four algorithmic steps:

- 1. Discretise the boundary. A number n of points lying on the boundary  $\partial\Omega$  are chosen so that the distance between two neighbouring points is roughly h. Should the domain have corners, the corresponding corner points must be chosen to preserve the geometric information as much as possible.
- 2. Insert points inside the domain. Points are inserted randomly in the domain. With prior knowledge of the solution, it seems appropriate to add more points in regions where the solution varies abruptly and less points where it is almost constant or linear. When such knowledge is not available, there are many possible ways to chose the interior points (for instance, in fig. 3.2, the interior points are chosen at random, which is far from optimal). We denote by  $S \subset \mathbb{R}^2$  the set of boundary and interior points.
- 3. Compute the Voronoï diagram. From the set S of points, the Voronoï diagram<sup>4</sup> is computed (fig. 3.2, middle). We can readily formalise its construction. For two points  $p, q \in S$  such that  $p \neq q$ , we denote by H(p,q) the half plane whose points are closer to p than they are to q,

$$H(\boldsymbol{p},\boldsymbol{q}) = \left\{\boldsymbol{x} \in \mathbb{R}^2 \text{ s.t. } |\boldsymbol{x} - \boldsymbol{p}| \leqslant |\boldsymbol{x} - \boldsymbol{q}|\right\}.$$

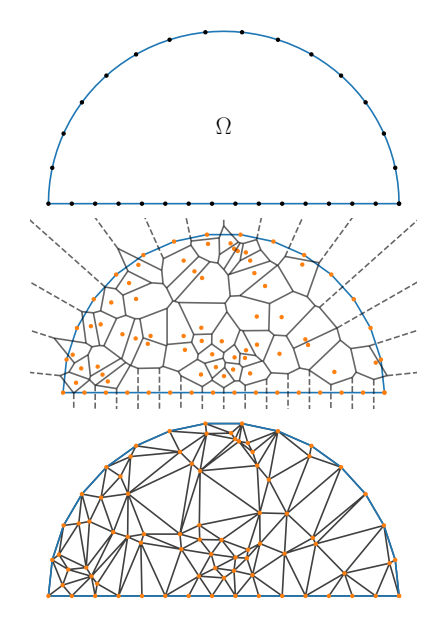


Figure 3.2 – A 2d domain  $\Omega$  and its boundary segmentation (up), interior points chosen at random and the corresponding Voronoï diagram (middle), and the Delaunay triangulation (down).

 $^{1}$ Courant et al. (1928)

 $^2 {\rm In}$  fact, this continuous problem is elliptic in the usual PDE sense (Evans 2010; Le Dret 2018). However, as  ${\rm Re} \to +\infty,$  the ellipticity condition becomes more and more degenerate.

<sup>3</sup>Delaunay (1934). There exist other methods to compute a triangulation. However, in 2d, it can be shown that Delaunay's triangulation is optimal, meaning that it maximises the angles of its constituting triangles (compared to other triangulations). This is shown in theorems 2.8 and 2.11 of Cheng et al. (2012).

<sup>4</sup>Voronoï (1908)

The Voronoï cell associated to  $p \in S$  it then

$$\operatorname{Vor}_S(\boldsymbol{p}) = \bigcap_{\boldsymbol{q} \in S - \{\boldsymbol{p}\}} H(\boldsymbol{p}, \boldsymbol{q}).$$

And the Voronoï diagram is the set of the Voronoï cells of all points of S.

4. Construct the triangulation. The Delaunay triangulation associated with S is the graph  $\mathcal{T}^h(\Omega) = (S, E)$  whose set of vertices is S and whose edges are obtained from the Voronoï diagram,

$$E = \left\{ (\boldsymbol{p}, \boldsymbol{q}) \in S^2 \text{ s.t. } \operatorname{Vor}_S(\boldsymbol{p}) \cap \operatorname{Vor}_S(\boldsymbol{q}) \neq \emptyset \right\},$$

*i.e.* two points in S share an edge in E if and only if their corresponding Voronoï cells are adjacent (fig. 3.2, down).

In practice, the Delaunay triangulation of a set of points is not computed in this manner<sup>1</sup>. However, the method presented above is easier to describe concisely. Examples of Delaunay meshes are shown in e.g. figures 3.3, 3.14 or 3.16. In 3d,  $\mathcal{T}^h(\Omega)$  is built in a similar manner. The main difference is that the boundary  $\partial\Omega$  is a surface which must first be triangulated. The step 1. of the algorithm presented above becomes thus trickier. The curious reader is encouraged to cast a glance at chapter 4 of Cheng et al. (2012).

Unsurprisingly, the Delaunay triangulation process yields triangles in 2d. On the other hand, in 3d, it yields tetrahedra. In the following, we shall use the word *simplex* to refer to a line segment in 1d, a triangle in 2d and a tetrahedron in 3d.

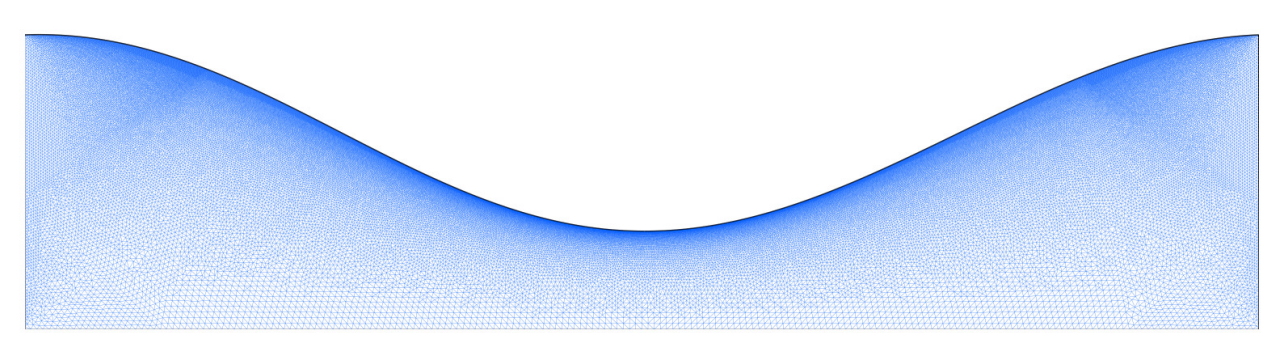


Figure 3.3 – A rather fine mesh computed from the initial domain of fig. 3.1 using the default 2d FreeFEM mesh generation method buildmesh. It contains  $N_v=113\,436$  vertices,  $N_t=222\,970$  triangles and  $N_e=336\,403$  edges.

I.3.2. Finite Element spaces. Once the domain  $\Omega$  has been discretised, we can now introduce a general method to expand a continuous function  $f:\Omega\to\mathbb{R}$  as a finite sum of basis functions  $\phi_j$   $(j=1,\cdots,N)$ , *i.e.* 

$$f(\boldsymbol{x}) = \sum_{j=1}^N f_j \phi_j(\boldsymbol{x}).$$

The choice of the basis functions  $\phi_j$  (and, incidently, the number of degrees of freedom N) correspond to choosing a Finite Element space. The basic idea of the FEM is to chose functions  $\phi_j$  whose support is spread over neighbouring triangles only. As shall be emphasised, the resulting matrix will be sparse and enjoy very nice properties.

<sup>1</sup>see the algorithms presented in chapters 3 and 5 of Cheng et al. (2012).

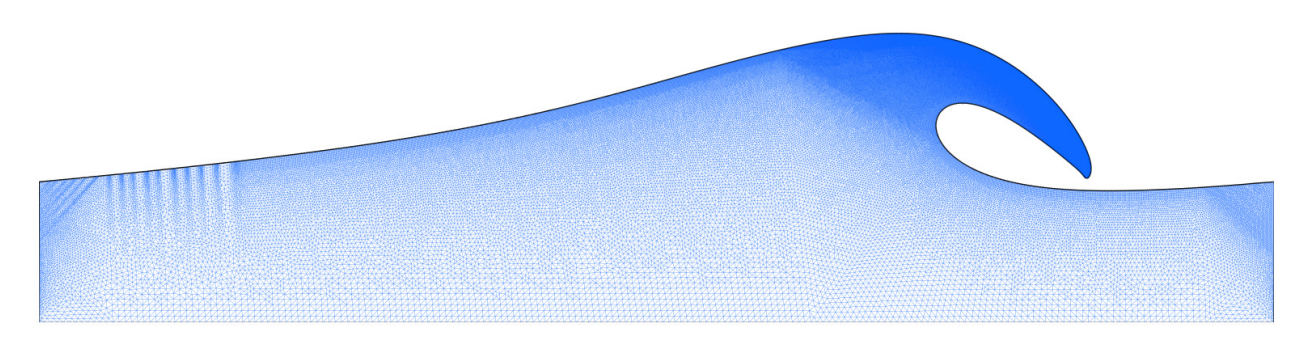


Figure 3.4 – A fine mesh corresponding to a breaking wave simulation (see chap 4) at Re =  $10^5$ . It contains  $N_v = 227\,275$  vertices,  $N_t = 450\,648$  triangles and  $N_e = 677\,920$  edges. Oscillations in the triangle density are visible at the left end of the mesh. They are a consequence of the remeshing procedure **PR** (soon to be discussed), which has been replaced by **MA** in the most recent version of the code.

 $\mathbb{P}^0$  elements. The easiest choice that can be made is to approximate f by a piecewise constant function. To do so, let  $N_s$  the number of simplexes. For  $j=1,\cdots,N_s$ , let  $\mathcal{T}^h_j\subset\mathcal{T}^h(\Omega)$  the j-th simplex, with barycentre  $\boldsymbol{x}_j$ . The associated basis function  $\phi_j$  is defined readily as

$$\phi_j(\boldsymbol{x}) = \begin{cases} 1 & \text{if } \boldsymbol{x} \in \mathcal{T}_j^h \\ 0 & \text{otherwise.} \end{cases}$$

The approximation  $\mathbb{P}_h^0[f]$  of f by  $\mathbb{P}^0$  elements elements is defined as

$$\mathbb{P}_h^0[f] = \sum_{j=1}^{N_s} f(\boldsymbol{x}_j) \phi_j.$$

Such approximation is obviously discontinuous. Therefore,  $\mathbb{P}^0$  is only  $L^2$ -conforming<sup>1</sup>, meaning that we can only expect a  $L^2$  convergence of  $\mathbb{P}^0_h[f]$  to f as the mesh typical size h goes to zero. Should we need  $H^1$  convergence, other element spaces must be used. A representation of the finite element basis functions is available in figure 3.5.

 $\mathbb{P}^1$  elements. To introduce the most commonly used  $H^1$ -conforming finite element space, we introduce the important concept of reference simplex  $\mathring{\mathcal{T}}$ . In 2d, this corresponds to the triangle whose vertices are (0,0), (1,0) and (0,1) (fig. 3.6). In 3d, the points (0,0,0), (1,0,0), (0,1,0) and (0,0,1) define the reference tetrahedron. Each point  $\boldsymbol{x}$  in the simplex  $\mathcal{T}_h^j$  can be projected to a point  $\boldsymbol{y}$  in reference simplex  $\mathring{\mathcal{T}}$  through a well-chosen diffeomorphism  $\Phi_j$  (fig. 3.10). In 2d, this affine transformation is given by

$$\Phi_{j}(\mathbf{y}) = \begin{bmatrix} a_{j,1} - c_{j,1} & b_{j,1} - c_{j,1} \\ a_{j,2} - c_{j,2} & b_{j,2} - c_{j,2} \end{bmatrix} \mathbf{y} + \begin{bmatrix} c_{j,1} \\ c_{j,2} \end{bmatrix}, \tag{3.4}$$

with  $\boldsymbol{a}_j, \boldsymbol{b}_j$  and  $\boldsymbol{c}_j$  the vertices of  $\mathcal{T}_h^j$  ( $\boldsymbol{a}_j$  has components  $(a_{j,1}, a_{j,2})$  and similar for  $\boldsymbol{b}_j$  and  $\boldsymbol{c}_j$ ). The inverse transformation can also be computed exactly. Surprisingly, the jacobian determinant of this transformation  $\det(\nabla \Phi_j)$  is exactly the area of  $\mathcal{T}_h^j$ . We shall take advantage of this important property afterward. The 3d transformation also enjoys these interesting particularities.

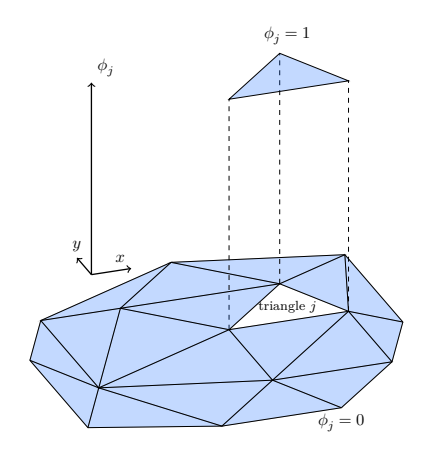


**Figure 3.5** – A  $\mathbb{P}^0$  basis function.

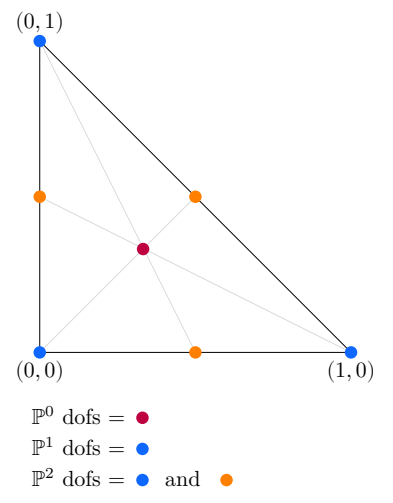


**Figure 3.6** – Position of the degrees of freedom on the reference cell for different finite element spaces.

 $^{1}\text{A finite element space }V_{h}\text{ is called }V\text{--}\\ \text{conforming if }V_{h}\subseteq V.$ 

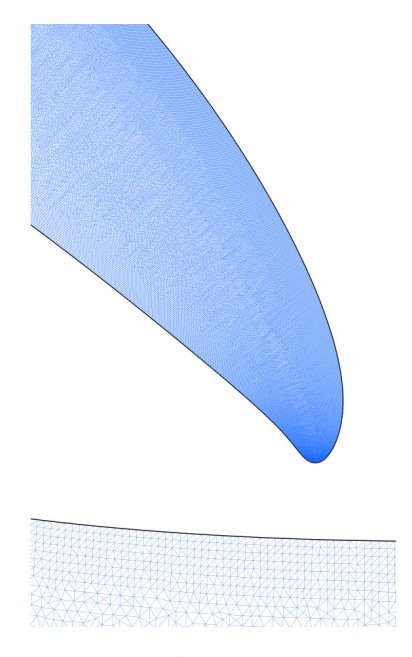


**Figure 3.7** – A zoom on the tip of the wave's mesh represented in fig. 3.4.

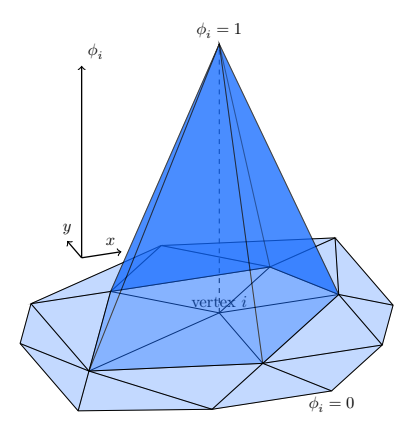


**Figure 3.8** – A  $\mathbb{P}^1$  basis function.

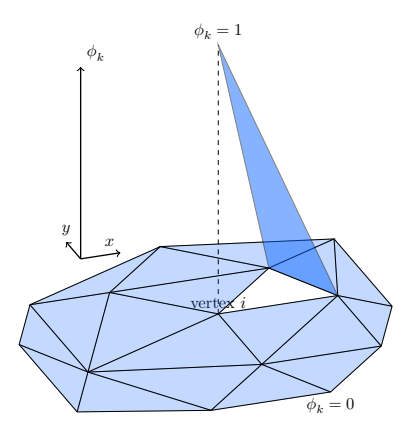


**Figure 3.9** – A  $\mathbb{P}^1_{dc}$  basis function.

Having introduced the transformation  $\Phi_j$ , we can now work on the reference cell. In 2d, let  $\mathring{\phi}_k$  (k=1,2 or 3) the functions defined on  $\mathring{\mathcal{T}}$  by

$$\begin{split} \mathring{\phi}_1 &= 1 - x - y \\ \mathring{\phi}_2 &= x \\ \mathring{\phi}_3 &= y. \end{split}$$

These reference basis functions vanish on all corner points of  $\mathring{\mathcal{T}}$  but one. Adaptation to 3d is straightforward. From  $\Phi_j$  and  $\mathring{\phi}_k$  we can build the set  $\mathbb{P}^1$  of  $H^1$ –conforming basis functions.

Let  $N_v$  the number of vertices of the triangulation  $\mathcal{T}^h$ . To each vertex  $\boldsymbol{x}_i$  we shall associate a basis function  $\phi_i$  defined as follows:

$$\phi_i(\boldsymbol{x}) = \begin{cases} \left[\mathring{\phi}_k \circ \Phi_j^{-1}\right](\boldsymbol{x}) & \text{if } \boldsymbol{x} \in \mathcal{T}_h^j \text{ and } \left[\mathring{\phi}_k \circ \Phi_j^{-1}\right](\boldsymbol{x}_i) = 1\\ 0 & \text{otherwise.} \end{cases}$$

That is,  $\phi_i$  is the function which is equal to 1 at  $\boldsymbol{x}_i$ , affine in the neighbouring triangles and 0 everywhere else (fig. 3.8). Therefore, there exists  $N_v$   $\mathbb{P}^1$  basis functions allowing to expand a function  $f \in H^1$  as

$$f = \sum_{i=1}^{N_v} f(\boldsymbol{x}_i) \phi_i.$$

This decomposition converges to f in  $H^1$  as  $h \to 0$  (Quarteroni and Valli 1994, sec. 3.4).

 $\mathbb{P}^2$  elements. These elements are built as the  $\mathbb{P}^1$  basis functions, but from quadratic reference functions  $\mathring{\phi}_k$  instead of affine ones. As with the  $\mathbb{P}^1$  reference functions, on the reference cell, each  $\mathring{\phi}_k$  vanishes on all degrees of freedom (blue and orange dots in figure 3.6) but one. It is worth noticing that the basis functions  $\phi_i$  are not  $H^2$ –conforming because of a discontinuity in their derivative at edges of the triangles. If  $N_e$  is the number of edges, then there are  $N_v+N_e$   $\mathbb{P}^2$  basis functions. The link between the number of edges  $N_e$  and the number of triangles  $N_t$  depends on the topology of the mesh through Euler's relation (Ern and Guermond 2021a, ch. 8).

We could, similarly, define  $\mathbb{P}^k$  elements of order k, using 3k degrees of freedom in 2d and 6k degrees of freedom in 3d, on the reference cell  $\mathring{\mathcal{T}}$ . These elements are sometimes called Lagrange's elements.

 $\mathbb{P}^1_{ ext{dc}}$  elements. The last finite element space that we would like to discuss shall be used to handle the derivative of the velocity. To each simplex, we associate d+1 basis functions (d being the ambient space dimension) defined as  $\mathring{\phi}_k \circ \Phi_j$ . The resulting basis functions  $\phi_i \in \mathbb{P}^1_{ ext{dc}}$  are piecewise affine (as function in  $\mathbb{P}^1$ ) but are discontinuous at all edges. An example is shown in figure 3.9. There are  $3N_t$  degrees of freedom in this space. Also note that these elements are only  $L^2$ -conforming.

I.3.3. Matrix assembly. Let us come back to the Naver-Stokes problem at hand. Having described the various finite element spaces used in the present work, we can provide the algorithm to create the stiffness matrices corresponding to the elliptic problems I.2.1 or I.2.2.

Having computed a triangulation (or tetrahedration) of the fluid domain  $\Omega(t)$ , each component of the velocity  $\boldsymbol{u}$  is decomposed using

 $\mathbb{P}^2$  elements while the pressure is represented by  $\mathbb{P}^1$  elements. This composite finite element space  $V_h=(\mathbb{P}^2)^d\times\mathbb{P}^1$  is called a Hood and Taylor space<sup>2</sup>.

As already stated, the divergence-free condition is difficult to handle using the FEM. The major difficulty lies in the fact that we must chose a composite finite element space satisfying the inf-sup criterion of Ladyženskaya, Babuška and Brezzi (LBB)<sup>3</sup>. This is a necessary condition for the existence of a solution to the discrete Navier-Stokes systems I.2.1 or I.2.2. Let us summarise it here. At time  $t \geq 0$ , for a pair  $(\boldsymbol{w},q)$  lying in elements spaces  $\boldsymbol{W}_h \times Q_h$  ( $\boldsymbol{W}_h$  being  $H^1$ –conforming and  $Q_h$   $L^2$ –conforming), let the bilinear form

$$b(\boldsymbol{w},q) = \int_{\mathcal{T}^h(\Omega^n)} q \boldsymbol{\nabla} \cdot \boldsymbol{w}.$$

This integral is well-defined since

$$q \in L^2\Big(\mathcal{T}^h\Big(\Omega^n\Big)\Big) \quad \text{and} \quad \boldsymbol{w} \in \Big[H^1\Big(\mathcal{T}^h\Big(\Omega^n\Big)\Big)\Big]^d.$$

The LBB condition asserts that the elliptic linear problems I.2.1 or I.2.2 have solutions if and only if there exists a constant  $\beta > 0$  such that

$$\inf_{q \in Q_h - \{0\}} \sup_{\boldsymbol{w} \in \boldsymbol{W}_h - \{0\}} \left\{ \frac{b(\boldsymbol{w}, q)}{\|q\|_{Q_h} \|\boldsymbol{w}\|_{\boldsymbol{W}_h}} \right\} > \beta.$$

Here, the norms on  $Q_h$  and  $\boldsymbol{W}_h$  are derived from the continuous conforming spaces. Note that the LBB condition also provides the well-posedness on the continuous level. The choice  $\boldsymbol{W}_h = (\mathbb{P}^2)^d$  and  $Q_h = \mathbb{P}^1$  satisfies this criterion (John 2016, ch. 3 and 4) but other choices could have been made.<sup>4</sup>

Knowing that our finite element space is well chosen, we can briefly describe the procedure to assemble the stiffness matrix **A**. We discuss the algorithm for the implicit problem I.2.1 first. At the n-th time iteration, the state  $(\boldsymbol{u}^n, p^n, \Omega^n)$  is known. We introduce the bilinear form  $a^n: (\mathbb{P}^2)^d \times (\mathbb{P}^2)^d \to \mathbb{R}$  defined by

$$a^n(\boldsymbol{u}^{n+1},\boldsymbol{v}) = \int_{\mathcal{T}^h(\Omega^n)} \left[ \frac{\boldsymbol{v} \cdot \boldsymbol{u}^{n+1}}{\delta t^n} + \boldsymbol{v} \cdot \boldsymbol{u}^n \cdot \boldsymbol{\nabla} \boldsymbol{u}^{n+1} + \frac{2}{\mathrm{Re}} \mathbf{S}(\boldsymbol{v}) : \mathbf{S}(\boldsymbol{u}^{n+1}) \right].$$

We also introduce the functional  $\ell^n : \mathbb{P}^2 \to \mathbb{R}$  describing the right-hand side (RHS) of I.2.1,

$$\ell^n(oldsymbol{v}) = \int_{\mathcal{T}^h(\Omega^n)} \left[ oldsymbol{g} \cdot oldsymbol{v} + rac{oldsymbol{v} \cdot oldsymbol{u}^n}{\delta t^n} 
ight].$$

The discrete equivalent of the implicit problem I.2.1 that must be solved to obtain the state  $(u^{n+1}, p^{b+1})$  is therefore rephrased as

$$a^{n}(\boldsymbol{u}^{n+1}, \boldsymbol{v}) + b(\boldsymbol{u}^{n+1}, q) + b(\boldsymbol{v}, p^{n+1}) = \ell(\boldsymbol{v}),$$
 (3.5)

for all  $\mathbf{v} \in (\mathbb{P}^2)^d$  and  $q \in \mathbb{P}^1$ .

We remind the reader that  $\mathcal{T}^h(\Omega^n)$  is the triangulated/tetrahedrated mesh after n time steps, on which the

 $^1$ We abuse the notation here by denoting both the continuous solution and the discrete-level solution as  $(\boldsymbol{u}^{n+1},p^{n+1}).$ 

<sup>2</sup>Hood and Taylor (1974)

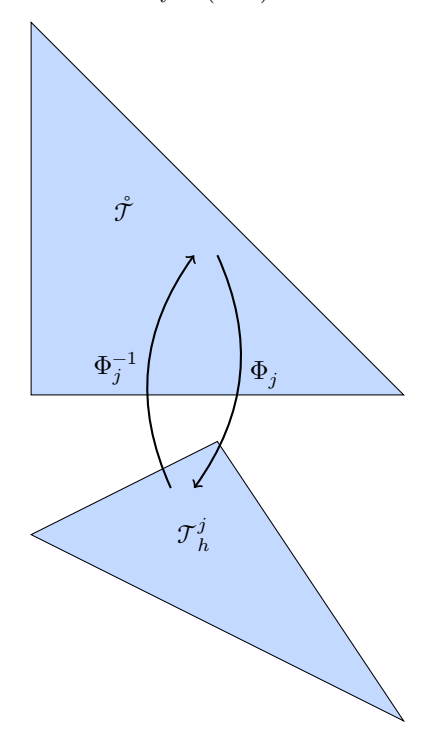


Figure 3.10 – The diffeomorphism  $\Phi_i$ .

<sup>3</sup>Ladyženskaya (1969), Babuška (1971), Brezzi (1974)

 $<sup>^4</sup>$ Unfortunately, the easiest Hood–Taylor space  $(\mathbb{P}^1)^d \times \mathbb{P}^0$  does not satisfies the LBB condition.

different quantities appearing in (3.5) can be written as

$$\begin{split} \boldsymbol{u}^{n+1} &= \sum_{j=1}^{N_v + N_e} \left[ u_{j,1}^{n+1} \hat{\boldsymbol{e}}_1 + u_{j,2}^{n+1} \hat{\boldsymbol{e}}_2 + u_{j,3}^{n+1} \hat{\boldsymbol{e}}_3 \right] \phi_j \qquad \quad \boldsymbol{v} = \sum_{j=1}^{N_v + N_e} \left[ v_{j,1} \hat{\boldsymbol{e}}_1 + v_{j,2} \hat{\boldsymbol{e}}_2 + v_{j,3} \hat{\boldsymbol{e}}_3 \right] \phi_j \\ \boldsymbol{u}^n &= \sum_{j=1}^{N_v + N_e} \left[ u_{j,1}^n \hat{\boldsymbol{e}}_1 + u_{j,2}^n \hat{\boldsymbol{e}}_2 + u_{j,3}^n \hat{\boldsymbol{e}}_3 \right] \phi_j \\ p^{n+1} &= \sum_{j=1}^{N_v} p_j^{n+1} \psi_j \qquad \qquad q = \sum_{j=1}^{N_v} q_j \psi_j, \end{split}$$

where we have distinguished the  $\mathbb{P}^2$  basis functions from the  $\mathbb{P}^1$  basis,  $\{\hat{e}_j\}_{j=1,\cdots,d}$  being the orthonormal basis of  $\mathbb{R}^d$  and where the terms in blue are only present in 3d. Inserting this decomposition into (3.5), the first term becomes

$$\int_{\mathcal{T}^h(\Omega^n)} \frac{\boldsymbol{v} \cdot \boldsymbol{u}^{n+1}}{\delta t} = \sum_{j=1}^{N_v+N_e} \sum_{k=1}^{N_v+N_e} \frac{\boldsymbol{u}_j^{n+1} \cdot \boldsymbol{v}_k}{\delta t^n} \cdot \int_{\mathcal{T}^h(\Omega^n)} \phi_j \phi_k.$$

In finite dimension, the condition "for all  $\mathbf{v} \in (\mathbb{P}^2)^d$ " is equivalent to replacing  $\mathbf{v}$  by  $\phi_k \hat{\mathbf{e}}_i$  and saying "for all  $k = 1, \dots, N_v + N_e$  and all  $i = 1, \dots, d$ ". We can apply the same procedure to the divergence-free condition, replacing q by any  $\psi_k$ . The above term can then be further simplified as

$$\int_{\mathcal{T}^h(\Omega^n)} \frac{\boldsymbol{v} \cdot \boldsymbol{u}^{n+1}}{\delta t} = \sum_{j=1}^{N_v + N_e} \hat{\boldsymbol{e}}_i \cdot \left( \frac{\mathrm{id}_{d \times d}}{\delta t^n} \cdot \int_{\mathcal{T}^h(\Omega^n)} \phi_j \phi_k \right) \cdot \boldsymbol{u}_j^{n+1}$$

We would like to reassure the worried reader, the number of indices will decrease at least as quick as it has increased. The other terms become

$$\begin{split} \int_{\mathcal{T}^h(\Omega^n)} \boldsymbol{v} \cdot \boldsymbol{u}^n \cdot \boldsymbol{\nabla} \boldsymbol{u}^{n+1} &= \sum_{j=1}^{N_v + N_e} \hat{\boldsymbol{e}}_i \cdot \left( \operatorname{id}_{d \times d} \int_{\mathcal{T}^h(\Omega^n)} \phi_k \ \boldsymbol{u}^n \cdot \boldsymbol{\nabla} \phi_j \right) \cdot \boldsymbol{u}_j^{n+1} \\ \int_{\mathcal{T}^h(\Omega^n)} \mathbf{S}(\boldsymbol{v}) : \mathbf{S}(\boldsymbol{u}^{n+1}) &= 2 \sum_{j=1}^{N_v + N_e} \hat{\boldsymbol{e}}_i \cdot \left( \operatorname{id}_{d \times d} \int_{\mathcal{T}^h(\Omega^n)} \boldsymbol{\nabla} \phi_k \cdot \boldsymbol{\nabla} \phi_j + \int_{\mathcal{T}^h(\Omega^n)} \boldsymbol{\nabla} \phi_j \otimes \boldsymbol{\nabla} \phi_k \right) \cdot \boldsymbol{u}_j^{n+1} \\ \int_{\mathcal{T}^h(\Omega^n)} p^{n+1} \boldsymbol{\nabla} \cdot \boldsymbol{v} &= \sum_{j=1}^{N_v} p_j^{n+1} \int_{\mathcal{T}^h(\Omega^n)} \psi_j \hat{\boldsymbol{e}}_i \cdot \boldsymbol{\nabla} \phi_k \\ \int_{\mathcal{T}^h(\Omega^n)} q \boldsymbol{\nabla} \cdot \boldsymbol{u}^{n+1} &= \sum_{j=1}^{N_v + N_e} \boldsymbol{u}_j^{n+1} \cdot \int_{\mathcal{T}^h(\Omega^n)} \psi_k \boldsymbol{\nabla} \phi_j \end{split}$$

We begin to see the block structure of the problem emerging. Our aim is now to express (3.5) using matrices. To this end, we introduce the unknown vector  $\mathbf{x}^{n+1} \in \mathbb{R}^{d(N_e+N_v)+N_v}$ ,

$$\mathbf{x}^{n+1} = egin{bmatrix} m{u}_1^{n+1} \ dots \ m{u}_{N_v+N_e}^{n+1} \ p_1^{n+1} \ dots \ p_{N_v}^{n+1} \end{bmatrix}.$$

We can then rewrite (3.5) as

$$\begin{bmatrix} \mathbf{M} & 0 \\ 0 & 0 \end{bmatrix} \mathbf{x}^{n+1} + \delta t^n \begin{bmatrix} \mathbf{B} & \mathbf{C} \\ \mathbf{C}^\top & 0 \end{bmatrix} \mathbf{x}^{n+1} = \delta t^n \begin{bmatrix} \mathbf{g} \\ 0 \end{bmatrix} + \begin{bmatrix} \mathbf{M} & 0 \\ 0 & 0 \end{bmatrix} \mathbf{x}^n, \tag{3.6}$$

with the matrices  $\mathbf{M}, \mathbf{B} \in \mathbb{R}^{d(N_v+N_e)\times d(N_v+N_e)}$  and  $\mathbf{C} \in \mathbb{R}^{d(N_v+N_e)\times N_v}$  whose components are given by

$$\begin{aligned} \mathbf{M}_{kd+\ell,jd+i} = & \delta_{i,\ell} \int_{\mathcal{T}^h(\Omega^n)} \phi_j \phi_k & \text{for } j,k \in \llbracket 1,N_v+N_e \rrbracket \text{ and } i,\ell \in \llbracket 0,d-1 \rrbracket \\ \mathbf{B}_{kd+\ell,jd+i} = & \delta_{i,\ell} \int_{\mathcal{T}^h(\Omega^n)} \left[ \phi_k \boldsymbol{u}^n \cdot \boldsymbol{\nabla} \phi_j + \frac{4}{\mathrm{Re}} \boldsymbol{\nabla} \phi_k \cdot \boldsymbol{\nabla} \phi_j \right] \\ & + \hat{\boldsymbol{e}}_{i+1} \cdot \frac{4}{\mathrm{Re}} \left( \int_{\mathcal{T}^h(\Omega^n)} \boldsymbol{\nabla} \phi_j \otimes \boldsymbol{\nabla} \phi_k \right) \cdot \hat{\boldsymbol{e}}_{\ell+1} & \text{for } j,k \in \llbracket 1,N_v+N_e \rrbracket \text{ and } i,\ell \in \llbracket 0,d-1 \rrbracket \\ \mathbf{C}_{kd+\ell,j} = & \int_{\mathcal{T}^h(\Omega^n)} \psi_j \hat{\boldsymbol{e}}_\ell \cdot \boldsymbol{\nabla} \phi_k & \text{for } k \in \llbracket 1,N_v+N_e \rrbracket, j \in \llbracket 1,N_v \rrbracket \text{ and } \ell \in \llbracket 0,d-1 \rrbracket, \end{aligned}$$

and with

$$\mathbf{g}_{kd+\ell} = \boldsymbol{g} \cdot \hat{\boldsymbol{e}}_{\ell} \int_{\mathcal{T}^h(\Omega^n)} \phi_k \qquad \qquad \text{for } k \in [\![1,N_v+N_e]\!] \text{ and } \ell \in [\![0,d-1]\!].$$

The Crank-Nicolson scheme I.2.2 is implemented readily as

$$\begin{bmatrix} \mathbf{M} & 0 \\ 0 & 0 \end{bmatrix} \mathbf{x}^{n+1} + \delta t^n \begin{bmatrix} \mathbf{B} & \mathbf{C} \\ \mathbf{C}^\top & 0 \end{bmatrix} \frac{\mathbf{x}^{n+1} + \mathbf{x}^n}{2} = \delta t^n \begin{bmatrix} \mathbf{g} \\ 0 \end{bmatrix} + \begin{bmatrix} \mathbf{M} & 0 \\ 0 & 0 \end{bmatrix} \mathbf{x}^n.$$

In the literature,  $\mathbf{M}$  is called the *mass matrix*. We notice that the  $\mathbf{C}$  matrix enforces the divergence-free condition and has absolutely no other purpose. Of course in order to complete this algebraic system, the correct set of boundary conditions must be implemented.

I.3.4. Structure of the stiffness matrix. Taking a look at the algebraic equation (3.6), we easily see that the stiffness matrix of eq. (3.3) is nothing but

$$\mathbf{A} = \begin{bmatrix} \mathbf{M} & 0 \\ 0 & 0 \end{bmatrix} + \delta t^n \begin{bmatrix} \mathbf{B} & \mathbf{C} \\ \mathbf{C}^\top & 0 \end{bmatrix}.$$

This matrix has an interesting symmetric block-structure, motivating the use a Schur complement—based<sup>1</sup> solver. In fact, we could even get a completely symmetric stiffness matrix **A** by using a symmetric version of the problem I.2.1 (Guermond et al. 2012). This has, however, not been tested yet.

At first sight, it seems that each constituting block of  $\bf A$  is dense. This is not the case since the support of each shape function  $\phi_j$ , or  $\psi_k$ , is only spread over a few triangles at most. Therefore, the product  $\phi_j\phi_k$  (or any other combination of  $\psi_k$ ,  $\nabla\phi_k$  and  $\nabla\psi_k$ ) is far from filling the entire rows and columns it lives in.  $\bf A$  is therefore a sparse matrix whose storage does not cause any major issue.

The main optimisations that allowed to greatly reduce the computational time rely on both the shape of the matrix and the ALE method that shall be presented in the next section.

# II. Arbitrary Lagrangian-Eulerian advection

In the previous section, the spurious discussion of the mesh-advection has been omitted. Unfortunately, the time has arrived to tackle this important, yet difficult, question: "Knowing the initial mesh  $\mathcal{T}^h(\Omega^0) = \mathcal{T}^h(\Omega(0))$ , how is computed the mesh  $\mathcal{T}^h(\Omega^n)$  after n time iterations?"

<sup>1</sup>Schur (1917)

#### II.1. General velocities on the continuous level

In chapter 1, sec. I.1, the proof of Reynold's transport theorem 1.1 relied on the Lagrangian space in which the control volume remains fixed, allowing to readily compute the time derivative under the integral. The basis idea of the Arbitrary Lagrangian–Eulerian method¹ is to write the PDE in a reference frame that is neither Eulerian nor Lagrangian. This method is rarely introduced in a comprehensive and rigorous manner. We propose to do so here.

<sup>1</sup>introduced originally in Noh (1963), and later extended by Hirt et al. (1974). A modern introduction to this method is available in Donea et al. (2004).

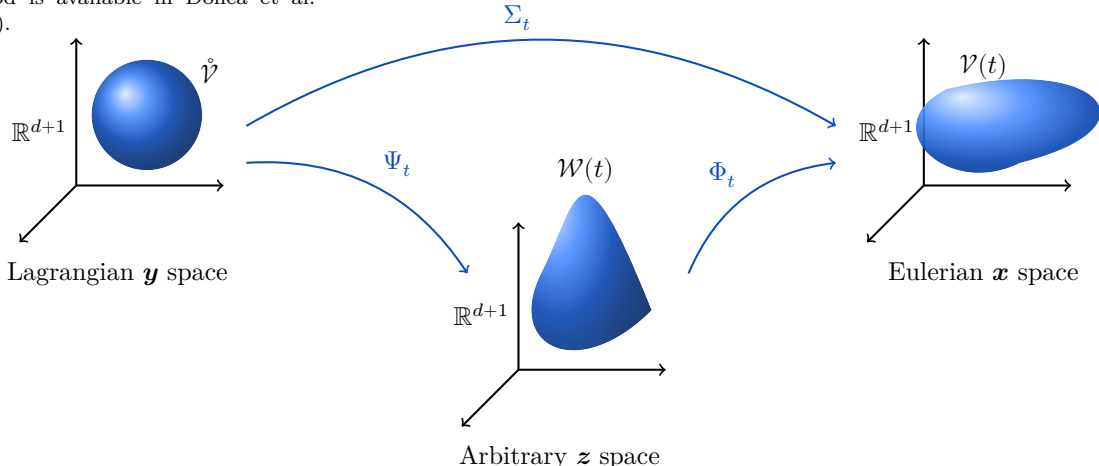


Figure 3.11 – The different spaces and diffeomorphisms used to motivate the Arbitrary Lagrangian–Eulerian method.

To introduce the ALE method, some notations are needed. As in sec. I.1 of chapter 1, let  $\mathring{\mathcal{V}} \subset \mathbb{R}^{d+1}$  a subset of the label space, also called the  $\boldsymbol{y}$  space previously, labelling the whole fluid at stake. Going from the label space to the physical space, *i.e.* the  $\boldsymbol{x}$  space, is done through the time-dependent diffeomorphism  $\Sigma_t$ . As discussed in chapter 2,  $\boldsymbol{x}$  and  $\boldsymbol{y}$  are merely time-dependent systems of coordinates. For an exterior observer, the fluid occupies the time-dependant domain  $\mathcal{V}(t) = \Sigma_t(\mathring{\mathcal{V}})$ .

We now introduce two new diffeomorphisms  $\Psi_t : \mathring{\mathcal{V}} \to \mathcal{W}(t)$  and  $\Phi_t : \mathcal{W}(t) \to \mathcal{V}(t)$  such that the diagram of fig. 3.11 commutes. The space  $\mathcal{W}(t)$  is called the arbitrary space, whose elements are denoted by z. In the following,  $\mathcal{W}(t)$  shall be the mesh. Having defined the quantities we need, we can state the underlying philosophy of the ALE method:

Solving the PDE (Euler or Navier-Stokes), expressed in W(t) using the  $\boldsymbol{x}$  variable.

We introduce (or recall) the following "velocities",

$$\begin{split} & \boldsymbol{u}(t,\boldsymbol{x}) = \left[ (\partial_t \Sigma_t) \circ \Sigma_t^{-1} \right] (\boldsymbol{x}) & \text{the fluid velocity} \\ & \boldsymbol{v}(t,\boldsymbol{x}) = \left[ (\partial_t \Psi_t) \circ \Psi_t^{-1} \right] (\boldsymbol{x}) \\ & \boldsymbol{w}(t,\boldsymbol{z}) = \left[ (\partial_t \Phi_t) \circ \Phi_t^{-1} \right] (\boldsymbol{z}). \end{split}$$

The quantities  $\boldsymbol{v}$  can be seen as the velocity of a point  $\boldsymbol{z}$  fixed in  $\mathcal{W}(t)$  from a physical observer in  $\mathcal{V}(t)$ , while  $\boldsymbol{w}$  is the physical velocity relative to a point in the  $\boldsymbol{z}$  space. We also set<sup>3</sup>

$$\boldsymbol{c}(t,\boldsymbol{x}) = \boldsymbol{u}(t,\boldsymbol{x}) - \boldsymbol{v}(t,\boldsymbol{x}),$$

<sup>2</sup>Denoting by  $\boldsymbol{x}$ ,  $\boldsymbol{z}$  and  $\boldsymbol{z}$  the elements of  $\mathcal{V}(t)$ ,  $\mathring{\mathcal{V}}$  and  $\mathcal{W}(t)$  respectively makes the changes of coordinates easier to see.

the relative velocity of a fluid element at  $\boldsymbol{x}$  with respect to the point  $\Psi_t^{-1}(\boldsymbol{x})$ . This last quantity will appear in the ALE formulation of the Navier-Stokes problem.

II.1.1. On the material derivative. We provide an interpretation of the material derivative in terms of the various diffeomorphisms introduced above. Let  $f:[0,T]\times\mathring{\mathcal{V}}\to\mathbb{R}$  a  $C^1$  functions in both time and (label) space. The lagrangian/material derivative corresponds to  $\partial_t f$  expressed at fixed  $\boldsymbol{x}$ . Indeed, pushing f to the eulerian  $\boldsymbol{x}$  space yields the function

$$F(t, \boldsymbol{x}) = f \big( t, \Sigma_t^{-1}(\boldsymbol{x}) \big).$$

Then the time derivative of f, in the x coordinate system, is<sup>1</sup>

$$\begin{split} \left(\partial_t f \circ \Sigma_t^{-1}\right) &(\boldsymbol{x}) = \partial_t \left(F \circ \Sigma_t\right) \circ \Sigma_t^{-1}(\boldsymbol{x}) \\ &= \partial_t F(t, \boldsymbol{x}) + \left(\partial_t \Sigma_t \circ \Sigma_t^{-1}(\boldsymbol{x})\right) \cdot \boldsymbol{\nabla}_{\boldsymbol{x}} F(t, \boldsymbol{x}) \\ &= \left(\partial_t F + \boldsymbol{u} \cdot \boldsymbol{\nabla}_{\boldsymbol{x}} F\right) (t, \boldsymbol{x}), \end{split}$$

the material derivate of F. Another way to see it is that

$$\left(\partial_t f \circ \Sigma_t^{-1}\right)\!\left(\boldsymbol{x}\right) = \left[\partial_t \!\left(f \circ \Sigma_t^{-1}\right) + \boldsymbol{u} \cdot \boldsymbol{\nabla}_{\boldsymbol{x}} \!\left(f \circ \Sigma_t^{-1}\right)\right]\!(t, \boldsymbol{x}).$$

The lagrangian derivative arises due to a time-dependent change of coordinate of the  $\partial_t f$  term. The exact same computations yields the lagrangian derivative in the z space,

$$\left(\partial_t f \circ \Phi_t^{-1}\right)\!\left(\boldsymbol{z}\right) = \left[\partial_t\!\left(f \circ \Phi_t^{-1}\right) + \boldsymbol{w} \cdot \boldsymbol{\nabla}_{\boldsymbol{z}}\!\left(f \circ \Phi_t^{-1}\right)\right]\!(t, \boldsymbol{z}).$$

II.1.2. The ALE framework. We are interested in solving the Navier-Stokes equations in an arbitrary z space. Indeed, it will correspond to the coordinate system of the moving mesh. However, as the Lagrangian frame, such set of coordinate might be highly non-euclidean, yielding a messy form of the Navier-Stokes equations which may not be very convenient to work with. The diffeomorphism  $\Psi_t$  allows to use the euclidean nature of the eulerian frame to easily compute the quantities arising in the z space.

Let  $U(t, \mathbf{z}) = \mathbf{u} \circ \Psi_t(\mathbf{z})$  the eulerian velocity pushed in the arbitrary space. We obtain readily that<sup>2</sup>

$$\begin{split} \partial_t \boldsymbol{u} &= (\partial_t \boldsymbol{U}) \circ \boldsymbol{\Psi}_t^{-1} - \boldsymbol{v} \cdot (\boldsymbol{\nabla}_{\boldsymbol{x}} \boldsymbol{\Psi}_t^{-1}) (\boldsymbol{\nabla}_{\boldsymbol{z}} \boldsymbol{U} \circ \boldsymbol{\Psi}_t^{-1}) \\ &= (\partial_t \boldsymbol{U}) \circ \boldsymbol{\Psi}_t^{-1} - \boldsymbol{v} \cdot \boldsymbol{\nabla}_{\boldsymbol{x}} \boldsymbol{u} \\ &= -\boldsymbol{u} \cdot \boldsymbol{\nabla} \boldsymbol{u} - \boldsymbol{\nabla} \boldsymbol{p} + \boldsymbol{g} + \frac{1}{\mathrm{Re}} \; \Delta \boldsymbol{u}. \end{split}$$

Thus, the equation for  $\partial_t U$ , recast in the eulerian frame, is<sup>3</sup>

$$(\partial_t \boldsymbol{U}) \circ \Psi_t^{-1} + \boldsymbol{c} \cdot \boldsymbol{\nabla} \boldsymbol{u} = -\boldsymbol{\nabla} \boldsymbol{p} + \frac{1}{\mathrm{Re}} \, \Delta \boldsymbol{u} + \boldsymbol{g}. \tag{3.7}$$

This is the fundamental equation of the ALE method. Fortunately, the many space derivative appearing in (3.7) are expressed in the x space, in which the differential operator are easily computed.

To the author's knowledge, equation (3.7) was never cast in this form before. Most authors use non-standard notations to make the time-derivative of  $\boldsymbol{u}$  appear, instead of  $\partial_t \boldsymbol{U}$ . This prevents the estimation of the error when replacing the first term with a finite-difference formula for the eulerian velocity (see next section). This also introduces misconceptions in the underlying philosophy.

<sup>3</sup>We show readily the link between  $\boldsymbol{c}$  and  $\boldsymbol{w}$ ,

$$\begin{split} \boldsymbol{c}(t, \boldsymbol{x}) &= \left[ \boldsymbol{w}(t) \cdot \boldsymbol{\nabla}_{\boldsymbol{z}} \boldsymbol{\Psi}_t \right] \circ \boldsymbol{\Psi}^{-1}(\boldsymbol{x}) \\ &= \left[ \left( \boldsymbol{\Psi}_t^{-1} \right)_* \boldsymbol{w}(t) \right] (\boldsymbol{x}). \end{split}$$

<sup>1</sup>To ease out the notations, it is implicitly understood that

$$(F\circ\Sigma_t)(\boldsymbol{x})=F\bigl(t,\Sigma_t(\boldsymbol{x})\bigr),$$

i.e. the composition operator  $\circ$  applies to the space-component of F. This notation is used for every functions of time and space.

<sup>2</sup>using the fact that

$$(\partial_t \Psi_t^{-1})(t, \boldsymbol{x}) = -\boldsymbol{v}(t, \boldsymbol{x}) \cdot \boldsymbol{\nabla}_{\boldsymbol{x}} \Psi_t^{-1}(\boldsymbol{x}),$$

which can be proved easily from

$$\Psi_t \circ \Psi_t^{-1} = 1.$$

<sup>3</sup>We recall that  $\boldsymbol{c} = \boldsymbol{u} - \boldsymbol{v}$ .

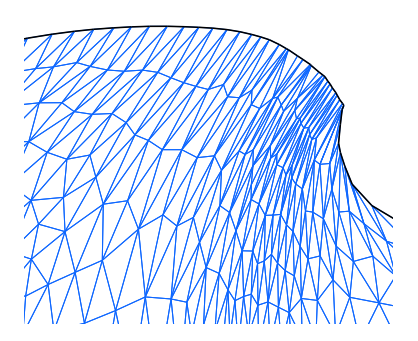


Figure 3.12 – As the mesh moves, some triangles get elongated, as in this (exaggerated) example. If no remeshing procedure is implemented, this eventually leads to triangles being reversed.

<sup>1</sup>For convenience, we omit the fact that  $\delta t^n$  varies between time steps, therefore only writing  $\delta t$  instead. Modifications to include an iteration-dependent time-step are straightforward.

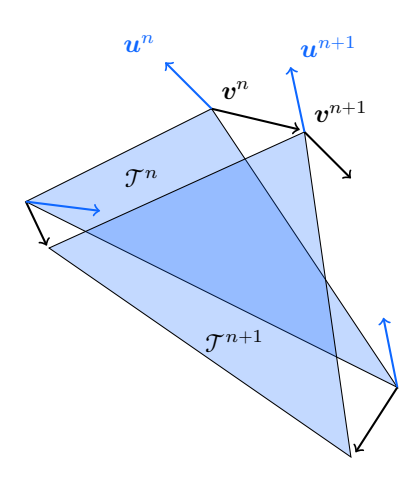


Figure 3.13 – A triangle  $\mathcal{T}^n$  after n time iterations moves with a chosen velocity  $\mathbf{v}^n$  and becomes  $\mathcal{T}^{n+1}$  at the (n+1)th iteration. The physical velocity  $\mathbf{u}^n$  (blue arrows) at time n is discretised at the vertices of  $\mathcal{T}^n$  while  $\mathbf{u}^{n+1}$  is associated with  $\mathcal{T}^n$ .

# II.2. Numerical analysis of the ALE scheme and implementation

Having obtained the master ALE equation (3.7), we discuss how it yields an efficient and useful numerical method. As already emphasised, in our case we are interested in having a lagrangian advection scheme for the boundary points lying on the free surface. To do so, however, all the points of the mesh must be advected at a velocity  $v^n$ . The choice of  $v^n$  is of fundamental importance to prevent the mesh's simplexes to get deformed too much (fig. 3.12). Before discussing the choices that were made in our case, we discuss the implementation scheme.

We can summarise the most basic, first order, ALE scheme as follows. Having computed the mesh velocity  $\boldsymbol{v}^n$  after n time iterations, we replace the spurious term  $(\partial_t \boldsymbol{U}) \circ \Psi_t^{-1}$  in (3.7) by a forward Euler scheme for  $\boldsymbol{u}$ , <sup>1</sup>

$$(\partial_t oldsymbol{U}) \circ \Psi_t^{-1} \sim rac{oldsymbol{u}^{n+1} - oldsymbol{u}^n}{\delta t}.$$

Then, the mesh is advected using a simple scheme: each vertex  $x_i$  is incremented with velocity  $v^n$  so that its coordinates become

$$\boldsymbol{x}_i \longrightarrow \boldsymbol{x}_i + \delta t \ \boldsymbol{v}^n(\boldsymbol{x}_i).$$

Therefore, at the end of the time iteration, the vector  $\boldsymbol{u}^{n+1}$  does not represent  $\boldsymbol{u}(t+\delta t,\boldsymbol{x})$  but the quantity

$$u(t + \delta t, x + \delta t \ v(t, x))$$

instead (fig. 3.13).

We can then formally show that such numerical scheme is first-order in time. Indeed,

$$\begin{split} \frac{\boldsymbol{u}^{n+1} - \boldsymbol{u}^n}{\delta t} &\sim \frac{1}{\delta t} \Big[ \boldsymbol{u} \Big( t + \delta t, \boldsymbol{x} + \delta t \ \boldsymbol{v}(t, \boldsymbol{x}) \Big) - \boldsymbol{u} \Big( t, \boldsymbol{x} \Big) \Big] \\ &= \frac{1}{\delta t} \Big[ \boldsymbol{u} \Big( t + \delta t, \Psi_t \circ \Psi_t^{-1} + \delta t \ \partial_t \Psi_t \circ \Psi_t^{-1} \Big) - \boldsymbol{u} \Big( t, \boldsymbol{x} \Big) \Big] \\ &= \frac{1}{\delta t} \Big[ \boldsymbol{u} \Big( t + \delta t, \Psi_{t + \delta t} + O(\delta t^2) \Big) \circ \Psi_t^{-1} - \boldsymbol{u} \Big( t, \boldsymbol{x} \Big) \Big] \\ &= \frac{1}{\delta t} \Big[ \boldsymbol{U} \Big( t + \delta t, \boldsymbol{\cdot} \Big) - \boldsymbol{U} \Big( t, \boldsymbol{\cdot} \Big) \Big] \circ \Psi_t^{-1} + O(\delta t) \\ &= \partial_t \boldsymbol{U}(t, \boldsymbol{\cdot}) \circ \Psi_t^{-1} + O(\delta t). \end{split}$$

This rather formal computation does not constitute a rigorous proof of the scheme's order. For instance, it was assumed that  $\Psi_{t+\delta t} \circ \Psi_t^{-1}$  is a well-defined quantity. Carrying out a full mathematical justification of this method would be an interesting future work. We could not find any such rigorous treatment in the literature.

Another interesting open question is concerned with a possible second-order ALE scheme, using a second-order Finite Difference formula for  $\boldsymbol{u}$  and a second-order advection scheme for the points of the mesh  $\mathcal{T}^h(\Omega^n)$ .

The first-order nature of the ALE scheme somehow explains the discrepancy we have observed with the Crank-Nicolson scheme described in I.2.2. It has been observed that this formulation does not preserve the energy, even after removing the viscous dissipation which can be

<sup>&</sup>lt;sup>2</sup>It also provides the consistency of the scheme.

computed explicitly (see chapter 4). This is because the ALE scheme introduces numerical dissipation.

So far, the ALE method was discussed to discretise the velocity equation. It can be easily extended to any evolution equation with a transport term. For instance, should we be interested in compressible fluids, the equation for density would be transformed as

$$\partial_t \rho + \boldsymbol{u} \cdot \boldsymbol{\nabla} \rho = 0 \longrightarrow \partial_t \rho + \boldsymbol{c} \cdot \boldsymbol{\nabla} \rho = 0.$$

Another way to obtain the ALE formulation of the problem at hand is to replace  $u^{n+1}$  in the time-discretised Navier-Stokes equation,

$$\frac{\boldsymbol{u}^{n+1} - \boldsymbol{u}^n}{\delta t} + \boldsymbol{u}^n \cdot \nabla \boldsymbol{u}^{n+1} = -\nabla p^{n+1} + \nu \Delta \boldsymbol{u}^{n+1} + \boldsymbol{g},$$

by  $\boldsymbol{u}(t+\delta t,\boldsymbol{x})$ . In that case, the missing term<sup>1</sup> arises naturally. This shorter "proof" does not say anything about the continuous problem. Therefore we chose to follow a different path.

 $^{1}i.e.$  the mesh velocity term  $-\boldsymbol{v}\cdot\boldsymbol{\nabla}\boldsymbol{u}^{n+1}.$ 

#### II.3. Two special choices of mesh velocities

Gathering all the considerations above, the implicit formulation of the problem that is actually numerically treated using the FEM at each time iteration is the following.

Given a  $\delta t^n > 0$  and a state  $(\boldsymbol{u}^n, p^n)$ , find  $\boldsymbol{u}^{n+1} \in \boldsymbol{H}^1_{\Gamma_b}(\Omega(t))$  and  $p^{n+1} \in L^2(\Omega(t))$  such that

$$\int_{\Omega^{n}} \left[ \boldsymbol{v} \cdot \frac{\boldsymbol{u}^{n+1} - \boldsymbol{u}^{n}}{\delta t^{n}} + \boldsymbol{v} \cdot \left( \boldsymbol{u}^{n} - \boldsymbol{v}^{n} \right) \cdot \boldsymbol{\nabla} \boldsymbol{u}^{n+1} + \frac{2}{\text{Re}} \left[ \mathbf{S}(\boldsymbol{v}) : \mathbf{S}(\boldsymbol{u}^{n+1}) - p^{n+1} \boldsymbol{\nabla} \cdot \boldsymbol{v} - q \boldsymbol{\nabla} \cdot \boldsymbol{u}^{n+1} - \boldsymbol{v} \cdot \boldsymbol{g} \right] d\boldsymbol{x} = 0, \quad (3.8)$$

for all  $\boldsymbol{v} \in \boldsymbol{H}^1_{\Gamma_h} \big( \Omega(t) \big)$  and  $q \in L^2(\Omega(t))$  and at all time  $t \in [0,T]$ .

We have emphasised the ALE correction in blue. This formulation is then cast into a finite-dimensional system using the method described in section I.3.3.

Unsurprisingly, if we choose  $\boldsymbol{v}^n=0$ , we recover the eulerian formulation of the problem. However the free-surface kinematic condition is not satisfied in that case: the water–void interface must move. To obtain this movement, two different methods were used, both with their strengths and weaknesses.

II.3.1. The elliptic mesh velocity problem. (Ell) Whenever the bottom topography is non-trivial (as in chapter 5 below), it is preferable to have non-moving vertices on the domain's bed. In this way, we prevent spurious, non-physical, geometrical deformations.

A way to build a mesh velocity  $v^n$  enjoying the features we are looking for, is to solve, numerically, at each time iteration, the following elliptic problem,<sup>2,3</sup>

$$\begin{cases}
\Delta \mathbf{v}^n = 0 & \text{in } \Omega^n \\
\mathbf{v}^n = \mathbf{u}^n & \text{on } \Gamma_i^n \\
\mathbf{v}^n = 0 & \text{on } \Gamma_b.
\end{cases}$$
(3.9)

In this manner, the advection is Eulerian on the bed  $\Gamma_b$  and Lagrangian on the interface  $\Gamma_i^n$ . The corresponding variational formulation is obtained readily.  $\mathbb{P}^1$  elements are used for this problem, yielding a

 $<sup>{}^2\</sup>Gamma^n_i$  being the free surface after n time steps.

 $<sup>^{3}</sup>$ We recall that periodic boundary conditions are used in the x direction.

<sup>1</sup>In fact, should we treat the non-linear term of the Navier-Stokes system explicitly, the stiffness matrix would be the Stokes' matrix, regardless of the chosen mesh velocity. However, this numerical treatment quickly led to in-

<sup>2</sup>Such algorithm cannot be easily implemented in FreeFEM since a direct access to the mesh is not currently permitted.

stabilities of numerical nature.

 $^3$  For the sake of completeness, we mention that the non-vanishing integrals can be computed using an exact Gauß quadrature since, by definition, the terms  $\phi_j \circ \Phi_k$  and  $\phi_i \circ \Phi_k$  are mere low-order polynomial in the reference simplex  $\mathring{\mathcal{T}}$ .

<sup>4</sup>We see from Reynolds' transport lemma 1.1 that the volume of an element being transported along such field does not change. This particularity is sometimes used to define a divergence-free vector field.  $dN_v \times dN_v$  matrix. Since the Navier-Stokes problem's matrix is of size  $(d(N_v+N_e)+N_v)^2,$  the cost of solving the mesh velocity problem is small compared to the Navier-Stokes problem's associated cost. This method has only been tested in 2d yet, but its 3d extension seems mandatory to consider non-flat topographies.

II.3.2. The fully Lagrangian problem. (Lag) Another choice can be made:  $\mathbf{v}^n = \mathbf{u}^n$ . This completely eliminates the non-linear term in the formulation (3.8), yielding the matrix usually associated with Stokes' equation, which is symmetric positive definite.<sup>1</sup>

The downfall of the fully lagrangian mesh advection is that, with Navier boundary conditions (1.14), the fluid elements are free to slip along the bottom boundary. While theoretically this does not cause any issue, having a small but finite time step could lead to elements not following the bed's geometry perfectly. This spurious deformation of the bottom boundary could be easily bypassed with a geometry-preserving slipping algorithm.<sup>2</sup>

A surprising aspect of the lagrangian mesh advection scheme, and more generally shared by every solenoidal velocities  $v^n$ , is that the stiffness matrix  $\mathbf{A}$  does not need to be recomputed at each time iteration. Indeed, schematically speaking, each term appearing in this matrix is a bilinear term of the form

$$\mathbf{A}_{i,j} = \int_{\mathcal{T}^h(\Omega^n)} \phi_i \phi_j.$$

During the matrix assembly, this integral is computed on every simplex separately using the reference simplex  $\mathring{\mathcal{T}}$ ,

$$\begin{split} \mathbf{A}_{i,j} &= \sum_{k=1}^{N_t} \int_{\mathcal{I}_k^h} \phi_i(\boldsymbol{x}) \phi_j(\boldsymbol{x}) \, \mathrm{d}\boldsymbol{x} \\ &= \sum_{k=1}^{N_t} \int_{\hat{\mathcal{I}}} \left( \phi_i \circ \Phi_k(\boldsymbol{y}) \right) \! \left( \phi_j \circ \Phi_k(\boldsymbol{y}) \right) \cdot \det \! \left( \boldsymbol{\nabla} \Phi_k(\boldsymbol{y}) \right) \mathrm{d}\boldsymbol{y}. \end{split}$$

Fortunately, the support of the basis functions  $\phi_j$  and  $\phi_i$  being spread over a few triangles only, the terms  $\phi_j \circ \Phi_k$  and  $\phi_i \circ \Phi_k$  often vanish so that only a reduced amount of term actually contribute to the above sum.<sup>3</sup> In 2d, we can see from (3.4) that  $\det(\nabla \Phi_k(\boldsymbol{y}))$  corresponds to (a constant multiple of) the triangle's area,

$$\det \left( \boldsymbol{\nabla} \Phi_k(\boldsymbol{y}) \right) = (a_{k,1} - c_{k,1}) (b_{k,2} - c_{k,2}) - (a_{k,2} - c_{k,2}) (b_{k,1} - c_{k,1}).$$

A similar result also holds in 3d. The mesh being transported along a solenoidal vector field, this last quantity does not vary throughout the simulation. This observation also applies to terms involving derivatives of  $\phi_j$ , and even to any other finite element basis functions product. Therefore, the quantity  $\mathbf{A}_{i,j}$  represent the correct quantity at all time. This observation saves non-negligible computational times in every simulation. This does not apply to the elliptic mesh advection scheme of sec. II.3.1 above, however. This also does not prevent the triangles getting elongated, as already discussed. This last issue is solved by recomputing, or adapting, the mesh, as will be discussed in the next section.

We have now described thoroughly our method to solve the freesurface Navier-Stokes system (1.54) with a Lagrangian interface advection scheme. The algorithm 3.1 contains a pseudo-code implementation.

```
Algorithm 3.1: Breaking Waves simulator
```

```
input: An initial time t
                 A final time T > t
                 An advection method advection method (elliptic II.3.1 or lagrangian II.3.2)
                 A time-stepping scheme time_scheme (implicit Euler I.2.1 or Crank-Nicolson I.2.2)
    output: A final mesh final_mesh
                 A final state final_state
 n \leftarrow 0;
                                                                                              /* Number of time iterations */
 2 \text{ mesh}(n=0) \leftarrow \text{ReadInitialMesh}(t);
                                                                                                                   /* Initial mesh */
 \mathbf{3} \ (\mathbf{u}^0, p^0) \leftarrow \text{ReadInitialState}(t) ;
                                                                                       /* Initial velocity and pressure */
 4 mesh(n) \leftarrow AdaptMesh(\mathbf{u}^0, p^0);
                                                                            /* Adapt the mesh to the current state */
 \mathbf{v}^0 is initialised:
                                                                                                                  /* Mesh velocity */
 6 A \leftarrow CreateNavierStokesMatrix(mesh(0), \mathbf{u}^0, p^0, \mathbf{v}^0, advection_method,time_scheme)
 7 while t < T do
         /* Beginning the time loop
                                                                                                                                               */
         \delta t^n \leftarrow \texttt{ComputeDT}(\texttt{mesh}(n), \mathbf{u}^n);
 8
 9
         t \leftarrow t + \delta t^n;
         /* Mesh advection (elliptic or lagrangian depending on the user's choice)
         if advection_method is elliptic then
10
              \mathbf{v}^n \leftarrow \text{numerical solution of (3.9)};
11
              A \leftarrow \text{CreateNavierStokesMatrix}(\text{mesh}(n), \mathbf{u}^n, p^n, \mathbf{v}^n, \text{advection\_method,time\_scheme});
12
         else
13
          | \mathbf{v}^n \leftarrow \mathbf{u}^n;
14
         mesh(n+1) \leftarrow AdvectMesh(mesh(n), \delta t^n, \mathbf{v}^n);
15
         /* Solving the Navier-Stokes problem
                                                                                                                                               */
         \begin{aligned} & \mathsf{rhs} \leftarrow \begin{bmatrix} \mathbf{g} \\ 0 \end{bmatrix} + \begin{bmatrix} \mathbf{M} & 0 \\ 0 & 0 \end{bmatrix} \begin{bmatrix} \mathbf{u}^n \\ p^n \end{bmatrix}; \\ & \begin{bmatrix} \mathbf{u}^{n+1} \\ p^{n+1} \end{bmatrix} \leftarrow \mathbf{A}^{-1} \; \mathsf{rhs} \; ; \end{aligned}
16
                                                                                       /* Navier-Stokes right-hand side */
                                                                                                        /* Solving the problem */
17
         SaveRestartFiles(mesh(n+1),\mathbf{u}^{n+1},p^{n+1});
18
         n \leftarrow n + 1;
19
20 final_mesh \leftarrow mesh(n);
21 final_state \leftarrow (\mathbf{u}^n, p^n);
```

# III. Implementation

We would now like to discuss the implementation of algorithm 3.1. It is done using the FreeFEM c++ interface. Through the time, the underlying method did not change but many optimisations were made. We try to describe them concisely here. We shall use references to this section in order to keep track of which method has been used to obtain the scientific results presented in the following chapters.

#### III.1. Recomputing the mesh

We already mentioned that, as a simulation goes on, the triangles get spuriously elongated (fig. 3.12, up). To solve this issue, two methods were used.

III.1.1. **Periodic Remeshing.** (PR) In the code that was used to obtain the results of Riquier and Dormy (2024b), the mesh is fully recomputed after a physical-time interval has elapsed.<sup>2</sup> When doing

<sup>5</sup>The underlying idea of doing the computations on a non-moving mesh corresponding to the Lagrangian frame is closely related to the Characteristic Mapping Method (CMM) (Krah et al. 2024; Yin, Mercier, et al. 2021; Yin, Schneider, et al. 2023)

<sup>1</sup>Hecht (2012)

<sup>&</sup>lt;sup>2</sup>This is done whenever output data are generated.

<sup>1</sup>leading to the uneven triangle density that can be seen at the left of figure 3.4 for instance. so, the interface points that moved out of the  $[0, L] \times \mathbb{R}$  box (due to lagrangian interface advection), are recast into this very box. The difficulty is that the new mesh generated in this manner does not encompass the former. Therefore the interpolation of the physical variables in the new mesh is quite tedious: it must be done invoking the periodicity in the x-direction. Unfortunately, when this is done, some artifacts appear near the left and right boundaries of the domain<sup>1</sup>. By chance, this did not yield any such artifact on the breaking region but it led us to drop out this method afterward.

III.1.2. **Mesh adaptation.** (MA) A better remeshing procedure is to adapt the mesh to the solution.<sup>2</sup> This must, however, be done with prior knowledge of the solution. For example, a straightforward mesh adaptation to an initially irrotational velocity would prevent the mesh to fully resolve a hypothetical boundary layer (*i.e.* a parabolic region in the flow) appearing at subsequent time.<sup>3</sup>

The solution that has been implemented is to adapt the mesh with respect to the velocity, pressure, and a third function f that varies quickly near the boundaries  $\Gamma(t) \subseteq \partial \Omega(t)$  on which many triangles are needed,

$$f(\boldsymbol{x}) = \exp\Bigl(-C \, \operatorname{dist}\bigl(\boldsymbol{x}, \Gamma(t)\bigr)\Bigr),$$

with C>0 a numerical factor controlling the number of triangles on the boundary after adaptation. It is related to the number of triangles on the same boundary before adaptation. The adaptation boundary  $\Gamma(t)$  is user-chosen. An example of such adapted mesh is visible in fig. 3.14 (to compare with the non-optimised mesh of fig. 3.4 which was computed with the **PR** method). In our cases, switching to the **MA** method successfully divided the number of degrees of freedom by roughly 4. Without this method, a 3d simulation would not be tractable.

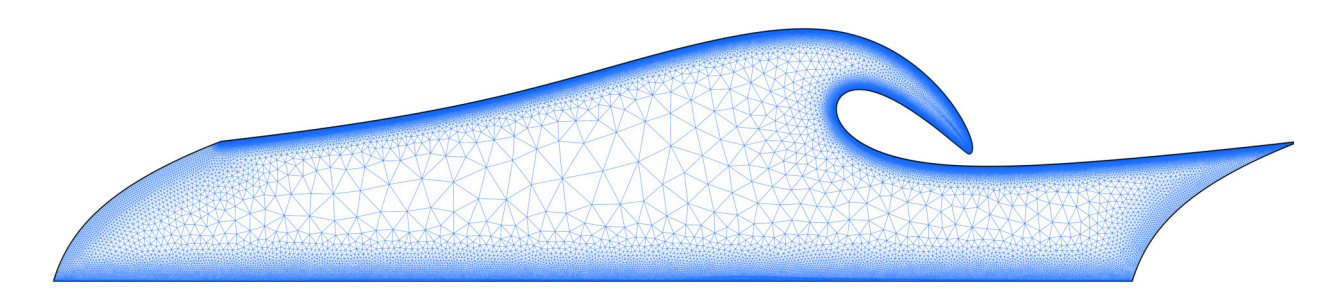


Figure 3.14 – A fine adapted mesh corresponding to a breaking wave simulation with a boundary layer on the bed (chap. 4) at Re =  $10^5$ . It contains  $N_v = 59\,532$  vertices,  $N_t = 117\,729$  triangles and  $N_e = 174\,258$  edges.

#### III.2. Parallelisation

Even with an optimised mesh, the number of degrees of freedom needed to carry out the simulations with the highest Reynolds number remains too high to work on a single thread. By chance, FreeFEM possesses a native interface with the PETSc<sup>4</sup> c++ library and native high performance domain decomposition methods.<sup>5</sup>Two different parallelisation schemes were used for the 2d code and a third one was implemented for the 3d case.

<sup>&</sup>lt;sup>2</sup>This method was suggested to the author by Georges Sadaka in May 2024.

<sup>&</sup>lt;sup>3</sup> A common issue with mesh adaptation is that, while it is well-suited for hyperbolic problems, for which the information travels at finite speed, it cannot guess where the information will lie in parabolic or elliptic problems. Usually, iterative methods are employed to bypass this issue but they are computationally costly.

<sup>&</sup>lt;sup>4</sup>Portable, Extensible Toolkit for Scientific Computation, see Balay, Abhyankar, et al. (2021a,b) and Balay, Gropp, et al. (1997)

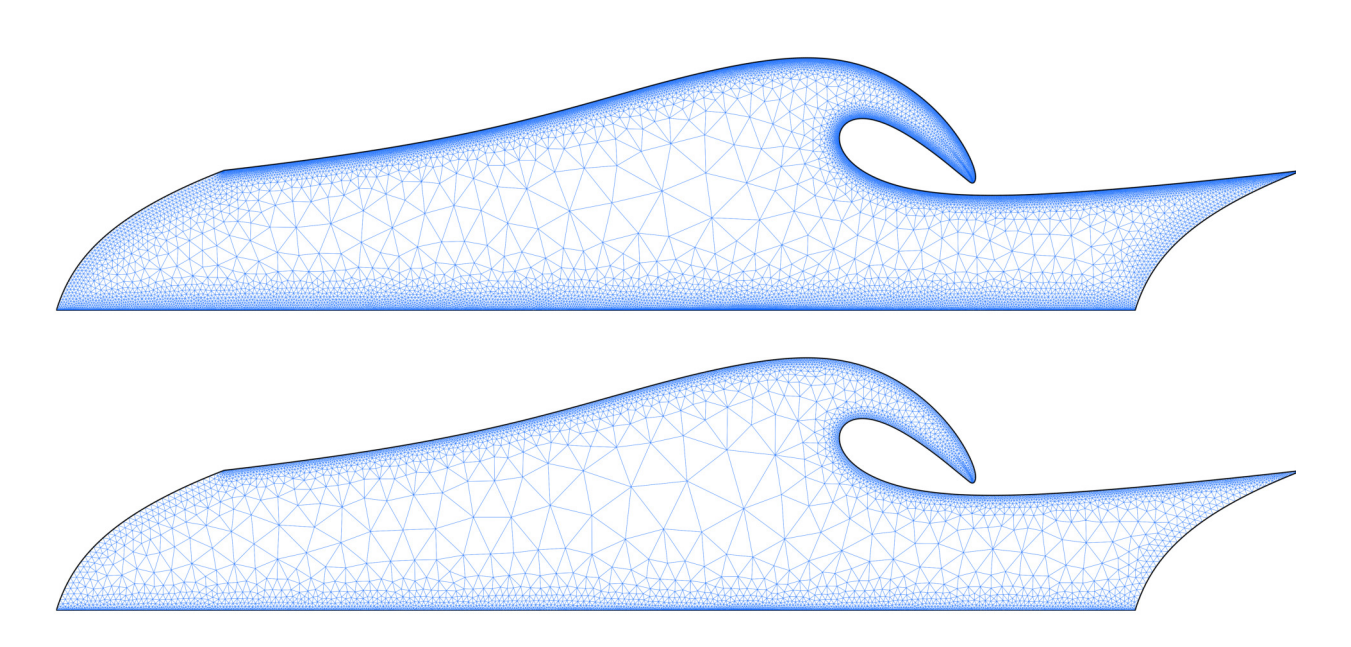


Figure 3.15 – The coarse meshes computed from the fine mesh of fig. 3.14. The mid-level mesh (up) contains  $N_v=25\,854$  vertices,  $N_t=47\,947$  triangles and  $N_e=73\,798$  edges. The coarsest-level mesh (down) contains  $N_v=10\,486$  vertices,  $N_t=17\,935$  triangles and  $N_e=28\,418$  edges.

Before discussing these method, we introduce the paradigm of multithreaded algebraic system solving. When one wants to solve the  $N \times N$ algebraic system (3.3), its is in fact completely equivalent to solve one of the *preconditioned* systems

$$\mathbf{P}^{-1}\mathbf{A}\mathbf{x} = \mathbf{P}^{-1}\mathbf{b}$$
 or 
$$\begin{cases} \mathbf{A}\mathbf{P}^{-1}\mathbf{y} &= \mathbf{b} \\ \mathbf{P}\mathbf{x} &= \mathbf{y}, \end{cases}$$
 (3.10)

with  $\mathbf{P}$  an invertible  $N \times N$  matrix that is, hopefully, easy to invert and which makes the product  $\mathbf{AP}^{-1}$  or  $\mathbf{AP}^{-1}$  quickly invertible. The left (respectively right) application of  $\mathbf{P}^{-1}$  is called *left-preconditioning* (res. *right-preconditioning*).

III.2.1. LU decomposition. (LU) Notice that, should we choose P = A in (3.10), then we obtain the desired solution. In a sense, A is the best preconditioner that can be chosen when it is easy to invert. In 2d, when the number of degrees of freedom is not too high, its is still possible to invert A directly using a parallel LU decomposition. This is done here using the MUMPS library. In 3d, the matrix assembly sometimes fails due to a lack of memory. This behavior was expected: it has already been observed in "large" 3d problems in, e.g. Nataf and Tournier (2023).

III.2.2. Non-nested geometric multigrid. (GMG) As the size of the system increases, any direct factorisation method like (LU) becomes slower.<sup>2</sup> In such case, iterative methods are prefered. The (flexible) GMRES algorithm<sup>3</sup> is chosen since we cannot always assure that the stiffness matrix is symmetric.

A preconditioner  $\mathbf{P}$  based on a Domain Decomposition Method (DDM) is chosen. The simplest of such preconditioner is arguably the Additive Schwarz Method  $(ASM)^{4,5}$ in which, loosely speaking, each MPI core solves the problem on a subregion of the mesh (also called a subdomain). The major difficulty is that the number of GMRES

<sup>&</sup>lt;sup>5</sup>Dolean et al. (2015), Jolivet, Hecht, et al. (2013), Jolivet, Roman, et al. (2021), and Jolivet and Tournier (2016)

<sup>&</sup>lt;sup>1</sup>MUltifrontal Massively Parallel sparse direct Solver, see Amestoy, Buttari, et al. (2019) and Amestoy, Duff, et al. (2001).

<sup>&</sup>lt;sup>2</sup>Computing the inverse of a  $N \times N$  matrix is done typically in  $O(N^3)$  operations.

<sup>&</sup>lt;sup>3</sup>Generalised Minimal RESidual (Saad and Schultz 1986).

<sup>&</sup>lt;sup>4</sup>Schwarz (1870)

<sup>5</sup>see the books of Dolean et al. (2015, ch. 1) and Mathew (2008, ch. 2) for comprehensive treatment of the subject.

<sup>1</sup>In practice, the two coarse levels are constructed through adaptation of the fine mesh shown in fig. 3.14.

<sup>2</sup>This last assertion has been verified up to 64 cores. This remains rather low.

<sup>3</sup>For technical reasons, storing only the decomposed mesh is not yet feasible. In all case, the global mesh must be created at some point and creating a coarse mesh globally before splitting it locally would lead to the cumbersome question of the interface precision. The author knows a way to solve this memory problem but did not implement it yet (doing so in FreeFEM would be difficult).

<sup>4</sup>see the review article of Xu and Zikatanov (2017, sec. 10) for a comprehensive (and complete) introduction.

iterations needed to converge to the solution increases with the number of MPI cores. This is due to the information taking more and more time to reach far subdomains (Bueler 2020). Introducing a so-called coarse correction usually prevents this problem to arise. The idea is to couple the problem at hand with a smaller subproblem which will allow the information to be transmitted quicker. Two types of coarse corrections have been used: one in 2d and another in 3d.

In 2d, a two-levels Geometric Multigrid method is utilised. Instead of computing only one mesh  $\mathcal{T}^h(\Omega^n)$  from the continuous domain  $\Omega^n$ , three triangulations are computed. Roughly speaking, this corresponds to building three meshes  $\mathcal{T}^{h_1,h_2,h3}(\Omega^n)$ , with  $h_1>h_2>h_3.^1$  Interpolations between two levels are handled by FreeFEM directly. These meshes are plotted in fig. 3.15.

In broad outline, to solve the Navier-Stokes problem on the fine mesh, the problem is first solved on the coarse mesh. After fine-tuning the coarse solver, this is usually done in about 50 ASM iterations on 32 MPI cores. Then, using this coarse solution as a preconditioner, a thiner one is computed on the middle mesh. Finally, using the middle (level one) solution to precondition the fine system completes one GM-RES iteration. With this method, the GMRES procedure converges to machine precision in  $6 \pm 2$  iterations, regardless of the number of MPI cores.<sup>2</sup>

III.2.3. Fieldsplitting and algebraic multigrid. (FS&AMG) In 3d, storing three meshes would be quite a burden.<sup>3</sup> Therefore the (GMG) method has been dropped out. Instead, we take advantage of the block-nature of the stiffness matrix.

A Schur complement–based fieldsplit solver is used to incorporate the divergence-free constraint. The pressure solver is a simple LU factorisation method while the velocity block makes use of the Geometric Algebraic Multigrid method (GAMG) implemented natively in PETSc.<sup>4</sup> By no mean we can state that this solver is optimal. It has, however, successfully provided the few three-dimensional simulations that appear in the present work.

This puts an end to this rather technical section on implementation. We did not want to dwell too much on the intricate details regarding parallelisation as it is not the subject of the present work. However, it seems important to have put in writing a thorough presentation of the method in a document that shall be accessible afterward. We now reward the patient reader with a plot of the 3d mesh corresponding to a breaking wave simulation in fig. 3.16. A description of the simulations that led to the meshes shown in figures 3.4, 3.14 and 3.16 shall be given later in chapter 4.

## IV. Code validation

In order to make sure that the method presented above works and that no mistake has been made when implementing it, some test cases are discussed in this section. As usual when carrying numerical studies, we must ensure that:

1. The numerical solution computed using the code is *identical*, up to some numerical error that should be estimated using the mesh's size h, to the analytical solution of the equations when it exists.

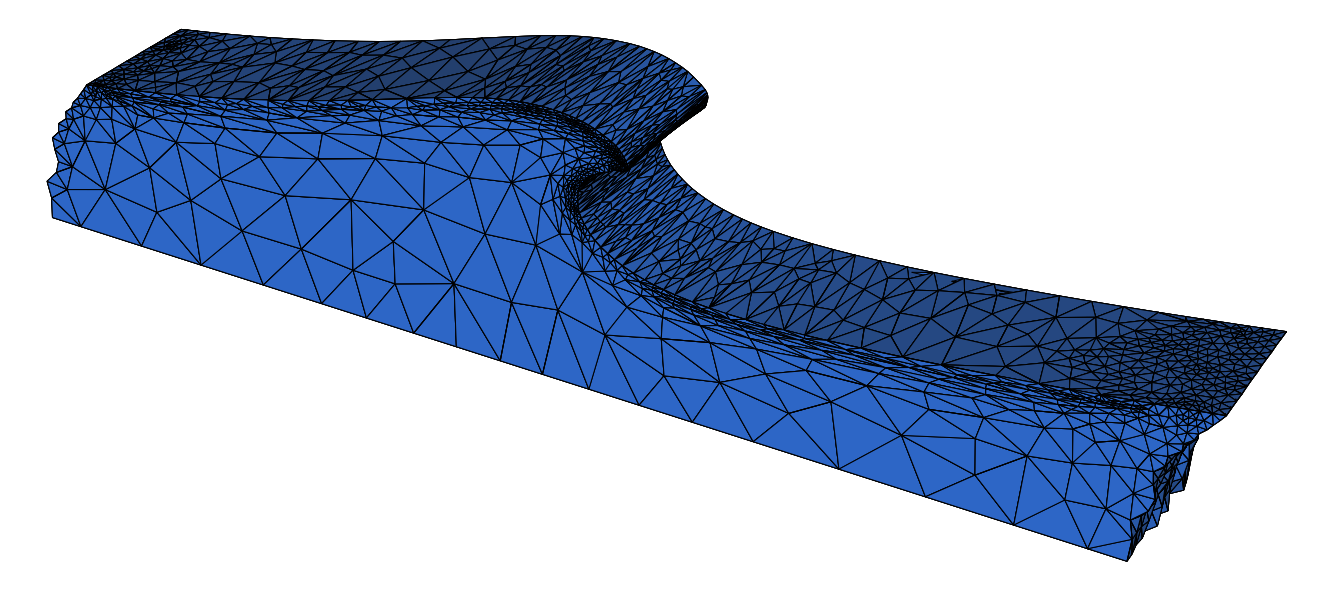


Figure 3.16 – The 3d mesh during a breaking wave simulation. It contains  $N_v = 4\,935$  vertices and  $N_t = 21\,838$  tetrahedra. Looking at the periodic boundaries, it seems that numerical convergence has not been achieved yet.

- 2. When no analytical solution is available, the numerical solution must at least converge to something as the mesh's size decreases,  $h \to 0$ .
- 3. If many other numerical studies based on different schemes were able to obtain similar results, the new method must do so too.

There does not exist any mathematical proof that our numerical scheme is convergent.<sup>1</sup> Even more, the author could not find any mathematical treatment of the ALE method described in sec. II. Therefore, testing our method and its implementation shall be made through numerical experiment and comparisons with analytical solutions and numerical results obtained using a different, independent, code.

## IV.1. Comparison to analytical solutions

Analytical solutions of the viscous water waves equations are scarce. When the viscous effects are small (*i.e.* when the Reynolds number is large), one could argue that the solution should remain close to the inviscid solution. By chance, a solution to the Euler system (1.53) has already been discussed: the linear wave solution<sup>2</sup> (1.25).

In figures 3.17 and 3.18 is shown a comparison between numerical simulations carried out at Re =  $10^5$ , with both the implicit and the Crank-Nicolson time-stepping schemes, and the first order (in  $\varepsilon$ ) solution up to 2 wave periods. The chosen amplitude is a=0.01. A small difference  $\|\eta_h-\eta\|_{L^\infty}\approx 10^{-4}$  between the numerical and theoretical solutions exists. However, as noted in Dormy and Lacave (2024), with such value of the amplitude a, a discrepancy of this intensity is not surprising since second-order terms in Stokes' solution are exactly of order  $\varepsilon^2=10^{-4}$ . We must also point out that both the Crank-Nicolson and the implicit euler time-stepping schemes yield identical results.

At Re =  $10^5$ , the viscous dissipation remains negligible. Indeed, a simple argument presented in §348 of Lamb (1932) shows that the

<sup>&</sup>lt;sup>1</sup>A finite element scheme is called convergent if as  $h \to 0$ , the numerical solution  $(\boldsymbol{u}_h, p_h)$  converges to the actual solution  $(\boldsymbol{u}, p)$  in some precise sense that won't be explicited here (see *e.g.* Temam (1984)).

<sup>&</sup>lt;sup>2</sup>Also corresponding the the first order Stokes wave (Stokes 1847, 1880).

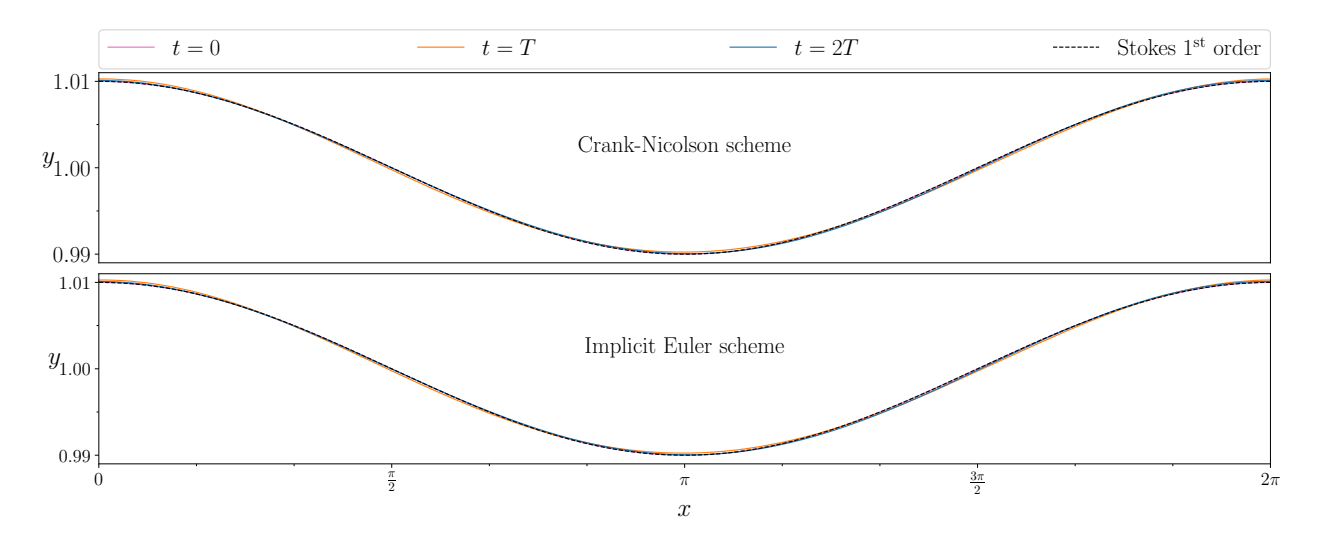


Figure 3.17 – Comparisons of Re =  $10^5$  Navier-Stokes simulations, obtained using the Crank-Nicolson scheme I.2.2 and the implicit Euler scheme I.2.1, with the linear wave analytical solution (1.25) with amplitude a=0.01, at t=T and t=2T, with  $T=2\pi/\omega$  the period. The vertical scale has been greatly exagerated compared to the horizontal one.

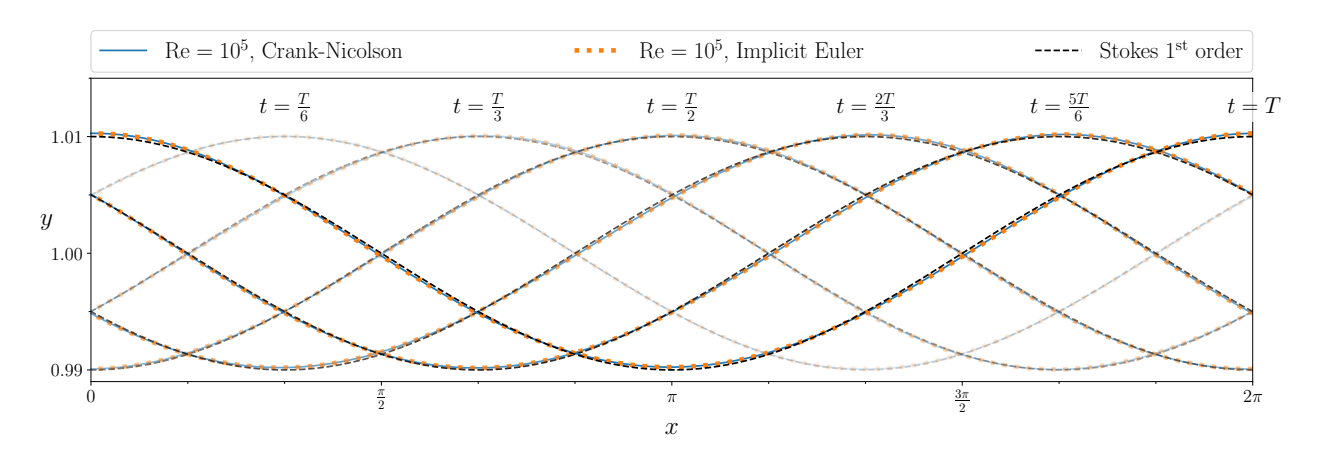
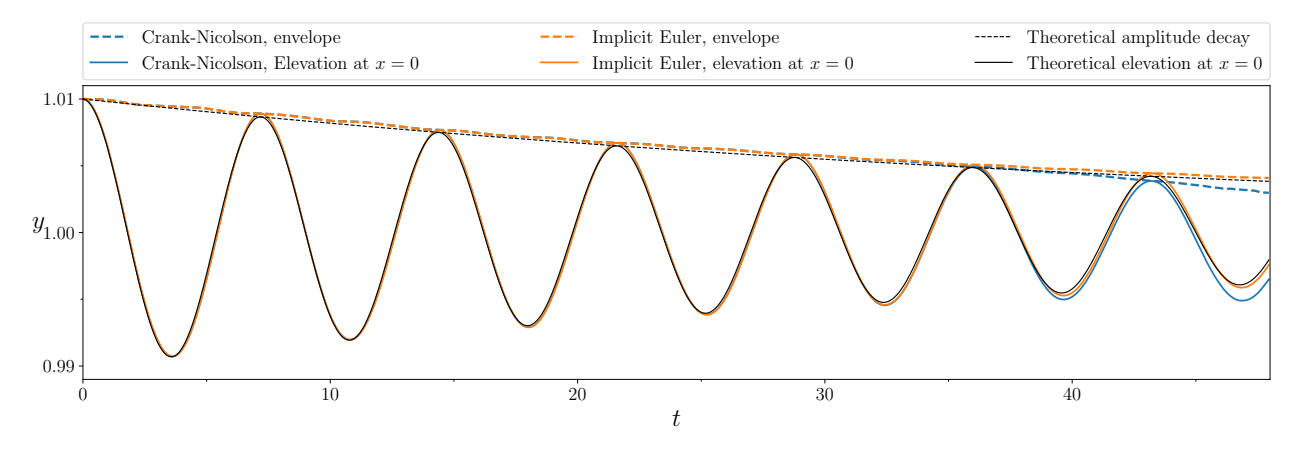


Figure 3.18 – Same as the above figure, but with different snapshots taken during the first period. The vertical scale has been greatly exagerated compared to the horizontal one.



**Figure 3.19** – Numerical simulation of a first order Stokes wave decaying due to viscous effects. The theoretical decay rate is derived in Lamb (1932), §348. The initial with amplitude is a = 0.01 again.

viscous decay rate  $\tau_{\nu}$  of a water waves of first-oder in  $\varepsilon$  is

$$\tau_{\nu} = \frac{\mathrm{Re}}{2k}.$$

The clever idea that leads to this decay rate lies in a simple quantification of the work that must be done to balance out the effects of viscosity. As the rate  $\tau_{\nu}$  grows linearly with the Reynolds number, it is not surprising that the simulation at Re =  $10^5$  can be compared with the inviscid solution.

In order to compare our numerical results with the decay rate presented above, we should let a numerical simulation up to time  $t \sim \text{Re}$ , as in Chen et al. (1999). While this cannot be done at  $\text{Re} = 10^5$  within accessible time, we have done for  $\text{Re} = 10^2$ . This simulation is presented in fig. 3.19. Once again, up to t=35, the difference between the numerical and the analytical solution remains of order  $\varepsilon^2$  so that we cannot distinguish the numerical error from the analytical one. However, at time  $t \sim 35$ , numerical instabilities (not shown) appear in the Crank-Nisolson simulation, leading to the discrepancy observed in fig. 3.19.

We could also try to compare a numerical result with the *cnoidal*-wave solution<sup>1</sup> of the Serre–Green and Naghdi system. This was done in *e.g.* Dormy and Lacave (2024). However, once again this analytical solution is not an exact solution of the Navier-Stokes system (1.54). Therefore we cannot conclude about whether the observed error is of numerical or analytical nature.<sup>2</sup>

#### IV.2. Numerical convergence

In order to ensure that our code converges as  $h \to 0$ , without proof that it does so to the mathematical solution, we increase gradually the number of points (thus decreasing h) on the free surface in a breaking wave simulation with initial datum (4.2) and amplitude a=0.5. This is done in figure 3.20. We readily see that the convergence is rather fast (theoretically in  $O(h^2)$ , as proved in Pironneau (1989)). The Re =  $10^6$  shows instabilities for N=1000 and N=2000, preventing these simulations to be carried out up to the splash.

#### IV.3. Cross-validation

We have at our disposition the Euler-based code of Dormy and Lacave (2024). In chapter 4, we shall investigate the convergence of the Navier-Stokes solution to Euler's solution by comparison of the free surfaces. This is done in fig. 4.6 for instance, starting from the same initial condition (4.2). Aside from the mathematical convergence which will be discussed later, the fact that two different methods yield comparable results shows that both should converge, as the discretisation length is decreased, to the same continuous solution. Indeed, it seems particularly improbable that two completely different numerical methods, trying to solve the same problem, could independently converge to something that is not the mathematical solution.

However, two methods yielding the same result remains not good enough. In the litterature, there exists a benchmark (Helluy et al. 2005) that has been established by several authors using six different numerical methods (based on both Euler's equations or the Navier-Stokes system). However, the results presented therein do not meet

Fig.	$N_{ m top}$	Re	Rem.	Adv.	
3.3 3.4 3.7	3 500	$10^{5}$	PR	Ell	
3.14 3.15	3 500	$10^{5}$	PR	Ell	
3.16	-	$10^{4}$	MA	Lag	

**Table 3.1** – Numerical parameters used for the different simulations appearing in this chapter.

Table 3.1 is the first example of simulation description table that can be seen in the present work. There shall be others in chapters 4 and 5. In such table,  $N_{\rm top}$  corresponds to the number of points on the interface, Re is the Reynolds number, Rem. stands for the remeshing procedure chosen from the two described in sec. III, and Adv. corresponds to the advection scheme chosen (elliptic II.3.1 or lagrangian II.3.2). There is no need to explicit the parallel scheme that has been used: GMG for 2d simulations, and FS&AMG in 3d. Also note that in 3d the number of faces on the free surface is not constant throughout the simulation.

<sup>1</sup>see e.g. Jiang and Bi (2017) for a review.

<sup>2</sup>The conclusion of this section is that we should have used the Implicit Euler scheme in every simulation shown in the present thesis. However, some old ones have been made with the CN scheme and we did not have the time to restart them with the current version of the code.

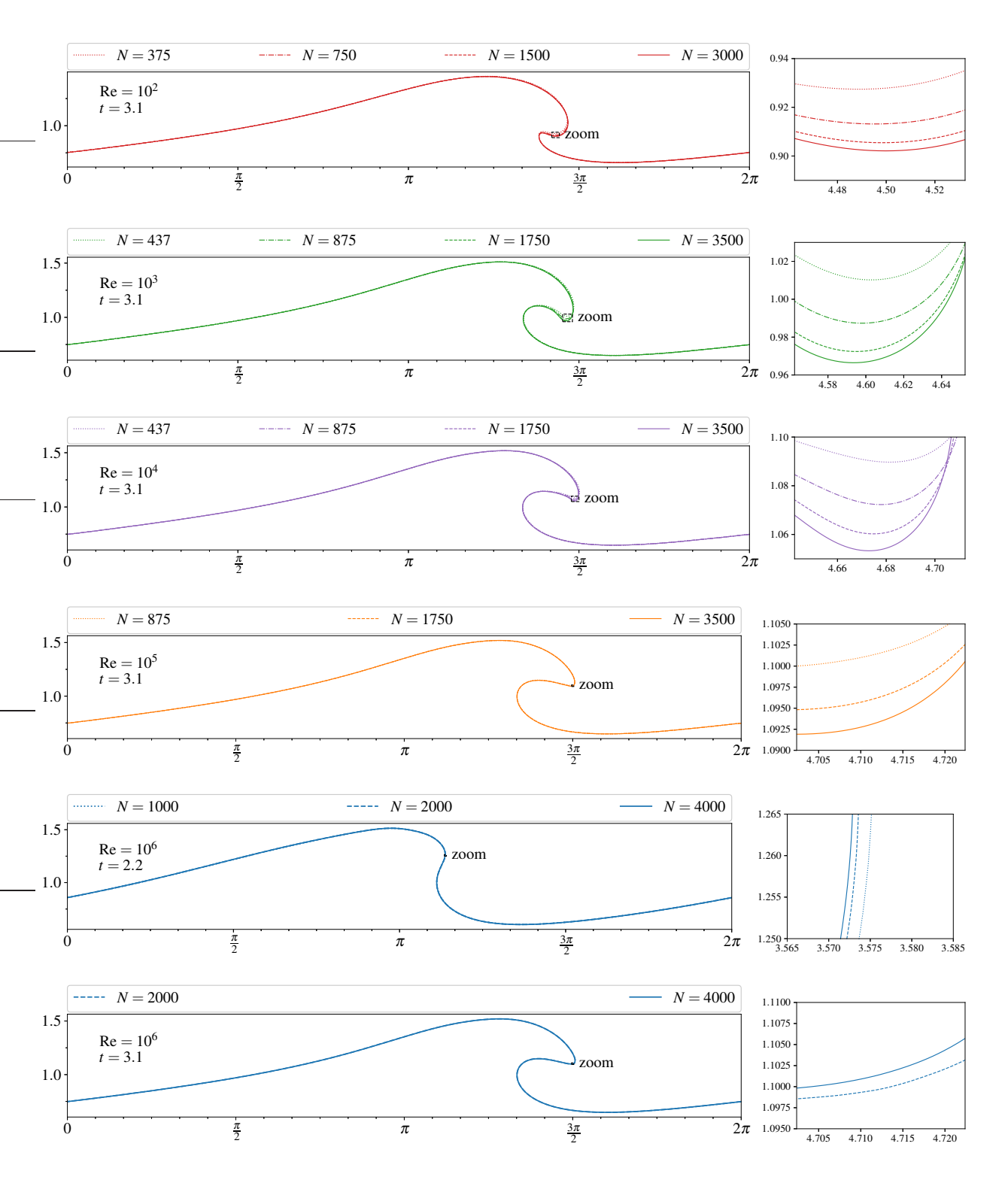


Figure 3.20 – Numerical convergence of the method, starting from the initial condition (4.2) with different values of Reynolds' number and different number of points N on the interface.

today's precision standards: none of their results could provide solutions as close as the one presented in figure 4.6. The author is currently establishing a new benchmark of this kind.

#### IV.4. Validating the 3d code

In order to assess that the three-dimensional version of the code yields correct results, we propose to compare a 3d simulation with a 2d one, starting from an initial datum that does not depend on y, built from the problem (4.1). The comparison between the two is visible in figure 3.21. It is rather clear that numerical convergence has not been achieved yet. However the difference between the two simulations is only attributable to the lack of numerical convergence.

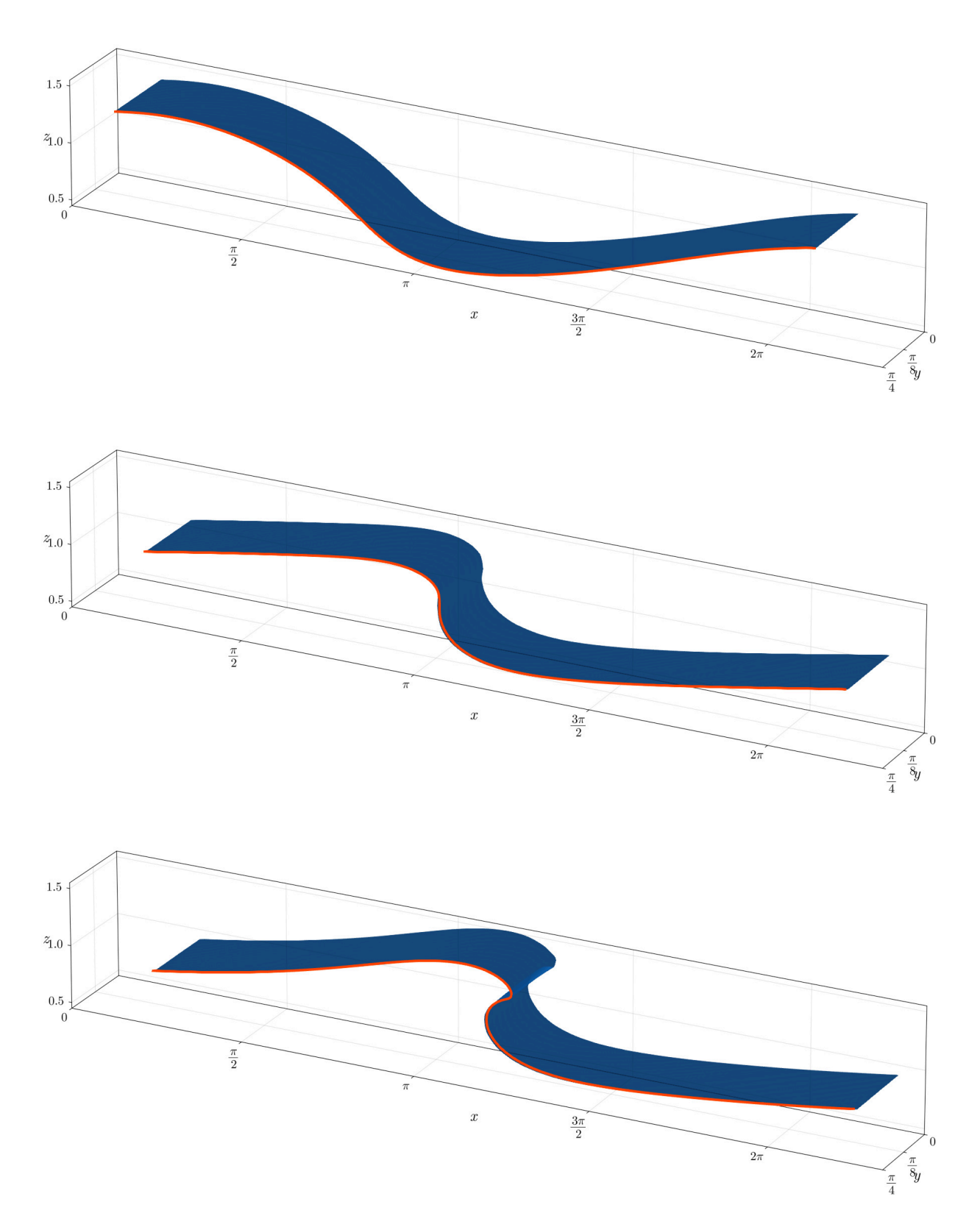


Figure 3.21 – Breaking wave simulation at Re =  $10^4$  for times t=1 (up), t=2 (middle) and t=2.6 (down), in 2d (orange line) and in 3d (blue surface). The initial condition shall be described in sec. I.1.2; the initial potential  $\psi_{\rm in}$  (4.1) is prescribed with an amplitude a=0.5.

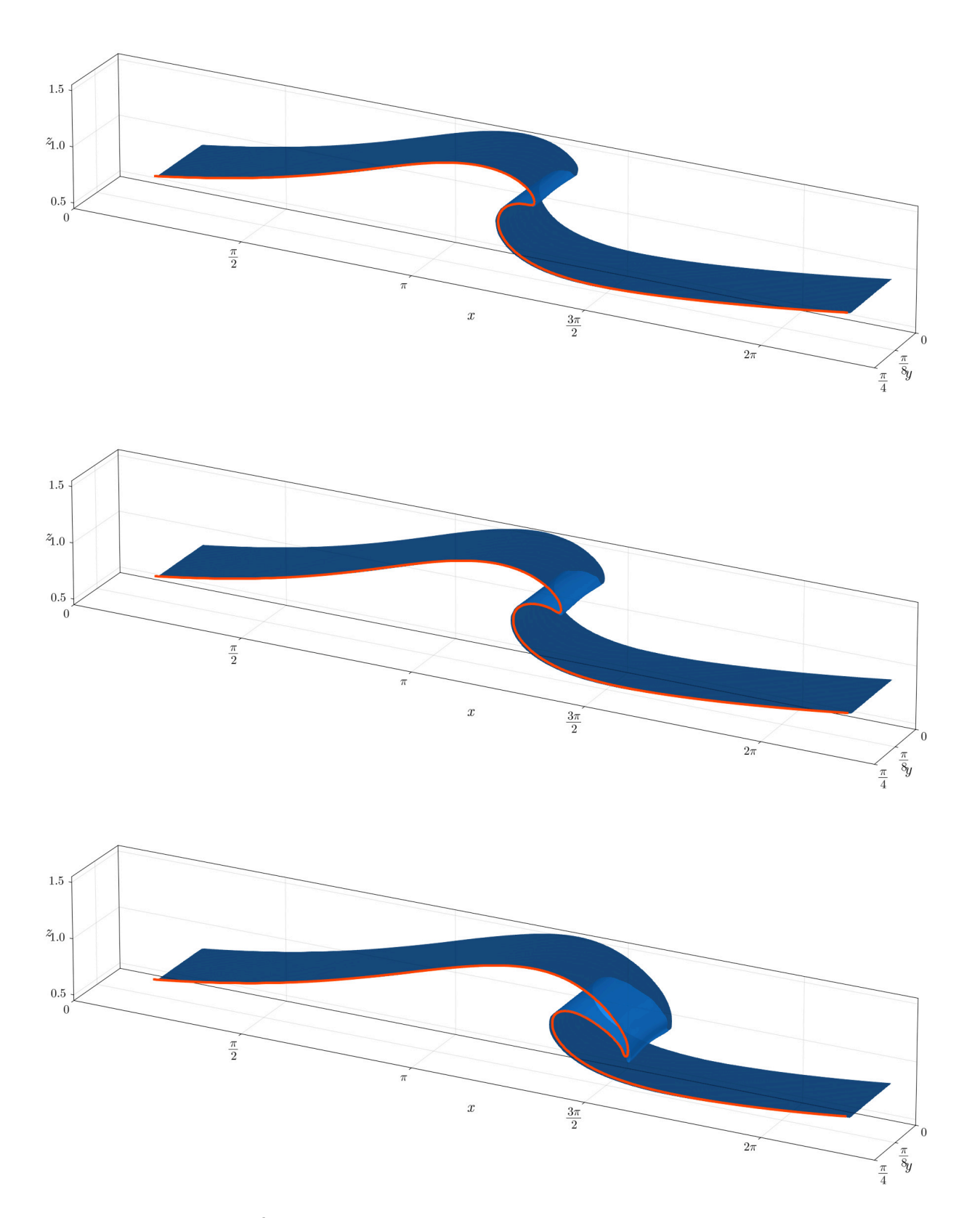


Figure 3.21 –  $\bigcirc$  – Continued, with times t=2.8~(up),~t=3~(middle) and t=3.5~(down).

# Chapter

# Viscosity and the shape of breaking Water Waves

"Might go somewhere sunny, sit on beach, look at ocean, collect seashells. [...] Might run tests on the seashells."

Mordin Solus, In: Mass Effect 3 (2012, dir. C. Hudson)

In the previous chapter, we discussed a numerical methods to solve (numerically) both the Navier-Stokes system (1.54) with a Lagrangian advection scheme for the interface. Using the Euler-based code of Dormy and Lacave (2024), comparing the solutions of both the viscous and inviscid systems as the Reynolds number becomes large is thus achievable.

The present chapter focuses on the viscous dissipation at the free surface, in the case of a breaking wave over a flat topography (on which the slip/Navier (1.14) or the no-slip/Dirichlet (1.15) condition is applied). Numerical experiments shows that, as the Reynolds number is increased, the viscous solution converges to the irrotational Euler solution, starting from an initially irrotational flow. This is due to the superficial, Navier-type, boundary layer (BL) being sufficiently well-behaved.

The value of the Reynolds number is increased up to Re =  $10^6$ . This value has never been achieved before in this context, to the author's knowledge. However, this does not even corresponds the slightest to a "real-world" plunging breaker. It corresponds to a water column of depth  $h_0 \sim 1$  [m]. The chosen initial condition is thus a wave of amplitude  $a \sim 0.5$  [m]. We are still very far from achieving numerical simulation of an overhanging wave of acceptable size, for which Re =  $10^7 \rightarrow 10^9$ .

Aside from the numerics, in the present chapter we also derive formally a link between the curvature of the interface and the size of the boundary layer. This is done through an asymptotic expansion in the BL's size  $\delta = \mathrm{Re}^{-\frac{1}{2}}$ .

# I. Initial conditions for breaking waves

To the author's knowledge, there exists no analytical, irrotational, solution of Euler's free-surface equations (1.53) exhibiting wave breaking. Therefore, no comparison with analytical solution is tractable.

The Stokes first order initial datum, computed from (1.25) setting t=0, does not yield promising results (a simulation with this initial condition is visible in fig. 4.2). Motivated by the idea of reproducing the results of Baker, Meiron, et al. (1982), we provide a general framework for constructing initially irrotational datum and apply it to prescribed velocity potentials or normal velocities that enjoy particular symmetries absent from Stokes' solution (at a given order).

This chapter is based on our study Riquier and Dormy (2024b).

<sup>1</sup>Gertsner's vortical solution (Gerstner 1802) exhibits breaking after a certain amplitude threshold has been passed. However the corresponding interface does not seem to be physical.

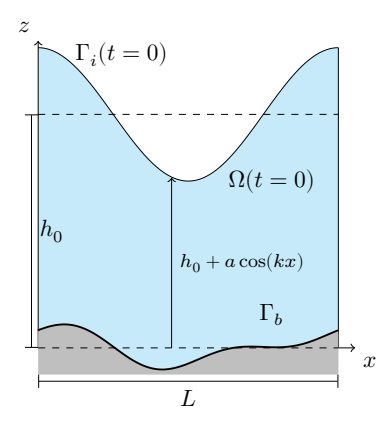


Figure 4.1 – Schematic representation of the initial domain in 2d (d=1). Periodic boundary conditions are enforced in the horizontal direction.

# <sup>1</sup>Recall that in the non-dimensional framework, $h_0 = 1$ .

Fig.	$N_{ m top}$	Re	Rem.	Adv.
4.2	3000	$10^{5}$	MA	Ell
4.3	4000	$10^{6}$	PR	Ell
4.4	3 000	$10^{5}$	MA	Ell

Table 4.1 – Numerical parameters used for the simulations used to compare the initial conditions. Rem. stands for the remeshing procedure, and Adv. for the advection scheme (see chapter 3).

#### I.1. Constructing the initial conditions

In the present chapter, we shall only consider the two-dimensional case. As we are interested in comparing Navier-Stokes simulations with irrotational Euler ones, the initial velocity  $u_0$  must be derived (numerically) from a potential  $\phi_0$ . Given an initial interface  $\gamma_{\rm in}$  (which shall always be the graph of a function), this is achieved by solving (using the FEM) any of the two following Laplace problem,

$$\begin{cases} \Delta \phi &= 0 & \text{in } \Omega(0) \\ \phi &= \psi_{\text{in}} & \text{on } \Gamma_i(0) \\ \partial_n \phi &= 0 & \text{on } \Gamma_b \end{cases}$$
 (4.D)

$$\begin{cases} \Delta \phi &= 0 & \text{in } \Omega(0) \\ \partial_n \phi &= \mathbf{u}_{\text{in}} \cdot \hat{\mathbf{n}} & \text{on } \Gamma_i(0) \\ \partial_n \phi &= 0 & \text{on } \Gamma_b, \end{cases}$$
 (4.N)

where (4.D) (respectively (4.N)) shall be called the Dirichlet initial problem (resp. Neumann initial problem). The functions  $\psi_{\rm in}$  and  $\boldsymbol{u}_{\rm in}$  are prescribed and the initial velocity is the  $\boldsymbol{u}_0 = \boldsymbol{\nabla}\phi_0$ . We could also prescribe the tangential velocity using the stream function instead. The initial domain is depicted in figure 4.1. We use a flat bottom,  $\Gamma_b = \{z=0\}$  throughout this chapter. We shall discuss non-trivial bottom later in chapter 5.

**Remark 4.1.** The Neumann problem (4.N) is difficult to solve numerically because the solution is defined up to a constant. This does not cause any major issue in 2d but the 3d solver of FreeFEM yields inconsistent results.

I.1.1. First order Stokes wave. Choosing the initial interface to be a cosine wave of amplitude a = 0.5, <sup>1</sup>

$$\eta_0(x) = 1 + a\cos(kx),$$

with k=1 (i.e. the wavelength/domain length is  $\lambda=2\pi$ ). Should we provide the initial trace of the velocity potential

$$\psi_{\rm in} = \frac{a\omega(k)}{k} \frac{\cosh\left(k\eta_0(x)\right)}{\sinh(kh_0)} \, \sin(x) \qquad {\rm with} \qquad \omega(k) = \sqrt{gk \tanh(kh_0)},$$

we would get Stokes' first order solution (1.25).

I.1.2. Symmetric initial conditions. A better-looking overhanging wave can be obtained by making the initial condition presented above symmetric with respect to the  $z=h_0$  axis, that is, choosing an initial superficial velocity (or potential) whose magnitude does not depend on z. The easiest way to do so is to take  $z=h_0$  in (1.25), yielding either

$$\psi_{\rm in} = \frac{a\omega(k)}{k} \frac{1}{\tanh(kh_0)} \sin(x), \tag{4.1}$$

or

$$\boldsymbol{u}_{\rm in} \cdot \hat{\boldsymbol{n}} = a\omega(k) \cdot \frac{\sin(kx)}{\sqrt{1 + k^2 a^2 \sin^2(kx)}} \left( 1 - \frac{ka}{\tanh(kh_0)} \cdot \cos(kx) \right). \tag{4.5}$$

However, the corresponding initial potential  $\phi_0$ , obtained through either (4.D) or (4.N), cannot be computed analytically any more.

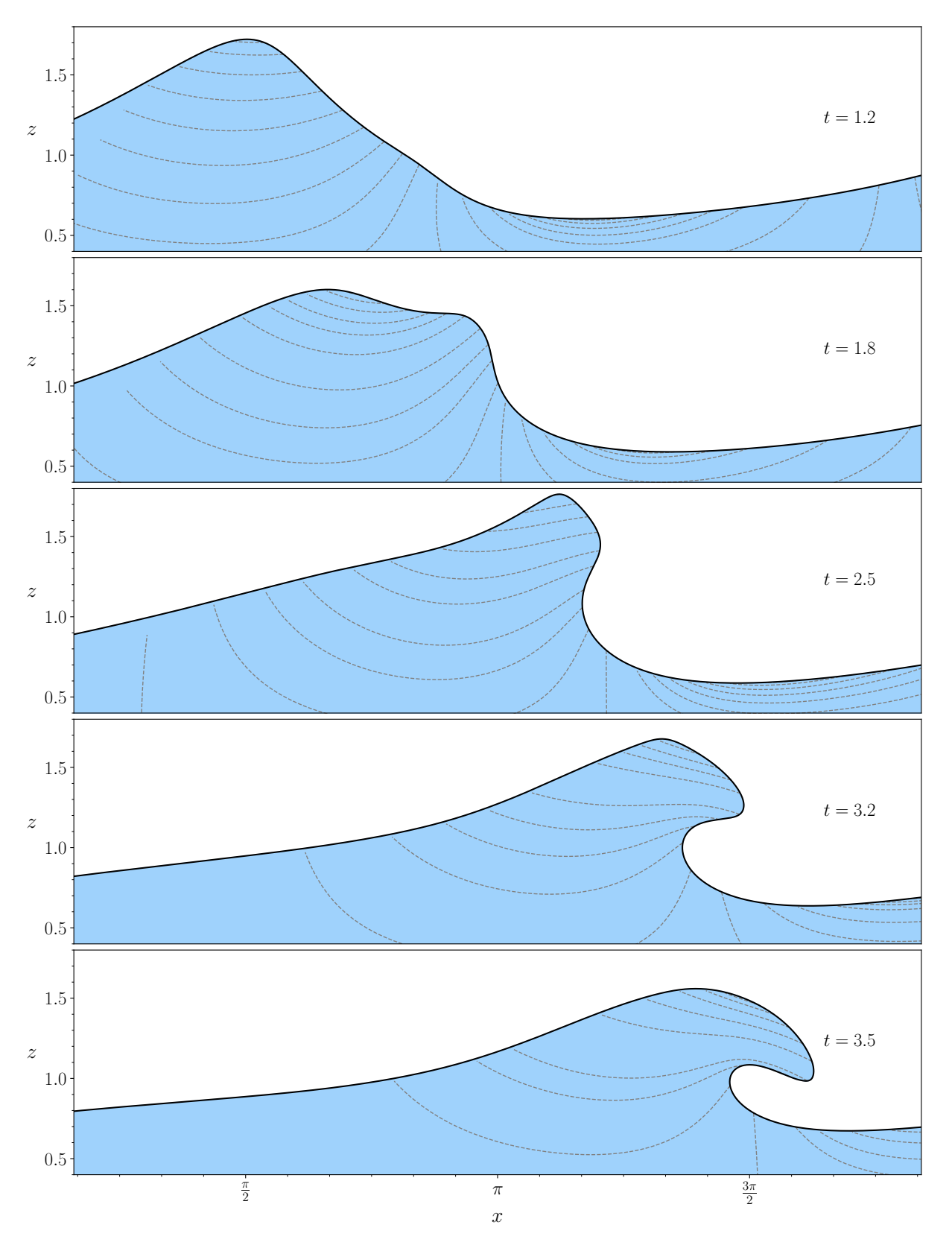


Figure 4.2 – Breaking wave simulation at  $Re = 10^5$  as a function of time. The dashed grey lines correspond to the streamlines of the flow. The initial condition is Stokes' first order solution, sec. I.1.1, with amplitude  $\varepsilon = 0.5$ .

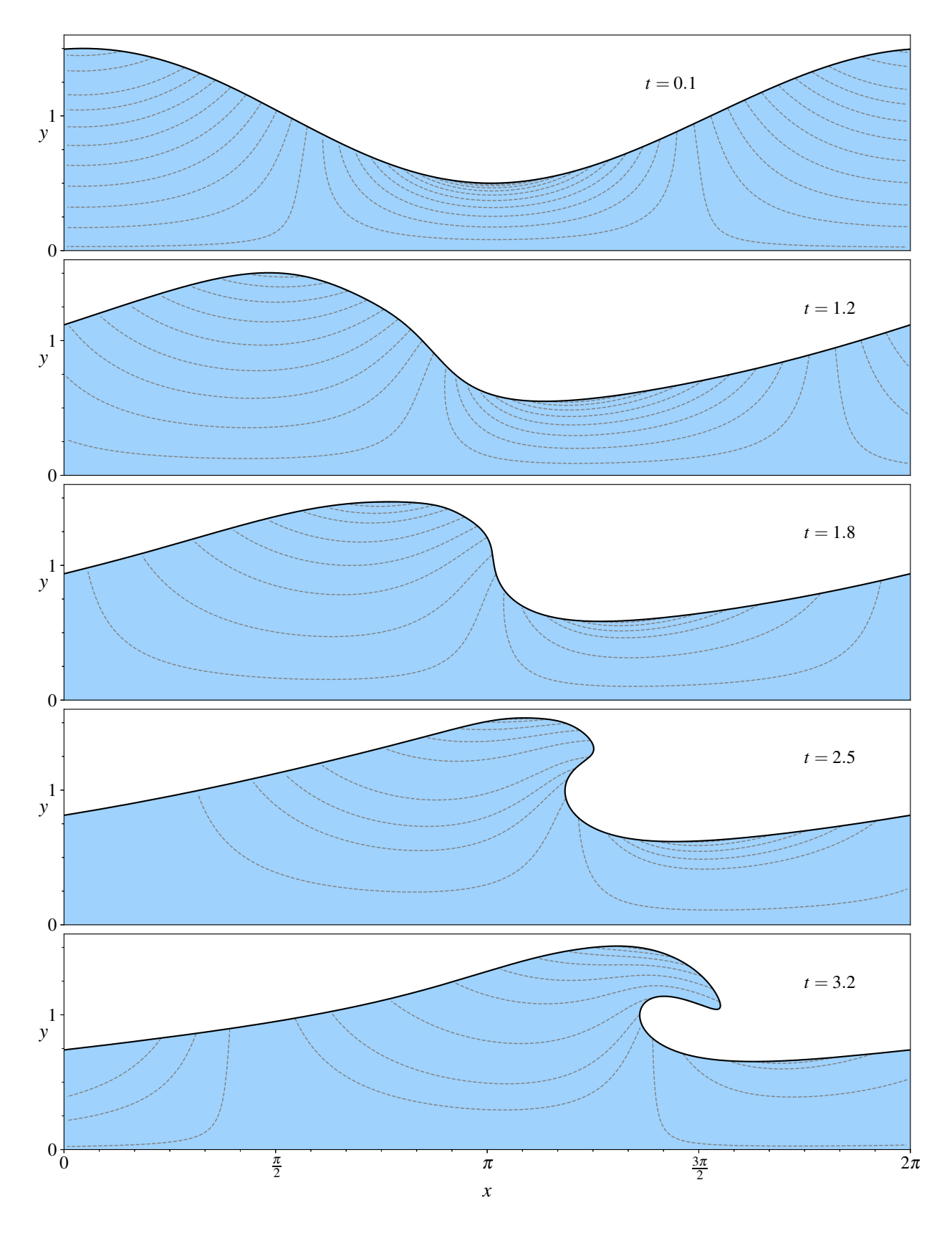


Figure 4.3 –  $\square$  – Breaking wave simulation at Re =  $10^6$  as a function of time. The dashed grey lines correspond to the streamlines of the flow. The initial condition is the symmetric one I.1.2 with prescribed normal velocity  $u_{\rm in} \cdot \hat{n}$  (4.2) and amplitude  $\varepsilon = 0.5$ .

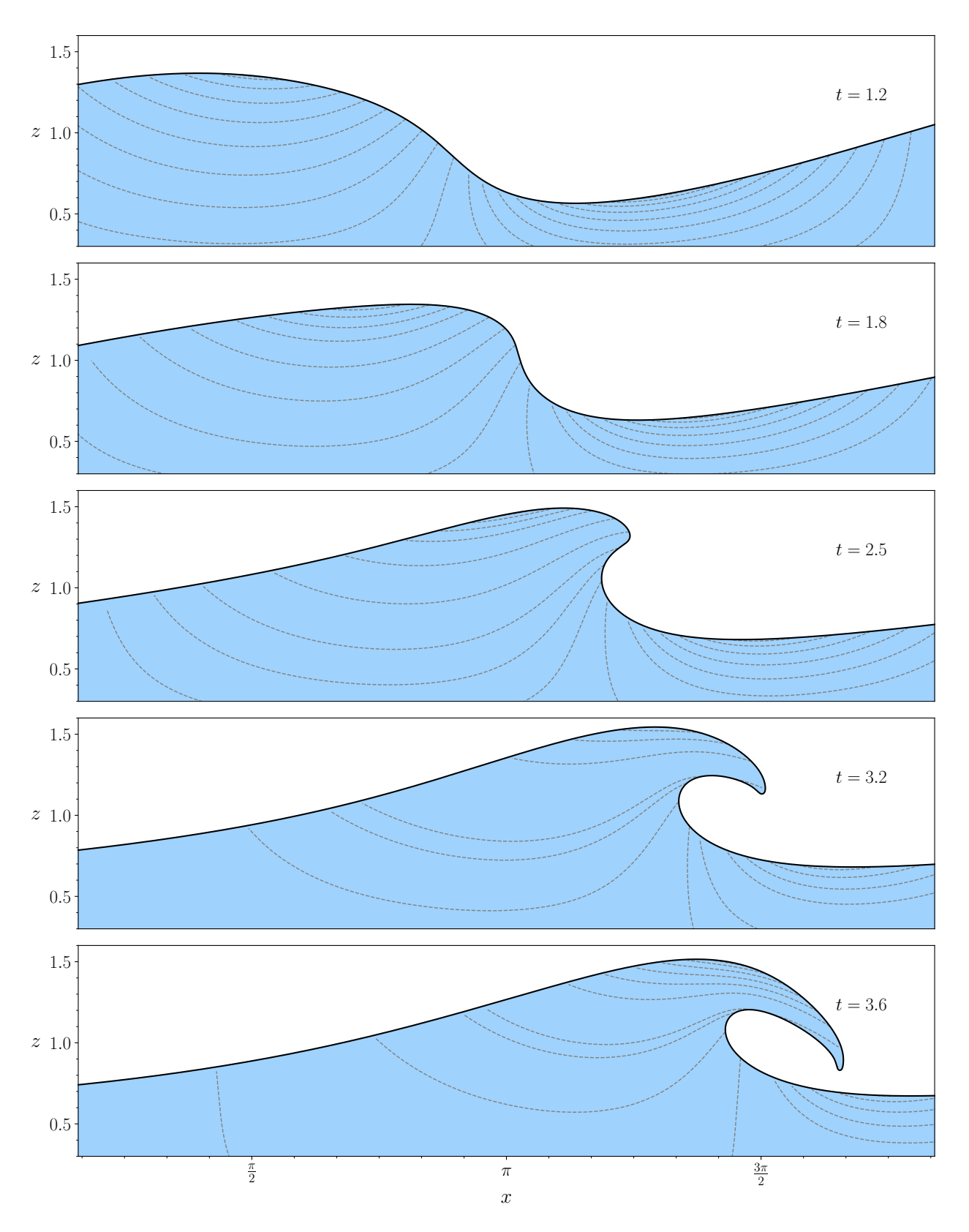


Figure 4.4 – Breaking wave simulation at Re =  $10^4$  as a function of time. The dashed grey lines correspond to the streamlines of the flow. The initial condition is the symmetric one I.1.2 with prescribed potential  $\psi_{\rm in}$  (4.1) and with amplitude  $\varepsilon = 0.5$ .

**Remark 1.** In figure 4.3, the vertical coordinate is denoted by y instead of z. Indeed, some figures in this chapter are reproduced from Riquier and Dormy (2024b), where different notations were used.

Remark 2. The camera symbol indicates that a video animation is available on the author's personal web page.

#### I.2. Comparison between different initial conditions

Simulations have been carried out with the first-order Stokes solution, sec. I.1.1 whose numerical solution is visible in figure 4.2, and with the prescribed symmetric initial data of sec. I.1.2. For the latter, the simulation with prescribed normal velocity  $\boldsymbol{u}_{\rm in} \cdot \hat{\boldsymbol{n}}$  (4.2) is shown in figure 4.3 while the one with prescribed potential  $\psi_{\rm in}$  (4.1) is plotted in 4.4. The last two simulations are effectively similar but not identical. The last simulation has also been carried out in 3d, see fig. 3.21.

We readily observe the spurious behaviour of Stokes' first order solution at large amplitude (fig. 4.2). In this chapter, all simulations shall be done using the prescribed initial normal velocity  $u_{\rm in} \cdot \hat{n}$  (4.2).

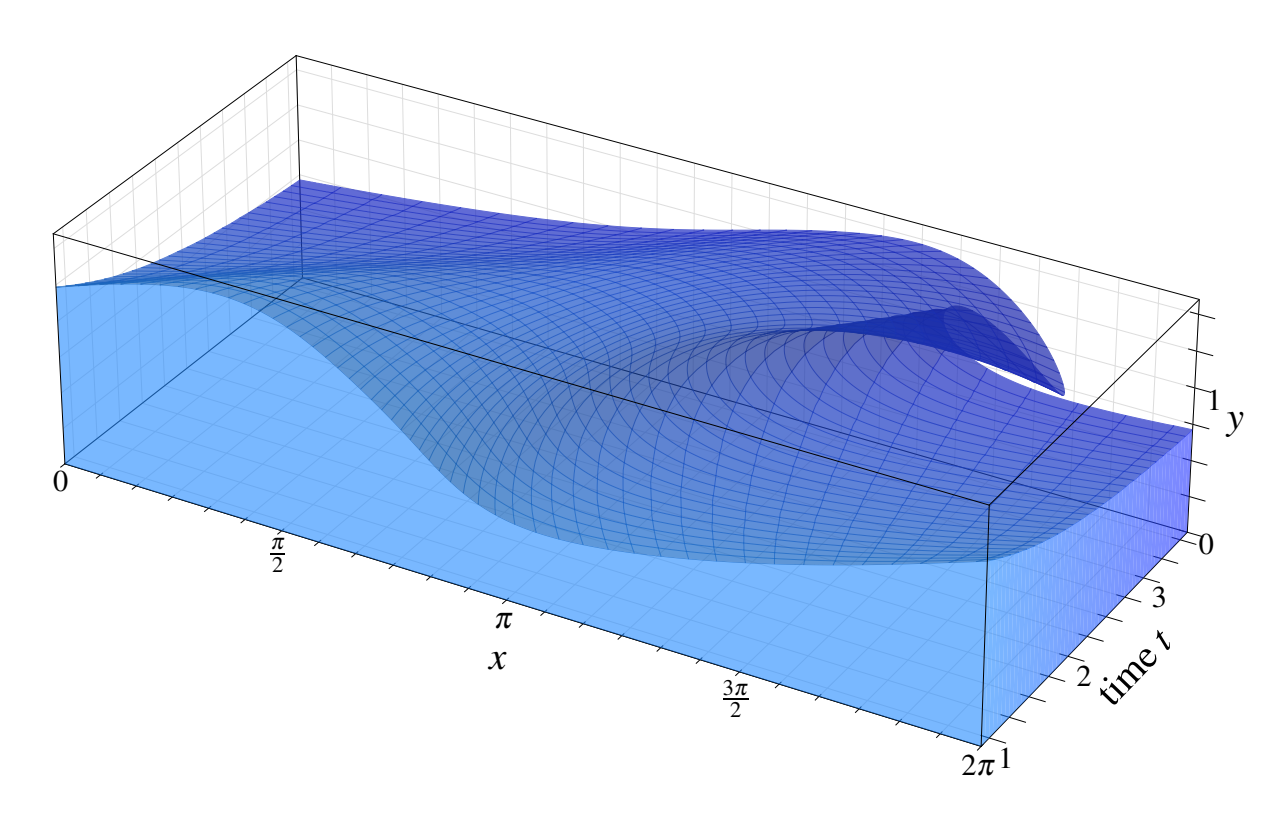


Figure 4.5 – 3d representation of the Re =  $10^6$  numerical solution whose initial velocity is computed by prescribing the normal velocity  $u_{in} \cdot \hat{n}$  (4.2).

Using the classification of Galvin (1968), the resulting wave is a plunging breaker. We note that the streamlines, shown in figs. 4.2, 4.4 and 4.3, initially wrap around the crests and the troughs of the wave. We mention that, due to the impenetrability condition (1.10), none of them can penetrate the water bed. If it seems to be the case in figs. 4.2 and 4.4, this is only because the vertical extent has been truncated in order to fit the figure in only one page.

In order to understand better the interface evolution with time, we propose a 3d representation in fig. 4.5.<sup>2</sup> It is interesting to compare this simulation with the one of Baker, Meiron, et al. (1982) (fig. 6 in their paper). They are indeed very similar. However, it is not clear

<sup>&</sup>lt;sup>1</sup>Because in general, as already mentioned, if  $\phi_{\rm in}$  is the harmonic function satisfying  $\phi_{\rm in} = \psi_{\rm in}$  on  $\Gamma_i(0)$ , then we do not have  $\partial_n \phi_{\rm in} = \boldsymbol{u}_{\rm in} \cdot \hat{\boldsymbol{n}}$ . Both quantities are not related through the Dirichlet-to-Neumann operator (1.40) (even up to a renormalisation).

<sup>&</sup>lt;sup>2</sup>Video animations are also available on the author's personal web page.

whether their initial condition corresponds to (4.2) or not. Indeed, in light of the rigorous treatment of Baker, Meiron, et al. (1982)'s vortex method which has been carried out in Dormy and Lacave (2024), the vortex sheet strength  $\gamma$  does not correspond, when the upper fluid's density is set to zero, to the water's mere tangential velocity at the interface. A solenoidal extension of the velocity (or stream function) in the "air" domain  $\Omega_{\rm a}(t)^1$  must be computed to obtain the initial vortex sheet. This can be carried out numerically but the result does not correspond to Baker, Meiron, et al. (1982)'s initial condition in the large amplitude regime.

<sup>1</sup>using the notations of chapter 1.

### II. The Re $\rightarrow +\infty$ limit

Simulations have been carried out (table 4.2) with values of the Reynolds number Re ranging from Re =  $10^2$  to Re =  $10^6$ . They are shown in fig. 4.6 and compared with the inviscid irrotational solution of Euler's system (1.53) computed with the dipole method of Dormy and Lacave (2024).

Safeguard against self-plagiarism. Some paragraphs in the following sections are reproduced from Riquier and Dormy (2024b) verbatim.

			# dofs at the <b>start</b>			# dofs at the <b>end</b>		
Re	$N_{\mathrm{top}}$	Scheme	# triangles	$({m u},p)$	$oldsymbol{v}$	# triangles	$({m u},p)$	$oldsymbol{v}$
$10^{2}$	3000	CN	195,314	886,913	198,514	780,572	3,520,574	783,722
$10^{3}$	3500	CN	221,748	1,007,116	$225,\!448$	$615,\!382$	2,675,923	$596,\!294$
$10^{4}$	3500	CN	$221,\!368$	1,005,406	225,068	$510,\!266$	$2,\!305,\!447$	513,966
$10^{5}$	3500	CN	222,970	$1,\!012,\!615$	$226,\!670$	450,648	2,037,166	$454,\!348$
$10^{6}$	4000	IE	272,948	$1,\!238,\!766$	277,148	$498,\!250$	$2,\!252,\!625$	$502,\!450$

Table 4.2 – Description of the simulations that led to the results presented in this chapter. N is the number of points on the interface. The column Scheme describes the time-stepping method that has been used (Crank-Nicolson or Implicit Euler). The number of degrees of freedom (dofs) for both the Navier-Stokes  $(\boldsymbol{u}, p)$  and the elliptic mesh velocity  $\boldsymbol{v}$  problems are presented, at both the beginning and the end of the simulation. The remeshing is done through the PR method (sec. III.1.1) and the mesh velocity is computed solving the elliptic problem of sec. II.3.1.

Before discussing the result presented in this figure, we would like to spend some time discussing the chosen definition of the Reynolds number.<sup>2</sup> Indeed, the flow associated with water waves is characterised by a large variety of fiducial length scales L and velocities U. Therefore, many Reynolds number can be defined and used when carrying out the non-dimensional version of the free-surface Navier-Stokes system. There is no right choice and we will not (and we cannot) argue that ours is better than another. It seems, based on the author's readings, that the community prefer the deep-water scaling where  $L = \lambda$ , the wavelength (Chen et al. 1999; Deike, Popinet, et al. 2015; Di Giorgio et al. 2022; Iafrati 2009; Mostert et al. 2022). As the vast majority of these studies include a topography,<sup>3</sup> this choice is questionable. We chose to use directly the shallow water scaling instead. The conversion between both Reynolds number is done through the shallowness parameter,<sup>4</sup>

$$\mathrm{Re}_\mathrm{dw} = \frac{\lambda \sqrt{g\lambda}}{\nu_\mathrm{w}} = \mu^{-\frac{3}{2}}\,\mathrm{Re} = (2\pi)^{\frac{3}{2}}\,\mathrm{Re}.$$

In all cases, the fiducial velocity is built upon the dispersion relation (i.e. from  $\omega(k)$ , eq. (1.25d)), which does not correspond to any typical

<sup>2</sup>We recall, in case it may be of use, that our definition of the Reynolds number

$$Re = \frac{LU}{\nu_w} = \frac{h_0 \sqrt{gh_0}}{\nu_w}.$$

<sup>3</sup>To our knowledge, no study proposed a numerical treatment of the freesurface Navier-Stokes system in an unbounded domain.

<sup>4</sup>The computational domain should also be adapted accordingly.

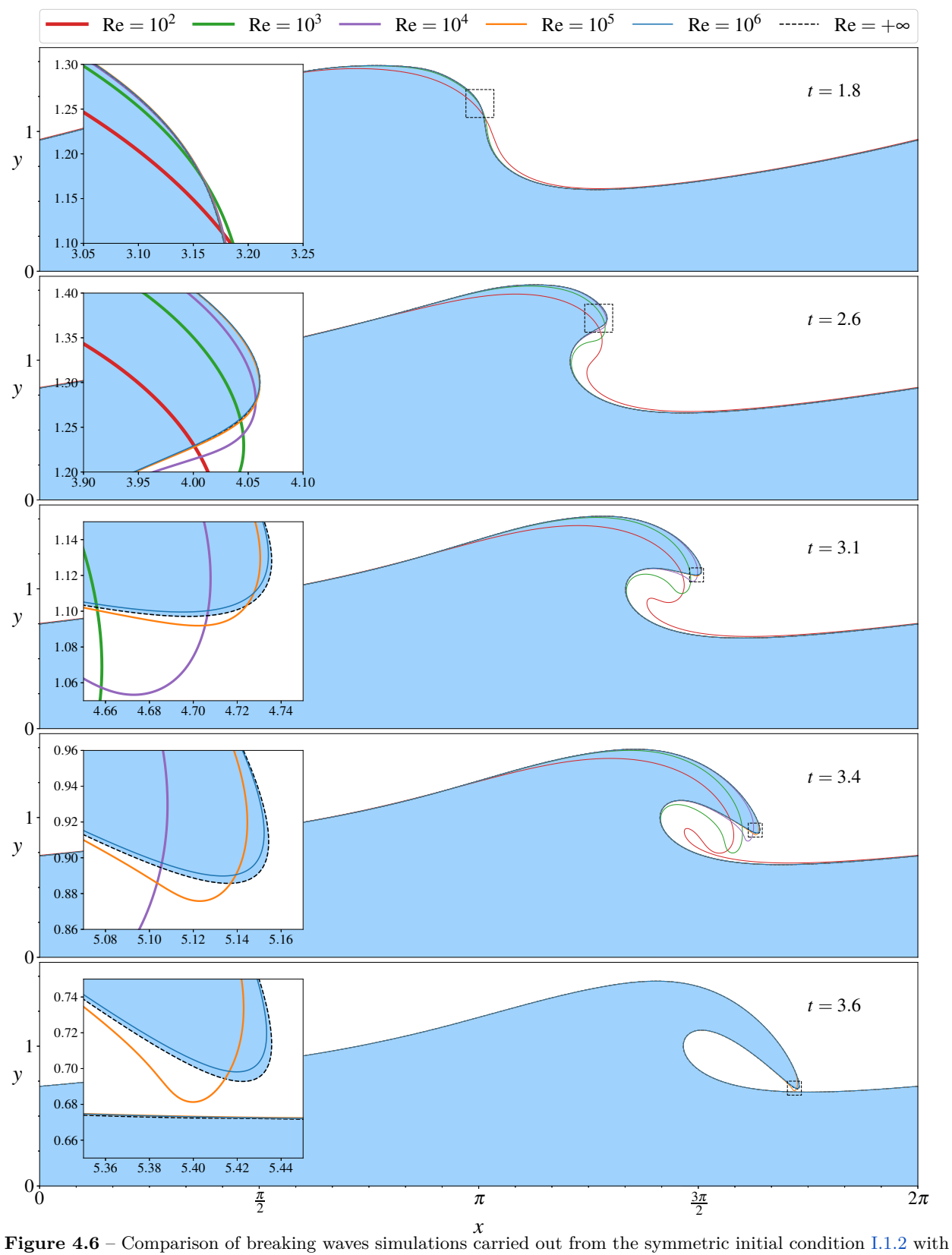


Figure 4.6 – Comparison of breaking waves simulations carried out from the symmetric initial condition 1.1.2 with prescribed normal velocity  $u_{\rm in} \cdot \hat{n}$  (4.2) and amplitude  $\varepsilon = 0.5$ , using different values of the Reynolds number. The Re =  $+\infty$  is the Euler solution computed using the dipole method described in Dormy and Lacave (2024).

value taken by the dimensional velocity field, in general. The arbitrariness of this construction of Reynolds' number should be remembered by the reader. In particular, it means that investigating the boundary layer structure, as shall be done anytime soon, won't be possible without the proper rescaling.<sup>1</sup>

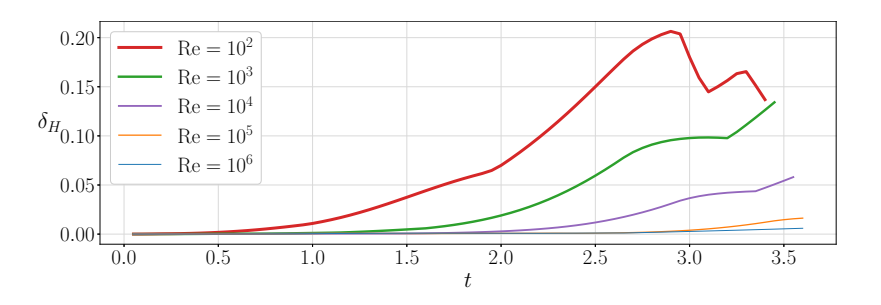
With that said, we can come back to figure 4.6. The interface-regularising effects of the viscous dissipation are clearly visible. The overhanging region takes a round shape and falls faster at larger dissipation (i.e. for decreasing Reynolds number). Perhaps more surprisingly, the effects of dissipation are localised near the plunging jet. The Euler interface appears to provide a limit solution towards which the Navier–Stokes solution converges as the Reynolds number is increased. Only a very small difference remains between the Euler solution and the Navier–Stokes solution for  $Re = 10^6$ . This minute difference may be due to the finiteness of Re but also possibly to some amount of numerical diffusion, as this extreme Reynolds number case is at the edge of our numerical resolution (see sec III below).

In order to quantify the convergence of the finite-Reynolds-number flow to the Euler solution, we must measure the differences between the various interface positions. We cannot use a standard norm to do that, since the interface is not a graph as soon as the wave overturns. We therefore rely (as in Dormy and Lacave (2024)) on the bidirectional Hausdorff distance between the curves. Let  $\alpha:[0,L_1]\to\mathbb{R}^d$  and  $\beta:[0,L_2]\to\mathbb{R}^d$  two parametric curves. An intuitive "distance" between the two is given by

$$\tilde{\delta}_H(\boldsymbol{\alpha},\boldsymbol{\beta}) = \max_{a \in [0,L_1]} \min_{b \in [0,L_2]} \, \Big| \boldsymbol{\alpha}(a) - \boldsymbol{\beta}(b) \Big|.$$

This map is however not a distance as it lacks the symmetric property. The standard counter-example is shown in figure 4.7. However, it can be symmetrised, yielding the Hausdorff distance,

$$\delta_H(\boldsymbol{\alpha},\boldsymbol{\beta}) = \max \Big\{ \tilde{\delta}_H(\boldsymbol{\alpha},\boldsymbol{\beta}), \tilde{\delta}_H(\boldsymbol{\beta},\boldsymbol{\alpha}) \Big\}.$$



In figure 4.8, the distance between the inviscid irrotational Euler solution and the Navier-Stokes solutions, computed with different values of the Reynolds number, is shown. The initial condition being identical, the distance is an increasing function of time until the splash happens (where both numerical methods stop). The time at which the effect of viscosity becomes significant increases as the Reynolds number increases.

No finite-time wedge-like singularity seems to be developing for the initial condition considered here, even in the case of the Euler solution. This can be assessed by introducing the minimum curvature radius

<sup>1</sup>The size of a boundary layer depends on the *physical* velocity, not on the group velocity (Batchelor 1967).

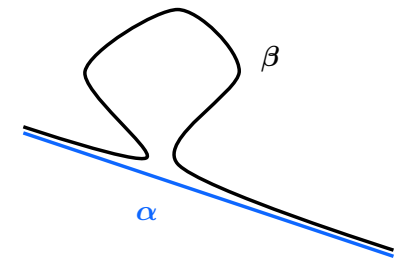


Figure 4.7 – Two planar curves  $\alpha$  and  $\beta$  such that  $\tilde{\delta}_H(\alpha, \beta) \neq \tilde{\delta}_H(\beta, \alpha)$ .

Figure 4.8 – Hausdorff distance  $\delta_H$  between the Navier-Stokes (numerical) solutions and Euler's solution.

Figure 4.9 – Minimum curvature radius of the interface after the breaking has happened, for all the Navier-Stokes simulations and Euler's one too.

 $R_c(t)$ . The curvature of the interface can be computed numerically, with a maximum corresponding to the crest. The minimum curvature radius  $R_c(t)$  is then the inverse of the maximum curvature.

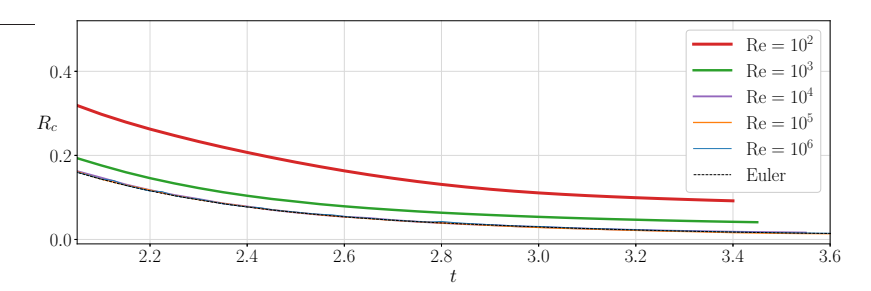


Figure 4.9 represents  $R_c$  as a function of time. Each simulation is interrupted when the interface self-intersects. Though  $R_c$  tends to zero for large enough Reynolds number, it remains strictly positive for all time in all our simulations. No finite-time singularity is obtained for this set-up. The low-Reynolds-number cases  ${\rm Re} < 10^4$  are characterised by a larger  $R_c(t)$ . The fact that the curves are indistinguishable in the figure for  ${\rm Re} \geqslant 10^4$ , and coincide with the Euler simulation, indicate that the lack of finite-time singularity for this configuration is not a consequence of viscosity and that the Bernoulli principle, accelerating the fluid near the tip of the wave (Pomeau and Le Berre 2012), does not lead to a finite-time cusp for such initial data. Further initial conditions and domain geometries thus need to be investigated to study the necessary conditions for the formation of such a singularity.

# III. Viscous dissipation near the free surface

To further characterise the difference between the Euler and Navier–Stokes solutions, we now investigate the spatial distribution of viscous dissipation. We readily obtain a local equation for the kinetic energy multiplying the Navier-Stokes momentum equation (1.54a) by  $\boldsymbol{u}$  and making use of some usefull identities, <sup>1</sup>

$$\begin{split} \left[\partial_t + \boldsymbol{u} \cdot \boldsymbol{\nabla}\right] \left(\frac{\boldsymbol{u}^2}{2}\right) - \boldsymbol{u} \cdot \boldsymbol{g} + \boldsymbol{u} \cdot \boldsymbol{\nabla} p &= \frac{1}{\mathrm{Re}} \cdot \boldsymbol{u} \cdot \Delta \boldsymbol{u} \\ &= -\frac{1}{\mathrm{Re}} \; \boldsymbol{u} \cdot \boldsymbol{\nabla}^\perp \omega \\ &= -\frac{1}{\mathrm{Re}} \; \left[\boldsymbol{\nabla} \cdot \left(\omega \boldsymbol{u}^\perp\right) + \omega^2\right]. \end{split}$$

Thus, the viscous dissipation is entirely contained in the vorticity's support. Before showing where the vorticity is located in the flow, we would like to discuss the global kinetic energy. This can be done readily by setting  $\mathbf{v} = \mathbf{u}$  (and q = p) in the variational formulation of the Navier-Stokes problem (3.1), yielding<sup>2</sup>

$$\int_{\Omega(t)} \left[ \left[ \partial_t + \boldsymbol{u} \cdot \boldsymbol{\nabla} \right] \left( \frac{\boldsymbol{u}^2}{2} \right) + \frac{2}{\mathrm{Re}} \ \mathbf{S}(\boldsymbol{u}) : \mathbf{S}(\boldsymbol{u}) - \boldsymbol{g} \cdot \boldsymbol{u} \right] \, \mathrm{d}\boldsymbol{x} = 0.$$

The gravity term can be simplified making use of Reynolds' transport lemma 1.1 (for steady gravity fields g),

$$\int_{\Omega(t)} \boldsymbol{u} \cdot \boldsymbol{g} \, \mathrm{d}\boldsymbol{x} = \int_{\Omega(t)} \boldsymbol{u} \cdot \boldsymbol{\nabla} \big( \boldsymbol{g} \cdot \boldsymbol{x} \big) \, \mathrm{d}\boldsymbol{x}$$

<sup>1</sup>namelly (B.3a) and the 2d version of (B.1d), that is

$$\begin{split} \boldsymbol{\nabla} \cdot \left( \boldsymbol{\omega} \boldsymbol{u}^{\perp} \right) &= \boldsymbol{\omega} \big( \boldsymbol{\nabla} \cdot \boldsymbol{u}^{\perp} \big) + \boldsymbol{u} \cdot \boldsymbol{\nabla}^{\perp} \boldsymbol{\omega} \\ &= - \boldsymbol{\omega} \big( \boldsymbol{\nabla}^{\perp} \cdot \boldsymbol{u} \big) + \boldsymbol{u} \cdot \boldsymbol{\nabla}^{\perp} \boldsymbol{\omega}. \end{split}$$

A minus sign slipped into Riquier and Dormy (2024b, eq. 5.2) without notifying the authors. It was not identified in the proofs either.

<sup>&</sup>lt;sup>2</sup>after making use of the weak incompressibility condition

$$\begin{split} &= \int_{\Omega(t)} \left[ \partial_t \left( \boldsymbol{g} \cdot \boldsymbol{x} \right) + \boldsymbol{u} \cdot \boldsymbol{\nabla} \left( \boldsymbol{g} \cdot \boldsymbol{x} \right) \right] \mathrm{d}\boldsymbol{x} \\ &= \frac{\mathrm{d}}{\mathrm{d}t} \int_{\Omega(t)} \boldsymbol{g} \cdot \boldsymbol{x} \, \mathrm{d}\boldsymbol{x} = -\frac{1}{2} \frac{\mathrm{d}}{\mathrm{d}t} \int_{\Omega(t)} \boldsymbol{\nabla} \cdot \left( z^2 \hat{\boldsymbol{z}} \right) \mathrm{d}\boldsymbol{x} \\ &= \frac{1}{2} \frac{\mathrm{d}}{\mathrm{d}t} \int_{\mathbb{T}} \left( \gamma_z(t,s) \right)^2 \hat{n}_z(t,s) \left| \partial_s \boldsymbol{\gamma}(t,s) \right| \mathrm{d}s, \end{split}$$

with  $\gamma(t, \cdot): \mathbb{T} \to \Gamma_i(t)$  a periodic parametrisation of the interface. Notice that we have used  $g = -\hat{y}$  above. Should we work with dimensions, a factor g would be present in front of each term. The bottom boundary term does not depend on time and is therefore chased off by the time-derivative.

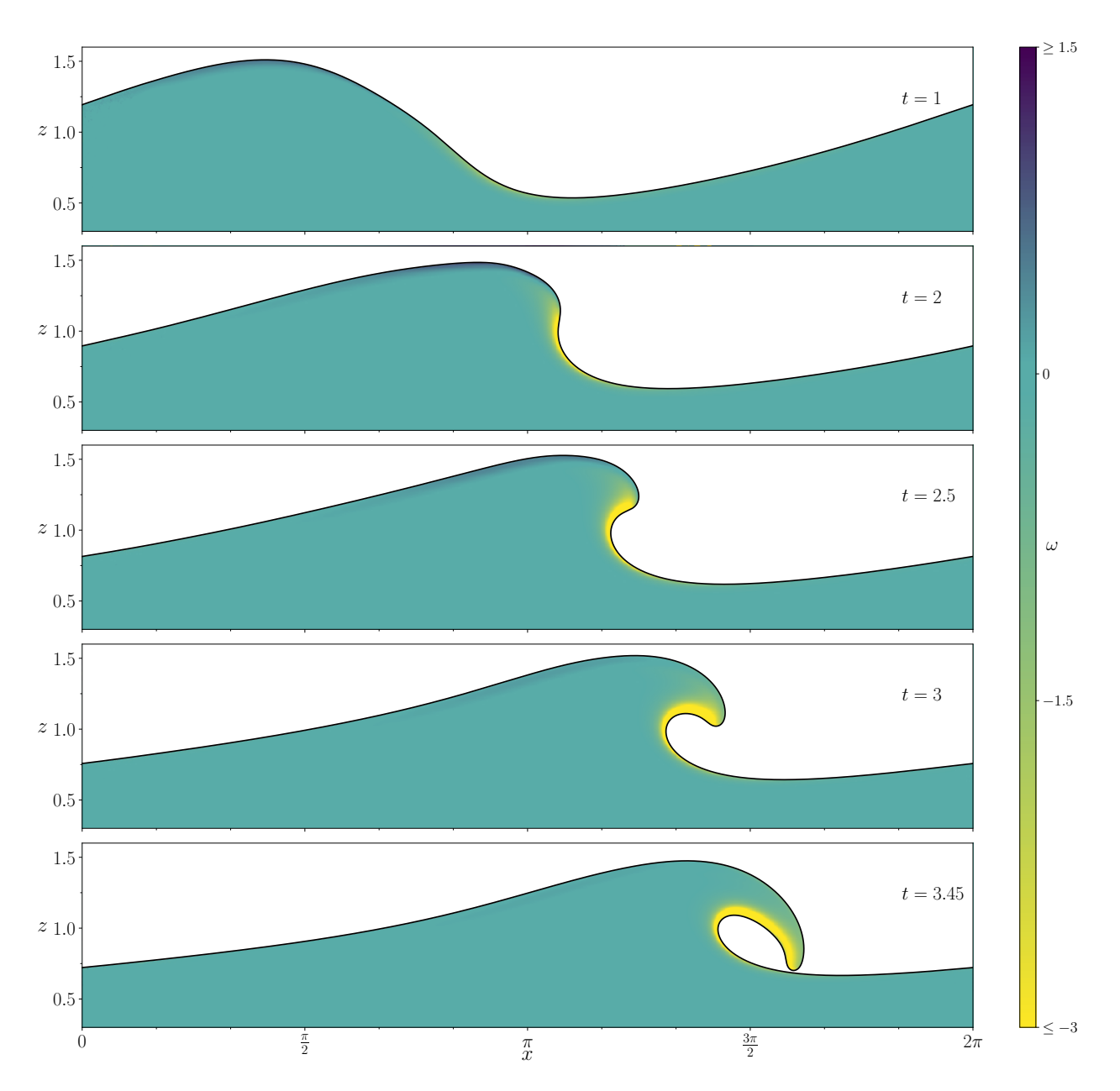


Figure 4.10 – Evolution of the vorticity  $\omega$  at Re = 10<sup>3</sup>. The color scheme has been truncated above and below to guarantee the overall coherence.

Finally, we obtain the following energy equation for the viscous water wave system (1.54),

$$\begin{split} \frac{1}{2} \frac{\mathrm{d}}{\mathrm{d}t} \left( \int_{\Omega(t)} \boldsymbol{u}^2 \right) + \frac{1}{2} \frac{\mathrm{d}}{\mathrm{d}t} \left( \int_{\mathbb{T}} \left( \gamma_z \right)^2 \hat{n}_z \big| \partial_s \boldsymbol{\gamma} \big| \right) \\ + \frac{2}{\mathrm{Re}} \underbrace{\int_{\Omega(t)} \mathbf{S}(\boldsymbol{u}) : \mathbf{S}(\boldsymbol{u})}_{\mathcal{E}'(\boldsymbol{u})} = 0. \quad (4.3) \end{split}$$

<sup>1</sup>Should we be interested in the surface tension, an additional term, namelly

$$\frac{1}{\mathrm{Bo}} \int_{\Gamma_i(t)} \kappa \, \boldsymbol{u} \cdot \hat{\boldsymbol{n}},$$

would lie on the right-hand side of (4.3).

<sup>2</sup>The enstrophy  $\mathcal{E}(\boldsymbol{u})$  is defined, depending on the author, as

$$\mathcal{E}(\boldsymbol{u}) = \int_{\Omega(t)} \left| \boldsymbol{\nabla} \boldsymbol{u} \right|^2 \quad \text{or} \quad \int_{\Omega(t)} \omega^2.$$

These two definitions are not always equivalent. It depends on the boundary conditions that are used.

<sup>3</sup>relating the convergence of Navier-Stokes solution to Euler's solution to the control of the enstrophy, Kato (1984). See also Kelliher (2007) for equivalent formulations.

<sup>4</sup>Stokes (1850)

The only difference with the inviscid case lies in the dissipation term<sup>1</sup> scaling as Re<sup>-1</sup>. A surprising aspect of (4.3) is that the energy dissipation due to viscosity does not correspond to the *enstrophy* of the flow.<sup>2</sup> This is due to the boundary conditions in water waves which do not correspond to any of the usual ones used in fluid dynamics textbooks. Even though the system at hand does not enter into the framework of Kato's theorem<sup>3</sup>, it seems reasonable to suppose that, if any Kato-like criterion exists, it would involve the quantity  $\mathcal{E}'(u)$  appearing in (4.3) instead of the enstrophy  $\mathcal{E}(u)$ . However, as the former differs from the latter through a boundary term, it may happen that this very term is easy to control so that Kato's original criterion would remain unchanged.

Using eq. (4.3), the numerical dissipation can be estimated. When the Reynolds number reaches 10<sup>4</sup>, it becomes comparable to the viscous dissipation. Therefore, energy considerations cannot be tracked efficiently with this method. The ALE scheme (sec. II of chap. 3) may be adapted to become second-order, through a higher-order advection scheme for the mesh for instance, in order to investigate the dissipation at high Reynolds number. This might be part of a future work but, to the author's knowledge, a second-order ALE scheme has not been found yet.

Coming back to the energy dissipation, figure 4.10 shows the vorticity in a breaking wave at  $Re = 10^3$ . It is confined in a sheet entirely lying in the vicinity of the free surface. Liu and Davie (1977) argued that, due to the oscillatory nature of the flow, the vorticity distribution shares similarities with the Stokes-type boundary layer<sup>4</sup> generated in the vicinity of a back-and-forth moving boundary. However, as we shall now show, the origin of this vorticity is different.

#### III.1. Vorticity generation at fluid interfaces

Lundgren and Koumoutsakos (1999) proposed an interesting interpretation about the origin of the vorticity sheet observed in figure 4.10 (extending the work of Longuet-Higgins 1992). We hereby extend their reasoning to the case of a single-fluid interface. The stress-free condition on  $\Gamma_i(t)$  (1.54c), taken in the tangential direction  $\hat{\tau}$ , can be rephrased as

$$\begin{split} 0 &= \hat{\pmb{\tau}} \cdot \pmb{\mathsf{S}}(\pmb{u}) \cdot \hat{\pmb{n}} & \text{on } \Gamma_i(t) \\ \Leftrightarrow & \omega &= -2\hat{\pmb{\tau}} \cdot \pmb{\nabla} \pmb{u} \cdot \hat{\pmb{n}} = -2\partial_s \big( \pmb{u} \cdot \hat{\pmb{n}} \big) + 2 \big( \pmb{u} \cdot \hat{\pmb{\tau}} \big) \kappa & \text{on } \Gamma_i(t), \ (4.4\text{a}) \end{split}$$

*i.e.* vorticity has two different origins on the free surface: a contribution from the exiting streamlines and another one from both the curvature and the tangential velocity (Longuet-Higgins 1992). A similar relation holds in  $3d.^5$  Coming back to fig. 4.10, we notice that

<sup>&</sup>lt;sup>5</sup>Lundgren (1989)

the strongest vorticity region (in yellow) is associated with an increasing curvature, together with a strong superficial current (not shown), yielding a high value of the second term in (4.4a).

Remark 4.2. The same argument applies to the slip/Navier boundary condition (1.54e) but the impenetrability condition (1.54d) yields

$$\omega = 2 \big( \boldsymbol{u} \cdot \hat{\boldsymbol{\tau}} \big) \kappa \qquad \text{on } \Gamma_b.$$

In the present case, the curvature of the topography vanishes everywhere so that no vorticity is generated on the bed. However, this does not hold in general and Navier-type boundary layer may appear.<sup>1</sup>

The relation (4.4a), alone, sheds light on the vorticity generation mechanism at hand. However, we can go further. Doing identical computations, we can also rewrite the normal component of the stress-free condition (1.54c) using the curvature, yielding

$$p + \frac{2}{\text{Re}} \left( \partial_s \left( \boldsymbol{u} \cdot \hat{\boldsymbol{\tau}} \right) + \kappa \left( \boldsymbol{u} \cdot \hat{\boldsymbol{n}} \right) \right) = 0 \quad \text{on } \Gamma_i(t).$$
 (4.4b)

An eventual surface tension term may also appear, should Bo  $< +\infty$ . Another enlightening relation can be obtained rapidly (lemma 4.3 below, fig. ??).<sup>2</sup>

Lemma 4.3 (Lundgren and Koumoutsakos, 1999). There holds

$$\frac{\mathrm{d}}{\mathrm{d}t} \int_{\Gamma_i(t)} \boldsymbol{u} \cdot \hat{\boldsymbol{\tau}} - \frac{\mathrm{d}}{\mathrm{d}t} \int_{\Gamma_h} \boldsymbol{u} \cdot \hat{\boldsymbol{\tau}} + \frac{1}{\mathrm{Re}} \int_{\Gamma_h \cup \Gamma_i(t)} \partial_n \omega = 0,$$

with the normal vectors defined as in fig. 1.6.

*Proof.* It is a direct consequence of both Stokes' theorem,

$$\int_{\Omega(t)} \omega = \int_{\partial \Omega(t)} \boldsymbol{u} \cdot \hat{\boldsymbol{\tau}},$$

and of the vorticity equation which, in 2d, yields readily

$$\frac{\mathrm{d}}{\mathrm{d}t} \int_{\Omega(t)} \omega = \frac{1}{\mathrm{Re}} \int_{\partial\Omega(t)} \partial_n \omega.$$

One just need to be careful with the orientations of normal vectors (and hence of the associated tangent ones too).  $\Box$ 

Remark 4.4. In the integral over the interface  $\Gamma_i(t)$ , we can replace  $\boldsymbol{u}\cdot\hat{\boldsymbol{\tau}}$  by the vortex sheet strength  $\gamma_i$  (Dormy and Lacave 2024).<sup>3,4</sup> The result is then closer to the one of Lundgren and Koumoutsakos (1999). In the same manner, we can also replace  $\boldsymbol{u}\cdot\hat{\boldsymbol{\tau}}$  by the bed's vortex sheet strength  $\gamma_b$  in the second integral appearing in lemma 4.3.

Lemma 4.3 provides an interesting interpretation of the vorticity sheet appearing in fig. 4.10: it corresponds to the free-surface vortex sheet  $\gamma_i$  diffusing in the bulk due to viscous effects. In other words, the viscosity introduces a defect in the conservation law for  $\gamma_i$  that is compensated by the bulk vorticity, so that we have formally

$$\frac{\mathrm{d}}{\mathrm{d}t} \int_{\mathrm{interface}} \gamma_i + \frac{\mathrm{d}}{\mathrm{d}t} \int_{\mathrm{fluid}} \omega = 0.$$

<sup>1</sup>We shall define the nomenclature regarding types of boundary layer soon, in secs. III.3.1 and III.3.2.

<sup>2</sup>In fact, Lundgren and Koumoutsakos (1999) obtained this result in the case of a two-fluids interface. Their proof involves manipulations of Euler's equation and (4.4) that are difficult to justify rigorously. Our approach seems somewhat simpler.

П

<sup>3</sup>Because, should we extend  $\boldsymbol{u}$  by  $\boldsymbol{u}_a$  in the air domain  $\Omega_a$ , as in Dormy and Lacave (2024), then

$$\int_{\Gamma_i(t)} \boldsymbol{u}_a \cdot \hat{\boldsymbol{\tau}} = 0.$$

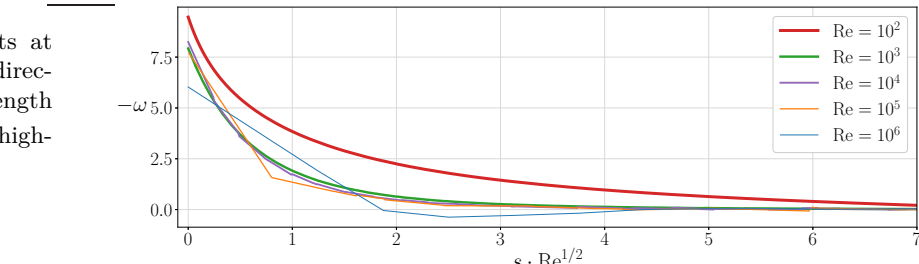
<sup>4</sup>With  $u_a$  the solenoidal extension of u in the air domain  $\Omega_a(t)$  obtained through a continuous extension of the stream function, we recall that the superficial vortex sheet strength is defined as

$$\begin{split} \left(\gamma_i \hat{\pmb{\tau}}\right) (t,s) &= \pmb{u} \Big(t, \pmb{\gamma}(t,s) \Big) \\ &- \pmb{u}_a \Big(t, \pmb{\gamma}(t,s) \Big). \end{split}$$

A similar interpretation holds for the bed's sheet too. However, in the absence of curvature, eq. (4.4a) yields the stronger statement that  $\gamma_b$  remains localised on the bottom boundary.

#### III.2. The free-surface boundary layer

In order to further characterise the vorticity sheet visible in fig. 4.10, we propose a magnification centered on the overturning region at t=2.9 for all values of Reynolds' number in fig. 4.13. The sheet's size seems to decrease with the viscosity. This observation can be made precise by plotting the vorticity strength along the black lines visible in fig. 4.13. This is shown in figure 4.11.



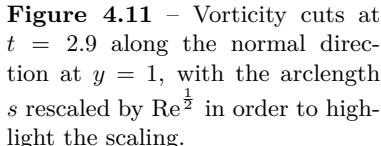
In fig. 4.11, we see readily that the sheet in the Re =  $10^6$  simulation is not fully resolved. Indeed, it is spread over one to three triangles. We also mention that, since  $\mathbb{P}^2$  basis functions have been used for the velocity  $\boldsymbol{u}$ , interpolation always happens when numerically computing  $\omega$  since piecewise linear elements with degrees of freedom lying on both the edges and the vertices of a triangle are not available in FreeFEM. We have chosen discontinuous  $\mathbb{P}^1_{\rm dc}$  elements instead (see chap. 3). We also notice that the Re =  $10^2$  result differ significantly from the others. This is due to its normal cut going in a different direction that the others. Indeed, the high (non-physical) value of the viscosity in this simulation yields a very different shape of the overturning region, looking like a phrygian cap.

Looking at both figures 4.11 and 4.12, we see that the size of the sheet scales as  $Re^{-\frac{1}{2}}$ . Therefore, it is in fact a boundary layer. As the vorticity remains uniformly bounded with the Reynolds number, this boundary layer is of *Navier* type (Iftimie and Sueur 2011). Since it happens to be well-mannered, meaning that is remains gently localised in the vicinity of the interface, we may conclude about the following (pointwise in time) convergence of the Navier-Stokes solution to Euler's irrotational solution for this particular initial condition, <sup>1</sup>

$$\begin{split} & \omega(t, {\:\raisebox{3.5pt}{\text{$\bullet$}}}) \xrightarrow[\text{Re} \to +\infty]{} 0 & \text{in } L^2 \big( \Omega(t) \big) \\ & {\:\raisebox{3.5pt}{\textbf{$u$}}}(t, {\:\raisebox{3.5pt}{\text{$\bullet$}}}) \xrightarrow[\text{Re} \to +\infty]{} {\:\raisebox{3.5pt}{\textbf{$\nabla$}}} \phi_E(t, {\:\raisebox{3.5pt}{\text{$\bullet$}}}) & \text{in } {\:\raisebox{3.5pt}{\textbf{$H$}}}^1_{\Gamma_b} \big( \Omega(t) \big), \end{split}$$

with  $\phi_E$  the velocity potential solution of Euler's irrotational problem with initial data  $\phi_0$ .<sup>2</sup> Regarding the interface, it is difficult to quantify the convergence without entering the spurious debate about reparametrisation. However, as already discussed in sec. II, the convergence can be stated in a space endowed with Hausdorff's distance.

We stress that a region of positive-valued vorticity is visible in fig. 4.13f. In fact, taking a closer look at figure 4.10, we see that positive vorticity appears first below the crest of the wave but quickly dissipates



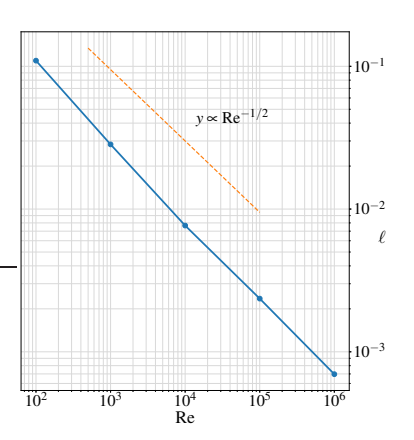


Figure 4.12 – Scaling of the vorticity sheet size  $\ell$  with the Reynolds number at t=2.9.

 $<sup>^{1}</sup>$ This can be seen as a conjecture.

<sup>&</sup>lt;sup>2</sup>We won't discuss convergence in function spaces involving time for the sake of simplicity.

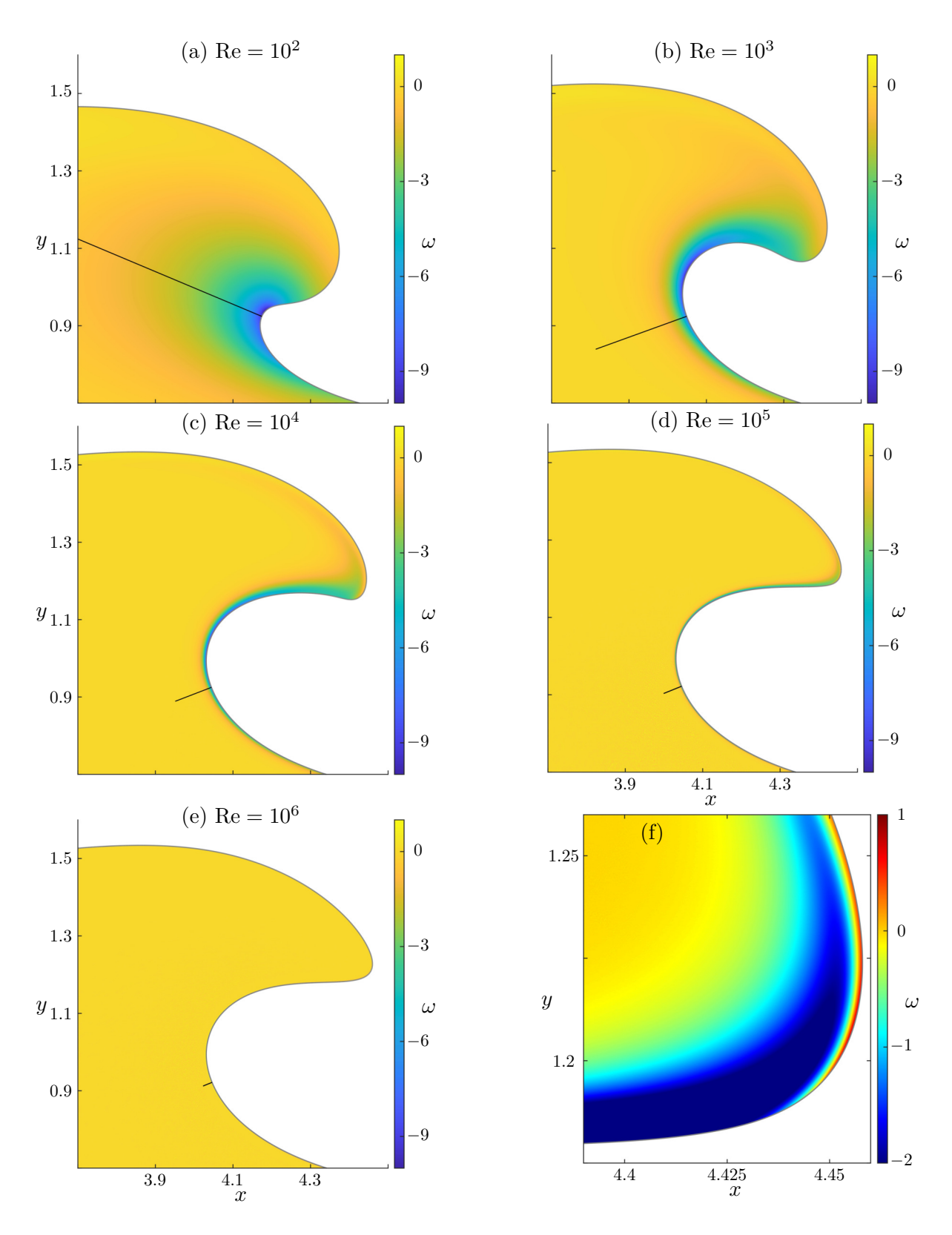


Figure 4.13 – (a–e) The vorticity  $\omega$  close to the wave's crest at time t=2.9 for different values of Reynolds' number. (f) A closer look at the tip of the wave when Re =  $10^5$ . The color scheme has been truncated above and below to guarantee the overall coherence.

away. In the meantime, as breaking occurs, the strong surface drift generates much more vorticity (owing to eq. (4.4a)) of opposite sign, therefore shadowing the positive region.

Interestingly the vorticity sheet becomes comparable in size with the minimum curvature radius  $R_c$  near Re =  $10^4$ , *i.e.* when the curvature radius, as a function of the Reynolds number, reaches its minimum (figure 4.9). This observation will lead us to find a link between the curvature radius and the boundary layer thickness in sec. IV.

As a final remark before moving on, we mention that we are not in a case in which the theorem of Masmoudi and Rousset (2017) applies, stating that the convergence of the viscous solution to the inviscid one happens as  $\text{Re} \to +\infty$  for small (in some norm), non-breaking, waves evolving in deep waters (*i.e.* without a bottom topography).

#### III.3. What about no-slip/Dirichlet conditions?

Starting from the same initial condition, we have carried out the exact same simulation with the Navier condition replaced by the noslip condition on the bed. The resulting wave is visible in fig. 4.14.

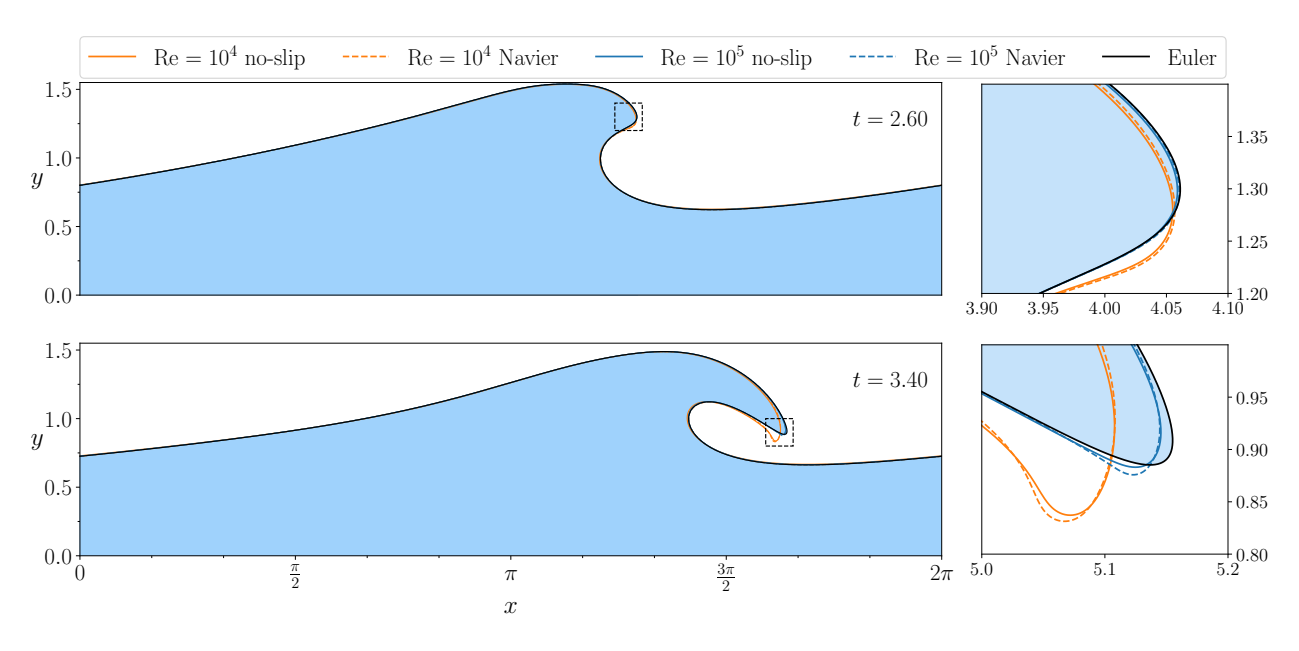


Figure 4.14 – Imposing the no-slip/Dirichlet and the slip/Navier boundary condition on the bed does not change the shape of the free surface.

One sees readily that, at each Reynolds number, the difference between the two interfaces remains small. We cannot conclude whether this gap is of physical or numerical nature.

However, imposing the no-slip/Dirichlet condition on the bottom yields a boundary layer of Dirichlet type (not shown), *i.e.* the vorticity is confined, once again, in a sheet of size  $\mathrm{Re}^{-\frac{1}{2}}$  but now scales as  $\mathrm{Re}^{\frac{1}{2}}$ . Therefore, we can only expect convergence of the following type (as in Kelliher 2007, 2008),<sup>1</sup>

$$\begin{split} & \omega(t, {\:\raisebox{3.5pt}{\text{\bullet}}}) \xrightarrow[\text{Re} \to +\infty]{} 0 & \text{in } H^{-1} \Big( \Omega(t) \Big) \\ & u(t, {\:\raisebox{3.5pt}{\text{\bullet}}}) \xrightarrow[\text{Re} \to +\infty]{} \nabla \phi_E(t, {\:\raisebox{3.5pt}{\text{\bullet}}}) & \text{in } \mathbf{L}^2 \Big( \Omega(t) \Big). \end{split}$$

 $^{1}$  where we set

$$\mathbf{L}^2 \Big( \Omega(t) \Big) = \Big[ L^2 \Big( \Omega(t) \Big) \Big]^2.$$

In fact, we can even say more about the vorticity. Indeed, we can argue that it converges in  $H^1\big(\Omega(t)\big)^\star$ , the topological dual of  $H^1\big(\Omega(t)\big)$ , to the bottom vortex sheet  $\gamma_b\delta_{\Gamma_b}$ . To see this, we introduce the Green function  $G(\boldsymbol{x},\boldsymbol{y})$  in the cylinder  $\mathbb{T}\times\mathbb{R}$ . Let  $\psi$  the stream function associated with  $\boldsymbol{u}$ . Dormy and Lacave (2024) showed that  $\psi$  can be extended continuously to the entire cylinder  $\mathbb{T}\times\mathbb{R}$  using the vortex sheets  $\gamma_i$  and  $\gamma_b$  already introduced, leading to the representation formula

$$\psi(t, \boldsymbol{x}) = \int_{\mathbb{T} \times \mathbb{R}} \varpi \left[ \boldsymbol{u}(t, \boldsymbol{\cdot}) \right] (\boldsymbol{y}) \ G(\boldsymbol{x}, \boldsymbol{y}) \, \mathrm{d} \boldsymbol{y}, \tag{4.7}$$

where the distribution  $\varpi[u]$  is the total vorticity<sup>2</sup> defined as

$$\varpi[\boldsymbol{u}] = \left(\boldsymbol{\nabla}\times\boldsymbol{u}\right) + \gamma_i[\boldsymbol{u}]\delta_{\Gamma_i(t)} + \gamma_b[\boldsymbol{u}]\delta_{\Gamma_b},$$

with the dependency of  $\gamma_i$  and  $\gamma_b$  in  $\boldsymbol{u}$  made explicit. Since the extension of  $\psi$  to the entire domain  $\mathbb{T} \times \mathbb{R}$  is harmonic in both  $\Omega_a(t)$  and  $\Omega_b$ , the first term's support lies in  $\overline{\Omega(t)}$  only.

III.3.1. Navier—type boundary layer. By this terminology, we mean the vorticity sheet appearing in the vicinity of a boundary supplemented with the slip/Navier boundary condition (1.14). The representation formula (4.7) for the stream function quickly yields

$$\begin{split} \boldsymbol{u}(t,\boldsymbol{x}) &= \int_{\mathbb{T} \times \mathbb{R}} \boldsymbol{\varpi}[\boldsymbol{u}](\boldsymbol{y}) \boldsymbol{\nabla}_{\boldsymbol{x}}^{\perp} G(\boldsymbol{x},\boldsymbol{y}) \, \mathrm{d} \boldsymbol{y} \\ &= \int_{\mathbb{T} \times \mathbb{R}} \boldsymbol{\varpi} \Big[ \boldsymbol{\nabla} \phi_E \Big](\boldsymbol{y}) \boldsymbol{\nabla}_{\boldsymbol{x}}^{\perp} G(\boldsymbol{x},\boldsymbol{y}) \, \mathrm{d} \boldsymbol{y} \\ &+ \int_{\mathbb{T} \times \mathbb{R}} \boldsymbol{\varpi} \Big[ \boldsymbol{u} - \boldsymbol{\nabla} \phi_E \Big](\boldsymbol{y}) \boldsymbol{\nabla}_{\boldsymbol{x}}^{\perp} G(\boldsymbol{x},\boldsymbol{y}) \, \mathrm{d} \boldsymbol{y}, \end{split}$$

with  $\nabla \phi_E$  the irrotational solution of Euler's system. On the bottom boundary  $\Gamma_b$ , both  $\boldsymbol{u} \cdot \hat{\boldsymbol{n}}$  and  $\nabla \phi_E \cdot \hat{\boldsymbol{n}}$  vanish. Regarding the tangential velocity, we can expect (Iftimie and Sueur 2011) a difference  $(\boldsymbol{u} - \nabla \phi_E) \cdot \hat{\boldsymbol{\tau}}$  of order  $\mathrm{Re}^{-\frac{1}{2}}$ , yielding the convergence of the Navier-Stokes bed's vortex sheet strength  $\gamma_b$  to Euler's one.

III.3.2. Dirichlet-type boundary layer. Imposing the no-slip/Dirichlet condition on  $\Gamma_b$  yields a boundary layer in which the vorticity formally scales as

$$\omega \equiv \operatorname{Re}^{\frac{1}{2}} \tilde{\omega} \left( t, s, \operatorname{Re}^{\frac{1}{2}} n \right),$$

with  $\tilde{\omega}$  of order O(1) as  $\mathrm{Re} \to +\infty$ , and with (s,n) the Frénet frame (see the following discussion, sec. IV). At the same time, since  $\boldsymbol{u}=0$  on  $\Gamma_b$ , the bed's vortex sheet strength  $\gamma_b$  vanishes identically everywhere, so that the representation formula (4.7) yields

$$\boldsymbol{u}(t,\boldsymbol{x}) = \int_{\mathbb{T}\times\mathbb{R}} \omega(t,\boldsymbol{y}) \boldsymbol{\nabla}_{\boldsymbol{x}}^{\perp} G(\boldsymbol{x},\boldsymbol{y}) \,\mathrm{d}\boldsymbol{y} + \int_{\Gamma_i(t)} \gamma_i(\boldsymbol{y}) \boldsymbol{\nabla}_{\boldsymbol{x}}^{\perp} G(\boldsymbol{x},\boldsymbol{y}) \,\mathrm{d}S(\boldsymbol{y}).$$

Thus, if convergence of the viscous solution to the inviscid irrotational one happens as  $\text{Re} \to +\infty$ , the former's vorticity  $\omega$  must become the latter's bed vortex sheet  $\gamma_b$ . This explains the pointwise divergence of the vorticity and its convergence in  $H^{-1}(\mathbb{T} \times \mathbb{R})$ .

 $^{1}$  *i.e.* we have

$$\boldsymbol{u} = \boldsymbol{\nabla}^{\perp} \psi$$
 and so  $-\Delta \psi = \omega$ .

<sup>2</sup>which is conserved in light of Lundgren and Koumoutsakos' result 4.3.

Vortex sheets and when to use them. As we were discussing lemma 4.3, we mentioned that  $\boldsymbol{u} \cdot \hat{\boldsymbol{\tau}}$  could be replaced by either  $\gamma_i$  (or  $\gamma_b$  depending on the considered integral). In fact the vortex sheet strengths  $\gamma_i$  and  $\gamma_b$  appear as soon as one is interested in a *continuous* extension of the stream function  $\psi$  in the entire cylinder  $\mathbb{T} \times \mathbb{R}$ .

In a sense, this continuous extension correspond to the very difference between Dormy and Lacave (2024)'s method and the Boundary Integral Method (BIM) where the representation formula for  $\psi$  is

$$\begin{split} \psi(t, \boldsymbol{x}) &= \int_{\Omega(t)} \omega(\boldsymbol{y}) G(\boldsymbol{x}, \boldsymbol{y}) \, \mathrm{d} \boldsymbol{y} \\ &+ \int_{\partial \Omega(t)} G(\boldsymbol{x}, \boldsymbol{y}) (\boldsymbol{u} \cdot \hat{\boldsymbol{\tau}}) (\boldsymbol{y}) \, \mathrm{d} S(\boldsymbol{y}) \\ &+ \int_{\partial \Omega(t)} \partial_{n, \boldsymbol{y}} G(\boldsymbol{x}, \boldsymbol{y}) \psi(\boldsymbol{y}) \, \mathrm{d} S(\boldsymbol{y}). \end{split}$$

(see e.g. Beer 2001; Bonnet 1995, for introductions to the BIM, even though the titles of these books misleads the reader into thinking that they are about the Boundary Element Method (BEM)) The difficulty with the above formula is that  $\psi$  appears in both the left- and right-hand sides. Introducing the solenoidal field  $\boldsymbol{u}_a$  in the air domain  $\Omega_a(t)$  bypasses this issue, at the cost of replacing  $\boldsymbol{u} \cdot \hat{\boldsymbol{\tau}}$  with  $\gamma_i$  or  $\gamma_h$ .

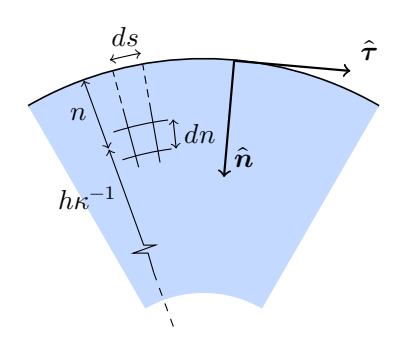


**Figure 4.15** – The Frénet frame in 2d. Geometrical interpretations of both quantities h and  $\kappa$ .

 $^{1}i.e.$  the smallest free-surface curvature radius reaches a minimum value with respect to the Reynolds number.

 $^2 \text{Indeed, denoting } u_n = \boldsymbol{u} \cdot \hat{\boldsymbol{n}}, \text{ we see easily that}$ 

$$\begin{split} \partial_t \Big( |\partial_s \pmb{\gamma}| \Big) &= \frac{\partial_s \pmb{\gamma}}{|\partial_s \pmb{\gamma}|} \cdot \partial_t \partial_s \pmb{\gamma} \\ &= \frac{\partial_s \pmb{\gamma}}{|\partial_s \pmb{\gamma}|} \cdot \partial_s \Big[ u_n \hat{\pmb{n}} + v \hat{\pmb{\tau}} \Big] \\ &= \frac{\partial_s \pmb{\gamma}}{|\partial_s \pmb{\gamma}|} \cdot \Big[ (\partial_s u_n) \hat{\pmb{n}} - u_n \kappa \hat{\pmb{\tau}} \\ &+ (\partial_s v) \hat{\pmb{\tau}} + v \kappa \hat{\pmb{n}} \Big] \\ &= -u_n \kappa + \partial_s v \stackrel{!}{=} 0, \end{split}$$

since the arc-length parametrisation is defined by the criterion  $|\partial_s \gamma| = 1$ . We have used many times the fact that

$$\partial_s \hat{\boldsymbol{\tau}} = \kappa \hat{\boldsymbol{n}},$$

by definition of the curvature.

Remark 4.5. The considerations of this section only apply in 2d. In the 3d case, the vortex stretching term in the vorticity equation must be handled carefully in order to obtain a result similar to lemma 4.3 (Lundgren and Koumoutsakos (1999) have done it in their appendix).

# IV. Regularisation of free surfaces due to viscosity

In sec. III.2, we observed that the strongest free-surface curvature, seen as a function of both time and Reynolds' number, reaches a maximum<sup>1</sup> around  $\text{Re} \approx 10^4$ , that is when the (Navier–type) boundary layer size becomes comparable to the radius of curvature. In the present section, we propose a general theory for interface regularisation due to viscosity, via parameter asymptotic expansion in terms of the boundary layer size

$$\delta = \frac{1}{\sqrt{\text{Re}}} \qquad \left(\delta = \frac{h_0}{\sqrt{\text{Re}}} \quad \text{in the dimensional world}\right),$$

and a basic scaling argument.

#### IV.1. Time evolution of the curvature

By regularisation, we mean that the curvature decreases due to viscous effects. In order to show this, we should derive an equation for the curvature evolution. This is done in Longuet-Higgins (1953, sec. 6). We propose to re-derive his equation in two different manners: using his  $\grave{a}$  la physicist approach and in a, less geometrical, more rigorous fashion.

IV.1.1. The Frénet frame. We start by rewriting some quantities in a curvilinear frame attached to the free-surface. We recall from chapter 2 that, should  $\gamma(t,s)$  denote a time-varying parametrisation of the free surface  $\Gamma_i(t)$ , we have

$$\partial_t \boldsymbol{\gamma}(t,s) = \Big( \hat{\boldsymbol{n}}(t,s) \cdot \boldsymbol{u} \Big( t, \boldsymbol{\gamma}(t,s) \Big) \Big) \hat{\boldsymbol{n}}(t,s) + v(t,s) \hat{\boldsymbol{\tau}}(t,s), \tag{4.8}$$

where v is an arbitrary slip vorticity. We assume that initially  $\gamma$  is parametrised using the arc-length. We preserve this parametrisation by choosing v such that<sup>2</sup>

$$\partial_s v(t,s) = \kappa(t,s) \Big( \hat{\boldsymbol{n}}(t,s) \cdot \boldsymbol{u} \Big( t, \boldsymbol{\gamma}(t,s) \Big) \Big).$$

We remark that v is defined up to a constant. Indeed, if all free-surface elements were sliding at the same constant velocity, this would not have any influence on the free-surface parametrisation. This peculiar choice of v has already been mentioned in lemma 2.13.

We work in the time-dependent Frénet frame (s,n) attached to the free surface (figure 4.15), where n corresponds to the coordinate in the normal direction (with unit velocity). The metric is implicitly defined by the relation

$$\mathrm{d}\boldsymbol{x}\otimes\mathrm{d}\boldsymbol{x}=\mathrm{d}\boldsymbol{n}\otimes\mathrm{d}\boldsymbol{n}+\left(1-\kappa\boldsymbol{n}\right)^{2}\mathrm{d}\boldsymbol{s}\otimes\mathrm{d}\boldsymbol{s}=\mathrm{d}\boldsymbol{n}\otimes\mathrm{d}\boldsymbol{n}+h^{2}\mathrm{d}\boldsymbol{s}\otimes\mathrm{d}\boldsymbol{s}.$$

The term h is called the shape factor. It can be viewed as the ratio between the distance of a point to the center of curvature and the

radius of curvature (fig. 4.15). This system possesses a coordinate singularity at  $n=\kappa^{-1}=R_c$  the curvature radius. This won't be an issue afterward as our analysis is concerned with boundary layers that are smaller that  $R_c$ . We mention that the curvature sign is chosen positive around waves' crests and negative around troughs (*i.e.* positive when convex inward).

For  $0 \le n < \kappa(t,s)^{-1}$ , we can decompose the velocity  $\boldsymbol{u}$  along the  $(\hat{\boldsymbol{\tau}},\hat{\boldsymbol{n}})$  frame as

$$\boldsymbol{u}(t,\boldsymbol{x}) = u_n(t,s,n)\hat{\boldsymbol{n}}(t,s) + u_{\tau}(t,s,n)\hat{\boldsymbol{\tau}}(t,s).$$

Following Massey and Clayton (1965) or Longuet-Higgins (1953), we can rewrite the Navier-Stokes system in the Frénet frame. This shall be done later in sec. V in order to understand the stability of boundary layers. However, for the time being, the divergence-free condition is enough. It becomes<sup>1</sup>

$$\nabla \cdot \boldsymbol{u} = \partial_s u_\tau + \partial_n (h u_n) = 0.$$

The relation between the stream function  $\psi$  and the velocity  $\boldsymbol{u}$  is thus<sup>2</sup>

$$u_{\tau} = -\partial_n \psi$$
 and  $u_n = h^{-1} \partial_s \psi$ .

The vorticity is then

$$\begin{split} \boldsymbol{\omega} &= \boldsymbol{\nabla}^{\perp} \cdot \boldsymbol{u} = \frac{1}{h} \Big( \partial_n \Big( h \boldsymbol{u}_{\tau} \Big) - \partial_s \boldsymbol{u}_n \Big) \\ &= -\frac{1}{h} \Big( \partial_n \Big( h \partial_n \psi \Big) - \partial_s \Big( h^{-1} \partial_s \psi \Big) \Big) = -\Delta \psi. \end{split}$$

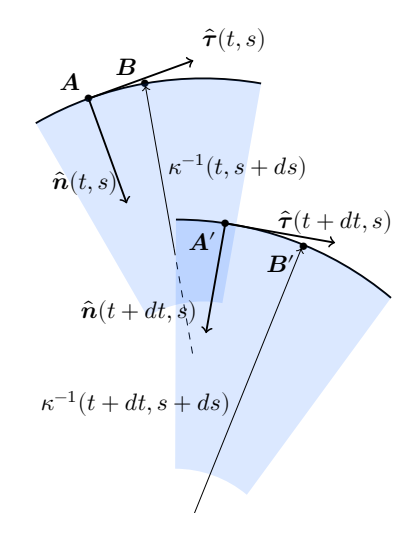


Figure 4.16 – Geometrical derivation of the curvature evolution equation: the frame at time t and t + dt.

<sup>1</sup>Differential operators expressed in any general orthogonal curvilinear system of coordinates can be found in appendix B.

<sup>2</sup>We can also define the velocity potential as

$$u_{\tau} = h^{-1} \partial_s \phi$$
$$u_n = \partial_n \phi.$$

IV.1.2. **Geometrical derivation.** We kindly ask the reader to forget about rigour until the next section. We now describe the method used by Longuet-Higgins (1953) in order to derive his curvature evolution equation. In order to follow the argument easily, a schematic representation of the configuration is provided in fig. 4.16.

Let us consider two points  $\mathbf{A} = \gamma(t, s)$  and  $\mathbf{B} = \gamma(t, s + ds)$  lying on the boundary  $\Gamma_i(t)$  and separated by an "infinitesimal" arc-length ds at time t. At time t + dt, they become  $\mathbf{A}' = \gamma(t + dt, s)$  and  $\mathbf{B}' = \gamma(t + dt, s + ds)$ .

From the evolution equation (4.8) of the parametrisation, we know that

$$\begin{array}{lclcrcl} {\bf A}' - {\bf A} & = & v(t,s) \, dt \, \hat{{\bf \tau}}(t,s) & + & u_n(t,s,0) \, dt \, \hat{{\bf n}}(t,s) & + & O(dt^2) \\ {\bf B}' - {\bf B} & = & v(t,s+ds) \, dt \, \hat{{\bf \tau}}(t,s+ds) & + & u_n(t,s+ds,0) \, dt \, \hat{{\bf n}}(t,s+ds) & + & O(dt^2). \end{array}$$

From the definition of the curvature, we see rather easily that

$$\hat{\boldsymbol{\tau}}(t,s+ds) = \hat{\boldsymbol{\tau}}(s,t) + \kappa(t,s) \, ds \cdot \hat{\boldsymbol{n}}(t,s) + O(ds^2)$$

$$\hat{\boldsymbol{n}}(t,s+ds) = \hat{\boldsymbol{n}}(t,s) - \kappa(t,s) \, ds \cdot \hat{\boldsymbol{\tau}}(t,s) + O(ds^2) ,$$

so that

$$\begin{array}{lcl} \boldsymbol{B}'-\boldsymbol{B} & = & dt \, \left[\boldsymbol{v}+\partial_s \boldsymbol{v}\cdot ds - \kappa \boldsymbol{u}_n\cdot ds\right](t,s,n=0)\cdot \hat{\boldsymbol{\tau}}(t,s) \\ & + & dt \, \left[\boldsymbol{u}_n+\partial_s \boldsymbol{u}_n\cdot ds + \kappa \boldsymbol{v}\cdot ds\right](t,s,n=0)\cdot \hat{\boldsymbol{n}}(t,s) & + & O(ds^2) + O(dt^2). \end{array}$$

Hence the vector going from  $\boldsymbol{A}$  to  $\boldsymbol{B}$  changes with time as

$$\boldsymbol{B}' - \boldsymbol{A}' = \underbrace{\boldsymbol{B} - \boldsymbol{A}}_{ds \cdot \hat{\boldsymbol{\tau}}} + ds \, dt \Big[ \partial_s \boldsymbol{v} - \kappa \boldsymbol{u}_n \Big] \cdot \hat{\boldsymbol{\tau}} + ds \, dt \Big[ \partial_s \boldsymbol{u}_n + \kappa \boldsymbol{v} \Big] \cdot \hat{\boldsymbol{n}} + O(ds^2) + O(dt^2), \tag{4.9}$$

all quantities being evaluated at t, s and n = 0 if needed. For small dt, it is possible to assume that the vector  $\mathbf{B} - \mathbf{A}$  remains of constant length (omitting  $O(ds \, dt + ds^2)$  terms). We can then write  $\mathbf{B}' - \mathbf{A}' = ds \cdot \hat{\mathbf{s}}(s, t + dt)$ . Let  $\Upsilon(t, s) \, dt$  be the angle by which the coordinate system at s is rotated between times t and t + dt. We can then write

$$\hat{\boldsymbol{\tau}}(t+dt,s) = \hat{\boldsymbol{\tau}}(t,s) + \Upsilon(t,s) dt \cdot \hat{\boldsymbol{n}}(t,s) + O(dt^2).$$

Inserted in relation (4.9), this gives the relations

$$\Upsilon = \partial_s u_n + \kappa v,\tag{4.10a}$$

$$0 = \partial_s v - \kappa u_n \qquad \text{(once again)}. \tag{4.10b}$$

Let  $\widehat{AB}$  be the angle between the normals  $\widehat{n}(t,s)$  and  $\widehat{n}(t,s+ds)$ ,  $\widehat{AA'}$  be the angle between the normals  $\widehat{n}(t,s)$  and  $\widehat{n}(t+dt,s)$ , etc. We have then

$$\begin{array}{cccc} \widehat{\boldsymbol{A}\boldsymbol{B}} & = & \kappa(t,s)\,ds & & \widehat{\boldsymbol{A}\boldsymbol{A'}} & = & \Upsilon(t,s)\,dt \\ \widehat{\boldsymbol{A'}\boldsymbol{B'}} & = & \left[\kappa + \partial_t\kappa\,dt\right]ds & & \widehat{\boldsymbol{B}\boldsymbol{B'}} & = & \left[\Upsilon + \partial_s\Upsilon\,ds\right]dt. \end{array}$$

From  $\widehat{AA'} + \widehat{A'B'} = \widehat{AB'} = \widehat{AB} = \widehat{BB'}$  and eq. (4.10), we get the main curvature evolution relation

$$\partial_t \kappa = \partial_s \Upsilon = \partial_{ss} u_n + v \partial_s \kappa - \kappa^2 u_n \qquad \text{(at } n = 0). \tag{4.11}$$

IV.1.3. Another derivation. We can obtain the same evolution equation using a more direct approach. We assume that the interface arc-length parametrisation  $\gamma$  is at least three time differentiable (even to the sense of distributions). We use the tangential velocity v defined in (4.8) so that the condition  $|\partial_s \gamma| = 1$  holds at all time  $t \ge 0$ . From the definition of the curvature, we see readily that

$$\partial_t \kappa = \left(\partial_t \partial_s \hat{m{ au}}\right) \cdot \hat{m{n}} + \partial_s \hat{m{ au}} \cdot \partial_t \hat{m{n}}.$$

A rapid computation yields

$$\begin{split} \partial_s \partial_t \hat{\pmb{\tau}} &= \partial_s \left( \partial_t \partial_s \pmb{\gamma} \right) \\ &= \partial_s \left[ \left( \partial_s u_n \right) \hat{\pmb{n}} + u_n \left( \partial_s \hat{\pmb{n}} \right) + \left( \partial_s v \right) \hat{\pmb{\tau}} + v \left( \partial_s \hat{\pmb{\tau}} \right) \right] \\ &= \partial_s \left[ \left( \partial_s u_n \right) \hat{\pmb{n}} - u_n \kappa \hat{\pmb{\tau}} + \left( \partial_s v \right) \hat{\pmb{\tau}} + v \kappa \hat{\pmb{n}} \right] \\ &= \left( \partial_{ss} u_n \right) \hat{\pmb{n}} - \left( \partial_s u_n \right) \kappa \hat{\pmb{\tau}} + \kappa \left( \partial_s v \right) \hat{\pmb{n}} + v \left( \partial_s \kappa \right) \hat{\pmb{n}} - v \kappa^2 \hat{\pmb{\tau}}, \end{split}$$

so that finally (recalling that  $u_n \kappa = \partial_s v$ )

$$\left(\partial_s\partial_t\hat{\boldsymbol{\tau}}\right)\cdot\hat{\boldsymbol{n}} = \partial_{ss}u_n - u_n\kappa^2 + v\partial_s\kappa,$$

which may give the reader a light feeling of dejà vu. To handle the second term, we notice that

$$\partial_t \hat{\boldsymbol{n}} = \left(\partial_t \hat{\boldsymbol{\tau}}\right)^{\perp} = -\left(\partial_s u_n\right) \hat{\boldsymbol{\tau}} - v \kappa \hat{\boldsymbol{\tau}},$$

meaning that

$$\partial_{\sigma}\hat{\boldsymbol{\tau}}\cdot\partial_{\tau}\hat{\boldsymbol{n}}=\kappa\hat{\boldsymbol{n}}\cdot\partial_{\tau}\hat{\boldsymbol{n}}=0.$$

We therefore recover Longuet-Higgins' relation (4.11) in a more straightforward manner, without resorting to some dark magic of any kind. Deriving an equivalent relation in the case of a general parametrisation is left as an exercise to the motivated reader. Ambrose and Masmoudi (2009a) also obtained an evolution equation for the mean curvature in 3d using the first and second fundamental forms.

#### IV.2. Asymptotic expansion and scaling

We observed that, in the case of water waves, the vorticity extends to a distance  $\delta = \text{Re}^{-\frac{1}{2}}$  from the interface. This vorticity boundary layer is created by the moving interface through (4.4a). We make use of the following decomposition (similar to Helmholtz (1858)'s decomposition with the potential being Euler's solution) for the velocity,

$$\boldsymbol{u} = \boldsymbol{\nabla} \phi_E + \boldsymbol{\nabla}^{\perp} \psi_{\mathrm{Re}},$$

i.e. the difference between Euler's irrotational solution and the Navier-Stokes solution is written as  $\nabla^{\perp}\psi_{\mathrm{Re}}$ . This is well-justified in fixed domains but since the fluid domain  $\Omega(t)$  depends on Re in itself, one must use extra care. Using either the Lagrangian framework or a continuous extension in the entire space (à la Dormy and Lacave (2024)) solves this issue. We propose to decompose  $\psi_{\mathrm{Re}}$  as

$$\psi_{\text{Re}}(t, s, n) = \psi_0(t, s, n) + \delta \psi_1(t, s, n) + \delta^2 \psi_2(t, s, n) + O(\delta^3).$$

Since the typical variation scale along the normal direction is  $\delta$ , we can further rewrite

$$\psi_{\mathrm{Re}}(t,s,n) \equiv \psi_{\mathrm{Re}}\left(t,s,\frac{n}{\delta}\right),$$

so that each application of the normal derivative reduces the order of the expansion in  $\delta$  by one. Having in mind the numerical results of sec. III.2 (and boundary layer theory in general), we see that both  $\psi_0$  and  $\psi_1$  are identically zero (in order to have a velocity of order  $O(\delta)$  and a vorticity O(1) as  $\delta \to 0$ ). Therefore

$$\psi_{\text{Re}} = \frac{1}{\text{Re}} \, \psi_2 + O(\text{Re}^{-\frac{3}{2}}) = \delta^2 \psi_2 + O(\delta^3).$$

This condition can then be introduced in the curvature evolution equation (4.11), yielding

$$\begin{split} \partial_t \kappa &= \partial_{ssn} \phi_E + \kappa^2 (\partial_n \phi_E) - h^{-1} (\partial_s \phi_E) (\partial_s \kappa) \\ &\quad + \partial_{ss} \left( h^{-1} \partial_s \psi_{\mathrm{Re}} \right) - v (\partial_s \kappa) + \kappa^2 h^{-1} (\partial_s \psi_{\mathrm{Re}}) \\ \Leftrightarrow &\quad O(\kappa \tau^{-1}) = \mathrm{potential} \\ &\quad + O\left( \delta^2 \right) + O(\kappa^2 \delta^2) + O(\kappa^2 \delta^2), \end{split} \tag{4.12}$$

where the scaling  $v = O(\kappa \delta^2)$  follows from the link (4.10b) between v and  $u_n$ . We recall that h = 1 for n = 0 (i.e. on the free surface) and we have denoted by  $\tau$  the typical regularising time. Rearranging the terms in the above equation, we get

$$\tau \sim O(\kappa \text{Re}) + O(\kappa^{-1} \text{Re}),$$

the former (respectively the latter) being the smallest on large scales (resp. small scales). Beware: we are interested in the smallest of the two terms.

For waves of (relatively) small amplitudes and large wavelengths  $\kappa \ll 1$ , as in the open ocean. In this case we have  $\tau$  scales as Re, in accordance with the usual decay rate used in sec. IV of chapter 3 (Lamb 1932; Liu and Davie 1977). On the other hand, for highly curved regions (in the simulations presented in this chapter,  $\kappa$  reaches values  $\sim 10^2 \to 10^3$ ), the second and third terms in (4.12) yield regularising effects happening in the course of the numerical experiment should  $\kappa^{-1} \text{Re} \sim 1 \to 10$ , in accordance with our observations at  $\text{Re} = 10^2$  and  $\text{Re} = 10^3$ . For higher values of Reynolds' number the numerical experiment is not long enough for the viscous effects to become important.

From the analysis above, we have understood the observations that were made when discussing the figure 4.9. The curvature evolution equation (4.11) seems like a natural candidate to investigate the link between viscosity and free surfaces in a more rigorous manner. It may even be appropriate in order to study a possible finite-time cusp—like singularity appearing in the free-surface Euler equation.

**Remark 4.6.** The analysis presented above generally applies to any interface involving a 2d viscous fluid. It is not restricted to the case of water waves.



# Irrotationality of Water Waves and topography

"Science compels us to explode the sun!"

Pye, In: Outer Wilds (2019, dir. A. Beachum and L. Verneau)

In the previous chapter, we have used numerical simulations to investigate the boundary layer appearing below the free-surface and concluded that, up to the splash, it remains sufficiently well-mannered not to perturb the bulk of the flow, which therefore remains irrotational. In his celebrated 1953 work, Longuet-Higgins noticed that a lack of irrotationality could come not only from the free surface, but from the water bed too:

"[Q]uite near the bottom the fluid is observed to be in motion with velocities comparable to that of the interior of the fluid, so that in general there must be a strong velocity gradient near the bottom. This implies that there is in fact strong vorticity in the neighbourhood of the bottom [...]. In an oscillating motion this vorticity will be of alternating sign; and the question then presents itself: will any of the vorticity spread into the interior of the fluid, or will it remain in a neighbourhood of the boundary?" (Longuet-Higgins 1953)

In the present chapter, we address this question. To do so we supply the no–slip/Dirichlet boundary condition (1.15) on the fluid's bottom boundary  $\Gamma_b$ . We have seen in sec. III.3 of chapter 4 that in the case of a breaking wave over flat bottom, this does not change our observations on short time scales. Therefore, we now use a non–flat topography, irregular at first and then smooth. We shall see that the associated boundary layer is unstable, leading to pairs of vortices being effectively shed in the bulk flow. This boundary layer separation prevents the convergence of the Navier-Stokes solution to Euler's irrotational one as the viscosity vanishes.

# I. Motivation: why should water waves be irrotational?

As we were motivating the Water Waves system (1.43), the key hypothesis was the irrotationality of the flow (**H11**), leading us to the introduction of a velocity potential  $\phi$  whose value on the free-surface  $\psi$  is the canonical variable used in the Zakharov–Craig and Sulem formulation of the problem.

Numerous reduced models typically used to study oceanic surface waves correspond in fact to asymptotic regimes of this set of equations. This chapter is based on our study Riquier and Dormy (2024a).

<sup>1</sup>*i.e.* when the shallowness  $\mu = h_0/\lambda$  is small,  $\mu \ll 1$ .

<sup>2</sup>whose well-posedness follows from the standard theory of quasilinear symmetrisable hyperbolic systems (Alinhac and Gérard 2007; Benzoni-Gavage and Serre 2007; Métivier 2008; Taylor 2011). Their justification as  $O(\mu^2)$  asymptotic regimes of the Water Waves equations (1.43) is done in Lannes (2013b, prop. 5.2) or Duchêne (2021, thm. 5.8).

 $^3$ Serre (1953), Green and Naghdi (1976). The well-posedness of this system has been established by e.g. Li (2006), Alvarez-Samaniego and Lannes (2009) or Duchêne and Israwi (2018). In these references, it is also shown that the Green-Naghdi system corresponds to a  $O(\mu^4)$  asymptotic regime of (1.43).

<sup>4</sup>Boussinesq (1872)

<sup>5</sup>Boussinesq (1877), Korteweg and de Vries (1895). The mathematical analysis of this equations, and its justification as a  $O(\mu^2)$  approximation of the Water Waves system (up to a certain time that might depend on  $\mu$ ) has been proved by e.g. Craig (1985) or Kano and Nishida (1986).

<sup>6</sup>Whitham (1967)

<sup>7</sup>Schrödinger (1926), Davey and Stewartson (1974), whose mathematical justification has been established in e.g. Craig, Sulem, and Sulem (1992) and Craig, Schanz, et al. (1997) respectively. The former is in fact also linked to the KdV equation (5.2) (Schneider 1998) and thus also appear in shallow water.

Figure 5.1 – The sequence of asymptotics that lead to reduced shallow water models. The first limit is far from completely understood.

A comprehensive discussion about shallow water asymptotics<sup>1</sup> can be found in Lannes (2020) or Duchêne (2021). To provide a complete self-contained introduction to the problem at hand, we hereby mention a few of these regimes and write them using the notations of chapter 1.

1. The Shallow Water equations (Barré de Saint-Venant 1871),<sup>2</sup>

$$\begin{cases}
\partial_t \eta + \vec{\nabla} \cdot (h\vec{u}) = 0 \\
\partial_t \vec{u} + \varepsilon \vec{u} \cdot \vec{\nabla} \vec{u} + g \vec{\nabla} \eta = 0,
\end{cases} (5.1)$$

commonly used in physics, written here on a flat topography with  $h = 1 + \varepsilon \eta$ . The *formal* derivation of these equations do not put emphasis on the presumed irrotationality of the flow, even though it is a direct consequence of the columnar motion.

2. The Serre-Green and Naghdi<sup>3</sup> system,

$$\left\{ \begin{array}{cccc} \partial_t \eta & + & \vec{\nabla} \cdot \left( h \vec{u} \right) & = & 0 \\ \left( \mathbf{id}_{d \times d} + \mu \mathbf{T}[h] \right) \partial_t \vec{u} & + & \varepsilon \vec{u} \cdot \vec{\nabla} \vec{u} + g \vec{\nabla} \eta + \mu \varepsilon \vec{\mathbf{Q}}(h, \vec{u}) & = & 0, \end{array} \right.$$

with  $\mathbf{T}[h]$  a matrix-like operator depending non-linearly on h, and  $\vec{\mathbf{Q}}(h, \vec{u})$  a nonlinear term (not explicitly written). Omitting the latter yields Boussinesq's system<sup>4</sup>. Notice that we recover the Shallow Water equations (5.1) by setting  $\mu = 0$ .

3. The Korteweg and de Vries equation,<sup>5</sup>

$$\partial_t u + \frac{3}{2} u \partial_x u + \frac{1}{6} \partial_{xxx} u = 0, \tag{5.2}$$

and their generalisation over non-flat topographies by Johnson (1973a,b), Shuto (1974) or Israwi (2010). Another worth mentioning scalar equation is Whitham's one,<sup>6</sup> relevant when one is interested in wave breaking (in the sense of a shock).

**Remark 5.1.** We choose not to discuss the *deep water* regimes (e.g. the nonlinear Schrödinger equation or the Davey and Stewartson model<sup>7</sup>) as their validity is not affected by the results of the present chapter.

Remark 5.2. We shall discuss the relevance of shallow water models incorporating the vorticity in the conclusion of the present chapter.

In chapter 4, we have seen that the free surface contributes little to the vorticity generation as long as no splash occurs, so that the flow should remain irrotational there. However, the Prandtl-like boundary layer lying in the vicinity of the bed might not be easy to neglect, even at high Reynolds number, because separation may happen. A fundamental difficulty is that such phenomenon is completely overlooked by the models mentioned above, which are derived following the procedure shown in figure 5.1. However the first limit presented in fig. 5.1 is far from trivial.

Since the results of Swann (1971) and Chemin (1996) about the Re  $\rightarrow +\infty$  limit in the entire space (in 3d and 2d respectively), it is known that all the difficulties with the vanishing viscosity limits stem from the boundaries (this can also be seen as a consequence of Kato (1984)'s theorem). We can argue that the free-slip/Navier condition should not cause any major issue, even for rough boundaries

(Gérard-Varet, Lacave, et al. 2018; Masmoudi and Rousset 2012), but no mathematical proof of this assertion seems currently available (the only work on the vanishing viscosity limit for free-surface flows that the author is aware of being the one of Masmoudi and Rousset (2017) in which there is no bottom topography). The case of no-slip/Dirichlet boundary condition is once again more tedious (Masmoudi 2007), even though this condition seems more physically relevant. The fundamental issue is that, on uneven topographies, the boundary layer may become unstable and separate, thus preventing the viscous solution to converge to Euler's irrotational one.

Coming back to the question addressed in the title of the present section: should water waves remain irrotational (and should the problem at hand enter the domain of validity of a certain asymptotic regime), we could use one of the asymptotic models mentioned before to significantly simplify its theoretical or numerical treatment. However, a deficit of irrotationality that does not disappear as  $\nu \to 0$  invalidates the use of such model, even in the correct asymptotic regime (the two limits in fig. 5.1 do not commute).

### II. Non-convergence to the irrotational solution

To investigate the high Reynolds number limit when the bottom boundary  $\Gamma_b$  is not flat, we make use of the method described in chapter 3 with the initial condition contructed from  $(4.\mathrm{N})$ , with an initial amplitude a=0.1. A larger value of a, like e.g. a=0.15, yields a overturning wave rather quickly when an obstacle lies on the bed. The simulation parameters used in the various simulations appearing in this chapter are available in tables 5.1 and 5.2.

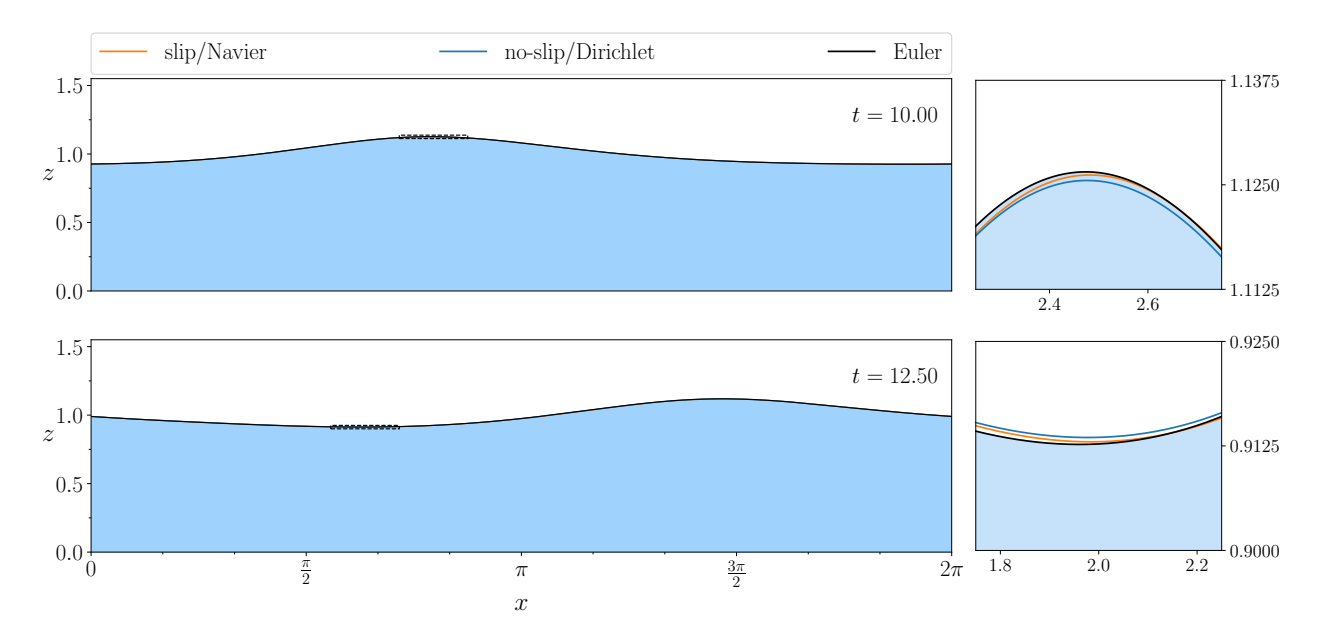


Figure 5.2 – Comparison between the slip/Navier and the no-slip/Dirichlet boundary conditions for a wave of amplitude a=0.1 over a flat topography at Re =  $10^5$ . [parameters: table 5.1]

<sup>&</sup>lt;sup>1</sup>Standard literature on boundary layer separation include Lagerstrom (1975), Sychev et al. (1998), Schlichting and Gersten (2017, sec. 2.6) or Ruban (2018, ch. 2). Regarding the mathematical literature, the reader can refer to the work of Dalibard and Masmoudi (2019) on Prandtl's equation.

<sup>&</sup>lt;sup>2</sup>To: we do not assert that the viscous solution does not converge to an inviscid one. We only state that, should separation happen, then the solution attained as  $\text{Re} \to +\infty$  will not be irrotational.

<sup>&</sup>lt;sup>3</sup>*i.e.* we prescribe the initial normal velocity on the interface, using the value described in sec. I.1.2.

Fig.	$N_{ m bot}$	$_{\mathrm{BC}}$	Rem.
5.2	100 1 000	slip no-slip	MA MA
Fig.	$N_{ m bot}$	Re	Rem.
	1000	$10^{2}$	PR
	1000	$10^{2.5}$	PR
	1000	$10^{3}$	PR
5.4	1000	$10^{3.5}$	PR
	1000	$10^{4}$	PR
	1000	$10^{4.5}$	PR
	1250	$10^{5}$	PR

Table 5.1 – Numerical parameters used for the simulations over a flat bottom and a sharp step. The mesh advection velocity is always computed by solving the elliptic problem (3.9). The number of points on the interface if always  $N_{\rm top}=3000$ .  $N_{\rm bot}$  corresponds to the number of points used to discretise the entire boundary  $\Gamma_b$ 

<sup>1</sup>One could use the value of Stokes first order solution (1.25) on the bottom z = 0 for  $U_b$ , yielding

$$U_b = a \cdot \sqrt{\frac{2gk}{\sinh(2kh_0)}}$$

for instance.

<sup>2</sup>Stokes (1850) studied the motion of a viscous fluid extending at infinity in the x direction whose tangential velocity along a wall at  $\{y=0\}$  is a cosine. The corresponding solution's vorticity scales as

$$\omega(t, y) \propto \operatorname{Re}^{\frac{1}{2}} \exp\left(-\operatorname{Re}^{\frac{1}{2}}y\right) f(t),$$

which becomes a vortex sheet as  $\text{Re} \to +\infty$ . The details of the computations can be found in *e.g.* Landau and Lifshitz (1987). This exact problem with a free surface has been studied by Yih (1968).

Figure 5.3 – Schematic representation of the numerical domain with a rectangular step. Periodic conditions are once again imposed on the left and right boundaries.

# II.1. Stability of the boundary layer laying over a flat topography: the non-breaking case

We start by investigating the boundary layer appearing in the vicinity of a flat topography, as in section III.3 of the previous chapter, but with a non-breaking wave that allows to carry out the simulation up to a greater time. This is the result shown in figure 5.2 for a Reynolds number  $Re=10^5$ , in which are compared the interfaces corresponding to the viscous solution and the inviscid irrotational one. A small gap with the Euler solution is visible for both the free-slip/Navier and the no-slip/Dirichlet simulations with the same magnitude (about  $\approx 10^{-4} h_0$ , pointwise).

Even though the latter seems to converge slower than the former, the stability of the bottom boundary layer (when using Dirichlet boundary conditions) does not seem to prevent convergence to the inviscid irrotational solution in this particular case. The discussion of sec. III.3.2, about the convergence of the bed's vorticity sheet to the bottom vortex sheet strength  $\gamma_b$  as Re  $\rightarrow +\infty$ , seems to hold.

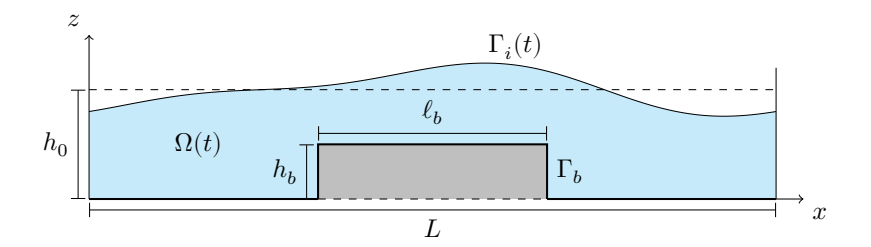
Surprisingly, the boundary layer remains laminar in the course of the simulation. This may be due to the oscillatory nature of the flow, as well as the periodicity of the domain. Indeed, defining a Reynolds number  $\mathrm{Re_{bl}}$  as in the theory of boundary layer over flat plate (Batchelor 1967, sec. 5.8),

$$\operatorname{Re}_{\mathrm{bl}} = \frac{LU_b}{\nu} = L^{\dagger}U_b^{\dagger}\operatorname{Re},$$

where L is the length of the domain and  $U_b$  is the characteristic velocity of the flow our of the boundary layer but close to the bottom, then  $\mathrm{Re_{bl}} \approx 5 \cdot 10^4$ , which is still still far from the turbulent separation threshold ( $\mathrm{Re_{bl,c}} \approx 5 \cdot 10^5$ ). This observation could lead to the conclusion that the boundary layer shall become unstable at higher values of Re. However, the oscillatory nature of the background flow may prevent this eventuality. Indeed, even though the Dirichlet boundary condition leads to a layer following Prandtl's scaling, the configuration is in fact closer to a Stokes–type oscillating boundary layer, which does not cause any issue in the inviscid limit. A way to understand the stabilisation process associated with oscillating flows is to notice that the local Reynolds number changes with time and vanishes periodically.

#### II.2. Adding a rectangular step on the bed

We now propose to add an obstacle on the water bed: a rectangular step of height  $h_b=0.5$  and length  $\ell_b=L/3$  (with  $L=2\pi$  as in chapter 3; see figure 5.3 for a schematic representation), on which the no-slip/Dirichlet boundary condition is prescribed.<sup>3</sup>



The initial condition is once again constructed by numerically solving the problem (4.N) with the prescribed normal velocity (4.2) and an amplitude a=0.1. This initial condition yields singularities on the salient edges of the step: the velocity is infinite there. We shall discuss this fact later, in sec. IV.2. Simulations are carried out with Reynolds numbers ranging from Re =  $10^2$  to Re =  $10^5$  (in multiplicative steps of size  $\sqrt{10}$  in order to emphasise the logarithmic nature of the convergence). We could not resolve higher values of the Reynolds number for reasons that shall be discussed below.

<sup>3</sup>This experimental configuration has been studied theoretically by Lamb (1932, §176) and experimentally by Grue (1992). An analytical solution for a steady potential flow behind a step is also computed in Feldmeier (2019), sec. 5.2.

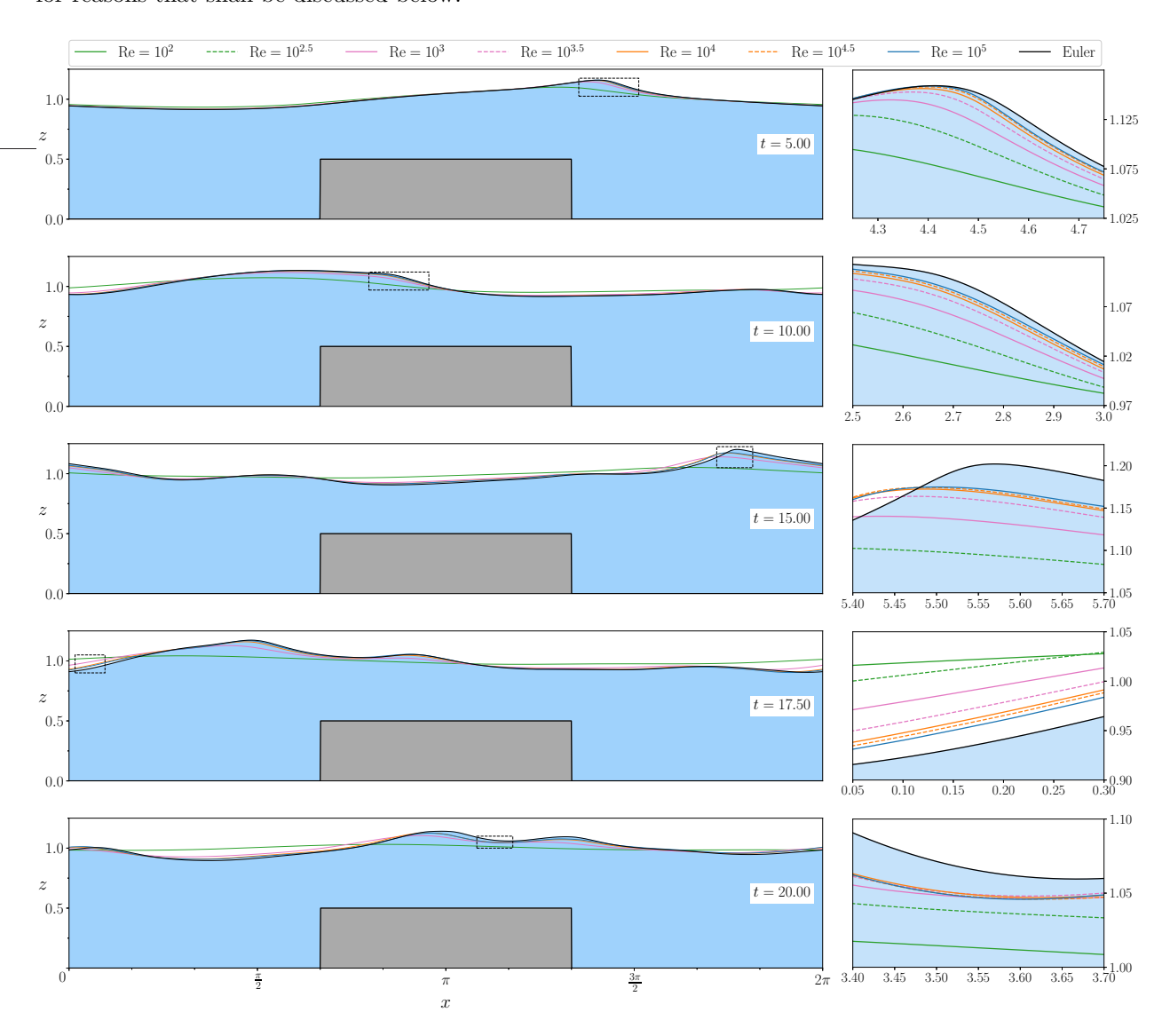


Figure 5.4 –  $\stackrel{\frown}{\square}$  – Time evolution of the free surfaces obtained by solving the Navier-Stokes problem (with Re ranging from  $10^2$  to  $10^5$ ) and Euler's one as well, making use of the numerical method of Dormy and Lacave (2024). [parameters: table 5.1]

Figure 5.4 shows the associated results at different times, all simulations beginning with the exact same initial condition. Interfaces comparisons are done with the inviscid irrotational solution, computed with the dipole method of Dormy and Lacave (2024). As in the flat bottom case, a small difference appears between each Navier-Stokes solution and Euler's one. However, this finite gap does not seem to

 $^{1}$ For two functions f, g defined on the torus, we write

$$\begin{split} d(f,g) &= \left\| f - g \right\|_{L^2(\mathbb{T})} \\ &= \left[ \int_{\mathbb{T}} \left( f - g \right)^2 (\theta) \, \mathrm{d}\theta \right]^{\frac{1}{2}}. \end{split}$$

disappear as the viscosity is decreased. The Navier-Stokes solution seems to converge to somethong that does not correspond to the inviscid irrotational one. In the following, we shall see that this is due to vorticity being emitted at the step's corners.

We can make the previous observation more quantitative by computing distances. In chapter 4, we made use of Hausdorff's distance since the waves were overturning. This is not the case here so we choose to use the standard  $L^2$  distance instead.<sup>1</sup> To this end, we denote by  $\gamma_{\rm Re}(t)$  (respectively  $\gamma_E(t)$ ) the parametrised interfaces at time t corresponding to the numerical solution of the free-surface Navier-Stokes problem (1.54) (respectively the inviscid irrotational Euler numerical solution). Following the procedure described in sec. III.2 of chapter 2, as long as the wave does not break (in the sense of definition 2.22), we can define  $\eta_{\rm Re}(t)$  (resp.  $\eta_E(t)$ ), the single-valued interface associated with  $\gamma_{\rm Re}(t)$  (resp.  $\gamma_E(t)$ ) at time t. We then define the relevant  $L^2$  distances

$$\begin{split} d_E(t; \mathrm{Re}) &= d \Big( \eta_E(t), \eta_\mathrm{Re}(t) \Big) \\ d_5(t; \mathrm{Re}) &= d \Big( \eta_\mathrm{Re=10^5}(t), \eta_\mathrm{Re}(t) \Big). \end{split}$$

These quantities can be computed numerically. They are plotted in figure 5.5.

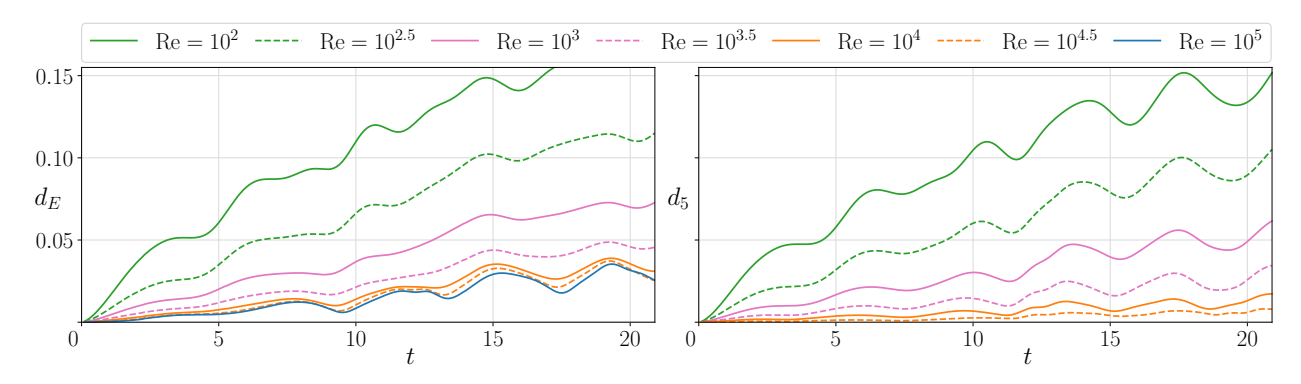


**Figure 5.5** – (left)  $L^2$  distance  $d_E$  between each Navier-Stokes solution and Euler's irrotational one as a function of time. (right) Evolution of the  $L^2$  distance  $d_5$  between the Re =  $10^5$  solution and the other Navier-Stokes solutions, for which Re  $< 10^5$ .

<sup>2</sup>but it still increases slowly with time

Safeguard against self-plagiarism. Some paragraphs in the following sections are reproduced from Riquier and Dormy (2024a) verbatim.

On the left part of fig. 5.5, we observe that the distance  $d_E$  to Euler's solution approaches a non-vanishing function of time, which slowly increases on average. At the same time, the distance  $d_5$  decreases with the Reynolds number<sup>2</sup>, thus exhibiting characteristics of a Cauchy sequence. We can therefore conclude that the Navier-Stokes solutions seem to converge, as  $\text{Re} \to +\infty$ , towards something that does not correspond to the Water Waves solution, even though the initial condition is irrotational.

### III. Boundary layer separation

To understand the lack of irrotationality that prevents the convergence to the inviscid irrotational solution, we show the flow's vorticity at  $\mathrm{Re}=10^5$  in figure 5.6.

The situation is rather clear: at the edges of the rectangular step, vorticity is shed from the boundary layer into the bulk. That is, the

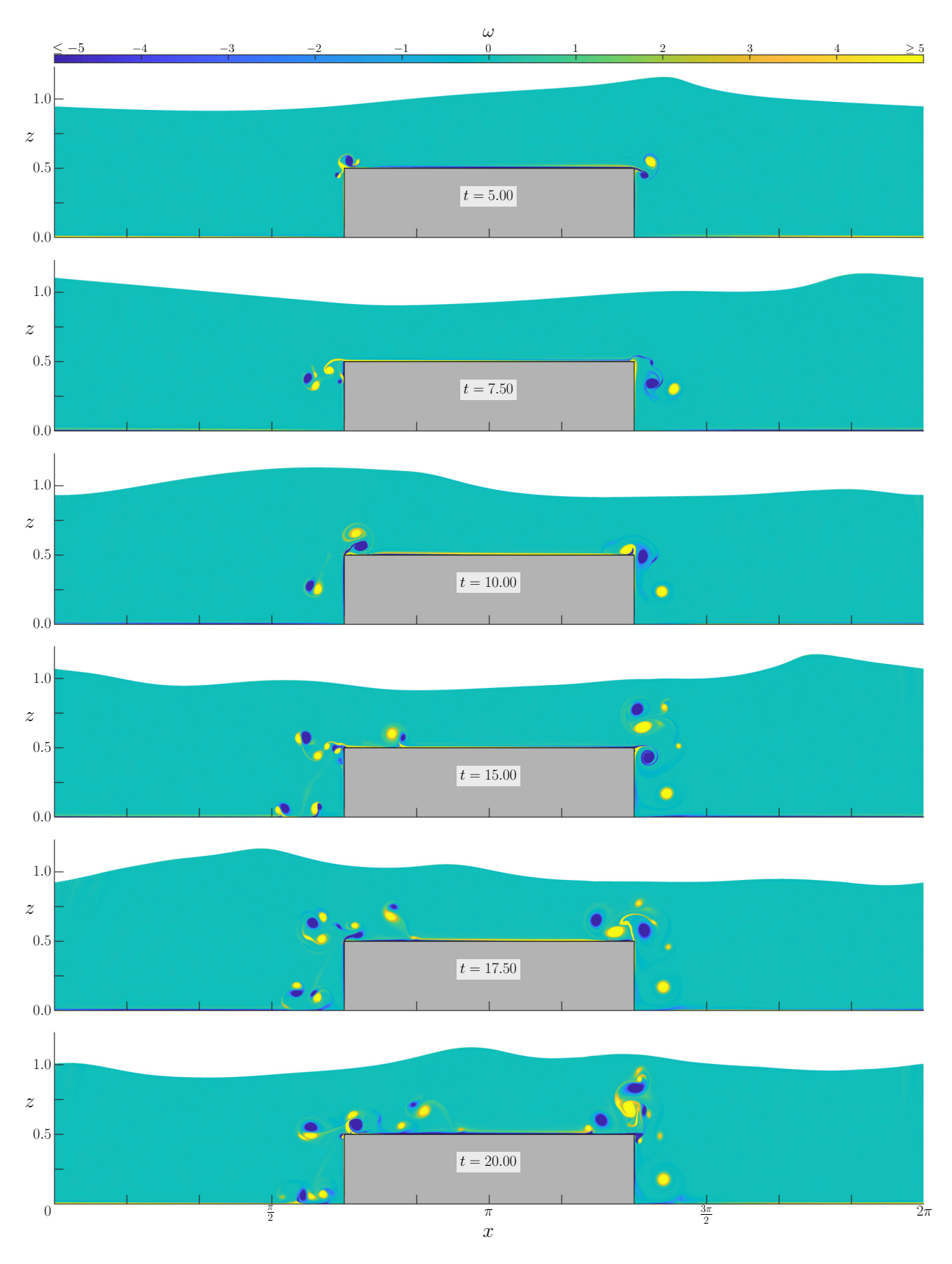
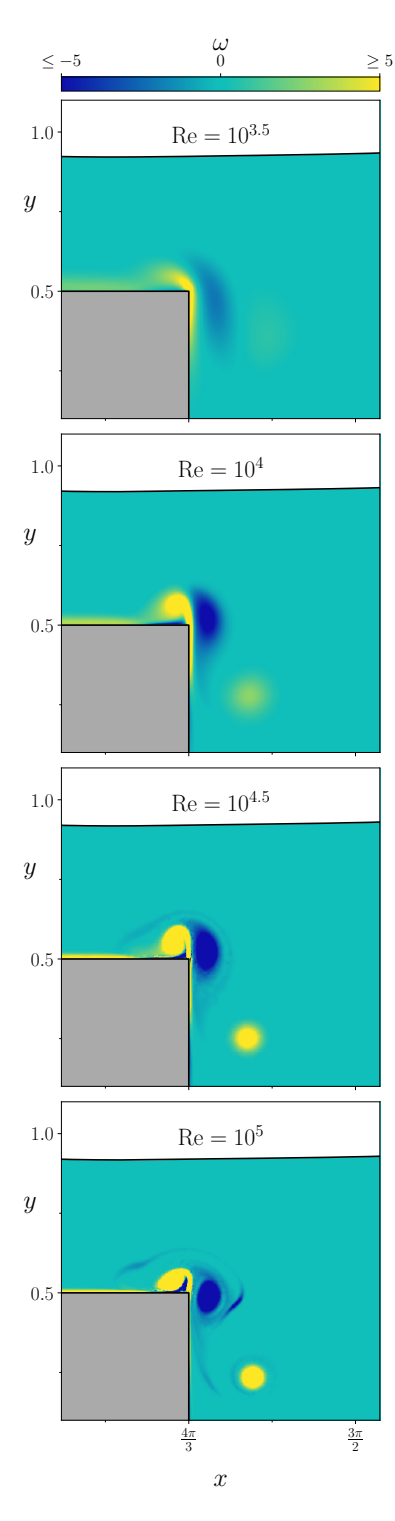


Figure 5.6 –  $\stackrel{\text{Ch}}{=}$  – Evolution of the vorticity  $\omega = \partial_x u_z - \partial_z u_x$  corresponding to the simulation with Re = 10<sup>5</sup>. The color scheme has been centered on the range [-5,5] to highlight the vortices. [parameters: table 5.1]



**Figure 5.7** – The vorticity  $\omega$  at fixed time t=10 for different values of Re close to the right edge of the step.

<sup>1</sup>In 3d the situation is somewhat different because the vortex lines are subject to the Crow (1970) instability or the elliptic instability (Moore and Saffman 1975). See the review article by Leweke et al. (2016).

background (potential) flow associated with the "passage" of a wave above a rectangular obstacle destabilises the boundary layer, which eventually separate. This separated vorticity takes the form of a continuous jet (a vortex layer) whose strength depends on the background flow's velocity. Once in the bulk, each filament winds-up onto itself because of the Kelvin–Helmhotz instability (Benjamin and Bridges 1997a,b; Bergmann et al. 2024; Birkhoff 1962; Caflisch et al. 2022; DeVoria and Mohseni 2018; Meiron et al. 1982; Sulem et al. 1981), yielding the "vortices" visible in fig. 5.6. We should stress that the physical mechanism through which a coiled vortex layer becomes a vortex core (or simply a vortex), is far from understood (Caflisch et al. 2022).

A comparison of the vorticity generated near the right edge of the shelf for different values of the Reynolds number Re is available in fig. 5.7. This vortical structure does not disappear as the viscosity is decreased. In fact this is rather the contrary: a vorticity layer is continuously shed into the bulk, with a width  $\sim \mathrm{Re}^{-\frac{1}{2}}$  and an intensity  $\sim \mathrm{Re}^{\frac{1}{2}}$  (Caflisch et al. 2022; Schlichting and Gersten 2017; Widmann and Tropea 2015). As  $\mathrm{Re} \to +\infty$ , it seems to converge, *i.e.* we notice some coherence between the different snapshots shown in fig. 5.7. We cannot assert, however, that it will remain so should the Reynolds number be increased further.

An enlightening analogy can be made with the flow around an aircraft's wing, for which the detachment of leading edge vortices has been extensively studied (see e.g. the thorough discussion in the introduction of Widmann and Tropea (2015), wherein the topological considerations of Foss (2004) are used). This is motivated by the streamlines visualisation available in fig. 5.8. In this case, the vortex layer coils in the vicinity of the edge too, yielding a vortical structure mainly concentrated in vortices.<sup>1</sup> Therefore, motivated by this rich theory, we shall talk about vortices afterward.

A surprising aspect that can be noticed in fig. 5.6 is that the separation actually takes the form of vortex pairs. This is due to the oscillatory nature of the flow, which is the subject of figure 5.8. Indeed, as the crest of a wave passes above the edge, the flow in this region undergoes a complete stream reversal. We remind the reader that, as can be noted in figures 4.2, 4.3 and 4.4, the streamlines globally wrap around the crests and the troughs of the free surface. Locally, in the vicinity of the obstacle the underlying irrotational flow gets through three different stages. First, at t=2 in fig. 5.8, in the vicinity of the edge it roughly corresponds to an up-going flow near a corner, whose velocity potential is well-known (Batchelor 1967, sec. 6.5, also shown in fig. 5.9). At a later time (about t = 4), as the inflection point of the interface passes above the salient edge, the direction of the stream changes. The streamlines no longer wrap around the topography. Instead the horizontal left-coming flow meets the vertical up-going one at the corner in a fashion similar to that of the rear tip of an aircraft's wing. These streamlines effectively guide the pair of vortices out of the boundary layer. Incidentally, this corresponds to the passage of the (outgoing) free streamline  $\psi = 0$  on the edge of the shelf. Finally, at subsequent times (around t = 6 in fig. 5.8), the underlying irrotational flow wraps once again around the corner, but now in the opposite direction.

Throughout the passage of a crest, the direction of the flow outside the boundary layer corresponds to the wave propagation direction and

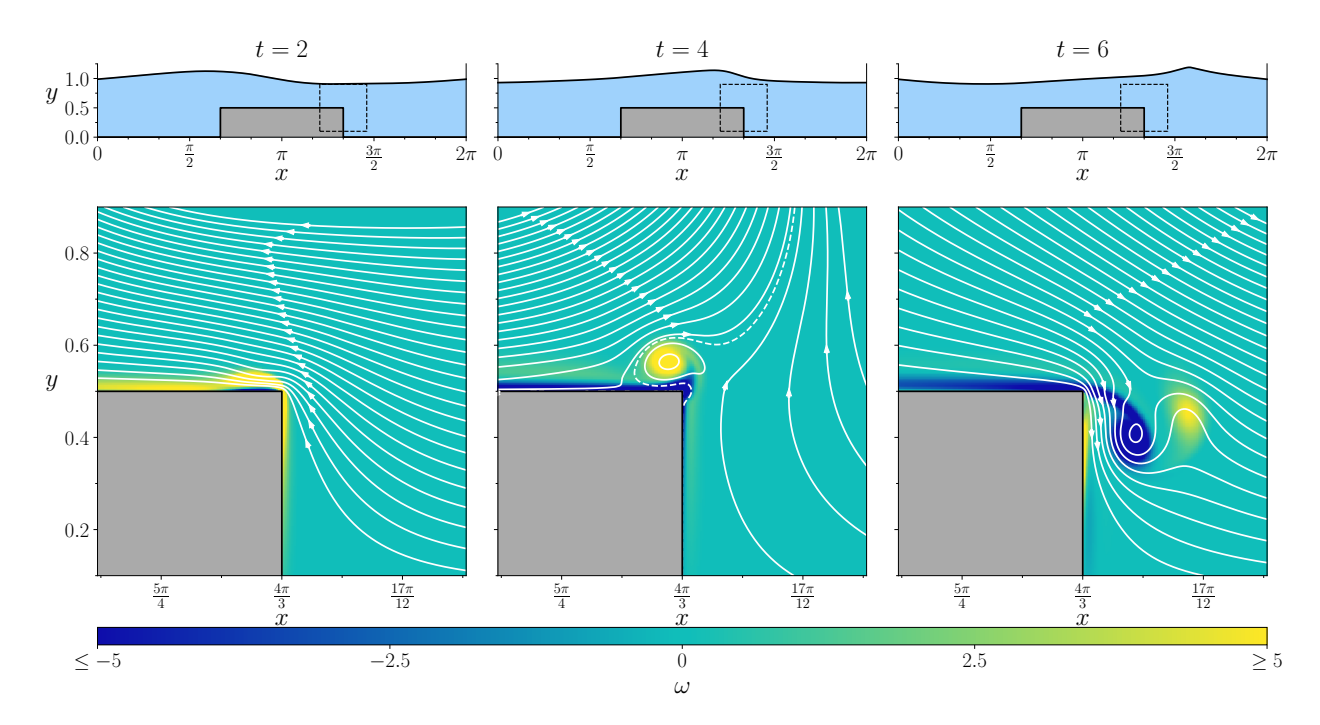


Figure 5.8 – The streamlines and the vorticity  $\omega$  in the vicinity of the right salient edge of  $\Gamma_b$ , for Re = 10<sup>4</sup>. The color scheme has been centered on the range [-5,5] to highlight the vortices. The  $\psi = 0$  line is drawn using dashes.

the vorticity generated in the boundary layer has a negative sign (fig. 5.8, right). As a trough passes above the edge, the stream's direction is opposite to the wave propagation so the vorticity has a positive sign (fig. 5.8, left). This empirically yields, as the vortices are separated from the boundary layer, the correspondence

 $\label{eq:crest} \operatorname{crest} \leftrightarrow \operatorname{negative\ vortex},$   $\operatorname{trough} \leftrightarrow \operatorname{positive\ vortex}.$ 

Of course, the mere presence of the obstacle has an important effect on the potential background flow too: the initially monochromatic wave does not remain so at subsequent times. We cannot assure that, as the initial wave will have collapsed into many smaller ones, the mechanism described above will remain that simple. In particular, some modes might not have a large-enough amplitude to change the direction of the bottom tangential velocity. This problem is somewhat similar to the complex dynamics happening as a solitary wave reaches an obstacle, which has been extensively studied in the literature (Grimshaw 2007; Johnson 1973b).

After being shed, the counter-rotating vortices do not move along a straight line (as they would do under their mutual influence) since they are subject to the background irrotational flow, which carries them in the vicinity of the free surface (fig. 5.10). A tiny disturbance (not shown) due to the presence of these vortices is noticed in the Re =  $10^5$  simulation. Further investigations are needed to precisely quantify the effects of vortices on free surfaces (we mention the recent work of Moffatt and Kimura (2024) regarding the similar problem of counter-rotating vortices acting on a vortex sheet).

Will the flow considered here become turbulent should the Reynolds number be increased further? That is, will more chaotic structure ap-

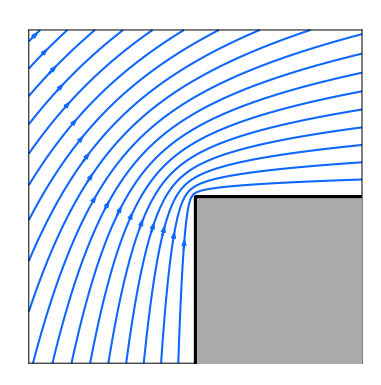


**Figure 5.9** – Analytical solution of Euler's irrotational equations near a corner.

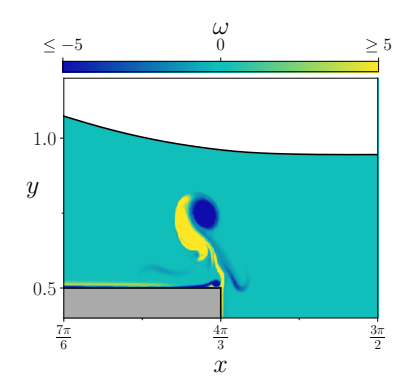


**Figure 5.10** – The vorticity  $\omega$  at fixed time t = 11.5 and Re =  $10^5$ .

pear at smaller viscosities? In a steady non-trivial background flow, this would be the case. Indeed the rich fluid dynamics literature regarding the flow downstream of a bluff body agree on this point (Schlichting and Gersten 2017). However, the flow considered here is oscillating. This should not prevent a turbulent behaviour to get triggered, but it would be of pulsating type. Indeed, as the background velocity goes back and forth in the vicinity of the bed, it vanishes periodically. In such moment, the associated Reynolds number does so too and turbulence cannot occur continually.

### IV. Separation from a smooth step

Boundary layer separation happening near a sharp corner is not surprising from the fluid dynamicist point of view (Batchelor 1967). Indeed, these vortical structures have already been observed numerically by Lin and Huang (2009, 2010) and experimentally by Chang et al. (2001, 2005). We now want to investigate whether this behaviour persists around edges of finite curvature. To that end, we consider smoothed out versions of the rectangular topography considered before, built usind the method of mollifiers introduced originally by Friedrichs (1944).

#### IV.1. Constructing the topography

We briefly describe the mollification of the topography for the sake of completeness. Let  $\gamma_b:(0,L_b)\to \mathbb{T}^2$  the periodic arc-length parametrisation of the sharp rectangular step consider in the previous section. It is a continuous function, differentiable almost everywhere. In fact, it is not differentiable at the salient edges of the step. Introduce the infinitely differentiable bump function  $\Phi$ , defined by  $\Phi$ 

$$\Phi(x) = \begin{cases} C \exp\left(-\frac{1}{1-x^2}\right) & \text{for } -1 < x < 1 \,, \\ 0 & \text{otherwise,} \end{cases}$$

with the normalisation constant C chosen so that  $\|\Phi\|_{L^1(\mathbb{R})} = 1$ . This function is represented in fig. 5.11. Let r > 0 a parameter that shall correspond to the minimum curvature radius of the step. The associated mollifier is then defined as

$$\Phi_r(x) = \frac{1}{r} \Phi\left(\frac{x}{r}\right),\,$$

and can be used to smooth out the function  $\gamma_b$  through a convolution,

$$\gamma_{b,r}(s) = \int_{-r}^{r} \Phi_{r}(\sigma) \gamma_{b}(s-\sigma) \, \mathrm{d}\sigma.$$

The parametrisation  $\gamma_{b,r}(s)$  obtained in this way is then used to defined a new topography. It is infinitely differentiable, with a minimum curvature radius roughly corresponding to r. Furthermore, as  $r \to 0$ , we have  $\gamma_{b,r}(s) \to \gamma_b(s)$ .

# IV.2. Does separation persist around smooth obstacles?

Yes it does! To see this, we have carried out numerical simulations with different values of r at fixed Re, and with different values of

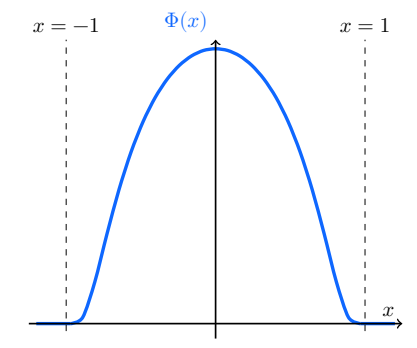


Figure 5.11 – The bump function used to mollify the topography.

<sup>1</sup>We could have used a gaussian to create the topography instead of the present bump function. However the latter has a compact support while the former does not.

Fig.	$N_{ m bot}$	r	Rem.
IV.2	1 250 1 250 1 000 1 000 1 000	0.1 0.2 0.3 0.5	PR PR PR PR PR

Table 5.2 – Numerical parameters used for the simulations over smoothed rectangular steps of curvature radii r. The mesh advection velocity is obtained through the methode Ell.. The number of points on the interface if always  $N_{\rm top}=3000$ .  $N_{\rm bot}$  corresponds to the number of points used to discretise the entire boundary  $\Gamma_b$ .

Re at fixed r. The numerical parameters for these simulations can be found in table 5.2. The associated vorticity at fixed time t=10 and for different values of Re is shown in figure 5.12. We also plot the evolution of the vorticity with time at fixed Reynolds number  $Re=10^5$  in figure 5.13. Three interesting regimes can be observed. First, on the topography with the smallest curvature (r=1), no separation happens. Then, looking at the r=0.5 and 0.3 results shown in fig. 5.12, one observes vorticity being separated from the boundary layer but remaining close by and slowly drifting on the sheet. Finally, in both the r=0.2 and 0.1 simulations, the boundary layer is completely separated: pairs of vortices are shed in the bulk, as with a sharp shelf topography, but with a smaller intensity.

The presence of these vortices is reminiscent of the von Kármán vortex street,<sup>2</sup> in which an adversary pressure gradient in the boundary layer leads to the emission of vortices past a cylinder when the Reynolds number is increased. We are, in fact, considering a rather similar situation except that vorticity stripping is not here associated with a steady stream, but instead results from an oscillation of the background flow with time.

The streamlines around the r=0.1 shelf are visible in figure 5.14. The qualitative discussion about fig. 5.8 still holds. However the separation mechanism here is somewhat different. Indeed, no singularity is present in the background flow now. The vortices are once again ejected far from the boundary layer as the free streamline  $\psi=0$ , whose relevance for the present problem is discussed by e.g. Ackerberg (1970, 1971), passes by.

We have already pointed out in sec. II.1 that the Reynolds number Re defined above, and generally used in the theory of Water Waves, is of no interested to study BL separation. Instead, another one, denoted  $\mathrm{Re}_b$ , should be defined from the length of the step  $\ell_b$  and the fiducial velocity of the background potential flow outside the boundary layer  $U_b$ ,

$$\operatorname{Re}_b = \ell_b U_b \operatorname{Re},$$

since Re plays the role of the inverse viscosity in the non-dimensional world. Why should the relevant length be  $\ell_b$  when it comes to boundary layers? The reason is that  $\ell_b$  corresponds roughly to the maximal length on which the topography is flat and parallel to the background flow. Such quantify is known to be relevant for the boundary layer generation mechanism (see e.g. Ruban 2018, sec. 1.1).

Having defined a relevant Reynolds number, we now investigate its scaling as the curvature increases. In particular, we put emphasis on the fiducial velocity  $U_b$ . It corresponds to the maximum background flow's velocity measured on the bed. For a flat bottom, we have already written the value of  $U_b$  using Stoke's first order solution. Unfortunately we cannot provide a closed formula for the case with a smooth step. However, we can easily extract its scaling regarding the value of r. The idea is as follows: we consider only the flow in a small neighbourhood  $\mathcal{V}_r$  of an r-mollified edge (looking, from afar, like the domain depicted in fig. 5.9) and introduce a diffeomorphism (even a conformal map)  $\Sigma_r: \mathcal{V}_r \to \mathbb{R}^2_+$ , with  $\mathbb{R}^2_+$  denoting the upper half-plane  $\{z>0\} \subset \mathbb{R}^2$  (fig. 5.15). Let

$$\tilde{\phi}(\boldsymbol{y}) = (\phi_r \circ \Sigma_r^{-1})(\boldsymbol{y}),$$

the velocity potential  $\phi_r$  expressed in the  $\mathcal{V}_r$  domain. We can assume

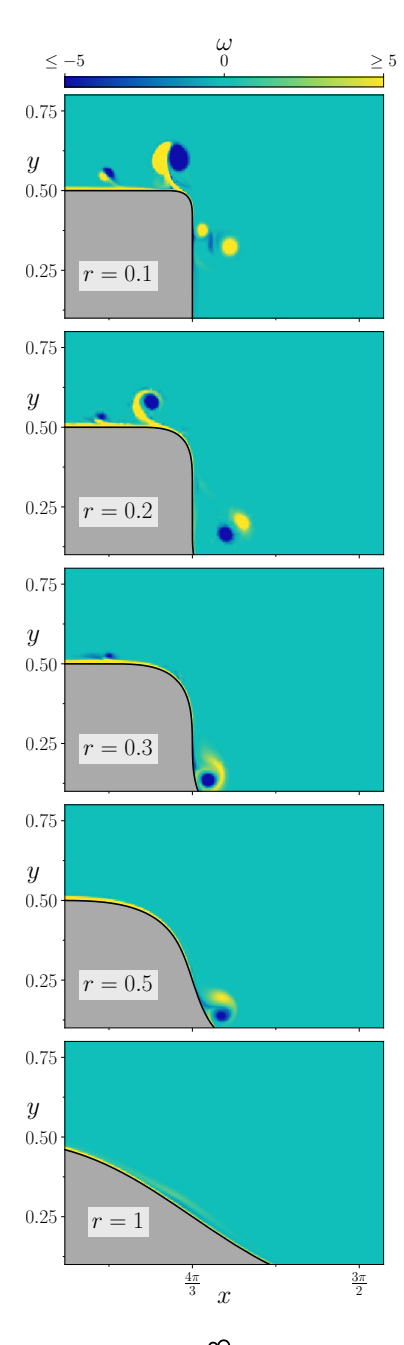


Figure 5.12 –  $\bigcirc$  – The vorticity around a smooth step at time t=10 and Re =  $10^5$  for different curvature radii r>0.

<sup>&</sup>lt;sup>1</sup>One could aptly say that the vortex is "riding" the sheet.

 $<sup>^{2}</sup>$ von Kármán (1911)

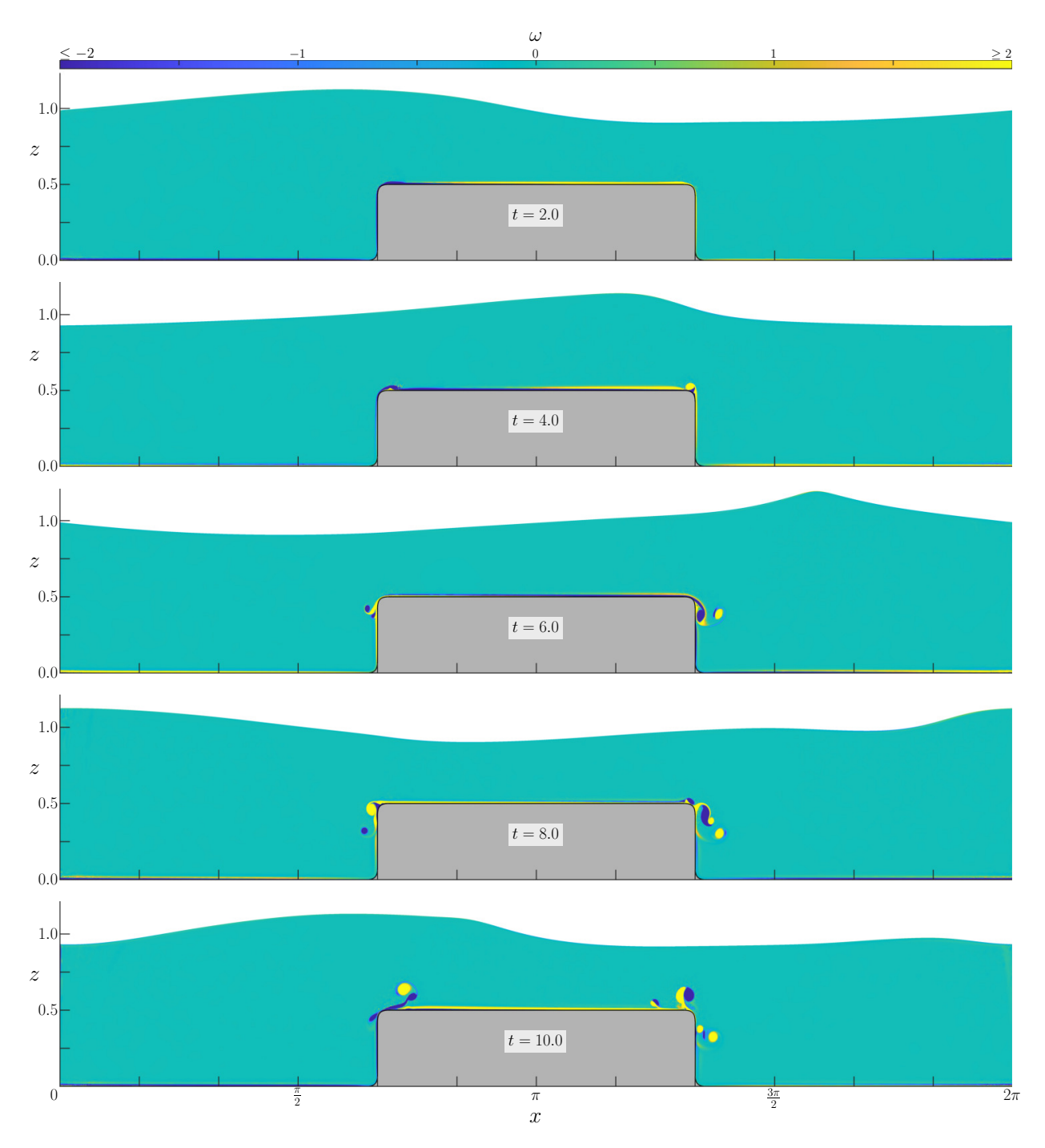


Figure 5.13 – Evolution of the vorticity in associated with the flow created by the passage of a wave over a mollified step with minimum curvature radius r = 0.1, for a Reynolds number Re =  $10^5$ . [parameters: table 5.2]

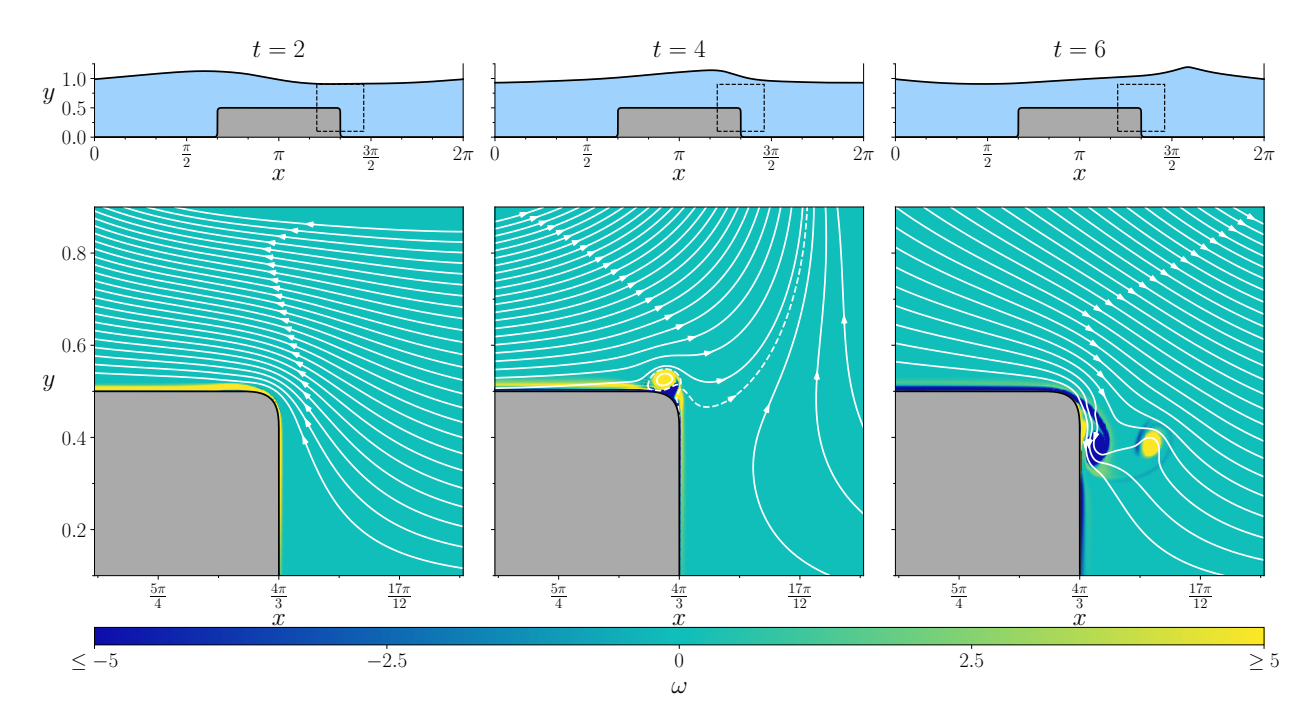


Figure 5.14 – The streamlines and vorticity  $\omega$  in the vicinity of the mollified step with curvature radius r = 0.1 for a Reynolds number Re =  $10^5$ . The free streamline  $\psi = 0$  is drawn using dashed lines. [parameters: table 5.2]

self-similarity of the domain,

$$\Sigma_r(\boldsymbol{y}) = \Sigma_1\left(\frac{\boldsymbol{y}}{r}\right),$$

meaning that we put the origin on the sharp tip at r=0 and the domains  $\Sigma_r$  are obtained from  $\Sigma_1$  by contraction. A simple calculation shows that the velocity  $\boldsymbol{u}_r$  scales according to 1

$$\begin{split} \boldsymbol{u}_r(\boldsymbol{x}) &= \boldsymbol{\nabla} \phi(\boldsymbol{x}) = \boldsymbol{\nabla}_{\boldsymbol{x}} \left[ \tilde{\phi} \circ \boldsymbol{\Sigma}_r \right] (\boldsymbol{x}) \\ &= \frac{1}{r} \, \boldsymbol{\nabla}_{\boldsymbol{x}} \boldsymbol{\Sigma}_1 \left( \frac{\boldsymbol{x}}{R_c} \right) \cdot \left[ \boldsymbol{\nabla}_{\boldsymbol{y}} \tilde{\phi} \circ \boldsymbol{\Sigma}_r \right] (\boldsymbol{x}) \\ &= \frac{1}{r} \boldsymbol{u}_1 \left( \frac{\boldsymbol{x}}{r} \right). \end{split}$$

Even though our domain is not self-similar with respect to r, the above computations applied in the vicinity of the curved edges. In these regions, the typical velocity  $U_b$  scales as  $O(r^{-1})$  and so does the bed's Reynolds number  $\mathrm{Re}_b$ . It is therefore not surprising to see separation appear once a certain viscosity-dependent curvature threshold has been reached.

The above considerations motivate the following assertion: at fixed Reynolds number, a curvature threshold exists above which separation shall happen. Equivalently, at fixed curvature, there exists a critical viscosity below which the vortices observed in this chapter may appear. A direct consequence of this conjecture is that the vanishing viscosity limit, the convergence to Euler's irrotational solution cannot hold as soon as the topography is not flat.

Before moving on to a general discussion about boundary layers equations around curved walls, we would like to emphasise that even though this work is two-dimensional, our conclusions apply to the 3d

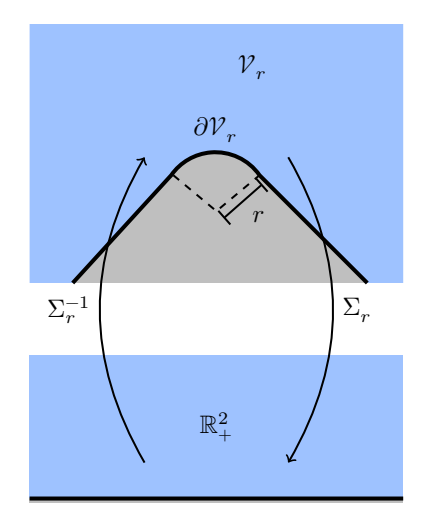


Figure 5.15 – Schematic representation of the domain  $\mathcal{V}_r$  and the diffeomorphism  $\Sigma_r$ .

<sup>&</sup>lt;sup>1</sup>The author would like to thank C. Lacave for his help with this argument.

#### <sup>1</sup>Squire (1933)

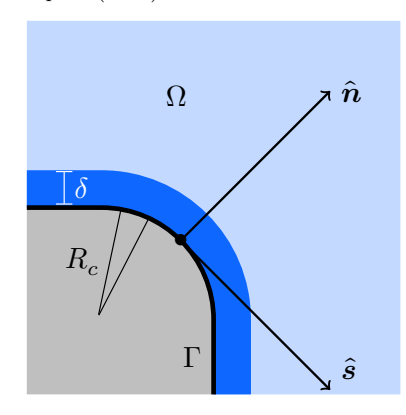


Figure 5.16 – Schematic representation of the Frénet frame (s,n) used around a concave wall (whose curvature radius is  $R_c$ ) with a boundary layer of size  $\delta$ .

case as well. Indeed, the flow associated with water waves in the near-shore regime is only weakly three-dimensional, in a sense that remains to be made precise, up to the splash. Furthermore, in light of Squire's result,  $^1$  the critical value of  $\mathrm{Re}_b$  can only be even lower for three-dimensional flows.

# V. A plea for a theory of boundary layers on curved concave walls

Before stating the conclusions of the present work, we would like to discuss more generally boundary layers appearing in the vicinity of no-slip boundaries with concave (in the sense depicted in fig. 5.16) geometries. Indeed, this problem does not fall into the regime of validity of Prandtl's equation (Blasius 1908; Prandtl 1904) or Görtler's equation (Floryan and Saric 1982; Görtler 1941; Saric 1994), as shall be emphasised soon. We therefore propose to write down boundary layer equations using the scaling laws observed in the previous sections.

#### V.1. The Navier-Stokes equations in the Frénet frame

We consider a viscous fluid in a fixed dimensional domain  $\Omega \subset \mathbb{R}^2$ , with  $C^2$  boundary  $\Gamma = \partial \Omega$  whose arclength parametrisation is denoted by  $\gamma_b(s)$ . Depending on the geometry, the domain of  $\gamma_b$  can be either  $\mathbb{T}$ ,  $\mathbb{R}$  or (0, L). Its curvature (taken positive for concave regions) at arclength s is  $\kappa(s)$  and the associated curvature radius is

$$R_c(s) = |\kappa^{-1}|(s).$$

Associated with the arclength parametrisation, we can introduce the Frénet frame (s, n) as in sec. IV of chapter 4. We remind the reader that n corresponds to the normal coordinate, defined up to the cut locus of the boundary (see sec. V.4.2 of chap. 1). In a neighbourhood of the boundary, this means that n extends up to  $R_c(s)$  when  $\kappa(s) < 0$ . We recall the line element of the Frénet frame,

$$d\mathbf{s} \otimes d\mathbf{s} = d\mathbf{s} \otimes d\mathbf{s} + (1 + \kappa(\mathbf{s})n)^2 dn \otimes dn,$$

which can be used to obtain closed expressions of every differential operator using the tedious formulas presented in appendix B. Using the definitions of this very appendix, we introduce the Lamé coefficient  $h_n(s,n) = 1 + \kappa(s)n$ . Expressed in this coordinate system, the dimensional Navier-Stokes equations become (Massey and Clayton 1965; Ruban 2018)

$$\partial_t u_s + \frac{1}{h_n} u_s \partial_s u_s + u_n \partial_n u_s + \frac{\kappa}{h_n} u_s u_n = -\frac{1}{\rho} \frac{\partial_s p}{h_n} + \nu \left[ \frac{1}{h_n^2} \partial_{ss} u_s + \partial_{nn} u_s + \frac{u_n \partial_s \kappa - n \partial_s \kappa \partial_s u_s}{h_n^3} + \frac{\kappa}{h_n} \partial_n u_s + \frac{2\kappa \partial_s u_n - \kappa^2 u_s}{h_n^2} \right]$$
 (5.3a)

$$\begin{split} \partial_t u_n + \frac{1}{h_n} \, u_s \partial_s u_n + u_n \partial_n u_n + \frac{\kappa u_s^2}{h_n} &= -\frac{1}{\rho} \, \partial_n p + \nu \left[ \frac{1}{h_n^2} \partial_{ss} u_n + \partial_{nn} u_n \right. \\ &+ \left. \frac{u_s \partial_s \kappa - n \partial_s \kappa \partial_s u_n}{h_n^3} + \frac{\kappa}{h_n} \partial_n u_n - \frac{2\kappa \partial_s u_s + \kappa^2 u_n}{h_n^2} \right] \end{split} \tag{5.3b}$$

$$\partial_s u_s + \partial_n (h_n u_n) = 0, \tag{5.3c}$$

where the velocity is written in the (s, n) coordinate system as

$$\boldsymbol{u}(t,s,n) = u_s(t,s,n)\hat{\boldsymbol{s}}(s) + u_n(t,s,n)\hat{\boldsymbol{n}}(s).$$

Our objective is to use the system presented above to formally study the validity of common boundary layer regimes, as well as motivate a new set of equations taking into account the scaling  $U_b \sim \kappa$  discussed in the previous section.

V.1.1. Introducing a background inviscid flow. We begin our journey by decomposing the velocity (and pressure) as the sum of a background inviscid flow  $(U_E, p_E)$  and a viscous perturbation  $(u_\nu, p_\nu)$ . We furthermore assume that  $\nabla^\perp \cdot U_E = 0$ , meaning that there exists a velocity potential  $\phi_E$  such that  $U_E = \nabla \phi_E$ . We do not suppose that  $U_E$  is steady. Since  $U_E$  solve Euler's equations,

$$\partial_t U_E + U_E \cdot \nabla U_E + \frac{1}{\rho} \nabla p_E = 0$$

$$\Delta \phi_E = 0$$

we obtain a perturbed equation for  $(\boldsymbol{u}_{\nu}, p_{\nu})$  readily,

$$egin{aligned} \partial_t oldsymbol{u}_
u + oldsymbol{U}_E \cdot oldsymbol{
abla} oldsymbol{u}_
u + oldsymbol{u}_
u \cdot oldsymbol{
abla} oldsymbol{U}_E + oldsymbol{u}_
u \cdot oldsymbol{
abla} oldsymbol{u}_
u + rac{1}{
ho} oldsymbol{
abla} p_
u = 
u \Delta oldsymbol{u}_
u = 0. \end{aligned}$$

V.1.2. Non-dimensionalisation. We assume that the domain possesses a characteristic length L which does not depend on the maximum curvature  $\kappa_{\max}$ . The problem at hand thus contains three difference fiducial lengths: L,  $R = \kappa_{\max}^{-1}$  and  $\delta$  the boundary layer thickness. Regarding the characteristic velocity, we choose  $U_1$ , the background flow's typical velocity when the curvature  $\kappa_{\max}$  is unity. A straightforward non-dimensionalisation of eqs. (5.3), coupled with the insertion of the decomposition discussed above, yields (instantly dropping the  $\natural$  superscripts usually denoting non-dimensional quantities)

$$\begin{split} \partial_t u_s &+ \frac{1}{h_{n,\beta}} \left( U_s \partial_s u_s + u_s \partial_s U_s + u_s \partial_s u_s \right) + \left( U_n \partial_n u_s + u_n \partial_n U_s + u_n \partial_n u_s \right) \\ &+ \beta \frac{\kappa}{h_{n,\beta}} \left( U_s u_n + u_s U_n + u_s u_n \right) + \frac{\partial_s p}{h_{n,\beta}} \\ &= \frac{1}{\text{Re}} \left[ \frac{1}{h_{n,\beta}^2} \partial_{ss} u_s + \partial_{nn} u_s + \beta \frac{u_n \partial_s \kappa - n \partial_s \kappa \partial_s u_s}{h_{n,\beta}^3} + \beta \frac{\kappa}{h_{n,\beta}} \partial_n u_s + \frac{2\beta \kappa \partial_s u_n - \beta^2 \kappa^2 u_s}{h_{n,\beta}^2} \right] \\ \partial_t u_n &+ \frac{1}{h_{n,\beta}} \left( U_s \partial_s u_n + u_s \partial_s U_n + u_s \partial_s u_n \right) + \left( U_n \partial_n u_n + u_n \partial_n U_n + u_n \partial_n u_n \right) \\ &+ \beta \frac{\kappa}{h_{n,\beta}} \left( 2U_s u_s + u_s^2 \right) + \partial_n p \\ &= \frac{1}{\text{Re}} \left[ \frac{1}{h_{n,\beta}^2} \partial_{ss} u_n + \partial_{nn} u_n + \beta \frac{u_s \partial_s \kappa - n \partial_s \kappa \partial_s u_n}{h_{n,\beta}^3} + \beta \frac{\kappa}{h_{n,\beta}} \partial_n u_n - \frac{2\beta \kappa \partial_s u_s + \beta^2 \kappa^2 u_n}{h_{n,\beta}^2} \right] \\ \partial_s u_s &+ \partial_n \left( h_{n,\beta} u_n \right) = 0, \end{split}$$

with  $(U_s, U_n)$  the background velocity expressed in the Frénet frame,  $(u_s, u_n)$  now representing the components of  $\mathbf{u}_{\nu}$  once non-dimensionalised, and where the following non-dimensional parameters appeared,

$$Re = \frac{U_1 L}{\nu}$$
 (Reynolds)  $\beta = \kappa_{max} L$  (curvature).

The Lamé coefficient  $h_n$  has become, through this non-dimensionalisation process, the factor

$$h_{n,\beta}(s,n) = 1 + \beta \kappa(s)n.$$

V.1.3. Introducing the boundary layer scaling. The final part of these computations consists in inserting the usual scaling laws of the components  $(u_s, u_n)$  in a boundary layer of (non-dimensional) size  $\delta = \operatorname{Re}^{-\frac{1}{2}}$ , namely

$$u_s \equiv u_s(t, s, N)$$
 and  $u_n \equiv \operatorname{Re}^{-\frac{1}{2}} u_n(t, s, N),$ 

into the above system, where we introduced the boundary layer variable  $N = n \operatorname{Re}^{\frac{1}{2}}$ . For now, we keep all the terms. Simplifications of this system using different assumptions regarding the parameter space  $(\operatorname{Re}, \beta)$  shall be carried out in the following section. In the end, we obtain the total boundary layer equations,

$$\begin{split} \partial_{t}u_{s} + \frac{1}{1 + \tilde{\beta}\kappa N} \left( U_{s}\partial_{s}u_{s} + u_{s}\partial_{s}U_{s} + u_{s}\partial_{s}u_{s} \right) + \left( U_{n}\partial_{N}u_{s}\sqrt{\mathrm{Re}} + u_{n}\partial_{N}U_{s} + u_{n}\partial_{N}u_{s} \right) \\ + \tilde{\beta}\frac{\kappa}{1 + \tilde{\beta}\kappa N} \left( U_{s}u_{n} + u_{s}U_{n}\sqrt{\mathrm{Re}} + u_{s}u_{n} \right) + \frac{\partial_{s}p}{1 + \tilde{\beta}\kappa N} \\ &= \left[ \frac{1}{\mathrm{Re}} \frac{\partial_{ss}u_{s}}{\left( 1 + \tilde{\beta}\kappa N \right)^{2}} + \partial_{NN}u_{s} + \frac{\tilde{\beta}}{\mathrm{Re}} \frac{u_{n}\partial_{s}\kappa - N\partial_{s}\kappa\partial_{s}u_{s}}{\left( 1 + \tilde{\beta}\kappa N \right)^{3}} + \frac{\tilde{\beta}\kappa\partial_{N}u_{s}}{1 + \tilde{\beta}\kappa N} + \frac{1}{\mathrm{Re}} \frac{2\tilde{\beta}\kappa\partial_{s}u_{n} - \mathrm{Re}\tilde{\beta}^{2}\kappa^{2}u_{s}}{\left( 1 + \tilde{\beta}\kappa N \right)^{2}} \right] \\ \partial_{t}u_{n} + \frac{1}{1 + \tilde{\beta}\kappa N} \left( U_{s}\partial_{s}u_{n} + u_{s}\partial_{s}U_{n}\sqrt{\mathrm{Re}} + u_{s}\partial_{s}u_{n} \right) + \left( U_{n}\partial_{N}u_{n}\sqrt{\mathrm{Re}} + u_{n}\partial_{N}U_{n}\sqrt{\mathrm{Re}} + u_{n}\partial_{N}u_{n} \right) \\ + \frac{\kappa\tilde{\beta}\mathrm{Re}}{1 + \tilde{\beta}\kappa N} \left( 2U_{s}u_{s} + u_{s}^{2} \right) + \mathrm{Re}\,\partial_{N}p \\ &= \left[ \frac{1}{\mathrm{Re}} \frac{\partial_{ss}u_{n}}{\left( 1 + \tilde{\beta}\kappa N \right)^{2}} + \partial_{NN}u_{n} + \frac{\tilde{\beta}}{\mathrm{Re}} \frac{u_{s}\partial_{s}\kappa\mathrm{Re} - N\partial_{s}\kappa\partial_{s}u_{n}}{\left( 1 + \tilde{\beta}\kappa N \right)^{3}} + \frac{\tilde{\beta}\kappa\partial_{N}u_{n}}{1 + \tilde{\beta}\kappa N} - \frac{2\tilde{\beta}\kappa\partial_{s}u_{s} + \tilde{\beta}^{2}\kappa^{2}u_{n}}{\left( 1 + \tilde{\beta}\kappa N \right)^{2}} \right] \\ \partial_{s}u_{s} + \partial_{N} \left( \left( 1 + \tilde{\beta}\kappa N \right)u_{n} \right) = 0, \end{split} \tag{5.5c}$$

where we have defined a new non-dimensional number

$$\tilde{\beta} = \frac{\beta}{\sqrt{\text{Re}}} = \kappa_{\text{max}} \, \delta, \tag{5.5d}$$

the ratio of the boundary layer's thickness and the minimum radius of curvature. We could neglect the  $U_n$  term because of the non-penetration condition stating that it should remain a small quantity in the vicinity of the boundary.

#### V.2. Formal asymptotic regimes

With the complete boundary layer equations (5.5) at our hand, we can rapidly investigate some formal asymptotic regimes. In particular, we would like to discuss the relevance of Prandtl's and Görtler's equations in the case of a curved concave boundary.

V.2.1. **Prandtl's equations.** In his original work, Prandtl (1904) was interested in the vorticity sheet appearing near a flat boundary ( $\tilde{\beta} = 0$ ). It is however sometimes argued that its regime of validity can be extended to curved boundaries as well.

In order to obtain Prandtl's system, in the form used e.g. by Sammartino and Caflisch (1998a), we must first set  $U_s = U_n = 0$ . This does not mean that the background flow identically vanishes, but rather that the decomposition discussed in sec. V.1.1 is not assumed. Doing so, we obtain as  $\tilde{\beta} \to 0$  and Re  $\to +\infty$ 

$$\begin{split} \partial_t u_s + u_s \partial_s u_s + u_n \partial_N u_s + \partial_s p - \partial_{NN} u_s &= O(\tilde{\beta}) + O\Big(\mathrm{Re}^{-1}\Big) \\ \partial_N p &= O(\tilde{\beta}) + O\Big(\mathrm{Re}^{-1}\Big) \\ \partial_s u_s + \partial_N u_n &= O(\tilde{\beta}), \end{split}$$

which are exactly Prandtl's equations (once the appropriate set of boundary conditions are added), valid for large values of Re and small values of  $\tilde{\beta}$ , which amounts to  $\delta \ll R$ , *i.e.* a boundary layer of small thickness compared to the minimum curvature radius. This does not correspond to the regime of interest.

There exists other formulations of Prandtl's system in the literature, obtained through other simplifying assumptions. Regarding the mathematical analysis of this system, Oleinik (1966) proved a first existence result under mild hypothesis regarding the initial data. Sammartino and Cafflisch (1998a) proved that this

system is well-posed for analytic initial data. Then Gérard-Varet and Dormy (2010) obtained an ill-posedness result in any Sobolev space. An intermediary result is the one of Gérard-Varet and Masmoudi (2015), in which local existence is obtained in some Gevrey space. Separation of the boundary layer has been studied later by Dalibard and Masmoudi (2019).

V.2.2. **Görtler's equations.** Görtler (1941) studied the stability of boundary layers on curved walls in 3d. We obtain a similar set of equations in 2d by keeping the  $O(\text{Re }\tilde{\beta})$  term appearing in (5.5) instead of discarding it. However, should we do so, the pressure term in (5.5b) would not possess the right scaling. This issue is commonly bypassed by assuming that the pressure  $p = O(\text{Re}^{-1})$  (Saric 1994). Furthermore, the nonlinear terms are also dropped out since most studies are only concerned with the linear stability analysis of the vorticity sheet. The corresponding asymptotic regime is then

$$\operatorname{Re} \to +\infty$$
 and  $\tilde{\beta} \to 0$  while  $\operatorname{Go} = \operatorname{Re} \cdot \tilde{\beta} = \operatorname{constant}$ ,

where the non-dimensional coefficient Go is called Görtler's number for obvious reasons. For a steady flow, this yields the following set of equations

$$\begin{split} U_s\partial_s u_s + u_s\partial_s U_s + U_n\partial_N u_s + u_n\partial_N U_s - \partial_{NN} u_s &= O(\tilde{\beta}) + O\Big(\mathrm{Re}^{-1}\Big) \\ U_s\partial_s u_n + u_s\partial_s U_n + U_n\partial_N u_n + u_n\partial_N U_n - \partial_{NN} u_n + 2\mathrm{Go}\kappa u_s U_s + \partial_N p &= O(\tilde{\beta}) + O\Big(\mathrm{Re}^{-1}\Big) \\ \partial_s u_s + \partial_N u_n &= O(\tilde{\beta}). \end{split}$$

This is exactly the system of equations obtained by Floryan and Saric (1982, eqs. 16–18) when studying theoretically the Görtler instability of the boundary layer, resulting in the appearance of longitudinal counterrotating vortices in the layer as Go reaches a threshold value.

Depending on the author, Görtler's number Go may be defined in a different manner. This is due to the many paths that can be taken when carrying out the non-dimensional set of equations.

V.2.3. Toward a boundary layer equation around curved concave walls. Neither Prandtl's nor Görtler's systems describe the present case, in which  $\beta \to \infty$  and the background flow is  $O(\beta)$ . In this limit, separation should occur at fixed value of Re once  $\beta$  reaches a threshold. In order to study the linear stability of eqs. (5.5) in the case of a finite value of both  $\beta$  and Re, we discard the non-linear terms (in  $u_s$  and  $u_n$ ) and impose the observed scaling

$$U_s(t,s,N) = \beta U(t,s) \qquad \text{and} \qquad U_n \ll 1,$$

yielding the "simpler" system

$$\begin{split} \left(1+\tilde{\beta}\kappa N\right)\partial_{t}u_{s}+\tilde{\beta}\sqrt{\mathrm{Re}}\left(U\partial_{s}u_{s}+u_{s}\partial_{s}U\right)+\tilde{\beta}^{2}\sqrt{\mathrm{Re}}\,\kappa\,Uu_{n}+\partial_{s}p&=\left[\frac{1}{\mathrm{Re}}\frac{\partial_{ss}u_{s}}{1+\tilde{\beta}\kappa N}+\left(1+\tilde{\beta}\kappa N\right)\partial_{NN}u_{s}\right.\\ &+\left.\frac{\tilde{\beta}}{\mathrm{Re}}\frac{u_{n}\partial_{s}\kappa-N\partial_{s}\kappa\partial_{s}u_{s}}{\left(1+\tilde{\beta}\kappa N\right)^{2}}+\tilde{\beta}\kappa\partial_{N}u_{s}+\frac{1}{\mathrm{Re}}\frac{2\tilde{\beta}\kappa\partial_{s}u_{n}-\mathrm{Re}\tilde{\beta}^{2}\kappa^{2}u_{s}}{1+\tilde{\beta}\kappa N}\right]\\ \left(1+\tilde{\beta}\kappa N\right)\partial_{t}u_{n}+\tilde{\beta}\sqrt{\mathrm{Re}}\,U\partial_{s}u_{n}+2\,\kappa\tilde{\beta}^{2}\mathrm{Re}^{\frac{3}{2}}\,Uu_{s}+\mathrm{Re}\left(1+\tilde{\beta}\kappa N\right)\partial_{N}p&=\left[\frac{1}{\mathrm{Re}}\frac{\partial_{ss}u_{n}}{1+\tilde{\beta}\kappa N}\right.\\ &+\left.\left(1+\tilde{\beta}\kappa N\right)\partial_{NN}u_{n}+\frac{\tilde{\beta}}{\mathrm{Re}}\frac{u_{s}\partial_{s}\kappa\mathrm{Re}-N\partial_{s}\kappa\partial_{s}u_{n}}{\left(1+\tilde{\beta}\kappa N\right)^{2}}+\tilde{\beta}\kappa\partial_{N}u_{n}-\frac{2\tilde{\beta}\kappa\partial_{s}u_{s}+\tilde{\beta}^{2}\kappa^{2}u_{n}}{1+\tilde{\beta}\kappa N}\right]\\ &\partial_{s}u_{s}+\partial_{N}\Big(\left(1+\tilde{\beta}\kappa N\right)u_{n}\Big)=0. \end{split}$$

This system does not seem easy to work with. However, studying its stability numerically for fixed values of  $\beta$  and Re seems tractable in order to obtain a criterion regarding boundary layer separation. The author is currently investigating this possibility.

### VI. Concluding remarks

In this chapter we have shed light on a physical phenomenon that has unfortunately been somewhat overlooked by numerous prior studies regarding water waves, mainly because its consequences greatly question the use of some two assumptions which are commonly made when studying water waves, namelly that the flow is both inviscid and irrotational.

This very lack of irrotationality, visible in figures 5.6, prevents to use the velocity potential  $\phi$  and the numerous models that stem from it (Water Waves, Shallow Water, K-dV or Boussinesq, to name a few of them). But what about models encompassing the vorticity evolution? Such models are scarce in the literature but they do exist. For instance, Castro and Lannes (2014, 2015) obtained a new formulation of the Water Waves equations (and shallow water asymptotic regimes) when vorticity is initially present in the flow. However their model does not encompass vorticity generation mechanisms. Another approach would be to consider viscous shallow water asymptotics. This is commonly made using the free-slip/Navier condition on the water bed (such models are discussed in e.g. the review of Bresch 2009). The author is only aware of two shallow water models mathematically justified from the Navier-Stokes equations with prescribed no-slip/Dirichlet condition on  $\Gamma_b$ , namelly the works of Bresch and Noble (2007) and Boutounet et al. (2008). In both studies, the inviscid limit cannot hold as the correction term is of order  $O(\mu \text{Re})$  (with  $\mu$  the shallowness), that is, the fluid domain is completely encompassed in the boundary layer. Furthermore, in the first mentioned study, the bottom topography is taken flat. A final approach worth mentioning is to include the turbulence effects, should they be present, directly inside the shallow water model, as in Kazakova and Richard (2019) and Richard et al. (2019). However, in these studies the bottom boundary condition is not the one considered here so the vorticity generation would not correspond to ours.

Setting aside the mathematical considerations regarding the vanishing viscosity limit, real-world water waves are characterised by a very high but finite Reynolds number. Indeed water is not an inviscid fluid. Therefore everything is not lost: for a given topography, there should exist a regime of validity for which the difference between the viscous and inviscid solutions remains small and the separation considered in this chapter does not happen. When using an inviscid model over a non-flat topography, one should still compute the Reynolds number which should be:

- 1. large enough as to control the difference between the Navier-Stokes solution and their model's solution.
- 2. small enough to prevent the separation to happen. This last point depends on the considered (at least  $C^2$ ) topography. The author is currently unable to provide a satisfying separation criterion, unfortunately.

This is schematised in figure 5.17. Of course, further investigations are needed to confirm that the boundary layer indeed separates in the smooth case. This should be done experimentally and numerically (with a different method).

As a final note, we stress that a simple way to reduce the uncanny effects of the vortices emitted by the wave would be to artifically introduce pairs of counter-rotating vortices in the flow. This possibility is currently being considered by the author but the major difficulty remains to estimate the strength of each vortex.

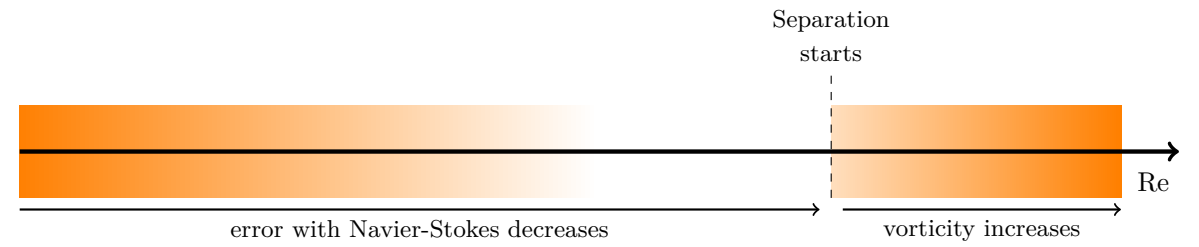


Figure 5.17 – Validity of an inviscid model for a given non-flat topography. The orange color represents the error between the solution computed with an irrotational inviscid model and the *physical Navier-Stokes* solution.

# Conclusions and perspectives

The present work focused on the description of breaking water waves (definition 2.22) using three different approaches. The first one (corresponding to chapter 2) was the most theoretical: we tried to extend a set of equations describing non-breaking water waves, the Zakharov-Craig-Sulem equations (1.43) which are commonly used, to the case of an overhanging wave. The second approach (chapter 3) was computational: we developed a numerical method to solve the single-fluid free-surface incompressible Navier-Stokes equations (1.54) with a Lagrangian advection scheme of the free surface that enabled the simulation of plunging breakers. The last part of our work (chapter 4) was more practical: we used the numerical method already mentioned to investigate the vanishing viscosity limit of a breaking wave arising from an irrotational initial condition.

The other two chapters were not directly related to the breaking phenomenon. In chapter 1 we motivated the various primitive equations commonly used to describe water waves with a particular emphasis on the near-shore regime. In the final part of our work (chapter 5), we discussed the irrotationality assumption which is commonly made to introduce the velocity potential  $\phi$  and hence simplify the equations greatly. We highlighted its incompatibility with a physical phenomenon that could arise in nature: boundary layer separation.

In the author's opinion, the threefold approach has a major limitation: it has raised more questions than it has successfully answered. Therefore, the present work may seem too phenomenological. This, in turns, leaves a bitter aftertaste of non-completeness, at least to the author. Unable to provide meaningful answers to our fabulous reader, we would like to, at least, raise their interest. To this end, we shall briefly discuss some of the questions that appeared throughout this thesis and that the author would like to tackle in the (hopefully near) future.

#### On the Breaking Waves equations

Regarding the Breaking Waves equations (that can also be called Craig's system), motivated in section II of chapter 2, almost all questions that could be asked remain unanswered. We have shown that they enjoy a non-canonical Hamiltonian structure and that they can be reduced to the classical Water Waves equations when no overhanging region exists. Aside from that, we are not currently able to say anything regarding any of the following topics:

1. Conserved quantities. Having at hand a conserved Hamiltonian functional (sec. II.3 of chapter 2), we could use the theory developed by Olver (1980) in order to obtain the Lagrangian counterparts of the Eulerian conserved quantities and their associated symmetries. We mention that the Lagrangian quantity obtained by Luke (1967) has already been extended to the breaking case by Bridges and

Donaldson (2011).

- 2. Well-posedness. Making use of a time-dependent diffeomorphism to a fixed domain (e.g. the Lagrangian frame), we could use an approach à la Lannes (2005, 2013b) to try to obtain a first existence and uniqueness result for system (2.18). The regularity of the solutions constructed in this manner should not be optimal, however. We currently do not see a straightforward way to find a lagrangian equivalent of the paralinearisation formula of the Dirichlet-to-Neumann operator obtained by Alazard and Métivier (2009) and thus reduce further the regularity of the solutions.
- 3. Shallow Water asymptotics. In sec. II.4 we non-dimensionalised the Breaking Waves equations, thus letting the shalowness parameter  $\mu$  appear. To investigate the  $\mu \ll 1$  asymptotic regimes, a straightforward adaptation of the commonly used averaging method (Lannes 2013b, ch. 5) will not work. Indeed, the free surface not being the graph of a function prevents a vertical averaging to be carried out.
- 4. Numerical analysis. Simulations of three-dimensional inviscid overhanging water waves are scarce (Guyenne and Grilli 2006, we mention once again the work of). With the two-dimensional Breaking Waves equations at hand, employing the Boundary Element Method (BEM) to compute the Dirichletto-Neumann operator seems tractable. The author has already started working on such method.

#### Boundary layer separation in water waves

The physical phenomenon highlighted in chapter 5 does not arise in most commonly used reduced models as it yields a finite difference between Euler's irrotational solution and the Navier-Stokes one. Therefore, we need to provide the community with criterion for the appearance of the vortices visible in figures 5.6 or 5.13. This is currently being investigating from the viewpoint of fluid mechanics by studying the stability of the steady Navier-Stokes equations with a boundary layer in the vicinity of a concave wall. The resulting criterion should, however, be geometry-dependent.

As mention in the conclusion of chapter 5, a way to decrease the effects of the separated "vortices" would be to manually add them to the inviscid flow. To to so, we first need to quantify the separated vorticity and then implement it in the potential code of Dormy and Lacave (2024) for instance, with hope of reducing the error between the two solutions. From the theoretical viewpoint, however, we cannot state that the separated Navier-Stokes solution should converge, as  $Re \to +\infty$  to the Water Waves system plus point vortices. We can however hope to reduce, in this manner, the difference between the irrotational and the viscous solution with Dirichlet boundary conditions.

Other unrelated questions arose during the last three years. We do not mention them here but the author surely hopes to have the chance to pursue his work on these issues with his collaborators.



## Mathematical tools and notations

For the sake of completeness, we provide in this first appendix a description of important mathematical notions that are used in this work. To this end we shall first introduce various notations related to functions spaces and recall some well-known properties from functional analysis. In a second step, completely independent from the first, we propose an brief introduction to the language and notations of differential geometry. We do not aim at self-containedness. Hence we provide references dedicated to each subject that are, in the author's opinion, clear and reliable sources.

### I. Functional setting

The various definitions and notations of this section can be found in the books and lecture notes of (in alphabetical order) Bahouri et al. (2011), Brezis (2010), Evans (2010), and Gallagher (2020), for instance.

#### I.1. Function spaces

Let  $d \geqslant 1$  and  $\Omega \subseteq \mathbb{R}^d$  an open set (with straightforward adaptations to the d-torus  $\mathbb{T}^d$ ) with boundary  $\partial \Omega$ . We only consider real-valued functions but adaptations to functions  $f: \Omega \to \mathbb{C}$  are easily made. If  $\alpha \in \mathbb{N}^d$  is a multi-index, we set

$$\left|\alpha\right| = \sum_{j=1}^{d} \alpha_j. \tag{A.1}$$

Let  $D_j$  the weak derivative with respect to the j-th coordinate of  $\mathbb{R}^d$ . For  $\alpha \in \mathbb{N}^d$  we define

$$D^{\alpha} = \prod_{j=1}^{d} D_j^{\alpha_j}. \tag{A.2}$$

We also set D to be the weak derivative equivalent of the  $\nabla$  operator. We then define:

- $C(\Omega)$  (or  $C(\bar{\Omega})$ ) the space of continuous function functions on  $\Omega$  (or  $\bar{\Omega}$ ).
- $C^k(\Omega)$  the space of continuous functions whose derivatives up to order  $k \in \mathbb{N}$  are continuous.
- $\mathcal{D}(\Omega)$  the space of smooth functions  $f \in C^{\infty}(\Omega)$  with compact support in  $\Omega$ .
- $\mathcal{D}^{\star}(\Omega)$  the space of distributions on  $\Omega$ .
- $\mathcal{S}(\mathbb{R}^d)$  the Schwarz class of functions.
- $\mathcal{S}^{\star}(\mathbb{R}^d)$  the set of tempered distributions.

—  $L^p(\Omega)$   $(1 \leqslant p \leqslant +\infty)$  is the usual Lebesgue space of functions  $f: \Omega \to \mathbb{R}$  such that

$$\left\| f \right\|_{L^p(\Omega)} = \begin{cases} \left( \int_{\Omega} \left| f \right|^p \right)^{\frac{1}{p}} & \text{for } p \neq +\infty \\ \text{ess sup} |f| & \text{for } p = +\infty \end{cases}$$
 (A.3)

—  $L^2(\Omega)$  is a Hilbert space for the inner product

$$\left\langle f, g \right\rangle_{L^2(\Omega)} = \int_{\Omega} fg$$
 (A.4)

—  $W^{k,p}(\Omega)$  for  $k \in \mathbb{N}, 1 \leq p \leq +\infty$  is the standard Sobolev space endowed with the norm

$$\left\|f\right\|_{W^{k,p}(\Omega)} = \begin{cases} \left(\sum_{|\alpha| \leqslant k} \left\|D^{\alpha} f\right\|_{L^{p}(\Omega)}^{p}\right)^{\frac{1}{p}} & \text{for } p \neq +\infty \\ \max_{|\alpha| \leqslant k} \left\|D^{\alpha} f\right\|_{L^{\infty}(\Omega)} & \text{for } p = +\infty \end{cases}$$

$$(A.5)$$

—  $H^k(\Omega) = W^{k,2}(\Omega)$  is the nonhomogeneous Sobolev space of order k. It is a Hilbert space for the scalar product

$$\left\langle f, g \right\rangle_{H^k(\Omega)} = \sum_{|\alpha| \le k} \left\langle D^{\alpha} f, D^{\alpha} g \right\rangle_{L^2(\Omega)} \tag{A.6}$$

- $H_0^k(\Omega)$  is the completion of  $\mathcal{D}(\Omega)$  for the  $H^k$ -norm. We can see functions in  $H_0^1(\Omega)$  as vanishing on the boundary (even though the reality is slightly more complicated, see *e.g.* thm. 5.5.1 in Evans (2010)).
- $H^{-k}(\Omega)$  is the topological dual of  $H_0^k(\Omega)$ .
- $\dot{W}^{k,p}(\Omega)$  is the homogeneous Sobolev space with norm

$$||f||_{\dot{W}^{k,p}(\Omega)} = \begin{cases} \left(\sum_{|\alpha|=k} ||D^{\alpha}f||_{L^{p}(\Omega)}^{p}\right)^{\frac{1}{p}} & \text{for } p \neq +\infty \\ \max_{|\alpha|=k} ||D^{\alpha}f||_{L^{\infty}(\Omega)} & \text{for } p = +\infty \end{cases}$$
(A.7)

This allows to define  $\dot{H}^k(\Omega) = \dot{W}^{k,2}(\Omega)$ .

— The Fourier transform of functions  $f \in L^1(\mathbb{R}^d)$  and its inverse are given by,

$$\mathcal{F}[f](\boldsymbol{\xi}) = \frac{1}{\sqrt{2\pi}^d} \int_{\mathbb{R}^d} f(\boldsymbol{x}) \cdot e^{-i\boldsymbol{x}\cdot\boldsymbol{\xi}} \, \mathrm{d}\boldsymbol{x} \qquad \text{with inverse} \qquad \mathcal{F}^{-1}[f](\boldsymbol{x}) = \frac{1}{\sqrt{2\pi}^d} \int_{\mathbb{R}^d} f(\boldsymbol{\xi}) \cdot e^{i\boldsymbol{x}\cdot\boldsymbol{\xi}} \, \mathrm{d}\boldsymbol{x}.$$

Using the Fourier transform we are able to define the  $\dot{H}^s(\mathbb{R}^d)$  and  $H^s(\mathbb{R}^d)$  Sobolev norms for all  $s \in \mathbb{R}$  as

$$\left\|f\right\|_{\dot{H}^{s}(\mathbb{R}^{d})} = \int_{\mathbb{R}^{d}} \left|\boldsymbol{\xi}\right|^{2s} \left|\mathcal{F}[f](\boldsymbol{\xi})\right|^{2} \mathrm{d}\boldsymbol{\xi} \qquad \text{and} \qquad \left\|f\right\|_{H^{s}(\mathbb{R}^{d})} = \int_{\mathbb{R}^{d}} \left(1 + |\boldsymbol{\xi}|^{2}\right)^{s} \left|\mathcal{F}[f](\boldsymbol{\xi})\right|^{2} \mathrm{d}\boldsymbol{\xi} \qquad (A.8)$$

It is easy to prove that whenever  $s \in \mathbb{N}$ , both definitions of  $\dot{H}^s(\mathbb{R}^d)$  (or  $H^s(\mathbb{R}^d)$ ) coincide.

**Remark A.1.** (Bahouri et al. 2011, props. 1.34 & 1.36) The space  $\dot{H}^s(\mathbb{R}^d)$  is a Hilbert space for s < d/2 only. Moreover we have the identification  $\dot{H}^{-s}(\mathbb{R}^d) \equiv \left(\dot{H}^s(\mathbb{R}^d)\right)^*$  only for |s| < d/2. These unappealing properties encouraged Lannes (2013b) (following Deny and Lions 1954) to work with the Beppo-Levi spaces instead (see next notation).

—  $\mathring{H}^k(\Omega)$  and  $\mathring{H}^s(\mathbb{R}^d)$ , the *Beppo-Levi* spaces, are both defined in the following fashion (with equivalence whenever  $s \in \mathbb{N}$  and  $\Omega = \mathbb{R}^d$ ),

$$\mathring{H}^{k+1}(\Omega) = \left\{ f \in \mathcal{D}^{\star}(\Omega) : Df \in H^{k}(\Omega) \right\} \tag{A.9a}$$

$$\mathring{H}^{s+1}(\mathbb{R}^d) = \left\{ f \in \mathcal{D}^{\star}(\mathbb{R}^d) : Df \in H^s(\mathbb{R}^d) \right\} \tag{A.9b}$$

In order to have separated Banach spaces, we must consider  $\mathring{H}^k(\Omega)/\mathbb{R}$  and  $\mathring{H}^s(\mathbb{R}^d)/\mathbb{R}$ . These spaces naturally represent a potential (defined up to a constant).

#### I.2. Pseudo-Differential operators

—  $S^m(\mathbb{R}^d)$   $(m \in \mathbb{R})$  is the class of symbols  $a \in C^\infty(\mathbb{R}^d \times \mathbb{R}^d)$  such that for all multi-indices  $\alpha, \beta \in \mathbb{N}^d$ , there is a constant  $C_{\alpha,\beta}$  such that  $\forall \boldsymbol{x}, \boldsymbol{\xi} \in \mathbb{R}^d$ ,

$$\left| D_{\boldsymbol{x}}^{\alpha} D_{\boldsymbol{\xi}}^{\beta} a(\boldsymbol{x}, \boldsymbol{\xi}) \right| \leqslant C_{\alpha, \beta} \left( 1 + \left| \boldsymbol{\xi} \right| \right)^{m - |\beta|}. \tag{A.10}$$

- $$\begin{split} & & S^{\infty}(\mathbb{R}^d) = \cup_{m \in \mathbb{R}} S^m(\mathbb{R}^d). \\ & & S^{-\infty}(\mathbb{R}^d) = \cap_{m \in \mathbb{R}} S^m(\mathbb{R}^d). \end{split}$$
- Op(a), for a symbol  $a \in S^m(\mathbb{R}^d)$ , is the pseudo-differential operator associated with a whose action on a function  $u \in \mathcal{S}(\mathbb{R}^d)$  is given by

$$Op(a)u(\mathbf{x}) = \frac{1}{\sqrt{2\pi}^d} \int_{\mathbb{R}^d} a(\mathbf{x}, \boldsymbol{\xi}) \mathcal{F}[u](\boldsymbol{\xi}) e^{i\mathbf{x}\cdot\boldsymbol{\xi}} d\boldsymbol{\xi}.$$
 (A.11)

#### I.3. Miscellaneous

The singular support of a function u, sing supp(u), is defined from

$$x \notin \text{sing supp } u \iff u \in C^{\infty} \text{ in a neighborhood of } x$$
 (A.12)

#### Differential Geometry 101 II.

We propose a concise introduction to the theory of smooth riemannian manifolds to motivate the somewhat unusual notations (for both the physicist and the applied mathematician) used in sections 1.V.4 and 2.II.1. These concepts arise naturally as one is interested in the theory of smooth d-dimensional surfaces embedded in  $\mathbb{R}^{d+1}$ , as is the case of the water-air interface. The following is based on the classical books of Boothby (1975), Tu (2011) and Lee (1997, 2013).

#### II.1. Smooth manifolds

**Definition A.2** (Locally Euclidean space). Let  $\mathcal{M}$  a topological space.  $\mathcal{M}$  is called locally Euclidean of dimension  $n \in \mathbb{N}^*$  if for every  $\vec{s} \in \mathcal{M}$ , there exists a neighbourhood  $U_{\vec{s}}$  of  $\vec{s}$  and a homeomorphism  $\varphi:U \to \varphi(U)$  where  $\varphi(U)$  is an open subset of  $\mathbb{R}^n$ . The couple  $(U_{\vec{s}},\varphi)$  is called a chart at  $\vec{s} \in \mathcal{M}$ .

**Definition A.3** (Smooth manifold). Let  $\mathcal{M}$  a topological space.  $\mathcal{M}$  is a n-dimensional smooth manifold

- 1. Second coutable and Hausdorff.
- 2. Locally Euclidean of dimension n with smooth transition maps (i.e. maps of the type  $\varphi \circ \psi^{-1}$ :  $\psi(U\cap V)\to \varphi(U\cap V)$  for two charts  $(U,\varphi)$  and  $(V,\psi)$ ).

We could define less regular manifolds invoking less regularity on the transition maps. For any chart  $(U,\varphi)$ , expanding the map  $\varphi$  as  $(x^1,\cdots,x^n)$  provides a local coordinate system on  $\mathcal{M}$ .

**Definition A.4** (Tangent space). Let  $\mathcal{M}$  a n-dimensional manifold and  $\vec{s} \in \mathcal{M}$ . The tangent space at  $\vec{s}$ , denoted  $T_{\vec{s}}\mathcal{M}$  is the set of all derivations of smooth functions on  $\mathcal{M}$  at  $\vec{s}$ . Elements of  $T_{\vec{s}}\mathcal{M}$  are called tangent vectors.

Let  $(U_{\vec{s}}, \{x^j\})$  a chart at  $\vec{s} \in \mathcal{M}$ , then a tangent vector  $X_{\vec{s}}$  is an expression having the following form,

$$X_{\vec{s}} = \sum_{i=1}^{n} v^{i} \left. \frac{\partial}{\partial x^{i}} \right|_{\vec{s}}.$$

On  $\mathbb{R}^n$ , it is equivalent to the usual notion of vector. However, this definition is far more general as it allows to set aside the representation of vectors as "arrows".

**Definition A.5** (Riemannian manifold). Let  $\mathcal{M}$  a n-dimensional smooth manifold. A metric  $\mathbf{g}$  is a map that assigns to each  $\vec{s} \in \mathcal{M}$  a positive-definite bilinear form  $\mathbf{g}(\vec{s}) : T_{\vec{s}}\mathcal{M} \times T_{\vec{s}}\mathcal{M} \to \mathbb{R}$  smoothly. The couple

#### II.2. Differential operations on manifold

At some points in chapters 1 and 2, we used notations commonly used to study (smoothed) Riemannian manifolds. We do not motivate all of them (we refer our reader to the books already mentioned) but we at least express them in some coordinate chart as to give a basic understanding of their meaning. We also provide relations to more common quantities when  $\mathcal{M} = \mathbb{R}^n$ . In the following,  $\mathcal{M}$  and  $\mathcal{N}$  will be smooth (possibly Riemannian) manifolds of dimensions m and n respectively, with coordinate charts  $(U, \{s^j\})$  and  $(V, \{r^j\})$ . The coordinates of  $\mathbb{R}^m$  are denoted as  $x^j$ .

— The differential of a smooth function  $f: \mathcal{M} \to \mathbb{R}$  at  $\vec{s} \in \mathcal{M}$  is a 1-form  $d_{\vec{s}}f: T_{\vec{s}}\mathcal{M} \to T_{f(\vec{s})}\mathbb{R} \simeq \mathbb{R}$ ,

$$\mathbf{d}_{\vec{s}} f = \frac{\partial f}{\partial s^1} \, \mathbf{d}_{\vec{s}} s^1 + \dots + \frac{\partial f}{\partial s^m} \, \mathbf{d}_{\vec{s}} s^m \qquad \sim \nabla f^{\top}$$

— The differential of a smooth map  $\Sigma: \mathcal{M} \to \mathcal{N}$  at  $\vec{s} \in \mathcal{M}$ , denoted by  $\Sigma_{\vec{s},*}: T_{\vec{s}}\mathcal{M} \to T_{\Sigma(\vec{s})}\mathcal{N}$ 

$$\Sigma_{\vec{s},*} \left( \left. \frac{\partial}{\partial s^j} \right|_{\vec{s}} \right) = \sum_{k=1}^n \frac{\partial (r^k \circ \Sigma)}{\partial s^j} \left. \frac{\partial}{\partial r^k} \right|_{\Sigma(\vec{s})} \sim (\nabla \Sigma)^\top = \mathbf{J} \Sigma.$$

It is also called the *pushforward*.

— The pullback of a 1-form  $\omega: T_{\Sigma(\vec{s})}\mathcal{N} \to \mathbb{R}$  by a map  $\Sigma: \mathcal{M} \to \mathcal{N}$  is a 1-form  $\Sigma^*\omega: T_{\vec{s}}\mathcal{M} \to \mathbb{R}$  obtained locally through

$$\Sigma^*\omega = \sum_{i,k} \omega_k(\Sigma) \frac{\partial (r^k \circ \Sigma)}{\partial s^j} \, \mathrm{d}_{\vec{s}} s^j \qquad \text{with} \qquad \omega = \sum_{k=1}^n \omega_k \, \mathrm{d}_{\Sigma(\vec{s})} r^k$$

— Let  $\vec{s} \in \mathcal{M}$ ,  $v \in T_{\vec{s}}\mathcal{M}$  a vector and  $\omega \in T_{\vec{s}}^{\star}\mathcal{M}$  a covector. Using the intrinsic metric **g** of  $\mathcal{M}$  we can define the *musical isomorphisms* between vectors and covectors as such,

$$\begin{split} \omega^{\sharp} \in \mathrm{T}_{\vec{s}} \mathcal{M} & \text{such that} & \mathbf{g}(\vec{s}) \Big( \omega^{\sharp}, u \Big) = \omega(u) & \text{for all } u \in \mathrm{T}_{\vec{s}} \mathcal{M}, \\ v^{\flat} \in \mathrm{T}_{\vec{s}}^{\star} \mathcal{M} & \text{such that} & \mathbf{g}(\vec{s}) \Big( v, u \Big) = v^{\flat}(u) & \text{for all } u \in \mathrm{T}_{\vec{s}} \mathcal{M}. \end{split}$$

— The gradient  $\vec{\nabla} f(\vec{s})$  of a smooth map  $f: \mathcal{M} \to \mathbb{R}$  at  $\vec{s} \in \mathcal{M}$  is a vector defined easily as

$$\vec{\nabla} f(\vec{s}) = (\mathbf{d}_{\vec{s}} f)^{\sharp}.$$

— Let  $\mathcal{Q}$  a third manifold, let  $\Sigma: \mathcal{M} \to \mathcal{N}$  and  $\Psi: \mathcal{N} \to \mathcal{Q}$  smooth maps. Then we have the *chain rule* expressed readily as

$$\left(\Psi \circ \Sigma\right)_{\vec{s},*} = \Psi_{\Sigma(\vec{s}),*} \circ \Sigma_{\vec{s},*} \qquad \qquad \sim \left(\boldsymbol{\nabla}(\Psi \circ \Sigma)\right)^\top = (\boldsymbol{\nabla}\Psi)^\top \cdot (\boldsymbol{\nabla}\Sigma)^\top$$



# A plenty of calculus identities

### I. Notations and disambiguations

- A scalar (differentiable) function  $f: \mathbb{R}^d \to \mathbb{R}$  with gradient  $\nabla f: \mathbb{R}^d \to \mathbb{R}^d$ .
- A vector field in  $\mathbb{R}^d$  is denoted using a boldface symbol, like  $e.g.\ \boldsymbol{u}:\mathbb{R}^d\to\mathbb{R}^d$ . The corresponding gradient tensor is  $\nabla \boldsymbol{u}$  while the jacobian matrix is  $\mathbf{J}\boldsymbol{u}=\nabla \boldsymbol{u}^{\top}$ . In cartesian coordinates, their components are given by

$$\left[\boldsymbol{\nabla}\boldsymbol{u}\right]_{i,j} = \frac{\partial u_j}{\partial x_i} \quad \text{and} \quad \left[\mathbf{J}\boldsymbol{u}\right]_{i,j} = \frac{\partial u_i}{\partial x_j}.$$

— A tensor field is a function  $\mathbf{T}: \mathbb{R}^d \to \mathbb{R}^{d \times d}$ . We do not consider any higher order tensor in the present work. Its divergence  $\nabla \cdot \mathbf{T}$  is a vector field which, written in cartesian coordinates, is

$$\left[\boldsymbol{\nabla}\cdot\boldsymbol{\mathsf{T}}\right]_{i} = \sum_{j=1}^{d}\frac{\partial T_{ji}}{\partial x_{j}}.$$

This convention is common in fluid dynamics textbooks.

— For vectors  $u, v \in \mathbb{R}^d$ ,  $u \cdot v = u^\top v$  is the usual euclidean scalar product. The · notation is also used with matrices, in the following manner

$$\boldsymbol{u} \cdot \boldsymbol{\mathsf{A}} = \boldsymbol{u}^{\top} \boldsymbol{\mathsf{A}} = \boldsymbol{\mathsf{A}}^{\top} \boldsymbol{u} \quad \text{and} \quad \boldsymbol{\mathsf{A}} \cdot \boldsymbol{u} = \boldsymbol{\mathsf{A}} \boldsymbol{u}.$$

— The tensor product  $\otimes$  is such that

$$\left[\boldsymbol{u}\otimes\boldsymbol{v}\right]_{i,j}=u_{i}v_{j}$$
 so that  $\nabla\boldsymbol{u}=\nabla\otimes\boldsymbol{u}.$ 

### II. A plenty of identities

#### II.1. First order identities

$$(\boldsymbol{u} \cdot \nabla) f = \boldsymbol{u} \cdot \nabla f$$
 
$$(\boldsymbol{u} \cdot \nabla) \boldsymbol{v} = \boldsymbol{u} \cdot \nabla \boldsymbol{v}$$
 (B.1a)

$$\nabla \cdot (f\boldsymbol{u}) = f \nabla \cdot \boldsymbol{u} + \boldsymbol{u} \cdot \nabla f$$

$$\nabla \times (f\boldsymbol{u}) = f \nabla \times \boldsymbol{u} + \nabla f \times \boldsymbol{u}$$

$$\nabla \times (f\boldsymbol{u}) = f \nabla \times \boldsymbol{u} + \nabla f \times \boldsymbol{u}$$

$$\frac{1}{2} \nabla (\boldsymbol{u} \cdot \boldsymbol{u}) = (\nabla \boldsymbol{u}) \cdot \boldsymbol{u}$$

$$= \boldsymbol{u} \cdot \nabla \boldsymbol{v} + \boldsymbol{v} \cdot \nabla \boldsymbol{u}$$

$$= \boldsymbol{u} \cdot \nabla \boldsymbol{u} + \boldsymbol{u} \times (\nabla \times \boldsymbol{u})$$
(B.1b)

$$+ \mathbf{u} \times (\nabla \times \mathbf{v}) + \mathbf{v} \times (\nabla \times \mathbf{u})$$

$$\nabla \cdot (\mathbf{u} \times \mathbf{v}) = (\nabla \times \mathbf{u}) \times \mathbf{v} - (\nabla \times \mathbf{v}) \times \mathbf{u}$$

$$\nabla \times (\mathbf{u} \times \mathbf{v}) = \mathbf{u} \nabla \cdot \mathbf{v} - \mathbf{v} \nabla \cdot \mathbf{u}$$

$$+ \mathbf{v} \cdot \nabla \mathbf{u} - \mathbf{u} \cdot \nabla \mathbf{v}$$
(B.1d)

#### II.2. Chain rule

Let  $\phi: \mathbb{R} \to \mathbb{R}$ ,  $f: \mathbb{R}^d \to \mathbb{R}$ ,  $u: \mathbb{R}^d \to \mathbb{R}^d$  and  $\mathbf{r}: \mathbb{R} \to \mathbb{R}^d$ . We use the notations  $\phi'$  and  $\mathbf{r}'$  as a short-hand for the one-dimensional derivative. Then we have

$$\nabla(\phi \circ f) = (\phi' \circ f)\nabla f \qquad (\mathbf{r} \circ \phi)' = (\mathbf{r}' \circ \phi)\phi'$$
 (B.2a)

$$(f \circ \mathbf{r})' = (\nabla f \circ \mathbf{r})' \cdot \mathbf{r}' \tag{B.2b}$$

$$(\boldsymbol{u} \circ \mathbf{r})' = \mathbf{r}' \cdot (\nabla \boldsymbol{u} \circ \mathbf{r})$$

$$\nabla (f \circ \boldsymbol{u}) = \nabla \boldsymbol{u} \cdot (\nabla f \circ \boldsymbol{u})$$

$$\cdot (\mathbf{r} \circ f) = \nabla f \cdot (\mathbf{r}' \circ f)$$

$$\nabla \times (\mathbf{r} \circ f) = \nabla f \times (\mathbf{r}' \circ f)$$
(B.2d)

$$\nabla \cdot (\mathbf{r} \circ f) = \nabla f \cdot (\mathbf{r}' \circ f) \qquad \qquad \nabla \times (\mathbf{r} \circ f) = \nabla f \times (\mathbf{r}' \circ f)$$
(B.2d)

#### II.3. Second order identities

$$\nabla \cdot \nabla f = \Delta f \qquad \Delta u = \nabla (\nabla \cdot u) - \nabla \times (\nabla \times u) \qquad (B.3a)$$

$$\nabla \cdot \left[ \nabla \boldsymbol{u} + \left( \nabla \boldsymbol{u} \right)^{\top} \right] = \Delta \boldsymbol{u} + \nabla \left( \nabla \cdot \boldsymbol{u} \right) \qquad \nabla \cdot \left( f \nabla g \right) = f \Delta g + \nabla f \cdot \nabla g$$
(B.3b)

### Common differential operators in arbitrary orthogonal coordinates systems

We propose to derive here expressions of various differential operators in a general d-dimensional coordinates system  $\{q^j\}_{j=1}^d$  whose line element is given by

$$\mathrm{d} \boldsymbol{s} \otimes \mathrm{d} \boldsymbol{s} = \sum_{j=1}^d h_j^2(q^1, \cdots, q^n) \, \mathrm{d} q^j \otimes \mathrm{d} q^j \\ \hspace{1cm} = \sum_{j=1}^d \mathrm{d} x^j \otimes \mathrm{d} x^j,$$

that is, the corresponding metric  $g_{ij}$  is diagonal with  $g_{jj} = h_j^2$ . A complete discussion of such framework is rarely done thoroughly in the literature. The relations obtained in this section are e.g. used in sec. V of chapter 5 to write the Navier-Stokes equations in the Frénet frame. Emphasis shall be put onto normalised and non-normalised vectors. To provide the clearest concise presentation possible, we compare every relation with its equivalent in cartesian form (with  $\{x^j\}_{j=1}^d$  the standard cartesian coordinates and  $e_k = \hat{e}_k$  the associated contravariant normalised basis vectors).

Let  $\boldsymbol{b}_k$   $(k=1,\cdots,d)$  the k-th contravariant, non-normalised, basis vector associated with the coordinate system  $\{q^j\}_{j=1}^d$ , defined through the relation

$$\mathrm{d}q^j(oldsymbol{b}_k) = \delta_k^j \qquad \qquad = \mathrm{d}oldsymbol{x}^j(oldsymbol{e}_k).$$

The set of 1-forms  $dq^j$  is sometimes called the *covariant* basis or *covectors* basis. Correspondence between vectors and covectors is done though the metric. We also introduce the normalised basis vectors and covectors defined by

$$\hat{m{b}}_j = rac{m{b}_j}{h_z}$$
  $\hat{m{e}}_j = \hat{m{e}}_j$ 

$$\mathrm{d}\hat{q}^j = h_i \mathrm{d}q^j \qquad \qquad \mathrm{d}\hat{x}^j = \mathrm{d}x^j.$$

Using these notations, we can decompose every vector field  $v : \mathbb{R}^n \to \mathbb{R}^n$  uniquely along the contravariant bases

$$\begin{split} \boldsymbol{v}(\boldsymbol{p}) &= \sum_{j=1}^d v^j(\boldsymbol{p}) \boldsymbol{b}_j(\boldsymbol{p}) \\ &= \sum_{j=1}^d \hat{v}^j(\boldsymbol{p}) \hat{\boldsymbol{b}}_j(\boldsymbol{p}) \\ &= \sum_{j=1}^d \hat{v}^j(\boldsymbol{p}) \hat{\boldsymbol{b}}_j(\boldsymbol{p}) \end{split}$$

From this decomposition, one understands readily the difficulty in working with such coordinates systems: contrary to the cartesian case, the basis vectors vary in space too. We also notice that denoting vector fields using a column vector, as is usually done in the standard cartesian frame, leads to ambiguities. Indeed, the normalised and non-normalised components  $v^j$  and  $\hat{v}^j = h_j v^j$  are different in general so one should be careful about what each quantity represents. We choose not to use the common matrix notations to bypass this eventual issue.

### III.1. The Christoffel symbols

As already pointed out, the basis vectors can, in general, vary in space. However, having assumed a diagonal metric, they remain orthogonal at each point  $p \in \mathbb{R}^n$ . Using this fact, we are able to obtain simple relations for the Christoffel symbols, relating the space derivatives of the basis vectors to other vectors as

$$\sum_{i=1}^{d} \Gamma^{j}_{k\ell} \boldsymbol{b}_{j} = \frac{\partial \boldsymbol{b}_{k}}{\partial q^{\ell}}$$
 (= 0 in cartesian coordinates).

In any standard textbook (e.g. the author used the book of Misner et al. (2017) to develop this appendix), the two following relations are proved,

$$\begin{split} &\Gamma^{j}_{\ k\ell} = 0 \quad \text{if } \ell \neq j \neq k \neq \ell \\ &\Gamma^{j}_{\ k\ell} = \Gamma^{j}_{\ \ell k} \qquad \qquad \text{(orthogonality)} \\ &\Gamma^{j}_{\ k\ell} = \frac{1}{2} \sum_{m=1}^{d} \frac{1}{g_{jm}} \left( \partial_{\ell} g_{km} + \partial_{k} g_{m\ell} - \partial_{m} g_{k\ell} \right) \qquad \qquad \text{(link with the metric)}. \end{split}$$

The last relation can be used to obtain closed forms for the Christoffel symbols in an orthogonal frame. Indeed, we prove easily that

$$\begin{split} &\Gamma^{j}_{\phantom{j}j\ell} = \frac{1}{h_{j}} \left(\partial_{\ell} h_{j}\right) \\ &\Gamma^{j}_{\phantom{j}kk} = \frac{2}{h_{j}} \left(\partial_{j} h_{j}\right) \delta^{j}_{k} - \frac{1}{h_{j}^{2}} h_{k} (\partial_{j} h_{k}), \end{split}$$

where  $\partial_j$  de notes the derivative with respect to  $q^j$ . The symmetric property of  $\Gamma^j_{k\ell}$  permits to write each one of its component using the metric diagonal elements  $h_j$  only. A word of caution here: we did not used Einstein's summation convention so repeated indices are not implicitly summed!

#### III.2. Differential operators

— The gradient of a differentiable function  $f: \mathbb{R}^d \to \mathbb{R}$  is given, in both the normalised and the non-normalised basis, by

$$oldsymbol{
abla} f = \sum_{j=1}^d rac{1}{h_j^2} rac{\partial f}{\partial q^j} oldsymbol{b}_j \qquad \qquad = \sum_{j=1}^d rac{1}{h_j} rac{\partial f}{\partial q^j} \hat{oldsymbol{b}}_j.$$

— The divergence operator of a vector field  $\boldsymbol{v}: \mathbb{R}^d \to \mathbb{R}^d$  is

$$\nabla \cdot \boldsymbol{v} = \frac{1}{\rho} \sum_{j=1}^{d} \frac{\partial}{\partial q^{j}} \left( \rho v^{j} \right) \qquad = \frac{1}{\rho} \sum_{j=1}^{d} \frac{\partial}{\partial q^{j}} \left( \frac{\rho}{h_{j}} \, \hat{v}^{j} \right) \qquad \text{with } \rho = \prod_{j=1}^{d} h_{j} = \sqrt{\det g}.$$

— When d=3, the *curl* of a vector field  $\boldsymbol{v}:\mathbb{R}^d\to\mathbb{R}^d$  is written as

$$\nabla \times \boldsymbol{v} = \frac{1}{h_1 h_2 h_3} \begin{vmatrix} \boldsymbol{b}_1 & \boldsymbol{b}_2 & \boldsymbol{b}_3 \\ \partial_1 & \partial_2 & \partial_3 \\ h_1^2 v_1 & h_2^2 v^2 & h_3^2 v^3 \end{vmatrix} = \frac{1}{h_1 h_2 h_3} \begin{vmatrix} h_1 \hat{\boldsymbol{b}}_1 & h_2 \hat{\boldsymbol{b}}_2 & h_3 \hat{\boldsymbol{b}}_3 \\ \partial_1 & \partial_2 & \partial_3 \\ h_1 \hat{\boldsymbol{v}}_1 & h_2 \hat{\boldsymbol{v}}^2 & h_3 \hat{\boldsymbol{v}}^3 \end{vmatrix}.$$

The d=2 analogue, denoted  $\nabla^{\perp} \cdot v$  in this work, is obtained readily from the  $\hat{b}_3$  component of the above relation.

— The tensor gradient of a vector field  $v: \mathbb{R}^d \to \mathbb{R}^d$  is more involved.

$$\begin{split} \boldsymbol{\nabla} \boldsymbol{v} &= \sum_{j=1}^d \mathrm{d} q^j \otimes \partial_j \boldsymbol{v} = \sum_{j=1}^d \sum_{k=1}^d \left[ \partial_j v^k + \sum_{\ell=1}^d \Gamma^k{}_{j\ell} v^\ell \right] \, \mathrm{d} q^j \otimes \boldsymbol{b}_k \\ &= \sum_{j=1}^d \sum_{k=1}^d \frac{1}{h_j} \left[ \partial_j \hat{v}^k - \frac{\hat{v}^k}{h_k} \left( \partial_j h_k \right) + \Gamma^k{}_{j\ell} \frac{h_k \hat{v}^\ell}{h_\ell} \right] \mathrm{d} \hat{q}^j \otimes \hat{\boldsymbol{b}}_k \end{split}$$

— The convection operator involving two vector field  $u, v : \mathbb{R}^d \to \mathbb{R}^d$  is obtained from the last point,

$$\begin{split} \boldsymbol{u} \cdot \boldsymbol{\nabla} \boldsymbol{v} &= \sum_{j=1}^d \mathrm{d} q^j(\boldsymbol{u}) \, \partial_j(\boldsymbol{v}) = \sum_{j=1}^d \sum_{k=1}^d u_j \left[ \partial_j v^k + \sum_{\ell=1}^d \Gamma^k{}_{j\ell} v^\ell \right] \, \boldsymbol{b}_k \\ &= \sum_{j=1}^d \sum_{k=1}^d \frac{\hat{u}^j}{h_j} \left[ \partial_j \hat{v}^k - \frac{\hat{v}^k}{h_k} \left( \partial_j h_k \right) + \Gamma^k{}_{j\ell} \frac{h_k \hat{v}^\ell}{h_\ell} \right] \, \hat{\boldsymbol{b}}_k \end{split}$$

— The divergence of a tensor field  $\mathbf{S}: \mathbb{R}^d \to \mathbb{R}^{d \times d}$ , with coordinates defined as

$$\mathbf{S} = \sum_{j,k=1}^d S_j^{\ k} \mathrm{d}q^j \otimes oldsymbol{b}_k = \sum_{j,k=1}^d \hat{S}_j^{\ k} \mathrm{d}\hat{q}^j \otimes \hat{oldsymbol{b}}_k,$$

and which yields a vector field, is defined as

$$\boldsymbol{\nabla}\cdot\mathbf{S} = \sum_{j,k=1}^d \frac{1}{h_j^2} \left[ \partial_j S_j^{\ k} - \sum_{\ell=1}^d \left( \Gamma^\ell_{\ jj} S_\ell^{\ k} + \Gamma^k_{j\ell} S_j^\ell \right) \right] \ \boldsymbol{b}_k.$$

— The laplacian of a scalar function  $f: \mathbb{R}^d \to \mathbb{R}$  is computed from the gradient and the divergence operators, yielding

$$\Delta f = \boldsymbol{\nabla} \cdot \boldsymbol{\nabla} f = \frac{1}{\rho} \sum_{i=1}^d \frac{\partial}{\partial q^j} \left( \frac{\rho}{h_j^2} \frac{\partial f}{\partial q^j} \right)$$

— The vector laplacian can be computed by a brave and adventurous person from

$$\Delta \boldsymbol{u} = \boldsymbol{\nabla} \cdot \boldsymbol{\nabla} \boldsymbol{u}.$$

# Bibliography

- ACKERBERG, R.C. (1970). Boundary-layer separation at a free streamline. Part 1. Two-dimensional flow. In: J. Fluid Mech. 44, pp. 211–225 (cit. on p. 149).
- (1971). Boundary-layer separation at a free streamline. Part 2. Numerical results. In: *J. Fluid Mech.* 46, pp. 727–736 (cit. on p. 149).
- AI, A., IFRIM, M., and TATARU, D. (2022). Two-dimensional gravity waves at low regularity II: Global solutions. In: *Ann. Inst. H. Poincaré C Anal. Non Linéaire* 39, pp. 819–884 (cit. on pp. 5, 19).
- (2024). Two dimensional gravity waves at low regularity I: Energy estimates. In: Ann. Inst. H. Poincaré C Anal. Non Linéaire. [published online] (cit. on pp. 5, 19).
- ALAZARD, T. (2021). Free surface flows in fluid dynamics. Lecture Notes for a course at UC Berkeley. URL: http://talazard.perso.math.cnrs.fr/CL.pdf (cit. on p. 48).
- (2024). The Water Waves Equations in Eulerian Coordinates. In: AI, A., ALAZARD, T., IFRIM, M., and TATARU, D. Free Boundary Problems in Fluid Dynamics. Vol. 54. Oberwolfach seminars. Birkhäuser, Cham, pp. 1–111 (cit. on p. 48).
- ALAZARD, T., BALDI, P., and HAN-KWAN, D. (2018). Control for water waves. In: J. Eur. Math. Soc. 20, pp. 657–745 (cit. on p. 20).
- Alazard, T., Burq, N., and Zuily, C. (2011a). Low regularity Cauchy theory for the water-waves problem: canals and swimming pools. In: *Journées Éq. Dériv. Partielles* 3 (cit. on p. 20).
- (**2011b**). Strichartz estimates for water waves. In: *Ann. Sci. Éc. Norl. Supér.* (4) **44**.5, pp. 855–903 (cit. on p. 19).
- (2013). The water-waves equations: from Zakharov to Euler. In: Progress in Nonlinear Differential Equations and Their Applications. Studies in Phase Space Analysis with Applications to PDEs 84, pp. 1–20 (cit. on p. 48).
- (2014a). On the Cauchy problem for gravity water waves. In: *Invent. Math.* 198, pp. 71–163 (cit. on pp. 5, 19).
- (2014b). On the water waves equations with surface tension. In: Duke Math. J. 158.3, pp. 413–499 (cit. on pp. 5, 19).
- Alazard, T. and Delort, J.-M. (2015a). Global solutions and asymptotic behavior for two dimensional gravity water waves. In: *Ann. Sci. Éc. Norm. Supér.* (4) 48.5, pp. 1149–1238 (cit. on pp. 5, 19).
- (2015b). Sobolev estimates for two dimensional gravity water waves. In: Astérisque 374 (cit. on pp. 5, 19).
- ALAZARD, T. and MÉTIVIER, G. (2009). Paralinearization of the Dirichlet to Neumann operator, and regularity of diamond waves. In: *Comm. Partial Differential Equations* 34.10–12, pp. 1632–1704 (cit. on pp. 19, 158).
- ALAZARD, T. and Shao, C. (2025). KAM via Standard Fixed Point Theorems. arXiv: 2312.13971 [math.AP] (cit. on p. 20).
- Alazard, T. and Zuily, C. (2024). Virial Theorems and Equipartition of Energy for Water Waves. In: SIAM J. Math. Anal. 56.4, pp. 5285–5329 (cit. on p. 20).
- ALINHAC, S. (1986). Paracomposition et Opérateurs Paradifférentiels. In: Comm. Part. Diff. Eq. 11.1, pp. 87–121 (cit. on p. 19).
- ALINHAC, S. and GÉRARD, P. (2007). Pseudo-differential Operators and the Nash-Moser Theorem. Vol. 82. Graduate Studies in Mathematics. American Mathematical Society (cit. on p. 140).
- ALLAIN, G. (1987). Small-Time Existence for the Navier-Stokes Equations with a Free Surface. In: *Appl. Math. Optim.* 16, pp. 37–50 (cit. on pp. 4, 17).

- ALVAREZ-SAMANIEGO, B. and LANNES, D. (2009). A Nash-Moser Theorem for Singular Evolution Equations. Applications to the Serre and Gree-Naghdi Equations. In: *Indiana Uni. Math. J.* 57.1, pp. 97–131 (cit. on p. 140).
- AMBROSE, D.A. and MASMOUDI, N. (2009a). The Zero Surface Tension Limit of Three-dimensional Water Waves. In: *Indiana Uni. Math. J.* 58.2, pp. 479–521 (cit. on pp. 5, 19, 136).
- (2009b). The Zero Surface Tension Limit of Two-dimensional Water Waves. In: Comm. Pure Appl. Math. LVIII, pp. 1287–1315 (cit. on pp. 5, 19).
- Ambrose, D.M., Camassa, R., Marzuola, J.L., McLaughlin, R.M., Robinson, Q., and Wilkening, J. (2022). Numerical algorithms for water waves with background flow over obstacles and topography. In: Adv. Comp. Math. 48.46 (cit. on p. 6).
- AMESTOY, P.R., BUTTARI, A., L'EXCELLENT, J.-Y., and MARY, T. (2019). Performance and Scalability of the Block Low-Rank Multifrontal Factorization on Multicore Architectures. In: *ACM Transactions on Mathematical Software* 45 (1), 2:1–2:26 (cit. on p. 107).
- AMESTOY, P.R., DUFF, I. S., KOSTER, J., and L'EXCELLENT, J.-Y. (2001). A Fully Asynchronous Multifrontal Solver Using Distributed Dynamic Scheduling. In: SIAM Journal on Matrix Analysis and Applications 23.1, pp. 15–41 (cit. on p. 107).
- Arsénio, D., Dormy, E., and Lacave, C. (2020). The vortex method for two-dimensional ideal flows in exterior domains. In: SIAM J. Math. Anal. 52.4, pp. 3881–3961 (cit. on p. 23).
- Babuška, I. (1971). Error-bounds for finite element method. In: *Numer. Math.* 16, pp. 322–333 (cit. on p. 97).
- BAHOURI, H., CHEMIN, J.-Y., and DANCHIN, R. (2011). Fourier Analysis and Nonlinear Partial Differential Equations. Vol. 343. A Series of Comprehensive Studies in Mathematics. Springer Berlin, Heidelberg (cit. on pp. 159, 160).
- BAKER, G. R., MEIRON, D., and ORSZAG, S. A. (1982). Generalized vortex methods for free-surface flow problems. In: *J. Fluid Mech.* 123, pp. 477–501 (cit. on pp. 2, 10, 23, 89, 117, 122, 123).
- Baker, G. R. and Xie, C. (2011). Singularities in the complex physical plane for deep water waves. In: *Journal of Fluid Mechanics* 685, pp. 83–116 (cit. on pp. 24, 68).
- BALAY, S., ABHYANKAR, S., and ADAMS, M. F. (2021a). PETSc Web page. URL: https://petsc.org/(cit. on p. 106).
- (2021b). *PETSc/TAO Users Manual*. Tech. rep. ANL-21/39 Revision 3.16. Argonne National Laboratory (cit. on p. 106).
- BALAY, S., GROPP, W. D., McInnes, L. C., and Smith, B. F. (1997). Efficient Management of Parallelism in Object Oriented Numerical Software Libraries. In: *Modern Software Tools in Scientific Computing*. Ed. by Arge, E., Bruaset, A.M., and Langtangen, H.P. Birkhäuser Press, pp. 163–202 (cit. on p. 106).
- BANNER, M.L. and PEREGRINE, D.H. (1993). Wave Breaking in Deep Water. In: Ann. Rev. Fluid Mech. 25, pp. 373–397 (cit. on p. 23).
- BARRÉ DE SAINT-VENANT, A. J. C. (1871). Théorie du mouvement non permanent des eaux, avec application aux crues des rivières et à l'introduction de marées dans leurs lits. In: *Comptes Rendus de l'Académie des Sciences* 73, 147-154 and 237-240 (cit. on pp. 5, 140).
- Basu, S. and Prasad, S. (2023). A connection between cut locus, Thom space and Morse–Bott functions. In: Algebraic & Geometric Topology 23.9, pp. 4185–4233 (cit. on p. 56).
- Batchelor, G. K. (1967). An Introduction to Fluid Dynamics. Cambridge University Press (cit. on pp. 21, 30, 45, 125, 142, 146, 148).
- BEALE, J.T. (1981). The initial value problem for the Navier-Stokes equations with a free surface. In: Comm. Pure Appl. Math. 34.3, pp. 359–392 (cit. on pp. 4, 17).
- (1984). Large-time regularity of viscous surface waves. In: Arch. Rational Mech. Anal. 84, pp. 307–352 (cit. on pp. 4, 17).
- Beck, G. and Lannes, D. (2022). Freely Floating Objects on a Fluid Governed by the Boussinesq Equations. In: Ann. Inst. H. Poincaré C Anal. Non Linéaire 39.3, pp. 575–646 (cit. on p. 20).
- BEER, G. (2001). Programming the Boundary Element Method. An Introduction for Engineers. John Wiley & sons (cit. on p. 133).
- Benjamin, T.B. (1967). Instability of periodic wavetrains in nonlinear dispersive systems. In: *Proc. R. Soc. Lond. A* 299.1456, pp. 59–76 (cit. on p. 23).

- BENJAMIN, T.B. and BRIDGES, T.J. (1997a). Reappraisal of the Kelvin-Helmholtz problem. Part 1. Hamiltonian structure. In: *J. Fluid Mech.* 333, pp. 301–325 (cit. on pp. 19, 146).
- (1997b). Reappraisal of the Kelvin–Helmholtz problem. Part 2. Interaction of the Kelvin–Helmholtz, superharmonic and Benjamin–Feir instabilities. In: *J. Fluid Mech.* 333, pp. 327–373 (cit. on pp. 19, 146).
- BENJAMIN, T.B. and FEIR, J.E. (1967). The disintegration of wave trains on deep water. Part 1. Theory. In: *J. Fluid Mech.* 27.3, pp. 417–430 (cit. on p. 23).
- BENJAMIN, T.B. and OLVER, P.J. (1982). Hamiltonian structure, symmetries and conservation laws for water waves. In: *J. Fluid Mech.* 125, pp. 137–185 (cit. on p. 77).
- BENNETT, A. (2006). Lagrangian Fluid Dynamics. Cambridge University Press (cit. on pp. 62, 64, 66).
- Benzoni-Gavage, S. and Serre, D. (2007). Multidimensional Hyperbolic Partial Differential Equations. First-order Systems and Applications. Oxford Mathematical Monographs. Oxford University Press (cit. on p. 140).
- BERGMANN, J., MAUREL-OUJIA, T., YIN, X.-Y., NAVE, J.-C., and SCHNEIDER, K. (2024). Singularity formation of vortex sheets in 2D Euler equations using the characteristic mapping method. *unpublished*. arXiv: 2404.02008 [physics.flu-dyn] (cit. on p. 146).
- Bernoulli, D. (1738). Hydrodynamica. sive de viribus et motibus fluidorum commentarii : opus academicum ab auctore, dum Petropoli ageret, congestum. Ed. by Dulsecker, J. R. printed by J. H. Decker (cit. on pp. 45, 46).
- BEYER, K. and GÜNTHER, M. (1998). On the Cauchy Problem for a Capillary Drop. Part I: Irrotational Motion. In: *Math. Methods Appl. Sci.* 21, pp. 1149–1183 (cit. on p. 19).
- BIRKHOFF, G. (1962). Hemlholtz and Taylor Instability. In: hydrodynamic Instability. Ed. by BIRKHOFF, G., BELLMAN, R., and LIN, C.C. Vol. 13. Proceedings of Symposia in Applied Mathematics. American Mathematical Society (cit. on p. 146).
- BLASER, A., BENAMRAN, R., VILLAS BÔAS, A.B., LENAIN, L., and PIZZO, N. (2024). Momentum, energy and vorticity balances in deep-water surface gravity waves. In: *J. Fluid Mech.* 997, A55 (cit. on p. 67).
- BLASIUS, H. (1908). Grenzschichten in Flüssigkeiten mit kleiner Reibung. In: Zeits. f. Math. u. Phys 56, pp. 1–37 (cit. on p. 152).
- BONNET, M. (1995). Équations intégrales et éléments de frontières. Applications en mécanique des solides et des fluides. Sciences et techniques de l'ingénieur. CNRS Éditions/Eyrolles (cit. on p. 133).
- Bony, J.-M. (1981). Calcul Symbolique et Propagation des Singularités pour les Équations aux Dérivées Partielles Non-Linéraires. In: *Ann. Sci. Éc. Norm. Sup. (4)* 14, pp. 209–246 (cit. on p. 19).
- BOOTHBY, W.M. (1975). An Introduction to Differentiable Manifolds and Riemannian Geometry. London: Academic Press, Inc. (cit. on p. 161).
- Boussinesq, J. (1872). Théorie des ondes et des remous qui se propagent le long d'un canal rectangulaire horizontal, en communiquant au liquide contenu dans ce canal des vitesses sensiblement pareilles de la surface au fond. In: *Journal de mathématiques pures et appliquées.* 2 17, pp. 55–108 (cit. on p. 140).
- (1877). Essai sur la Théorie des Eaux Courantes. Vol. 23. Mémoires présentés par divers savants de l'Académie des Sciences de l'Institut National de France 1 (cit. on p. 140).
- BOUTOUNET, M., CHUPIN, L., NOBLE, P., and VILA, J.-P. (2008). Shallow waters viscous flows for arbitrary topography. In: *Comm. Math. Sci.* 6.1, pp. 29–55 (cit. on p. 156).
- BRECHNER, E. L. (1992). General Offset Curves and Surfaces. In: Geometry Processing for Design and Manufacturing. Ed. by BARNHILL, R. E. Society for Industrial and Applied Mathematics. Chap. 5, pp. 101–121 (cit. on p. 55).
- Bresch, D. (2009). Shallow-Water Equations and Related Topics. In: *Handbook of Differential Equations*. Vol. 5: Evolutionary Equations. Ed. by Dafermos, C.M. and Pokorný, M. Elsevier. Chap. 1 (cit. on p. 156).
- BRESCH, D. and Noble, P. (2007). Mathematical Justification of a Shallow Water Model. In: *Methods and Applications of Analysis* 14.2, pp. 87–118 (cit. on p. 156).
- (2011). Mathematical Derivation of Viscous Shallow-Water Equations with Zero Surface Tension. In: *Ind. Univ. Math. J.* 60.4, pp. 1137–1169 (cit. on pp. 4, 17).
- Brezis, H. (2010). Functional Analysis, Sobolev Spaces and Partial Differential Equations. 1st ed. Universitext. Springer New York, NY (cit. on p. 159).

- Brezzi, F. (1974). On the existence, uniqueness and approximation of saddle-point problems arising from Lagrangian multipliers. In: Rev Française Automat Informat Recherche Opérationnelle Sér. Rouge 8, pp. 129–151 (cit. on p. 97).
- BRIDGES, T.J. and DONALDSON, N.M. (2011). Variational Principles for Water Waves from the Viewpoint of a Time-dependent Moving Mesh. In: *Mathematika* 57, pp. 147–173 (cit. on pp. 77, 80, 157).
- BUELER, Ed (2020). PETSc for Partial Differential Equations: Numerical Solutions in C and Python. Philadelphia, PA: Society for Industrial and Applied Mathematics (cit. on p. 108).
- Caflisch, R.E., Gargano, F., Sammartino, M., and Sciacca, V. (2022). Complex singularity analysis for vortex layer flows. In: *J. Fluid Mech.* 932, A21 (cit. on p. 146).
- Castro, Á, Córdoba, D., Fefferman, C., Gancedo, F., and Gómez-Serrano, J. (2013). Finite time singularities for the free boundary incompressible Euler equations. In: *Ann. of Math.* (2) 178.3, pp. 1061–1134 (cit. on p. 20).
- (2019). Splash singularities for the free boundary Navier-Stokes equations. In: Ann. PDE 5.12 (cit. on p. 20).
- CASTRO, Å and LANNES, D. (2014). Fully nonlinear long-wave models in the presence of vorticity. In: J. Fluid Mech. 759, pp. 642–675 (cit. on pp. 18, 156).
- (2015). Well-posedness and shallow-water stability for a new Hamiltonian formulation of the water waves problem con vorticity. In: *Indiana Uni. Math. J.* 64.4, pp. 1169–1270 (cit. on pp. 18, 156).
- CHANG, K.-A., HSU, T.-J., and LIU, P.L.-F. (2001). Vortex generation and evolution in water waves propagating over a submerged rectangular obstacle Part I. Solitary waves. In: *Coastal Engineering* 44, pp. 13–36 (cit. on p. 148).
- (2005). Vortex generation and evolution in water waves propagating over a submerged rectangular obstacle Part II: Cnoidal waves. In: *Coastal Engineering* 52, pp. 257–283 (cit. on p. 148).
- CHEMIN, J.-Y. (1995). Fluides parfaits incompressibles. In: Astérisque 230 (cit. on p. 18).
- (1996). A remark on the inviscid limit for two-dimensional incompressible fluids. In: Commun. Partial Differential Equations 21.11–12, pp. 1771–1779 (cit. on pp. 20, 140).
- CHEN, G., KHARIF, C., ZALESKI, S., and LI, J. (1999). Two-dimensional Navier-Stokes simulation of breaking waves. In: *Physics of Fluids* 11.1, pp. 121–133 (cit. on pp. 2, 24, 37, 89, 90, 111, 123).
- CHENG, S.-W., DEY, T.K., and SHEWCHUK, J. (2012). Delaunay Mesh Generation. CRC Press LLC (cit. on pp. 93, 94).
- CLAMOND, D. (2007). On the Lagrangian description of steady surface gravity waves. In: *J. Fluid Mech.* 589, pp. 433–454 (cit. on p. 67).
- COURANT, R., FRIEDRICHS, K., and LEWY, H. (1928). Über die partiellen Differenzengleichungen der mathematischen Physik. In: *Mathematische Annalen* 100.1. (in German), pp. 32–74 (cit. on p. 93).
- COUTAND, D. and SHKOLLER, S. (2007). Well-Posedness of the Free-Surface Incompressible Euler Equations with or without Surface Tension. In: *J. Amer. Math. Soc.* 20.3, pp. 829–930 (cit. on pp. 5, 18).
- (2014). On the Finite-Time Splash and Splat Singularities for the 3-D Free-Surface Euler Equations. In: Commun. Math. Phys. 325, pp. 143–183 (cit. on p. 20).
- (2016). On the Impossibility of Finite-Time Splash Singularities for Vortex Sheets. In: Arch. Rational Mech. Anal. 221, pp. 987–1033 (cit. on p. 20).
- (2019). On the splash singularity for the free-surface of a Navier–Stokes fluid. In: Ann. Inst. H. Poincaré C, Anal. non linéaire 36.2, pp. 475–503 (cit. on pp. 20, 45, 89).
- CRAIG, W. (1985). An existence theory for water waves and the Boussinesq and Korteweg-de Vries scaling limits. In: *Comm. PDEs* 10, pp. 787–1003 (cit. on pp. 19, 140).
- (2000). Problèmes de petits diviseurs dans les équations aux dérivées partielles. In: *Panoramas & Synthèses* 9 (cit. on pp. 18, 20).
- (2017). On the Hamiltonian for Water Waves. *Unpublished*. arXiv: 1612.08971 [math.AP] (cit. on pp. 2, 6, 19, 25, 61, 66, 68, 77, 80, 157).
- CRAIG, W., SCHANZ, U., and SULEM, C. (1997). The modulational regime of three-dimensional water waves and the Davey-Stewartson system. In: *Ann. Inst. Henri Poincaré. C: Analyse non linéaire* 14.5, pp. 615–667 (cit. on pp. 19, 51, 140).
- Craig, W. and Sulem, C. (1993). Numerical simulation of gravity waves. In: *Journal of Computational Physics* 108, pp. 73–83 (cit. on pp. 2, 5, 18, 46–48, 51, 60, 68, 139).
- Craig, W., Sulem, C., and Sulem, P.-L. (1992). Nonlinear modulation of gravity waves: a rigorous approach. In: *Nonlinearity* 5, pp. 497–522 (cit. on pp. 19, 140).

- Crank, J. and Nicolson, P. (1947). A practical method for numerical evaluation of solutions of partial differential equations of the heat conduction type. In: *Proc. Cambridge Phil. Soc.* 43, pp. 50–67 (cit. on p. 92).
- Crow, S.C. (1970). Stability theory for a pair of trailing vortices. In: AIAA Journal 8.12, pp. 2172–2179 (cit. on p. 146).
- D'ALEMBERT, J. L. R. (1752). Essai d'une nouvelle théorie de la résistance des fluides. Ed. by L'AÎNÉ, David (cit. on p. 33).
- Dalibard, A.-L., Dietert, H., Gérard-Varet, D., and Marbach, F. (2017). High frequency analysis of the unsteady interactive boundary layer model. In: *SIAM J. Math. Anal.* 50.4, pp. 4203–4245 (cit. on p. 21).
- Dalibard, A.-L. and Masmoudi, N. (2019). Separation for the stationary Prandtl equation. In: *Pub. Math. IHÉS* 130, pp. 187–297 (cit. on pp. 21, 141, 155).
- Dalibard, A.-L. and Saint-Raymond, L. (2018). Mathematical Study of Degenerate Boundary Layers: A Large Scale Ocean Circulation Problem. In: *Memoirs Amer. Math. Soc.* 253.1206 (cit. on p. 22).
- DAVEY, A. and STEWARTSON, K. (1974). On three-dimensional packets of surface waves. In: *Proc. R. Soc. London A* 338.1613, pp. 101–110 (cit. on p. 140).
- DE GENNES, P.-G., BROCHARD-WYART, F., and Quéré, D. (2002). Gouttes, bulles, perles et ondes. Belin (cit. on p. 92).
- DE POYFERRÉ, T. (2019). A Priori Estimates for Water Waves with Emerging Bottom. In: Arch. Rational Mech. Anal. 232, pp. 763–812 (cit. on p. 20).
- DEIKE, L., MELVILLE, W. K., and POPINET, S. (2016). Air entrainment and bubble statistics in breaking waves. In: *J. Fluid Mech.* 801, pp. 91–129 (cit. on pp. 2, 24, 37).
- Deike, L., Popinet, S., and Melville, W. K. (2015). Capillary effects on wave breaking. In: *J. Fluid Mech.* 769, pp. 541–569 (cit. on pp. 2, 24, 37, 90, 123).
- DELAUNAY, B. (1934). Sur la sphère vide. In: Bull. Acad. Sci. URSS 6, pp. 793–800 (cit. on p. 93).
- DELORT, J.-M. (1991). Existence de Nappes de Tourbillons en Dimension Deux. In: J. American Math. Soc. 4.3, pp. 553–586 (cit. on pp. 18, 22).
- Deng, Y., Ionescu, A.D., Pausader, B., and Pusateri, F. (2017). Global solutions of the gravity-capillary water-wave system in three dimensions. In: *Acta Math.* 219, pp. 213–402 (cit. on p. 19).
- Deny, J. and Lions, J.-L. (1954). Les espaces du type de Beppo Levi. In: Annales de l'institut Fourier 5, pp. 305–370 (cit. on p. 160).
- DESJARDINS, B., LANNES, D., and SAUT, J.-C. (2020). Normal mode decomposition and dispersive and nonlinear mixing in stratified fluids. In: *Water Waves* 3.1, pp. 153–192 (cit. on p. 18).
- DEVORIA, A.C. and MOHSENI, K. (2018). Vortex sheet roll-up revisited. In: *Journal of Fluid Mechanics* 855, pp. 299–321 (cit. on p. 146).
- DI GIORGIO, S., PIROZZOLI, S., and IAFRATI, A. (2022). On coherent vortical structures in wave breaking. In: *J. Fluid Mech.* 947, A44 (cit. on pp. 2, 24, 37, 90, 123).
- DIETERT, H. and GÉRARD-VARET, D. (2022). On the ill-posedness of the triple deck model. In: SIAM J. Math. Anal. 54.2, pp. 2611–2633 (cit. on p. 21).
- DOLD, J.W. (1992). An efficient Surface-Integral Algorithm Applied to Unsteady Gravity Waves. In: *J. Comp. Phys.* 103, pp. 90–115 (cit. on p. 23).
- Dold, J.W., Peregrine, D.H., Morton, K.W., and Baines, M.J. (1986). An Efficient Boundary Integral Method for Steep Unsteady Water Waves. In: *Numerical Methods for Fluid Dynamics II*. Oxford University Press, pp. 671–679 (cit. on pp. 2, 23).
- DOLEAN, V., JOLIVET, P., and NATAF, F. (2015). An Introduction to Domain Decomposition Methods. Philadelphia: SIAM (cit. on pp. 9, 107, 108).
- Donea, J., Huerta, A., Ponthot, J.-Ph., and Rodriguez-Ferran, A. (2004). Arbitrary Lagrangian-Eulerian methods. In: *The Encyclopedia of Computational Mechanics*. Ed. by Stein, E., Borst, R., and Hughes, T.J.R. Vol. 1. Wiley. Chap. 14, pp. 413–437 (cit. on p. 100).
- DORMY, E. and LACAVE, C. (2024). Inviscid Water-Waves and interface modeling. In: *Quarterly of Applied Mathematics* 82, pp. 583–637 (cit. on pp. 2, 10, 12, 23, 26, 109, 111, 117, 123–125, 129, 133, 137, 143, 158).
- Drivas, T.D., Iyer, S., and Nguyen, T.T. (2024). The Feynman–Lagerstrom Criterion for Boundary Layers. In: *Arch. Rational Mech. Anal.* 248.55 (cit. on p. 22).

- Duchêne, V. (2021). Many Models for Water Waves. A unified theoretical approach. AMS Open Math Notes. URL: https://www.ams.org/open-math-notes/omn-view-listing?listingId=111309 (cit. on pp. 6, 20, 140).
- DUCHÊNE, V. and ISRAWI, S. (2018). Well-posedness of the Green-Naghdi and Boussinesq-Peregrine systems. In: *Ann. Math. Blaise Pascal* 25.1, pp. 21–74 (cit. on p. 140).
- EBIN, D.G. (1987). The equations of motions of a perfect fluid with free boundary are not well posed. In: Comm. Part. Diff. Eq. 12.10, pp. 1175–1201 (cit. on p. 19).
- ERN, A. and GUERMOND, J.-L. (2021a). Finite Elements I. Approximation and Interpolation. Springer Cham (cit. on pp. 90, 96).
- (2021b). Finite Elements II. Galerkin Approximation, Elliptic and Mixed PDEs. Springer Cham (cit. on p. 90).
- (2021c). Finite Elements III. First-Order and Time-Dependent PDEs. Springer Cham (cit. on p. 90).
- EULER, L. (1757). Principes Généraux du Mouvement des Fluides. In: *Mémoires de l'Académie royale des sciences et des belles lettres de Berlin* 11, pp. 274–315 (cit. on pp. 33, 60).
- (1768). Institutionum calculi integralis volumen primum. St. Petersburg: Imperial Academy of Sciences (cit. on p. 92).
- EVANS, L. C. (2010). Partial Differential Equations. 2nd ed. Vol. 19. Graduate Studies in Mathematics. Providence, R.I.: American Mathematical Society (cit. on pp. 34, 93, 159, 160).
- FEFFERMAN, C., IONESCU, A, and LIE, V. (2016). On the absence of splash singularities in the case of two-fluid interfaces. In: *Duke Mathematical Journal* 165.3, pp. 417–462 (cit. on pp. 20, 45, 89).
- FELDMEIER, A. (2019). Theoretical Fluid Dynamics. Theoretical and Mathematical Physics. 2020 corrected publication. Springer Nature Switzerland (cit. on p. 143).
- FEYNMAN, R.P., LEIGHTON, R.B., and SANDS, M. (1965). The Feynman Lectures on Physics; Vol. I. Addison-Wesley Publishing Company (cit. on p. 15).
- FLORYAN, J.M. and SARIC, W.S. (1982). Stability of Gortler Vortices in Boundary Layers. In: AIAA J. 20.3, pp. 316–324 (cit. on pp. 152, 155).
- FONTELOS, M. A. and DE LA HOZ, F. (2010). Singularities in water waves and the Rayleigh-Taylor problem. In: *Journal of Fluid Mechanics* 651, pp. 211–239 (cit. on p. 24).
- Foss, J.F. (2004). Surface selections and topological constraint evaluations for flow field analyses. In: *Experiments in Fluids* 37, pp. 883–898 (cit. on p. 146).
- Fradin, T. (2025). Well-posedness of the Euler equations in a stably stratified ocean in isopycnal coordinates. Preprint. url: https://hal.science/hal-04615812 (cit. on p. 18).
- FRIEDRICHS, K. O. (1944). The identity of weak and strong extensions of differential operators. In: *Trans. Amer. Math. Soc.* 55, pp. 132–151 (cit. on p. 148).
- Fujita, H. and Kato, T. (1964). On the Navier-Stokes initial value problem. I. In: Arch. Rational Mech. Anal. 16, pp. 269–315 (cit. on p. 16).
- Galerkin, B. (1915). On electrical circuits for the approximate solution of the Laplace equation. In: *Vestnik Inzh.* 19. (in Russian), pp. 897–908 (cit. on p. 90).
- GALLAGHER, I. (2020). Analyse Fonctionnelle. Lecture Notes for a course at ENS Paris. URL: https://www.math.ens.psl.eu/~gallagher/AnalyseFonctionnelle%202019-2020.pdf (cit. on p. 159).
- Gallagher, I. and Gallay, T. (2005). Uniqueness for the two-dimensional Navier-Stokes equation with a measure as initial vorticity. In: *Math. Ann.* 332, pp. 287–327 (cit. on p. 22).
- Gallagher, I., Gallay, T., and Lions, P.-L. (2005). On the uniqueness of the solution of the twodimensional Navier-Stokes equation with a Dirac mass as initial vorticity. In: *Math. Nachr.* 278, pp. 1665–1672 (cit. on p. 22).
- Galvin, C. J. (1968). Breaker Type Classification on Three Laboratory Beaches. In: *Journal of Geophysical Research* 73.12, pp. 3651–3659 (cit. on pp. 8, 22, 82, 83, 122).
- GÉRARD-VARET, D. and DORMY, E. (2010). On the ill-posedness of the Prandtl equation. In: J. Amer. Math. Soc. 23, pp. 591–609 (cit. on pp. 21, 155).
- GÉRARD-VARET, D., IYER, S., and MAEKAWA, Y. (2023). Improved well-posedness for the Triple-Deck and related models via concavity. In: *J. Math. Fluid Mech.* 25.3, A69 (cit. on p. 21).
- GÉRARD-VARET, D. and LACAVE, C. (2013). The Two-Dimensional Euler Equations on Singular Domains. In: Arch. Ration. Mech. Anal. 209.1, pp. 131–170 (cit. on pp. 4, 18).
- GÉRARD-VARET, D., LACAVE, C., NGUYEN, T.T., and ROUSSET, F. (2018). The vanishing viscosity limit for 2D Navier–Stokes in a rough domain. In: J. Math. Pures Appl. 119, pp. 45–84 (cit. on pp. 21, 141).

- GÉRARD-VARET, D. and MASMOUDI, N. (2015). Well-posedness for the Prandtl system without analyticity or monotonicity. In: Ann. Sci. Éc. Norm. Sup. (4) 48.6, pp. 1273–1325 (cit. on pp. 21, 155).
- GERMAIN, P., MASMOUDI, N., and SHATAH, J. (2012). Global solutions of the gravity water waves equation in dimension 3. In: *Annals of Mathematics* 175, pp. 691–754 (cit. on p. 19).
- GERSTNER, F. J. VON (1802). Theorie der Wellen. In: Abhandlunger der Königlichen Böhmischen Gesellschaft der Wissenschaften (cit. on pp. 67, 117).
- GOLDSTEIN, S. (1948). On laminar boundary-layer flow near a position of separation. In: Q. J. Mech. Appl. Math. 1.1, pp. 43–69 (cit. on p. 21).
- GÖRTLER, H. (1941). Instabilität laminarer Grenzchichten an Konkaven Wiinden gegenber gewissen dreidimensionalen Störungen. In: J. Appl. Math. Mech. (ZAMM) 21, pp. 250–252 (cit. on pp. 152, 155).
- Granger, R. A. (1995). Fluid Mechanics. Dover New York (cit. on p. 30).
- Green, A. E. and Naghdi, P. M. (1976). A derivation of equations for wave propagation in water of variable depth. In: *Journal of Fluid Mechanics* 78.2, pp. 237–246 (cit. on pp. 5, 111, 140).
- GREEN, G. (1828). An Essay on the Application of Mathematical Analysis to the Theories of Electricity and Magnetism. Nottingham, England: T. Warehouse (cit. on p. 50).
- GRILLI, S.T., SKOURUP, J., and SVENDSEN, I.A. (1989). An efficient boundary element method for non-linear water waves. In: *Engineering Analysis with Boundary Elements* **6**.2, pp. 97–107 (cit. on pp. 2, 23).
- GRIMSHAW, R. (2007). Solitary waves propagating over variable topography. In: *Tsunami and Nonlinear Waves*. Ed. by Kundu, A. Springer, Berlin, Heidelberg (cit. on p. 147).
- GRUE, J. (1992). Nonlinear water waves at a submerged obstacle or bottom topography. In: *J. Fluid Mech.* 244, pp. 455–476 (cit. on p. 143).
- GRUE, J. and KOLAAS, J. (2017). Experimental particle paths and drift velocity in steep waves at finite depth. In: *J. Fluid Mech.* 810.R1 (cit. on p. 21).
- GUERMOND, J.-L., LÉORAT, J., LUDDENS, F., and NORE, C. (2012). Remarks on the stability of the Navier-Stokes equations supplemented with stress boundary conditions. In: *European Journal of Mechanics B/Fluids* 39, pp. 1–10 (cit. on pp. 91, 99).
- Guo, Y. and Tice, I. (2013a). Almost exponential decay of periodic viscous surface waves without surface tension. In: *Arch. Ration. Mech. Anal.* 207.2, pp. 459–531 (cit. on pp. 4, 17).
- (2013b). Decay of viscous surface waves without surface tension in horizontally infinite domains. In: *Analysis and PDE* **6**.6, pp. 1429–1533 (cit. on pp. 4, 17).
- (2013c). Local Well-Posedness of the Viscous Surface Wave Problem without Surface Tension. In: *Analysis and PDE* **6**.2, pp. 287–369 (cit. on pp. 4, 17).
- GUYENNE, P. and GRILLI, S. T. (2006). Numerical study of three-dimensional overturning waves in shallow water. In: *Journal of Fluid Mechanics* 547, pp. 361–388 (cit. on pp. 23, 158).
- GUYON, É., HULIN, J.-P., and PETIT, L. (2012). *Hydrodynamique Physique*. 3rd ed. EDP Sciences/CNRS Éditions (cit. on pp. 21, 30).
- HECHT, F. (2012). New development in FreeFem++. In: J. Numer. Math. 20.3-4, pp. 251-265. URL: https://freefem.org/ (cit. on pp. 8, 25, 105).
- Helluy, P., Golay, F., Caltagirone, J.-P., Lubin, P., Vincent, S., D., Drevard, Marcer, R., Fraunié, P., Seguin, N., Grilli, S., Lesage, A.-C., Dervieux, A., and Allain, O. (2005). Numerical Simulation of Wave Breaking. In: *ESAIM: Math. Mod. & Num. Analysis* 39.3, pp. 591–607 (cit. on pp. 25, 111).
- HELMHOLTZ, H. von (1858). Ueber Integrale der hydrodynamischen Gleichungen, welche den Wirbelbewegungen entsprechen. In: *Journal für den reine und angewandte Mathematik* 55, pp. 25–55 (cit. on pp. 43, 137).
- (1867). On the Integrals of Hydrodynamical Equations, which Express Vortex Motions. In: *Phil. Magazine* 33. This is a translation of his 1858 paper (above reference), pp. 485–512 (cit. on p. 43).
- (1868). Über discontinuierliche Flüssigkeits-Bewegungen. In: Monatsberichte der Königlichen Preussische Akademie der Wissenschaften zu Berlin 23, pp. 215–228 (cit. on pp. 36, 37).
- HIRT, C.W, AMSDEN, A.A, and COOK, J.L (1974). An arbitrary Lagrangian-Eulerian computing method for all flow speeds. In: *Journal of Computational Physics* 14.3, pp. 227–253 (cit. on pp. 2, 9, 31, 100).
- HÖLDER, E. (1933). Über die unbeschränkte fortsetzbarkeit einer stetigen ebenen bewegung in einer unbegrenzten inkompressiblen flüssigkeit. In: *Mathematische Zeitschrift* 37, pp. 727–738 (cit. on p. 18).

- HOOD, P. and TAYLOR, C. (1974). Navier–Stokes equations using mixed interpolation. In: *Finite element methods in flow problems*. Ed. by Oden, J.T., Gallagher, R.H., Zienkiewicz, O.C., and Taylor, C. Huntsville Press, University of Alabama, pp. 121–132 (cit. on p. 97).
- HOPF, E. (1950). Über die Anfangswertaufgabe für die hydrodynamischen Grundgieichungen. In: *Math. Nachr* 4, pp. 213–231 (cit. on p. 16).
- HUERRE, P. (2012). Mécanique des fluides Tome 1. Lecture notes. École Polytechnique (cit. on p. 30).
- IAFRATI, A. (2009). Numerical study of the effects of the breaking intensity on wave breaking flows. In: *Journal of Fluid Mechanics* 622, pp. 371–411 (cit. on pp. 2, 24, 90, 123).
- IFTIMIE, D. and Planas, G. (2006). Inviscid limits for the Navier–Stokes equations with Navier friction boundary conditions. In: *Nonlinearity* 19.4 (cit. on pp. 4, 21, 36).
- IFTIMIE, D. and SUEUR, F. (2011). Viscous boundary layers for the Navier–Stokes equations with the Navier slip conditions. In: Arch Rational Mech Anal 199, pp. 145–175 (cit. on pp. 4, 21, 36, 130, 133).
- IONESCU, A.D. and PUSATERI, F. (2015). Global solutions for the gravity water waves system in 2d. In: *invent. math.* 199, pp. 653–804 (cit. on p. 19).
- Iooss, G. and Plotnikov, P.I. (2009). Small divisor problem in the theory of three-dimensional water gravity waves. In: *Mem. Amer. Math. Soc.* 200.940 (cit. on p. 20).
- (2011). Asymmetrical tridimensional travelling gravity waves. In: Arch. Rat. Mech. Anal. 200.3, pp. 789–880 (cit. on p. 20).
- IOOSS, G., PLOTNIKOV, P.I., and TOLAND, J.F. (2005). Standing waves on an infinitely deep perfect fluid under gravity. In: *Arch. Rat. Mech. Anal.* 177.3, pp. 367–478 (cit. on p. 20).
- IPCC (2019). Special Report on the Ocean and Cryosphere in a Changing Climate. Cambridge University Press (cit. on pp. 1, 15).
- (2023). Climate Change 2023: Synthesis Report. Contribution of Working Groups I, II and III to the Sixth Assessment Report of the Intergovernmental Panel on Climate Change. Tech. rep. IPCC, Geneva, Switzerland (cit. on pp. 1, 15).
- ISRAWI, S. (2010). Variable depth KdV equations and generalizations to more nonlinear regimes. In: ESAIM: Math. Mod. & Num. Analysis 44.2, pp. 347–370 (cit. on p. 140).
- Janssen, P. (2004). The Interaction of Ocean Waves and Wind. Cambridge University Press (cit. on pp. 3, 37).
- JIANG, B. and BI, Q. (2017). Classification of traveling wave solutions to the Green–Naghdi model. In: *Wave Motion* 73, pp. 45–56 (cit. on p. 111).
- JILLIANS, W.J. (1989). The superharmonic instability of Stokes waves in deep water. In: *J. Fluid Mech.* 204, pp. 563–579 (cit. on p. 23).
- JOHN, V. (2016). Finite Element Methods for Incompressible Flow Problems. Vol. 51. Springer Series in Computational Mathematics. Springer Cham (cit. on pp. 90, 92, 97).
- Johnson, R.S. (1973a). On an asymptotic solution of the Korteweg-de Vries equation with slowly varying coefficients. In: *J. Fluid Mech.* **60**, pp. 813–824 (cit. on p. 140).
- (1973b). On the development of a solitary wave moving over an uneven bottom. In: *Mathematical Proceedings of the Cambridge Philosophical Society* 73.1, pp. 183–203 (cit. on pp. 140, 147).
- (1997). A Modern Introduction to the Mathematical Theory of Water Waves. Cambridge University Press (cit. on pp. 30, 39, 40).
- Jolivet, P., Hecht, F., Nataf, F., and Prud'homme, C. (2013). Scalable domain decomposition preconditioners for heterogeneous elliptic problems. In: *Proceedings of the International Conference on High Performance Computing, Networking, Storage and Analysis. SC '13.* Denver, Colorado: Association for Computing Machinery (cit. on p. 107).
- JOLIVET, P., ROMAN, J.E., and ZAMPINI, S. (2021). KSPHPDDM and PCHPDDM: Extending PETSc with advanced Krylov methods and robust multilevel overlapping Schwarz preconditioners. In: *Computers & Mathematics with Applications* 84, pp. 277–295 (cit. on p. 107).
- Jolivet, P. and Tourner, P.-H. (2016). Block iterative methods and recycling for improved scalability of linear solvers. In: *Proceedings of the International Conference for High Performance Computing, Networking, Storage and Analysis. SC '16.* Salt Lake City, Utah: IEEE Press (cit. on p. 107).
- Kano, T. and Nishida, T. (1986). A Matematical Justification for Korteweg-de Vries equation and Boussinesq equation of Water Surface Waves. In: Osaka J. Math. 23, pp. 389–413 (cit. on p. 140).

- Kato, T. (1984). Remarks on Zero Viscosity Limit for Nonstationary Navier-Stokes Flows with Boundary. In: *Seminar on Nonlinear Partial Differential Equations*. Ed. by Chern, S. S. Springer New York, pp. 85–98 (cit. on pp. 21, 128, 140).
- KAZAKOVA, M. and RICHARD, G.L. (2019). A new model of shoaling and breaking waves: one-dimensional solitary wave on a mild sloping beach. In: *J. Fluid Mech.* 862, pp. 552–591 (cit. on p. 156).
- Kelliher, J.P. (2007). On Kato's conditions for vanishing viscosity. In: *Ind. Uni. Math. J.* 56.4, pp. 1711–1721 (cit. on pp. 22, 128, 132).
- (2008). Vanishing viscosity and the accumulation of vorticity on the boundary. In: *Comm. Math. Sci.* **6**.4, pp. 869–880 (cit. on p. 132).
- KELVIN, Lord (W. Thomson) (1867). On Vortex Atoms. In: *Proc. Roy. Soc. Edinburgh* VI, pp. 94–105 (cit. on p. 43).
- (1869). On Vortex Motion. In: Trans. Roy. Soc. Edinburgh 25, pp. 217–260 (cit. on p. 43).
- (1871). Hydrokinetic solutions and observations. In: *Philosophical Magazine* 42, pp. 362–377 (cit. on pp. 36, 37).
- KINSMAN, B. (1965). Wind Waves. their generation and propagation on the ocean surface. Prentice-Hall (cit. on p. 37).
- KORTEWEG, D.J. and DE VRIES, G. (1895). XLI. On the change of form of long waves advancing in a rectangular canal, and on a new type of long stationary waves. In: *The London, Edinburgh, and Dublin Philosophical Magazine and Journal of Science* 39.240, pp. 422–443 (cit. on pp. 5, 140).
- Krah, P., Yin, X.-Y., Bergmann, J., Nave, J.-C., and Schneider, K. (2024). A Characteristic Mapping Method for Vlasov-Poisson with Extreme Resolution Properties. In: *Communications in Computational Physics* 35.4, pp. 905–937 (cit. on p. 105).
- Kuksin, S.B. (2000). Analysis of Hamiltonian PDEs. Oxford University Press (cit. on pp. 8, 18).
- LADYŽENSKAYA, O.A. (1958). Solution in the large to the boundary-value problem for the Navier–Stokes equations in two space variables. In: *Soviet Physics Dokl.* 123.3. [originally in Russian], pp. 1128–1131 (cit. on p. 16).
- (1969). The mathematical theory of viscous incompressible flow. 2nd ed. Vol. 2. Mathematics and its Applications. New York/London/Paris: Gordon and Breach (cit. on p. 97).
- LAGERSTROM, P.A. (1975). Solutions of the Navier-Stokes Equation at Large Reynolds Number. In: SIAM J. Appl. Math. 28.1, pp. 202–214 (cit. on p. 141).
- LAGRANGE, J. L. (1781). Mémoire sur la théorie du mouvement des fluides. In: Nouveaux Mémoires de l'Académie royale des Sciences et Belles-Lettres de Berlin (cit. on p. 31).
- LAMB, H. (1932). Hydrodynamics. 6th ed. Dover Publications (cit. on pp. 9, 30, 37, 109, 110, 137, 143).
- LANDAU, L. D. and LIFSHITZ, E. M. (1987). Fluid Mechanics. 2nd ed. Vol. 6. Course of Theoretical Physics. Pergamon (cit. on pp. 21, 30, 142).
- LANNES, D. (2005). Well-Posedness of the Water Waves Equations. In: *J. Amer. Math. Soc.* 18.3, pp. 605–654 (cit. on pp. 5, 19, 48, 80, 158).
- (2013a). A Stability Criterion for Two-Fluid Interfaces and Applications. In: Arch. Rational Mech. Anal. 208, pp. 481–567 (cit. on p. 20).
- (2013b). The Water Waves Problem: Mathematical Analysis and Asymptotics. Vol. 188. Mathematical Surveys and Monographs. American Mathematical Society (cit. on pp. 5, 6, 19, 20, 39, 48–51, 80, 82, 140, 158, 160).
- (2020). Modeling Shallow Water Waves. In: Nonlinearity 33, R1–R57 (cit. on pp. 6, 140).
- LANNES, D. and MING, M. (2015). The Kelvin-Helmholtz Instabilities in Two-Fluids Shallow Water Models. In: *Hamiltonian Partial Differential Equations and Applications*. Ed. by GUYENNE, P., NICHOLLS, D., and SULEM, C. Vol. 75. *Fields Institute Communications*. Springer (cit. on p. 20).
- (2024). Well posedness of F. John's floating body problem for a fixed object. arXiv: 2407.18082 [math.AP] (cit. on p. 20).
- LAPLACE, P. S. (1798 (an VII)). Traité de mécanique céleste. Tome II. Livre III. Paris: De L'Imprimerie de Crapelet. Chap. 2 (cit. on p. 45).
- LAX, P. D. and MILGRAM, A. N. (1955). Parabolic Equations. In: Contributions to the Theory of Partial Differential Equations. Ed. by Bers, L., Trust, S., and John, F. Vol. 33. Annals of Mathematics Studies. Princeton University Press. Chap. IX, pp. 167–190 (cit. on p. 48).
- LE DRET, H. (2018). Nonlinear Elliptic Partial Differential Equations. An Introduction. Springer Cham (cit. on p. 93).

- LEE, J.M. (1997). Riemannian Manifolds. An Introduction to Curvature. 1st ed. Vol. 176. Graduate Texts in Mathematics. Springer New York (cit. on p. 161).
- (2013). Introduction to Smooth Manifolds. 2nd ed. Vol. 218. Graduate Texts in Mathematics. Springer New York (cit. on p. 161).
- LERAY, J. (1934a). Essai sur le mouvement d'un liquide visqueux emplissant l'espace. In: J. Maths. Pures et Appliquées 13, pp. 331–418 (cit. on p. 16).
- (1934b). Sur le mouvement d'un liquide visqueux emplissant l'espace. In: *Acta Math.* 63, pp. 193–248 (cit. on p. 16).
- Leweke, T., Le Dizès, S., and Williamson, C.H.K. (2016). Dynamics and Instabilities of Vortex Pairs. In: *Annu. Rev. Fluid Mech.* 48, pp. 507–541 (cit. on p. 146).
- LI, Y.A. (2006). A Shallow-Water Approximation to the Full Water Wave Problem. In: Comm. Pure Appl. Math. LIX, pp. 1225–1285 (cit. on p. 140).
- LIN, M.Y. and HUANG, L.H. (2009). Study of water waves with submerged obstacles using a vortex method with Helmholtz decomposition. In: *Inter. J. Num. Meth. Fluids* **60**, pp. 119–148 (cit. on p. 148).
- (2010). Vortex shedding from a submerged rectangular obstacle attacked by a solitary wave. In: *J. Fluid Mech.* 651, pp. 503–518 (cit. on p. 148).
- LINDBLAD, H. (2005). Well-posedness for the motion of an incompressible liquid with free surface boundary. In: *Annals of Maths.* 162, pp. 109–194 (cit. on pp. 5, 18).
- LIONS, J.-L. and MAGENES, E. (1968). Problèmes aux limites non homogènes et applications. Vol. 1. Dunod (cit. on p. 50).
- LIONS, J.-L. and PRODI, G. (1959). Un théorème d'existence et unicité dans les équations de Navier-Stokes en dimension 2. In: C. R. Acad. Sci. Paris 248, pp. 3519–3521 (cit. on p. 16).
- Liu, A.-K. and Davie, S. H. (1977). Viscous attenuation of mean drift in water waves. In: *Journal of Fluid Mechanics* 81, pp. 63–84 (cit. on pp. 128, 137).
- Longuet-Higgins, M.S. (1953). Mass Transport in Water Waves. In: *Phil. Trans. R. Soc. London A*, *Math. Phys. Sci.* 245.903, pp. 535–581 (cit. on pp. 134, 135, 139).
- (1978). The instabilities of gravity waves of finite amplitude in deep water I. Superharmonics. In: *Proc. R. Soc. Lond. A* 360, pp. 471–488 (cit. on pp. 2, 23).
- (1980a). A technique for time-dependant free-surface flows. In: *Proc. R. Soc. Lond. A* 371, pp. 353–378 (cit. on p. 24).
- (1980b). On the forming of sharp corners at a free surface. In: *Proc. R. Soc. Lond. A* 371, pp. 441–451 (cit. on p. 24).
- (1982). Parametric solutions for breaking waves. In: J. Fluid Mech. 121, pp. 403–424 (cit. on p. 24).
- (1992). Capillary rollers and bores. In: J. Fluid Mech. 240, pp. 659–679 (cit. on pp. 2, 128).
- LONGUET-HIGGINS, M.S. and COKELET, E.D. (1976). The deformation of steep surface waves on water, I. A numerical method of computation. In: *Proc. R. Soc. Lond. A* 350, pp. 1–26 (cit. on pp. 2, 23, 89).
- (1978). The deformation of steep surface waves on water, II. Growth of normal-mode instabilities. In: *Proc. R. Soc. Lond. A* 364, pp. 1–28 (cit. on pp. 2, 23, 89).
- Lubin, P. and Glockner, S. (2015). Numerical simulations of three-dimensional plunging breaking waves: generation and evolution of aerated vortex filaments. In: *Journal of Fluid Mechanics* 767, pp. 364–393 (cit. on pp. 2, 24, 90).
- Lubin, P., Kimmoun, O., Véron, F., and Glockner, S. (2019). Discussion on instabilities in breaking waves: Vortices, air-entrainment and droplet generation. In: *Eur. J. Mech.* 73, pp. 144–156 (cit. on p. 24).
- LUKE, J.C. (1967). A variational principle for a fluid with a free surface. In: J. Fluid Mech. 27.2, pp. 395–397 (cit. on p. 157).
- LUNDGREN, T.S. (1989). A Free Surface Vortex Method with Weak Viscous effects. In: *Mathematical Aspects of Vortex Dynamics*. Ed. by Caflisch, R.E. Philadelphia: SIAM (cit. on p. 128).
- LUNDGREN, T.S. and KOUMOUTSAKOS, P. (1999). On the generation of vorticity at a free surface. In: *J. Fluid Mech.* 382, pp. 351–366 (cit. on pp. 2, 128, 129, 133, 134).
- Majda, A.J. and Bertozzi, A.L. (2002). Vorticity and Incompressible Flow. Cambridge University Press (cit. on p. 18).
- MARUSIC, I. and BROOMHALL, S. (2021). Leonardo da Vinci and Fluid Mechanics. In: Annual Review of Fluid Mechanics 53, pp. 1–25 (cit. on p. 31).

- MASMOUDI, N. (2007). Chapter 3 Examples of Singular Limits in Hydrodynamics. In: ed. by DAFERMOS, C.M. and FEIREISL, E. Vol. 3. *Handbook of Differential Equations: Evolutionary Equations*. North-Holland, pp. 195–275 (cit. on p. 141).
- MASMOUDI, N. and ROUSSET, F. (2012). Uniform Regularity for the Navier-Stokes Equation with Navier Boundary Condition. In: Arch. Rational Mech. Anal. 203, pp. 529–575 (cit. on pp. 4, 21, 141).
- (2017). Uniform Regularity and Vanishing Viscosity Limit for the Free Surface Navier–Stokes Equations. In: Arch Rational Mech Anal 223, pp. 301–417 (cit. on pp. 4, 5, 17, 20, 132, 141).
- MASSEY, B.S. and CLAYTON, B.R. (1965). Laminar Boundary Layers and Their Separation From Curved Surfaces. In: *Journal of Basic Engineering* 87.2, pp. 483–493 (cit. on pp. 135, 152).
- MATHEW, T.P.A. (2008). Domain Decomposition Methods for the Numerical Solution of Partial Differential Equations. Vol. 61. Lecture Notes in Computational Science and Engineering. Springer Berlin, Heidelberg (cit. on p. 108).
- MCALLISTER, M.L., DRAYCOTT, S., CALVERT, R., DAVEY, T., DIAS, F., and VAN DEN BREMER, T.S. (2024). Three-dimensional wave breaking. In: *Nature* 633, pp. 601–615 (cit. on p. 22).
- McLean, J.W. (1982). Instabilities of finite-amplitude water waves. In: J. Fluid Mech. 114, pp. 315–330 (cit. on p. 23).
- McLean, J.W., Ma, Y.C., Martin, D.U., Saffman, P.G., and Yuen, H.C. (1981). Three-Dimensional Instability of Finite-Amplitude Water Waves. In: *Phys. Rev. Letters* 46.13 (cit. on p. 23).
- MEIRON, D.I., BAKER, G.R., and ORSZAG, S.A. (1982). Analytic structure of vortex sheet dynamics. Part 1. Kelvin-Helmholtz instability. In: *J. Fluid Mech.* 114, pp. 283–298 (cit. on p. 146).
- MÉTIVIER, G. (2008). Para-differential Calculus and Applications to the Cauchy Problem for Nonlinear Systems. Lecture Notes. Università di Pisa, 2007. URL: https://cel.hal.science/cel-00287554 (cit. on p. 140).
- MING, M. and WANG, C. (2021). Water-Waves Problem with Surface Tension in a Corner Domain II: The Local Well-Posedness. In: *Comm. Pure Appl. Math.* 74, pp. 225–285 (cit. on p. 20).
- MING, M. and ZHANG, Z. (2009). Well-posedness of the water-wave problem with surface tension. In: *J. Math. Pures Appl.* 92, pp. 429–455 (cit. on p. 19).
- MISNER, C.W., THORNE, K.S., and WHEELER, J.A. (2017). *Gravitation*. 2nd ed. Princeton University Press (cit. on p. 165).
- MOFFATT, H.K. and KIMURA, Y. (2024). Spiral wind-up of vortex sheets. In: *Geophys. Astro. Fluid Dyn.*, pp. 1–14 (cit. on p. 147).
- Monaghan, J.J. (1994). Simulating Free Surface Flows with SPH. In: J. Comp. Phys. 110, pp. 399–406 (cit. on p. 23).
- MOORE, D.W. and SAFFMAN, P.G. (1975). The Instability of a Straight Vortex Filament in a Strain Field. In: *Proc. R. Soc. London A* 346.1646, pp. 413–425 (cit. on p. 146).
- Moser, J. (1966). A rapidly convergent iteration method and non linear differential equations. In: *Ann. Scuola Norm. Sup. Pisa* 20, pp. 499–535 (cit. on p. 20).
- MOSTERT, W., POPINET, S., and DEIKE, L. (2022). High-resolution direct simulation of deep water breaking waves: transition to turbulence, bubbles and droplets production. In: *J. Fluid Mech.* 942, A27 (cit. on pp. 2, 24, 37, 90, 123).
- Nalimov, V.I. (1974). The Cauchy-Poisson problem. In: *Dynamika Splosh. Sredy* 18, pp. 605–654 (cit. on p. 19).
- NASH, J. (1956). The imbedding problem for Riemannian manifolds. In: *Annals of Mathematics* 63, pp. 20–63 (cit. on p. 20).
- NATAF, F. and TOURNIER, P.-H. (2023). A GenEO Domain Decomposition method for Saddle Point problems. In: *Comptes Rendus. Mécanique* 351, pp. 1–18 (cit. on p. 107).
- NAVIER, C. L. M. H. (1821). Sur les Lois des mouvements des fluides, en ayant égard à l'adhésion des molécules. In: *Annales de Chimie et de Physique* 19, pp. 244–260 (cit. on pp. 16, 29, 33, 60).
- NEW, A. L. (1983). A class of elliptical free-surface flows. In: *Journal of Fluid Mechanics* 130, pp. 219–239 (cit. on p. 24).
- New, A.L., McIver, P., and Peregrine, D.H. (1985). Computations of overturning waves. In: *J. Fluid Mech.* 150, pp. 233–251 (cit. on p. 23).
- NGUYEN VAN YEN, N., FARGE, M., and SCHNEIDER, K. (2011). Energy Dissipating Structures Produced by Walls in Two-Dimensional Flows at Vanishing Viscosity. In: *Phys. Rev. Letters* 106.184502 (cit. on p. 21).

- NGUYEN VAN YEN, N., WAIDMANN, M., KLEIN, R., FARGE, M., and SCHNEIDER, K. (2018). Energy dissipation caused by boundary layer instability at vanishing viscosity. In: *J. Fluid Mech.* 849, pp. 676–717 (cit. on p. 21).
- NICHOLS, B.D. and HIRT, C.W. (1975). Methods for Calculating Multi-Dimensional, Transient Free Surface Flows Past Bodies. In: *Proc. Of the First International Conference on Numerical Ship Hydrodynamics, Gaithersburg, Maryland* (cit. on p. 24).
- NISHIDA, T. and TERAMOTO, Y. (2004). Global in time behavior of viscous surface waves: horizontally periodic motion. In: J. Math. Kyoto Univ. 44.2, pp. 271–323 (cit. on pp. 4, 17).
- Noh, W.F. (1963). CEL: A time-dependant, two-space dimensional, coupled Eulerian-Lagrangian code. In: *Methods in Computational Physics*. Ed. by Alder, B., Fernbach, S., and Rotenberg, M. Vol. 3. New York: Academic Press, pp. 117–179 (cit. on p. 100).
- OLEINIK, O.A. (1966). On the mathematical theory of boundary layer for an unsteady flow of incompressible fluid. In: *J. Appl. Math. Mech.* 30.5, pp. 951–974 (cit. on pp. 21, 154).
- OLVER, P.J. (1980). On the Hamiltonian structure of evolution equations. In: *Math. Proc. Cambridge Phil. Soc.* 88, pp. 71–88 (cit. on pp. 8, 77, 80, 157).
- OSHER, S. and SETHIAN, J.A. (1988). Fronts Propagating with Curvature Dependent Speed: Algorithms based on Hamilton-Jacobi Formulations. In: *J. Comp. Phys.* 79, pp. 12–49 (cit. on p. 24).
- PEREGRINE, D.H. (1983). Breaking Waves on Beaches. In: Ann. Rev. Fluid Mech. 15, pp. 149–178 (cit. on p. 23).
- PIRONNEAU, O. (1989). Finite Element Methods for Fluids. John Wiley & sons (cit. on pp. 90, 111).
- Poincaré, H. (1886). Sur les résidus des intégrales doubles. In: C.R. hebdo. Acad. Sc. 102, pp. 202–204 (cit. on p. 45).
- (1887). Sur les résidus des intégrales doubles. In: Acta Math. 9, pp. 321–380 (cit. on p. 45).
- POMEAU, P., LE BERRE, M., GUYENNE, P., and GRILLI, S. (2008). Wave-breaking and generic singularities of nonlinear hyperbolic equations. In: *Nonlinearity* 21.5, T61–T79 (cit. on p. 23).
- POMEAU, Y. and LE BERRE, M. (2012). Topics in the theory of wave-breaking. In: *Panoramas & Synthèses* 38, pp. 125–162 (cit. on pp. 24, 126).
- POPINET, S. (2003). Gerris: a tree-based adaptative solver for the incompressible Euler equations in complex geometries. In: *J. Comp. Phys.* 190, pp. 572–600 (cit. on p. 24).
- (2009). An accurate adaptative solver for surface-tension-driven interfacial flows. In: *J. Comp. Phys.* 228, pp. 5838–5866 (cit. on p. 24).
- PRANDTL, L. (1904). Über Flüssigkeitsbewegung bei sehr kleiner Reibung. In: Verhandlungen des III. Internationalen Mathematiker-Kongresses Heidelberg 1904, pp. 484–491 (cit. on pp. 21, 152, 154).
- QUARTERONI, A. and Valli, A. (1994). Numerical Approximation of Partial Differential Equations. Springer Series in Computational Mathematics. Springer Berlin, Heidelberg (cit. on p. 96).
- REYNOLDS, O. (1903). Papers on mechanical and physical subjects. Vol. 3: The sub-mechanics of the universe. Cambridge University Press (cit. on p. 30).
- RICHARD, G.L., DURAN, A., and FABRÈGES, B. (2019). A new model of shoaling and breaking waves. Part 2. Run-up and two-dimensional waves. In: *J. Fluid Mech.* 897, pp. 146–194 (cit. on p. 156).
- RIESZ, F. (1909). Sur les opérations fonctionnelles linéaires. In: Comptes rendus de l'Académie des Sciences 149, pp. 974–977 (cit. on p. 49).
- RIQUIER, A. and DORMY, E. (2024a). Irrotationality of Water Waves and Topography. Submitted. arXiv: 2411.09291 [physics.flu-dyn] (cit. on pp. 89, 139, 144).
- (2024b). Numerical study of a viscous breaking water wave and the limit of vanishing viscosity. In: *Journal of Fluid Mechanics* 984, R5 (cit. on pp. 10, 89, 91, 105, 117, 122, 123, 126).
- Ruban, A.I. (2018). Fluid Dynamics. Part 3: Boundary Layers. Oxford University Press (cit. on pp. 21, 141, 149, 152).
- SAAD, Y. and SCHULTZ, M.H. (1986). GMRES: A Generalized Minimal Residual Algorithm for Solving Nonsymmetric Linear Systems. In: SIAM Journal on Scientific and Statistical Computing 7.3, pp. 856–869 (cit. on p. 107).
- Salmon, R. (1988). Hamiltonian Fluid Mechanics. In: Ann. Rev. Fluid Mech. 20, pp. 225–256 (cit. on p. 62).
- (2020). More Lectures on Geophysical Fluid Dynamics. Avalaible online. URL: https://pordlabs.ucsd.edu/rsalmon/More.Lectures.pdf (cit. on p. 62).

- SAMMARTINO, M. and CAFLISCH, R.E. (1998a). Zero Viscosity Limit for Analytic Solutions, of the Navier-Stokes Equation on a Half-Space. I. Existence for Euler and Prandtl Equations. In: *Comm. Math. Phys.* 192, pp. 433–461 (cit. on pp. 21, 154).
- (1998b). Zero Viscosity Limit for Analytic Solutions, of the Navier-Stokes Equation on a Half-Space. II. Construction of the Navier-Stokes Solution. In: *Comm. Math. Phys.* 192, pp. 463–491 (cit. on pp. 21, 22).
- SARIC, W.S. (1994). Görtler Vortices. In: Annual Rev. Fluid Mech. 26, pp. 379–409 (cit. on pp. 152, 155). SCHLICHTING, H. and GERSTEN, K. (2017). Boundary-Layer Theory. With contributions from Egon Krause and Herbert Oertel Jr. 9th ed. Springer-Verlag Berlin Heidelberg (cit. on pp. 21, 141, 146, 148).
- SCHNEIDER, G. (1998). Approximation of the Korteweg-de Vries Equation by the Nonlinear Schrödinger Equation. In: *J. Diff. Eqs.* 147, pp. 333–354 (cit. on p. 140).
- Schrödinger, E. (1926). Quantisierung als Eigenwertproblem. In: Annalen der Physik 4.79, pp. 361–376 (cit. on p. 140).
- Schur, I. (1917). Über Potenzreihen die im Inneren des Einheitskreises beschränkt sind. In: *J. reine u. angewandte Mathematik* 147, pp. 205–232 (cit. on p. 99).
- Schwarz, H. A. (1870). Gesammelte mathematische abhandlungen. In: Vierteljahrsschrift der naturforschenden gesselschaft in Zürich 15, pp. 272–286 (cit. on p. 107).
- SEENATH, A. (2025). Fundamental limitations of shoreline models. In: Nature Water (cit. on p. 1).
- SERRE, F. (1953). Contribution à l'étude des écoulements permanents et variables dans les canaux. In: La Houille Blanche 39.3, pp. 374–388 (cit. on pp. 5, 111, 140).
- SETHIAN, J.A. (1999). Level set methods and fast marching methods. 2nd ed. Cambridge University Press (cit. on p. 24).
- Shuto, N. (1974). Nonlinear Long Waves in a Channel of Variable Section. In: Coastal Engineering in Japan 17.1, pp. 1–12 (cit. on p. 140).
- SOLONNIKOV, V.A. (1977). Solvability of the problem of the motion of a viscous incompressible fluid bounded by a free surface. In: *Izv. Akad. Nauk SSSR Ser. Math.* 41. [originally in russian, later translated in english in *Math. USSR Izv.* 11, pp. 1323–1358], pp. 1388–1424 (cit. on p. 17).
- Squire, H.B. (1933). On the Stability for Three-Dimensional Disturbances of Viscous Fluid Flow between Parallel Walls. In: *Proc. R. Soc. Lond. A* 142.847, pp. 621–628 (cit. on p. 152).
- STEWARTSON, K. (1958). On Goldstein's Theory of Laminar Separation. In: Q. J. Mech. Appl. Math. 11.4, pp. 399–410 (cit. on p. 21).
- (1974). Multistructured boundary layers on flat plates and related bodies. In: Adv. Appl. Mech. 14, pp. 145–239 (cit. on p. 21).
- STOKES, G.G. (1845). On the Theories of the Internal Friction of Fluids in Motion, and of the Equilibrium and Motion of Elastic Solids. In: *Trans. Cambridge Philos. Soc.* 8, pp. 287–319 (cit. on pp. 16, 29, 33, 60).
- (1847). On the theory of oscillatory waves. In: *Transactions of the Cambridge Philosophical Society* 8, pp. 441–455 (cit. on pp. 22, 67, 109).
- (1850). On the Effect of the Internal Friction of Fluids on the Motion of Pendulums. In: *Transactions of the Cambridge Philosophical Society* 9 (cit. on pp. 128, 142).
- (1880). Supplement to a paper on the theory of oscillatory waves. In: *Mathematical and Physical Papers, Volume 1.* Cambridge University Press, pp. 314–326 (cit. on pp. 67, 109).
- SULEM, C., SULEM, P.-L., BARDOS, C., and FRISCH, U. (1981). Finite Time Analyticity for the Two and Three Dimensional Kelvin-Helmholtz Instability. In: *Commun. Math. Phys.* 80, pp. 485–516 (cit. on p. 146).
- SWANN, S.H.G. (1971). The Convergence with Vanishing Viscosity of Nonstationary Navier-Stokes flow to Ideal Flow in  $\mathbb{R}^3$ . In: *Trans. Amer. Math. Soc.* 157, pp. 373–397 (cit. on pp. 20, 140).
- Sychev, V.V., Ruban, A.I., Sychev, V.V., and Korolev, G.L. (1998). Asymptotic Theory of Separated Flows. Cambridge University Press (cit. on pp. 13, 21, 141).
- TANAKA, M. (1983). The stability of steep gravity waves. In: J. Phys. Soc. Japan 156.9, pp. 3047–3055 (cit. on pp. 2, 23).
- (1985). The stability of steep gravity waves. Part 2. In: J. Fluid Mech. 156, pp. 281–289 (cit. on pp. 2, 23).
- TANAKA, M., DOLD, J.W., LEWY, M., and PEREGRINE, D.H. (1987). Instability and breaking of a solitary wave. In: J. Fluid Mech. 185, pp. 235–248 (cit. on pp. 2, 23).

- TAYLOR, G. (1950). The instability of liquid surfaces when accelerated in a direction perpendicular to their planes. In: *Proc. Roy. soc. London Ser. A* 201, pp. 192–196 (cit. on p. 19).
- Taylor, M.E. (2011). Partial Differential Equations III. Nonlinear Equations. Vol. 117. Applied Mathematical Sciences. Springer New York (cit. on p. 140).
- TEMAM, R. (1984). Navier-Stokes Equations: Theory and Numerical Analysis. AMS Chelsea Publishing (cit. on pp. 17, 92, 109).
- Tu, L.W. (2011). An Introduction to Manifolds. 2nd ed. Universitext. Springer New York (cit. on p. 161). Vinje, T. and Brevig, P. (1981). Numerical simulation of breaking waves. In: Adv. Water Resources 4, pp. 77–82 (cit. on pp. 2, 23).
- VON KÁRMÁN, T. (1911). Ueber den Mechanismus des Widerstandes, den ein bewegter Körper in einer Flüssigkeit erfährt. In: Nachrichten von der Gesellschaft der Wissenschaften zu Göttingen, Mathematisch-Physikalische Klasse, pp. 509–517 (cit. on pp. 21, 149).
- VORONOÏ, G. (1908). Nouvelles applications des paramètres continus à la théorie des formes quadratiques. Premier mémoire. Sur quelques propriétés des formes quadratiques positives parfaites. In: *Journal für die Reine und Angewandte Mathematik* 1908.133 (cit. on p. 93).
- WHITHAM, G.B. (1967). Variational methods and applications to water waves. In: *Proc. R. Soc. London A* 299.1456, pp. 6–25 (cit. on p. 140).
- WIDMANN, A. and TROPEA, C. (2015). Parameters influencing vortex growth and detachment on unsteady aerodynamic profiles. In: *J. Fluid Mech.* 773, pp. 432–459 (cit. on pp. 21, 146).
- WIEGEL, R.L. (1964). Oceanographical engineering. Prentice-Hall (cit. on pp. 8, 22, 82, 83).
- Wolibner, W. (1933). Un théorème sur l'existence du mouvement plan d'un fluide parfait, homogène, incompressible, pendant un temps infiniment long. In: *Mathematische Zeitschrift* 37, pp. 698–726 (cit. on p. 18).
- Wu, S. (1997). Well-posedness in Sobolev spaces of the full water wave problem in 2-D. In: *Invent. Math.* 130.1, pp. 39–72 (cit. on p. 19).
- (1999). Well-posedness in Sobolev spaces of the full water wave problem in 3-D. In: *J. Amer. Math. Soc.* 12.2, pp. 445–495 (cit. on p. 19).
- (2009). Almost global wellposedness of the 2-D full water wave problem. In: *Invent. Math.* 177, pp. 45–135 (cit. on p. 19).
- (2010). Global wellposedness of the 3-D full water wave problem. In: *Invent. Math.* 184, pp. 125–220 (cit. on p. 19).
- (2019). Wellposedness of the 2D full water wave equation in a regime that allows for non- $C^1$  interfaces. In: *Invent. Math.* 217, pp. 241–375 (cit. on p. 19).
- Xu, J. and Zikatanov, L. (2017). Algebraic multigrid methods. In: *Acta Numerica* 26, pp. 591–721 (cit. on p. 108).
- YAKUBOVICH, E.I. and ZENKOVICH, D.A. (2001). Matrix approach to Lagrangian fluid dynamics. In: *J. Fluid Mech.* 443, pp. 167–196 (cit. on p. 63).
- Yih, C.-S. (1968). Instability of unsteady flows or configurations. Part 1. Instability of a horizontal liquid layer on an oscillating plane. In: *J. Fluid Mech.* 31, pp. 737–751 (cit. on p. 142).
- YIN, X.-Y., MERCIER, O., YADAV, B., SCHNEIDER, K., and NAVE, J.-C. (2021). A Characteristic Mapping method for the two-dimensional incompressible Euler equations. In: *Journal of Computational Physics* 424, p. 109781 (cit. on p. 105).
- YIN, X.-Y., SCHNEIDER, K., and NAVE, J.-C. (2023). A Characteristic Mapping Method for the three-dimensional incompressible Euler equations. In: *Journal of Computational Physics* 477, p. 111876 (cit. on p. 105).
- Yosihara, H. (1982). Gravity Waves on the Free Surface of an Incompressible Perfect Fluid of Finite Depth. In: *Publ. RIMS, Kyoto Univ.* 18, pp. 49–96 (cit. on p. 19).
- Yudovich (1963). Non-stationary flows of an ideal incompressible fluid. In: Z. Vy cisl. Mat. i Mat. Fiz. 3.6, pp. 1032–1066 (cit. on p. 18).
- ZAKHAROV, V. E. (1968). Stability of periodic waves of finite amplitude on the surface of a deep fluid. In: *Journal of Applied Mechanics and Technical Physics* 9, pp. 190–194 (cit. on pp. 2, 5, 18, 46, 47, 51, 60, 68, 139).
- ZHANG, P. and ZHANG, Z. (2008). On the Free Boundary Problem of Three-Dimensional Incompressible Euler Equations. In: *Comm. Pure Appl. math.* 61.7, pp. 877–940 (cit. on pp. 5, 18).

#### **ABSTRACT**

The first part of this thesis will be devoted to the motivation of a set of equations that describes overhanging waves in the inviscid irrotational regime, with either a one-dimensional or a two-dimensional free surface. This is done by setting aside the commonly used Eulerian framework and working in Lagrangian coordinates instead. This should be seen as an extension of the Zakharov-Craig-Sulem formulation of the Water Waves problem. The non-canonical Hamiltonian structure of these partial differential equations is investigated and it is shown that in the absence of breaking, they can be reduced to the usual set of equations. Emphasis is put on the various physical assumptions that are made along the way. In a second moment, we come back to these very hypotheses and put them to the test. This is done numerically using a Navier-Stokes based computational framework based on the Finite-Element Method (FEM). The major novelty compared to other studies lies in the use of the Arbitrary Lagrangian-Eulerian method (ALE), which diminishes the interpolation error greatly. The viscosity can therefore be decreased to values that allow the comparison with the inviscid solution (computed using another wode, based on potential theory in the complex plane) to be carried out.

Over a flat topography, it is found that both the free-surface and bed boundary layers are sufficiently well-behaved as to not perturb the bulk irrotational flow. Water being characterised by a relatively small viscosity, the consequence is that, in this regime the inviscid models accurately describe the oceanic flow. We do not prove this assertion rigorously, however. Difficulties seem to arise, however, when a non-flat topography is considered. Indeed, the typical velocities associated with the wave are high enough to eventually trigger boundary layer separation near curved-enough portions of the bed, resulting in vorticity being shed in the initially irrotational flow, far from the topography. The convergence to the inviscid solution is therefore compromised.

#### **KEYWORDS**

Water Waves, Wave Breaking, Finite element Method, Mathematical Modelling

#### RÉSUMÉ

Dans un premier temps, nous allons introduire un ensemble d'équations à dérivées partielles qui décrivent l'évolution de la surface libre de l'océan, l'eau étant considérée comme non-visqueuse, le tourbillon étant supposé évanescent et l'air étant complètement négligé. Ces équations, que nous nous proposons d'appeler équations des vagues déferlantes, sont obtenues formellement à partir de principes physiques généraux (description continue de la matière, densité homogène et uniforme de l'eau, etc.). La structure hamiltonienne non-canonique de ce système sera par la suite explicitée. Nous montrerons aussi que, en l'absence de déferlement, elles se réduisent à une formulation bien-connue du problème, dite de Zakharov, Craig et Sulem.

Pour arriver à ce système d'équations, deux hypothèses importantes doivent être réalisées : négliger la viscosité et supposer un tourbillon nul. La seconde partie de ce travail consistera en une discussion de ces dernières. Pour cela, nous adopterons une approche numérique permettant d'approximer la solution des équations de Navier--Stokes à surface libre. Le schéma mis au point diffère de ceux qu'il est coutume d'utiliser pour ce problème. En effet il met en œuvre la méthode Lagrangien--Eulerien Arbitraire (ALE) pour l'advection et la discrétisation est réalisée par la Méthode des Éléments Finis (FEM).

Ce schéma numérique sera d'abord utilisé pour étudier la couche limite apparaissant sous l'interface eau--vide, lorsque le fond de l'eau est plat. Il nous sera alors possible de conclure que le tourbillon ainsi généré n'empêche nullement la solution de faible viscosité de converger vers la solution irrotationnelle de l'équation d'Euler, étant donné que son support devient arbitrairement petit.

Par contre, l'étude de topographies non-plate mettra en lumière un phénomène physique absent du système limite : le décollement de la couche limite présente au fond de l'eau. En effet, il peut arriver que l'écoulement irrotationnel associé au passage d'un train d'onde d'amplitude finie ait une vélocité suffisamment importante pour venir arracher des tourbillons des régions de forte courbure et les transporter jusqu'à proximité immédiate de la surface. Ce phénomène ne semble pas disparaître dans la limite de viscosité évanescente et contrecarre, de ce fait, la convergence vers la solution irrotationnelle.

## **MOTS CLÉS**

Vagues océaniques, Déferlement, Éléments finis, Modélisation mathématique

